

The  
**Flow Stability of Shear Layers**  
in a  
**Differentially Rotating Container**

by

**Tony Dai Vo**



---

---

A Thesis submitted to Monash University  
for the degree of  
*Doctor of Philosophy*

---

---

April 2014

Department of Mechanical and Aerospace Engineering  
Monash University



*For Sally.*



# Statement of originality

This thesis contains no material that has been accepted for the award of a degree or diploma in this or any other university. To the best of the candidate's knowledge and belief, this thesis contains no material previously published or written by another person except where due reference is made in the text of this thesis.

---

Tony D. Vo

April 2014



# Copyright notices

## Notice 1

Under the Copyright Act 1968, this thesis must be used only under the normal conditions of scholarly fair dealing. In particular no results or conclusions should be extracted from it, nor should it be copied or closely paraphrased in whole or in part without the written consent of the author. Proper written acknowledgement should be made for any assistance obtained from this thesis.

## Notice 2

I certify that I have made all reasonable efforts to secure copyright permissions for third-party content included in this thesis and have not knowingly added copyright content to my work without the owner's permission.



*“It is not the process of linearization that limits insight. It is the nature of the state we choose to linearize about.”*

Eric Eady.



*Still a stranger to stability.*



# Abstract

A numerical study of flows in a differentially rotating container is presented. The container is comprised of a cylindrical rotating tank coupled with differentially rotating disks placed flush with the top and bottom horizontal boundaries of the tank. The tank and the disk share the same axis of rotation. The differential speed imposed by the disks produce shear layers that are susceptible to instabilities. Flow transitions in the axisymmetric flow including steady, unsteady and time-periodic states are investigated. In addition, non-axisymmetric flows are examined via quasi-two-dimensional and three-dimensional models.

The flow conditions in this configuration are characterised primarily by the Rossby and Ekman numbers, which are non-dimensional parameters. The Rossby number,  $Ro$ , describes the balance between inertial to Coriolis forces, while the Ekman number,  $E$ , describes the balance between viscous to Coriolis forces. A third non-dimensional parameter, the Reynolds number, which is the ratio of inertial to viscous forces, is also used to characterise the onset of several critical flow transitions. The aspect ratio of the tank, defined by the ratio of the disk radius to the tank height, is explored between  $1/6 \leq A \leq 2$ . Additionally, Rossby numbers between  $-4 \leq Ro \leq 0.6$  and Ekman numbers ranging between  $5 \times 10^{-5} \leq E \leq 3 \times 10^{-3}$  are primarily investigated.

A spectral-element method is employed to compute axisymmetric flows on a semi-meridional mesh. The numerous meshes used throughout the study are validated through grid resolution studies under computationally demanding flow conditions. Achieving grid independence for such flow conditions ensures that the flow solutions obtained for a wide range of  $Ro$  and  $E$  are accurate.

The axisymmetric base flow is obtained for a range of  $Ro$  and  $E$ , and in various aspect ratio containers. The vertical structure of the flow reveals that small- $|Ro|$  flows demonstrate strong axial independence in accordance with the Taylor–Proudman theorem. This theorem becomes invalid at sufficiently large  $|Ro|$  with distinct depth-dependent features displayed in the positive and negative- $Ro$  regime. The transition from reflectively symmetric flow to symmetry-broken flow is determined and reveals an independence on the aspect ratio. Measurements of the Stewartson layer thickness across the explored parameter space have established trends away from  $Ro \approx 0$  for the first time. Transition to unsteady and time-dependent flow from these steady-state flows has been achieved by either increasing the Rossby number or decreasing the Ek-

man number, both of which serve to increase an internal Reynolds number based on the shear layer thickness and velocity differential.

Interest in the developing non-axisymmetric three-dimensional structures on an underlying axisymmetric base flow motivates an application of a linear stability analysis technique. The eigenmodes extracted from the analysis describe the growth rates and the mode shapes of the wavenumber instability. The differentially rotating flow under investigation exhibits an instability typical of barotropic instability as its primarily linear instability mode, with typical dominant scaled azimuthal wavenumbers ranging between  $1 \leq kA \leq 6$ . The instability deforms the base flow in such a way that a polygonal structure described by the most unstable wavenumber is seen precessing around the centre of the tank. Secondary instability modes are also present, and often display depth-dependent structures with higher azimuthal wavenumbers. Increases to the aspect ratio demonstrates a shift in preference to lower-wavenumber structures and to a more stable flow. Provided that the shear layer in the axisymmetric base flow is not affected by the confining walls, the growth rate data universally collapses when the azimuthal wavenumber is scaled by the aspect ratio.

Non-axisymmetric studies are conducted using a spectral-element-Fourier method. Nonlinear effects are seen to encourage the coalescence of vortices, resulting in the selection of smaller azimuthal wavenumbers with increased forcing. Thus, the resultant wavenumber generally illustrates a larger difference compared to the predicted linear mode when the described flow conditions move further away from the linear instability threshold. The vacillation process typically occurs through unit increments and reversing the forcing yields an increasing wavenumber configuration with observable hysteresis. The transition from axisymmetric to non-axisymmetric flow is determined to be supercritical from the application of a Stuart–Landau model. The simulations reveal the laborious growth of the instabilities in the flow and suggests that under typical experimental parameters, many months may be required for a stable flow state to saturate! Thus, these results may have implications for the experimental results previously reported in the literature.

Computations of a quasi-two-dimensional model are used to compare the qualitative and quantitative results of the axisymmetric and three-dimensional flows. Due to the inability of the quasi-two-dimensional model to capture the vertical structure of the flow, the linear stability analysis expresses the same characteristics between positive and negative- $Ro$  flows. The predicted dominant azimuthal wavenumber demonstrates strong agreement with those obtained by the axisymmetric model. Contrasts between the quasi-two-dimensional model and the three-dimensional model are performed, with the same trends being established from both models such that increasing the forcing conditions produces a lower-wavenumber structure.

# Acknowledgments

The writing of this thesis embodies the conclusion to this PhD, after which I feel deeply indebted to the many people who have encouraged, inspired and supported my studies. It is with much pleasure and thankfulness that I acknowledge the efforts of those who have contributed invaluable to the writing of this thesis.

Firstly, I would like to express my sincere gratitude to my supervisor, Associate Professor Gregory J. Sheard, for all his enlightening guidance, generous support and understanding patience throughout this PhD. In difficult times, he has always been able to offer positivity and provide me the much needed reassurance and encouragement. The immense amount of his personal time dedicated to the continual development of the spectral-element code critical to this thesis is often taken for granted. Thus, I thank and truly appreciate his persistence and enthusiasm. Additionally, his high standards and constant refinements to my research methods have illustrated to a great extent, what scientific research entails. Without these qualities, this thesis would not have advanced to its present state.

I would also like to thank Dr. Luca Montabone, whose expertise in atmospheric physics has provided a fresh prospective to this research. His willingness to share knowledge during the developing stages of my learning led to stimulating discussions that have enhanced my understanding. My thanks also extend to Dr. Ana Aguiar for her aid during the initial stages of this PhD.

This research would not have been possible without the financial support from the Department of Mechanical and Aerospace Engineering, Monash University, for which I am very grateful. Furthermore, the research environment and resources provided have greatly assisted in the accomplishment of this PhD. I would also like to acknowledge the Monash e-Research Centre, the National Computational Infrastructure and the Victorian Life Sciences Computation Initiative for granting access to their high performance computing facilities, which were crucial to this research.

I thank all of the students, academics and colleagues with whom I have shared an office, corridor, or a late night, for sharing their research insights, life and friendship. These moments have made my learning enjoyable and memorable.

Finally, to my parents, Võ Đại Hải and Trịnh Thị Tuyết, I am forever indebted to them for instilling me with the importance of empathy, generosity, kindness, self-discipline and hard work. Without their sacrificial love, unwavering support, and com-

mitment to my growth and learning, I could not have lived so freely. To my brother David, and sister Dana, I thank them for their unrelenting love, support and understanding. My warmest thanks goes to Sally Han, my partner and best friend, for providing me during this time more love, support, and encouragement than I could have ever deserved, or have hoped for. To all of them, I dedicate this thesis.

# Publications relating to thesis

VO, T., MONTABONE, L. & SHEARD, G.J. 2014 Linear stability analysis of a shear layer induced by differential coaxial rotation within a cylindrical enclosure. *Journal of Fluid Mechanics* **738**, 299-334.

VO, T., MONTABONE, L. & SHEARD, G.J. 2012 Linear instabilities on model polar vortices generated in a differential-disk rotation configuration. In *Proceedings of the Ninth International Conference on CFD in the Minerals and Process Industries* (Eds: C.B. Solnordal, P. Liovic, G.W. Delaney and P.J. Witt, Pub: CSIRO, ISBN: 978-922173-01-0), Melbourne Convention and Exhibition Centre, Melbourne, Australia, 10-12 December 2012.

VO, T., MONTABONE, L. & SHEARD, G.J. 2012 Numerical investigation of the stability of model polar vortices in a split-disk system. In *Proceedings of the Eighteenth Australasian Fluid Mechanics Conference* (Eds: P.A. Brandner & B.W. Pearce, Pub: Australasian Fluid Mechanics Society, ISBN: 978-0-646-58373-0 (USB)), Launceston, Tasmania, Australia, 3-7 December 2012, Paper 299.

VO, T., MONTABONE, L. & SHEARD, G.J. 2012 Instabilities on model polar vortices generated in a rotating tank source-sink configuration. In *Australia-New Zealand Rotating Flows Workshop*, Mudbrick Winery, Waiheke Island, Auckland, New Zealand, 9-10 January 2012.

VO, T., SHEARD, G.J. & MONTABONE, L. 2011 Stability of a rotating tank source-sink setup to model a polar vortex. In *Mechanical, Industrial, and Manufacturing Engineering: Selected, peer reviewed paper from 2011 International Conference on Mechanical, Industrial, and Manufacturing Engineering (MIME 2011)* (Eds: M. Ma, Pub: Information Engineering Research Institute, USA, ISBN: 978-0-9831693-1-4, ISSN: 2070-1918), Rydges Hotel, Melbourne, Australia, 15-16 January 2011, 251-254.



# Nomenclature

Symbol	Description
$\S$	Thesis section
$\int$	Integration
$\log_{10}$	Logarithm to the base of 10
$\log_e$	Natural logarithm
$\nabla$	Vector gradient operator (grad)
$\nabla^2$	Del squared (or div grad) operator
$\sum_{i=a}^b$	Sum of arguments with $i$ incrementing from $a$ to $b$
$\infty$	Infinity
$\alpha$	Exponent of the Rossby number used in power-law fitting, Width of the jet
$\alpha_j$	The $j^{\text{th}}$ coefficient used in the third-order backwards multi-step scheme
$\beta$	Exponent of the Ekman number used in power-law fit, Linear topographic parameter
$\beta_j$	The $j^{\text{th}}$ coefficient used in the third-order backwards multi-step scheme
$\Gamma$	Circulation
$\gamma$	Parabolic topographic parameter, Ratio of shear zone radius to characteristic length
$\Delta x$	Change in a given variable $x$
$\delta$	Boundary/shear layer thickness, Small positive constant
$\delta_E$	Ekman layer thickness
$\delta_{Ha}$	Hartmann layer thickness
$\delta_{\text{vel}}$	Shear-layer thickness derived from the relative azimuthal velocity profile

*Continued on the next page.*

*Continued from previous page.*

<b>Symbol</b>	<b>Description</b>
$\delta_{\text{vort}}$	Shear-layer thickness derived from the radial gradient of axial vorticity profile
$\epsilon$	Threshold of the maximum change in velocity between successive time steps
$\varepsilon$	Relative percentage error
$\zeta$	Relative vorticity
$\theta$	Angle of the sloping bottom boundary relative to the horizontal, Azimuthal cylindrical polar coordinate, Latitude
$\theta_0$	Reference latitude
$\lambda$	Wavelength
$\lambda_\theta$	Azimuthal wavelength
$\mu$	Floquet multiplier, Fluid viscosity
$\nu$	Kinematic viscosity
$\xi$	Spatial coordinate
$\rho$	Fluid density, Real and non-negative amplitude
$\rho_{\text{sat}}$	Saturated real and non-negative amplitude
$\sigma$	Aspect ratio of the bottom disk radius to the cylindrical tank radius, Complex growth rate of the azimuthal wavelength disturbance, Electrical conductivity
$\sigma_{\text{peak}}$	Peak growth rate
$\sigma_{\text{pos } Ro}$	Growth rate associated with a positive- $Ro$ flow
$\sigma_{\text{neg } Ro}$	Growth rate associated with a negative- $Ro$ flow
$\sigma_{Ro=0}$	Growth rate associated with a zero-Rossby number flow (solid-body rotation)
$\sigma_R$	Real component of the growth rate
$\tau$	Shear stress Time period of integration
$\Phi$	Rayleigh's discriminant

*Continued on the next page.*

*Continued from previous page.*

<b>Symbol</b>	<b>Description</b>
$\phi$	Phase of a real and non-negative amplitude, Wave amplitude
$\phi^*$	Complex conjugate of the wave amplitude
$\psi$	Streamfunction
$\psi'$	Streamfunction perturbation
$\mathbf{\Omega}$	Anti-symmetric part of the decomposed velocity-gradient tensor
$\Omega$	Planetary rotation rate, Tank rotation rate
$\Omega_1$	Angular velocity of the disk
$\Omega_2$	Angular velocity of the tank
$\Omega_i$	Angular velocity of the inner cylinder
$\Omega_o$	Angular velocity of the outer cylinder
$\overline{\Omega}$	Mean rotation rate
$\omega$	Angular oscillation frequency of the linear mode, Differential rotation, Vorticity
$\omega_{\text{sat}}$	Saturated angular oscillation frequency of the linear mode
$\omega_z$	Axial vorticity
$\omega_{z,0}$	The $z$ -component of the vorticity to zeroth order Rossby number
$\omega_{z,bc}$	The $z$ -component of the vorticity field boundary condition
$\omega_{z,\text{disk}}$	Axial vorticity of the disk
$\omega_{z,\text{tank}}$	Axial vorticity of the tank
$\omega'$	Vorticity of the bottom plate boundary
$\mathcal{A}(\tau)$	Linear time integration operator over time period $\tau$
$A$	Aspect ratio of the disk radius to tank height, Complex amplitude
$a$	Ageostrophic component, Disk radius, Inner cylinder radius
$B$	Vertical magnetic component

*Continued on the next page.*

*Continued from previous page.*

<b>Symbol</b>	<b>Description</b>
$b$	Outer cylinder radius
$c$	Landau constant, Vertical intercept of a linear curve, Zonal propagation speed
$c_i$	Imaginary component of the zonal propagation speed
$c_r$	Real component of the zonal propagation speed
$c^*$	Complex conjugate of the zonal propagation speed
$d$	Fluid depth, Separation distance between the source and the sink
$E$	Ekman number
$E_k$	Energy contained in the $k^{\text{th}}$ azimuthal wavenumber
$\mathcal{F}$	Fourier transform in the azimuthal direction
$\mathbf{F}$	External forcing term
$F$	Pumping rate
$Fr$	Froude number
$f$	Angular frequency, Coriolis parameter
$f_0$	Constant Coriolis parameter at reference latitude
$f_d$	Disk frequency
$f_g$	Daughter wave frequency
$f_m$	Parent wave frequency
$G$	Coefficient of the forcing term linear with the velocity field
$g$	Geostrophic component, Gravity
$g'$	Velocity component or pressure
$H$	Angular momentum per unit mass, Height/depth of the fluid, Height/depth of the fluid at the split-disk radius, Spacing between two parallel plates
$Ha$	Hartmann number
$H_{\text{tank}}$	Height of the tank sidewall

*Continued on the next page.*

*Continued from previous page.*

<b>Symbol</b>	<b>Description</b>
$h_0$	Initial water height
$i$	Imaginary number ( $i = \sqrt{-1}$ )
$i$	Spatial index of a data point
$J$	Number of azimuthal Fourier planes, Order of the scheme, Richardson number
$j$	Spatial index of a data point
$k$	Azimuthal cylindrical polar wavenumber, Cartesian $y$ -direction wavenumber
$k_c$	Azimuthal wavenumber at the onset of instability
$k_{\text{peak}}$	Azimuthal wavenumber corresponding to the maximum growth rate
$k^*$	Average azimuthal wavenumber weighted by energy
$L$	Lagrange polynomial, Length scale, Shear-layer thickness
$L_D$	Rossby deformation radius
$L^*$	Dimensionless jet width
$l$	Non-dimensional parameter used to characterise hysteretic transitions
$Ma$	Mach number
$m$	Gradient of a linear curve, Modulated oscillating state
$N$	Azimuthal mode, Buoyancy frequency, Initial equilibrium state, Interaction parameter, Number of Fourier modes, Total number of data points, Value equating to three times the number of mesh nodes
$N_p$	Polynomial degree

*Continued on the next page.*

*Continued from previous page.*

<b>Symbol</b>	<b>Description</b>
$n$	Azimuthal cylindrical polar wavenumber Number of Ekman layers, Number of Hartmann layers, Positive integer value
$nV$	Noisy vortex
$O(X)$	Order of magnitude X
$P$	First positive invariant of the velocity-gradient tensor, Kinematic pressure, Period-doubled state
$P_m$	Legendre polynomial
$\bar{P}$	Mean kinematic pressure
$p$	Pressure
$\bar{p}$	Mean pressure
$p'$	Pressure perturbation
$Q$	Second positive invariant of the velocity-gradient tensor
$q$	Potential vorticity
$R$	Reynolds number, Shear zone radius, Third positive invariant of the velocity-gradient tensor
$R_d$	Disk radius
$R_i$	Reynolds number based on the inner cylinder rotation rate
$R_o$	Reynolds number based on the outer cylinder rotation rate
$R_t$	Tank radius
$Re$	Reynolds number
$Re_c$	Critical Reynolds number
$Re_E$	Reynolds number based on the Ekman layer thickness
$Re_{E^{1/3}}$	Reynolds number based on the $E^{1/3}$ Stewartson layer thickness
$Re_i$	Internal Reynolds number
$Re_{i,c}$	Critical internal Reynolds number
$Ro$	Rossby number
$Ro_c$	Critical Rossby number describing the onset of instability

*Continued on the next page.*

*Continued from previous page.*

<b>Symbol</b>	<b>Description</b>
$Ro_{c1-c2}$	Critical Rossby number describing the transition of reflectively symmetric to symmetry-broken flow
$Ro_{\text{mode II}}$	Critical Rossby number describing the onset of the mode II waveband
$Ro_{I-II}$	Critical Rossby number describing the dominance of mode I and mode II transition
$r$	Radial cylindrical polar coordinate
$r_0$	Split-disk radius
$r_i$	Inner sphere radius
$r_m$	Mean radius of the jet
$r_o$	Outer sphere radius
<b>S</b>	Symmetric part of the decomposed velocity-gradient tensor
$s$	Slope of the bottom topography
$T$	Taylor vortex, Time period
$T^*$	Ratio of the Ekman friction time to the eddy turnover time
$t$	Time
$t^*$	Reference time
$U$	Velocity scale
$U_0$	Maximum jet velocity
$U_B$	Non-dimensional lower boundary tangential velocity
$\bar{\mathbf{U}}$	Axisymmetric base velocity field
$U_\infty$	Velocity value sufficiently far from the boundary
<b>u</b>	Velocity vector
<b>u<sub>0</sub></b>	Forcing velocity due to electrical conduction
<b>u<sub>a</sub></b>	Ageostrophic velocity vector
<b>u<sub>bc</sub></b>	Velocity vector of the boundary condition
<b>u<sub>bc,B</sub></b>	Velocity vector of the bottom boundary condition
<b>u<sub>bc,T</sub></b>	Velocity vector of the top boundary condition
<b>u<sub>g</sub></b>	Geostrophic velocity vector
<b>u'</b>	Velocity perturbation vector

*Continued on the next page.*

*Continued from previous page.*

<b>Symbol</b>	<b>Description</b>
$\mathbf{u}'_k$	$k^{\text{th}}$ perturbation field
$\hat{\mathbf{u}}'_k$	$k^{\text{th}}$ Complex Fourier coefficient
$\hat{\mathbf{u}}'_k$	$k^{\text{th}}$ eigenvector
$\bar{\mathbf{u}}$	Mean velocity vector
$\mathbf{u}_\perp$	Interior velocity field relative to the boundary velocity
$u$	Axial cylindrical polar velocity component, Cartesian $x$ -direction velocity component, Horizontal velocity component
$u_\theta$	Azimuthal velocity
$u_{\theta,\text{rel}}$	Azimuthal velocity relative to the tank
$u_{\theta-\text{rel}}$	Azimuthal velocity relative to the tank
$u_{\theta-\text{rel}, \text{max}}$	Maximum azimuthal velocity relative to the tank
$u_{\theta-\text{rel}, \text{min}}$	Minimum azimuthal velocity relative to the tank
$u_{i,j}$	Variable $u_i$ differentiated with respect to the $j^{\text{th}}$ direction
$u_{\text{sound}}$	Speed of sound
$u_z$	Axial velocity
$V$	Volume of the computational domain
$v$	Cartesian $y$ -direction velocity component, Radial cylindrical polar velocity component, Tangential velocity component
$\bar{v}$	Tangential velocity of the basic flow
$\tilde{v}$	Transformed radial velocity component
$w$	Azimuthal cylindrical polar velocity component, Weak fluctuation
$w^*$	Disk speed
$w_1$	Vertical velocity to the first order of Rossby number
$w_d$	Vertical velocity induced by the disk
$w_j$	The $j^{\text{th}}$ weighting coefficient of the Gauss–Lobatto–Legendre quadrature
$\tilde{w}$	Transformed azimuthal velocity component

*Continued on the next page.*

*Continued from previous page.*

<b>Symbol</b>	<b>Description</b>
$x$	Cartesian eastward coordinate
$y$	Cartesian northward coordinate
$z$	Cartesian upward coordinate, Axial cylindrical polar coordinate
$z_s$	An arbitrary point in the flow



# Contents

<b>1</b>	<b>Introduction</b>	<b>1</b>
1.1	Overview of the problem . . . . .	1
1.2	Existence of barotropic instability . . . . .	3
1.2.1	Tropical cyclone eyewalls . . . . .	3
1.2.2	Planetary vortices . . . . .	6
1.2.2.1	Earth’s polar stratosphere . . . . .	6
1.2.2.2	Other atmospheres . . . . .	8
1.3	Governing parameters and flow approximations . . . . .	11
1.3.1	Governing parameters . . . . .	11
1.3.2	Coriolis variation approximations . . . . .	12
1.3.3	Geostrophic and quasi-geostrophic approximations . . . . .	14
1.3.3.1	Taylor–Proudman theorem . . . . .	15
1.4	Boundary and shear layers . . . . .	16
1.5	Barotropic instability . . . . .	19
1.5.1	Inviscid flows . . . . .	20
1.5.2	Viscid and frictional effects . . . . .	22
1.6	Centrifugal instability . . . . .	25
1.7	Vortex identification and eduction methods . . . . .	27
1.7.1	Intuitive definitions . . . . .	28
1.7.1.1	Pressure minimum . . . . .	28
1.7.1.2	Streamlines and pathlines . . . . .	29
1.7.1.3	Vorticity magnitude . . . . .	29
1.7.1.4	Discussion of intuitive methods . . . . .	30
1.7.2	Velocity-gradient tensor based definitions . . . . .	30
1.7.2.1	$\lambda_2$ criterion . . . . .	31
1.7.2.2	$Q$ criterion . . . . .	32
1.7.2.3	$\Delta$ and $\lambda_{ci}$ criteria . . . . .	32
1.7.2.4	Discussion on velocity-gradient tensor based methods . . . . .	33
1.8	Aims of the study . . . . .	34
1.9	Structure of the thesis . . . . .	35

<b>2</b>	<b>A Review of the Literature</b>	<b>37</b>
2.1	Transition to turbulence in shear flows . . . . .	37
2.2	Hollow vortex core flow . . . . .	41
2.3	Source-sink flow . . . . .	47
2.3.1	Transport through boundary and shear layers . . . . .	47
2.3.2	Unstable flow . . . . .	48
2.4	Differential rotating flow . . . . .	55
2.4.1	Internal rotation . . . . .	55
2.4.2	Single end-wall rotation . . . . .	57
2.4.3	Double end-wall rotation . . . . .	60
2.4.4	Short cylinders . . . . .	70
2.4.5	Spherical shells and spheroids . . . . .	75
2.4.6	Keplerian flow . . . . .	83
2.5	Review summary . . . . .	84
2.6	Hypotheses and testing . . . . .	86
<b>3</b>	<b>Numerical methodology</b>	<b>89</b>
3.1	Governing equations . . . . .	89
3.2	Quasi-geostrophic model . . . . .	90
3.2.1	Effect of the Ekman layer . . . . .	91
3.2.2	Magnetohydrodynamic flow analogy . . . . .	94
3.3	Spectral-element method . . . . .	95
3.3.1	Spatial discretisation . . . . .	96
3.3.2	Time discretisation . . . . .	97
3.4	Linear stability analysis . . . . .	99
3.4.1	Base flow . . . . .	99
3.4.2	Linear perturbations . . . . .	99
3.4.3	Mode stability . . . . .	101
3.5	Spectral-element-Fourier method . . . . .	103
3.6	Stuart–Landau modelling . . . . .	105
3.7	Geometric model . . . . .	107
3.7.1	Differential-disk configuration . . . . .	107
3.7.1.1	Governing equations and parameters . . . . .	108
3.7.1.2	Domain and boundary conditions . . . . .	110
3.7.2	The quasi-geostrophic model . . . . .	111
3.7.3	Spatial and temporal resolution refinement . . . . .	113
3.8	Chapter summary . . . . .	114

<b>4</b>	<b>Axisymmetric flow in a differential-disk rotating system</b>	<b>117</b>
4.1	Grid independence study . . . . .	118
4.2	Simulating the configuration used by Früh & Read . . . . .	119
4.2.1	Steady-state axisymmetric flow structure . . . . .	120
4.2.2	Vertical shear-layer profile and thickness . . . . .	124
4.2.3	Time-dependent axisymmetric flow structure . . . . .	131
4.2.3.1	Unsteady flow in the positive-Rossby-number regime . . . . .	132
4.2.3.2	Unsteady flow in the negative-Rossby-number regime . . . . .	134
4.2.4	Smoothed velocity profile forcing . . . . .	140
4.3	Varying the aspect ratio . . . . .	141
4.3.1	Axisymmetric flow structure . . . . .	142
4.3.2	Vertical shear-layer profile and thickness . . . . .	144
4.3.3	Time-dependent axisymmetric flow structure . . . . .	147
4.3.4	Universal regime diagram . . . . .	152
4.4	Flow on the $\beta$ -plane . . . . .	156
4.4.1	Axisymmetric flow structure . . . . .	157
4.5	Summary . . . . .	159
<b>5</b>	<b>Linear instability of flow in a differential-disk rotating system</b>	<b>163</b>
5.1	Simulating the configuration used by Früh & Read . . . . .	164
5.1.1	Positive-Rossby-number regime . . . . .	164
5.1.1.1	Growth rates . . . . .	164
5.1.1.2	Global instability mode shapes . . . . .	168
5.1.1.3	Visualising the linear instability modes on horizontal planes . . . . .	171
5.1.1.4	Preferred azimuthal wavenumbers . . . . .	173
5.1.2	Negative-Rossby-number regime . . . . .	179
5.1.2.1	Growth rates . . . . .	179
5.1.2.2	Linear instability modes and visualisation on horizontal planes . . . . .	180
5.1.2.3	Preferred azimuthal wavenumbers . . . . .	183
5.1.3	The internal Reynolds number and characterisation of the pre- ferred wavenumber regime diagrams . . . . .	185
5.2	Varying the aspect ratio . . . . .	188
5.2.1	Growth rates . . . . .	188
5.2.2	Linear instability modes and visualisation on horizontal planes . . . . .	193
5.2.3	Preferred azimuthal wavenumbers . . . . .	196
5.3	Linear stability of flow on a $\beta$ -plane . . . . .	199
5.4	Summary . . . . .	202

<b>6</b>	<b>Non-axisymmetric flow in a differential-disk rotating system</b>	<b>205</b>
6.1	In the vicinity of instability onset . . . . .	207
6.2	Flow conditions further beyond the instability onset . . . . .	214
6.2.1	Increasing the Rossby number . . . . .	214
6.2.2	Decreasing the Ekman number . . . . .	219
6.3	Varying the Rossby number . . . . .	225
6.3.1	Large-Ekman-number regime . . . . .	225
6.3.2	Small-Ekman-number regime . . . . .	232
6.4	Flow sensitivity . . . . .	235
6.4.1	Perturbing the axisymmetric solution . . . . .	236
6.4.2	Hysteresis effects . . . . .	240
6.5	Bifurcation analysis . . . . .	243
6.5.1	The mode I transition . . . . .	243
6.5.2	The mode II, III and $\beta$ -plane transition . . . . .	245
6.6	Chapter summary . . . . .	246
<b>7</b>	<b>Quasi-two-dimensional modelling</b>	<b>249</b>
7.1	Grid independence study . . . . .	250
7.2	Quasi-two-dimensional axisymmetric flow structure . . . . .	251
7.2.1	Vertical shear-layer profile and thickness . . . . .	254
7.3	Linear stability analysis . . . . .	257
7.3.1	Growth rates . . . . .	257
7.3.1.1	Positive-Rossby-number regime . . . . .	257
7.3.1.2	Negative-Rossby-number regime . . . . .	260
7.3.2	Global instability mode shapes and visualisation on horizontal planes . . . . .	266
7.3.3	Preferred azimuthal wavenumbers . . . . .	269
7.3.4	The Rossby and Ekman numbers dependence on the preferred azimuthal wavenumber and wavelength . . . . .	272
7.4	Smoothing the imposed velocity profile . . . . .	274
7.4.1	The axisymmetric flow structure, vertical profile and shear-layer thickness . . . . .	274
7.4.2	Linear instability and visualising global instability modes on hor- izontal planes . . . . .	275
7.5	Non-axisymmetric flow structure . . . . .	279
7.6	Chapter summary . . . . .	282

<b>8</b>	<b>Conclusions and direction for future research</b>	<b>287</b>
8.1	Key results from axisymmetric base flow simulations . . . . .	288
8.1.1	The vertical structure of the flow and universality of the aspect ratio . . . . .	288
8.1.2	Scaling of the Stewartson layer thickness . . . . .	288
8.1.3	Time-dependent flow structure . . . . .	289
8.2	Key results from the linear stability analysis . . . . .	289
8.2.1	Mode I and II linear instabilities . . . . .	289
8.2.2	Scaling the azimuthal wavenumber against the aspect ratio . . .	290
8.2.3	Scaling of the unstable azimuthal wavelength . . . . .	290
8.2.4	The critical $Ro/E^{3/4}$ parameter . . . . .	290
8.3	Key results from three-dimensional direct numerical simulation . . . . .	291
8.3.1	Significance of nonlinear effects . . . . .	291
8.3.2	Experimental implications and limitations . . . . .	291
8.4	Key results from quasi-two-dimensional modelling . . . . .	292
8.4.1	The vertical flow structure and $E^{1/4}$ layer thickness . . . . .	292
8.4.2	Significance of $ Ro $ in describing positive and negative-Rossby-number growth rates and the preferred azimuthal wavenumbers .	292
8.4.3	Non-axisymmetric flow structure . . . . .	293
8.5	Future research . . . . .	293
<b>A</b>	<b>The Ekman solution</b>	<b>297</b>
<b>B</b>	<b>Scaling of the governing equations</b>	<b>301</b>
B.1	Governing equations scaled by the tank rotation rate . . . . .	302
B.2	Governing equations scaled by the disk rotation rate . . . . .	304



# Chapter 1

## Introduction

This thesis presents the results of a numerical investigation of the structure and stability of shear layers arising in rotating flows. The following sections outline an overview of the problem and describes common flows related to the origin of this work. Governing non-dimensional parameters and instabilities relating to these flows are also established, followed by the aims of this current study. The structure of this thesis concludes this preliminary chapter.

### 1.1 Overview of the problem

Hydrodynamic stability occupies a central position in the field of fluid mechanics as instability phenomena are widely seen across disciplines of engineering and science, and frequently observed in nature. Its main concerns are in studying a saturated base flow forced by disturbances and examining the resultant flow development and end state. Since the distinguished investigations by Helmholtz, Kelvin, Rayleigh and Reynolds in the 19<sup>th</sup> century, advancements in hydrodynamic stability have been steady and ongoing. Rotating flows is one such category of flows that encompasses a class of interesting instabilities and has gauged key interest from researchers.

Rotating flows are abundant in nature and are renowned for their instabilities leading to the formation of intriguing structures of geometric shape, for which a comprehensive understanding is desired. These flows are generally influenced by external disturbances that induce a differential rotation to the bulk fluid motion. Consequently, shear and boundary layers are developed within the flow in order to accommodate the changes in velocity. These layers are significant in governing the state and evolution of the flow.

Flows that are influenced greatly by rotation are most clearly observable in the large-

scale structures present in atmospheric and oceanic flows. The thin atmosphere exhibits fluid motions that are predominant in the horizontal direction while vertical motions are weak in comparison. Thus, such flows have been largely approximated by two-dimensional and quasi-two-dimensional models. As such, any external horizontal forcing acting on these approximately two-dimensional flows are likely to produce vertical shear layers. These shear layers may become unstable resulting in an instability deforming the shear layer. An unstratified flow disturbed by horizontal forces encourages a shear-layer instability that is known as barotropic instability. However, atmospheric flows are stratified, which lend its potential energy to a second type of instability. This instability is known as baroclinic instability and it is common for it to coexist with barotropic instability in altering the base flow.

Barotropic and baroclinic instabilities are best recognised in the range of weather systems experienced on Earth. Mechanisms of these instabilities arise from many factors including wind shear, land topography, Coriolis parameter variation and the pole-equator temperature gradient. Interests in these instabilities are caused by the need to predict and understand geophysical phenomena. Baroclinic instability originates from perturbations that grow in rotating stratified fluids that are forced by a horizontal temperature gradient. In contrast, barotropic instability occurs in barotropic flows due to a horizontal shear forcing. Although barotropic flows are recognised as simpler systems to study in comparison to baroclinic flows, they are dynamically similar (McWilliams 1991; Vallis 2006). Thus, understanding barotropic instability can provide important insights in the flow structure and mechanisms of baroclinic problems. Despite this perceived simplicity, barotropic instability is still not fully understood, even in its linear-growth regime. The aims of this thesis are in examining the barotropic shear-layer instability.

An important aspect of barotropic instability is displayed in the extensive range of scales at which it can be observed. Given the difficulty in monitoring and obtaining relevant data on Earth and extraterrestrial planets, laboratory experiments have been the primary choice for prior research. The reason for this is because laboratory experiments enable complete control over the flow conditions, which can be quite extensive. However, physical and geometrical complexities paired with limited measuring techniques demand the implementation of theoretical and numerical simulations. Previously, simulating three-dimensional flows have been computationally expensive, though with the

continual advancement in computational power has made solving the governing equations within a reasonable time frame more realisable. The main benefit in adopting a numerical approach is in the immense flow details that are available. The numerical solutions are able to provide flow information on a fine scale, which would otherwise be unattainable through experiments. Both the experimental and numerical methods clearly play a complimentary role in the study of shear-layer instability.

## 1.2 Existence of barotropic instability

In order for barotropic instability to develop, there must exist some form of horizontal shear forcing imposed on the flow. These horizontal shear forces are commonly observed in the large-scale atmospheric and oceanic flows on Earth. Lesser-known examples of barotropic instability have been observed in astrophysical systems, planetary cores, planetary atmospheres and industrial processes. It is clear from this list that the scales driven by barotropic instability differ vastly. The following sections provides a brief insight into previously observed phenomena as a consequence of barotropic instability.

### 1.2.1 Tropical cyclone eyewalls

The formation of a tropical cyclone is complex and often described through a sequence of stages (e.g. Montgomery & Farrell 1993; Gray 1998). The formation generally involves environments of enhanced vorticity, humidity, convection and warm sea surface temperatures and may be perturbed by weather fronts and trade winds (Tory & Frank 2010). It may originate from a tropical storm that is comprised of waves, which are susceptible to instability (Schär & Davies 1990). These instabilities generate an increase to the wind speeds and the spatial structure that may eventually form a tropical cyclone. This structure rotates cyclonically with a warm low-pressure core, surrounded by colder high-pressure air. For hurricanes, the system is sustained by the ocean's heat and water evaporation at the surface. A hurricane may extend 450 km in diameter with speed typically ranging between 33 m/s and 70 m/s. The Saffir–Simpson Hurricane Wind Scale classifies these two extreme speed cases as Category 1 and Category 5. The scale was developed by Herbert Saffir and Robert Simpson to provide a measure of the strength of a hurricane.

At the centre of this seemingly violent system is a region of calm weather, known as the “eye”. Hurricane eyes are characterised by a low pressure region typically of

30 to 60 km in diameter where cooler air is drawn downwards. The border of this typically circular structure is known as the eyewall, and extends in the vertical while being surrounded by extreme weather conditions. The eye and eyewall have exhibited many interesting features, which have fascinated scientists as the general mechanisms forming these structures are not well known. Of particular interest is in understanding mesovortices which have been observed in the eyewall (e.g. Lewis & Hawkins 1982; Kossin & Schubert 2004).

In observing film from land-based and airborne radars, initial investigations by Lewis & Hawkins (1982) frequently observed hurricane eyes which were not circular but rather polygonal in shape. In particular, a pentagonal shaped eyewall was detected in Hurricane Debbie (1969) and Hurricane Anita (1977). Other observed shapes include squares and hexagons. Considering that these polygonal structures were often incomplete, it was believed that these astonishing structures were attributed to artifacts of the radar systems used. However, further observations evidently exemplified the existence of polygons in the eyewall. It was then proposed that the polygonal patterns are a result of the interference of horizontally propagating internal gravity waves.

As noted by Kossin & Schubert (2001), Willoughby *et al.* (1982) recognised that the azimuthal mean velocity is characterised by a “U-shaped” profile within the radius corresponding to the maximum tangential wind of the hurricanes. Outside of this radius, the azimuthal mean velocities are seen to decrease significantly. Correspondingly, an annular ring of high vorticity in the eyewall exists surrounded by low vorticity. This annular ring is generally circular but has demonstrated polygonal configurations indicative of deformations due to barotropic instability. The presence of barotropic instability related to the large shearing forces near the edge of the eyewall was also suggested by Muramatsu (1986) who observed distinct polygonal eyewall in Typhoon Wynne (1980).

An unforced barotropic non-divergent model of rings exhibiting elevated vorticity was investigated by Schubert *et al.* (1999). Numerical results of linear stability analysis and direct numerical simulations demonstrated polygonal eyewalls near the radius of maximum tangential velocity as a result of barotropic instability. This work was extended by Kossin & Schubert (2001) using a two-dimensional barotropic model of hurricane-like vortices. The eyewall was represented by a thin annulus of vorticity that is surrounded by nearly irrotational flow. Their results revealed that these flows sustain barotropic instability at high wavenumbers and large growth rates. A nonlinear



FIGURE 1.1: Hurricane Isabel with six mesovortices in the eye (one at the centre and five surrounding it). These vortices form a starfish pattern. This figure is reproduced from Kossin & Schubert (2004), courtesy of Dr. Jim Kossin.

---

analysis of the flow illustrated the ring of vorticity rolling up into mesovortices which were capable of undergoing merging processes and displaying long-lived polygonal configurations.

Previous findings of these polygonal configurations using simple barotropic models were complemented with the observations of a hurricane that formed during September 6-19 of 2003. The deadly tropical cyclone, named Hurricane Isabel was captured photographically via the eastern Geostationary Operational Environmental Satellite (GOES-12) using super rapid scan operations. The images revealed the existence of mesovortices at the eye-eyewall interface with the number of vortices ranging from an initial 8 to a 4-vortex configuration after coalescence. Figure 1.1 illustrates Hurricane Isabel with six mesovortices in the eye. These vortices often arranged themselves into a polygonal configuration similar to those obtained by previous numerical studies implementing barotropic models. These observations strongly suggests that mesovortices arise primarily due to barotropic instability.

Although these models are highly idealised, the simplistic barotropic models have revealed important characteristics in the formation of polygonal structures in tropical

cyclone eyewall regions.

## 1.2.2 Planetary vortices

### 1.2.2.1 Earth's polar stratosphere

The combination of the temperature gradient, Coriolis parameter variation and conservation of angular momentum on Earth causes circumpolar jets to develop. This occurs especially during the Winter months as the temperature drops and the wind speeds increase, resulting in a circumferential jet around a cyclonic vortex at polar latitudes. The planetary-scale vortex is known as a polar vortex and is characterised by a low pressure core. Polar vortices are formed in both hemispheres on Earth with its development initiating typically at the start of Autumn, peaking in Winter and subsequently decaying with the onset of Spring. The large-scale structures extend into the stratosphere and usually exhibit stable, long-lived and is typically circular features.

It is well known that strong coherent vortices are able to trap fluid inside their cores and isolate it from surrounding flow (Provenzale 1999). This property poses issues for the climate conditions on Earth as polar vortices are most prominent during Winter, which exacerbates chlorine build-up over the poles of the planet. The chlorine is formed via the reaction between nitric acid in polar stratospheric clouds (PSC) and the chlorofluorocarbons. The onset of spring weakens the strength of the polar vortex, eventually leading to the break up of the structure. Thus, chlorine is released and catalyses the process of ozone destruction leading to deterioration of the ozone layer. Consequently, climate variability has been observed in polar latitudes of the southern hemisphere (e.g. Thompson & Solomon 2002). The effects propagate equatorward impacting countries such as Australia (Karoly 2003) through prolonged drought conditions (Murphy & Timbal 2008). The significant consequence of polar vortices on mankind has garnered increasing interest in understanding the dynamics of polar vortices in recent decades.

The polar vortices generated in the northern and southern hemispheres have revealed differences in their strength and size. The Antarctic polar vortex often exhibits greater wind speeds, a larger spatial structure, and has superior longevity (Waugh & Polvani 2010). These differences are accounted for by the hemispheric differences in the land-sea contrast and the topographic features. Small-scale waves such as gravity waves are generated from the topography that act to perturb the polar vortex through

the interactions with large-scale Rossby waves. Since there are more obstructions such as mountains and buildings present in the polar latitudes of the northern hemisphere, more waves are generated that act to disrupt and break up the polar vortex structure. This is a reason for why sudden stratospheric warming occurs more frequently in the northern hemisphere. In contrast, the polar vortex in the southern hemisphere is not hampered by any such waves and therefore maintains its strength throughout the Winter season. Hence, ozone depletion is more problematic above the Antarctic. Furthermore, the wave activity can influence the spatial and temporal properties of the polar vortex such that the ozone levels and its distribution which affect the atmospheric circulations and climate (Ialongo *et al.* 2012).

The significant temperature differences between the hemispheres also plays a role in the dynamics of the polar vortex. Air masses are considerably colder in the southern hemisphere which creates conditions that are favorable for PSC formation. These clouds form approximately below 195 K which is exhibited for five months on average in the southern hemisphere. In contrast, conditions capable of stratospheric cloud formation are only sustained approximately for only two months in the northern hemisphere (Waugh & Polvani 2010). Moreover, there is greater temperature variability in the northern hemisphere compared to the southern hemisphere. Additionally, ozone depletion is also dependent on the volume of air on which PSCs can form (Harris *et al.* 2010), and so a larger polar vortex has a greater potential to promote ozone loss.

As the polar vortices on Earth become unstable, their circular structures deform into polygonal shapes which are typically ovals and dipoles. The splitting of the polar vortex in the southern hemisphere into two separate vortices in 2002 is a phenomenal event that was not expected since the southern structure is generally stable. The dynamics of this rare event have been thoroughly studied with details presented in Charlton *et al.* (2005), Groß *et al.* (2005) and Newman & Nash (2005). This splitting demonstrated similar patterns to those observed in the northern hemisphere when the polar vortex experiences a major warming of the azimuthal wavenumber 2 type.

Unlike the polar vortices on Earth, extraterrestrial planets have sustained long-lived structures exhibiting higher wavenumber polygonal shapes. Two well-known examples are of Venus' dipolar vortices and Saturn's northern polar hexagonal configuration, both of which are described in the next section.

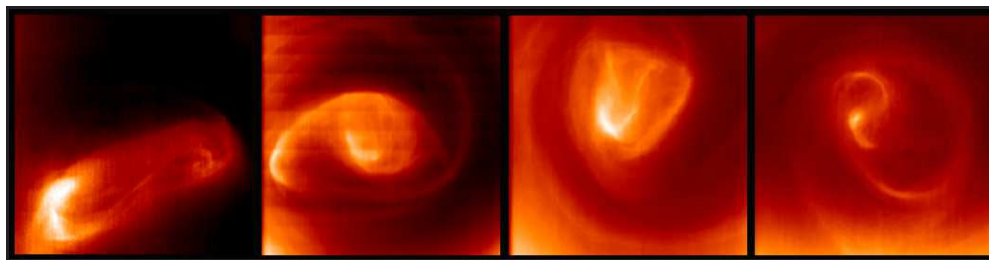


FIGURE 1.2: The changes in the structure of Venus’ south polar vortex over several days are illustrated via infrared images. The left frame represents the well-known dipolar structure. This figure is a reproduction, courtesy of Itziar Garate Lopez. Credit: ESA/VIRTIS/INAF-IASF/Obs. de Paris-LESIA/Universidad del País Vasco (I. Garate Lopez).

---

### 1.2.2.2 Other atmospheres

The displayed features on Earth and Venus are vastly different, despite the similarity in the size of the planets. For example, Venus rotates at a much slower rate and in the opposite direction to Earth. In addition, its planetary rotation is slower than its atmosphere (known as a super-rotating atmosphere), which is predominantly comprised of carbon dioxide. Also, Venus does not experience any pronounced seasonal forcing which largely plays a role in the formation of polar vortices on Earth.

Venus’ dipole in the northern hemisphere was first observed using ground-based observations in 1962 (Murray *et al.* 1963) with a spectral coverage of 8-14  $\mu\text{m}$ . Spacecraft observations were obtained a decade later on the Mariner 10 in 1974 and mapped by Pioneer Venus Orbiter (Taylor *et al.* 1980) in the middle atmosphere. Later observations revealed a similar dipole-structure phenomenon at the south pole (Piccioni *et al.* 2007). Observations at a wavelength of 5.05  $\mu\text{m}$  acquired in 2006 demonstrates the dipoles being represented by an inverse “S” shape. The dipolar structures are enclosed within a cold “collar” which is approximately 5000 km in diameter. This long-lived structure is also reported to be at least 20 km high (Garate-Lopez *et al.* 2013) and its internal structure is constantly varying on a daily time scale (Luz *et al.* 2011). Its chaotic character is unlike the polar vortices on other planets such as Earth and Saturn which are more stable. This variability is shown in figure 1.2. Although this structure has been observed for many years, the phenomenon on Venus remains mysterious.

A polar vortex on Saturn during its Spring season was first observed in the 1980s through images captured by the Voyager spacecraft (Godfrey 1988). The structure of the vortex represents a hexagon at a latitude of  $78^\circ$  in the northern hemisphere. The

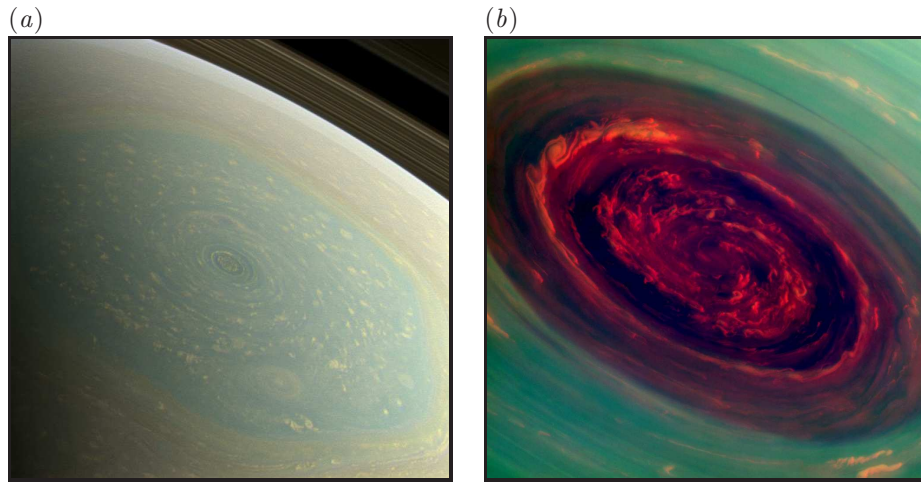


FIGURE 1.3: (a) The hexagonal polar vortex as seen on Saturn's north pole during its Spring. The hexagon border is seen at  $77^\circ$  north latitude and spans approximately 25,000 km across with each side being 13,800 km long. A natural-color view is shown to illustrate what the human eye would observe on Saturn. (b) A closeup false-color image the hexagon's eye which demonstrates the large storm systems. The eye is approximately 2,000 km across with cloud speeds as fast as 150 m/s. Credit: NASA/JPL-Caltech/Space Science Institute.

---

Cassini spacecraft which arrived in the Saturn system in 2004, rediscovered the hexagonal structure in 2007 (Baines *et al.* 2007, 2009) through thermal fields and demonstrated that the structure is persistent throughout Saturn's annual solar variation. This suggests that the polar vortex is insensitive to seasonal changes. The straight sides of the hexagon are approximately 13,800 km in length which is larger than the diameter of Earth. The emergence of Spring in recent times has enabled new amazing images to be captured due to sunlight directed towards the north pole. Images of the hexagonal structure and its central eye are illustrated in figure 1.3. This long-lived structure provides an appreciation of the grand scales at which polar vortices can exist.

In addition to the hexagonal structure, a large dark spot was observed south of the hexagon in the images captured by the Voyager in 1980 and ground-based observations in 1990 (Sanchez-Lavega *et al.* 1993). It was proposed by Allison *et al.* (1990) that this vortex-like feature is responsible for the generation of a azimuthal wavenumber six Rossby wave. However, imagery by the Cassini captured decades later have not been able to identify the same dark spot. Thus, the validity of a planetary wave mechanism being responsible for the hexagonal polar vortex is in doubt and the mechanism of the hexagon remains uncertain. It is quite possible that the dark spot is completely

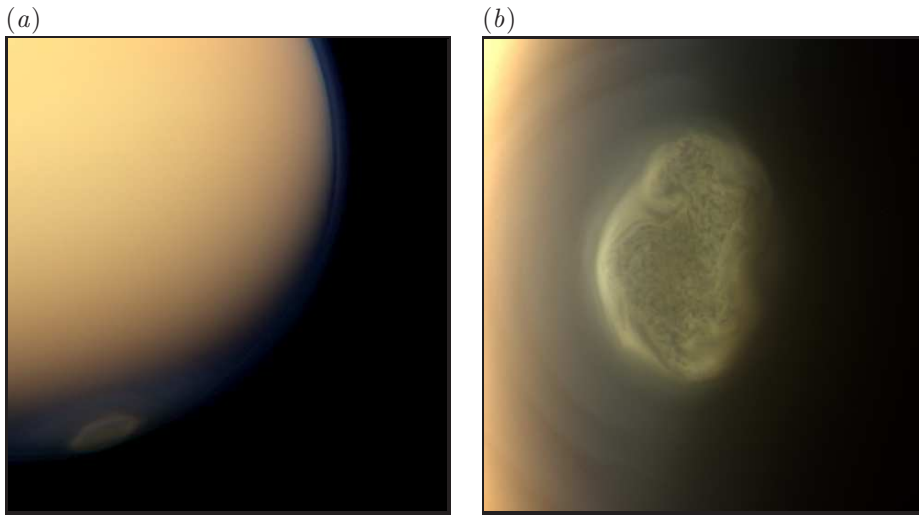


FIGURE 1.4: (a) A natural-color view of Titan revealing the position of its southern polar vortex. (b) A closeup true color image of the south polar vortex. Credit: NASA/JPL-Caltech/Space Science Institute.

---

unrelated to the formation and subsistence of the polar vortex.

Unlike the northern hemisphere which habitats a hexagonal configuration, the southern hemisphere displays a hurricane-like eyewall structure. This structure was picked up as a localised hot spot by the Keck I telescope in 2004 (Orton & Yanamandra-Fisher 2005) and was observed in 2006 by the Cassini spacecraft (Dyudina *et al.* 2008, 2009; Fletcher *et al.* 2008). The observations revealed an hurricane eye-like structure surrounded by two cloud walls that extend through the troposphere and stratosphere. Its structure consists of features in common with terrestrial hurricanes and Venus' polar vortices in terms of its warm core, structure and cyclonic rotation. This is in contrast with Earth's seasonal polar vortices which has a low temperature core.

Unique to Saturn is its largest moon Titan which has recently exhibited a polar vortex structure on its south pole during the Winter season. The south polar vortex was observed during Cassini's flyby of Titan on June 27, 2012 and is believed to be a permanent structure. The thickness of the atmosphere on Titan is what makes it unique and perhaps it is the reason for why it is able to sustain and produce these vortical structures. The atmosphere rotates faster than the moon's surface which is analogous to Venus' super-rotating atmosphere. These features in addition to its minor temperature contrast between the poles and the equator displays similarities to Venus.

Further out in the solar system, a hot spot was observed at the south pole of

Neptune. These cloud features were seen to split into two during 2007 via the Keck near-infrared images. Orton *et al.* (2007) and Hammel & Lockwood (2007) analysed the structures and suggested that the higher temperatures may be representative of a vortex, similar to that of Venus’ polar vortices or Earth’s polar vortex during the event of a sudden stratospheric warming. Closer links were drawn towards Venus’ south pole which habitats a long-lived hot polar vortex.

It may be possible that polar vortices exist on other planets and moons. However, at this point in time, there is insufficient observation and detection to suggest that this phenomenon is more widespread. Well-known structures of Saturn’s ribbon at  $47^\circ$  and Jupiter’s Great Red Spot may be a related phenomenon, as are the dark spots on the icy planets of Neptune and Uranus. Despite the vast interest in these planetary scale structures, there is still a great deal that is not understood. Particularly, the origin of these polar vortical shapes and the mechanisms which sustain these long-lived structures remains unknown. It has been proposed that these wave-like structures emerge from either a barotropic or baroclinic instability, or a complex interaction of both (Montabone *et al.* 2009; Aguiar *et al.* 2010).

### 1.3 Governing parameters and flow approximations

Many atmospheric and oceanic motions are strongly influenced by Coriolis effects arising from the rotation of the planet. For an incompressible rotating flow, the Navier–Stokes equations are described by

$$\begin{aligned} \frac{\partial \mathbf{u}}{\partial t} + (\mathbf{u} \cdot \nabla) \mathbf{u} + \mathbf{f} \times \mathbf{u} &= -\nabla P + \nu \nabla^2 \mathbf{u}, \\ \nabla \cdot \mathbf{u} &= 0, \end{aligned} \tag{1.1}$$

where  $\mathbf{u}$  is the velocity field,  $t$  is time,  $P$  is the kinematic pressure,  $\nu$  is the fluid kinematic viscosity, and  $\mathbf{f}$  is the Coriolis parameter. The Coriolis parameter is representative of the background vorticity which is non-uniform due to the spherical shape of the planet and its rotation. That is, the vertical component of the Coriolis parameter varies with latitude  $\theta$ , given by  $f = 2\Omega \sin \theta$ , where  $\Omega$  is the planetary rotation.

#### 1.3.1 Governing parameters

The terms in the momentum equation (1.1) from left to right, describe the unsteady acceleration, convective acceleration, Coriolis force, pressure gradient and viscous forces. A scaling estimate between the convective acceleration and viscous forces to Coriolis

forces yields two non-dimensional parameters given by

$$\frac{(\mathbf{u} \cdot \nabla)\mathbf{u}}{\mathbf{f} \times \mathbf{u}} \sim \frac{U^2}{L} \frac{1}{fU} = \frac{U}{fL} = Ro, \quad (1.2)$$

$$\frac{\nu \nabla^2 \mathbf{u}}{\mathbf{f} \times \mathbf{u}} \sim \frac{\nu U}{L^2} \frac{1}{fU} = \frac{\nu}{fL^2} = E, \quad (1.3)$$

where  $L$  and  $U$  represent the length and velocity scales, respectively. The ratio between the inertial and Coriolis forces is known as the Rossby number,  $Ro$ , and provides a measure of rotational importance on the system. A small Rossby number indicates that the flow is dominated by Coriolis effects. The Ekman number,  $E$ , indicates an interaction between frictional forces and Coriolis forces within the system.

An additional parameter can be defined based on the ratio of the Rossby and Ekman number. The resulting parameter is known as the Reynolds number,  $Re$ , given by

$$\frac{Ro}{E} = \frac{U}{fL} \frac{fL^2}{\nu} = \frac{UL}{\nu} = Re, \quad (1.4)$$

and describes the ratio of inertial to viscous forces.

### 1.3.2 Coriolis variation approximations

Flows that are characterised by a very small  $Ro$  and small  $E$  can be described by the quasi-geostrophic potential vorticity equation (1.15), which expresses the conservation of potential vorticity. The potential vorticity is defined as

$$q = \frac{f + \zeta}{H(r)}, \quad (1.5)$$

where  $f$  is the planetary vorticity,  $\zeta$  is the relative vorticity and  $H$  is the fluid depth. The planetary vorticity represents the vorticity associated with the background rotation while the relative vorticity is associated with motions relative to the background rotation. Thus for a constant fluid depth, the absolute vorticity, which is the addition of the planetary and relative vorticity, must remain constant. The change in either vorticity component can be demonstrated by considering a column of fluid in the northern hemisphere that has an associated potential vorticity. This column experiences a larger Coriolis force when it is displaced northward and therefore the relative vorticity is reduced to conserve potential vorticity. The reverse is true when the column moves southward.

The simplest treatment of incorporating the Coriolis variation into the model is by adopting a constant value for  $f$  (i.e.  $f = 2\Omega$ ). This is known as the  $f$ -plane

approximation. In order to include latitudinal variation of the Coriolis parameter, a Taylor expansion of  $f$  about a central latitude  $\theta_0$  must be considered. To first order, this approximation, known as the  $\beta$ -plane approximation, is given by

$$f \simeq f_0 + \beta y, \quad (1.6)$$

where  $f_0 = 2\Omega \sin \theta_0$ ,  $\beta$  is the topographic parameter and  $y$  is the northward coordinate. The topographic parameter is related to the variation of the Coriolis parameter with latitude, and is defined as

$$\beta = \frac{2\Omega}{R} \cos \theta_0, \quad (1.7)$$

where  $R$  is the radius of the planet. Two special cases are developed at the extreme latitudes of  $\theta_0 = 0$  and  $\theta_0 = \pi/2$ . The former is known as the equatorial  $\beta$ -plane. It is noted that for the latter case, the  $\beta$  parameter vanishes. Thus in order to capture the variation of the Coriolis parameter in this case, the second order term in the Taylor expansion of  $f$  is required. To second order with a reference latitude of  $\theta_0 = \pi/2$ , the Coriolis parameter is given by

$$f \simeq f_0 - \gamma(x^2 + y^2), \quad (1.8)$$

where  $x$  and  $y$  are the eastward and northward coordinates, respectively, and  $\gamma = \Omega/R^2$ .

In a laboratory setting, a flat cylindrical rotating tank with a constant fluid depth will exhibit a constant vertical component of background vorticity. By conservation of potential vorticity (1.5), the relative vorticity will also be constant. These conditions mimic the  $f$ -plane approximation. However, to achieve the dynamic similarity with that of planets (i.e. a decrease in relative vorticity at higher latitudes) in a rotating tank (constant  $f$ ), the fluid depth must vary. Specifically, the fluid depth must increase with increasing radius such that the relative vorticity of a fluid column translating towards deeper regions (larger  $H$ ) will decrease. By selecting the appropriate profile for the topography, the appropriate variation of the Coriolis effect can be attained. For the  $\beta$ -plane, the topography is linear whereas for the  $\gamma$ -plane the topography is parabolic. This dynamic similarity has been exploited by many authors in various media including air, water and plasma (van Heijst 1994; Sansón & van Heijst 2002; Rasmussen *et al.* 2006; Montabone *et al.* 2009; Aguiar *et al.* 2010).

### 1.3.3 Geostrophic and quasi-geostrophic approximations

Large-scale atmospheric and oceanic flows are generally governed by Rossby and Ekman numbers less than unity. Motions in the thin layer of the atmosphere are dominated by horizontal motions where vertical motions may become negligible. Applying these approximations yield simplified models that can be used to accurately describe planetary or oceanic fluid dynamics. Assuming that  $Ro \ll 1$  and  $E \ll 1$ , the Navier–Stokes equations (1.1) can be simplified to the geostrophic approximation. That is, the convective and viscous terms are neglected and the time derivative and Coriolis force balances the pressure gradient. For time-independent flows, the balance of forces in the horizontal direction reduces to

$$\mathbf{f} \times \mathbf{u} = -\nabla p, \quad (1.9)$$

where  $\mathbf{u}(x, y, z) = (u, v, w)$  is the velocity field with  $u$  and  $v$ , the horizontal velocity components, and  $w$  denoting the vertical velocity component and  $p$  is the pressure. Equation 1.9 represents geostrophic balance and describes the geostrophic velocity in terms of the pressure gradient and the Coriolis parameter. The accompanying vertical force balance is given by the hydrostatic approximation,

$$\rho g = -\frac{\partial p}{\partial z}, \quad (1.10)$$

where  $g$  represents the gravity. The prevailing horizontal motions cause the vertical velocities to become negligible. In addition to the momentum equations, the conservation of mass

$$\frac{\partial \rho}{\partial t} + (\mathbf{u} \cdot \nabla)\rho + w \frac{\partial \rho}{\partial z} = 0, \quad (1.11)$$

forms the planetary geostrophic equations. Here,  $\rho$  is the fluid density. Appropriate boundary conditions used together with these equations may provide accurate geostrophic fluid motion such as large-scale oceanic systems.

Unfortunately, the geostrophic equations cannot describe all of the atmospheric and oceanic flows since certain flows are not characterised by Rossby numbers that are sufficiently small. That is, the inertial accelerations cannot be ignored and the flow is no longer in geostrophic balance. Thus, the governing equations are required to describe ageostrophic effects, which is known as the quasi-geostrophic vorticity equation. Assuming that the velocity field is comprised of a geostrophic and a ageostrophic component, the horizontal velocities can be written as  $u = u_g + u_a$  and  $v = v_g + v_a$  where

subscripts ‘ $a$ ’ and ‘ $g$ ’ denote ageostrophic and geostrophic properties, respectively. To first order (terms comparable to  $O(Ro)$ ), the horizontal momentum equations after neglecting lower order terms becomes

$$\frac{\partial \mathbf{u}_g}{\partial t} + (\mathbf{u}_g \cdot \nabla) \mathbf{u}_g + f_0 \times \mathbf{u}_a + \beta y \times \mathbf{u}_g = 0. \quad (1.12)$$

Taking the curl of the horizontal momentum equations yields the vorticity equation,

$$\left( \frac{\partial}{\partial t} + \mathbf{u} \cdot \nabla \right) \zeta + \beta v = f_0 \frac{\partial w}{\partial z}, \quad (1.13)$$

where  $\zeta = \partial v / \partial x - \partial u / \partial y$  is the relative vorticity. The absolute vorticity is comprised of the planetary vorticity and the relative vorticity ( $\xi = f_0 + \beta y + \zeta$ ). A streamfunction is introduced such that  $u = -\partial \psi / \partial y$  and  $v = \partial \psi / \partial x$ . The ageostrophic vertical velocity is given by

$$w_a = -\frac{f_0}{N^2} \left( \frac{\partial}{\partial t} + \mathbf{u}_g \cdot \nabla \right) \frac{\partial \psi}{\partial z}, \quad (1.14)$$

where  $N$  is the buoyancy frequency. Noting that  $\beta v_g = \mathbf{u}_g \cdot \nabla (f_0 + \beta y)$  and  $\zeta = \nabla^2 \psi$  and combining it with equation 1.14, the horizontal momentum equation (1.12) becomes the quasi-geostrophic potential vorticity equation defined as

$$\left( \frac{\partial}{\partial t} + \mathbf{u} \cdot \nabla \right) \left\{ \nabla^2 \psi + f_0 + \beta y + \frac{\partial}{\partial z} \left( \frac{f_0}{N^2} \frac{\partial \psi}{\partial z} \right) \right\} = 0. \quad (1.15)$$

The quantity inside the braces is known as the quasi-geostrophic potential vorticity which is comprised of the relative vorticity, planetary vorticity and stratification. This is a materially conserved quantity in the absence of friction and diabatic heating.

### 1.3.3.1 Taylor–Proudman theorem

An important characteristic arising from geostrophic balance (1.9) is that the flow may become two-dimensional in planes perpendicular to the axis of rotation. This can be demonstrated by taking the curl of equation 1.9 which assumed incompressible flow. This is represented by

$$\nabla \times (\mathbf{f} \times \mathbf{u}) = -\nabla \times \nabla p. \quad (1.16)$$

Recognising that the curl of the pressure gradient is identically zero (since the pressure gradient is a scalar), the expansion of equation 1.16 yields

$$(\nabla \cdot \mathbf{u})\mathbf{f} - (\mathbf{f} \cdot \nabla)\mathbf{u} + (\mathbf{u} \cdot \nabla)\mathbf{f} - (\nabla \cdot \mathbf{f})\mathbf{u} = 0. \quad (1.17)$$

The spatial derivatives of the Coriolis parameter are zero as  $\mathbf{f}$  is not a function of position. Rather,  $\mathbf{f}$  has a single component that is parallel to the axis of rotation such that

$$\mathbf{f} = 2\boldsymbol{\Omega} = (0, 0, 2\Omega), \quad (1.18)$$

where  $\Omega$  is a scalar. Paired with the continuity result of an incompressible flow ( $\nabla \cdot \mathbf{u} = 0$ ), the resulting equation is given by

$$(2\boldsymbol{\Omega} \cdot \nabla)\mathbf{u} = 2\Omega \frac{\partial \mathbf{u}}{\partial z} = 0. \quad (1.19)$$

Equivalently, the result is  $\partial \mathbf{u} / \partial z = 0$  which implies that the velocity field  $\mathbf{u}$  is independent of  $z$ , which is the direction parallel to the axis of rotation. This result is known as the Taylor–Proudman theorem after Joseph Proudman who derived this theoretical result in 1915 and Sir Geoffrey Ingram Taylor who demonstrated it experimentally.

For a rotating system with solid boundaries perpendicular to the axis of rotation, the axial derivatives of the radial and azimuthal velocities are zero. Furthermore, the zero axial velocity present at the impenetrable boundary is enforced throughout the domain. Therefore, the flow can be described by two-dimensional motion in planes perpendicular to the rotation axis well away from the boundaries. It should be noted that details of the boundaries have not been specified here. That is, irrespective of the boundary profile (e.g.  $f$ -plane,  $\beta$ -plane or  $\gamma$ -plane), the fluid motion remains independent along the axis of rotation rather than the common misconception of fluid columns being perpendicular to the local normal. The theorem is invalid in the proximity of the boundaries due to the presence of boundary layers which are viscous. Boundary and shear layers are described in the next section.

## 1.4 Boundary and shear layers

Systems with viscous fluids are able to develop boundary layers. As the name suggests, these layers form on the boundaries of the system and serve as a transitional zone in smoothing out velocities from the boundary to the surrounding flow and to transport mass. An intuitive example of this is of a flow over a flat plate where the boundary layer develops at the leading edge and continues to grow downstream. However, these layers do not always need to be attached to the boundary. Such layers are known as free or detached shear layers and can exist in rotating flows.

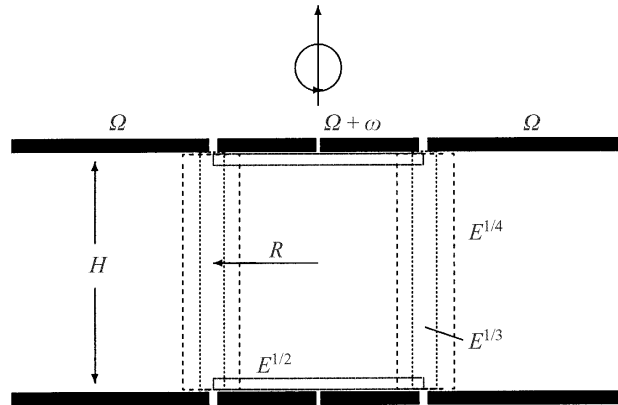


FIGURE 1.5: Illustration of the Stewartson and Ekman layers in this differential-disk rotating configuration. The tank rotates at a rate of  $\Omega$  while the disks rotate at  $\Omega + \omega$ . The thickness of each layer is indicated and scaled against the Ekman number,  $E$ . This figure is reproduced from Fröh & Read (1999) with permission from Dr. Wolf-Gerrit Fröh and the Cambridge University Press.

A shear layer can be produced through mechanical forcing by imparting differential velocities on parts of a stationary or rotating flow. An example of this is given by two concentric spheres which rotate about the same axis with slightly differing angular velocities. This configuration was first considered by Proudman (1956). By superimposing a small angular velocity perturbation onto one of the spheres, three different regions of the flow can be observed. The most important of which is a cylindrical shear layer which circumscribes the inner sphere. From the balance of fluid entering and leaving the boundary layers on the surfaces, it was inferred that a return of fluid may occur in the shear layer. Proudman (1956) was unable to determine the thickness of the shear layer but proposed that the thickness is of  $O(Re^{-1/4})$  where  $Re$  is the Reynolds number.

Stewartson (1957) embarked on studying a simpler system to determine the thickness of the shear layer. The configuration considered was comprised of two coaxial disks rotating differentially to rotating plates. An illustration of the configuration considered is shown in figure 1.5. The two disks rotate in the same orientation at a different angular velocity compared to the tank walls. A vertical shear layer is produced to smooth out the discontinuity in angular velocity at the disk-tank interface similar to that produced in the concentric spheres configuration. The shear layer was found to be a nesting of two vertical layers. The thick outer layer had a thickness of  $O(Re^{-1/4})$  which func-

tioned to smooth out the discontinuity in angular velocity across the layer. The thin layer has a thickness of  $O(Re^{-1/3})$  which is embedded inside the  $Re^{-1/4}$  layer. The purpose of the thinner layer is to complete the meridional circulation of the fluid in the layer. The thickness scaling of these Stewartson layers are often represented through the Ekman number, which is proportional to the reciprocal of  $Re$ . Hence, the layers are often referred to as the  $E^{1/3}$  and  $E^{1/4}$  layers, respectively. In addition to these shear layers, boundary layers are formed at the top and bottom horizontal boundaries which are known as Ekman layers. These have thicknesses which scale with  $E^{1/2}$ .

The Stewartson and Ekman layers are also present in source-sink configurations where fluid is continuously pumped into and withdrawn from the system. These layers arise primarily due to the mass transport of fluid required from the source port to the sink port. According to the Taylor–Proudman theorem, which was explained in detail in § 1.3.3.1, the vertical motions are inhibited due to the dominant rotation. Thus the only regions where vertical transport can occur is in the vertical shear layers. This theory has been complimented by several investigations of source-sink flow in a rotating fluid including that of Hide (1968). That particular study revealed that the injected fluid is only transported through the vertical Stewartson layers and the horizontal Ekman layers for small flux values (small  $Ro$ ). An example route from the source entry to the sink exit and the shear layers is illustrated in figure 1.6.

It should be noted that the Stewartson  $E^{1/4}$  layer is a depth-independent structure while the  $E^{1/3}$  layer is not. Thus, the quasi-geostrophic vorticity equation (1.15) cannot describe the structure of the thin  $E^{1/3}$  layer. The significance of the  $E^{1/3}$  layer is still not completely known. Indeed in many differential-disk rotation set-ups, both the  $E^{1/3}$  and  $E^{1/4}$  Stewartson layers exist. However, it is believed that there are several conditions and configurations which can eliminate the  $E^{1/4}$  layer. For the case of counter-rotating disks (Stewartson 1957; Baker 1967), it has been found that the  $E^{1/3}$  alone is enough to sustain the shear. This is in contrast to the requirement of both layers in the co-rotating case. The argument behind this is due to the zero depth-averaged azimuthal velocity in the counter-rotating case. Therefore, there is no discontinuity at the split-disk radius and no need for the  $E^{1/4}$  layer. The counter-rotating experiments by Baker (1967) found that the vertical shear-layer thickness scales with  $E^{0.4}$ . It was claimed that this result is consistent with the theoretical result of  $E^{1/3}$ . The attainment of a thicker shear-layer scaling compared to theoretical predictions are not unusual in

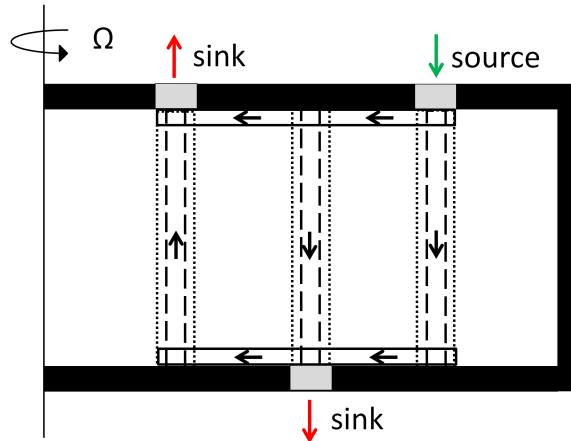


FIGURE 1.6: Meridional semi-plane of an example rotating source sink configuration. Transport and direction of flow are illustrated by the arrows in the shear and boundary layers. The horizontal and vertical shear layers are the Ekman and Stewartson layers, respectively. The scaling of each layer is the same as that shown in figure 1.5. This figure is adapted from Matsuda *et al.* (1975).

experiments as viscosity acts to broaden the shear layer. Also, the measurements are limited by the visualisation techniques and the classification of the shear-layer edge.

The depth-averaged azimuthal velocity value will differ between different configurations. This may alter which shear layer is of primary importance but also may introduce additional shear layers. For example, a differentially-rotating spherical system has an additional  $E^{2/7}$  Stewartson layer and a  $E^{2/5}$  thickening of the Ekman layer around the equator (Stewartson 1966). It may be that these additional shear layers have a significant effect on the stability of the flow. In fact, in a source-sink system, the  $E^{1/4}$  is independent on the fluid injection and withdrawal method whereas there is a notable dependence with the  $E^{1/3}$  layer (Conlisk & Walker 1981; van Heijst 1984). Thus, the knowledge of individual shear layers is significant, particularly for numerical investigations, as the quasi-geostrophic approximation does not model any depth-dependent structures.

## 1.5 Barotropic instability

The following section provides equations and criteria commonly used in studying barotropic instability for both viscous and inviscid flows. Many prior studies have investigated

inviscid flows due to the simplicity introduced by neglecting viscous dissipation.

### 1.5.1 Inviscid flows

A time-dependent inviscid barotropic flow influenced by rotation in two-dimensional space is described by

$$\begin{aligned}\frac{\partial \mathbf{u}}{\partial t} + (\mathbf{u} \cdot \nabla) \mathbf{u} + \mathbf{f} \times \mathbf{u} &= -\nabla P, \\ \nabla \cdot \mathbf{u} &= 0.\end{aligned}\tag{1.20}$$

Decomposing the flow variables of velocity and pressure into a mean  $(\bar{u}, \bar{v}, \bar{p})$  and perturbation components  $(u', v', p')$  yields

$$\begin{aligned}u &= \bar{u}(y) + u'(x, y, t), \\ v &= v'(x, y, t), \\ p &= \bar{p}(y) + p'(x, y, t),\end{aligned}\tag{1.21}$$

and linearising the governing equations acquires

$$\begin{aligned}\frac{\partial u'}{\partial t} + \bar{u} \frac{\partial u'}{\partial x} + v' \frac{d\bar{u}}{dy} - (f_0 + \beta y)v' &= -\frac{1}{\rho} \frac{\partial p'}{\partial x}, \\ \frac{\partial v'}{\partial t} + \bar{u} \frac{\partial v'}{\partial x} + (f_0 + \beta y)\bar{u} + (f_0 + \beta y)u' &= -\frac{1}{\rho} \frac{\partial p'}{\partial y}, \\ \frac{\partial u'}{\partial x} + \frac{\partial v'}{\partial y} &= 0.\end{aligned}\tag{1.22}$$

The products of the perturbation have been neglected due to their negligible contributions. The perturbation velocities are related to the streamfunction via  $u' = -\partial\psi'/\partial y$  and  $v' = \partial\psi'/\partial x$ , which allows the horizontal momentum equations to combine into a single equation

$$\left( \frac{\partial}{\partial t} + \bar{u} \frac{\partial}{\partial x} \right) \nabla^2 \psi' + \left( \beta - \frac{d^2 \bar{u}}{dy^2} \right) \frac{\partial \psi'}{\partial x}.\tag{1.23}$$

Taking the normal mode approach, the streamfunction takes the form

$$\psi'(x, y, t) = \phi(y)e^{ik(x-ct)},\tag{1.24}$$

where  $\phi$  is the wave amplitude,  $k$  is the wavenumber and  $c$  may be complex with its real component representing the propagation speed. This form transforms equation 1.23 into the second-order ordinary differential equation

$$\frac{d^2 \phi}{dy^2} - \left( k^2 \phi + \frac{\beta - \frac{d^2 \bar{u}}{dy^2}}{\bar{u} - c} \right) \phi = 0.\tag{1.25}$$

Equation 1.25 is known as the Rayleigh–Kuo equation. The addition of Coriolis variation via the  $\beta$  parameter by Kuo (1949) produces a generalised expression to an earlier equation developed by Rayleigh (1880). As a result, equating  $\beta = 0$  in the Rayleigh–Kuo equation attains Rayleigh’s equation. Likewise, the Orr–Sommerfeld equation,

which includes the effects of viscosity, is another generalisation of the Rayleigh equation, which describes linear two-dimensional instabilities in a viscous parallel flow such as pipe flow (e.g. Meksyn & Stuart 1951; Niino & Misawa 1984; Drazin & Reid 2004). The Orr–Sommerfeld equation is described by

$$(\bar{u} - c) \left( \frac{d^2}{dy^2} - k^2 \right) \phi - \frac{d^2 \bar{u}}{dy^2} = -\frac{i}{kRe} \left( \frac{d^2}{dy^2} - k^2 \right)^2 \phi, \quad (1.26)$$

where  $Re$  is the Reynolds number.

Assuming that the flow is bounded between two walls  $(y_1, y_2)$  in which there is no permeation ( $v' = 0$ ) results in a zero streamfunction. Therefore, the wave amplitude at the boundaries are  $\phi(y_1) = \phi(y_2) = 0$ . The boundary conditions coupled with equation 1.25 represents an eigenvalue problem. A property of the Rayleigh–Kuo equation is that if  $c = c_r + ic_i$  is an complex eigenvalue, then so is its complex conjugate  $c^*$ . Thus complex eigenvalues come in pairs. This implies that if any complex eigenvalue can be found then the base flow must be unstable as an imaginary component of  $c_i > 0$  must exist. This is demonstrated in the streamfunction  $\psi = \phi e^{ik(x-c_r t)} e^{kc_i t}$  via the complex expansion of  $c$ .

Multiplying equation 1.25 by the wave amplitude conjugate  $\phi^*$  and integrating over the domain  $(y_1, y_2)$  produces

$$\int_{y_1}^{y_2} \left[ \left| \frac{d\phi}{dy} \right|^2 + k^2 |\phi|^2 \right] dy + \int_{y_1}^{y_2} \frac{\beta - \frac{d^2 \bar{u}}{dy^2}}{\bar{u} - c} |\phi|^2 dy = 0. \quad (1.27)$$

A more practical form can be achieved by multiplying the second integral of equation 1.27 by  $(\bar{u} - c^*)/(\bar{u} - c^*)$ , and upon expansion obtains the following expression

$$\begin{aligned} \int_{y_1}^{y_2} \left[ \left| \frac{d\phi}{dy} \right|^2 + k^2 |\phi|^2 \right] dy + \int_{y_1}^{y_2} \frac{(\beta - \frac{d^2 \bar{u}}{dy^2})(\bar{u} - c_r)}{|\bar{u} - c|^2} |\phi|^2 dy \\ + ic_i \int_{y_1}^{y_2} \frac{\beta - \frac{d^2 \bar{u}}{dy^2}}{|\bar{u} - c|^2} |\phi|^2 dy = 0. \end{aligned} \quad (1.28)$$

There are two possible scenarios to satisfy the imaginary term of equation 1.28. It is required that either  $c_i$  vanishes or the integral does. However,  $c_i \neq 0$  if the flow is unstable as stated previously. Therefore only the latter option is viable for an unstable flow. Since the magnitudes of  $\bar{u} - c$  and  $\phi$  are positive, the term

$$\beta - \frac{d^2 \bar{u}}{dy^2} \quad (1.29)$$

must change sign somewhere within the domain  $(y_1, y_2)$  for the imaginary term to be satisfied. This condition is known as the Rayleigh–Kuo condition and again is a gen-

eralised condition of Rayleigh's inflexion point theorem discovered earlier by Rayleigh (1880); that is,  $d^2\bar{u}/dy^2$  must change sign in the domain to permit instability.

These criteria are a physical representation of the gradient of absolute vorticity which is comprised of the planetary vorticity (Coriolis parameter) and the relative vorticity. In cylindrical coordinates, the vorticity in the  $r$ - $\theta$  plane is given by  $1/r[\partial(rv)/\partial r - \partial u/\partial\theta]$ , where  $u$  and  $v$  represent the radial and azimuthal velocity components respectively. Therefore an equivalent instability criterion in cylindrical coordinates for a flow governed only by  $v(r)$  is that

$$\frac{d^2v}{dr^2} + \frac{1}{r} \frac{dv}{dr} - \frac{v}{r^2} - \frac{df}{dr} = 0, \quad (1.30)$$

be satisfied. It must be noted that the absolute vorticity changing sign is a necessary but not sufficient condition. This was demonstrated by Drazin & Howard (1966) through an analysis using a  $\bar{u} = \sin(y)$  velocity profile. Additionally, a stricter criterion based on Rayleigh's criterion was derived by Fjørtoft (1950) (see Drazin 2002; Schmid & Henningson 2001). The necessary condition for instability follows  $\bar{u}''(\bar{u} - \bar{u}_s) < 0$  somewhere in the flow, where  $\bar{u}_s = \bar{u}(z_s)$  and  $z_s$  is a point in the flow where  $\bar{u}''(z_s) = 0$ .

It should be noted that these criteria are only valid for a barotropic inviscid flow. The development of linear stability theory for inviscid plane-parallel shear flows by Rayleigh (1880) is able to describe the initial structure of the instability in inflectional shear flows. However, it failed when applied to flows such as Poiseuille flow due to the viscous processes which are involved and necessary for the initial instability of certain flows. Hence, a theoretical criterion (equation 1.26) was formulated by Orr (1907) and Sommerfeld in 1908 (Drazin & Reid 2004) which incorporates viscous effects.

### 1.5.2 Viscid and frictional effects

The development of a more complete theory for the linear stability of barotropic flow was achieved by incorporating the effects of both the Ekman friction and internal viscous diffusion. The Ekman friction is associated with the friction within the Ekman boundary layers. Prior studies had considered either inviscid flow, Ekman friction only or internal diffusion only (see Niino & Misawa (1984) for references). As concluded by Niino & Misawa (1984), the effects of both factors are significant and alter the critical Reynolds number and corresponding azimuthal wavenumbers. Thus prior studies which had not considered both effects have encountered quantitative inconsistencies. A brief

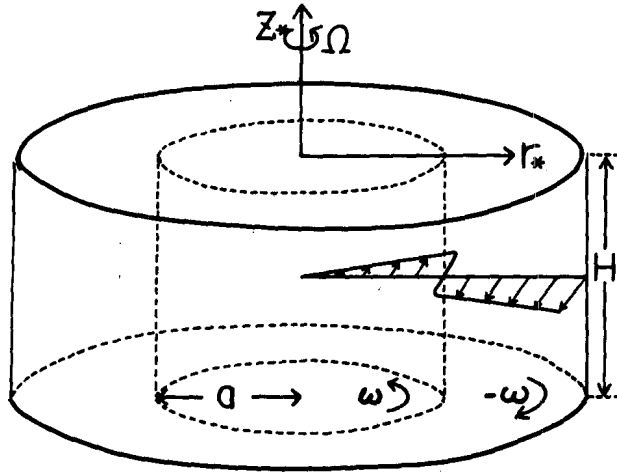


FIGURE 1.7: Idealised configuration of the differential experiment used for theoretical consideration. This figure is reproduced from Niino & Misawa (1984) with permission from the © American Meteorological Society.

description and derivation of the basic flow stability is described in this section. A more complete walkthrough can be found in Niino & Misawa (1984).

The theoretical model developed by Niino & Misawa (1984) considers a flat cylindrical container of depth  $H$ . The upper boundary located at  $z = H$  and the bottom boundary located at  $z = 0$  rotate at an angular rate of  $\Omega$  and  $\Omega \pm \omega$ , respectively. For radii less than the shear zone radius  $R$ , the differential rotation imposed is in the same direction as that of the lid while beyond  $R$ , the differential rotation imposed is in the opposite direction. Thus, a shear layer is developed via the angular discontinuity at  $r = R$ . A schematic of the idealised configuration is shown in figure 1.7. Given that  $\omega \ll \Omega$  (small  $Ro$ ), the flow field can be described by the non-dimensional quasi-geostrophic vorticity equation written as

$$\frac{\partial}{\partial t} \nabla^2 \psi + \frac{Re}{r} \left( \frac{\partial \psi}{\partial \theta} \frac{\partial}{\partial r} \nabla^2 \psi - \frac{\partial \psi}{\partial r} \frac{\partial}{\partial \theta} \nabla^2 \psi \right) + \nabla^2 \psi + \frac{1}{2r} \frac{\partial}{\partial r} (r U_B) = \nabla^4 \psi \quad (1.31)$$

where  $\psi$  is the streamfunction in the horizontal plane and  $U_B$  is the non-dimensional tangential velocity at the lower boundary. The terms  $\nabla^2 \psi$  and  $\nabla^4 \psi$  represent the Ekman friction and internal diffusion effects, respectively. The variables have been non-dimensionalised as  $r' = Lr$ ,  $z' = Hz$ ,  $U'_B = UU_B$ ,  $\psi' = UL\psi$ ,  $\Delta\Omega' = (\omega/2)\Delta\Omega$  and  $t' = E^{-1/2}/(2\Omega)t$ , where the primes denote dimensional quantities. Here,  $L$  and  $U$  are

the characteristic length and velocity of the basic flow, respectively, defined as

$$L = \left(\frac{E}{4}\right)^{1/4} H \text{ and } U = \frac{\omega R}{2}. \quad (1.32)$$

The Reynolds number is defined as  $Re = UE^{1/2}/(2\Omega L) = UL/\nu$ , which was reported as the only parameter required to determine the stability of this system if the ratio of the shear zone radius to the characteristic length is asymptotically large, denoted by  $\gamma = R/L$ . The tangential velocity boundary condition imposed at the bottom boundary in producing a shear layer is given by

$$U_B = \begin{cases} \frac{-2r}{\gamma} & \text{for } r < \gamma \\ \frac{2r}{\gamma} & \text{for } r > \gamma \end{cases} \quad (1.33)$$

while for a jet, the velocity boundary condition is given by

$$U_B = \begin{cases} 0 & \text{for } r < \gamma - \alpha \\ \frac{-2r}{\gamma} & \text{for } |r - \gamma| < \alpha \\ 0 & \text{for } r > \gamma + \alpha \end{cases} \quad (1.34)$$

where  $2\alpha$  is the dimensionless width of the jet (gap between the outer edges of the two disks). For steady and axisymmetric base flows, the governing equation becomes

$$\nabla^2\psi + \frac{1}{2r} \frac{\partial}{\partial r}(rU_B) = \nabla^4\psi. \quad (1.35)$$

Integration of equation 1.35 with respect to  $r$  yields

$$\bar{v} = \begin{cases} -e^y + 1 + O(y/\gamma) & \text{for } y < 0 \\ e^{-y} - 1 + O(y/\gamma) & \text{for } y > 0 \end{cases} \quad (1.36)$$

where  $\bar{v}$  is the tangential velocity of the basic flow and  $y = r - \gamma$ . This is only true if  $\gamma$  is sufficiently large. If the shear zone layer is small in comparison to the characteristic length, the curvature of the geometry becomes significant and the basic flow field no longer satisfies equation 1.36.

As these velocity profiles satisfy the inviscid Rayleigh–Kuo criterion at  $y = 0$ , it is expected that these flows are unstable to barotropic instabilities under sufficient forcing conditions. An added perturbation to the streamfunction substituted into equation 1.31 and neglecting second-order terms (i.e.  $O(\psi'^2)$ ) leads to

$$\frac{\partial}{\partial t} \nabla^2\psi' + \frac{Re}{r} \left( \bar{v} \frac{\partial}{\partial \theta} \nabla^2\psi' - \frac{\partial}{\partial r} \left[ \frac{1}{r} \frac{d}{dr}(\bar{v}r) \right] \frac{\partial\psi'}{\partial \theta} \right) + \nabla^2\psi' = \nabla^4\psi', \quad (1.37)$$

where  $\psi'$  is the perturbation added to the streamfunction variable.

By following a normal mode approach similar to that of the previous section for inviscid flows and assuming a sufficiently large  $\gamma$ , equation 1.37 can be simplified to

$$[ikRe(\bar{v} - c) + 1] \left( \frac{d^2\phi}{dy^2} - k^2\phi \right) - ikRe\frac{d\bar{v}}{dy}\phi = \left( \frac{d^2}{dy^2} - k^2 \right)^2 \phi, \quad (1.38)$$

where  $\phi$  is the wave amplitude and  $k$  is the wavenumber. In fact, this equation is the Orr–Sommerfeld equation (1.26) with the added Ekman friction term. These equations are only valid for large  $\gamma$ ; further details and derivations can be found in Niino & Misawa (1984) regarding smaller  $\gamma$ . The results of their study are detailed in the next chapter (§ 2.4.2).

## 1.6 Centrifugal instability

Centrifugal instabilities are another important type of hydrodynamic instability that arise in swirling flows. Similar to parallel flows, the classical swirling flow is the circular Couette flow. Rayleigh (1916) was the first to consider the stability of swirling flows to axisymmetric infinitesimal perturbations. It was found that a pure rotational flow having a velocity field  $V(r)$  that is solely azimuthal and varies only in  $r$ , is unstable to infinitesimal axisymmetric disturbances if

$$\frac{d\kappa^2}{dr} > 0, \quad (1.39)$$

for every  $r$  in the domain, where  $\kappa = rV$  is the swirl function or circulation. That is, the circulation of the flow should not decrease as  $r$  increases away from the axis of rotation. Rayleigh derived this criterion through an energy argument which will be described via the example given by Drazin (2002). Consider two fluid rings of the same volume in an inviscid flow at different radii ( $r_1$  and  $r_2$ ). Each ring possesses an angular momentum per unit mass given by

$$H = rV(r). \quad (1.40)$$

By Kelvin’s circulation theorem, the circulation  $\Gamma = 2\pi H$ , will be conserved when the ring is perturbed. Therefore,  $H$  is conserved. The total kinetic energy per unit volume is

$$\frac{1}{2}\rho V(r_1)^2 + \frac{1}{2}\rho V(r_2)^2 = \frac{1}{2}\rho \left( \frac{H_1^2}{r_1^2} + \frac{H_2^2}{r_2^2} \right). \quad (1.41)$$

The resulting kinetic energy after the interchange of the two fluid rings is given by

$$\frac{1}{2}\rho \left( \frac{H_1^2}{r_2^2} + \frac{H_2^2}{r_1^2} \right). \quad (1.42)$$

The difference is therefore proportional to

$$(H_2^2 - H_1^2) \left( \frac{1}{r_1^2} - \frac{1}{r_2^2} \right). \quad (1.43)$$

Taking  $r_2 > r_1$  without loss of generality, the interchange can only release energy and hence generate instability if  $H_1^2 > H_2^2$ . That is, instability can occur only if

$$\frac{dH^2}{dr} < 0, \quad (1.44)$$

somewhere in the flow and is stable if

$$\frac{dH^2}{dr} > 0, \quad (1.45)$$

is met for all  $r$  in the domain. Hence, a rotating, inviscid fluid described only by azimuthal flow is stable with respect to axisymmetric perturbations if the square of the circulation increases monotonically with radius. This is Rayleigh's circulation criterion for instability. This criterion was later strengthened by Synge (1933), who mathematically determined that the Rayleigh's criterion for stability is in fact sufficient (Drazin 2002; Billant *et al.* 2005). The stability condition is given by

$$\Phi = r^{-3} \frac{d\kappa^2}{dr} > 0, \quad (1.46)$$

where  $\Phi$  is the Rayleigh's discriminant. Note that equation 1.46 is equivalent to equation 1.45, in that the square of the circulation should nowhere decrease as the radius increases. A development of Synge's proof can be found in Green (1995). It should be noted that Rayleigh's argument considered only axisymmetric perturbations in inviscid flows. The flow may still be unstable to non-axisymmetric perturbations even if equation 1.46 is satisfied. A discontinuous velocity profile which inhibits instability via a Kelvin–Helmholtz instability mechanism is such an example (Drazin 2002).

The circulation theorem was extended by Kloosterziel & van Heijst (1991) to a swirling flow imposed on a rotating fluid. That is, the azimuthal velocity consists of a background rotation  $\Omega r$  and a vortex velocity field  $v_\theta(r)$ , and the vorticity is given by the combination of the background vorticity  $f = 2\Omega$  and the relative fluid vorticity  $\omega_z$ . For a vortex whose centre remains on the axis of rotation, the extended criterion can be generalised to the possibility of an instability generated if the product of the absolute velocity and absolute vorticity is negative anywhere in the domain. In mathematical form, the resulting criterion is

$$(v_\theta + \Omega r)(\omega_z + 2\Omega) < 0. \quad (1.47)$$

The general circulation theorem described is limited in that the azimuthal flow is only a function of radius. The range of the domain for which equation 1.47 is true serves as a guideline for the regions of possible instability. Although the criterion is restricted to axisymmetric perturbations, studies have found it as a useful guide even for three-dimensional disturbances (see Carnevale *et al.* 1997; Smyth & Peltier 1994; van Heijst & Clercx 2009).

The effect of axial flow in addition to swirling flow was investigated by Howard & Gupta (1962). This extension derived a sufficient condition for linear stability, given by

$$J = \frac{\Phi}{\left(\frac{du}{dr}\right)^2} > \frac{1}{4}, \quad (1.48)$$

where  $u$  represents the axial velocity component and  $J$  is known as the Richardson number. Violation of this criterion does not guarantee instability but it is necessary. This is a generalised condition to Rayleigh's criterion. That is, the Richardson number criterion of a zero or constant axial component of velocity is equivalent to Rayleigh's circulation criterion (equation 1.46).

Linear stability theory of non-axisymmetric perturbations on columnar vortices have been investigated. The most notable study stems from Leibovich & Stewartson (1983) who considered the stability of inviscid columnar vortex flows involving azimuthal and axial shear in unbounded domains to three-dimensional perturbations. Through the use of asymptotic theory, they were able to derive a sufficient condition for instability given by

$$w \frac{d\Omega}{dr} \left[ \frac{d\Omega}{dr} \frac{d\Gamma}{dr} + \left( \frac{du}{dr} \right)^2 \right] < 0, \quad (1.49)$$

at any point in the flow, where  $\Omega$  represents the angular velocity,  $\Gamma = rw$ , with  $w$  the azimuthal velocity and  $u$  the axial velocity. Also, it is emphasised that the condition is only sufficient and not necessary. Their results were applied to a trailing vortex flow and claim to be comparable to the linear stability analyses carried out by Lessen *et al.* (1974) and the extended studies by Duck & Foster (1980).

## 1.7 Vortex identification and eduction methods

Vortices are abundant in the field of fluid mechanics due to the rotational nature of many practical and existing natural flows. Intuitive examples include tornadoes, hurricanes, Kelvin–Helmholtz vortex rolls, Jupiter's Great Red Spot and wing-tip vortices.

The vortices are generated from various flow instabilities such as those governed by shear, centrifugal and baroclinic processes. The gathered interest in these flows arise from the importance in the roles that the vortical configurations play. These motions enable kinetic energy production, mixing, diffusion and the transport of mass, heat and momentum. Achieving an understanding of how these structures are generated, subsequently evolve and interact is most desired.

The familiar examples previously stated are relatively easily recognised, not due solely to their spatial scales, but rather their distinctive rotating cores. This view contributes to the general perception that a vortex is described by a region of circulating fluid. However, not all rotating motions can be categorised as vortices. An accepted view of what constitutes a vortex is still in much debate with studies working towards a desired universal definition. Despite the difficulty in obtaining a vortex definition, it is clear that at the basic level the word “vortex” is accompanied by thoughts of rotating characteristics.

In order to accurately study flows characterised by vortical features, the vortices within the flow must first be identified and visualised. However, the dual combination of the importance of vortex dynamics and the inconsistent definitions of a vortex presents complexity in visualising and locating vortices. Thus various criteria and techniques have been developed by many authors with considerable progress, though a definitive solution for vortex visualisation still remains elusive. A background into several common methods are described in the following sections as it is important to understand and correctly interpret results from any numerical models. Moreover, several of these methods have been used to advance the research in this thesis.

### **1.7.1 Intuitive definitions**

Jeong & Hussain (1995) recount several techniques for visualising vortices and their inadequacies which they denote as intuitive. These techniques are based on pressure, velocity and vorticity, which are easily calculated or measured. The intuitive approaches are briefly reviewed below.

#### **1.7.1.1 Pressure minimum**

For a steady inviscid planar two-dimensional flow, a rotating flow generally exhibits minimum pressure at the axis of circulating motion. This low pressure arises from the balance of centrifugal force and radial pressure gradient in a steady inviscid planar

flow. However, unsteady, three-dimensional viscous flows cannot adopt the low pressure approach as pressure may have a minimum in all directions at a point or in a plane perpendicular to the vortex axis. Also, if multiple vortices co-exist within the flow, it would be difficult to educe all the vortices if their respective pressure minima differed. This issue was demonstrated by Robinson (1991) where no appropriate pressure level exists in identifying all vortices within a turbulent boundary layer. Importantly, the pressure representation method is inadequate as low pressure does not necessarily imply a swirling structure and vice versa.

### 1.7.1.2 Streamlines and pathlines

A vortical structure can be identified and represented by closed or spiraling streamlines and pathlines in certain flows. This detection method was proposed by Lugt (1979). However, this approach is dependent on the frame of reference used. Indeed, this approach is problematic with the existence of multiple swirling structures as these structures may undergo nonlinear processes. The characterisation via pathlines introduces a vulnerable inadequacy as the production of these circular lines requires that a particle complete a full revolution around the vortex centre. It is clear that this is not always evident, particularly in unsteady and transitional flows. Jeong & Hussain (1995) illustrate the varying streamlines resulting from a Lamb vortex when viewed from different reference frames. Also, it is stated that multiple vortices travelling at different velocities will increase the complication in locating and displaying them.

### 1.7.1.3 Vorticity magnitude

A commonly utilised intuitive measure to educe vortex cores is through the illustration of the vorticity magnitude, defined as  $\omega = |\nabla \times \mathbf{u}|$ . In specific cases, vortex structures have been identified by regions of high vorticity. Hence, regions with vorticity above a user selected threshold of the vorticity magnitude correspond to vortical structures. The arbitrariness of the chosen threshold poses similar problems present with the low pressure definition. That is, the existence of multiple vortices introduces issues in identifying all vortical structures within the flow. Also, indications of vorticity are ambiguous as there is no distinction between rotation due to pure shearing motions and rotation due to swirling motions. Thus, a combination of background shear and vortical activity with the same order of magnitude will evidently mask actual vortex structures. According to Jeong & Hussain (1995), Lugt (1979) has shown that the

maximum vorticity magnitude in planar wall-bounded flows only occurs at the wall surface for where coincidence of vortex cores cannot exist.

#### 1.7.1.4 Discussion of intuitive methods

For simple flows with *a priori* knowledge of the motions, these intuitive techniques may be adequate in providing required insight if used appropriately. Indications of vortical structures are also made possible from using a combination of these intuitive identification and visualisation techniques. Complementary results may strongly signify the existence of a vortex and their location. In short, employing any of the intuitive methods described requires proper attention.

Issues and counter-examples with the definitions described above have been effectively exposed by authors such as Jeong & Hussain (1995) and Cucitore *et al.* (1999). In response to the inadequacies, Jeong & Hussain (1995) suggest that a vortex core should satisfy the following requirements:

1. A vortex core must have net vorticity and therefore net circulation. Thus, the potential flow regions are excluded from vortex cores and a zero cross-section is a potential vortex.
2. The geometry of the identified vortex core should be Galilean invariant.

Galilean invariance implies that the dynamics remain the same regardless of the inertial frame used. It is noted that the three intuitive techniques described fails to satisfy at least one of these two conditions. Thus, definitions based on the Galilean invariant velocity-gradient tensor have been proposed by numerous authors. These methods are presented in the next section.

#### 1.7.2 Velocity-gradient tensor based definitions

Advancements in vortex identification have been driven largely through the desire to understand turbulent motions. Turbulence has been recognised as spatially coherent and temporally evolving vortical motions, rather than just random noise. The majority of the vortex identification, visualisation, criteria and definitions used to investigate such flows have been developed over the last two decades. An overview list of studies has been conveniently tabulated in Kolář (2011) with further listings found in Jiang *et al.* (2005). A large number of these proposed methods have been derived mathematically and usually take advantage of the velocity-gradient tensor  $\nabla\mathbf{u}$ . In determining

vortex structures and their definition requirements, Kolář (2011) has summarised the requirements which include validity for compressible flows, determination of the swirl orientation, Galilean invariance and vortex-axis location. Despite the acknowledgement of these requirements, the definitions proposed have been unable to satisfy all the requirements. Thus, no single study or definition has been proven to be definitive, though it has been noted that the use of multiple methods may be effective (Stegmaier *et al.* 2005). Although existing definitions do not grant a universal solution, they do have the potential of providing useful insight. Indeed, as noted by Chong *et al.* (1990), there may never be a definition of a vortex that will admit universal acceptance.

The most popularly used criteria, namely the  $\lambda_2$  (Jeong & Hussain 1995),  $\Delta$  (Chong *et al.* 1990) and  $Q$  criterion (Hunt *et al.* 1988), are region-type as opposed to line-type methods. These criteria are founded on the properties of the velocity-gradient tensor and are briefly described in the following sections.

#### 1.7.2.1 $\lambda_2$ criterion

The  $\lambda_2$  criterion was developed by Jeong & Hussain (1995) on the basis that a low pressure represents a vortex core. They circumvent the inadequacies of the intuitive low pressure definition previously described, by considering the Navier–Stokes equations without the unsteady irrotational straining and viscous terms. Exclusion of these terms will prevent a pressure minimum arising in the absence of a vortex and retain a pressure minimum within the vortex.

The velocity-gradient tensor  $\nabla \mathbf{u}$  is computed and decomposed into a symmetric part  $\mathbf{S}$  and antisymmetric part  $\mathbf{\Omega}$ , defined by

$$\nabla \mathbf{u} = \mathbf{S} + \mathbf{\Omega}, \quad (1.50a)$$

$$S_{i,j} = \frac{1}{2} (u_{i,j} + u_{j,i}), \quad (1.50b)$$

$$\Omega_{i,j} = \frac{1}{2} (u_{i,j} - u_{j,i}). \quad (1.50c)$$

The subscript indices  $i$  and  $j$  represent the positional components and the notation  $u_{i,j}$  denotes  $u_i$  differentiated with respect to the  $j^{\text{th}}$  direction. Equivalently,  $u_{i,j} = du_i/dx_j$  where  $x$  is the position vector.

Physically,  $\mathbf{S}$  and  $\mathbf{\Omega}$  represent the strain-rate tensor and rotation tensor, respectively. A vortex is defined as a connected fluid region with two negative eigenvalues of  $(\mathbf{S}^2 + \mathbf{\Omega}^2)$ . Since,  $(\mathbf{S}^2 + \mathbf{\Omega}^2)$  is symmetric, it only has three real eigenvalues labelled

as  $\lambda_1$ ,  $\lambda_2$  and  $\lambda_3$ . The classification of these eigenvalues is related to their magnitudes such that  $\lambda_1 \geq \lambda_2 \geq \lambda_3$ . A presence of a vortex core requires that two of the eigenvalues is negative. Thus, the definition of the vortex identification is equivalent to  $\lambda_2 < 0$ . Hence, a field of negative  $\lambda_2$  values is used in visualising the vortical structures in the flow. A restriction with the  $\lambda_2$  definition is that the flow considered is incompressible.

### 1.7.2.2 $Q$ criterion

Hunt *et al.* (1988) developed the  $Q$  criterion which identifies a vortex as connected fluid regions with the second positive invariant of  $\nabla \mathbf{u}$ . For incompressible flows, the second invariant  $Q$  is given by

$$Q = \frac{1}{2} (u_{i,i}^2 + u_{i,j}u_{j,i}) = -\frac{1}{2}u_{i,j}u_{j,i} = \frac{1}{2} (\|\boldsymbol{\Omega}\|^2 - \|\mathbf{S}\|^2). \quad (1.51)$$

Thus, positive  $Q$  values indicate that the vorticity magnitude dominates the strain-rate magnitude. Therefore this situation guarantees that no vortex will be incorrectly deduced from shear flows. However, it has been noted that  $Q > 0$  does not necessarily imply a region of minimum pressure. Hence, Hunt *et al.* (1988) also proposed an additional requirement such that the pressure in the region should be lower than the ambient pressure, if a vortical structure is to be identified.

In many cases, it has been shown that the vortex identification results from the  $Q$  and  $\lambda_2$  criterion are similar far from a wall (e.g. a Bödewadt vortex (Cucitore *et al.* 1999)). The similarity arises from both definitions describing a balance between the rotation and deformation rates of a fluid element; the  $Q$  criterion compares global values whereas the  $\lambda_2$  criterion calculates the balance in the plane of interest. However great differences between the definitions are illustrated when vortices with strong core dynamics exists. In this case, the  $Q$  criterion becomes erroneous.

### 1.7.2.3 $\Delta$ and $\lambda_{ci}$ criteria

The  $\Delta$  criterion was proposed by Chong *et al.* (1990), which identifies a vortex as regions in which the eigenvalues of  $\nabla \mathbf{u}$  are complex (a pair of complex conjugates). In a local reference frame moving with a fluid particle, the eigenvalues determine the streamline pattern. In particular, a pair of complex conjugate eigenvalues represents streamlines that are closed or spiralling. The eigenvalues  $\lambda$  of  $\nabla \mathbf{u}$  satisfies the characteristic equation

$$\lambda^3 + P\lambda^2 + Q\lambda + R = 0, \quad (1.52)$$

where  $P$ ,  $Q$  and  $R$  are the three invariants of  $\nabla\mathbf{u}$ . The  $Q$  invariant (second invariant) has been previously defined (§ 1.7.2.2) while  $P$  (first invariant) and  $R$  (third invariant) are given by  $P = -\nabla \cdot \mathbf{u}$  and  $R = -\text{Det}(\nabla\mathbf{u})$ , respectively. For incompressible flows where  $P = 0$ , the resulting discriminant for equation 1.52 is given by

$$\Delta = \left(\frac{1}{2}R\right)^2 + \left(\frac{1}{3}Q\right)^3. \quad (1.53)$$

Complex eigenvalues exist when the discriminant is positive ( $\Delta > 0$ ).

An extension of this definition has been developed by Zhou *et al.* (1999) known as the swirling strength criterion or  $\lambda_{ci}$  criterion. The criterion identifies vortical regions from the imaginary part of the complex conjugate eigenvalue ( $\lambda = \lambda_{cr} \pm \lambda_{ci}$ ), which is a measure of the local swirling rate inside the vortex. The real component  $\lambda_{cr}$  provides an indication of the compression or stretching strength of the vortex.

An enhancement to the swirling strength criterion has been proposed by Chakraborty *et al.* (2005) which is based on the non-local criterion proposed by Cucitore *et al.* (1999). Chakraborty *et al.* (2005) state three requirements for the identification of a vortex core in three dimensional flow, which are

1. The identification criterion should be Galilean invariant
2. The local flow in the frame of reference translating with the vortex should be swirling
3. The separation between the swirling material points inside the vortex core should remain small.

The first two requirements are satisfied for the  $\Delta$  and  $\lambda_{ci}$  criteria. However, only the enhanced  $\lambda_{ci}$  definition satisfies all three.

#### 1.7.2.4 Discussion on velocity-gradient tensor based methods

The widely used  $\lambda_2$ ,  $Q$  and  $\Delta$  criterion have been described together with extensions of the  $\Delta$  criterion. These approaches are based on the properties of the velocity-gradient tensor  $\nabla\mathbf{u}$ . Although the criteria are Galilean invariant, the results still vary with time-dependent rotations. This objectivity has been investigated by Haller (2005) who derived a definition that is objective and does not require a user-defined threshold, unlike the  $\nabla\mathbf{u}$  based definitions. However, it is not as widely used due to its large computational resource requirements in calculating tracer trajectories.

Importantly, each of the  $\nabla\mathbf{u}$  based definitions require a user-defined threshold to reveal the appropriate vortices. Consequently, the size and boundary of the vortices are quite arbitrary and subjective. Multiple studies have investigated the feasibility and accuracy of these definitions. At least one counter-example exists for each technique which provides erroneous or ambiguous results. The application and discussion of these methods can be found in Jeong & Hussain (1995), Cucitore *et al.* (1999) and Dubief & Delcayre (2000).

Evidently, there has not yet been a proposed definition which offers a universal solution in identifying and visualising vortical structures. Like intuitive methods, these proposed definitions are unable to fulfill many of the vortex detection and visualisation requirements. However, appropriate uses of existing definitions are still able to offer significant information about the flows. Depending on the flow type, certain techniques may be more suitable and therefore knowledge of the flow is beneficial. In addition, a combination of these methods (including intuitive methods) becomes effective in understanding the physics of the flow structure.

## 1.8 Aims of the study

The purpose of this research is to numerically study the stability of shear layers produced in rotating flows. These shear layers are produced via differential rotation forcing imposed on a rotating flow. The basic axisymmetric flows are numerically computed and solved using a spectral-element method. In this study, the base flow is governed by the axisymmetric Navier–Stokes equations, which permit the development of depth-dependent structures. This is a distinct difference to prior numerical studies which have strictly enforced depth independence through the implementation of two-dimensional quasi-geostrophic models. Thus, observations of the shear-layer structure are made in accordance to the changes in any of the governing parameters ( $Ro$  and  $E$ ). In addition, comparisons of these observations will be performed to determine the validity of the quasi-two-dimensional model.

Linear stability analysis will uncover the most unstable azimuthal mode specific to a flow condition. The structure of this mode can be visualised in isolation to the base flow, which is particularly difficult in an experimental setting. A wide examination of the parameter space with the determination of the preferential mode will allow a mapping of the unstable linear mode as a function of  $Ro$  and  $E$ . Linear stability analysis will

also reveal other global instabilities that have not yet been recognised in the literature. Differences in flow structure and instability between positive and negative  $Ro$  will be investigated. Again, comparisons between the axisymmetric and the quasi-two-dimensional model relating to the preferred azimuthal wavenumbers will be established to investigate the significance of the  $E^{1/4}$  and  $E^{1/3}$  Stewartson layers.

Three-dimensional direct numerical simulations are undertaken to monitor the effects and significance of nonlinear effects. These nonlinear effects may change the stable azimuthal structure observed and may also prohibit certain instability modes or types from growing. The sensitivity of the flow to initial conditions will also be examined by perturbing the axisymmetric steady-state base flows and saturated flows with white noise and a variety of unstable linear modes.

Although the parameter condition of these numerical flows do not quantitatively match those in nature where Reynolds numbers are very high, qualitative details may still provide insights to natural atmospheric flows. In addition, the implementation of the quasi-two-dimensional model permits a larger parameter space to be studied, and the results of which will be compared to the axisymmetric and three-dimensional model. More importantly, this numerical study aims to draw a connection between numerical and previous experimental results. The previous experimental studies are described in the next chapter in addition to the review of these aims specific to the past literature. The key findings from this numerical study will further increase the fundamental knowledge of shear layers in rotating flows.

## 1.9 Structure of the thesis

This thesis is comprised of eight chapters. Following this introductory chapter, Chapter 2 presents a thorough review of the literature surrounding unstable Stewartson layers that resemble those of planetary vortices. Chapter 3 details the numerical methodologies used throughout this research and its validation. The numerical results form Chapters 4-7 with the first three result chapters dedicated to the three-dimensional modelling of the differential-disks double end-wall configuration. Chapter 4 describes the structure of the axisymmetric base flow and Chapter 5 establishes its linear stability. Chapter 6 presents results relating to the significance of nonlinear effects in these rotating systems. A comparison of the axisymmetric and non-axisymmetric simulations in the prior chapters to the results of the quasi-two-dimensional model are revealed in

Chapter 7. Concluding remarks are provided in Chapter 8 in addition to suggestions for future research.

## Chapter 2

# A Review of the Literature

A review of the literature involving structures resembling those of polar vortices that have been reproduced experimentally and numerically are described in this chapter. This review is structured as follows.

§ 2.1 reviews investigations into the stability of conceptually simple shear flows. The purpose of this section is to provide an introduction and an appreciation of the complexity of flow stability and the pursuit of an understanding of flow transitions. The remaining sections focus on rotating flows which have been able to reproduce structures that exhibit features similar to those observed in planetary polar vortices. That is, flows which facilitate instabilities capable of causing deformations in the azimuthal direction. This begins with a review of hollow vortex core flows in § 2.2. Following this, the generation of non-hollow vortical structures in a source-sink configuration is described in § 2.3. § 2.4 presents studies pertaining to the differential-disk rotation apparatus and contributes to bulk of this chapter as it is closely related to the research of this thesis.

This chapter concludes with a summary of the related work in § 2.5 and the proposed aims and hypotheses of the project in § 2.6.

### 2.1 Transition to turbulence in shear flows

Shear flows engender great interest due to their intriguing stability behaviour. Such flows are able to exhibit a wide variety of flow states, for which an understanding is desired from a fundamental point of view. Conceptually, some of the simplest examples include Couette, Poiseuille and Taylor–Couette flow. Plane Couette flow involves fluid between two parallel plates with shear imparted by the movement of one or both plates at a constant speed in opposite directions (Leutheusser & Chu 1971; Daviaud *et al.*

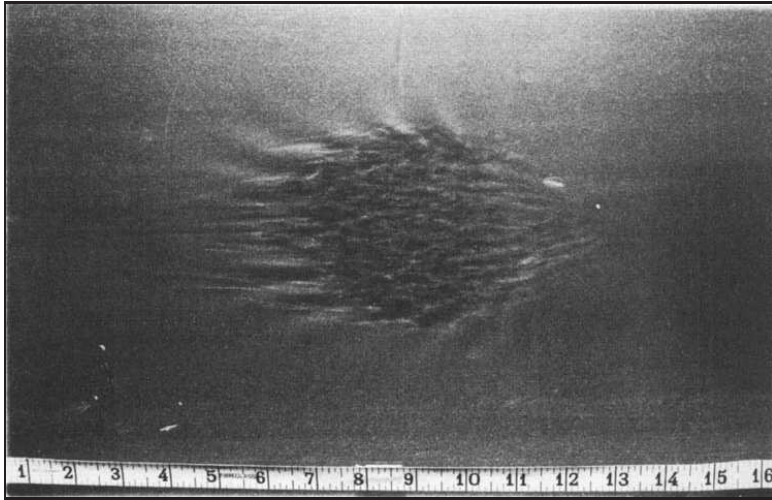


FIGURE 2.1: An illustration of a turbulent spot at the onset of instability in a plane Poiseuille flow. This figure is reproduced from Carlson *et al.* (1982) with permission from the Cambridge University Press.

---

1992). For plane Poiseuille flow, the plates are stationary and the flow is driven by a non-zero pressure gradient in the streamwise direction (Carlson *et al.* 1982). The Taylor–Couette flow is described by a viscous fluid in an annulus driven by two rotating cylinders (Taylor 1923).

The Couette, Poiseuille, and Taylor–Couette flow have been central in investigating the mechanisms and processes in the transition from laminar to turbulent flow. The transition point, generally measured by a flow parameter, is of particular interest due to the large differences in properties between the laminar and the turbulent flow regimes. The presence of irregular fluctuations in velocity provides an increase in mixing and the transfer of heat, mass and momentum which is of considerable importance in many engineering applications (Jiménez 2004; Dimotakis 2005; Avila *et al.* 2011). Indeed it was the observed flow disruptions in a pipe flow by Reynolds (1883) that pioneered such hydrodynamic stability research. Although investigations began over a century ago, many of the phenomena remain unanswered with new discoveries and validations still being achieved in recent times (e.g. Kuik *et al.* 2010; Moxey & Barkley 2010). These classical problems have become fundamental in fluid mechanics.

Linear stability analysis has been a useful tool in providing an indication of where the instability transition occurs as a function of one or more flow parameters; this is typically measured by the Reynolds number based on the centreline velocity and half

the channel width for Couette and Poiseuille flow (Nishioka *et al.* 1975; Carlson *et al.* 1982). However, the onset of turbulence may not always be predicted using linear stability analysis. Plane Poiseuille flow is such an example whereby the flow has been determined to become linearly unstable to Tollmien–Schlichting waves at  $Re_c = 5772.22$  (Orszag 1971; Bayly *et al.* 1988) through the solution of the Orr–Sommerfeld equation (1.26). However, experiments have demonstrated turbulence at much smaller values of  $Re$  than those predicted by linear stability analysis. Thus, subcritical instability occurs in plane Poiseuille flow. Orszag & Kells (1980) were able to establish a transition to turbulence around  $Re = 1000$  given that the disturbances are of finite amplitude via direct numerical simulation. In contrast, Nishioka *et al.* (1975) was able to maintain laminar flow up to a Reynolds number of  $Re = 8000$ . Flow visualisation of the structures in this turbulent regime was first captured by Carlson *et al.* (1982) with a determined onset described approximately by  $Re = 1000$ . The most prominent structure was a turbulent spot, which is illustrated in figure 2.1.

In contrast to plane Poiseuille flow, plane Couette flow has been determined to be linearly stable to all  $Re$  (Romanov 1973). Despite this, turbulence has been observed in experiments at relatively small  $Re$ . Pipe Poiseuille flow is also believed to be linearly stable for all Reynolds numbers. Given the difficulty in designing an apparatus that can produce pure plane Couette flow, there is limited experimental literature regarding its transition to turbulent flow. The first flow visualisations were obtained by Tillmark & Alfredsson (1992) through the use of an infinite-belt type channel with counter-moving walls. The determined transition point was  $Re_c = 360 \pm 10$ . Two prior experiments without visualisation ascertained critical values of  $Re_c = 280 \pm 20$  and  $Re_c = 750$  by Leutheusser & Chu (1971) and Reichardt (1956), respectively. The large discrepancies in these values may be attributed to the set-up of the experiments, the differences in the inlet disturbance amplitudes, experimental noise, and the monitoring techniques used. Numerical work concerning the transitional point was investigated by Orszag & Kells (1980) who found  $Re_c \approx 1250$ . Direct numerical analysis by Lundbladh & Johansson (1991) found that turbulent spots could be sustained at a Reynolds number as low as  $Re = 375$ , which is close in value to the experimental studies of Tillmark & Alfredsson (1992) and Daviaud *et al.* (1992) of  $Re = 370 \pm 10$ . Although plane Couette and plane Poiseuille flow present qualitatively similar features, the quantitative characteristics are very different.

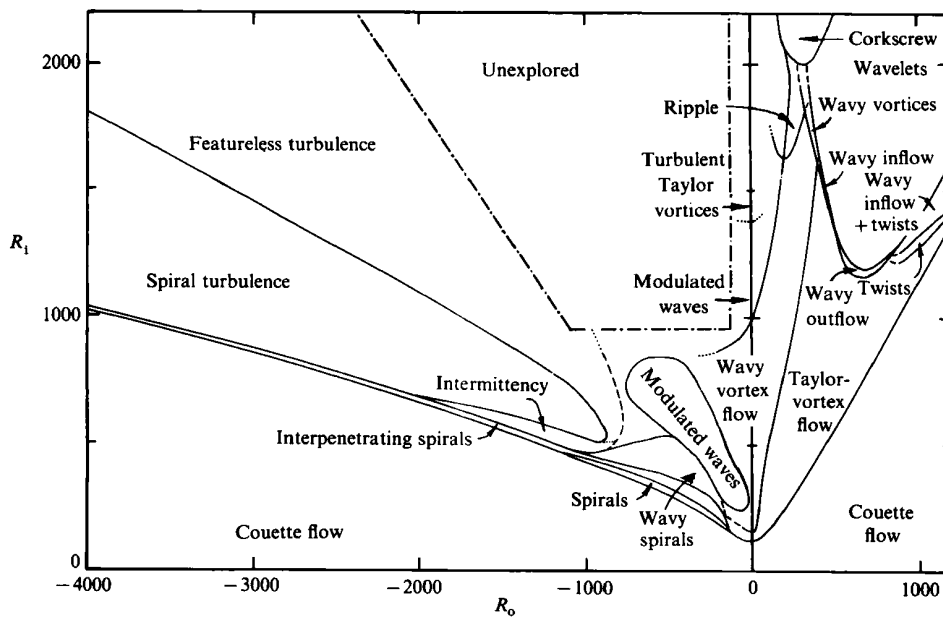


FIGURE 2.2: An illustration of the various regimes that may exist in a Taylor–Couette flow. The parameters  $R_i = a(b - a)\Omega_i/\nu$  and  $R_o = b(b - a)\Omega_o/\nu$  represent the inner (subscript  $i$ ) and outer (subscript  $o$ ) Reynolds numbers, respectively, where  $a$  is the inner radius,  $b$  is the outer radius and  $\Omega$  represents the rotation rate. This figure is reproduced from Andereck *et al.* (1986) with permission from Dr. David Andereck and the Cambridge University Press.

A succession of bifurcations to flow states that are not turbulent may exist between the laminar and turbulent flow regime. Such bifurcations are evident in the Taylor–Couette flow. According to Rayleigh’s criterion (§ 1.6), it is possible for the Taylor–Couette flow to be unstable for any inner cylinder rotation rate, provided the outer cylinder is stationary. The investigation of this flow was pioneered by Taylor (1923) who found remarkable agreement between his numerical and experimental results. For low rotation rates of the inner cylinder, the flow is stable and demonstrates a laminar Couette-like flow. This state is known as a circular Couette flow. The flow becomes unstable to axisymmetric perturbations when the angular velocity of the inner cylinder exceeds a critical value. This unstable flow exhibits axisymmetric toroidal vortices and is known as the Taylor vortex flow. Further increases to the angular speed promoted transitions to other flow states such as wavy vortex flows and spiral vortex flows. Since this pioneering work, a vast number of studies have been conducted and many more flow states have been discovered. A highlighted study stems from the work of Coles (1965) who established that these periodic flows are non-unique to Reynolds numbers and

that for a given  $Re$ , twenty or more different flow states could be produced. A perfect illustration of how complicated this forced-flow can become is shown in figure 2.2. The figure represents a regime diagram of the different flow states as functions of the Reynolds numbers based on the inner and outer rotation rates.

This section has briefly presented the variety of thrilling phenomena that can exist in even the simplest of shear flows. These canonical flows have been developed with the aim of understanding flow transitions from laminar to structured unstable flows, and eventually turbulent flow. This is significant as certain engineering applications aim to either avoid or generate turbulent environments, typically with the aim of improving efficiency. Further details and examples of these flows can be found in texts such as Chandrasekhar (1961), Schmid & Henningson (2001), Drazin & Reid (2004) and references therein.

## 2.2 Hollow vortex core flow

Free surface flows in a rotating container may demonstrate a parabolic deformation of hollow depression at the centre. The balance between the horizontal pressure gradient and the centrifugal forces explains this result. However, this parabolic deformation may exhibit an azimuthal polygonal shape for certain conditions when a rotating base and a stationary side wall are employed. This simple confinement has exhibited structures that resemble those observed in geophysical, astrophysical and industrial environments (e.g. Lopez *et al.* 2004; Jansson *et al.* 2006; Cogan *et al.* 2011; Tophøj *et al.* 2013).

A rotating disk located near the base of a stationary open container was qualitatively investigated by Vatistas (1990). The apparatus is illustrated in figure 2.3. The motion of the disk imparts centrifugal forces in the flow that pushes the fluid outwards towards the fringe of the container. The receding fluid at the centre exposes the disk for which the perimeter of the hollow core reveals a polygonal stationary state. It was found that for low angular velocities, the core was always filled and displayed a circular shape. With increasing angular velocity, an elliptical shape was initially formed. Further increases causes a greater surface depression that ultimately results in a hollow core exhibiting polygonal modes on the disk. It was also found that polygonal shapes with lower azimuthal wavenumbers are sustained over a wider range of angular frequencies compared to the higher-wavenumber polygonal structures. The decreasing frequency bandwidth at higher wavenumbers caused difficulty in visualising stationary

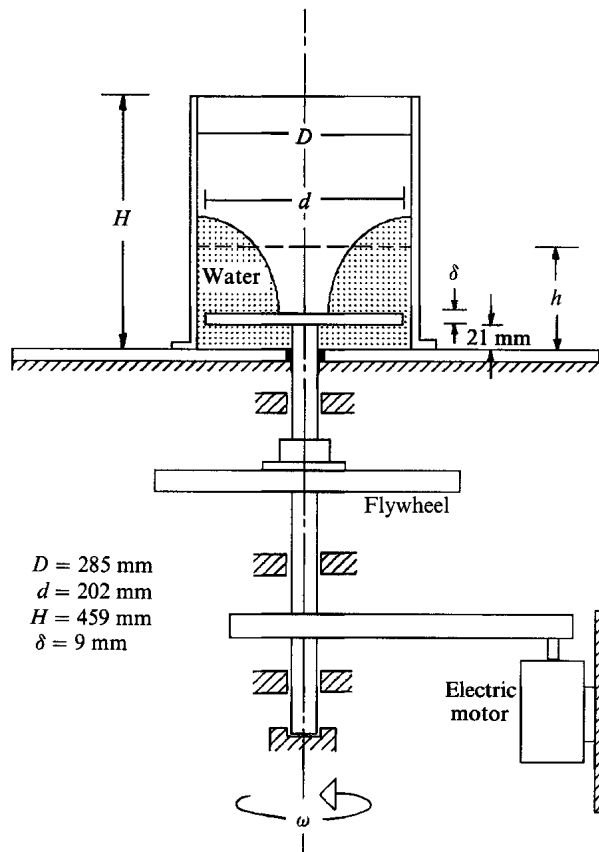


FIGURE 2.3: A schematic of the apparatus used to create hollow vortex cores. This figure is reproduced from Vatistas (1990) with permission from Dr. Georgios H. Vatistas and the Cambridge University Press.

states greater than wavenumber 6. It was also noted that the surface tension rounded off the crests and troughs of the waves, which prohibited clear structural identification. Evidently an alternative apparatus is required for studying a larger range of stationary states.

An extension of the study with a variety of viscous fluids was performed by Vatistas *et al.* (1992). A working fluid of water ( $\nu = 1.00 \times 10^{-6} \text{ m}^2/\text{s}$ ) produced similar results described in Vatistas (1990). Again, stationary states beyond the  $N = 6$  mode were not seen as the flow would change transient states over time while greater rotation rates displayed chaotic flow characteristics. Two different oils were used in the experiments, characterised by a viscosity of  $\nu = 5.67 \times 10^{-5} \text{ m}^2/\text{s}$  and  $\nu = 6.4 \times 10^{-4} \text{ m}^2/\text{s}$ . Both fluids exhibited completely different behaviors in comparison to water. For the less viscous oil, core patterns between  $N = 1$  and  $N = 11$  were observed. Unlike water, the

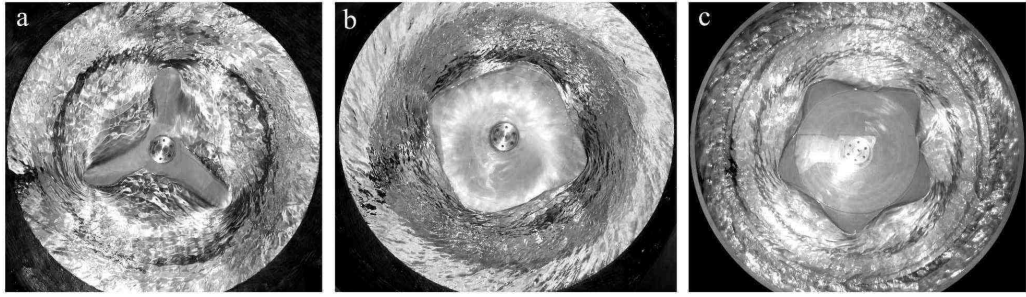


FIGURE 2.4: Typical examples of polygonal patterns observed in water when viewed from above. Illustrated polygons of a (a) wet triangle, (b) a square and (c) a pentagon. This figure is reproduced from Jansson *et al.* (2006) with permission from Thomas R. N. Jansson and the American Physical Society.

unstable mode observed did not increase orderly with increasing rotation rate, rather the changes were abrupt. Sub-harmonically modulated states were also encountered. Fluctuations in preferable states were observed for experiments of different depths, spin up and spin down. These differences clearly express the existence of hysteresis in the flow. The oil with a greater viscosity demonstrated highly stable flow typically exhibiting a circular core. Stationary waves were only seen for large depths at high disk speeds. The flow evolution was found to be affected by the disk speed, the kinematic viscosity and the initial liquid height. Explanations for the major differences in preferential modal trend seen between water and oil were not provided, although a suggestion would be that of the Ekman number difference which is related to the fluid viscosity.

The symmetry breaking of the free surface to azimuthal disturbances was also explored by Jansson *et al.* (2006) in a cylindrical tank. The disturbances were induced by the rotation of the entire bottom plate of the tank with stationary sidewalls. The difference between this set-up and the one used by Vatistas (1990) is the considerable gap between the rotating disk and the base (see figure 2.3). Two different set-ups of varying cylinder radius were studied. This had been a neglected parameter in previous studies. The difference between the two radii cases investigated is approximately a factor of 1.5. A working fluid of water exhibited typical hollow vortex cores with azimuthal wavenumbers ranging between  $N = 2-6$ , with several examples reproduced in figure 2.4.

Unlike Vatistas (1990), who reported stationary and mixed states, Jansson *et al.* (2006) observed spontaneous breaking of axial symmetry on the surface. The state

of the flow was defined by two control parameters, the rotation frequency and the height of the undisturbed fluid. These key parameters were used to map the azimuthal wavenumber of various stationary states observed. In agreement with past experiments, it was seen that an increasing rotation rate leads to an increasing azimuthal wavenumber for a fixed initial height. The primary height of the fluid was found to have an effect with a decrease in azimuthal wavenumber with increasing height for a fixed rotation rate. These relationships described both “dry” and “wet” polygons where dry polygons are formed on the surface of the disk and wet polygons formed above the disk. The transition lines between polygonal states were demonstrated on a phase diagram as a function of the rotation rate and the initial fluid depth. The transition between the observed wavenumbers are described roughly by a positive linear relationship for both radii cases. The transition lines and observed states were seen to vary with radii and viscosity. Slight differences were seen between the two radii cases with water, while a large discrepancy was demonstrated with ethylene glycol, which is 15 times more viscous than water. Only azimuthal wavenumbers from  $N = 0$  to  $N = 3$  was demonstrated for ethylene glycol. It is possible that the viscosity diffuses and dissipates the perturbations that lead to the formation of higher modes. Also, it was suggested that the vortices that form on the periphery of the polygonal sides are due to the shear layer induced by the stationary side wall, which is susceptible to a Kelvin–Helmholtz–Rayleigh type instability.

Vatistas (1990) and Jansson *et al.* (2006) investigated rotating flow in different configurations and of differing aspect ratio. The aspect ratio is defined as  $\sigma = R_d/R_t$  where  $R_d$  is represents the radius of the bottom rotating disk and  $R_t$  represents the cylindrical tank radius. The effect of varying the aspect ratio was reported by Vatistas *et al.* (2008). For  $\sigma < 1$ , the flow reveals a circular vortex core for low rotation rates. Gradual increases in rotation transforms the circular state ( $N = 0$ ) into a precessing circular core ( $N = 1$ ). Further increases leads to successive polygonal states up to hexagons ( $N = 6$ ). Modes above  $N = 6$  were not clearly seen as higher rotation rates are said to amplify dynamical noise that wash out the sharp spectral peaks. Mixed states are evident between pure modes, which is in agreement with observations of Vatistas (1990). As for  $\sigma = 1$ , the spontaneous symmetry breaking seen by Jansson *et al.* (2006) was confirmed. The experiments demonstrated that high-wavenumber structures only exist over a short bandwidth of rotation rates. This is particularly true

for wavenumber 6 which appears to exist only between disk speeds of 225-227 rpm as compared to wavenumber 3 which exists over a span of approximately 35 rpm. Hence, identifying the existence of a mode 7 structure would be very difficult. Vatistas *et al.* (2008) have reported that their results are in great agreement with theoretical work of vortices arranged in a circular row with an exterior boundary (see references therein). Those studies have found stability for  $N < 6$  states and instability for  $N > 8$  states. The  $N = 7$  state has been found to be both stable and unstable depending on the type of analysis performed.

The continuation of the work of Vatistas *et al.* (2008) and Abderrahmane *et al.* (2009) is detailed in Abderrahmane *et al.* (2011) with the focus on pattern transition. With water as the working fluid, three parameters that influence the resulting structure of the flow were determined to be the initial water height  $h_0$ , disk frequency  $f_d$ , and the disk radius  $R_d$ . A combination of these parameters yield the dimensionless Froude number given by

$$Fr = \frac{R_d f_d}{2\pi\sqrt{gh_0}}, \quad (2.1)$$

where  $g$  denotes the gravity. This non-dimensional parameter was deemed most appropriate for dictating the state of the flow. It was observed that increases in  $Fr$  yields transitions from a lower-wavenumber to higher-wavenumber polygonal pattern. Increasing  $Fr$  is achieved by either one of increasing the disk rotation, lowering the initial height or increasing the disk radius, while the other parameters remain fixed. An in-depth study of the transitions from  $N = 2$  to 3 and  $N = 4$  to 5 was reported in Abderrahmane *et al.* (2009) and the phenomena generalised in Abderrahmane *et al.* (2011). A spectral analysis of the time series of the polygonal structure revealed two distinct wave frequencies, namely the dominant parent wave frequency  $f_m$ , and a lesser daughter wave frequency  $f_g$ . The spectral peaks are determined by the parent's wave harmonics and the subtraction/addition of the parent wave to the daughter wave. The power spectra of the transitions from  $N = 2$  to  $N = 3$  and  $N = 3$  to  $N = 4$  are reproduced in figure 2.5. As  $Fr$  increases and evolves towards the higher state, the amplitude of the daughter wave becomes comparable and eventually dominates the parent wave. The flow was found to be in a state of synchronisation with the locking of the parent and daughter waves when the ratio of  $f_m/f_g$  is rational. The ratio of  $f_m/f_g$  was determined to be

$$\frac{f_m}{f_g} = \frac{N-1}{N}, \quad (2.2)$$

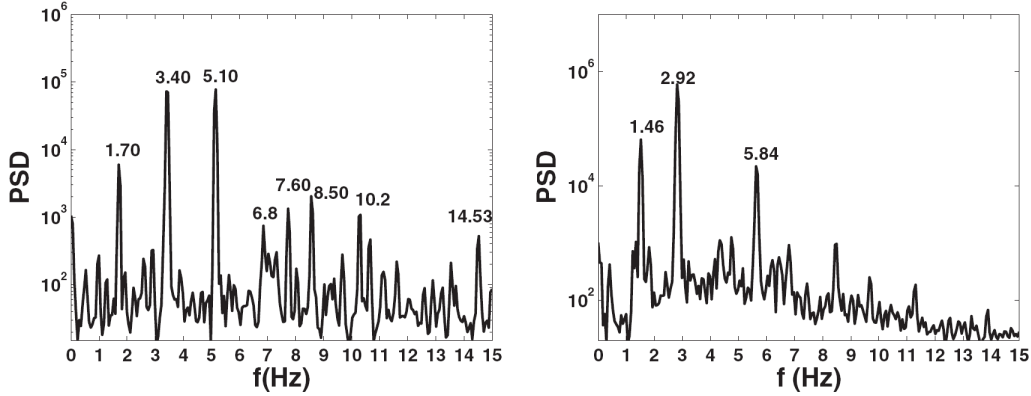


FIGURE 2.5: The power spectrum of the radial displacement during the transition phase from (left)  $N = 3$  to  $N = 4$  with frequency locking between two intrinsic modes  $f_m = 3.4$  Hz and  $f_g = 5.1$  Hz, and (right)  $N = 2$  to  $N = 3$  with frequency locking between  $f_m = 1.46$  Hz and  $f_g = 2.92$  Hz. This figure is reproduced from Abderrahamne *et al.* (2009) with permission from the American Physical Society.

where  $N$  is the mode of the initial equilibrium state. For the subsequent transition, the  $f_g$  becomes  $f_m$ . Thus two processes are involved from the transition from mode  $N$  to  $N + 1$ . Initially, the pattern is characterised by the ratio  $f_m/f_g$ , which is irrational and the dynamics are quasi-periodic. As  $Fr$  increases, the daughter wave strengthens and the ratio  $f_m/f_g$  approaches a rational value. The rational value represents the transition from  $N$  to  $N + 1$  where the parent wave and daughter wave locks and exhibit synchronicity. It was further found that the frequency of the disk to the polygon frequency was equal to  $1/3$ , which is independent of the Froude number. This is in agreement with what has been found by Miraghaie *et al.* (2003), although it is in contrast to the findings of Jansson *et al.* (2006), Poncet *et al.* (2007) and Vastistas *et al.* (2008).

Despite these previous studies, the instability leading to polygonal formation is still unexplained. Bergmann *et al.* (2011) set out to fill the knowledge gap by investigating the development of a triangular polygon. The apparatus used was similar to that used by Jansson *et al.* (2006). It was noted that the generated polygon structure is robust and stable, and was developed using three different approaches. The approaches were of either increasing rotation rate from rest, starting from a manually destroyed fully developed triangle or decreasing the rotation rate from an initially high rotation rate. All three approaches resulted in the same eventual structure of a triangle, which implies

that the flow is insensitive to initial conditions.

The instability forming these surface polygons are not thought to be of pure barotropic instability and Kelvin–Helmholtz instability. This is because these instabilities occur primarily in two-dimensional flows whereas the instability producing these hollow core vortices appear to be three-dimensional. This may be the primary reason for why there is a lack of numerical studies concerning these flows. However, great insight into the formation of these structures can potentially be provided from understanding two-dimensional instabilities forming similar polygonal structures. It may be possible that extremely wet polygons are structures resulting from a two-dimensional instability, which then manifest into three-dimensional structures as the depth of the fluid depresses towards base.

Attention is now turned to the class of vortex flows central to this thesis, that of non-hollow vortex core studies, which are described in the sections to follow.

## 2.3 Source-sink flow

Vortex structures closely resembling polar vortex structures have been generated in rotating systems forced by fluid injection and extraction. The flows produced from these configurations are known as source-sink flows. Typically, these involve a rotating tank with ports located on the boundaries of the tank that can either act as sources (fluid injection) or sinks (fluid extraction). Initially, these experimental configurations were used primarily in investigating the transport of mass through boundary and shear layers. Following this, studies investigating the instability and appearance of source-sink flows were conducted. Both of these aspects are described in this section, with particular attention focused on the latter.

### 2.3.1 Transport through boundary and shear layers

Various distributions of sources and sinks in a rotating container have been studied by numerous authors both theoretically and experimentally. This type of forcing provides a closer relationship to problems of atmospheric and oceanic current flows. These flows are also applicable to industry such as those involving gas centrifuges and chemical bio-reactors. As noted by Matsuda *et al.* (1975), compressibility effects are significant in gas centrifuges. However, they find that the structure of the shear layers in the flow remain essentially unchanged compared to those under incompressible conditions.

Thus, many theoretical works have considered incompressible flows as they are simpler to study. Also, the fluid motion is assumed to be very slow compared to the angular velocity of the system (small  $Ro$ ) such that nonlinear effects can be neglected.

Barcilon (1967) investigated the flow induced by radially pumping and withdrawing fluid through the vertical side wall of a rotating cylinder. The cylinder is filled with a viscous incompressible fluid. Theoretical consideration of this configuration found that vertical transport is achieved via the Stewartson  $E^{1/3}$  layer while the horizontal transport occurs in the interior. This is in contrast to the experimental results of Hide (1968) who found horizontal motion confined to the Ekman layer. This contradiction could be due to the difference in configuration considered between the two authors. Hide (1968) studied a cylindrical rotating system with a vertical line source and vertical line sink under various arrangements. Barcilon (1967) claims that the simple experimental set-up failed to demonstrate any significant motion in the Ekman layer, visualised through dye. In addition, any dye introduced into the flow interior was shown to transit towards the sink via the interior region.

Later theoretical work by Hashimoto (1975) considered an incompressible viscous fluid in a rotating circular cylinder. The majority of mass transport was observed to occur through the horizontal and vertical shear layers. The sources and sinks were represented as concentric circles on the top and bottom surfaces. The positioning of the sources and sinks along the radius were varied and the effect of a discontinuity in angular velocity across the entry and exit points was explored. The discontinuity in the angular velocity produced  $E^{1/3}$  and  $E^{1/4}$  Stewartson layers around the periphery of the sources and sinks. These results were observed experimentally by van Heijst (1984) in which a ring source is located in the fluid interior while a ring sink is prescribed around the bottom corner.

### 2.3.2 Unstable flow

Prior studies have focused on investigating the transport of fluid in the shear layers and its respective vertical structure produced via a source-sink forcing. The stability of these shear layers and the possible deformations were not examined. Sommeria *et al.* (1988) and Meyers *et al.* (1989) proposed that Jupiter's Great Red Spot may be related to a westward jet on a background shear. Thus, they experimentally studied the stability of a jet. Their particular arrangement involves a rotating annular tank with 3

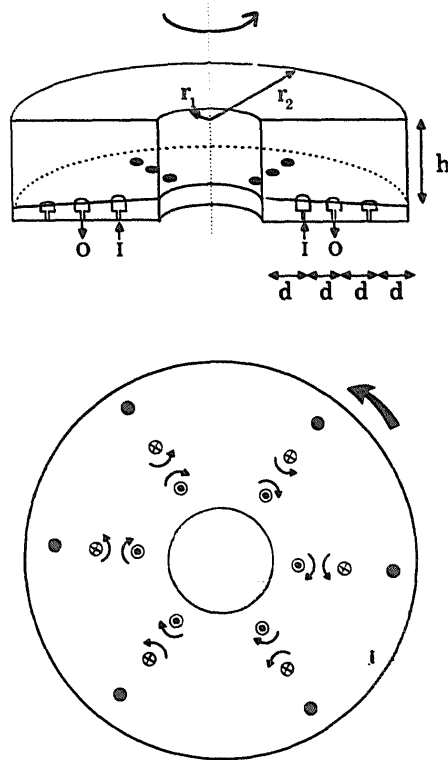


FIGURE 2.6: (Top) A cross section of the tank used for source-sink experiments. (Bottom) A top-down view of the configuration with the expected flow direction above each port where partially filled circles represent sources, crossed circles represent sinks and filled circles represent inactive ports. This figure is reproduced from Meyers *et al.* (1989) with permission from Dr. Steven Meyers and Elsevier.

rings comprised of 6 holes each at its base which could act as either a source or a sink. A schematic of the configuration is shown in figure 2.6. This particular configuration could induce a continuous circulation that mimics the mass transfer between tropical latitudes to the polar latitudes. Fluid jets which are susceptible to instability are formed as a result of the continuous poleward flux.

Water was used as the working fluid to match the density of the polystyrene latex spheres used for streak photography. A conical base was used to replicate the  $\beta$ -effect and free-surface effects were ignored by using a solid lid. Experiments achieved small Rossby number flows by rapidly rotating the tank. At low pumping rates, vortices developed above the sources and sinks and remained stationary relative to the original sink or source. The vortices only begin to drift with the flow when the forcing is increased beyond a sufficient value. The drift of the vortices develops a jet that is sus-

ceptible to instabilities. An unstable jet portrays a waviness in the azimuthal direction with its borders resembling a polygon. Two dimensionless parameters were chosen to characterise the flow conditions, namely the jet width  $L^*$ , and the ratio of the Ekman friction time to an eddy turnover time  $T^*$ . These are defined as

$$L^* = \frac{c_2}{r_m} F^{1/3} \Omega^{-1/6}, \quad (2.3)$$

$$T^* = \frac{h_0 c_1}{2c_2 \nu^{1/2}} (F \Omega)^{1/3}, \quad (2.4)$$

where  $c_1 = (s d^2 / 2 \pi^2 \nu h_0 r_m^2)^{1/3}$ ,  $c_2 = (d h_0 / 4 \pi s r_m \nu^{1/2})^{1/3}$ ,  $F$  as the pumping rate,  $r_m$  is the radial position of the jet,  $d$  as the separation distance between the sources and the sink,  $s$  as the slope of the bottom topography and  $h_0$  is the mean depth of the tank. The constants of  $c_1$  and  $c_2$  were determined by physical arguments. Specifically, the torque arising from the action of the Coriolis force on the radially pumped fluid is balanced by the torque arising from the dissipation in the boundary layers. Thus, the width and maximum velocity of the jet are only approximations.

At a sufficient pumping rate, the rotating flow becomes unstable to barotropic instability, which develops a polygonal structure comprised of multiple vortices. Vortices were primarily observed in a westward forcing (inner ports acting as sources). These vortices began to merge upon further increasing of the pumping rate. During the merging process, a particular vortex increases its speed which causes it to subsequently pass through the other vortices. Upon each vortex-vortex interaction, the faster vortex imparts an amount of its energy until it is completely consumed. Thus a structure of 5 vortices would become 4, then 3 and eventually a monopole provided the pumping rate was increased gradually and sufficiently. At each step, the remaining vortices become stronger and larger, filling up a larger portion of the tank. The number of vortices observed under particular flow conditions were mapped on a regime diagram as a function of  $L^*$  and  $T^*$ . A range of 1 to 5 vortices was observed in the parameter space explored with  $L^*$  ranging between  $0.3 \leq L^* \leq 0.45$  and  $T^*$  ranging between  $20 \leq T^* \leq 80$ . The resulting monopole vortex displayed a similar appearance to that of Jupiter's Great Red Spot. In addition, a few similar properties were observed between the experimental vortex and Jupiter's spot. These include that the primary monopole consumed any introduced vortices of lesser strength, that the vortex has vorticity of the same sign compared to the background rotation, and that the spot's length to width ratio is approximately 2. Also, the vortex was observed to be very robust. Dye introduced into

the vortex remained in the vortex for long time periods while dye introduced outside the vortex quickly mixed with the background flow. The arrangement of the sources and sinks was claimed to have no effect on the resulting structure, provided the momentum and energy production and the velocity of the flow with respect to the forcing ports remained the same. That is, closing all the ports on one side of the tank produced structures similar to those created if all ports were open.

Sommeria *et al.* (1989) and Sommeria *et al.* (1991) furthered their previous work with a primary focus on eastward jets. The work was motivated by Earth's oceanic and atmospheric flows, which are dominated by Coriolis forces. They used the same apparatus as that in Sommeria *et al.* (1988). The vortices produced above each port remained stationary for  $F < 15 \text{ cm}^3/\text{s}$  and began to drift for  $F > 15 \text{ cm}^3/\text{s}$ , which resulted in a jet. Radial pumping towards the centre of the tank (inner ports acting as sinks) produces an eastward jet while radial pumping away from the centre (inner ports acting as sources) produces a westward jet. From the obtained data, the azimuthal profiles of the jets exhibited a  $\text{sech}^2$  profile with differences between westward and eastward jets. The maximum jet velocity and the width of the jet were revised as

$$U_0 = \left(\frac{b}{a^2}\right)^{1/3} \left(\frac{sd^2}{2\pi^2\nu h_0 r_m^2}\right)^{1/3} (\Omega F)^{2/3}, \quad (2.5)$$

$$L = \left(\frac{1}{ab}\right)^{1/3} \left(\frac{dh_0}{4\pi s r_m \nu^{1/2}}\right)^{1/3} \Omega^{-1/6} F^{1/3}, \quad (2.6)$$

where  $a = 2$  and  $b = -1/2$  for an eastward jet and  $a = 2$  and  $b = 3/2$  for a westward jet.

Assuming that the jet has a velocity profile described by  $U(y) = U_0 \text{sech}^2(y/L)$  yields a development of an instability criterion through a normal mode approach. This velocity profile is known as the Bickley jet and the normal mode approach follows that detailed in § 1.5.1. That is, the gradient of absolute vorticity ( $\beta - d^2U(y)/dy^2$ ) must change sign somewhere in the flow for the possibility of instability. Although  $\beta$  is positive, changing its sign is mathematically equivalent to reversing the flow direction. Hence, a westward jet corresponds to  $U(y) = -U_0 \text{sech}^2(y/L)$  with  $\beta > 0$ . The analysis determined that an eastward jet is unstable for  $\beta^* < 2/3$  and a westward jet is unstable for  $\beta^* > 2$ . Here  $\beta^*$  is the  $\beta$ -effect non-dimensionalised by  $L^2/U_0$ . Thus, the  $\beta$ -effect is required to be three times stronger to stabilise a westward jet compared to an eastward jet with a  $\text{sech}^2$  profile. In other words, a jet with a narrow width would be stable for an eastward jet but unstable for a westward jet, assuming that they both

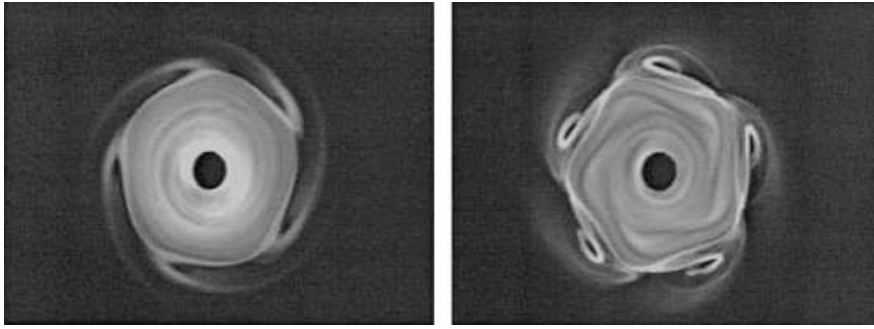


FIGURE 2.7: Visualisation of vortex chains in the presence of pumping for (left)  $Re = -42$  and (right)  $Re = 110$ . This figure is reproduced from van de Konijnenberg *et al.* (1999) with permission from the Cambridge University Press.

---

exhibit a  $\text{sech}^2$  profile. From a linear stability analysis, the wavelength of a sinusoidal instability for a marginally stable eastward jet on a  $\beta$ -plane is given by  $\lambda = \pi L \sqrt{2}$ . Many analytical solutions for the Bickley jet can be found in Maslowe (1991), Burns *et al.* (2002), Engevik (2004), Drazin & Reid (2004) and references therein. Consequently the wavenumber can be predicted and for the range of  $L$  obtained, the wavenumber dependence on  $\Omega$  and  $F$  compared qualitatively well to the experimental observations. However, there were quantitative discrepancies which are attributed to the flow being highly nonlinear with large amplitude waves resembling wavenumbers structures of 3 to 8 for an unstable eastward jet. Increasing either  $\Omega$  or  $F$  has the same effect as decreasing the Rossby number, which has demonstrated a preference to higher-wavenumber structures (further described in § 2.4).

Van de Konijnenberg *et al.* (1999) briefly investigated the effects of fluid pumping via a source-sink arrangement. The experiments were performed on a tank with a parabolic base, where a portion of the tank can rotate independently of the tank rotation. In addition, a port is situated at the centre of the base to facilitate fluid pumping while fluid is naturally withdrawn from the periphery of the tank. Results from the differential-disk rotation forcing of this study are covered in § 2.4. In the absence of differential rotation, fluid was pumped from the centre port which produced a westward jet. Thus for negative- $Re$  flows, the effects of the shear from both the rotation of the fluid and the radial pumping combine to cause the shear layer to become more unstable as compared to the case of no pumping. Hence, for a particular  $|Re|$ , the negative counterpart will exhibit a lower number of vortices as the greater instability of

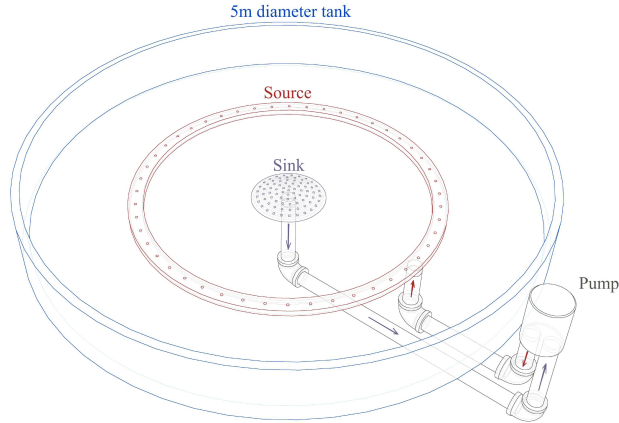


FIGURE 2.8: A sketch of the source-sink experimental configuration. The sink has a parabolic colander-like surface while the source is represented by a flat ring. This figure is reproduced from “Evolution of coherent modes in the dynamics of planetary polar vortices” proposal for the 6<sup>th</sup> EC framework programme integrated infrastructure initiative Hydralab III, with permission from Dr. Luca Montabone.

---

the jet causes an elongation of the vortices and an increase in vortex-vortex interaction. The opposite effect was observed for  $Re > 0$  where only higher wavenumber modes were reproducible in the comparative parameter space. Dye visualisation revealed that the vortices are more distinct when the jet is westward (positive  $Re$ ), as illustrated in figure 2.7.

Montabone *et al.* (2010a) conducted experiments on the 5 m Coriolis rotating tank at Norwegian University of Science and Technology in Trondheim, which has fluid pumping and extraction capabilities. Later work by Montabone *et al.* (2010b) was conducted on a larger Coriolis platform with a diameter of 13 m in Grenoble. A figure of the Trondheim apparatus is shown in figure 2.8. The tank incorporates a source ring with ports situated at a constant radius and a central circular sink. The sink is able to facilitate a flat platform or a parabolic colander-like profile. The former and latter topographic features are used to mimic to the  $f$ -plane and  $\gamma$ -plane, respectively. Also, the sink can partially be covered in order to change the usual circular sink into a ring-shaped sink.

The poleward flux and conservation of angular momentum results in the production of a jet that is susceptible to barotropic instability under sufficient forcing. This leads to the formation of vortices that rearrange themselves into polygonal shapes, ranging

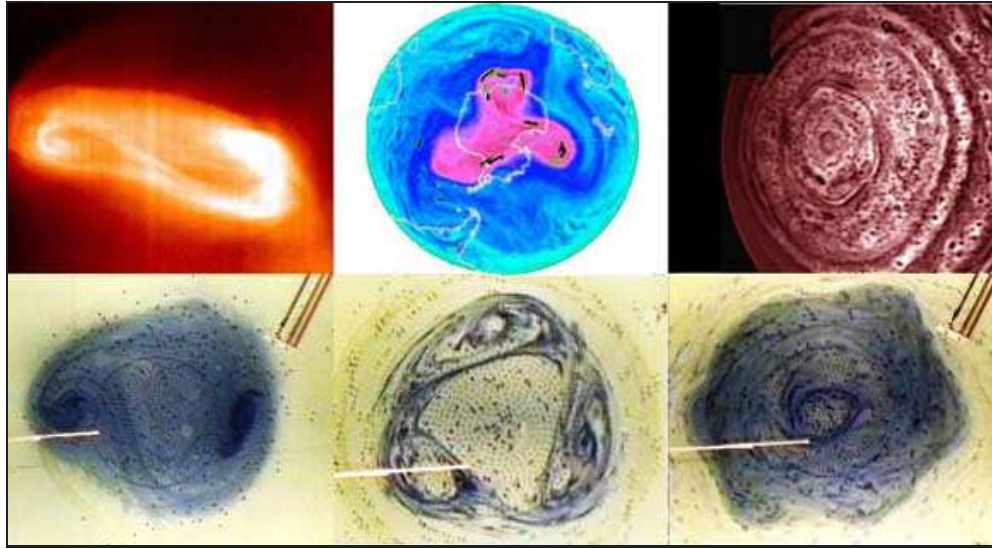


FIGURE 2.9: Top panels: Polar vortices as observed in nature on Venus, Earth and Saturn from left to right. Bottom panels: The laboratory counterparts of the natural polar vortices as produced in the source-sink system. From left to right, the structures are of a dipole, triangle and a hexagon. This figure is reproduced from Montabone *et al.* (2009) with permission from Dr. Luca Montabone.

---

from dipoles to hexagons. It is reported that these are “minimal energy” configurations, although it is believed that the term here is used loosely as no results support this claim. Injection of dye in the polygon or the vortices demonstrate a strong prohibition of fluid leaving and entering the structure. The governing parameters for this system are the Rossby number and the flow rate. Although the Ekman number is expected to have some importance with the preferential structures, the effect of this parameter was not explored. The qualitative results for these experiments reinforce the idea of barotropic instability being a plausible mechanism for the origin of polar vortices.

Visualisation of the laboratory vortical structures are presented in figure 2.9 along side their natural polar vortex counterparts. Interestingly, distinct vortices are seen bordering the polygon only for the triangular configuration while for the hexagon, the dye reveals a structure which is not as sharp. It is unclear whether this is a consequence of the location of the dye injection or if these visualisations are due to the manifestation of the flow itself. For the dipole, two strong vortices are seen rotating inside a larger patch of dye. It may well be that the dye has been introduced inside the hexagonal interior as well as the bordering satellite vortices. It is unclear whether these satellite vortices are present for the hexagon. In fact, no satellite vortices have been observed

for the hexagon on Saturn.

It is clear that there remains much to understand about flows developed via source-sink forcing, especially those that are influenced by barotropic instability. The complexity of the apparatus combined with limited measurement techniques and the many unknown variables such inlet and outlet flow profiles are contributing factors for the lack of results from this configuration to date. The next section details results from a more well-defined configuration, namely the differential-disk rotation apparatus.

## 2.4 Differential rotating flow

After the discovery of the shear layers in the original apparatus used by Stewartson (1957), numerous authors have experimentally reproduced the shear layers under various differential rotation configurations to observe the instabilities present. It is recalled that Stewartson only considered the limit of infinitesimally small  $\Delta\Omega$  ( $Ro \rightarrow \infty$ ) where the flow is highly stable due to the insignificance of the inertial forces. For sufficiently larger forcing, an instability forms and alters the flow structure. The instabilities in these system often cause the initially circular shear layer to deform into a ring of vortices that rearrange themselves around a polygon-shaped interior. These aesthetic structures usually extend the entire depth of the system and are representative of the polar vortices observed in nature. A review of the different configurations used to recreate these polar vortical structures and the stability of the flow are presented in this section.

### 2.4.1 Internal rotation

Hide & Titman (1967) first visualised polygonal patterns in a fluid-filled cylindrical rotating tank with a submerged differentially rotating disk. The disk was suspended by a connecting rod attached from above. The configuration is illustrated in figure 2.10. Through theoretical considerations of small- $Ro$  and small- $E$  conditions, the expected shear and boundary layers and their locations were determined. Vertical shear layers around the periphery of the disk and horizontal layers along the surface of the disk, the base and the lid were noted theoretically and observed experimentally. The former layers characterise Stewartson layers and the latter describe Ekman layers. For flows with very small Rossby and Ekman numbers, the flow is steady, axisymmetric and highly geostrophic outside of the shear layers. As the forcing of  $|Ro|$  is increased or as  $E$  is decreased, the flow approaches an unsteady state. This is true for both positive

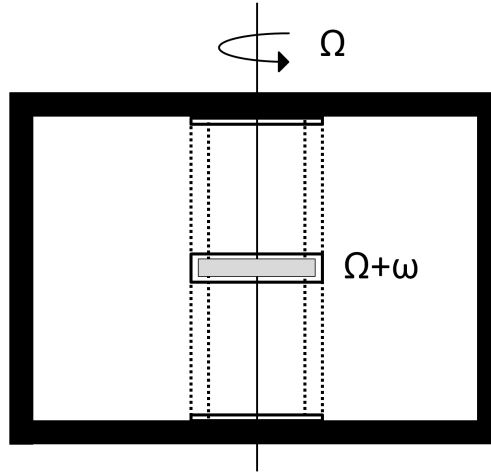


FIGURE 2.10: Schematic diagram of the experimental set up. The tank and disk rotate at different rates of  $\Omega$  and  $\Omega + \omega$ , respectively. The solid lines around the disk, lid and base of the tank represent the Ekman boundary layers. The dotted lines represent the Stewartson layers. This figure is adapted from Hide & Titman (1967).

and negative Rossby numbers; where positive and negative  $Ro$  correspond to the disk rotating faster and slower compared to the tank rotation, respectively.

The stability of the flow was determined experimentally via the threshold of the critical Rossby number at various Ekman numbers. That is, an axisymmetric flow is considered to be stable while flow is regarded as unstable once this axisymmetry is broken. It is noted that only three readings were recorded for negative-Rossby-number flows and it is claimed that there are little differences between the critical  $|Ro|$  threshold value between the positive and negative- $Ro$  regimes. An empirical relationship for the instability threshold is provided by  $|Ro| \sim 16.8E^{0.568}$ . Changing the disk radius did not influence this threshold relationship. The effects of the disk thickness and depth location were not investigated. Above the instability threshold, positive- $Ro$  flows demonstrated an instability in the vertical Stewartson layers that exhibited multiple vortices. These vortices generally arranged themselves into polygonal configurations when viewed along the axis of rotation and extends through the entire depth of the tank. As  $Ro$  is further increased, the number of vortices decreases with the size of each vortex becoming larger. The minimum number of vortices that was observed reached a limit of two. In contrast, negative- $Ro$  flows did not illustrate any polygonal patterns but instead only portrayed an off-axis ellipse in the unstable regime. The number of vortices were mapped onto a

$Ro$ - $E$  regime diagram for positive- $Ro$  flows only and revealed a weak dependence of  $E$  on the preferential azimuthal wavenumber.

#### 2.4.2 Single end-wall rotation

Niino & Misawa (1984) demonstrated that carefully conducted experiments can be explained by linear stability theory where effects of Ekman friction and internal viscosity are both considered. This approach is in contrast with previous studies of jets (Busse 1968; Dunst 1973) where linear theory incorporating either Ekman friction or viscosity alone were unable to obtain quantitative agreement between the theory and the experimental results. Their model has been previously described in § 1.5.2. In solving the Orr–Sommerfeld equation with added Ekman friction (equation 1.38), the stability of the shear layer and jet was determined as a function of  $Re$ ,  $k$  and  $\gamma$ . Here,  $k$  denotes the azimuthal wavenumber while  $\gamma$  represents the aspect ratio of the disk radius to the length scale  $L = (E/4)^{1/4}H$ . The stability curves are illustrated in figure 2.11. It was established that the curvature has an effect on the stability of the shear layer in that the critical  $Re$  decreases with increasing  $\gamma$ . Accordingly, the wavenumber also increases with decreasing  $\gamma$ . The effect of curvature on the flow’s stability is lost for  $\gamma > 25$  as its neutral stability curve closely matches that for  $\gamma = \infty$ . Thus, the stability can be described solely by  $Re$ . Their model demonstrated a higher critical Reynolds number and a lower corresponding critical wavenumber in comparison to a model that considers Ekman friction only. This is true for the case of  $\gamma = \infty$  for both the shear layer and the jet with  $k_c$  and  $Re_c$  being approximately half and double, respectively. They attribute this result solely on the incorporation of internal viscosity to their model. The critical  $Re$  for the shear layer and jet was determined theoretically to be  $Re_c = 11.6$  and  $Re_c = 15.5$ , respectively.

Their theoretical results displayed good agreement with the experiments, which reinforces the importance of the effects of internal viscosity. Their experimental apparatus involved a rotating cylinder where three disks of varying sizes were situated at the base. The production of a shear layer was achieved by rotating two disks at the same rate, but in opposite directions. A jet was developed by differentially rotating a single disk. The  $Re_c$  determined from the experiments for the shear layer and the jet was  $Re_c = 11.7 \pm 0.5$  and  $Re_c = 15.2 \pm 1.1$ , respectively. These values are very close to the theoretically established ones. The number of vortices varied between 2 to 8

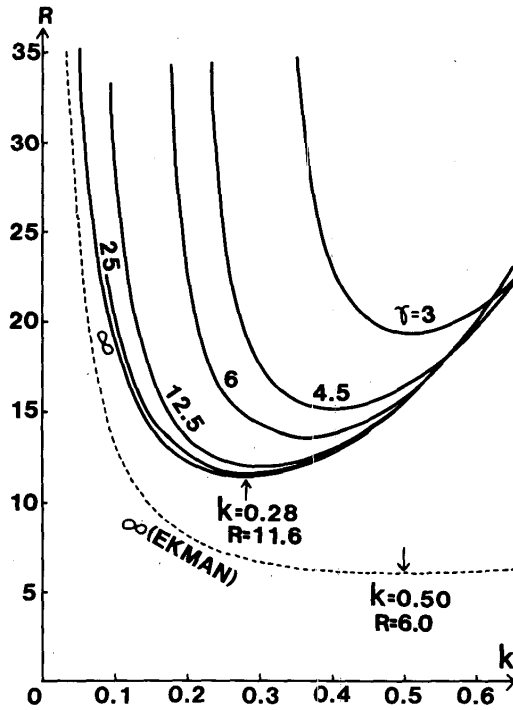


FIGURE 2.11: Neutral stability curves of a shear layer as a function of the Reynolds number  $R$ , the wavenumber  $k$ , and an aspect ratio  $\gamma$ . Here,  $\gamma = a/L$  where  $a$  is the disk radius and  $L = (E/4)^{1/4}H$  is the shear-layer thickness and  $H$  is the tank height. The dashed line represents the neutral stability curve for when Ekman friction is only considered. This figure is reproduced from Niino & Misawa (1984) with permission from the © American Meteorological Society.

for the shear layer and 6 to 13 for the jet. For both, the number of vortices decreased with increasing  $Re$ . The neutral curves they obtained via linear stability theory did not compare well with the experimental results of Hide & Titman (1967). It was proposed that the thickness of the disk may be the cause of the discrepancy.

Van de Konijnenberg *et al.* (1999) studied the stability of a circular shear layer produced via differential rotation in addition to a source-sink forcing. Their experimental set-up involves a fluid contained in a parabolic-shaped bowl atop a turntable. The parabolic surface is comprised of two sections, an inner portion that is able to rotate independently to that of the outer section. By rotating the tank at a nominal rate of 7.53 rad/s, the effects of the curved bottom boundary are mitigated and the results of the experiments are dynamically similar to those on an  $f$ -plane. Rotation rates lesser and greater than this nominal rate correspond to cases dynamically similar to  $\beta < 0$  and  $\beta > 0$ , respectively. A Reynolds number based on the thickness of the Stewartson

$E^{1/4}$  layer was used to measure the stability of the shear layer. The critical Reynolds number identified as the transition from stable to unstable flow found was of a higher value compared to that found by Niino & Misawa (1984). An explicit reason for this quantitative difference was not given though the authors did suggest that the curvature of the system may have influenced the results. Above the  $Re_c$ , the shear layer becomes unstable and forms discrete vortices which rearrange themselves into a polygon. This is indicative of barotropic instability and has been observed in previous studies. As the Reynolds number is increased, the number of vortices that form decreases with an azimuthal wavenumber 2 structure being the lowest observed.

The presence of the parabolic topography was found to be that of a stabiliser. For positive Reynolds numbers and  $\beta > 0$ , the number of vortices that appear is greater than those compared to the  $\beta = 0$  case. The same stabilising effect is seen for negative Reynolds numbers of  $\beta < 0$ . Recall that as the flow becomes more unstable, the vortices are likely to interact and coalesce, which yields a lower number of vortices. The stabilisation from the  $\beta$ -effect is not seen for opposing signs of  $Re$  and  $\beta$ . The introduction of pumping from the centre has a similar destabilising effect on the vortices. It was found that an azimuthal flow induced by the pumping of the same sense of the interior rotation yields a smaller number of vortices less than that compared to the non-pumping state. The authors note that this is a consequence of easier interaction between vortices after becoming elongated and less coherent. A two-dimensional model which incorporates an approximation of Ekman pumping and the  $\beta$ -effect illustrated the same trends seen in the experiments. The governing vorticity equation is given by

$$\frac{\partial \omega}{\partial t} + \mathbf{u} \cdot \nabla \omega - \beta u_r = \frac{\sqrt{\nu \Omega}}{H} (\omega^* - \omega) + \nu \nabla^2 \omega, \quad (2.7)$$

where  $\mathbf{u}$  is the velocity field,  $\omega$  is the vorticity and  $\omega^*$  is the vorticity of the bottom plate. Due to the two-dimensionality of the equation, the Ekman layer is not directly simulated. Instead, an additional linear friction term is added on the right hand side of the equation to capture the frictional effects induced by the Ekman layer (further described in § 3.2). This model is known as a quasi-two-dimensional model. The number of vortices observed in the numerical simulation was often lower than those observed experimentally. Van de Konijnenberg *et al.* (1999) argue that this difference is due to the simplicity of the model governing the flow whereby the  $E^{1/3}$  Stewartson layer is not simulated.

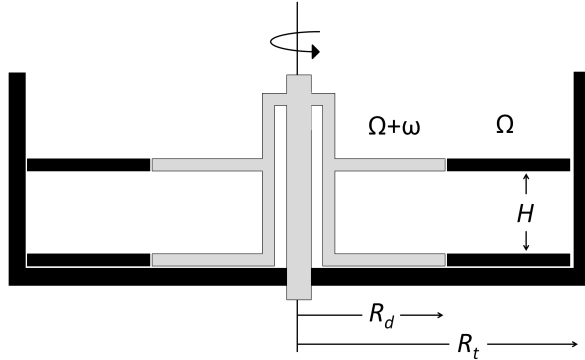


FIGURE 2.12: A schematic diagram of the differential rotating disk set-up used by Fröh & Read (1999). The key dimensions are the disk radius  $R_d$ , tank radius  $R_t$ , and tank height  $H$ . The disks (grey) and tank rotate about the central axis (vertical dashed line) at a rate of  $\Omega + \omega$  and  $\Omega$ , respectively. This figure is adapted from Fröh & Read (1999).

### 2.4.3 Double end-wall rotation

Double end-wall rotations in a rotating container have been investigated with the first being considered by Stewartson (1957) in investigating the vertical shear layers at the disk-tank interface in the limit of  $Ro \rightarrow 0$ . Fröh & Read (1999) investigated the same configuration with a focus on the unstable regime. The differentially forced disks rotate in unison having the same rotation rate and direction. A schematic of the apparatus is shown in figure 2.12. The depth of the fluid was set to  $H = 10$  cm and the radius of the disks and tank were  $R_d = 15$  cm and  $R_t = 30$  cm, respectively. Two working fluids were used; a mixture of water and glycerol with a kinematic viscosity of  $\nu = 1.66 \times 10^{-6}$  m<sup>2</sup>/s, and water ( $\nu = 1 \times 10^{-6}$  m<sup>2</sup>/s).

Upon sufficient differential forcing of the disks, the shear layer becomes unstable and forms a ring of multiple vortices. The vortices are arranged in such a way that an appearance of a polygon is seen in the interior while the vortices form the perimeter edge. Both positive and negative- $Ro$  flows were studied such that the disks rotated faster and slower than the tank, respectively. The parameter space ranged between  $0.01 \leq |Ro| \leq 1.0$  and  $2 \times 10^{-5} \leq E \leq 2 \times 10^{-3}$ , or equivalently,  $10 \leq Re \leq 10^5$  or  $1 \times 10^3 \leq Re_i \leq 2 \times 10^3$ , where  $Re_i$  is the internal Reynolds number following Niino & Misawa (1984), for which the length scale is based on the thickness of the shear layer ( $L = (E/4)^{1/4}H$ ). Accordingly, the internal Reynolds number is given by

$$Re_i \equiv \sqrt{2}RoE^{-3/4}, \quad (2.8)$$

where

$$Ro = \frac{R_d \omega}{2\bar{\Omega}H}, \quad (2.9)$$

$$E = \frac{\nu}{\bar{\Omega}H^2}. \quad (2.10)$$

Here,  $R_d$  is the radius of the disk,  $\omega$  is the differential rotation of the disk,  $H$  is the height of the tank,  $\bar{\Omega} = \Omega + \omega/2$  is the mean fluid rotation and  $\Omega$  is the tank rotation rate. The Reynolds number is defined as  $Re = UL/\nu$ .

The flow was seeded with latex beads and monitored using laser-Doppler velocimetry (LDV) and particle image velocimetry (PIV). LDV was used for experiments with water to obtain high-precision time series while a PIV was used for the water/glycerol mixture to obtain horizontal flow fields. Regime diagrams of the preferential azimuthal wavenumber as a function of  $Ro$  and  $E$  were produced with the equation of the stability threshold determined to be  $|Ro_c| = 27(\pm 1)E^{0.72 \pm 0.03}$ . Due to the minimal differences between positive and negative  $Ro_c$ , the threshold equation is representative for both positive and negative- $Ro$  regimes. Stable solutions with azimuthal wavenumbers between 2 to 8 were observed for both flow regimes. In addition, time-dependent flow categorised as weak fluctuations, period-doubled, modulated and highly irregular zones were demonstrated. The highly irregular flows, noisy vortices and anomalous period flows were more prominent in the negative- $Ro$  parameter space. It was found that the flow states and the preferential vortex numbers at onset did not depend strongly on the sign of  $Ro$ . This observation is in contrast with several prior studies, especially in comparison to the internally forced experiments of Hide & Titman (1967).

The coverage of their parameter space was accomplished by slowly scanning through the  $Ro$  range while keeping  $E$  constant. The two regime diagrams are shown in figure 2.13. In general, their parameter space concluded that a decrease in wavenumber can be achieved by either increasing  $Ro$  or  $Re$  and to a lesser extent, decreasing  $E$ . This transitional trend has been consistently observed in shear-layer experiments irrespective of the forcing mechanism and geometry (e.g. Hide & Titman 1967; Niino & Misawa 1984; van de Konijnenberg *et al.* 1999). The experiments were the first to confirm that the transition through supercritical instability is of a Hopf bifurcation. Multiple wavenumbers were mapped in the same region on the regime diagram due to the strong hysteresis observed during spin-up and spin-down of the differential forcing. The dotted lines on their regime diagrams represented hysteretic transitions.

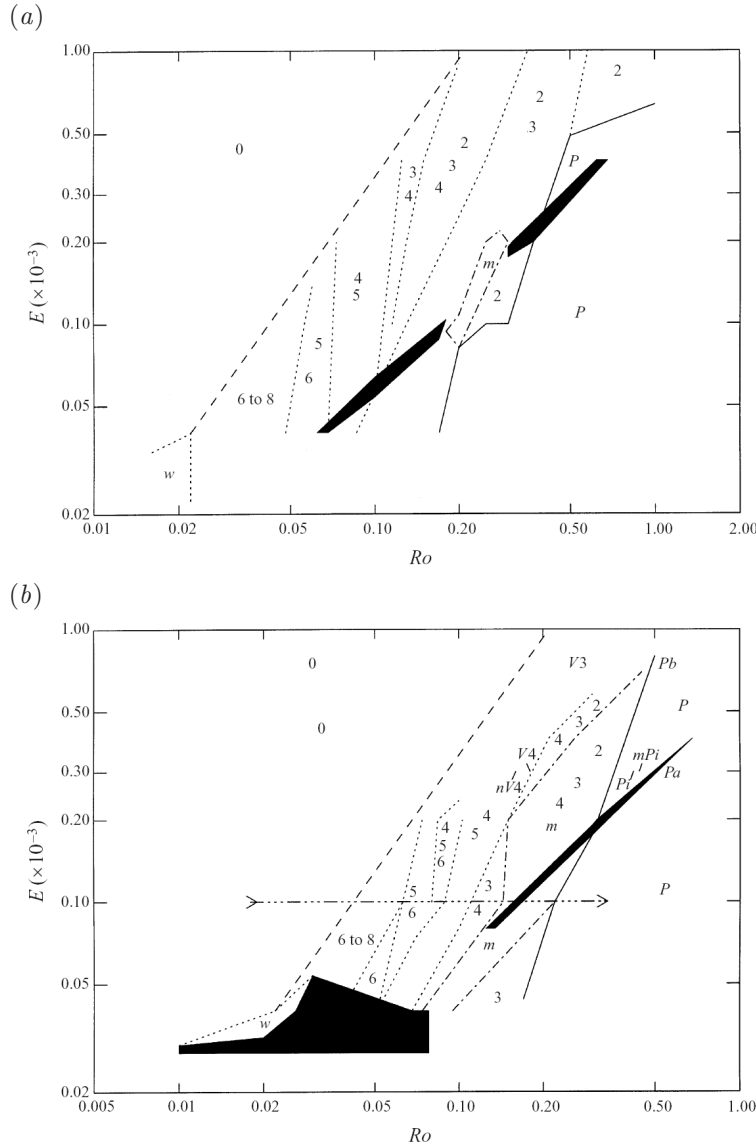


FIGURE 2.13: Regime diagrams of the unstable azimuthal wavenumber as a function of Ekman number with (a) positive Rossby numbers and (b) negative Rossby numbers. The numbers represent the unstable mode seen in that region of parameter space. The black regions represent highly irregular flow, 0 the axisymmetric stable flow,  $m$  the modulated oscillating states,  $P$  period-doubled solutions,  $nV$  as noisy vortices and  $w$  as weak fluctuations in velocity. Solid lines denote transitions without any noticeable hysteresis while the dashed lines represent hysteretic transitions. This figure is reproduced from Fröh & Read (1999) with permission from Dr. Wolf-Gerrit Fröh and the Cambridge University Press.

It should be noted that the claim of the critical internal Reynolds number being  $Re_{i,c} = 19E^{-0.03} \approx 24 \pm 2$  is based on a variant of equation 2.8. The definition of  $Re_i$  used by Fröh & Read (1999) is a factor of 2 smaller than the one defined in equation 2.8. It is also noted that the governing parameters between these systems are not consistently defined across the literature, as some authors use  $\Omega$  while others use  $f = 2\Omega$  in their definitions of  $Ro$  and  $E$ . Further, Fröh & Read (1999) use neither and instead opted for a mean fluid rotation rate. Therefore, a scaling of results is required when conducting comparisons between studies which use different length and velocity scales in addition to different conditions. Further details on these comparisons are discussed later in § 5.1.3.

The work of Fröh & Read (1999) was extended by Fröh & Nielsen (2003), who focused their attention on the time-dependent aspects of these differentially rotating flows. The same apparatus from the prior experiments was used and the numerical model adopted follows that of Bergeron *et al.* (2000) (described later in § 2.4.4). The boundary conditions used were a no-slip condition for both the inner and outer side boundaries and a smoothing function connecting the disk and tank azimuthal velocities assumed a tanh profile. Experimental and numerical simulations were run at an Ekman number of  $10^{-4}$ . Time-dependent flows were found in the form of two and three-vortex flows. All flows with four or more vortices were found to be steady with the appropriate symmetry. In addition, irregular weak fluctuations and highly irregular flows were observed. The latter type of flow was observed to be similar in appearance to Taylor vortices. As these structures were reproducible in both positive and negative- $Re$  regimes, it was noted that they cannot be Taylor vortices. This is due to all  $Re < 0$  flows being stable to the Taylor–Couette instability. The weak fluctuating and highly irregular flows were not investigated numerically due to the limitation of the quasi-geostrophic model.

The numerical and laboratory results demonstrated a decrease in azimuthal wave-number with increasing  $Re$  for a constant  $E$ . Here, the  $Re$  was redefined to be  $Re = 12^{-1/4}RoE^{3/4}$  by choosing a length scale of  $L = (E/12)^{1/4}H$ . In converting the  $Ro < 0$  regime diagram of Fröh & Read (1999) to their  $Re$  definition, the critical Reynolds number was determined to be  $|Re_c| = 36 \pm 3$ . The enstrophy contained in each azimuthal mode was monitored in numerical simulations, which demonstrated saturation for steady type flows. The mode with the largest energy saturation was

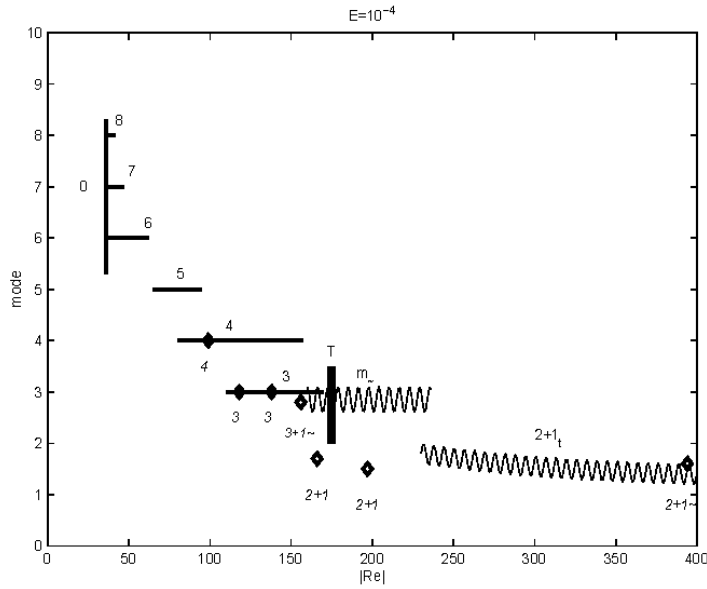


FIGURE 2.14: A comparison between experimental (lines) and numerically (diamonds) results of the observed flow state in a differential disk-rotation configuration. The flow condition is of  $E = 1 \times 10^{-4}$ . The numbers represent the instability wavenumber,  $T$  as the presumed Taylor vortices,  $m$  as modulated states, and a combination of two modes representing a distorted time-dependent flow. The labels above the lines refer to experimental results while the labels below the lines refer to the numerical results. This figure is reproduced from Fröh & Nielsen (2003) with permission from Dr. Wolf-Gerrit Fröh and Copernicus Publications.

exhibited through the vorticity contours. It should also be noted that the dominant mode differs to that of the mode in the linear regime where the enstrophy increases exponentially. Beyond a certain  $Re$ , the enstrophy in several modes becomes comparable and this induces time-dependent flow. This is characterised by two or more modes in competition and exhibited vortices that are of non-equal strength or size occurring in combination with vortices developing from the central rod used to drive the disks in their apparatus. The same was observed in the measurements of amplitude through a laser Doppler anemometry of the various modes.

The number of vortices observed in the experiments and the simulations agreed well with each other. The experimental and numerical results are summarised in figure 2.14 for  $E = 1 \times 10^{-4}$ . Here, the lines represent experimental steady vortex flows, “ $T$ ” as the interruption of the Taylor-like vortices and the oscillating lines representing time-dependent flows with the associating mode number. The diamonds depict the numerical results. Despite the quantitative agreement, there are qualitative disagreements demon-

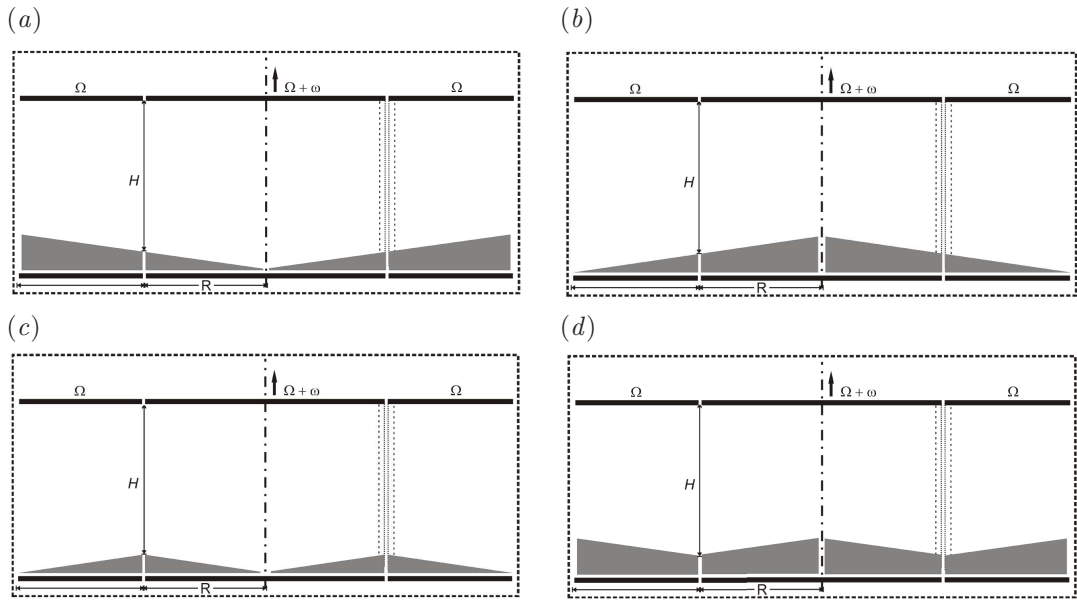


FIGURE 2.15: The various configurations investigated by Aguiar (2008). Two monotonic and two non-monotonic slopes are shown. (a)  $\beta < 0$  configuration, (b)  $\beta > 0$  configuration, (c)  $\beta^\mp$  configuration where  $\{\beta < 0, r < R\}$  and  $\{\beta > 0, r > R\}$  and (d)  $\beta^\pm$  configuration where  $\{\beta > 0, r < R\}$  and  $\{\beta < 0, r > R\}$ . This figure is reproduced from Aguiar (2008) with permission from Dr. Ana Aguiar.

strated through the types of flows found. For the three vortex flows, experiments were able to produce only the symmetric mode while the numerical simulations captured a weakly distorted flow. The numerical results also demonstrated smaller-scale vortex structures that were generated at the central rod, which interacted with the larger vortices. The experimental visualisations were unable to capture these smaller vortices, although they claim that these structures gave rise to the time-dependent behaviours of the flows.

Aguiar (2008) investigated cases with various bottom topography in a rotating cylindrical tank with differential disk forcing. The apparatus they used was an upgraded version of the differentially-rotating apparatus used for studying barotropic instability by Fröh & Read (1999). Four different types of topography were investigated, namely  $\beta < 0$ ,  $\beta > 0$ ,  $\beta^\mp$  and  $\beta^\pm$ . With increasing radius, the respective configurations are described by increasing depth, decreasing depth, increasing depth ( $r < R_d$ ) and decreasing depth ( $r > R_d$ ), and decreasing depth ( $r < R_d$ ) and increasing depth ( $r > R_d$ ). Schematics of these cases are reproduced in figure 2.15. All of these configurations were investigated for both positive and negative  $Ro$ .

The flow exhibited polygonal and vortex structures that were sharp and stable for cases where the monotonic  $\beta$  and the  $Ro$  are of the same sign. For opposing signs of  $Ro$  and  $\beta$ , the edges of the polygon were more curved and the vortices appeared distorted. Regime diagrams of the opposing  $Ro$  and  $\beta$  also suggests that the distorted two-vortex flows were more prominent over a larger region of the parameter space. These period-doubling flows were either rare or non-existent for same signed  $Ro$  and  $\beta$ . This may be due to the presence of Rossby waves which would interact with the shear layer and distort the resulting structure, as seen by van de Konijnenberg *et al.* (1999). Aguiar (2008) note that the main difference between positive and negative  $Ro$  for each sign of  $\beta$  is the radial position of where the Rayleigh–Kuo criterion is violated (§ 1.5.1). It was concluded that flow patterns have a more stable and sharp appearance when the Rayleigh–Kuo criterion is violated at a radius outside the disk radius ( $r = R_d$ ). This occurs when  $Ro$  and  $\beta$  are of the same sign. The onset of instability displayed a qualitative agreement against the theoretical result of  $Ro_c \propto \beta E^{1/2}$  (Schaeffer & Cardin 2005) when compared to the  $\beta = 0$  case ( $Ro_c \propto E^{3/4}$ ). The regime diagram obtained experimentally for  $\beta > 0$  and positive  $Ro$  is demonstrated in figure 2.16 where the solid blue line represents  $\beta = 0$  and the red dashed line represents the non-zero  $\beta$  value.

Similar differences were seen for non-monotonic bottom topography. For  $Ro > 0$  &  $\beta^\pm$  and  $Ro < 0$  &  $\beta^\mp$ , the polygonal structures appeared robust and sharp. However, for  $Ro < 0$  &  $\beta^\pm$  and  $Ro > 0$  &  $\beta^\mp$ , the structures were more distorted with period-doubling flows being predominant. The Rayleigh–Kuo criterion was again suggested for this cause. It was observed that  $\beta$  and the relative vorticity,  $d^2u/dy^2$ , share the same sign on either side of the shear layer for the cases of  $Ro > 0$  &  $\beta^\mp$  and  $Ro < 0$  &  $\beta^\pm$ . Thus,  $\beta - d^2u/dy^2 = 0$  is violated on both sides of the shear layer which becomes susceptible to complex and irregular flows such as period-doubling. In contrast, the reverse cases only violate the instability criterion at the  $r = R$ , similar to the  $f$ -plane scenario. Indeed, the average  $\beta$  for these non-monotonic topographies is zero. This may be the reason for why there is a better qualitative agreement of the instability threshold when scaled against  $E^{3/4}$  ( $\beta = 0$ ) compared to  $\beta E^{1/2}$  (non-zero  $\beta$ ). The results of the monotonic and non-monotonic geometries suggests that the value of  $\beta$  at the location of the shear layer has an effect on the stability of the shear layer. Also, the range of azimuthal wavenumbers observed between positive and negative  $Ro$  under the various configurations did not demonstrate any strong asymmetry as observed by

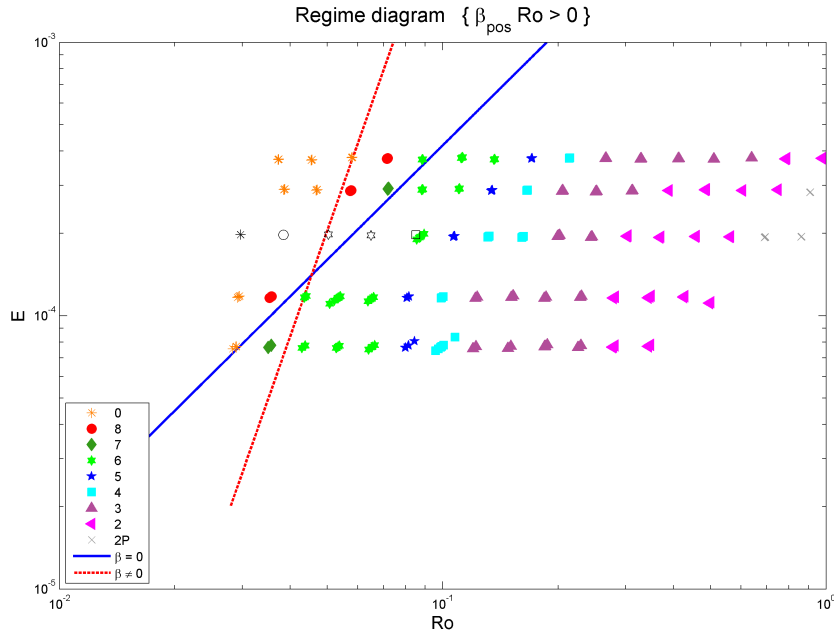


FIGURE 2.16: Unstable azimuthal wavenumbers observed experimentally for the  $\beta > 0$  configuration, mapped onto a  $Ro$ - $E$  regime diagram. The solid blue line represents  $\beta = 0$  and the red dashed line represents the non-zero  $\beta$  value of the bottom topography. Solid filled and hollow symbols represent two different time-varying forcing used to obtain the results. This figure is reproduced from Aguiar (2008) with permission from Dr. Ana Aguiar.

---

Hide & Titman (1967) and Hollerbach (2003) (results of which are described later in § 2.4.5).

Aguiar *et al.* (2010) had a focus on explaining the origin of Saturn’s northern polar hexagon. Measured profiles of Saturn’s mean zonal wind and absolute vorticity gradient profiles from cloud tracking were used in their linear stability analysis. From the vorticity profile as illustrated in figure 2.17, violations of the Rayleigh–Kuo criterion can be observed at multiple locations. This suggests that barotropic instability may be possible on Saturn. However, the location of the hexagon vortex ( $77.5^\circ$  N) and the Ribbon wave ( $47^\circ$  N) does not occur at the latitudinal locations of where the vorticity gradient equals  $\beta$ . Instead, these structures have been observed at latitudes where the velocities are large and sharp changes occur over a narrow latitudinal band.

Growth rates as a function of zonal wavenumber and the Rossby deformation radius  $L_D$  were obtained through the linear analysis. For  $L_D = \infty$  (pure barotropic flow), the wavenumber with the largest growth rate was predicted to be  $k = 13$ . The maximum growth rate and associating wavenumber decreases with decreasing  $L_D$  in

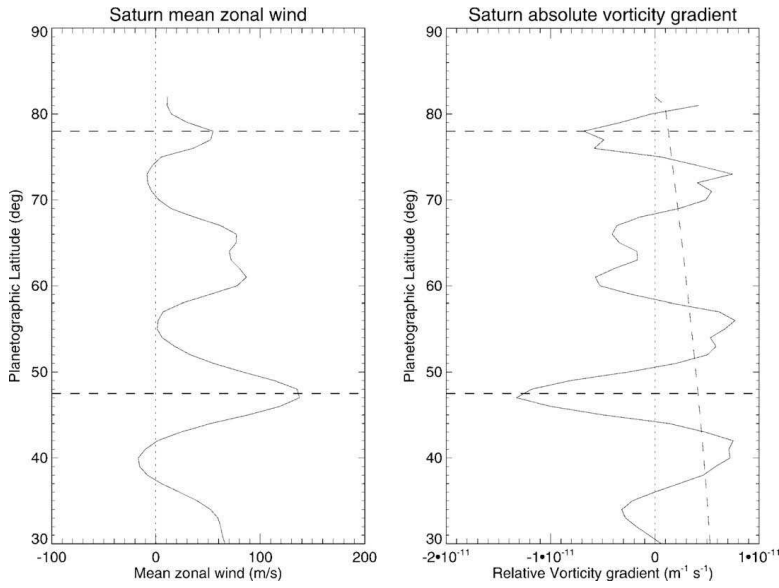


FIGURE 2.17: Mean zonal wind and the relative vorticity gradient profiles measured from Voyager cloud tracking measurements of Saturn’s northern hemisphere. The two horizontal lines at  $77.5^\circ$  and  $47^\circ$  represent the latitudes of the polar vortex’s hexagonal border and Saturn’s ribbon structure, respectively. The diagonal dashed line in the right plot represents the planetary vorticity gradient,  $\beta$ . This figure is reproduced from Aguiar *et al.* (2010) with permission from Dr. Ana Aguiar and Elsevier.

the range of  $0 \leq k \leq 20$ . Beyond these wavenumbers, the growth rate appears to grow continually. Also, for  $L_D = 2000$  km or less, the large-scale instability was suppressed and the growth rate increased linearly with increasing wavenumber. For comparative properties of Saturn where  $L_D = 2500$ , the predicted peak wavenumber is  $k = 6$  which is consistent with the spacecraft observations. The same analysis was performed for southern latitudes of Saturn and yielded peak growth rates at non-finite wavenumbers. It is claimed that this is in agreement with the monopole observed at the south pole.

The experiments conducted in that study were performed on the same apparatus used in Früh & Read (1999) and Aguiar (2008). Several modifications were made to the equipment to accommodate depth variations and jet generation with a differential rotating ring. The  $\beta$ -effect was mimicked by a linearly sloping bottom of approximately  $5^\circ$ . In this barotropic jet configuration, the tank including the entire base rotates at a rate of  $\Omega$  while the ring rotates at  $\Omega + \omega$ . The working fluid was of a water/glycerol mixture and fluorescein dye was injected at the radial location of the disk or ring edge at the bottom boundary for visualisation purposes. Correlation imaging velocimetry was used to obtain flow fields and compute the velocity and vorticity fields. The profiles

were found to be independent of depth except in the vicinity of the Ekman layers. The features in these profiles displayed similarities with those measured on Saturn. The vorticity gradient indicated a strong negative peak with weak positive peaks on either side similar to the latitudes between  $72^\circ$  and  $82^\circ$  on Saturn.

A regime diagram of the preferential azimuthal wavenumber as a function of  $Ro$  and  $E$  for the differential-ring configuration with  $\beta = 0$ . Only the positive- $Ro$  regime was explored with wavenumbers ranging from 2-8. The majority of the parameter space was comprised of steady-wave states. The same dependencies were observed in this differential-ring configuration as compared to the differential-disks configuration. That is, a decrease in azimuthal wavenumber is achieved by primarily increasing  $Ro$  or decreasing  $E$ . The onset of instability was compared against the empirical relationship obtained by Fröh & Read (1999) of  $Ro_c = 27E^{0.72}$ . The experimental data points showed good agreement for moderately small  $E$  but lost conformity at larger  $E$  values. An empirical fit for the instability threshold was not provided.

With a length and velocity scale of  $L = (E/4)^{1/4}H$  and  $U = R\omega/4$ , respectively, the critical Reynolds number was determined to be approximately  $Re_{i,c} \sim 27$ . The value  $Re_{i,c} \sim 37$  stated in the paper is a typographical error and the boundary condition  $d\psi/dz = 0$  should read  $d\psi/dy = 0$  (*personal communication*). The reported critical internal Reynolds number of  $Re_{i,c} = 27$  is close to that claimed by Fröh & Read (1999) ( $Re_{i,c} = 24$ , although it should be noted that the velocity scales are different between the two configurations). At the largest values of  $Re$  investigated, time-dependent flows were observed for modes 2 and 3. This is in agreement with experiments from Fröh & Nielsen (2003), where time-dependent flows were only found for wavenumbers less than 4.

The velocity field of a wavenumber 6 structure demonstrated a prominent hexagonal ring with no clear indication of vortices at its boundary. However, the relative vorticity field clearly displays a presence of vorticity patches around the border of the hexagon. The ring is bounded by positive vorticity in the interior while the satellite vortices on the outside exhibit negative vorticity. Their dye-streak visualisations reinforce the presence of these vortices. Similar to previous experiments, the structure demonstrates prohibition of mass transport across the polygonal ring. It was observed that structures produced on a  $\beta$ -plane appear much sharper around the borders of the polygon compared to structures developed on an  $f$ -plane which adopt a wavy form.

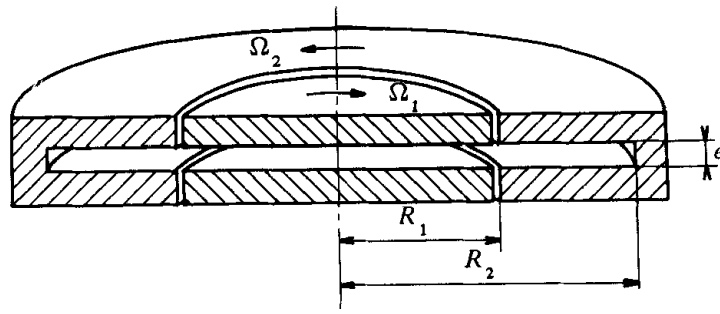


FIGURE 2.18: A schematic cross section of an experimental apparatus investigating differential rotating flows in containers of small depths. This figure is reproduced from Rabaud & Couder (1983) with permission from Prof. Marc Rabaud and the Cambridge University Press.

The qualitative results from the instability of the jet and shear layer illustrate that barotropic instability is certainly plausible for the origin of Saturn's hexagon assuming that baroclinic effects are negligible. Despite the large differences in the Reynolds and Ekman numbers between the laboratory experiments and Saturn, the range of Rossby numbers under which a wavenumber 6 was sustained is comparable.

#### 2.4.4 Short cylinders

The previous section described studies involving double end-wall differential rotation in containers which have a depth much greater than the Ekman layer thickness. This section details the results of flow under the influence of differential rotation in containers of small depths.

The instability of a circular shear layer was considered experimentally by Rabaud & Couder (1983). The configuration investigated is shown in figure 2.18, which involves a rotating container with differentially rotating disks. The working fluid is air. However, the major difference between this configuration and those of previous sections is that the height of the enclosure is very small compared to the tank radius. In fact, the height is usually of the order of the Ekman layer thickness or smaller. This difference causes the developing Ekman layers to fill up the entire cell, which suggests that the centrifugal and Coriolis forces have no influence on the stability of the flow. The experimental conditions in previous studies were governed by small Rossby and Ekman numbers, which indicates the dominance of the Coriolis force in the system. Despite the differences in conditions, the shear layer is observed to undergo a Kelvin–Helmholtz

type instability. The resultant structure is of a ring of vortices originating from the shear layer at the disk radius which is similar to that seen by other differential rotating experiments (e.g. Hide & Titman 1967; Fröh & Read 1999; Aguiar *et al.* 2010). An illustration of an unstable structure is shown in figure 2.19. It was observed that modal transitions of the flow can occur abruptly, thereby bypassing several modes entirely. The transitions is seen to be dependent on the rate of increase or decrease of the angular velocities. That is, a quasi-static increase in the difference in angular velocities between the disks and the tank results in successive transitions described by  $k \rightarrow k - 1$ . The difference in angular velocities is incorporated in the definition of the Reynolds number, which is given by

$$Re = \frac{|\Omega_2 - \Omega_1| R_d H}{\nu} \quad (2.11)$$

where  $\Omega_2$  represents the angular velocity of the tank,  $\Omega_1$  is the angular velocity of the disks,  $R_d$  is the disk radius and  $H$  is the tank height. The Reynolds number is the sole parameter used to characterise the stability of the flow. A decrease in  $Re$  yields transitions described by  $k \rightarrow k + 1$ , although with strong hysteresis. For a wavenumber of even parity, the transition from an  $k$ -fold symmetry is replaced by a  $k/2$  symmetry in its intermediate state before realising an eventual structure. The resulting structure is dependent on the rate of spin up/down. For example, the intermediate state of a wavenumber 6 structure involves a state where three vortices are enlarged while the remaining three vortices are reduced in size. Provided that the rate of increase in the forcing is large, then the  $k/2$  pairing occurs resulting in a  $k = 3$  structure. In contrast, a small rate in forcing increase yields a  $k - 1 = 5$  structure.

Various tank depths were investigated for which short depths have demonstrated a critical Reynolds number of  $Re_c = 85 \pm 5$  while for larger depths,  $Re_c = 110 \pm 10$ . The selection of the azimuthal wavenumber that appears shortly beyond the instability threshold was found to depend on the aspect ratio of the shear layer. An empirical relationship for the wavenumber seen at the threshold of stability was given by  $k_c = 0.85R_d/H$ . In addition, a phenomenon was observed when the outer cylinder radius is comparable to the inner disk radius whereby the lateral friction along the side walls causes the mode to oscillate between its initial wavenumber  $k$  and a wavenumber  $2k$  state.

The experimental rig used by Rabaud & Couder (1983) was further investigated by Chomaz *et al.* (1988). Enhancements were made to the apparatus to allow a wider range

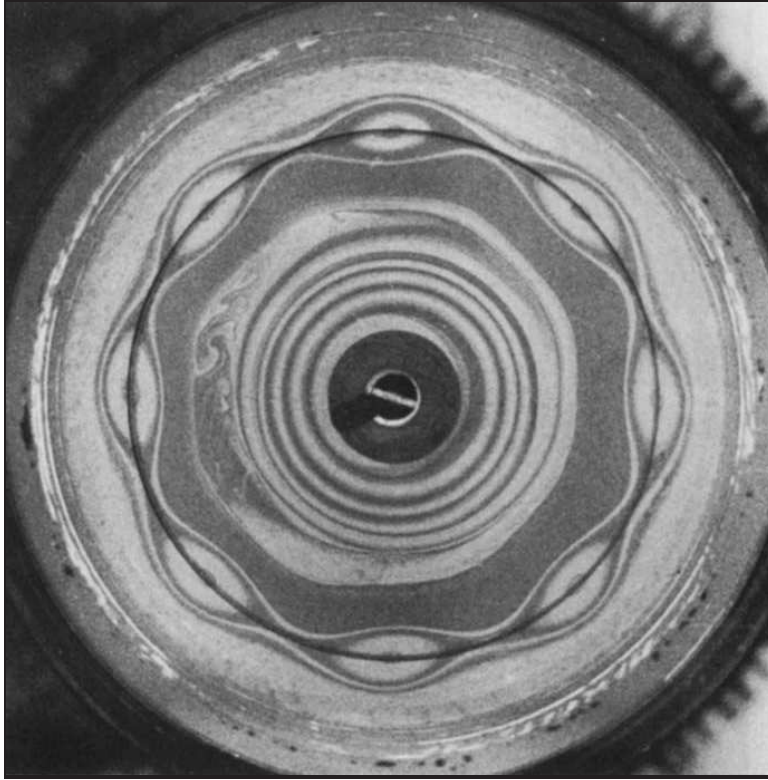


FIGURE 2.19: A wavenumber 8 structure visualised via a soap film placed at mid-depth. This figure is reproduced from Rabaud & Couder (1983) with permission from Prof. Marc Rabaud and the Cambridge University Press.

of aspect ratios between  $2/13 \leq A \leq 1/12$  to be explored. Their results complement those found by Rabaud & Couder (1983) and they determined the critical Reynolds number to be  $Re_c = 80 \pm 2$ . The wavenumber observed at the transition from axisymmetric to unsteady flow is governed by the empirical relationship  $k_c \sim (0.77 \pm 0.03)A$ . In addition, they obtained empirical laws that fit tabulated data of angular velocity of the vortical structure from Rabaud & Couder (1983). It follows that the wavenumber pattern moves relative to the laboratory frame at

$$\Omega_v = \alpha_k \Omega_1 + \beta_k \Omega_2, \quad (2.12)$$

where

$$\alpha_k = \frac{1}{2} - \frac{0.7}{k}, \quad (2.13)$$

$$\beta_k = \frac{1}{2} + \frac{0.7}{k}, \quad (2.14)$$

with  $\Omega_1$  and  $\Omega_2$  representing the disk and tank angular velocities, respectively. It was found that the aspect ratio of the cell, defined by the ratio of disk radius to cell

depth, influences the dynamical behavior of the flow. Differences were observed in the transition in flow states for large and small cells. The formation from one wavenumber to another occurs through localised processes in taller cells whereas successive breaking of the symmetry is demonstrated in shorter cells.

Two-dimensional numerical simulations were conducted to demonstrate that the characteristics of the instability observed experimentally can be captured numerically. The median plane was modelled numerically by a modification to the two-dimensional Navier–Stokes equations with the addition of drag due to the friction on the horizontal boundaries. This Ekman friction is modelled through a forcing term. A parabolic vertical dependence characteristic of Poiseuille flow between the two disks is assumed for the velocity deviation from solid-body rotation. Thus the forcing term is given by

$$\mathbf{F} = \nu \frac{\partial^2 \mathbf{u}}{\partial z^2} \sim \frac{8\nu}{H^2}(\mathbf{u}_0 - \mathbf{u}), \quad (2.15)$$

where  $\mathbf{u}$  is the velocity field and  $\mathbf{u}_0$  represents the velocity boundary conditions. As  $\mathbf{u}_0$  is discontinuous, a linear smoothing function was applied between the disk and tank angular velocity over a width of  $H$ . The numerical results demonstrated an initially circular shear layer deforming into polygonal structures as the Reynolds number is increased beyond the instability threshold. The experimental trend of decreasing  $k$  with increasing  $Re$  was also observed. Although several qualitative results were in agreement, generally the quantitative results were not in agreement. The instability threshold value was determined to be  $Re_c = 55 \pm 10$ , which is significantly different compared to the experimental findings ( $Re_c \sim 80$ ). The authors fault this discrepancy on the simplicity of the model and due to the uncertainty with the width definition of the shear layer. The spatial resolution was also believed to contribute to the discrepancy. Bergeron *et al.* (2000) further investigated the disconnection between the experimental and numerical results and stated that the model was insufficient.

The set-up from Rabaud & Couder (1983) and Chomaz *et al.* (1988) was also considered by Bergeron *et al.* (1996) from a numerical and theoretical perspective. A numerical scheme based on a fully de-aliased spectral method was employed to solve the vorticity evolution equation which includes an Ekman forcing. The adopted Ekman forcing follows that of Chomaz *et al.* (1988) (equation 2.15) with linear interpolation between the disk and tank angular velocities. The linear interpolation occurs over a region of width  $H$  centred around the disk radius. Further details of the numerical scheme can be found in Chomaz *et al.* (1988) and Bergeron *et al.* (2000). The two-dimensional

domain of the mid-plane was simulated, which allows for a direct comparison with the visualisation obtained via prior experiments. Direct numerical simulations were performed to determine the number of vortices present for a particular flow condition and the stability threshold. The first 20 modes were initially excited with random phases and low amplitudes. The critical Reynolds number was determined to be  $Re_c = 86.178$  analytically and  $Re_c = 86.3 \pm 0.1$  numerically, which demonstrate great similarity. The analytical result also bodes well against the prior experimental studies (Rabaud & Couder 1983; Chomaz *et al.* 1988). In addition, the first unstable azimuthal wavenumber obtained via linear stability analysis is in agreement with the empirical rule deduced by Rabaud & Couder (1983) ( $k_c \sim (0.77 \pm 0.03)A$ ). It was found that the value of  $Re_c$  varies over a broad range in relation to the aspect ratio of the apparatus and with the interpolated velocity forcing. This is significant as the latter variable can be tweaked to achieve the critical Reynolds numbers obtained by the experiments.

Bergeron *et al.* (2000) furthered the investigation by studying the effects of the boundary conditions imposed on the inner rod and outer walls. They employed a tank aspect ratio of  $A = 2/13$ . Results from free-slip boundary conditions are compared to the previously obtained no-slip boundary conditions. Moreover, the effect of various interpolation profiles between the disk and tank angular velocities were studied. The linear interpolation used previously attributes a discontinuity in the vorticity profile. Thus, a  $\tanh(r/\Delta r)$  and a cubic interpolation was considered for interpolation between the disk and tank angular velocities, where  $\Delta r$  represents a normalisation length ( $\Delta r = 0.4H$ ). The cubic interpolation provides a continuous profile for vorticity as well as illustrating a well-defined transition region while the  $\tanh$  involves continuous derivatives for all orders. However, it is unclear why the cubic interpolation profile was favoured against a  $\tanh$  profile (and *vice versa*) in certain cases as it is not explicitly stated, and a direct comparison of the results associated with the two interpolation profiles were not highlighted in the paper.

The value of  $Re_c = 81.1 \pm 0.1$  for the free-slip case was lower than that obtained with the no-slip condition ( $Re_c = 86.3 \pm 0.1$ ). Good agreement was shown again between the asymptotic analysis and the numerical study with an analytically determined value of  $Re_c = 80.6$  for the free-slip case. A comparison of  $Re_c$  with prior experiments suggests that the no-slip boundary conditions are most suited to simulating an experimental environment. This is not surprising; the primary difference observed in the vorticity

contours between slip and no-slip conditions were in the vorticity strands developing off of the inner rod and outer walls. These strands are able to develop into vortices, particularly those originating from the inner wall at high values of  $Re$ . At high  $Re$ , the flow becomes time-dependent and the introduction of the vortex shedding interacts with the primary polygonal vortex structure. Strong hysteresis was also observed while investigating the effects of spin-up and spin-down. The rate of spin-up was seen to affect the transition between stable and unstable flow. That is, low spin-up rates reduce the number of vortices by one while higher spin-up rates are able to cause a transitional jump of multiple vortices. This effect was also observed by Rabaud & Couder (1983).

#### 2.4.5 Spherical shells and spheroids

It is interesting that Hide & Titman (1967) found substantially different structures between the two forcing directions (positive and negative  $Ro$ ) while Fröh & Read (1999) found little difference. Much of the body of theoretical work has considered very small  $|Ro|$ , or in the limit of  $Ro \rightarrow 0$ . According to Hollerbach (2003), the governing equations used (Busse 1968) in barotropic and quasi-geostrophic form do not depend on sign of  $\Delta\Omega$ . Thus, there is no difference between positive and negative  $Ro$  in the linear theory. Hollerbach (2003) set out to determine the cause of this difference by considering fluid flow in a spherical shell with differential-rotation forcing through numerical simulations. A general schematic of the spherical shell configuration is illustrated in figure 2.20. The incompressible Navier–Stokes equations were solved in the  $r$ - $z$  plane to obtain the basic state of the flow. The boundary conditions were  $\mathbf{u} = r \sin \theta$ ,  $\theta \in [-\pi/2, \pi/2]$  at the inner radius  $r_i$  (inner sphere surface) and  $\mathbf{u} = 0$  at the outer radius  $r_o$  (outer sphere surface) in a rotating frame of reference. This basic state reveals a Stewartson layer that circumscribes the inner sphere. It adopts a nested structure of the  $E^{1/3}$  and  $E^{1/4}$  layers much like that in the planar configuration, although with an intermediate  $E^{2/7}$  layer. Upon sufficient forcing, the Stewartson layer adopts a wavy instability similar to that observed in the planar configuration. The length and velocity scales were chosen as  $(r_o - r_i)$  and  $\Omega(r_o - r_i)$  such that the Rossby and Ekman numbers are defined as

$$Ro = \frac{\Delta\Omega}{\Omega}, \quad (2.16)$$

$$E = \frac{\nu}{\Omega(r_o - r_i)^2}, \quad (2.17)$$

where  $\Omega$  and  $\Delta\Omega$  are the rotation rate and differential rotation rate, respectively.

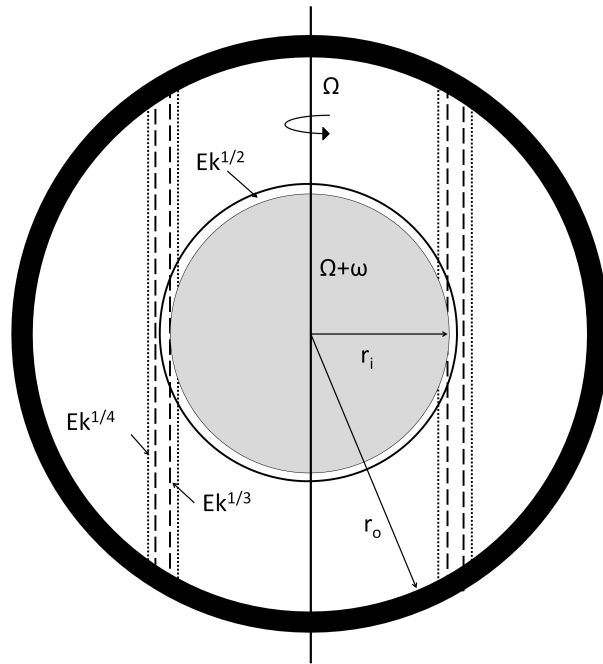


FIGURE 2.20: A schematic diagram of the differential spherical shell set-up. The key dimensions are the inner sphere radius  $r_i$  and outer sphere radius  $r_o$ . The inner sphere (grey) and outer sphere (black) rotate about the central axis (vertical solid line) at a rate of  $\Omega + \omega$  and  $\Omega$ , respectively. The vertical shear layers represent the Stewartson layers which have thicknesses scaling with  $E^{1/4}$  and  $E^{1/3}$ . An additional thickness of  $E^{2/7}$  exists, although not shown here. An Ekman layer of thickness  $E^{1/2}$  surrounds the inner sphere.

The stability curves for numerous wavenumbers were determined and plotted as a function of  $Ro$  and  $E$ . This was achieved by obtaining the axisymmetric base states for a pair of  $Ro$  and  $E$  conditions. A specific wavenumber is then considered and time-stepped through the linearized Navier–Stokes equations until the dominant eigenmode is obtained. If the chosen mode was found to grow, then  $Ro$  was decreased. This method was repeated until the conditions of the instability onset were established. Hollerbach (2003) determined that  $Ro_c \propto E^{0.65}$  for positive  $Ro$  while it is  $Ro_c \propto E^{0.45}$  for negative  $Ro$ . In addition, the most unstable modes for the range of  $E$  explored ( $10^{-5} \leq E \leq 10^{-2}$ ) was  $3 \leq k \leq 8$  for positive  $Ro$  and  $1 \leq k \leq 2$  for negative  $Ro$ . The stability curves they obtained are reproduced in figure 2.21. The significant difference between the two forcing signs resembles the findings of Hide & Titman (1967), especially with  $k = 1$  being the most unstable throughout the majority of the parameter space for negative  $Ro$ . It should be noted that  $Ro_c$  of positive and negative- $Ro$  flows found

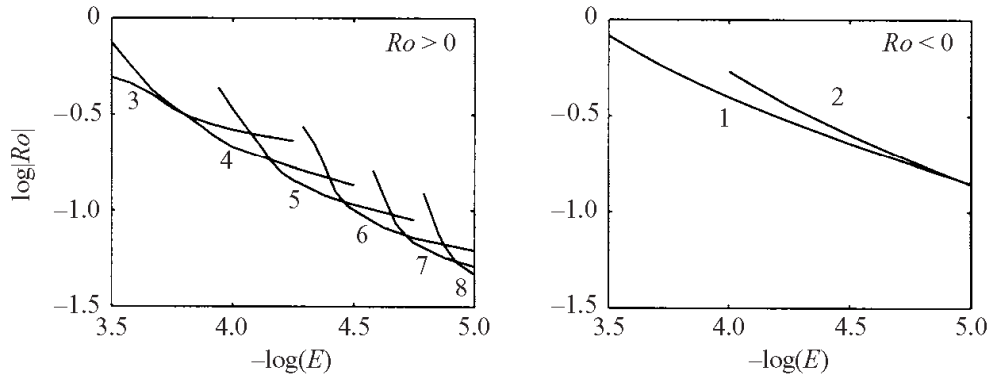


FIGURE 2.21: Stability curves of the most unstable azimuthal wavenumbers as a function of  $Ro$  and  $E$ , for the spherical shell configuration. The left and right plots are of the positive and negative- $Ro$  regimes, respectively. The most unstable modes differ significantly between the two regimes. The base flow is of the spherical shell configuration with  $r_i = 1/2$  and  $r_o = 3/2$ . This figure is reproduced from Hollerbach (2003) with permission from Prof. Rainer Hollerbach and the Cambridge University Press.

by Hide & Titman (1967) was found to be the same which is different here.

Multiple tests were conducted to establish the cause of this wavenumber asymmetry between positive and negative  $Ro$ . Initial tests investigated aspects of the basic state in which the nonlinearity was removed by setting  $Ro = 0$  in the governing equations of the base flow while allowing it to vary in the linearised equations. Other tests involved artificially removing the meridional circulation from the Stewartson and Ekman layers. The significance of the Ekman layers was proposed because of its thinner structure which may become unstable before Stewartson layers. However, this is not the case. The results of these initial tests suggests that all these factors do not greatly impact the asymmetry observed in flow states between the positive and negative- $Ro$  instability curves.

The last aspect of the base flow that was tested was attributed to the depth-independent structure of the Stewartson layer. Thus, the effects of the geometry was modelled by mapping the flow of a particular  $r_i/r_o$  ratio configuration onto a different  $r_i/r_o$  configuration. This is achieved by varying  $r_i$  while keeping  $r_o = 3/2$  constant. A full-sphere and a thin-shell arrangement was examined with  $r_i = 0$  and  $r_i = 4/5$ , respectively. An inner radius of  $r_i = 1/2$  was used as a reference case. Consequently, the shear layer is no longer situated at the edge of the inner sphere. This change resulted in the instability curves for negative and positive  $Ro$  displaying similar characteristics

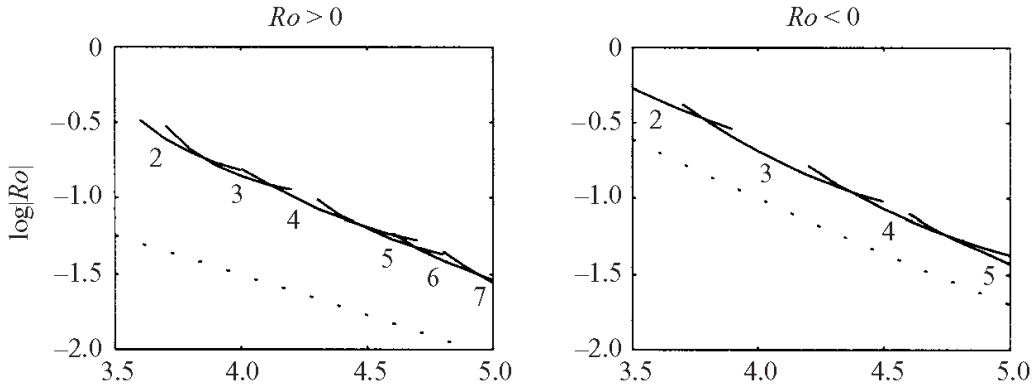


FIGURE 2.22: Stability curves of the most unstable azimuthal wavenumbers as a function of  $Ro$  and  $E$ , for the spherical shell configuration. The left and right plots are of the positive and negative  $Ro$  regime, respectively. The most unstable modes are similar between the two regimes. The base flow of the spherical shell configuration has been imposed onto the full-sphere configuration with  $r_o = 3/2$  by extending the solution to all of  $z$ . This figure is reproduced from Hollerbach (2003) with permission from Prof. Rainer Hollerbach and the Cambridge University Press.

---

for both the full-shell and thin-shell geometry. The stability curves for the full sphere is shown in figure 2.22. For all cases, they find  $|Ro_c| \propto E^{0.7}$  which is in closer agreement with Fröh & Read (1999) and Busse (1968).

The critical aspect of the geometry was determined to be in the variation in height across the shear layer. In the full shell geometry, the height of the shear layer decreases with increasing radius across the shear layer while for the thin shell, the fluid height continually increases with increasing radius. However, for the reference case which exhibits the Stewartson layer at the edge of the inner sphere, the depth decreases radially away from the edge in both directions. At the actual edge, the change in depth against radius is considered as  $dh/dr = \infty$ . Thus it was concluded that if the height of the fluid “does not change, or changes gradually, then positive and negative  $Ro$  will be much the same, whereas if it changes abruptly, then negative  $Ro$  will be anomalous”. This would indeed explain the discrepancy between the experiments of Hide & Titman (1967) and Fröh & Read (1999). In the internal forcing experiments, the shear layer abruptly changes across the disk edge while for the double end-wall configuration, the shear layer remains constant. However, this still does not explain why Hide & Titman (1967) found similar  $Ro_c$  for positive and negative- $Ro$  flows.

Since the depth of the fluid was found to be the critical factor in the differences

between instabilities of the Stewartson layer, it seemed to suggest that potential vorticity may be the key diagnostic used to understand the underlying physics of this discrepancy. This is due to the conservative property of potential vorticity in inviscid flows which incorporates a variable fluid depth (equation 1.5). However, the analyses by Hollerbach (2003) involving potential vorticity proved inconclusive.

Hollerbach *et al.* (2004) extended the investigation by conducting physical experiments to compliment their numerical results. The apparatus is of concentric spheres with  $r_i = 26.7$  mm and  $r_o = 40$  mm, which is filled with a silicone oil with viscosity of  $3.3 \times 10^{-6}$  m<sup>2</sup>/s. The Ekman numbers achieved experimentally were larger than those in Hollerbach (2003) but were nevertheless considered small enough to create well-defined Stewartson layers. The focus of their study was on the nonlinear regime of positive  $Ro$ . The linear onset and the nonlinear equilibrium were obtained numerically with strong experimental agreement. The unstable azimuthal wavenumber was seen to decrease with increasing  $Ro$  and decreasing  $E$ . Decreasing  $Ro$  and increasing  $E$  displayed the opposite trend, though the observed wavenumbers were different due to hysteresis effects. A steady-state flow was achieved by allowing the flow to settle for 10-15 minutes after changing the inner sphere rotation. Azimuthal wavenumbers ranging from 3-6 were produced in the experimental parameter space of  $0.2 \leq Ro \leq 0.8$  and  $8 \times 10^{-4} \leq E \leq 3 \times 10^{-3}$ .

Recall that these azimuthal wavenumbers reported by Hollerbach *et al.* (2004) correspond to the number of sides of a polygon. That is, the initially circular Stewartson layer may become distorted into a triangle ( $k = 3$ ), square ( $k = 4$ ), pentagon ( $k = 5$ ), etc. The spatial structures of these unstable flows were visualised in the  $r$ - $\theta$  plane using the streamfunction of the vertically integrated horizontal flow and vertical velocity from the numerical results, and photographs of the experimental flow. Visualisation with aluminium flakes revealed sharp, defined and robust polygonal structures, and the edges were more distinct for higher-wavenumber structures. This may be attributed to the shear magnitude in the Stewartson layer. It was found that the shear remains relatively constant throughout the axisymmetric regime. However, as soon as non-axisymmetric modes were established, the magnitude of shear decreased quite dramatically. It continued to decrease with decreasing wavenumber (i.e. increasing  $Ro$ ). However, this diagnostic alone does not explain the why the wavenumber transitions occur since a given amount of shear is not unique to a particular wavenumber.

In regards to discrepancy between positive and negative- $Ro$  structures, Hollerbach (2003) suggested additional testing to reinforce his conclusion about the changes in depth across the shear layer. It was noted that the abrupt change in depth with increasing radius is positive when negative- $Ro$  flows are anomalous. Thus, it is questioned whether positive- $Ro$  flows would be the anomalous case if  $dh/dr < 0$ . This can be achieved by increasing the disk thickness in the double end-wall rotation configuration. Other variations of depth variation across the shear layer induced by linear and non-monotonic topography were proposed. Thus  $dh/dr$  switches between positive and negative values. Aguiar (2008) investigated cases with various bottom topography configurations in a rotating cylindrical tank with differential disk forcing. Details of the study can be found in § 2.4.3. Although no anomalous cases were observed, the suggested criterion of  $dh/dr \rightarrow \infty$  at  $r = R$  being the cause of the anomaly was discredited.

Aguiar (2008) also investigated rotating disks at the caps of a spheroid to observe the effect of instability onset with varying disk spacing. A linear dependence of the critical Rossby number with disk spacing was obtained, with negative  $Ro$  revealing a higher  $Ro_c$  threshold when compared to positive  $Ro$ . The difference in  $Ro_c$  between the two directions of forcing became more apparent as the disks approached one another. Unfortunately, due to the complex geometry, the structures of the flow were unable to be visually captured. The range of azimuthal wavenumbers for each sign of  $Ro$  could not be determined to confirm whether the anomaly observed by Hide & Titman (1967) existed.

Schaeffer & Cardin (2005) developed a quasi-geostrophic model which enforces mass conservation, includes Ekman friction, and is able to handle finite slopes at the end-walls. Four configurations were studied numerically; a flat cylindrical container, an exponential base with a constant  $\beta = -1$ , a split sphere (with differentially rotating polar end caps) and a sphere with flat disks placed at the polar regions. Experimental set-ups involved a sphere with flat disks instead of polar caps and a spherical shell geometry (such as that in figure 2.20). Their primary focus was validating the quasi-geostrophic model at very small Ekman number flows. The smallest  $E$  considered was  $E = 1 \times 10^{-10}$ .

Asymptotic analysis of the quasi-geostrophic equation revealed several scalings for the onset of the instability and critical azimuthal wavenumbers. It was assumed that

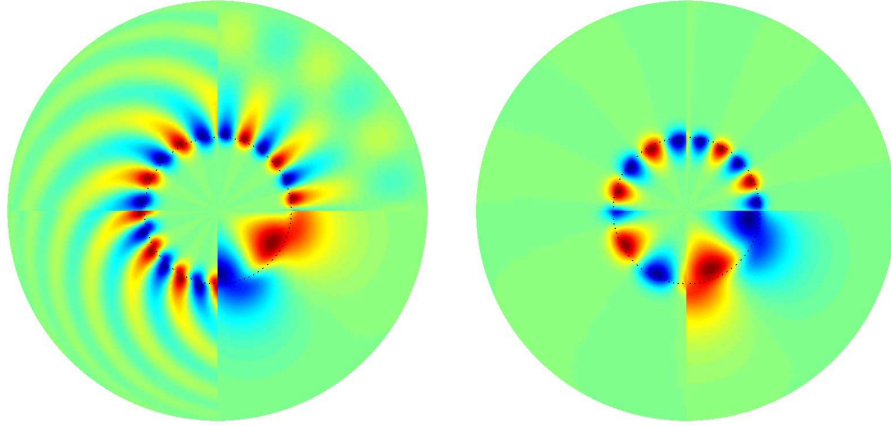
(a) Positive  $Ro$ (b) Negative  $Ro$ 

FIGURE 2.23: Top-down views of the radial velocity for the first unstable mode at  $E = 10^{-6}$  in various geometries for (a)  $Ro > 0$  and (b)  $Ro < 0$ . Clockwise from the top left quadrant, the geometries are of the split-sphere, a constant  $\beta = -1$ , flat container ( $\beta = 0$ ) and spherical case with flat disks. The dotted circle represents the split radius. Red, blue and green contours represent positive, negative and zero values, respectively. Figure courtesy of Dr. Nathanaël Schaeffer and is a colour version of that produced in Schaeffer & Cardin (2005).

the wavenumber of the perturbation is comparable to the thickness of the shear layer at the stability threshold. That is,  $k \sim \delta^{-1} \sim E^{-1}$  where  $\delta$  represents the Stewartson  $E^{1/4}$  layer. Thus, a balance between the nonlinear forcing and the viscous damping for the  $f$ -plane configuration yields  $Ro_c \sim E^{3/4}$ . This is in agreement with the linear theory of Busse (1968). Through the same analysis with an incorporated  $\beta$ -effect, the stability threshold was determined to be

$$Ro_c \sim 2\beta E^{1/2}. \quad (2.18)$$

Furthermore, the critical frequency was found to scale with  $E^{1/2}$  for flat topography while it scales with  $2\beta/k$  when a  $\beta$ -plane is considered. The latter relationship follows a Rossby wave dispersion. It is noted that these frequency scales have not been reported in previous investigations as it may be difficult to distinguish the critical frequency from those of advection which have comparable amplitudes.

For the split-sphere case, the model considers a spherical container filled with fluid, which has a split radius at  $r = r_0$ . For  $r < r_0$ , the end caps rotate differentially at  $\Omega \pm \omega$  while for  $r > r_0$ , the boundary rotates at  $\Omega$ . The instability threshold was obtained as a function of  $Ro$  for  $1 \times 10^{-10} \leq E \leq 1 \times 10^{-5}$ . The onset of instability agrees against  $Ro_c \propto E^{1/2}$ . However, negative- $Ro$  flows demonstrated a stronger stability compared

to positive- $Ro$  flows with negative  $Ro_c$  being approximately three times greater than positive  $Ro_c$ . The trend is reversed for wavenumbers, in that the unstable wavenumber is higher for positive  $Ro$  compared to negative  $Ro$ . It is noted that the critical Rossby wave develops mainly outside of  $r_0$  when  $Ro > 0$ , as illustrated in figure 2.23. This is explained by considering the conservation of potential vorticity (§ 1.3.2). For  $\beta > 0$  and  $Ro > 0$ , the Stewartson layer is a layer of negative vorticity which implies that the perturbations will be damped with increasing radius (increasing  $H$ ) as the relative vorticity will be increased. The opposite is true for  $Ro < 0$ . For  $\beta < 0$  and  $Ro > 0$ , perturbations will be amplified by the decrease in vorticity with increasing radius (decreasing  $H$ ). As the value of  $\beta$  is always negative in the split-sphere case, the instability is promoted in the larger region ( $r > r_0$ ) which may explain why  $k$  is greater for positive  $Ro$ .

The perturbation was found to exhibit spiraling vorticity cells which extend from the origin of the shear layer to the outer boundaries in the spherical configurations (split-sphere and sphere with flat disks as seen in panels (a) and (d) of figure 2.23). This spiral structure is a prograde Rossby wave and is a consequence of the variable  $\beta$  with increasing radius. This is only seen for positive  $Ro$ . While not observed by Aguiar (2008), it has been noted that these structures do exist in thermal convection of spherical shells (Cardin & Olson 1994). It is surprising to note that the study of Hollerbach *et al.* (2004) did not observe any of these spiral patterns in their numerical work after imposing  $z$ -independent solutions onto a full sphere. When  $Ro < 0$ , the spherical configurations demonstrated instabilities growing towards the centre instead which were not spiral in appearance. Non-spiralling vorticity cells which extend to the outer boundaries were obtained for  $Ro > 0$  and a constant negative  $\beta$  (figure 2.23(b)).

The numerical work by Hollerbach (2003) was complimented by the experimental results of the differentially rotating spherical shell in the study by Schaeffer & Cardin (2005). Good agreement was obtained in the results of the critical wavenumbers and the critical Rossby number. The  $|Ro_c|$  for negative- $Ro$  flows was approximately three times larger than that of positive- $Ro$  flows. This difference can be explained by the strength of the Rossby waves. It was stated that for  $Ro > 0$ , the waves are stronger on either side of the shear layer as the depth decreases when moving away from this tangent cylinder. The region of  $r > r_0$  is favoured due to the influence of the larger  $|\beta|$  compared to the  $|\beta|$  in  $r < r_0$ . However, there is no deeper region around the shear

layer for  $Ro < 0$ , and therefore the instability is damped radially away from the shear layer. Thus a stronger forcing is needed to induce instability in  $Ro < 0$  flow.

The numerical simulations of the  $f$ -plane found that there were no differences between positive and negative- $Ro$  flows. The models of their flat case followed those of Niino & Misawa (1984) and Früh & Read (1999). Their numerical results showed pleasing agreement with experimental results from Niino & Misawa (1984) in relation to the critical Rossby number and critical wavenumber for various Ekman numbers. However, the  $Ro_c$  values they obtain were about half that of Früh & Read (1999) even though the critical wavenumber was in agreement. This lower  $Ro_c$  was argued to be as a consequence of the missing  $E^{1/3}$  layer in the quasi-geostrophic model. The spatial structure of the instability did not show any preferred direction of growth with vortical structures originating at the shear radius. This can be seen in figure 2.23(c). The numerically determined critical wavenumbers scaled with the asymptotic result of  $E^{-1/4}$ .

The quasi-geostrophic modelling of the sphere with disk end-walls did not show good agreement with  $Ro_c$ , though it does appear to scale with  $E^{1/2}$ . It was stated that the onset was determined visually by various independent people. Similar to other spherical experiments, the visualisation of these instabilities have made it difficult to determine the actual azimuthal wavenumber and frequencies. The determination of the instability onset found that the numerical quasi-geostrophic results were a factor of 2 less than the experimental results for  $Ro < 0$  and less by a factor of 3 for  $Ro > 0$ .

In conclusion, Schaeffer & Cardin (2005) found that the geometrical effects hypothesised by Hollerbach (2003) are due to symmetry breaking in the Rossby wave propagation mechanism, rather than any abrupt changes to the depth derivatives associated with the geometry. That is, depending on the sign of  $Ro$  and  $\beta$ , the instability will develop on one side of the shear layer and this symmetry breaking is independent of whether there are abrupt changes in the height of the container. If this is the case, the discrepancies in spatial structures between positive and negative  $Ro$  investigated by Hide & Titman (1967) remains unexplained as Rossby waves are not sustained in flat containers.

#### 2.4.6 Keplerian flow

The majority of the studies described in this chapter have focused on creating the Stewartson layer and studying its stability. However, there is also interest in investigating

whether the effects of the Stewartson layer or the layer itself can be avoided. An ongoing debate in astrophysics concerns the nonlinear stability of astrophysical disks that adopt a Keplerian rotation, namely  $\Omega \propto r^{-3/2}$ . In order for accretion in astrophysical disks to occur, the loss of momentum from mass gravitating towards the disk centre must be balanced by outward angular momentum transfer (Avila 2012). However, the Keplerian velocity profile is linearly stable according to the Rayleigh–Kuo criterion (described in § 1.5.1) and the laminar aspect of the flow is not sufficient to cause accretion. Thus, the observed rates of angular momentum transport may be related to a nonlinear mechanism of the flow. Hence there is great interest in determining the nonlinear stability of Keplerian flows.

It has been proposed that the Keplerian profile could be reproduced in Taylor–Couette type configurations. One such configuration involves using multiple split-rings for the end plates, each rotating independently. Provided enough rings are used, a smooth angular velocity profile can be obtained as each Stewartson layer merges to fill the entire tank and a Keplerian flow can be forced by supplying appropriate boundary rotations. A numerical study by Hollerbach & Fournier (2004) at small  $Ro$  flow suggested that the influence of the Stewartson layers at each split disk and the end effects would be too significant and practically unavoidable for small  $E$ . These results are supported by the numerical work of Avila (2012), who also states that current split-ring configurations used to approximate profiles from accretion disks demonstrate turbulent flow at moderate Reynolds numbers. Recent experiments (Paoletti & Lathrop 2011; Paoletti *et al.* 2012) demonstrated finite-amplitude instabilities in a container with independent rotating cylinders. This is in conflict to the prior experimental results of Ji *et al.* (2006) and Schartman *et al.* (2012), who were not able to observe any such instabilities even at very large Reynolds numbers and argue that the end-walls used by Paoletti & Lathrop (2011) were insufficiently designed. Thus, there still remains the question on whether a truly Keplerian flow would be nonlinearly unstable or not.

## 2.5 Review summary

Various configurations that have been able to produce vortical structures resembling large-scale polar vortices have been discussed in this chapter. A common feature involved in all the configurations is rotation. For a large rotation rate of a base with stationary side walls, hollow vortex cores were produced. Primarily, the intersection

between the base and the fluid's free surface demonstrated polygonal patterns. For fluid-filled containers of small fluid flux or small differential rotations, a ring of vortices bounding an interior polygon was observed. These flows are highly two-dimensional due to the Taylor–Proudman theorem which make them particularly favored for investigation.

The general trend is that with increasing dominance of the inertial forces (increasing  $Ro$  and  $Re$ ), the flow transitions from an axisymmetric stable state to a non-axisymmetric state. Experiments typically observed azimuthal wavenumbers ranging from 6-8 at the onset of transition which decreases with increasing  $Re$  down to a wavenumber of 2. The internal Reynolds number has been found to provide an accurate indication of where the transition from the stable to unstable regime occurs. However, it does not describe the wavenumber transitions. Also, it does not entirely describe the instability onset for flows in a  $\beta$ -plane. Thus, both the Rossby and Ekman numbers are required in order to describe the state of these flows. It should be noted that due to the various configurations studied by many authors, the definitions of  $Ro$ ,  $Re$  and  $E$  are not universal. The definitions often vary in terms of the length and velocity scales they employ. Thus, care must be taken when comparing quantitative results between the different systems.

Many similarities have been demonstrated between the experiments and nature, despite the quantitative differences in the range of governing parameters. The velocity and vorticity profiles have shown similarities with spacecraft measurements (Aguiar *et al.* 2010), along with the resulting structures. All visualisations from experimental investigations appear to show a chain of vortices at the polygon boundary. However, Aguilar *et al.* (2010) find that their vorticity and dye-visualisation demonstrate vortices at the boundary while the velocity field does not display any strong presence. Thus, the vortex elucidation would be significant in such a case. On Saturn, no satellite vortices have been observed. Whether or not these vortices are very thin or do not exist is still unknown.

Although not detailed in this thesis, there exist studies of barotropic vortices in rotating systems which have used vortex creation techniques different to that of source-sink and differential-rotation forcing. An overview of the methods can be found in van Heijst & Clercx (2009) with detailed results in the references within Kloosterziel & van Heijst (1991), Hopfinger & van Heijst (1993) and Beckers & van Heijst (1998).

## 2.6 Hypotheses and testing

A number of questions arise from the literature which require answering in order to further understand the fundamental processes in these shear dominant rotating flows. Several hypotheses are listed below.

1. The vertical structure of the flow transitions from depth-independent to depth-dependent flow as  $|Ro|$  increases. Successive transitions involve time-dependent flows.
2. Flow conditions in the proximity of the instability threshold are dominated by linear instabilities and its preferential azimuthal wavenumber can accurately be determined by a linear stability analysis. Moving away from the instability threshold either by increasing  $Ro$  or decreasing  $E$  causes a larger difference between the azimuthal wavenumber predicted by the linear stability analysis and that of three-dimensional direct numerical simulation.
3. Varying the aspect ratio of the container will result in different preferential azimuthal wavenumbers.
4. The preferential wavenumbers determined by linear stability analysis on a two-dimensional model are agreeable with those determined by linear stability analysis on a quasi-two-dimensional model.

The following studies will be conducted in this thesis to test these hypotheses.

1. Solutions for the axisymmetric base flows will be obtained for a wide range of flow conditions characterised by  $Ro$  and  $E$ . The vertical structure of the flow will be examined for both steady-state and time-dependent flows. Differences between the positive and negative- $Ro$  regime will be examined. In addition, the effect of varying the aspect ratio and the topography will be investigated.
2. Linear stability analysis will be conducted on the steady-state axisymmetric base flows. The onset of instability and the transitions between the preferred azimuthal wavenumbers will be determined. Various instability types will be revealed through the growth rate data as a function of azimuthal wavenumber.
3. Three-dimensional direct numerical simulation will be performed for selected

cases. The non-axisymmetric flow structures revealed in these solutions will be compared to their linear stability analysis counterparts.

4. Flows modelled by quasi-two-dimensional equations are simulated on a quasi-one-dimensional domain. The stability of the flow will be determined through linear stability analysis and computations on a two-dimensional  $r$ - $\theta$  plane will demonstrate non-axisymmetric structures.

In essence, progress of the results chapters are as follows: steady-state basic flows are obtained for a wide range of flow conditions including positive and negative  $Ro$  for the double-disk differential-rotation configuration. The vertical flow structure, shear-layer measurements and its time dependence are examined in Chapter 4. Linear stability analysis is performed on these basic flows to characterise their linear stability. The onset of linear instability and the trends of the preferential azimuthal wavenumbers as functions of  $Ro$  and  $E$  are established in Chapter 5. Three-dimensional direct numerical simulation is used to resolve any nonlinear instabilities and deduce any effects they may have in comparison to their linear counterparts. These results are reported in Chapter 6. Similar analyses from chapters 4-6 are performed on quasi-two-dimensional flows. The differences in flow structure and stability between three-dimensional and quasi-two-dimensional flow are explored in Chapter 7.



## Chapter 3

# Numerical methodology

This chapter provides an overview of the various governing flow approximations and the numerical techniques used to solve them in this thesis. § 3.1 and § 3.2 covers the general governing equations of the rotating flows investigated. The spectral-element technique employed for spatial discretisation and time integration is introduced in § 3.3. A background into linear stability analysis and three-dimensional direct numerical simulation techniques are provided in § 3.4 and § 3.5, respectively. Following this, a Stuart–Landau model used to investigate weakly nonlinear dynamics in the vicinity of a bifurcation point is presented in § 3.6. It should be noted that the focus of the thesis is not on the development of the computational techniques used throughout the study, rather, they serve as a tool to investigate these research problems.

Flows within a differential-disk configuration with two rotating end-walls are primarily investigated. Descriptions of the axisymmetric and quasi-two-dimensional differential-disk models are provided in § 3.7. In addition, the governing equations, reference scales and the boundary conditions implemented in this study are detailed. A description of the validation methods used to ensure sufficient spatial and temporal resolution conclude this chapter with the results detailed in the chapters to follow.

### 3.1 Governing equations

Several assumptions are made in forming the governing equations describing the flows studied in this thesis. It is assumed that the fluid is a continuum with length scales that are sufficiently larger than the molecule size. The fluid itself is considered to be Newtonian, having a direct proportionality between the viscous stresses and the strain

rate. This relationship is given by

$$\tau = \mu \frac{du}{dy}, \quad (3.1)$$

where  $\tau$  represents the shear stress,  $\mu$  is the dynamic viscosity of the fluid and  $u$  is the velocity component parallel to the direction of shear. Many common liquids and gases such as air and water behave as Newtonian fluids, while other fluids including polymer melts, blood, paint and toothpaste exhibit non-Newtonian behaviour (see Deshpande *et al.* 2010, and references therein).

The rotating flows investigated here are assumed to remain well below the threshold Mach number beyond which compressibility effects become significant ( $Ma \simeq 0.3$ ), and so will be treated as being incompressible (Anderson 2007). The Mach number is a dimensionless quantity that represents the ratio between a specified speed to the local speed of sound ( $u_{\text{sound}} = 340.3$  m/s in air at Standard Sea Level conditions).

Taking these assumptions into consideration, the governing equations are described by the time-dependent incompressible Navier–Stokes equations. In an inertial frame of reference, the equations are written in vector form as

$$\frac{\partial \mathbf{u}}{\partial t} + (\mathbf{u} \cdot \nabla) \mathbf{u} = -\nabla P + \nu \nabla^2 \mathbf{u}, \quad (3.2)$$

$$\nabla \cdot \mathbf{u} = 0, \quad (3.3)$$

where  $\mathbf{u}$  is the velocity field,  $P = p/\rho$  is the kinematic pressure,  $p$  is the pressure,  $\rho$  the fluid density and  $\nu = \mu/\rho$  is the fluid kinematic viscosity. These equations are respectively derived from the principles of conservation of momentum and mass. From left to right, the terms in equation 3.2 represent the unsteady acceleration, advection, pressure gradient and diffusion contributions. The terms on the left side of the equation are known as convective terms, which are responsible for the physical transport of properties through an ordered bulk motion. This is in contrast to the diffusion term on the right which disperses fluid properties in all directions. It should also be noted that the advection term is a nonlinear quantity. The continuity equation 3.3 states that there is no net flux of mass.

## 3.2 Quasi-geostrophic model

For very small-Ekman-number flows, the shear and boundary layers, which scale with Ekman number, are very thin. This is most true of the Ekman layers at the confining

end-walls, for which the thickness scales with  $E^{1/2}$ , whereas other shear layers identified in these flows scale with the less aggressive  $E^{1/3}$  and  $E^{1/4}$  scaling. Thus resolving such structures in a full three-dimensional domain is computationally expensive. Therefore, a simpler flow model is required in order to study flows that are described by small  $E$ . This is achieved by making several assumptions. A popular model used in the literature is the two-dimensional quasi-geostrophic model, which enforces depth independence by assuming flow conditions of small  $E$  and small  $Ro$ . That is, quasi-geostrophic flow is computed on a two-dimensional domain.

In a three-dimensional rotational flow, there are regions described by geostrophic and ageostrophic features. Boundary and shear layers are ageostrophic while the bulk interior is characterised by geostrophic motion. For small  $E$  and  $Ro$ , the flow is depth-independent according to the Taylor–Proudman theorem. Therefore, modelling the mid-depth of a three-dimensional domain alone will neglect the effects of any end-walls. Thus the justification for the use of a quasi-geostrophic model involves the addition of an external forcing term which mimics the frictional effects resulting from the boundary and detached shear layers; specifically, the frictional effects from the Ekman layers. The modified governing momentum equation takes the form

$$\frac{\partial \mathbf{u}}{\partial t} + (\mathbf{u} \cdot \nabla) \mathbf{u} = -\nabla P + \nu \nabla^2 \mathbf{u} + \mathbf{F} + G\mathbf{u}, \quad (3.4)$$

where  $\mathbf{F}$  and  $G$  are external forcing terms. These terms are used to describe an averaged frictional effect imposed by the boundaries at a particular distance from the mid-depth. These terms represent the Ekman friction as it describes the decrease or increase in azimuthal velocity due to the Ekman layers. The quasi-two-dimensional model has been developed based on the Ekman solution (Appendix A). Interestingly, the same model can be derived based on an analogous magnetohydrodynamic flow. Both approaches are described in the following sections.

### 3.2.1 Effect of the Ekman layer

Consider a solid-body rotating flow in a cylindrical container. A sufficient rotation causes the flow to suppress any variation in the direction along the rotation axis as stated by the Taylor–Proudman theorem. Any differential forcing in rotation of the base or lid of the container causes Ekman layers to form, which in turn causes the velocity of the flow to match those at the boundaries. Thus, there is a variation in velocity along the depth of the tank. Within the boundary layer, the profile is assumed to be

exponential while it remains constant in the interior of the flow. This depth-independent velocity only occurs in cylinders which have a large height to radius aspect ratio. For small aspect ratios, the flow is dominated by the boundary layers and therefore the velocity profile is assumed to take on a parabolic profile which is characteristic of Poiseuille flow between two plates. This parabolic profile has been adopted in quasi-two-dimensional models previously by Chomaz *et al.* (1988) and Bergeron *et al.* (2000).

The exponential assumption is based on the steady solution of the Ekman boundary layer flow which is an exact solution of the Navier–Stokes equations. The Ekman flow belongs to a family of flows over an infinite disk that includes the Bödewadt and von Kármán flows (see Schlichting 1979; del Arco *et al.* 2005; Lopez *et al.* 2009). In addition, consider the flow being forced at  $\mathbf{u} = U_\infty$  sufficiently far above an infinite stationary flat plate in a rotating reference frame. An Ekman layer develops on the plate to accommodate the transition of the flow velocity to zero at the plate. This general geostrophic Ekman layer problem has a dimensional velocity field solution given by

$$u = U_\infty(1 - e^{-z/\delta} \cos(z/\delta)), \quad (3.5)$$

$$v = U_\infty e^{-z/\delta} \sin(z/\delta), \quad (3.6)$$

where  $\delta$  represents the Ekman layer thickness  $\delta = \sqrt{\nu/\Omega}$ ,  $u$  and  $v$  represents the horizontal and tangential velocity components, respectively, and  $z$  is the vertical directional component. As  $z \rightarrow \infty$ , the velocity components exponentially approaches the geostrophic velocity ( $u \rightarrow U_\infty$  and  $v \rightarrow 0$ ). However, within the boundary layer, there is a flow that is transverse to the interior flow. A plot of  $u$  against  $v$  as a function of  $z/\delta$  would demonstrate the Ekman spiral which suggests that for small  $z/\delta$  the flow is approximately 45 degrees to the left of the interior velocity. Thus, the region which is affected by viscosity is of the  $O(\delta)$ . Furthermore, the vertical velocity induced by the disk in a geostrophic flow is given by

$$w_d = -\frac{\sqrt{E}}{2} \frac{\partial U_\infty}{\partial y}. \quad (3.7)$$

A more detailed derivation can be found in Appendix A following Pedlosky (1987).

Similarly, the velocity solutions can be determined for a quasi-geostrophic flow between two parallel plates located at  $z = 0$  and  $z = 1$  with boundary conditions of  $\mathbf{u}_{bc} = (u_{bc}, v_{bc}, 0)$ . The non-dimensional velocity field for the top boundary layer is

given by

$$u_T = u_0(x, y) + e^{\frac{1-z}{\sqrt{E}}} \left[ (u_{bc,T} - u_0) \cos \left( \frac{1-z}{\sqrt{E}} \right) + (v_{bc,T} - v_0) \sin \left( \frac{1-z}{\sqrt{E}} \right) \right], \quad (3.8)$$

$$v_T = v_0(x, y) + e^{\frac{1-z}{\sqrt{E}}} \left[ (v_{bc,T} - v_0) \cos \left( \frac{1-z}{\sqrt{E}} \right) - (u_{bc,T} - u_0) \sin \left( \frac{1-z}{\sqrt{E}} \right) \right], \quad (3.9)$$

where the ‘ $bc, T$ ’ subscript represents velocity boundary condition of the top boundary, and the ‘0’ subscript represents the first order term of the Taylor expansion of the velocity components. For example, the velocity component  $w$  is expanded in powers of the Rossby number such that  $w = w_0 + Ro w_1 + Ro^2 w_2 + \dots$ . That is, retaining only the 0 subscript terms results in the quasi-geostrophic equations. Similarly, the velocity solution for the bottom boundary layer is given by

$$u_B = u_0(x, y) + e^{\frac{z}{\sqrt{E}}} \left[ (u_{bc,B} - u_0) \cos \left( \frac{z}{\sqrt{E}} \right) + (v_{bc,B} - v_0) \sin \left( \frac{z}{\sqrt{E}} \right) \right], \quad (3.10)$$

$$v_B = v_0(x, y) + e^{\frac{z}{\sqrt{E}}} \left[ (v_{bc,B} - v_0) \cos \left( \frac{z}{\sqrt{E}} \right) - (u_{bc,B} - u_0) \sin \left( \frac{z}{\sqrt{E}} \right) \right], \quad (3.11)$$

where the subscript ‘ $bc, B$ ’ subscript represents velocity boundary condition of the bottom boundary. Note that with the appropriate initial conditions ( $v_0 = 0$ ), boundary conditions ( $u_{bc} = v_{bc} = 0$ ) and scalings, equations 3.10 and 3.11 are the same as equations 3.5 and 3.6, respectively. This can be seen by scaling the axial coordinate with  $z^* = zH$ , where the asterisk denotes a dimensional variable. More importantly, inclusion of quasi-geostrophic effects by retaining terms of  $O(Ro)$  yields a vertical velocity induced by the Ekman layer on the top and bottom surfaces given by

$$w_1(x, y, 1) = \frac{\sqrt{E}}{2Ro} (\omega_{z,bc} - \omega_{z,0}), \quad (3.12)$$

$$w_1(x, y, 0) = \frac{\sqrt{E}}{2Ro} (\omega_{z,0} - \omega_{z,bc}), \quad (3.13)$$

respectively, where  $\omega$  represents the vorticity. Hence, the non-dimensional governing vorticity equation is given by

$$\frac{\partial \omega_{z,0}}{\partial t} + (\mathbf{u} \cdot \nabla) \omega_{z,0} = \frac{\sqrt{E}}{Ro} (\omega_{z,bc} - \omega_{z,0}) + \frac{1}{Re} \nabla^2 \omega. \quad (3.14)$$

Equation 3.14 states that the total rate of change of the relative vorticity is due to the vortex tube stretching induced by the Ekman layers  $\partial w / \partial z$ , and the horizontal diffusion of vorticity  $Re^{-1} \nabla^2 \omega_{z,0}$ . Equation 3.14 is identical to the governing equation used by Fröh & Nielsen (2003) in studying quasi-two-dimensional rotating flows. Indeed, this

equation can be recast in terms of the velocity components such that the first two terms on the right hand side respectively correspond to the last two forcing terms in equation 3.4. Consequently, the three-dimensional problem has been reduced to a two-dimensional problem, and simultaneously the need to resolve the thinnest structure in the flow (the Ekman layers) has been eliminated.

### 3.2.2 Magnetohydrodynamic flow analogy

A somewhat analogous flow to rotating flow between two parallel plates is that of magnetohydrodynamic flow between two plates subjected to a strong transverse magnetic field. The magnetic field acts to suppress motions along the field direction similar to that of rotation in the hydrodynamic case. The velocity profile in the magnetohydrodynamic case also exhibits exponential behaviour in the boundary layers and is constant in the interior (Sommeria & Moreau 1982; Poth erat *et al.* 2000, 2005). Boundary and shear layers in these flows are known as Hartmann and Shercliff layers, which are analogous to Ekman and Stewartson layers, respectively. The same dilemma arises in that for high Hartmann number ( $Ha$ ) flows, the Hartmann layer becomes very thin as it scales reciprocally with the  $Ha$ . The Hartmann number is the ratio of electromagnetic to viscous forces. To overcome the computational requirements in simulating high  $Ha$  flow, quasi-two-dimensional models have been developed. The non-dimensional governing equations derived by Sommeria & Moreau (1982) is given by

$$\frac{\partial \mathbf{u}}{\partial t} + (\mathbf{u} \cdot \nabla) \mathbf{u} = -\nabla P + \frac{N}{Ha^2} \nabla^2 \mathbf{u} + \frac{N}{Ha} (\mathbf{u}_0 - n \mathbf{u}_\perp), \quad (3.15)$$

where  $N = \sigma B^2 H / (\rho U)$  is the interaction parameter,  $B$  the vertical magnetic component,  $H$  the spacing between parallel plates,  $\rho$  the fluid density,  $U$  a typical velocity,  $Ha = HB\sqrt{\sigma/\rho\nu}$ ,  $\sigma$  the electrical conductivity,  $\nu$  the kinematic viscosity,  $\mathbf{u}$  is the velocity field,  $\mathbf{u}_0$  is the forcing velocity due to electrical conduction through the out-of-plane walls,  $\mathbf{u}_\perp$  is the interior velocity field relative to the boundary velocity and  $n$  represents the number of Hartmann layers. The last term on the right hand side of the equation is known as the Hartmann friction term. The scaling follows  $\mathbf{u}^* = \mathbf{u}U$ ,  $t^* = tH/U$ ,  $P^* = pU$  and  $\nabla^* = \nabla/H$  where variables with asterisk superscripts represent dimensional variables. Hence, the dimensional equation is defined as

$$\frac{\partial \mathbf{u}^*}{\partial t^*} + (\mathbf{u}^* \cdot \nabla^*) \mathbf{u}^* = -\nabla P^* + \nu \nabla^{*2} \mathbf{u}^* + Ha \frac{\nu}{H^2} [\mathbf{u}_0^* - n \mathbf{u}_\perp^*]. \quad (3.16)$$

In recognising the similarities in the velocity profile between magnetohydrodynamic flow and rotating hydrodynamic flow, a relationship for the Ekman friction can be derived. The thickness of the boundary layer in magnetohydrodynamic flow and hydrodynamic flow is given by  $\delta_{Ha} = H/Ha$  and  $\delta_E = \sqrt{E}H$ , respectively. Equating the dimensional thickness expressions and substituting, the dimensional quasi-two-dimensional for rotating flows can be written as

$$\frac{\partial \mathbf{u}^*}{\partial t^*} + (\mathbf{u}^* \cdot \nabla) \mathbf{u}^* = -\nabla P^* + \nu \nabla^{*2} \mathbf{u}^* + \frac{1}{\sqrt{E}} \frac{\nu}{H^2} [n(\mathbf{u}_b^* - \mathbf{u}^*)], \quad (3.17)$$

where  $\mathbf{u}^*$  is the velocity field,  $\mathbf{u}_b^*$  is the velocity at the boundaries, and  $n$  is the number of friction (Ekman) layers. Note that there is no additional forcing term which is comparable to  $\mathbf{u}_0^*$  in the hydrodynamic case and that the friction is modelled solely on the difference in rotation between the boundary and the interior velocity. The last term on the right side of the equation represents the Ekman friction term, which becomes more pronounced with an increasing number of Ekman layers. Equation 3.14 can be obtained by scaling equation 3.62 with  $\mathbf{u}^* = \mathbf{u}R\omega$ ,  $\nabla^* = 2\nabla/R$ ,  $t^* = t/(2\omega)$  and  $p^* = R^2\omega^2 p$  for flow between two parallel plates ( $n = 2$ ). Comparing equations 3.4 and 3.17, the external forcing terms are given by  $\mathbf{F} = (\sqrt{E}/Ro)\mathbf{u}^*$  and  $G = \sqrt{E}/Ro$ .

Thus, rotating flows influenced by the presence of Ekman layers can be computed on a two-dimensional domain if described by quasi-geostrophic equations. Although the geostrophic model captures the frictional effects of the Ekman layer, the model itself still does not directly involve vertical velocities. Hence, the quasi-geostrophic model can only model the thicker  $E^{1/4}$  layer and not the  $E^{1/3}$  layer. The significance of the  $E^{1/3}$  layer is still not clearly known although several authors have typically attributed discrepancies between numerical and experiments to this exclusion (Schaeffer & Cardin 2005). Despite this omission, the numerical results have been found to be qualitatively accurate and have proven that the quasi-two-dimensional model is a valuable tool.

### 3.3 Spectral-element method

The governing equations are discretised and solved via a spectral-element method (Karniadakis *et al.* 1991; Karniadakis & Sherwin 2005). Similar to finite-element methods, the domain space is discretised into macro elements which are then further discretised into  $N_p \times N_p$  nodes through basis functions. However, spectral-element methods employ high-order Lagrangian interpolants which allows a higher convergence rate and higher

accuracy. The method can be thought of as a high-order finite-element method which adopts geometric flexibility from finite elements and the spectral convergence acquired from spectral methods.

The software used to discretise and solve the governing equations throughout the study is an in-house formulation that has been developed by Associate Professor Gregory J. Sheard. The software exists in an Open Multiprocessing (OpenMP) and a Message Passing Interface (MPI) environment, namely *Viper* and *Vmpir*, respectively. The code has been validated in prior studies (e.g. Sheard *et al.* 2005; Sheard & Ryan 2007; Sheard 2009) and the techniques of the spectral-element method are reviewed in the following sections. Further details of the techniques can be found in Karniadakis *et al.* (1991) and Karniadakis & Sherwin (2005).

### 3.3.1 Spatial discretisation

The two-dimensional computational domain is discretised into quadrilateral elements. The elements are able to adopt curvilinear sides through parametric mapping but are required to respect quadrilateral properties. Consequently, no element corner is allowed to have an inner angle equal to or larger than  $180^\circ$ . A refinement of the flow solution is achieved by increasing the interpolating polynomial degree imposed within each of the elements or increasing the number of elements. The former is known as a  $p$ -refinement technique and the latter as an  $h$ -refinement technique. Depending on the geometry of the domain, a pure  $h$ - or  $p$ -refinement of the mesh may be inappropriate as dense elements may be generated unnecessarily in regions of small velocity gradients. Therefore, a combination of both refinement techniques is used to balance solution accuracy and computational expense, which is known as the  $h$ - $p$  method (Karniadakis & Sherwin 2005).

The Lagrange polynomials are defined as

$$L_i(\xi) = \prod_{j=0, j \neq i}^N \frac{(\xi - \xi_j)}{(\xi_i - \xi_j)}, \quad (3.18)$$

where  $\xi$  is the spatial coordinate,  $i$  and  $j$  represent the spatial indices of the data points and  $N$  is the total number of data points.

Within each element, the Gauss–Lobatto–Legendre quadrature is employed for integration. The Gauss–Lobatto–Legendre quadrature points include points fixed at the element edges to facilitate a continuous solution between adjoining elements. In one

dimension, the Gauss–Lobatto–Legendre quadrature is exact for polynomials of degree  $2N_p - 3$ . In addition, the Gauss–Lobatto–Legendre quadrature points are the roots of the equation

$$(1 - \xi)(1 + \xi)P'_m(\xi) = 0 \quad \text{with} \quad -1 \leq \xi \leq 1, \quad (3.19)$$

where  $P_m$  is the Legendre polynomial. Using Rodriguez's formula, the polynomial can be written as

$$P_m = \frac{1}{2^m m!} \frac{d^m}{d\xi^m} (\xi^2 - 1)^m \quad \text{where} \quad m = 0, 1, 2, \dots \quad (3.20)$$

Galerkin weighted residual methods are used to form equations for the flow solution at the nodal points in the domain. A nodal weight function is used to multiply the nodal equations and are integrated in space. The weighting functions are non-zero only within the local element, and therefore the integral is only dependent on the local and immediate neighbouring nodal points. The weighting coefficients of the Gauss–Lobatto–Legendre quadrature are given by

$$w_j = \frac{2}{m(m+1)} \frac{1}{[P_m(x_j)]^2} \quad \text{where} \quad j = 0, 1, 2, \dots, m, \quad (3.21)$$

and in combination with the quadrature points, the integrals can be determined using Gauss–Lobatto–Legendre quadrature in two dimensions.

### 3.3.2 Time discretisation

A backwards differentiation scheme is used to time integrate the equations, where the momentum equation is evaluated at the future time step  $(n+1)$  while the time derivative term is replaced by a backward differentiation formula, such that

$$\frac{\alpha_0 \mathbf{u}^{(n+1)} - \sum_{q=1}^J \alpha_q \mathbf{u}^{(n-q+1)}}{\Delta t} = -[(\mathbf{u} \cdot \nabla) \mathbf{u}]^{(n+1)} - \nabla P^{(n+1)} + \nu \nabla^2 \mathbf{u}^{(n+1)} + \mathbf{F}^{(n+1)} + G \mathbf{u}^{(n+1)}, \quad (3.22)$$

where  $\mathbf{F}$  is a forcing term,  $G$  is the coefficient of the forcing term linear with the velocity field,  $J$  denotes the order of the scheme and  $\alpha$  are the corresponding coefficients. In this study, a third-order backwards differentiation scheme is used which adopt coefficients provided in Table 3.1.

An operator-splitting method involving a three-step splitting scheme is used to temporally discretise the Navier–Stokes equations. The splitting scheme integrates each term on the right hand side of equation 3.22 separately over one time step. The

---

Coefficient	Value
$\alpha_0$	11/6
$\alpha_1$	-3
$\alpha_2$	3/2
$\alpha_3$	-1/3
$\beta_0$	3
$\beta_1$	-3
$\beta_2$	1

---

TABLE 3.1: Coefficients for the third-order backwards multi-step scheme.

---

three substeps are referred to here as the advection, pressure and diffusion substeps. This three-step splitting scheme has been described in Karniadakis *et al.* (1991) and has been used widely thereafter (e.g. Barkley *et al.* 2002; Carmo & Meneghini 2006; Blackburn *et al.* 2008; Blackburn & Sheard 2010). The solution to the Navier–Stokes equations can be obtained by solving the pressure and velocity fields through these substeps.

The first substep involves the advection term that is evaluated through

$$\frac{\mathbf{u}^* - \sum_{q=1}^J \alpha_q \mathbf{u}^{(n-q+1)}}{\Delta t} = -[(\mathbf{u} \cdot \nabla) \mathbf{u}]^{(n+1)} + \mathbf{F}^{(n+1)} + G\mathbf{u}^{(n+1)}, \quad (3.23)$$

where  $\mathbf{u}^*$  is the intermediate velocity field. It is not convenient to solve equation 3.23 implicitly due to the nonlinear term on the right hand side of the equation. Instead, this term is replaced by an explicit projection from previous time steps. Hence,  $\mathbf{u}^*$  is obtained from

$$\frac{\mathbf{u}^* - \sum_{q=1}^J \alpha_q \mathbf{u}^{(n-q+1)}}{\Delta t} = \sum_{q=0}^{J-1} \beta_q [-(\mathbf{u} \cdot \nabla) \mathbf{u} + \mathbf{F} + G\mathbf{u}]^{(n-q)}, \quad (3.24)$$

where  $\beta$  are coefficients, as provided in Table 3.1.

The second sub-step solves

$$\frac{\mathbf{u}^{**} - \mathbf{u}^*}{\Delta t} = -\nabla P^{(n+1)}, \quad (3.25)$$

where  $\mathbf{u}^{**}$  is the second intermediate field. The pressure is obtained through a Poisson equation which is derived by taking the divergence of equation 3.25 and enforcing the divergence-free condition on the second intermediate velocity field. With the appropriate boundary conditions for the pressure field, the pressure field can be obtained through

$$\nabla^2 P^{(n+1)} = \frac{1}{\Delta t} \nabla \cdot \mathbf{u}^*, \quad (3.26)$$

which may then be used with equation 3.25 to calculate  $\mathbf{u}^{**}$ .

The third sub-step known as the diffusion sub-step calculates the effects of viscous diffusion and the forcing terms through the means of a Helmholtz equation on which the velocity boundary conditions are imposed on the  $\mathbf{u}^{(n+1)}$  field,

$$\frac{\alpha_0 \mathbf{u}^{(n+1)} - \mathbf{u}^{**}}{\Delta t} = \nu \nabla^2 \mathbf{u}^{(n+1)}. \quad (3.27)$$

Thus, the calculated pressure and velocity fields at the time step  $(n + 1)$  are obtained, and the procedure is repeated as necessary to advance the flow.

### 3.4 Linear stability analysis

The growth or decay of three-dimensional perturbations introduced into steady-state or periodic solutions of the base flow can be obtained through a linear stability analysis. The adopted method follows Barkley & Henderson (1996) and Sheard (2011), and has been successfully implemented in both Cartesian and cylindrical coordinate systems (e.g. Sheard *et al.* 2005; Blackburn & Sheard 2010; Cogan *et al.* 2011). The present implementation is described in the following sections, specifically for the task of determining the stability of an axisymmetric base flow to infinitesimal non-axisymmetric ( $\partial/\partial\theta \neq 0$ ) disturbances.

#### 3.4.1 Base flow

In assuming that the base flow is axisymmetric ( $r$ - $z$  plane), the derivative terms in the azimuthal direction are zero. To compute these flows, an initial condition of solid-body rotation with a rate matching that of the outer tank walls is imposed together with appropriate boundary conditions. The flow is evolved through time-stepping until steady-state or time periodic conditions are reached. Flows are considered to be steady state once the maximum change in velocity magnitude in the solution decreased below  $1 \times 10^{-12}$ . The majority of the axisymmetric flows investigated herein reached a steady state.

#### 3.4.2 Linear perturbations

The linear stability analysis formulation begins by decomposing the flow variables into the sum of the axisymmetric base flow and an arbitrarily small three-dimensional disturbance,  $\mathbf{u} = \overline{\mathbf{U}}(x, y, t) + \delta \mathbf{u}'(x, y, z, t)$ , where  $\delta$  is a small positive constant. Note

that  $\bar{\mathbf{U}}$  is two-dimensional and  $\mathbf{u}'$  is three-dimensional. Substitution of these decompositions into equations 3.2 and 3.3, and retaining terms of  $O(\delta)$  (terms of  $O(\delta^2)$  may be neglected as they are negligible for small  $\mathbf{u}'$ ) yields the linearised Navier–Stokes equations,

$$\begin{aligned} \frac{\partial \mathbf{u}'}{\partial t} + (\bar{\mathbf{U}} \cdot \nabla) \mathbf{u}' + (\mathbf{u}' \cdot \nabla) \bar{\mathbf{U}} &= -\nabla P' + \nu \nabla^2 \mathbf{u}', \\ \nabla \cdot \mathbf{u}' &= 0. \end{aligned} \quad (3.28)$$

The linearised equations are similar to the full Navier–Stokes flow except for the dual advection term. If instead terms of  $O(1)$  are retained, one recovers the Navier–Stokes equations for the axisymmetric base flow,

$$\begin{aligned} \frac{\partial \bar{\mathbf{U}}}{\partial t} + (\bar{\mathbf{U}} \cdot \nabla) \bar{\mathbf{U}} &= -\nabla \bar{P} + \nu \nabla^2 \bar{\mathbf{U}}, \\ \nabla \cdot \bar{\mathbf{U}} &= 0. \end{aligned} \quad (3.29)$$

It is noted that equations 3.29 do not depend on the perturbation field.

As the geometry of the system is homogeneous in  $\theta$ , it is convenient to represent the three-dimensional perturbation as a Fourier series. That is, the perturbation is comprised of a series of complex sine waves. The series is given by

$$\mathbf{u}'_k(z, r, \theta, t) = \sum_{k=-\infty}^{\infty} \hat{\mathbf{u}}'_k(z, r, t) e^{ik\theta}, \quad (3.30)$$

where  $\hat{\mathbf{u}}'$  represents the complex Fourier coefficients,  $k$  the azimuthal wavenumber,  $\theta$  the azimuthal direction and  $i$  is the imaginary unit. It is imperative due to the presence of non-zero azimuthal velocities in the base flows computed in this study that the complex Fourier coefficients be retained to correctly capture azimuthal precession of the perturbation fields on the swirling base flows. The wavenumber is related to the wavelength,  $\lambda$ , through  $k = 2\pi/\lambda$ , where  $\lambda$  is normalised by an appropriate length scale. In a planar Cartesian flow, the wavelengths in the out-of-plane direction can take any real number. However, in a cylindrical coordinate system, the wave perturbation is restricted to integer azimuthal wavenumbers since it must conform to the azimuthal symmetry of the geometry. Given that equation 3.28 is linear in  $\mathbf{u}'$ , azimuthal Fourier modes are only dependent on the base flow and not on other Fourier modes. Thus, each azimuthal Fourier mode can be computed individually and independently. In addition, as the Fourier coefficients are two-dimensional for a single Fourier mode, they can be computed on the same two-dimensional domain used in computing the base flow.

### 3.4.3 Mode stability

The evolution of a single Fourier mode can be determined by time integrating in Fourier space (that is, replacing velocities  $\mathbf{u}'$  by Fourier coefficients  $\hat{\mathbf{u}}'$ ). The evolution of the perturbation field over a time period is obtained by operating on its current state, characterised by

$$\hat{\mathbf{u}}'_k(t + \tau) = \mathcal{A}(\tau)\hat{\mathbf{u}}'_k(t), \quad (3.31)$$

where  $\tau$  is the time period and  $\mathcal{A}$  is the linear time integration operator. The stability of the flow may be determined by casting the evolution of the perturbation field as an eigenmode problem,

$$\mathcal{A}(\tau)\hat{\mathbf{u}}'_k = \mu_k \hat{\mathbf{u}}'_k, \quad (3.32)$$

where  $\mu_k$  and  $\hat{\mathbf{u}}'_k$  are the eigenvalues and eigenvectors of the system, respectively. Stability is dictated by the eigenmode with the largest eigenvalue magnitude. The eigenvalue can either be real or complex. A positive real eigenvalue characterises the instability mode as synchronous, which retains its structure and sign but can grow or decay over time. An instability mode defined by a real negative eigenvalue is of a subharmonic nature, which undergoes a change in amplitude and sign attenuation but preserves its structure. In fact, the period of the perturbation field is twice that of the base flow. Lastly, an instability mode described by a complex eigenvalue is quasi-periodic which contributes an incommensurate frequency into the flow. This frequency results in a perturbation field period that is incommensurate with the base flow period. For rotating flows, the leading eigenvalues are typically complex for azimuthal wave perturbations due to the precession of the perturbation around the swirling base flow. Further details of instability mode classifications can be found in Elston *et al.* (2004), Sheard *et al.* (2005) and Blackburn & Sheard (2010).

Operator  $\mathcal{A}$  is an extremely large matrix made up of  $N \times N$  elements where  $N$  is quantified as being 3 times the number of mesh nodes (one for each velocity component). As an example, a mesh comprised of 500 node points would result in operator  $\mathcal{A}$  having 225 million elements. Therefore, for most practical problems  $\mathcal{A}$  is impractical to compute and construct explicitly.

A flow problem can contain numerous pairs of eigenvalues and eigenvectors. However, the leading eigenmode is of primary interest as it is either the fastest growing or slowest decaying mode. The leading eigenvalue can be determined using a number

of methods, including the power iteration and Arnoldi methods. These methods are iterative in that they rely on repeated time integration over  $\tau$  to resolve the leading one (power iteration) or more (Arnoldi iteration) eigenvalues. The power method continues through this process until it isolates the largest eigenvalue magnitude, representative of the fastest growing mode. The Arnoldi method constructs a Krylov subspace and resolves a requested number of the complex leading eigenvalues. The stability analysis technique adopted here uses the implicitly restarted Arnoldi method implemented through the ARPACK package (Lehoucq *et al.* 1989; Blackburn & Sheard 2010; Sheard 2011).

For a steady-state or periodic base flow, the eigenvalues correspond to the amplification factors from one time period to the next. These amplification factors are known as Floquet multipliers,  $\mu$ .<sup>1</sup> The amplitude of the leading Floquet multiplier provides an indication of the stability of the specified wavenumber. For  $|\mu| < 1$ , the mode is stable as the mode amplitude will decrease over each period. Similarly, a mode is unstable if  $|\mu| > 1$  and neutrally stable if  $|\mu| = 1$ . According to Floquet theory, the perturbation fields satisfy the relationship

$$g'(t + \tau) = e^{(\sigma\tau)}g'(t), \quad (3.33)$$

where  $g'$  represents either one of the velocity components ( $u', v', w'$ ) or pressure ( $p'$ ) and  $\sigma$  is the complex growth rate. Thus, any growth or decay of a perturbation from one period to the next is exponential. The complex growth rate is given by  $\sigma = \sigma_R + i\omega$  where the subscript “ $R$ ” denotes the real component of the growth rate and  $\omega$  is the angular frequency of the linear mode. The value of  $\tau$  is arbitrarily chosen for steady-state solutions while  $\tau$  represents the period for periodic flows.

Steady-state base flows can also be frozen in time and thus do not need to be evolved with the perturbation field, producing an increase in computational efficiency. Since the Floquet multiplier is the periodic amplification factor, equation 3.33 can be rewritten as

$$\mu_k \equiv e^{(\sigma_R + i\omega)\tau}, \quad (3.34)$$

which relates the growth rate, period and Floquet multiplier to each other. Stability is determined only by the real part of the growth rate, which is evaluated from  $\sigma_R =$

---

<sup>1</sup>Floquet theory is developed for time-periodic base flows, but it is used throughout to describe the eigenvalues resulting from linear stability analysis of either steady-state or time-periodic base flows.

$\log |\mu|/\tau$ . Since only the real component of the growth rate is considered throughout this study, the subscript “ $R$ ” is omitted hereafter.

In a typical study, the base flow is governed by at least one non-dimensional parameter. For example, the flow in a pipe is characterised by the Reynolds number. Therefore, the linear stability of the base flow would be characterised by the dependence of the Floquet multiplier on the Reynolds number and the perturbation wavenumber. The direction of the wavelength is in the out-of-plane direction to the two-dimensional plane on which the base flow is computed. The onset of instability can be determined by exploring  $\mu_k$  over a wide range of  $Re$  and wavenumber. The critical  $Re_c$  corresponds to  $|\mu_k| = 1$  (or  $\sigma = 0$ ), which represents neutral stability.

### 3.5 Spectral-element-Fourier method

The geometries considered in this thesis possess an azimuthal homogeneity and therefore, an efficient approach to compute the non-axisymmetric flow in the geometry is to use a spectral-element-Fourier method (Blackburn & Sherwin 2004). The same spectral-element method described in previous sections is used to discretise the flow in the two-dimensional  $r$ - $z$  plane. The third dimension is constructed through a Fourier expansion of the velocity and pressure fields. In cylindrical coordinates, the two-dimensional  $r$ - $z$  plane is expanded in the azimuthal  $\theta$  direction. The number of Fourier modes represents the spatial resolution in the third dimension. Details of the spectral-element-Fourier technique can be found in Karniadakis (1990), Blackburn & Sherwin (2004) and Karniadakis & Sherwin (2005). A brief overview of the method is described here.

The velocity and pressure fields are decomposed with a Fourier expansion in  $\theta$ , such that

$$\begin{pmatrix} u(z, r, \theta, t) \\ v(z, r, \theta, t) \\ w(z, r, \theta, t) \\ p(z, r, \theta, t) \end{pmatrix} = \sum_{j=-J/2}^{J/2-1} \begin{pmatrix} u_j(z, r, t) \\ v_j(z, r, t) \\ w_j(z, r, t) \\ p_j(z, r, t) \end{pmatrix} e^{ik_j\theta}, \quad (3.35)$$

where  $J$  is the number of azimuthal Fourier planes considered in the non-axisymmetric computation and  $k$  is the azimuthal wavenumber of the  $\theta$ -periodic domain. For the cylindrical formulation employed in this thesis, the smallest possible azimuthal wavenumber number is 1, corresponding to an azimuthal wavelength of  $2\pi$  ( $\lambda = 2\pi/k$ ). Substitution of equation 3.35 into the governing Navier–Stokes equations (3.2) and

expressed in cylindrical coordinates yields

$$\frac{\partial u_j}{\partial t} = \mathcal{F}_j [-(\mathbf{u} \cdot \nabla)\mathbf{u}]_z - \frac{\partial P_j}{\partial z} + \nu \left( \nabla_{rz}^2 - \frac{k^2 j^2}{r^2} \right) u_j, \quad (3.36)$$

$$\frac{\partial v_j}{\partial t} = \mathcal{F}_j [-(\mathbf{u} \cdot \nabla)\mathbf{u}]_r - \frac{\partial P_j}{\partial r} + \nu \left[ \left( \nabla_{rz}^2 - \frac{k^2 j^2 + 1}{r^2} \right) v_j - \frac{2ikj}{r^2} w_j \right], \quad (3.37)$$

$$\frac{\partial w_j}{\partial t} = \mathcal{F}_j [-(\mathbf{u} \cdot \nabla)\mathbf{u}]_\theta - \frac{ikj}{r} P_j + \nu \left[ \left( \nabla_{rz}^2 - \frac{k^2 j^2 + 1}{r^2} \right) w_j - \frac{2ikj}{r^2} v_j \right], \quad (3.38)$$

where  $\mathcal{F}$  is a Fourier transform in the azimuthal direction. The Laplacian operator in cylindrical coordinates is defined as

$$\nabla_{rz}^2 = \frac{\partial^2}{\partial z^2} + \frac{1}{r} \frac{\partial}{\partial r} \left( r \frac{\partial}{\partial r} \right) + \frac{1}{r^2} \frac{\partial^2}{\partial \theta^2} = \frac{\partial^2}{\partial z^2} + \frac{1}{r} \frac{\partial}{\partial r} \left( r \frac{\partial}{\partial r} \right) - \frac{k^2 j^2}{r^2} \quad (3.39)$$

and the nonlinear terms are expressed as

$$[-(\mathbf{u} \cdot \nabla)\mathbf{u}]_z = \mathcal{F}_j \left[ -u \left( \frac{\partial u}{\partial z} + \frac{\partial v}{\partial r} + \frac{ikjw}{r} \right) \right], \quad (3.40)$$

$$[-(\mathbf{u} \cdot \nabla)\mathbf{u}]_r = \mathcal{F}_j \left[ -v \left( \frac{\partial u}{\partial z} + \frac{\partial v}{\partial r} + \frac{ikjw}{r} \right) \right], \quad (3.41)$$

$$[-(\mathbf{u} \cdot \nabla)\mathbf{u}]_\theta = \mathcal{F}_j \left[ -w \left( \frac{\partial u}{\partial z} + \frac{\partial v}{\partial r} + \frac{ikjw}{r} \right) \right]. \quad (3.42)$$

A set of complex transformations on the velocity fields are required in order to decouple equations 3.36 to 3.38. Following Tomboulides & Orszag (2000) and Blackburn & Sherwin (2004), the change of variables are given by

$$\tilde{v}_j = v_j + iw_j, \quad (3.43)$$

$$\tilde{w}_j = v_j - iw_j. \quad (3.44)$$

Applying this transformation yields a set of equations that are linear in  $u_j$ ,  $\tilde{v}_j$  and  $\tilde{w}_j$  except in the nonlinear terms for which there is a coupling. The equations are given by

$$\frac{\partial u_j}{\partial t} = \mathcal{F}_j [-(\mathbf{u} \cdot \nabla)\mathbf{u}]_z - \frac{\partial p_j}{\partial z} + \left( \nabla_{rz}^2 - \frac{k^2 j^2}{r^2} \right) u_j, \quad (3.45)$$

$$\frac{\partial \tilde{v}_j}{\partial t} = \tilde{\mathcal{F}}_j [-(\mathbf{u} \cdot \nabla)\mathbf{u}]_r - \left( \frac{\partial}{\partial r} - \frac{kj}{r} \right) p_j + \left( \nabla_{rz}^2 - \frac{(kj+1)^2}{r^2} \right) \tilde{v}_j, \quad (3.46)$$

$$\frac{\partial \tilde{w}_j}{\partial t} = \tilde{\mathcal{F}}_j [-(\mathbf{u} \cdot \nabla)\mathbf{u}]_\theta - \left( \frac{\partial}{\partial r} + \frac{kj}{r} \right) p_j + \left( \nabla_{rz}^2 - \frac{(kj-1)^2}{r^2} \right) \tilde{w}_j, \quad (3.47)$$

with the Fourier-transformed nonlinear terms undergoing a change of variables. The  $\theta$ -derivatives are evaluated using the property  $\partial u / \partial \theta = \mathcal{F}^{-1} [ikj\mathcal{F}\{u\}]$  while the  $r$  and  $z$ -derivatives are evaluated on the spectral-element plane in the standard fashion. The

same time integration method described earlier in § 3.3.2 is used in this solver. The velocity fields are transformed to real space to evaluate the nonlinear terms, while the remainder of the time step is evaluated in Fourier space. To stabilise the computation, the inverse transform during the nonlinear solve is projected onto a higher-resolution space, with the option of one additional Fourier mode, or numerous additional modes to satisfy the two-thirds antialiasing rule being facilitated. The latter option is employed throughout this thesis, such that a simulation of 48 Fourier modes for pressure and diffusion corresponds to 71 Fourier modes used for antialiasing of the advection terms.

### 3.6 Stuart–Landau modelling

A Stuart–Landau model is used to investigate the weakly nonlinear dynamics in the vicinity of a bifurcation point. The Stuart–Landau equation describes the time variance of the complex amplitude  $A$  of an unstable mode which is related to the growth rate  $\sigma$  of that particular mode and can be used to establish the nature of non-axisymmetric transitions. That is, whether the transitions are supercritical or subcritical. The Stuart–Landau equation is defined as

$$\frac{dA}{dt} = (\sigma + i\omega)A - l(1 + ic)|A|^2A + \dots, \quad (3.48)$$

where  $\omega$ ,  $l$ , and  $c$  are all real. Here,  $\omega$  is the angular oscillation frequency during the linear growth regime and  $c$  is the Landau constant, which is a non-dimensional parameter. The quantity  $l$  is dimensional and its sign can be used to categorise whether a transition is supercritical or subcritical. Supercritical and subcritical transitions are also known as non-hysteretic and hysteretic transitions, respectively, as it describes the hysteretic nature in the vicinity of the critical transition. The term on the left of equation 3.48 represents the change in complex amplitude over time while the terms on the right represents the series expansion. If the first term from the expansion is the only term retained, then exponential behaviour is predicted by linear stability analysis such that  $A$  grows or decays monotonically. If the second term is retained and  $l$  is positive, then a saturated solution is described with  $|A| = (\sigma/l)^{1/2}$ . This corresponds to a supercritical transition as  $|A| > 0$  is only possible for  $\sigma > 0$  (i.e. beyond neutral stability). If  $l$  is negative, then higher terms are required to describe the saturation of the flow, and the possibility of bi-stability ( $|A| = 0$  or  $|A| > 0$  possible for some  $\sigma < 0$ ). This corresponds to subcritical behaviour.

The Stuart–Landau model has been used extensively in the investigations of bluff-body wake transitions and have been detailed and applied to stability analyses (Provansal *et al.* 1987; Le Gal *et al.* 2001; Sheard *et al.* 2004; Thompson & Le Gal 2004). However, this type of modelling has also been used for instabilities in any weakly nonlinear rotating flow similar to those studied here (van de Konijnenberg *et al.* 1999; Bergeron *et al.* 2000). Thus, a brief overview of its application will be provided here.

It is proposed that the complex amplitude takes the form of

$$A(t) = \rho(t)e^{i\phi(t)}, \quad (3.49)$$

where  $\rho$  is the real and non-negative amplitude of  $A$ , and  $\phi$  is its phase. Substituting this expression into equation 3.48 and splitting the Stuart–Landau equation into the real and imaginary parts yields

$$\frac{d \log(\rho)}{dt} = \sigma - l\rho^2 + \dots, \quad (3.50)$$

$$\frac{d\phi}{dt} = \omega - lc\rho^2 + \dots \quad (3.51)$$

It should be noted that for steady-state transitions, only the real components of the Stuart–Landau equation need to be considered, whereas for time-periodic flows, the imaginary components are required. Given that  $|A| = (\sigma/l)^{1/2}$  at saturation, the real amplitude does not change in time and can be written as  $\rho_{\text{sat}} = (\sigma/l)^{1/2}$ . Also at saturation, the flow solution reaches a time-periodic state which has a constant angular oscillation frequency  $\omega_{\text{sat}}$ . This value is given by  $\omega_{\text{sat}} = \omega - lc\rho_{\text{sat}}^2 = \omega - \sigma c$ . The term  $\sigma c$  represents the shift in angular frequency in relation to that of its linear growth regime. This expression can be rearranged such that the Landau constant can be determined from numerical computations. This is given by

$$c = \frac{\omega - \omega_{\text{sat}}}{\sigma}. \quad (3.52)$$

Equation 3.50 takes on a linear function of  $\rho^2$  that is directly related to  $|A|$ . Therefore, it is possible to apply this Stuart–Landau model to numerical results that measure  $|A|$ . To do this, the amplitude variable  $|A|$  must first be specified. In applying the Stuart–Landau model,  $|A|$  has been defined as different parameters in different studies. Such parameters include various velocity components measured at a particular point in the flow, and the  $L_2$  norm. In this study, the  $L_2$  norm is adopted such that the amplitude

is computed from

$$|A| = \left[ \int_V \mathbf{u}^2 dV \right]^{1/2}, \quad (3.53)$$

where  $V$  is the volume of the computational domain.

By observing a plot of  $d \log |A| / dt$  against  $|A|^2$ , the values of  $\sigma$  and  $l$  are given by the vertical axis intercept and the gradient at the vertical intercept, respectively. This is valid for times where  $|A|$  is sufficiently small. Therefore,  $l$  is determined close to the vertical axis. Assuming that the amplitude of the mode is initially small and saturates at a future time, the plot should demonstrate an initial point starting on the vertical axis with an end point on the horizontal axis. A positive slope (negative  $l$ ) at the vertical axis indicates that the transition is subcritical, whereas a negative slope (positive  $l$ ) indicates a supercritical transition.

### 3.7 Geometric model

The following section describes the differential-disk models used to investigate the stability of shear layers produced by differential rotation. The governing equations, parameters, reference scaling and boundary conditions are described. Validation of the spatial resolution for all numerical models used throughout this project can be found in the preliminary sections of their respective chapters.

#### 3.7.1 Differential-disk configuration

A number of differential-disk rotating configurations have been used experimentally, which have been covered in § 2.4. In this study, the double-disk geometry used by Fröh & Read (1999) has been adopted. A closed cylindrical tank of radius  $R_t$ , and height  $H$ , has disks of radius  $R_d$  attached to its boundaries. The circular disks sit flush with the top and bottom boundaries with axes aligned with the axis of rotation of the tank. The tank and disks rotate independently at angular speeds of  $\Omega$  and  $\Omega + \omega$ , respectively, relative to a stationary reference frame. The proportions of the tank are scaled to match the set-up employed by Fröh & Read (1999), which had  $R_t = 30$  cm,  $R_d = 15$  cm and  $H = 10$  cm. A schematic diagram of the model is given in figure 3.1. The tank is entirely filled with a working fluid that is assumed to be incompressible and Newtonian and characterised by the kinematic viscosity  $\nu = \mu / \rho$ , where  $\mu$  is the dynamic viscosity and  $\rho$  is the fluid density.

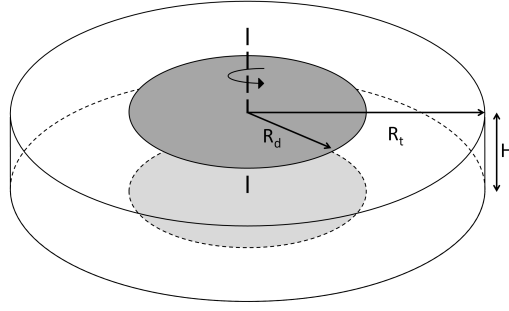


FIGURE 3.1: A schematic diagram of the  $f$ -plane differential rotating disk set-up under investigation. The key dimensions are the disk radius  $R_d$ , tank radius  $R_t$ , and tank height  $H$ . The disks and tank rotate about the central axis (dashed line) at a rate of  $\Omega + \omega$  and  $\Omega$ , respectively.

### 3.7.1.1 Governing equations and parameters

The flow is governed by the time-dependent incompressible Navier–Stokes equations (3.2 and 3.3). Scaling lengths by  $R_d$ , velocity by  $R_d\Omega$ , time by  $\Omega^{-1}$  and pressure by  $\rho(R_d\Omega)^2$  yields the dimensionless equations governing momentum and mass conservation given as

$$\begin{aligned} \frac{\partial \mathbf{u}}{\partial t} + (\mathbf{u} \cdot \nabla) \mathbf{u} &= -\nabla P + \frac{EA^2}{1 - ARo} \nabla^2 \mathbf{u}, \\ \nabla \cdot \mathbf{u} &= 0, \end{aligned} \quad (3.54)$$

where  $\mathbf{u} = (u_z, u_r, u_\theta)$  is the velocity vector,  $P$  is the kinematic pressure, and the aspect ratio of the shear layer is given by  $A = H/R_d$ . The Rossby and Ekman numbers are defined respectively as

$$Ro = \frac{R_d\omega}{2\bar{\Omega}H}, \quad (3.55)$$

$$E = \frac{\nu}{\bar{\Omega}H^2}, \quad (3.56)$$

where  $\bar{\Omega} = \Omega + \omega/2$  is the appropriate mean rotation rate following Fröh & Read (1999) and Aguiar (2008). The parameter  $\bar{\Omega}$  calculated from averaging the rotation rate prescribed in each quadrant in the  $r$ - $z$  plane (i.e.  $\bar{\Omega} = (2\Omega + 2(\Omega + \omega))/4$ ). This method has also been adopted by Aguiar *et al.* (2010) with  $\bar{\Omega} = \Omega + \omega/4$  describing the mean rotation rate of the flow in a differential-ring configuration whereby only one disk is differentially forced.

Remarkably, different mathematical forms of the diffusion coefficient are achieved depending on the choice of reference quantities, the choice of which have implications for the numerical tractability of the system. That is, mathematical singularities ex-

---

Reference quantity	Parameter
Length	$R_d$
Velocity	$R_d\Omega$
Time	$1/\Omega$
Pressure	$R_d\Omega^2\rho$
Diffusion coefficient	$E A^2/(1 - ARo)$
Normalised disk rotation	$(ARo + 1)/(1 - ARo)$
Normalised tank rotation	1
Available $Ro$ range	$Ro < 1/A$

---

TABLE 3.2: Reference quantities employed throughout this study and the associated limitations in the available  $Ro$  range.

---

ist due to the denominator of the diffusion coefficient (which must also be positive), which limits the available  $Ro$  range that can be investigated. Table 3.2 summarises the reference quantities employed and the  $Ro$  range available throughout this study. As indicated in Table 3.2, negative- $Ro$  flows are best investigated using reference quantities based on the tank rotation rate. Similarly, positive- $Ro$  flows are best investigated using reference quantities based on the disk rotation rate (see Appendix B). In this study, the denominator of the diffusion coefficient limits studies to be in the range of  $ARo < 1$ . It is possible to explain this constraint by taking the limit of  $ARo \rightarrow 1$ , such that

$$\begin{aligned}
ARo &= 1, \\
\frac{\omega}{2\Omega + \omega} &= 1, \\
\frac{\omega/\Omega}{2 + \omega/\Omega} &= 1, \\
\frac{\omega}{\Omega} &= 2 + \frac{\omega}{\Omega}.
\end{aligned} \tag{3.57}$$

Dividing equation 3.57 through by  $\omega/\Omega$  yields

$$\begin{aligned}
1 &= \frac{2}{\omega/\Omega} + 1, \\
\frac{2}{\omega/\Omega} &= 0, \\
\frac{\omega}{\Omega} &= \infty,
\end{aligned} \tag{3.58}$$

Thus,  $ARo = 1$  is the limit as  $\omega \rightarrow \infty$  for a constant  $\Omega$ . Therefore, the constraints on computable  $Ro$  is not purely attributed to the reference scales used, rather it is the unique definition of  $\bar{\Omega}$  used in  $Ro$ , which produces these singularities.

The Rossby and Ekman number are used to characterise the flow conditions in this configuration. In addition, a Reynolds number for the shear layer can be defined based on the azimuthal velocity difference across the layer ( $R_d\omega$ ) and a suitable length scale. Using a length scale of  $H$  yields a parameter known as the external Reynolds number, which can be expressed in terms of  $Ro$  and  $E$  and is defined as

$$Re = \frac{R_d\omega L}{\nu} = \frac{2Ro}{E}, \quad (3.59)$$

following Fröh & Read (1999). It should be restated that the choice of length and velocity scales has varied between studies (see § 2.4.3). Using a length scale of  $L = (E/4)^{1/4}H$  yields an internal Reynolds number defined as

$$Re_i = \frac{R_d\omega L}{\nu} = \frac{\sqrt{2}Ro}{E^{3/4}}. \quad (3.60)$$

This parameter is particularly significant in describing the onset of instability on an  $f$ -plane (see Niino & Misawa 1984; Fröh & Read 1999). The same non-dimensional parameter definitions are also applicable to the  $\beta$ -plane case. However, an extra parameter is required, known as the  $\beta$  parameter, and is defined as

$$\beta = \frac{2\bar{\Omega} \tan \theta}{H}, \quad (3.61)$$

with  $\bar{\Omega} = \Omega + \omega/2$ , following Aguiar *et al.* (2010). The height  $H$  used in equation 3.61 represents the height of the shear layer at the disk-tank interface, rather than the full height of the tank.

### 3.7.1.2 Domain and boundary conditions

The flow is computed on an axisymmetric meridional semi-plane that has been discretised into quadrilateral elements (as shown in figure 3.2). The boundaries of the domain are solid and impermeable with the exception of the axis of symmetry (at the left of the frames in figure 3.2). The boundary condition treatment of the symmetry of axis is as per Blackburn & Sherwin (2004); zero radial and azimuthal velocities are exactly enforced as a Dirichlet boundary condition, whereas a zero Neumann condition is imposed on the axial velocity. The remaining boundaries have azimuthal velocity profiles imposed on them to induce a split-disk forcing. A single component of velocity in the azimuthal direction of  $u_\theta = r(\Omega + \omega)$  is imposed on the disks while  $u_\theta = r\Omega$  is imposed on the tank walls. A high order Neumann boundary condition is also imposed for the pressure following Karniadakis *et al.* (1991). The mesh density is concentrated in areas

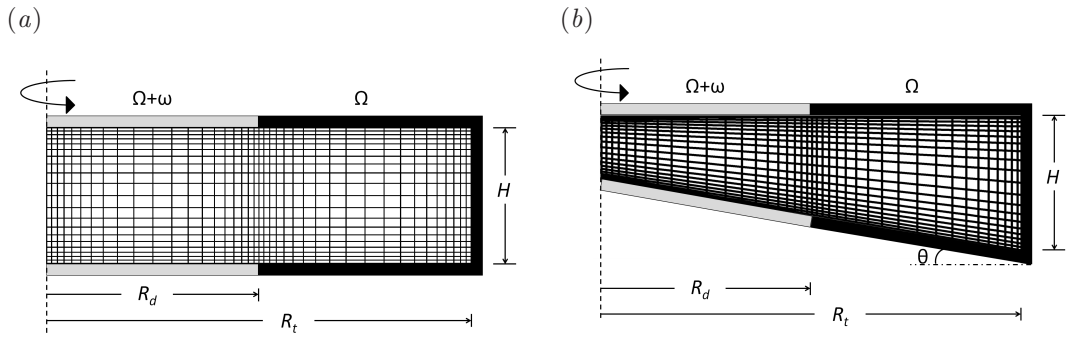


FIGURE 3.2: The spatially discretised semi-meridional mesh used in the numerical simulations is illustrated for (a) the  $f$ -plane and (b) the  $\beta$ -plane with an angled sloping bottom of angle  $\theta$ . The disks (grey) and tank (black) rotate about the central axis (dashed line) at a rate of  $\Omega + \omega$  and  $\Omega$ , respectively.

where shear layers are expected to emerge and evolve. An initial field of  $\mathbf{u} = (0, 0, r\Omega)$  is imposed as an initial condition at time  $t = 0$ .

### 3.7.2 The quasi-geostrophic model

An efficient alternative to the full non-axisymmetric simulations is the employment of a two-dimensional quasi-geostrophic model to compute the flow on a horizontal plane. The model integrates out the vertical direction for which the frictional effects are instead modelled by external forcing terms. Thus, the model only simulates the flow in the  $r$  and  $\theta$  dimensions. In using the length and time scales adopted in table 3.2, the two-dimensional quasi-geostrophic equation (3.17) can be written in dimensionless vector form as

$$\frac{\partial \mathbf{u}}{\partial t} + (\mathbf{u} \cdot \nabla) \mathbf{u} = -\nabla P + \frac{A^2 E}{1 - ARo} \nabla^2 \mathbf{u} + \frac{2\sqrt{E}}{1 - ARo} (\mathbf{u}_b - \mathbf{u}). \quad (3.62)$$

The last term on the right hand side of the equation is a forcing term describing the Ekman friction from the boundary layers on the horizontal boundaries.

For axisymmetric flows, only the  $r$  dimension is required to be simulated since there is no variation in the  $\theta$  and  $z$  directions. Therefore, it is possible to compute the flow on a one-dimensional domain. With the axisymmetric solver described in § 3.3, the one-dimensionality is achieved by adopting a quasi-one-dimensional domain. That is, the height of the domain is much smaller than the radial length of the domain such that the aspect ratio of the mesh is  $A = 0.01/2 = 0.005$ . It is emphasised that the aspect ratio of the mesh is not representative of the aspect ratio of the tank under investigation, which is given by  $A = H/R_d$ . Instead, the mesh is a representative slice

of the axial-invariant flow which can be used to model flow for any  $A$ . An aspect ratio of  $A = 2/3$  is considered for the quasi-two-dimensional model (Chapter 7). In addition, a zero axial velocity is imposed on the horizontal boundaries while the tank's rotation rate is applied to the tank wall. As normal, the left-hand boundary represents the axis of rotation and symmetry. Here, the boundary condition incorporated in the external forcing term is given by

$$\mathbf{u}_b = \begin{cases} \frac{(\Omega + \omega)r}{\Omega R_d} & \text{for } r/R_d \leq 1 \\ r/R_d & \text{for } r/R_d > 1 \end{cases} \quad (3.63)$$

This boundary condition expresses a rotation rate corresponding to the disk for radii less than the disk radius  $R_d$  while a tank rotation is set for radii greater than  $R_d$ . Thus, the boundary condition is discontinuous across  $R_d$ . This is the same condition set on the two-dimensional axisymmetric mesh described in the previous section.

For non-axisymmetric flows, the  $r$ - $\theta$  domain is mapped to a two-dimensional Cartesian grid. The mesh used for these simulations is shown in figure 3.3. The solver used throughout this study only accepts quadrilateral elements. Thus, it is inevitable that the mesh adopts a four-fold symmetry. This was found to present problems for traditional boundary conditions which include a discontinuous azimuthal velocity forcing across the radius at the disk-tank interface. The discontinuity exacerbates the four-fold symmetry of the mesh and feeds energy into wavenumbers which are harmonics of wavenumber 2. Hence the resulting simulations did not reliably capture the azimuthal wavenumber once the flow saturates. To circumvent this issue, a smoothing to the forcing is applied through the use of a hyperbolic tangent function over the transition zone. Hence, the boundary condition in equation 3.63 is replaced by

$$\mathbf{u}_b = \frac{\Omega r + \frac{r}{2} \left[ 1 - \tanh \left( \frac{r - R_d}{\delta} \right) \right] \omega}{\Omega R_d}, \quad (3.64)$$

for all  $r$ , where  $\delta$  represents the thickness of the  $E^{1/4}$  Stewartson layer. Following the length scale used in determining the internal Reynolds number (equation 3.60), the thickness is given by  $\delta = (E/4)^{1/4} H$ . An advantage in using a hyperbolic tangent profile is that the derivative of any order is continuous (Bergeron *et al.* 2000). This exact type of smoothing has been previously applied by van de Konijnenberg *et al.* (1999) and Früh & Read (1999). An initial condition corresponding to a flow characterised by  $\mathbf{u}_b$  is prescribed for the axisymmetric and non-axisymmetric flows.

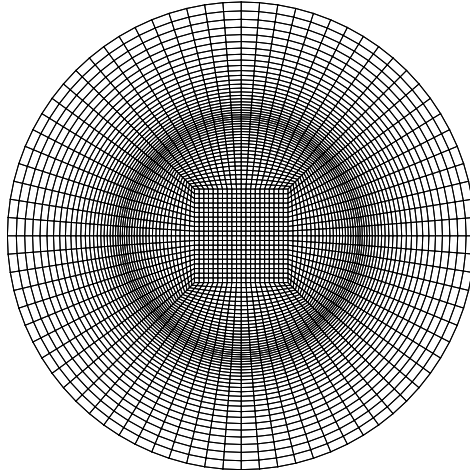


FIGURE 3.3: The spatially discretised semi-meridional mesh used for quasi-two-dimensional numerical simulations. Macro elements are shown in the  $r$ - $\theta$  plane.

---

Limitations of the present approach are that it is inconvenient to track the modal energies of each wavenumber. Also, a direct comparison cannot be made with the full non-axisymmetric solutions since the forcing conditions imposed here are smoothed and not discontinuous.

### 3.7.3 Spatial and temporal resolution refinement

The Navier–Stokes equations are solved in cylindrical coordinates using a nodal spectral-element discretisation in space and a third-order time-integration scheme based on backward differentiation (Karniadakis *et al.* 1991). Imposed upon each macro element are Lagrangian tensor-product polynomial shape functions. The polynomial degree  $N_p$  is varied to control spatial resolution and is interpolated at the Gauss–Lobatto–Legendre quadrature points. Thus, a higher  $N_p$  results in a finer grid. The cylindrical formulation of the solver employed here has been validated in previous studies (Sheard & Ryan 2007; Sheard 2009).

A grid independence study for each mesh have been performed and the results are presented in the preliminary sections of each respective chapter (§ 4.1 and § 7.1). An error threshold between  $0.1\% \lesssim \varepsilon \lesssim 1\%$  is achieved to ensure temporal and spatial accuracy of the flow field solutions. The quantities used to measure solution convergence include norms, several integrated variables, leading eigenvalues of the most unstable wavenumber determined from a linear stability analysis and monitored parameters at

specific points in the flow. It is emphasised that although these quantities do not directly measure error, the differences between their values at different levels of resolution can be used to quantify the uncertainty due to the finite resolution used in the simulations.

The  $L_2$  norm is an integral of the velocity magnitude throughout the entire computational domain. Given that it captures the global velocity field, it is a useful parameter for monitoring solution convergence. Another global quantity this study employs to monitor convergence is the volume integral of the azimuthal velocity relative to the tank rotation. Since the flows studied here are dominant in rotation, the relative azimuthal velocity can capture subtle changes in the solution with varying resolution that may be occluded by the strong background rotation dominating a traditional  $L_2$  norm. A third global parameter used herein is the leading eigenvalues of a specific azimuthal wavenumber obtained via linear stability analysis performed on the base flow. The linear stability analysis technique was described in § 3.4. In addition, the components of velocity and vorticity have been monitored at specific points in the flow to provide an indication of solution convergence with grid resolution. Measurements have been obtained both inside and outside of the shear and boundary layers.

The number of azimuthal Fourier modes, and therefore the azimuthal resolution required to obtain accurate solutions in three-dimensional direct numerical simulations is largely dependent on the flow conditions. Generally, either increasing  $Ro$  or decreasing  $E$  requires an increase in the number of Fourier modes as increases in  $Re_i$  typically present smaller scale structures. For several flow conditions, test cases with several different numbers of Fourier modes have been computed to ensure that the solutions are accurate. The solutions corresponding to the optimal amount of Fourier modes for each case is presented in this thesis as it illustrates the furthest time-integrated flow state.

### 3.8 Chapter summary

Numerical methods used throughout this thesis have been described in this chapter. The general governing equations of three-dimensional and quasi-two-dimensional flow have been presented. The spectral-element method has been established to investigate two-dimensional base flows while a linear stability analysis method is used to examine the flows' stability to three-dimensional perturbations. A formulation of the spectral-

element-Fourier method used for non-axisymmetric flow simulation and a description of the Stuart–Landau model have also been covered.

The differential-disk configurations have been illustrated and detailed, which includes the  $f$ -plane,  $\beta$ -plane and the quasi-two-dimensional model. The flow parameters, reference scales and governing equations used throughout the thesis have been discussed. Interestingly, the choice of scales for length, velocity and time can have numerical limitations on the range of flow conditions available. The boundary conditions imposed on the axisymmetric  $r$ - $z$  mesh and the  $r$ - $\theta$  mesh have been provided.

Finally, quantitative measures adopted to monitor solution convergence with varying spatial resolution have been described. These measures have been used in the grid resolution studies for each differential-disk model. The results of the grid independence study for each model can be found in their respective results sections (§ 4.1 and § 7.1).

The next chapter highlights the flow structures of axisymmetric base flows in a differential-disk rotating configuration with dimensions matching those studied by Früh & Read (1999). Both the positive and negative- $Ro$  regimes are explored. In addition, the effect of varying the aspect ratio on the flow structure is examined. Differences between the flows produced on an  $f$ -plane and the  $\beta$ -plane are also highlighted.



## Chapter 4

# Axisymmetric flow in a differential-disk rotating system

The experiments carried out by Fröh & Read (1999) focused on the number of vortices present for a specific flow condition and with the assumption of the vertical structure being axially-independent for small- $Ro$  flows. The Taylor–Proudman theorem becomes invalid at larger  $Ro$ , and therefore the flow loses its depth independence. Previous experiments have monitored only flow in horizontal planes, and past numerical simulations have primarily solved the two-dimensional quasi-geostrophic equations where there is no depth dependence by definition. In order to gain a deeper understanding of the structures in these rotating flows, the full three-dimensional motions must be simulated to elucidate the vertical structures of the flow.

This chapter presents axisymmetric computations of the basic flow states for a variety of flow conditions in a cylindrical differentially-disk rotating system. The validation of the mesh used throughout this chapter is presented in § 4.1. § 4.2 highlights flow characteristics in a container of the same aspect ratio studied by Fröh & Read (1999), namely  $A = 2/3$ , and discusses the flow structures evident upon the breaking of axial independence and the onset of time-dependent flows. Measurements for the shear layers are conducted and time periodic flows are also presented in this section. In § 4.3, a similar analysis is performed on containers of aspect ratios ranging between  $1/6 \leq A \leq 2$  to investigate the effect of varying the aspect ratio. Finally, in § 4.4 a comparison between structures produced on the  $f$ -plane and  $\beta$ -plane is presented.

Various results from this chapter have been published in Vo *et al.* (2014).

## 4.1 Grid independence study

The flows reported in this chapter have been computed on semi-meridional domains. The geometries of the  $f$ -plane and  $\beta$ -plane meshes have been described earlier in § 3.7.1. The mesh describing an  $A = 2/3$  domain encompasses 800 mesh elements (20 axial elements and 40 radial elements). The number of elements stated here refer to the macro elements, and does not include the collocation points within elements. The mesh adopts bi-exponent profiles for the element vertex distribution on the horizontal boundaries either side of  $r = 1$  and on the side boundaries. The dimensions of the smallest macro element is  $0.0215 \times 0.02325$  (axial  $\times$  radial), which resides at the intersection of the horizontal boundary layer and the vertical shear layer. For other aspect ratio meshes, the number of elements in the axial direction is changed while the number of elements in the radial direction remains constant since the radial length of the domain does not change. These meshes assume the same ratio of the mesh height to the number of axial elements (i.e.  $(2/3)/(20)=1/30$ ). That is, an aspect ratio of  $A = 2$  has 60 axial elements and 40 radial elements with the smallest element having dimensions of  $0.0147 \times 0.02325$  (axial  $\times$  radial). All angles of the  $\beta$ -plane mesh adopt the same number of elements and distribution as the  $A = 2/3$   $f$ -plane mesh.

To ensure grid independence, the convergence of several global parameters with increasing element polynomial order has been computed. A reference case featuring a small  $E = 8.33 \times 10^{-5}$  and a constant  $Ro = -0.833$  is considered. This case is at the more challenging end of the parameter range covered by this thesis, as smaller  $E$  produces thinner shear layers, and thus requiring higher resolution. Therefore achieving grid independence for this case ensures solution accuracy for larger  $E$  cases.

Three measures for convergence are adopted: the volume integral of the azimuthal velocity relative to the tank ( $u_{\theta,rel} = u_{\theta} - \Omega r$ ) across the domain, the leading eigenvalue magnitude obtained by the linear stability analysis of a perturbation with azimuthal wavenumber  $k = 12$ , and the  $L_2$  norm taken as the integral of the velocity magnitude throughout the domain. The values are obtained once the flow has reached a steady state. The relative percentage error  $\varepsilon$  against a high-resolution reference case with element polynomial degree  $N_p = 14$  is plotted in figure 4.1. The results demonstrate a decreasing error with increasing  $N_p$ . The relatively larger errors of the linear stability analysis eigenvalue reflect the fact that higher resolution is typically required to capture the smaller-scale features of the instability mode structure. A threshold criterion of

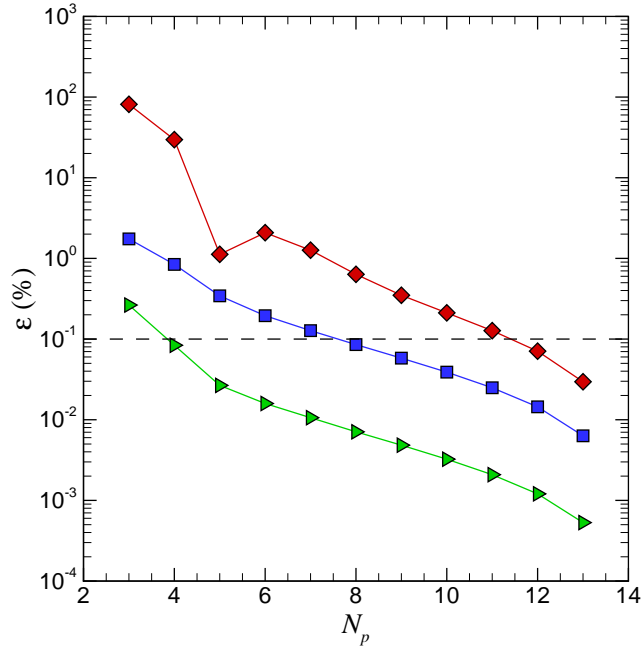


FIGURE 4.1: The relative percentage error  $\varepsilon$  in the global variables of the integral of the relative azimuthal velocity ( $\square$ ),  $L_2$  norm ( $\triangleright$ ) and the leading eigenvalue magnitude ( $\diamond$ ) of the case study  $(Ro, E) = (-0.833, 8.33 \times 10^{-5})$ . A decreasing trend with increasing polynomial degree  $N_p$  is seen with all variables. An error of  $\varepsilon = 0.1\%$  is marked by the horizontal dashed line.

$O(0.1\%)$  is sought to ensure that solution error due to finite spatial resolution is much smaller than likely laboratory sources of error. This is approximately satisfied with  $N_p = 11$ , which is used hereafter.

## 4.2 Simulating the configuration used by Fröh & Read

Fröh & Read (1999) considered a double end-wall differentially-rotating configuration with a disk radius of  $R_d = 15$  cm and a tank height of  $H = 10$  cm. This corresponds to a container aspect ratio of  $A = 2/3$ . This section highlights the numerical results of this configuration and aspect ratio.

Steady-state solutions were obtained on the meridional semi-plane for a variety of flow conditions. Time-evolved solutions are taken to have reached steady-state when velocity variations are less than  $10^{-12}$  between successive time steps. Simulations have been performed for Rossby numbers between  $-4.0 < Ro < 0.6$  and Ekman numbers between  $5 \times 10^{-5} < E < 3 \times 10^{-3}$ . Negative and positive  $Ro$  correspond to the inner disks rotating slower and faster than the tank, respectively. Counter-rotation between

the disks and tank is described when  $\omega < -\Omega$ , corresponding to  $Ro < -R_d/H = -1/A$ . Different characteristics of the flow were observed for small and large- $Ro$  flows for both positive and negative- $Ro$  regimes. The transition of these characteristics for positive and negative  $Ro$  occur at significantly different onset values. A description of these distinct features are divided into positive and negative  $Ro$  at small and large  $Ro$ .

#### 4.2.1 Steady-state axisymmetric flow structure

Typical contours of the axial velocity  $u_z$  and axial vorticity  $\omega_z$  for various positive- $Ro$  flows at  $E = 3 \times 10^{-4}$  are shown in figure 4.2. Ekman pumping is observed at the disk-tank interface ( $r = 1$ ) where fluid is drawn radially towards the interface in the Ekman layer and is ejected axially into the interior. To replace the fluid along the horizontal boundaries, fluid from the interior is directed back into the Ekman layer on either side of the pumping region to complete the circulation. Provided that  $Ro$  is small, the contours of axial velocity demonstrate reflective symmetry about the mid-plane, where the two axial jets within the Stewartson layer meet. That is, the point  $(r/R_t, z/H) \approx (0.5, 0.5)$  exhibits features similar to a hyperbolic equilibrium point. The plane of  $z/H = 0.5$  can also be thought of as an imaginary boundary upon which axial jets are impinging on either side.

Interesting dynamics are also demonstrated at  $r \approx 1$  in the contours of  $\omega_z$ . For the smaller positive- $Ro$  cases (e.g. figure 4.2(a)), the concentrated vorticity portrays significant depth independence, which is surrounded by uniform vorticity. The interior of the flow is dominated by a depth-independent azimuthal velocity field. Thus the base flow is highly two-dimensional away from the lid and base and portrays characteristics consistent with a barotropic flow. The characteristics of the base flow at small  $Ro$  are in agreement with the Taylor–Proudman theorem. Large changes in  $E$  are required to induce the same effect to the flow structure in comparison to  $Ro$  variations. Increasing  $E$  causes a larger shear-layer region to develop and also promotes depth independence, similar to decreasing  $Ro$ . In contrast, thin detached shear layers are present at very small  $E$ .

As the positive Rossby number is increased in magnitude, the flow begins to lose its reflective symmetry about the horizontal mid-plane. The negative-vorticity regions located at the disk-tank interface grow into strands, which are initially symmetric about the mid-depth. Eventually, the strands elongate into the flow interior and the flow loses

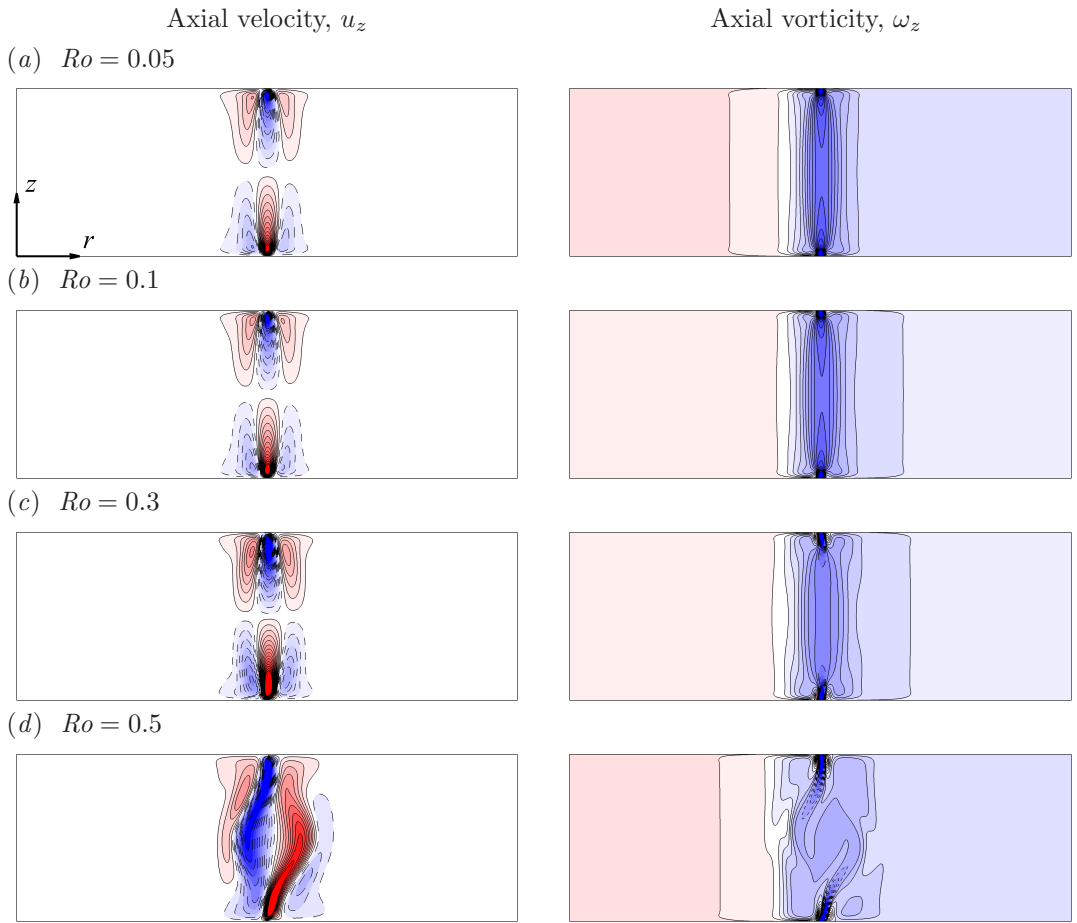


FIGURE 4.2: Structure of the axisymmetric flows visualised on the semi-meridional  $r$ - $z$  plane. Axial velocity (left) and axial vorticity (right) are shown for  $E = 3 \times 10^{-4}$  at (a)  $Ro = 0.05$ , (b)  $Ro = 0.1$ , (c)  $Ro = 0.3$ , and (d)  $Ro = 0.5$ . For the axial velocity plots, equi-spaced contour levels are plotted between  $\pm 0.1 |Ro| (\Omega + \omega)$ , while for the axial vorticity plots, equi-spaced contour levels are plotted between  $2\bar{\Omega} \pm 10\omega$ . Blue and red contour shading represent low and high values, respectively, while solid and dashed contour lines identify positive and negative contour levels, respectively. The domain shown represents the entire semi-meridional plane with  $0 \leq r \leq 2$  and  $0 \leq z \leq 2/3$ . Images are to scale.

---

reflective symmetry about the mid-depth. This behaviour is shown in figure 4.2(d). Further increases to  $Ro$  cause “hooks” to develop at the tips of the negative vortical strands. These are represented by a strand branching back towards the horizontal boundaries from the tip of the strand. This flow feature has only been observed in small  $E$  flows, which form thin detached shear layers. At larger  $E$  and sufficient  $Ro$  forcing, a detached negative-vorticity region is instead present at mid-depth in the shear-layer region. These distinct features which are observed through the progression of increasing  $Ro$ , affect the linear stability of the flow. The linear stability of this flow

is discussed in the next chapter (Chapter 5).

The breaking of the initially vertical band of axial vorticity into diagonal strands may be explained by the dynamics exhibited through the contours of axial velocity. The breaking of the mid-plane reflective symmetry is illustrated in the contours of figure 4.2(*d*), such that the vertical jets fed by axial pumping from each disk now bypass each other (compare figure 4.2(*a*) to (*d*)). It is suspected that the hyperbolic point in the flow is lost due to the axial velocity within the shear layer exceeding some threshold value. As  $Ro$  is increased, the axial pumping velocity is also increased in magnitude. Thus, with sufficient forcing, the axial jets are free to bypass each other. A similar transition has been observed in flows with jets impinging on a horizontal boundary (e.g. Chiriac & Ortega 2002; Hsieh *et al.* 2006). In such studies for small Reynolds numbers, the flow is steady and symmetric about the centreline of the impinging jet. However, as the Reynolds number is increased, the flow becomes unsteady as represented by the distortion of the jet. In addition, vortices are expelled on both sides of the jet in an alternating fashion, induced by a lateral “flapping” of the jet.

Contours of axial velocity and axial vorticity for various negative- $Ro$  flows at  $E = 3 \times 10^{-4}$  are reproduced in figure 4.3. Unlike positive- $Ro$  flows, increases to the magnitude of Rossby number in the negative- $Ro$  regime have a lesser effect on the base flow over a wide range of  $Ro$  values. The flow preserves its reflective symmetry about the mid-plane for the majority of flow conditions computed in this study. This is portrayed in the contours of  $Ro = -1.0$  and  $E = 3 \times 10^{-4}$  (figure 4.3(*b*)). Despite having a significantly larger  $Ro$  magnitude compared to figure 4.2(*d*), the flow still retains its reflective symmetry in the horizontal mid-plane.

The ability for the flow to retain its reflective symmetry about the mid-plane may be explained by the sign of the vorticity generated at the disk-tank interface. For positive- $Ro$  flows, the decrease in angular velocity from the disk to the tank at the disk-tank interface introduces a region of negative vorticity, which develops at larger  $Ro$ . This is not observed for negative  $Ro$ , as the increase in angular velocity at the disk-tank interface produces positive axial vorticity in the vicinity. As this region is surrounded by the same-signed vorticity, it is not encouraged to grow into the interior. If this explanation holds true, the two-dimensionality of the flow is expected to break if the disk and tank rotate in opposite directions. This occurs when  $\omega \leq -\Omega$  or, equivalently,  $Ro \leq -1/A$  ( $Ro \leq -1.5$  in the present system). Alternatively, this explanation can be

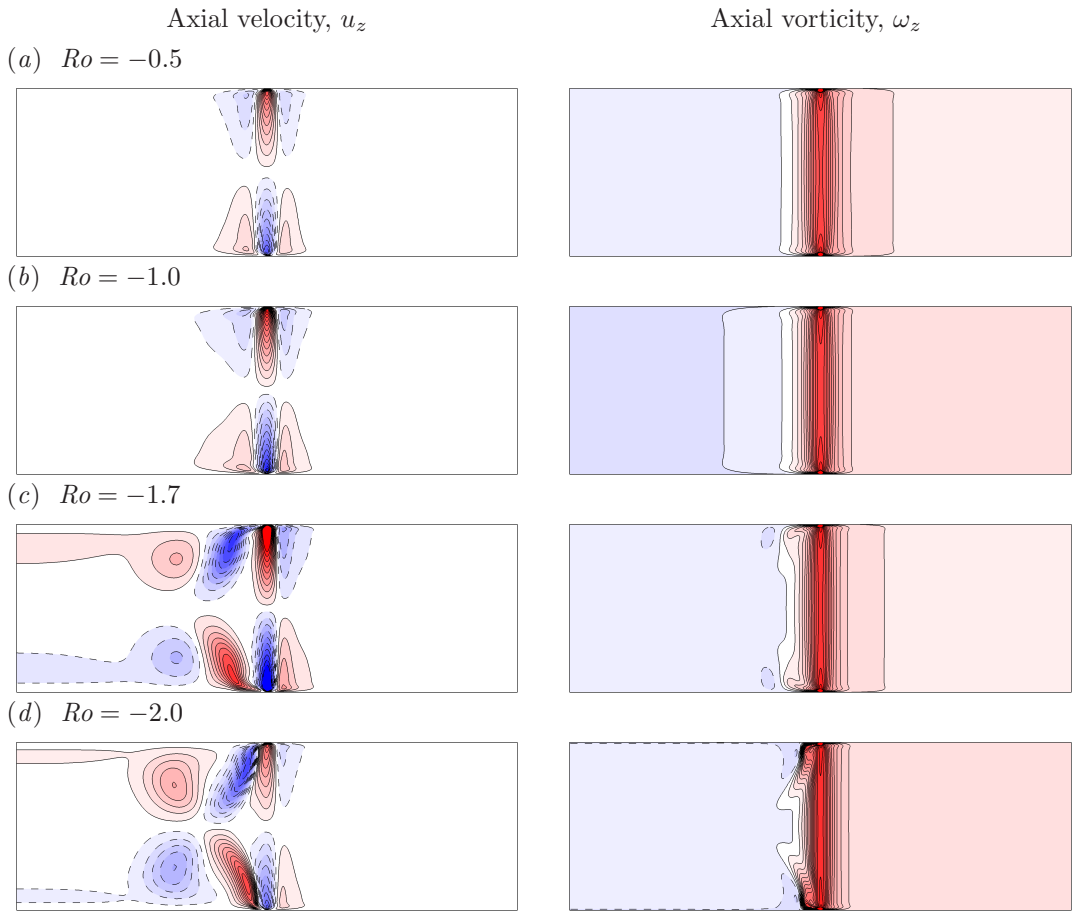


FIGURE 4.3: Structure of the axisymmetric flows visualised on the semi-meridional  $r$ - $z$  plane. Axial velocity (left) and axial vorticity (right) are shown for  $E = 3 \times 10^{-4}$  at (a)  $Ro = -0.5$ , (b)  $Ro = -1.0$ , (c)  $Ro = -1.7$ , and (d)  $Ro = -2.0$ . Contour levels are as per figure 4.2. The domain shown represents the entire semi-meridional plane with  $0 \leq r \leq 2$  and  $0 \leq z \leq 2/3$ . Images are to scale.

---

referenced to the axial pumping invoked by the disks and the stability of the hyperbolic point at  $z/H = 0.5$  and  $r = 1$ .

The axial velocity and axial vorticity contours for a Rossby number flow with opposing disk and tank rotations are illustrated in panels (c) and (d) of figure 4.3. For these counter-rotating cases, distinct features are seen in regions enclosed by the disks ( $r \leq 1$ ). In addition to the vertical column of axial vorticity around  $r = 1$ , there are vorticity patches and strands angled towards the axis of rotation and the interior flow originating from a point along the disk boundary. The vorticity strand is positive while the patch adjacent to it and the horizontal boundary is negative. As the negative Rossby number increases in magnitude, the negative-vorticity patch enlarges,

which forces the positive-vorticity strand to incline more towards the vertical shear layer. With regards to the axial velocity, an extra circulation is seen towards the centre of the tank. However, there still remains a reflectional symmetry about  $z/H = 0.5$ , which is broken in the positive- $Ro$  regime. Recall that large negative- $Ro$  flows may demonstrate a strong Ekman pumping. Thus, following the earlier explanation of the hyperbolic point, the reflective symmetry about the mid-plane may be broken if the Rossby number is sufficiently decreased in the negative regime.

### 4.2.2 Vertical shear-layer profile and thickness

Profiles of the relative azimuthal velocity extracted at mid-depth are shown in figure 4.4(a). The profiles consistently feature three distinct regions. The two regions of linearly increasing and zero relative azimuthal velocity outside of the shear layer around  $r = 1$  typify the rotation rates of the disk and tank, while the region inside the shear layer represents an interface zone over which the profiles smoothly vary from the disk to the outer tank profiles. As  $|Ro|$  increases, the amplitude of the velocities increases, with the location of the peak remaining relatively constant for all  $|Ro| < 0.1$  investigated. The radial position of the peak relative azimuthal velocity for larger  $Ro$  shifts closer towards the centre of the tank due to the breaking of reflective symmetry in the flow. Decreasing  $E$  induces the same effect although the changes are less pronounced compared to  $Ro$  variations. For  $|Ro| < 0.1$  the profiles of azimuthal velocity are identical at other depths, excluding the vicinity of boundary layers.

The mid-depth axial vorticity profiles corresponding to the cases in figure 4.4(a) are shown in figure 4.4(b). A minimum in axial vorticity is observed at  $r = 1$  for  $Ro < 0.1$ , with constant vorticity on either side. At the higher magnitudes of positive  $Ro$ , the vorticity profile demonstrates multiple troughs. Indeed, at these higher  $|Ro|$  flows, the profiles are no longer depth-independent.

The radial gradients of axial vorticity for positive- $Ro$  cases are calculated and shown in figure 4.4(c), which demonstrates  $\partial\omega_z/\partial r$  changing sign at least once within the domain. The common root observed in all cases appears at  $r = 1$  where the vorticity gradient changes sign, whereas it approaches zero when moving away from  $r = 1$ . This suggests the possibility of barotropic instability developing at the radial location of the disk-tank interface due to the Rayleigh–Kuo criterion (described in § 1.5.1), which is explored in detail in Chapter 5. Additional intersections of the horizontal axis are

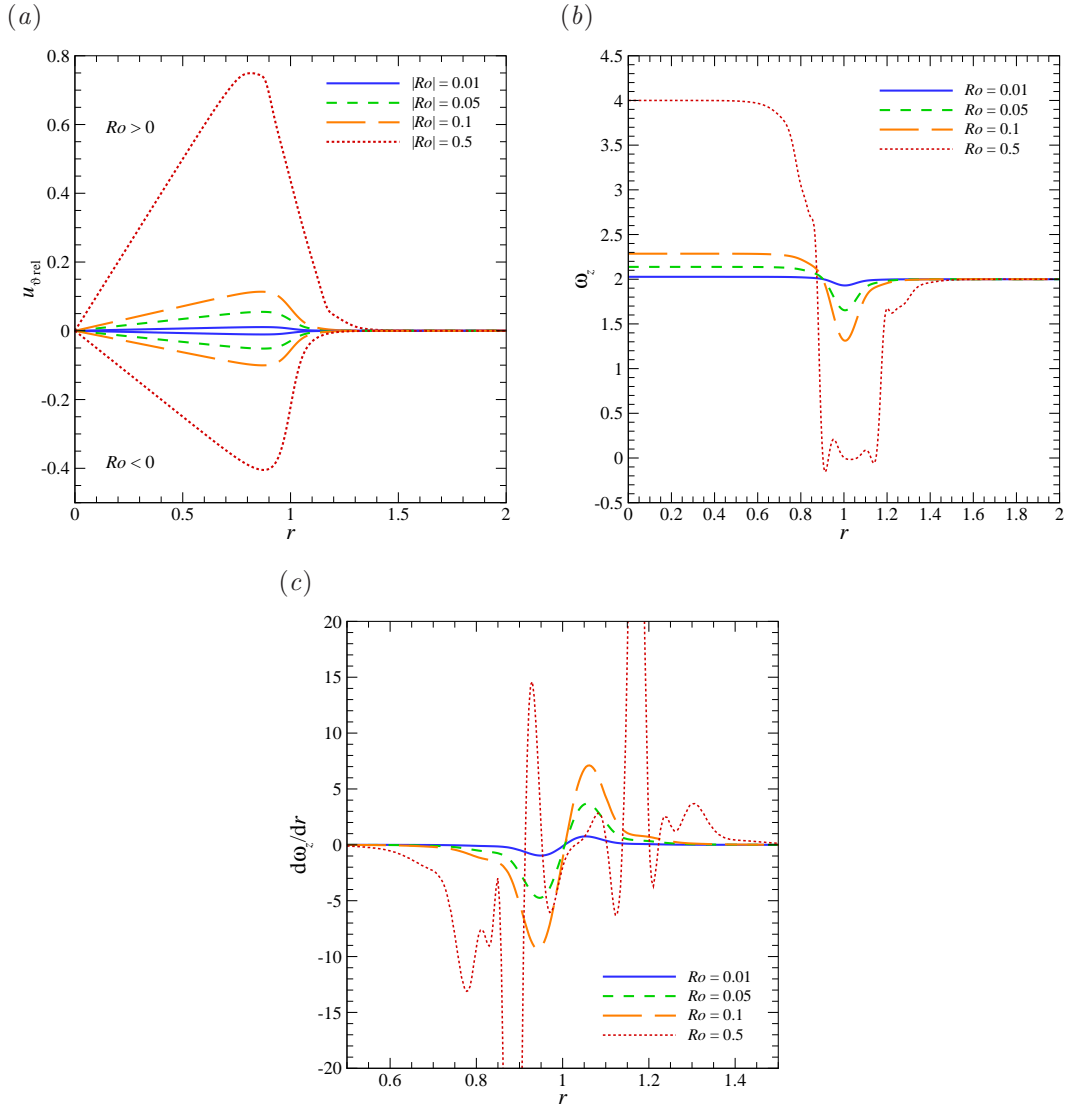


FIGURE 4.4: (a) Azimuthal velocity relative to the rotating tank against radius extracted at  $z/H = 0.5$  for  $E = 3 \times 10^{-4}$  at various  $Ro$ . Curves above and below the zero-line axis correspond to positive and negative  $Ro$ , respectively. (b) The axial vorticity profiles and (c) its radial gradient as a function of radius for various positive  $Ro$  only (negative- $Ro$  data have been omitted for clarity). Root crossings of  $d\omega_z/dr$  are observed at  $r = 1$ .

evident at higher positive  $Ro$ . Similar trends are observed for negative- $Ro$  flows, though they are not included in the plot for clarity. The vorticity gradient consistently changes sign at  $r = 1$  for small  $Ro$ , while multiple root crossings are observed at larger negative  $Ro$ .

From figure 4.4, it is clear that the profiles of azimuthal velocity and axial vorticity remain continuous across the disk-tank interface. The discontinuity imposed by

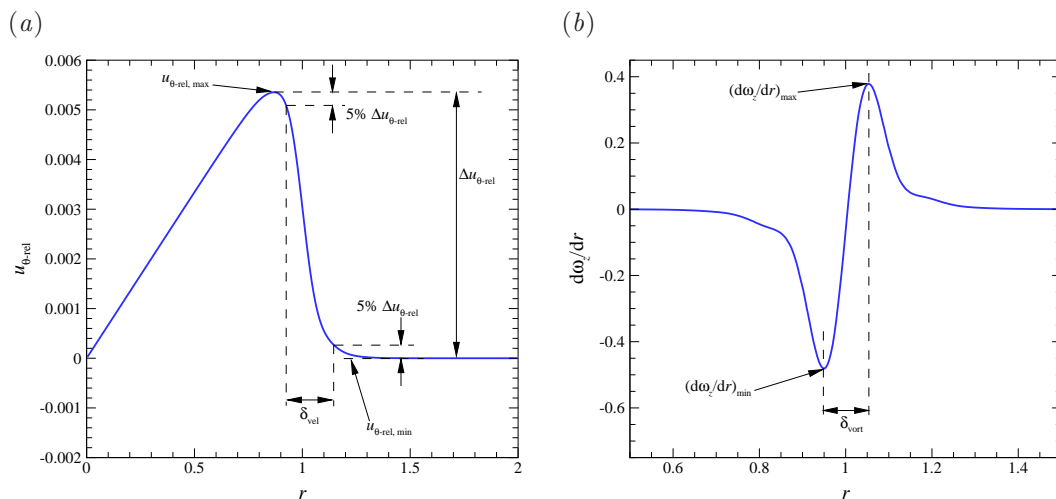


FIGURE 4.5: The techniques used to measure the thicknesses of (a) the shear-layer associated with azimuthal velocity and (b) the shear layer associated with axial vorticity. (a) The relative azimuthal velocity  $u_{\theta-rel}$  plotted against  $r$ . Here  $\Delta u_{\theta-rel}$  is the difference between the maximum and minimum values obtained by the velocity profile at mid-depth. The thickness  $\delta_{vel}$  is taken as the absolute value of the difference between the radial locations where  $u_{\theta-rel}$  first reaches within 5% of the maximum and minimum  $u_{\theta-rel}$  values moving away from the disk-tank interface ( $|r - 1|$  increasing from zero). (b) The radial derivative of the axial vorticity plotted against  $r$ . The thickness  $\delta_{vort}$  is taken as the absolute value of the difference between the radial locations of the maximum and minimum values of  $d\omega_z/dr$  bracketing the disk-tank interface at  $r = 1$ .

the boundary at this interface is smoothed out via the vertical detached shear layers. Indeed, this is the role of the Stewartson layers. Theoretical analysis by Stewartson (1957) identified two nested shear layers of thicknesses scaling with  $E^{1/3}$  and  $E^{1/4}$  for infinitesimal  $Ro$ . The function of the thinner  $E^{1/3}$  layer is to complete the meridional circulation of the Ekman pumping/suction, which in turn removes the vorticity singularity, while the role of the thicker  $E^{1/4}$  layer serves to smooth out the discontinuity in angular velocity between the inner and outer sections (Smith 1984; Vooren 1992; Schaeffer & Cardin 2005).

Aside from theoretical analysis, the only experimental investigation that has been able to retrieve a thickness scaling of the shear layers was conducted by Baker (1967). The range of Rossby numbers that Baker investigated was very small, ranging over  $0.0041 < Ro < 0.038$ . The scalings of the thick and thin layers determined in that study were proportional to  $E^{0.25 \pm 0.02}$  and  $E^{0.4 \pm 0.1}$ , respectively. Those scalings were determined by measuring the shear-layer thickness from azimuthal and axial velocity

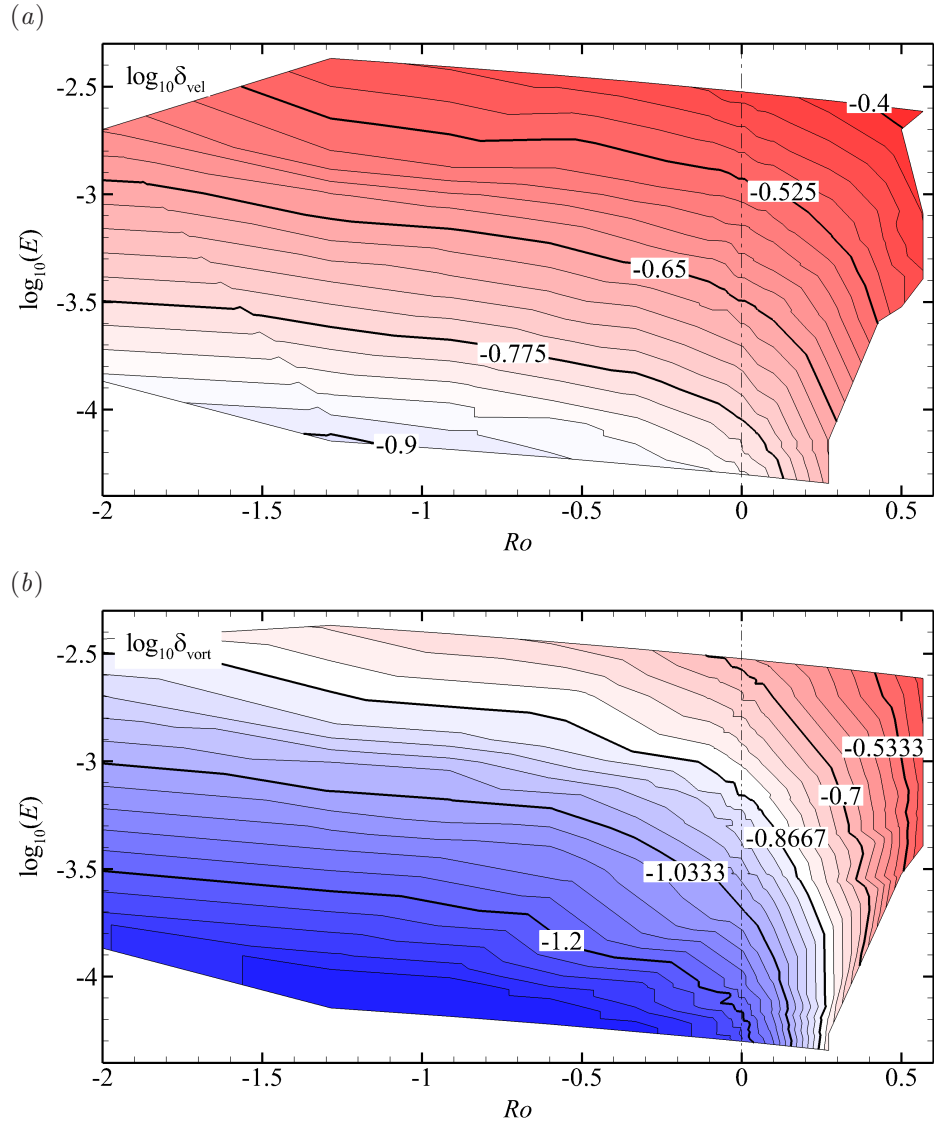


FIGURE 4.6: Contours of the base-10 logarithm of vertical shear-layer thickness plotted on axes of  $\log_{10}(E)$  against  $Ro$ . Contour plots of (a)  $\log_{10} \delta_{\text{vel}}$  and (b)  $\log_{10} \delta_{\text{vort}}$ , respectively, with thicknesses as defined in figure 4.5. In both plots, small to large thickness is represented by blue to red contours, respectively, and thickness values take the same contour shading in both plots. Contour line intervals are  $1/4$  and  $1/3$  of the vertical axis scale in panels (a) and (b), respectively. This follows the respective expected shear-layer scalings of  $E^{1/4}$  and  $E^{1/3}$ . The data agree with these scalings when the vertical contour line spacing matches the vertical axis tick mark spacing. A vertical dash-dotted line corresponds to the Stewartson limit of  $|Ro| \rightarrow 0$ , demonstrating that a finite-shear-layer thickness is produced in this limit.

profiles measured using electrodes, respectively, though the precise criterion used to define the edges of the shear layer was not made clear. The issue of an ill-defined shear-layer edge may be the cause of a lack of numerical validation, and is further exacerbated by the frequent use of a quasi-geostrophic model which neglects the axial flow producing the  $E^{1/3}$  layer. Additionally, there has been no mention in the literature of how the shear-layer thickness scales at higher  $Ro$ . It is evident from figure 4.2 that the thin barotropic shear layer obtained for small  $|Ro|$  breaks down at large  $|Ro|$ , so presumably this would affect the thickness scalings.

Since the functions of the  $E^{1/4}$  and  $E^{1/3}$  layers are to smooth out the azimuthal velocity and axial vorticity discontinuities, respectively, it is proposed that their respective thicknesses can be determined from the profiles of the azimuthal velocity and the radial gradient of axial vorticity from the axisymmetric base flow. The techniques used to measure the thicknesses are illustrated in figure 4.5, where  $\delta_{\text{vel}}$  represents the thickness of the  $E^{1/4}$  layer and  $\delta_{\text{vort}}$  represents the  $E^{1/3}$  thickness. The thickness  $\delta_{\text{vel}}$  is taken as the absolute value of the difference between the radial locations of where  $u_{\theta-\text{rel}}$  first reaches within 5% of the maximum and minimum  $u_{\theta-\text{rel}}$  values on either side of the disk-tank interface ( $r = 1$ ). Although this 5% threshold has been chosen arbitrarily, it has been determined that the relevant results obtained through this approach are quite insensitive to the threshold value used provided that it is small (e.g.  $< 10\%$ ). The thickness  $\delta_{\text{vort}}$  is determined by the absolute difference between the radial positions of the minimum and maximum values of  $d\omega_z/dr$ .

Figure 4.6 maps  $\log_{10}(\delta_{\text{vel}})$  and  $\log_{10}(\delta_{\text{vort}})$  on axes of  $\log_{10}(E)$  and  $Ro$ . In each case a regular increase in thickness with Ekman number is observed, and additionally a continuous increase in thickness with Rossby number through both the negative and positive-Rossby-number ranges is found. These plots confirm that the Stewartson layers adopt a finite thickness in the limit as  $|Ro| \rightarrow 0$ . This feature is not without precedent in fluid mechanics. For instance, it is well known (Schlichting 1979) that at a stagnation point in plane flow (Hiemenz flow) the boundary layer has a finite thickness at the stagnation point, despite the velocity differential across the boundary layer going to zero.

For all negative Rossby numbers (and small positive Rossby numbers), an approximately uniform vertical spacing between contour levels in both plots in figure 4.6 is seen. The contour-level spacing further indicates that the shear-layer scalings are

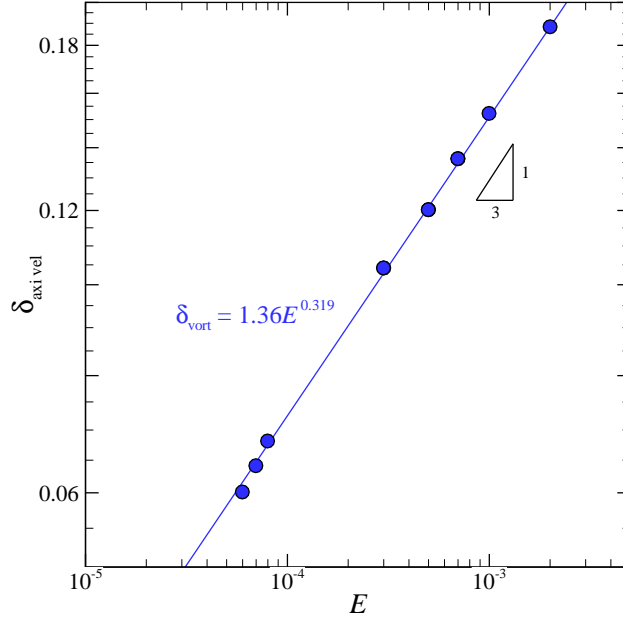


FIGURE 4.7: The thickness based on the axial velocity profile as a function of  $E$ . The Rossby number examined is close to zero at  $Ro = 0.01$ .

approximately consistent with their theoretical  $E^{1/4}$  and  $E^{1/3}$  values. For example, power-law fits of  $\delta_{\text{vel}}$  and  $\delta_{\text{vort}}$  against Ekman number for a very small Rossby number ( $Ro = 0.005$ ) yields  $\delta_{\text{vel}} = 1.31E^{0.22}$  and  $\delta_{\text{vort}} = 1.26E^{0.31}$ , respectively. The exponents of  $E$  are in good agreement with those predicted by theory.

So why is it that an  $E^{1/3}$  scaling is detected from the axial vorticity profile when Baker (1967) used the axial velocity profile to measure the  $E^{1/3}$  layer? Within the Stewartson layers, fluid circulates axially towards mid-depth at positive Rossby numbers, and towards the horizontal boundaries at negative Rossby numbers. Recirculation is therefore confined to one vertical half of the enclosure, and near to mid-depth, the fluid pumped axially through the  $E^{1/3}$  layer migrates horizontally near the mid-plane to complete its meridional circulation away from the Stewartson layers. The change in angular momentum as this fluid migrates radially inwards or outwards at mid-depth then modifies the axial vorticity profile, which is believed to drive the detection of an  $E^{1/3}$  scaling in the shear-layer thickness measured from the radial profile of axial vorticity in figure 4.6(b). Moreover, a similar analysis conducted on the axial velocity profiles yields an  $E$  exponent comparable to that of  $\delta_{\text{vort}}$ , namely 0.319. The data for the thickness derived from the axial velocity profile for  $Ro = 0.01$  are illustrated in

figure 4.7.

Another feature observable in figure 4.6 is that, at larger positive Rossby numbers, the measured thicknesses begin to lose their dependence on the Ekman number (contours of constant thickness approach the vertical). This Ekman-number-independent behaviour also manifests itself in the stability of the flow to azimuthal perturbations discussed later in Chapter 5. By inspection of the axisymmetric flows shown in figure 4.2 (and similar plots at other  $(Ro, E)$  pairs not shown here), it becomes apparent that this Ekman-number-independent regime corresponds to the symmetry-broken axisymmetric flows (see figure 4.2(*d*)).

Across the negative-Rossby number range, the thicknesses change gradually. As Rossby numbers approach zero and increase through the range of positive values, thickness increases at an accelerating rate. This behaviour can be explained by the nonlinear relationship between differential angular velocity ( $\omega$ ) and  $Ro$ . While  $\omega$  appears directly in the numerator of the Rossby number definition (equation 3.55), it also enters in the denominator through the definition of  $\bar{\Omega}$ . Rearranging equation 3.55 for the normalised differential rotation gives

$$\frac{\omega}{\bar{\Omega}} = \frac{2Ro}{1/A - Ro}, \quad (4.1)$$

which has an asymptotic minimum  $\omega/\bar{\Omega} = -2$  as  $Ro \rightarrow -\infty$ , and an asymptotic maximum  $\omega/\bar{\Omega} = \infty$  as  $Ro \rightarrow 1/A$  (which corresponds to  $Ro \rightarrow 1.5$  with the enclosure dimensions adopted in the present section). The similarity in Rossby number dependence between the relationship described by equation 4.1 and the thickness measurements in figure 4.6 highlights  $\omega/\bar{\Omega}$  as an important parameter in describing the dependence of the shear-layer thickness against Rossby number.

Universal relationships for the shear-layer thicknesses are now developed. As established from figure 4.6,  $\delta_{\text{vel}}/E^{1/4}$  and  $\delta_{\text{vort}}/E^{1/3}$  are approximately constant. When plotted against  $\omega/\bar{\Omega}$ , approximately linear trends were found for these normalised thickness quantities for  $Ro \lesssim 0$ . Least-squares fits to the data obtained the trends displayed in figure 4.8. These trends hold well for all negative Rossby numbers and positive Rossby numbers exhibiting reflective symmetry about the mid-plane in the axisymmetric flows. Once the symmetry is broken, the measured shear layer becomes thicker than the universal curve, which results from the widening of the shear layer away from the lid and base (this effect can be seen when comparing panels (*d*) to (*a*) in figure 4.2). This is observed in figure 4.8 in the upward departure of measured thickness data from

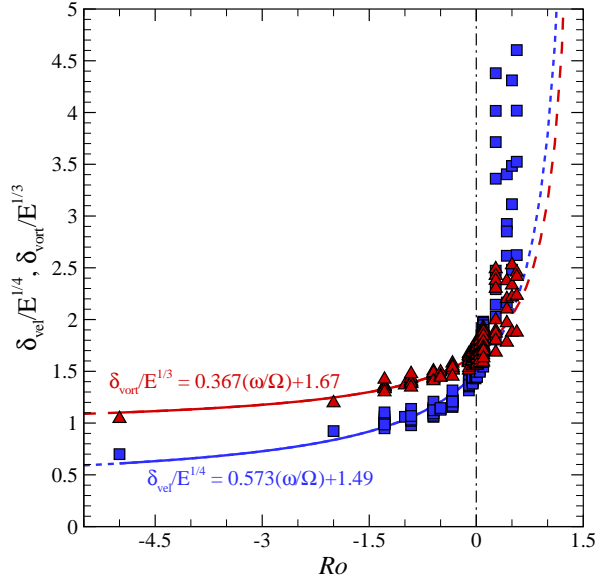


FIGURE 4.8: Partial collapse of the shear-layer thickness data onto universal trends as functions of  $E$  and  $Ro$ . The plot shows  $\delta_{\text{vel}}/E^{1/4}$  ( $\square$ ) and  $\delta_{\text{vort}}/E^{1/3}$  ( $\triangle$ ) against  $Ro$ . Analysis determined that while the axisymmetric flows remained depth-independent, the scaled shear-layer thicknesses varied linearly with  $(\omega/\Omega)$ . The relationships obtained from least-squares fits to the data are included on the plot. Solid lines show the Rossby number range where the universal fits hold, and dashed lines extrapolate these fits for comparison against the data that deviates from these trends at higher  $Ro$ .

the universal relationships.

### 4.2.3 Time-dependent axisymmetric flow structure

It has been described that with increasing  $|Ro|$  magnitude, the flow transitions from reflectively symmetric to symmetry-broken flow. For positive- $Ro$  flow, the depth dependence is characterised by the diagonal strands of negative vorticity that stem from the disk-tank interface. In contrast, negative- $Ro$  flows illustrate the development of negative-vorticity patches adjacent to the horizontal boundary and the vertical positive-vorticity band at the disk-tank interface when axial invariance of the axial vorticity is broken. It has been observed that further increases to  $|Ro|$  causes the axisymmetric flow to become time-dependent. Details of the time-dependent flow structures in the positive and negative- $Ro$  regimes are described separately in the following sections.

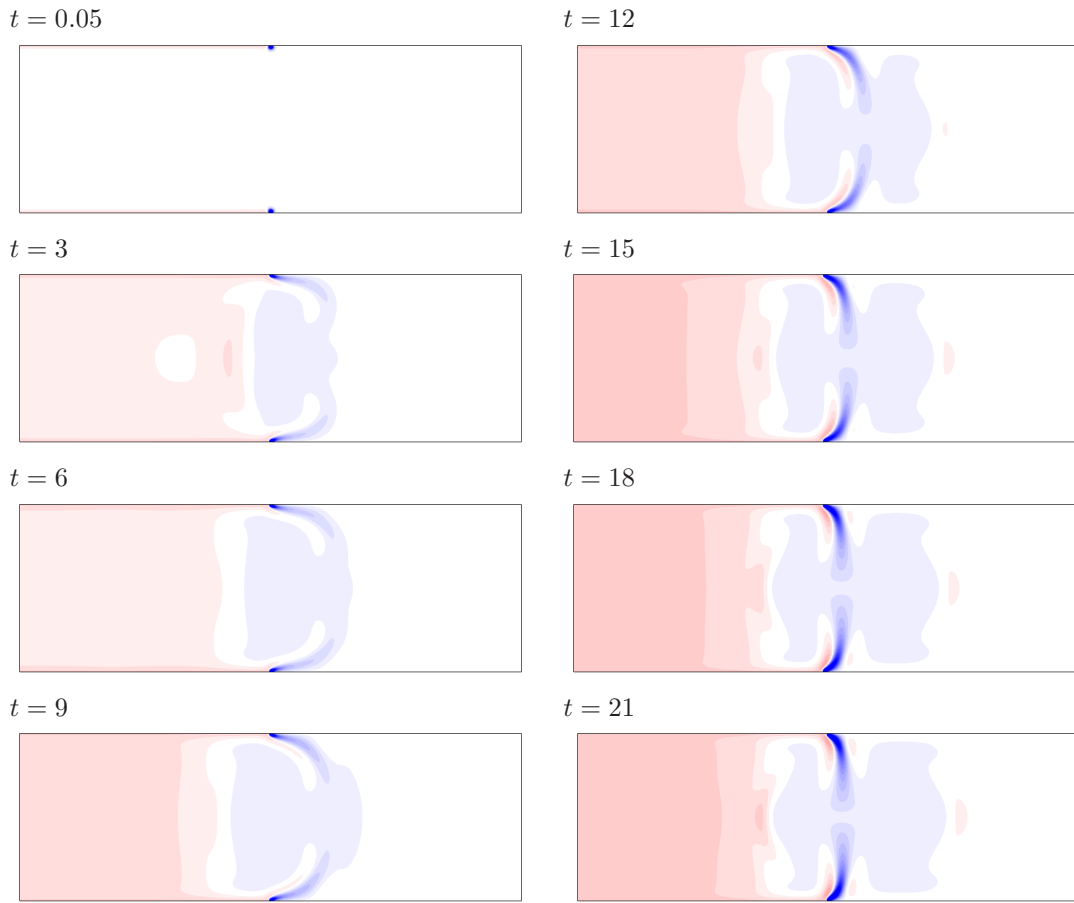


FIGURE 4.9: Snapshots of axial vorticity during the start up of the flow with conditions  $Ro = 0.924$  and  $E = 1 \times 10^{-3}$ . Sequence begins from top to bottom and left to right. Contour levels are as per figure 4.2.

---

#### 4.2.3.1 Unsteady flow in the positive-Rossby-number regime

A representative flow condition that illustrates time-dependent flow is characterised by  $(Ro, E) = (0.924, 1 \times 10^{-3})$ . This flow is analysed in detail here, describing the developments of the flow from solid-body rotation at the tank's angular rate through to time-dependent flow.

Snapshots of axial vorticity contours at the startup of the flow (solid-body rotation) to the near-onset of time-periodic flow are illustrated in figure 4.9. Initially, a small zone of negative axial vorticity is generated at the disk-tank interface, while a thin layer of positive axial vorticity forms on the disk boundaries ( $t = 0.05$ ). The fluid bound between the two differentially rotating disks develops positive axial vorticity while the localised negative-vorticity zones at the disk-tank interface grow into strands. These negative-vorticity strands initially extend horizontally, but then progressively

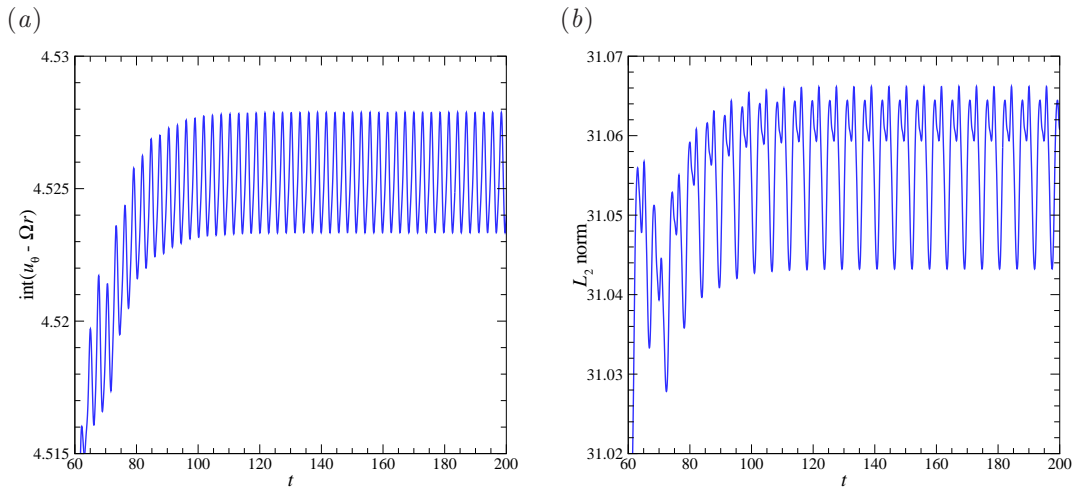


FIGURE 4.10: (a) The integral of the azimuthal velocity relative to the tank and (b) the  $L_2$  norm of the flow with conditions  $Ro = 0.924$  and  $E = 1 \times 10^{-3}$  measured over time.

---

shift towards the vertical as the flow develops. The flow reaches a fully developed state marking the end of the transient startup phase of the simulation at  $t = 21$ . After this time, the strands begin to divert away from the vertical in a similar manner to the flow shown in figure 4.2(d). However, due to the higher  $Ro$  here, the flow is unable to remain steady and develops an instability. The unsteadiness manifests as an oscillation of the negative-vorticity strands which begin to flap past each other twice per cycle. In addition, the axial vorticity contours reflect the fact that the strands are aligned with jets of axial velocity from the top and bottom boundaries. Thus, the instability develops as a breaking of the hyperbolic zone at the point where the jets meet. It turns out here that the unsteadiness saturates to a perfect periodicity.

The periodicity of the flow is easily identifiable through profiles of the integral of azimuthal velocity relative to the tank and the  $L_2$  norm over time. These profiles are illustrated in figure 4.10. For clarity, only  $60 \leq t \leq 200$  is shown. Both profiles demonstrate strong periodicity beyond approximately  $t = 100$ . The measured periods from the integral measure and the  $L_2$  norm are  $T_{\text{int}} = 2.8406$  and  $T_{L_2} = 5.6812$ , respectively. These periods differ by a factor of exactly 2. The  $L_2$  norm yields a longer period as it incorporates all three velocity components for its measure. Since the integral measure of the azimuthal velocity considers only one component, it is possible that the energy in that integral is repeated throughout half of the actual flow period. In addition, the complete period of  $T = 5.6812$  corresponds to a frequency of  $f = 0.176$ ,

which is less than twice the frequency of the background flow, namely  $f = 0.768 (1/\overline{\Omega})$ . Thus, inertial waves in the form of shear layers may be present (see Lopez & Marques (2014) and references therein). However, it would be difficult to identify inertial waves since the oscillation of the flow occurs over a large region rather than a localised point. Therefore, the inertial waves would likely be a disturbance that does not prorogate at a constant angle to the rotation axis, rather a distorted wave due to the motion of the vorticity strands.

The structure of the axisymmetric base flow over a complete period ( $T = 5.6812$ ) is illustrated in figure 4.11 through axial vorticity contours. The top centred panel is a reference frame at  $t = t^*$  and successive panels are snapshots through time equally spaced at intervals of  $T/8$ . Throughout a complete period, the negative axial vorticity strands flap past each other twice. A similar motion is exhibited in the azimuthal component of vorticity whereby the positive and negative-vorticity strands oscillates about  $r = 1$ . This feature is demonstrated in figure 4.12. Similar to the structure of the steady-state base flows, there exists a dominant layer of azimuthal vorticity on the horizontal boundaries of the disks and tank that varies slightly throughout the period. These layers are generated through the radial pumping (inwards) of fluid due to the Ekman layer dynamics.

#### 4.2.3.2 Unsteady flow in the negative-Rossby-number regime

Periodic flows were not observable at large  $|Ro|$  in the negative- $Ro$  regime. The integral of the azimuthal velocity relative to the tank and the  $L_2$  norm data are shown in figure 4.13 with flow conditions  $Ro = -3.0$  and  $E = 3 \times 10^{-4}$ . The flow has been allowed to develop over a long time period. It is evident from both plots that a periodic state is not established. Between  $400 \lesssim t \lesssim 1000$ , the flow appears to begin exhibiting periodic-like features, where the measured variables oscillate regularly. However, even in this region the oscillation is not perfectly periodic. During this time, the positive diagonal vorticity bands on the inner side of the primary vertical strand elongate and contract very slightly, and the flow maintains reflective symmetry about the axial mid-plane. Contours of axial velocity and axial vorticity at an instant in this regime are shown in figure 4.14. At the same time, the negative vorticity (dotted line) close to the axis of rotation also expands and contracts, although over a larger region. Similarly, the regions of positive and negative axial velocity near the axis of rotation shrink and

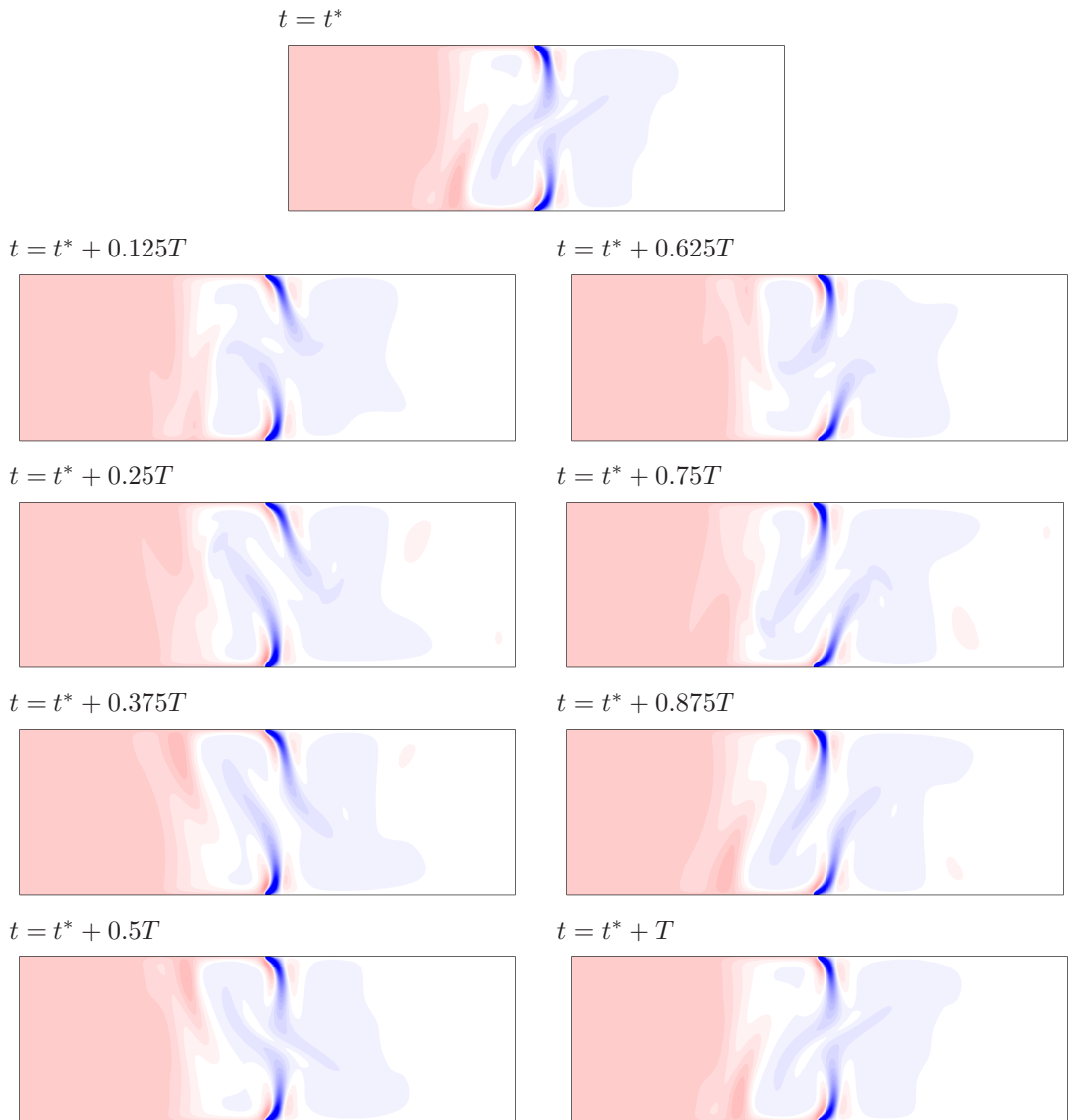


FIGURE 4.11: Snapshots of axial vorticity throughout a complete period with flow with conditions  $Ro = 0.924$  and  $E = 1 \times 10^{-3}$ . The top centred panel represents the reference flow condition at  $t = t^*$ . The period of the flow is given by  $T = 5.6812$ . Contour levels are as per figure 4.2.

---

grow over time while the axial velocity strands at the disk-tank interface elongate and contract. These modulations are the cause of the nearly-periodic behaviour over  $400 \lesssim t \lesssim 1000$ . Beyond  $t \simeq 1000$ , the measured variables begin to demonstrate chaotic behaviour.

The flow beyond  $t \simeq 1000$  begins to illustrate greater spatial changes within the flow, especially those involving the axial vorticity strands at the disk-tank interface. The diagonal vorticity strands oscillate over a larger region and their tips expel a packet of

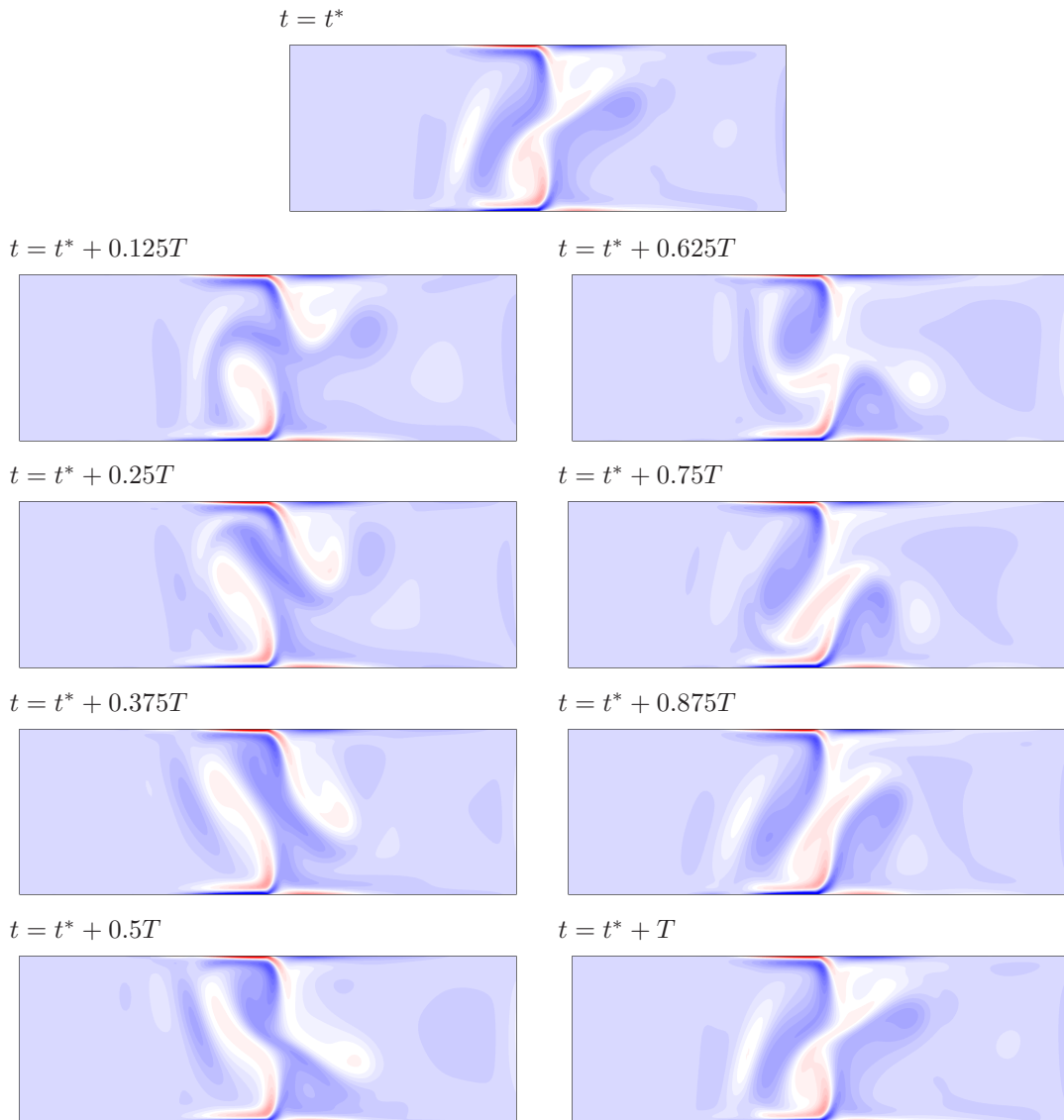


FIGURE 4.12: Snapshots of azimuthal vorticity throughout a complete period with flow with conditions  $Ro = 0.924$  and  $E = 1 \times 10^{-3}$ . The time of these panels correspond directly to those in figure 4.11. Contour levels are as per the axial vorticity contours in figure 4.2.

---

positive vorticity that convects towards the axis of rotation. Interestingly, this packet of positive vorticity is accompanied by a packet of negative vorticity of a similar size. The negative vorticity is generated from the high negative vorticity produced across the disk-tank interface beneath the positive-vorticity strand. Therefore during this flow phase, a pair of positive and negative vortices is produced from the persistent structures at  $r = 1$  which then migrates towards the axis of rotation. They are carried on the returning flow expelled radially inward from the vertical jets within the remnants of the Stewartson layer. As this is a high negative- $Ro$  flow, the Ekman layer on the disks

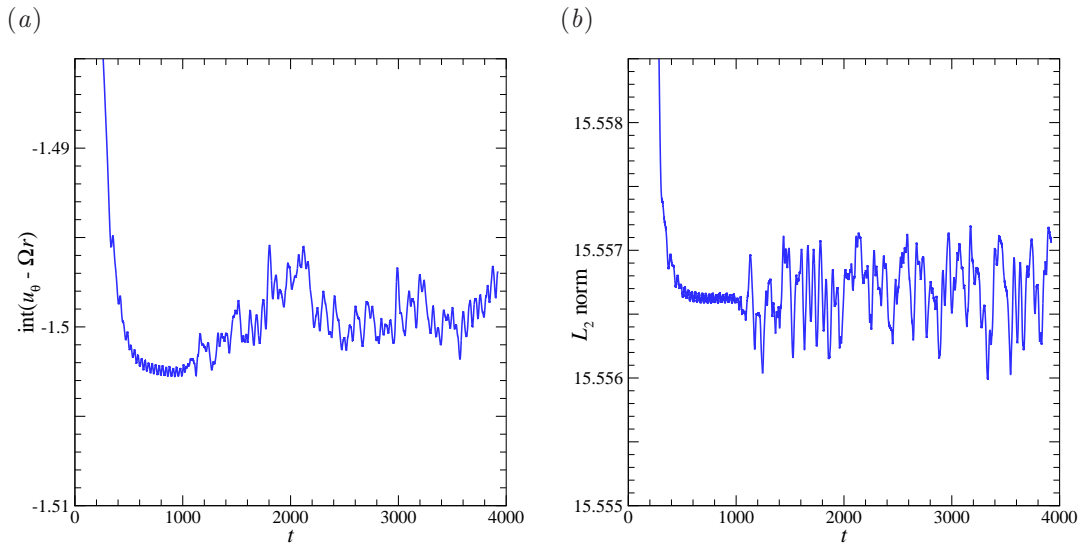


FIGURE 4.13: (a) The integral of the azimuthal velocity relative to the tank and (b) the  $L_2$  norm of the flow with conditions  $Ro = -3.0$  and  $E = 3 \times 10^{-4}$  measured over time.

---

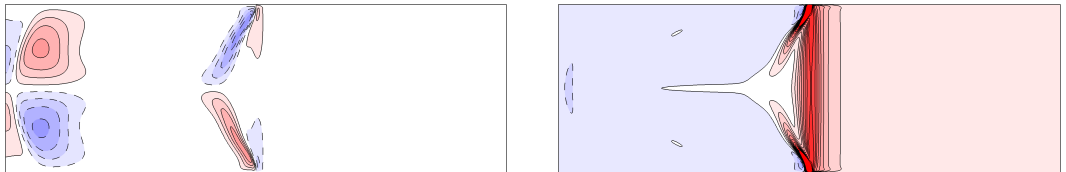


FIGURE 4.14: Contours of axial velocity (left) and axial vorticity (right) at  $t = 600$  with flow conditions of  $Ro = -3.0$  and  $E = 3 \times 10^{-4}$ . Contour levels are as per figure 4.2.

---

express strong fluid pumping into the interior flow.

Despite the profiles of figure 4.13, the qualitative features of the flow are somewhat periodic. This vortex pair shedding motion is very similar to that of the wake of flow over a cylinder (e.g. Sheard *et al.* 2005; Rao *et al.* 2013). An illustration of these vortex pairs can be seen in figure 4.15. The production of a vortex pair alternates between the bottom positive vortex strand and the top negative vortex patch ( $t = 3898$ ), and the top positive strand and the bottom negative patch ( $t = 3910$ ). As the vortex pair travels towards  $r = 0$ , it deforms and elongates with the occasional coalescence with the existing, previously generated vortex pair in the flow. The vortices eventually weaken and decay prior to reaching the axis of rotation, as the returning radial flow diverts vertically towards the top and bottom boundaries to complete the circulation.

Stronger chaotic features are exhibited as the magnitude of the Rossby number is

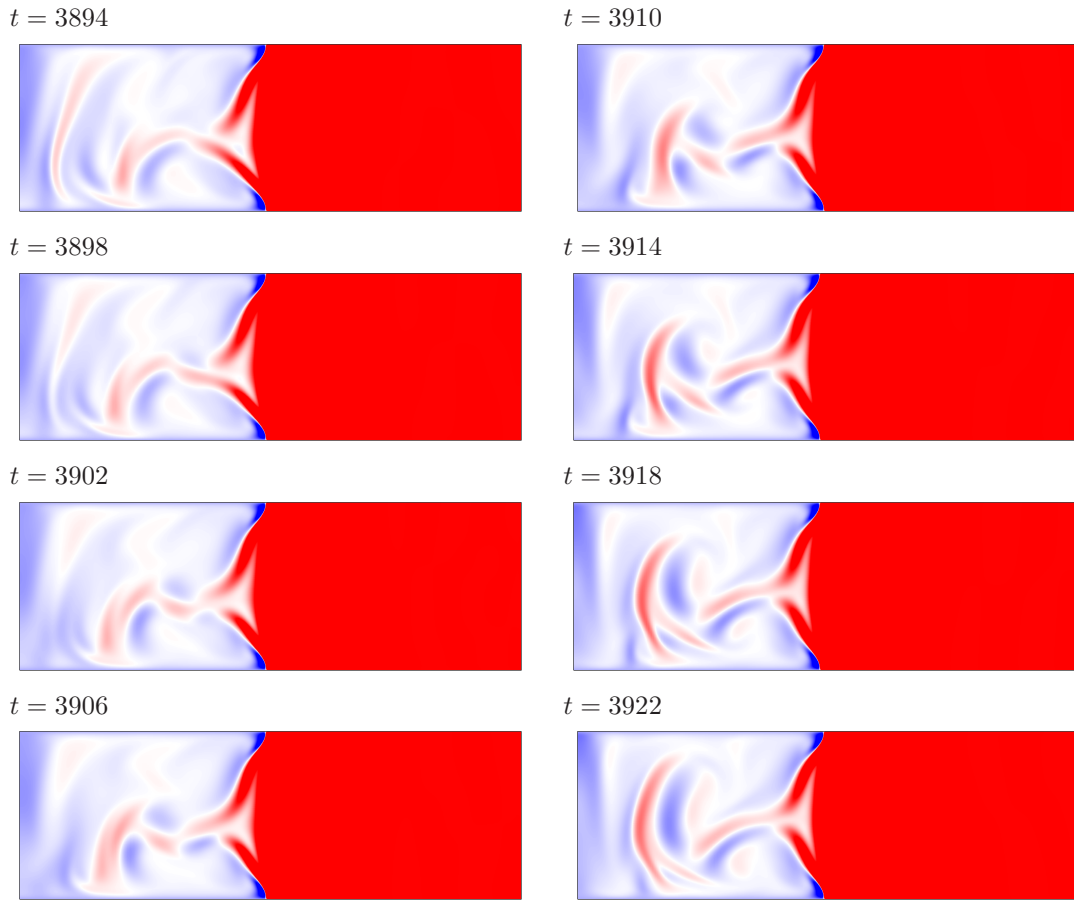


FIGURE 4.15: Snapshots of axial vorticity throughout  $3894 \leq t \leq 3922$  for  $Ro = -3.0$  and  $E = 3 \times 10^{-4}$ . Contour levels are between  $-2\Omega \leq \omega_z \leq 2\Omega$  with red and blue contours representing positive and negative values, respectively.

---

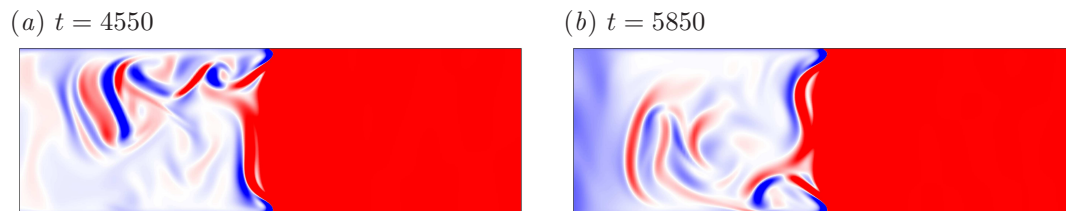


FIGURE 4.16: Axial vorticity contours at  $(a) t = 4550$  and  $(b) t = 5850$  demonstrating the flow features present in chaotic-like flow. The flow conditions are of  $Ro = -5$  and  $E = 3 \times 10^{-4}$ . Contour levels are between  $-2\Omega \leq \omega_z \leq 2\Omega$  with red and blue contours representing positive and negative values, respectively.

---

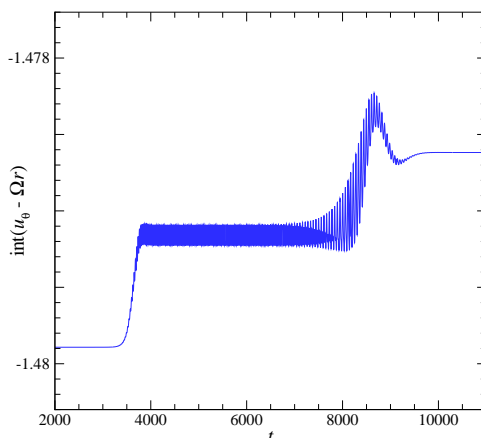


FIGURE 4.17: The integral of the azimuthal velocity relative to the tank for flow conditions at  $Ro = -2.5$  and  $E = 3 \times 10^{-4}$  measured over time.

---

increased to  $Ro = -5$ . At this flow condition, the reflective spatio-temporal symmetry about the mid-plane is lost since one of the positive-vorticity strands dominates and elongates further into the interior. The strand which dominates alternates irregularly over time. An illustration of this is shown in figure 4.16 at  $t = 4550$  and  $t = 5850$ . The production of vortex pairs is still seen to originate from bands extending from the disk-tank interface. However, since the bands are of unequal length, the patches of vorticity does not primarily travel along the mid-plane, rather many of the vortical motions occur near to a horizontal boundary. That is, the interface between the two bands is no longer centred at the mid-plane. As expected based on this observed flow behaviour, the integrals of the relative azimuthal velocity and the  $L_2$  norm demonstrate erratic behaviour over this region (not shown).

The transition from steady-state axisymmetric base flows to this irregular time-dependent flows in the negative- $Ro$  regime is not instantaneous. An interesting flow condition at  $Ro = -2.5$  and  $E = 3 \times 10^{-4}$  exhibited both steady-state and time-dependent behaviour. Eventually, the flow saturated to a steady state. The integral of relative azimuthal velocity for this case is shown in figure 4.17. Initially, steady-state behaviour is demonstrated whereby the change in velocities between each time step consistently decreases over time. This is observed for  $t \lesssim 2000$ . However, beyond this time, the velocity fluctuations increase rapidly and a state of quasi-periodicity is established over a large time frame ( $4000 \lesssim t \lesssim 8000$ ). During this time, motions similar to those illustrated in figure 4.15 are observed. After  $t \gtrsim 10000$ , changes in the

flow begin to decrease, eventually saturating towards a steady-state. This axisymmetric steady-state condition illustrate structures similar to those demonstrated in figure 4.3.

#### 4.2.4 Smoothed velocity profile forcing

The previous sections have presented solutions which have had discontinuous boundary conditions imposed. That is, the disk rotates at a rate of  $\Omega + \omega$  while the tank rotates at  $\Omega$ , and the interface between the two boundaries share a single element edge. The physical set-up of this system requires a finite gap between the disk and the tank in order for the two boundaries to rotate independently. Hence, the transition from the disk's angular velocity to the tank's angular velocity occurs smoothly over a finite radial distance. This transition has been modelled using various functions in previous quasi-two-dimensional models (see § 3.7.2). The smoothed angular velocity boundary condition used here is given by

$$\mathbf{u}_b = \Omega r + \frac{r}{2} \left[ 1 - \tanh \left( \frac{r - R_d}{\delta} \right) \right] \omega, \quad (4.2)$$

where  $\delta = (E/4)^{1/4} H$  represents the thickness of the  $E^{1/4}$  Stewartson layer.

Figure 4.18 highlights the differences between the steady-state solutions obtained using discontinuous and smoothed boundary conditions via axial vorticity contours. Minor differences are observed between the contours, most of which are present around  $r = 1$ . It should be noted that the contour levels used are exactly the same for both the discontinuous and smoothed solutions. For  $Ro = 0.1$ , the solutions portray very similar features with the discontinuous case exhibiting a lower value of vorticity around  $r = 1$ . This is expected as the smoothing of the angular velocity assists in evening out the vorticity across the interface. As the  $Ro$  magnitude is increased to  $Ro = 0.5$ , the symmetry-breaking of the flow is seen in both the discontinuous and the smoothed cases where the negative-vorticity strands stemming from the disk-tank interface elongate into the interior. This suggests that the negative-vorticity strands which were first observed in the solutions with discontinuous forcing are not artifacts of insufficient numerical discretisation (due to the discontinuous boundary condition). However, the effect of the angular velocity smoothing appears to have truncated the negative-vorticity strands. Indeed, increasing the  $Ro$  magnitude for the smoothed boundary condition case causes the flow structure to become more like its discontinuous counterpart such that the strands become elongated at a greater angle to the vertical. That is, smoothing of the angular velocity boundary condition acts to delay the onset of transition from

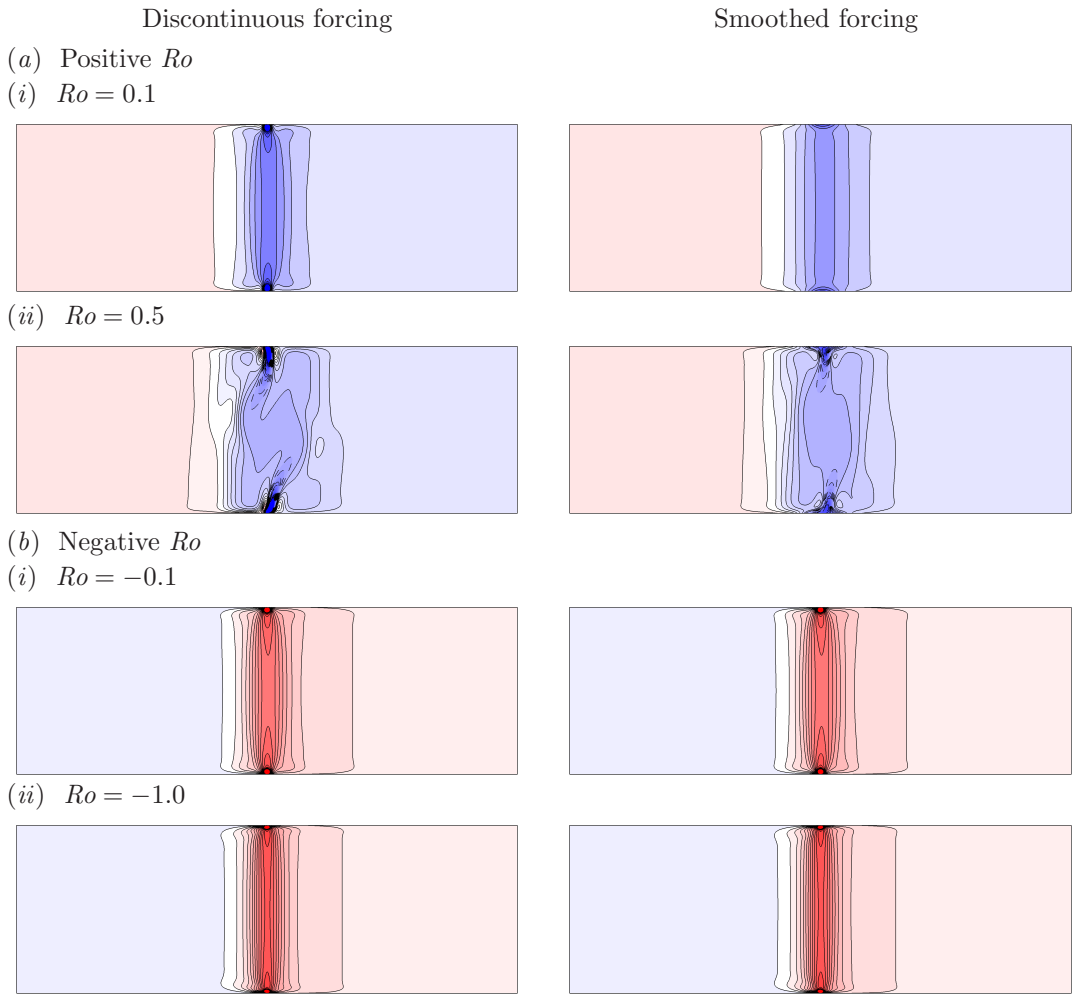


FIGURE 4.18: Structure of the axisymmetric flows visualised on the semi-meridional  $r$ - $z$  plane. Steady-state portrayed through axial vorticity for the discontinuous boundary condition (left) and smoothed condition (right) for  $E = 5 \times 10^{-4}$  at (a)(i)  $Ro = 0.1$ , (ii)  $Ro = 0.5$  and (b)(i)  $Ro = -0.1$ , (ii)  $Ro = -1.0$ . Contour levels are as per figure 4.2 with the same number of contour levels used between the two forcing cases.

---

reflectively symmetric to symmetry-broken flow. The same delay effect is observed for flow conditions in the negative- $Ro$  regime.

### 4.3 Varying the aspect ratio

The effect of varying the aspect ratio is numerically investigated by varying the height of the tank while keeping the disk radius constant. The motivation for this originates from the definition of the Stewartson layer thickness, which scales linearly with height (i.e.  $\delta_{\text{vel}} \propto E^{1/4}H$ ). The height of the container can be expressed through the non-dimensional parameter  $A$ , and therefore the effect of varying  $A$  in relation to the

Stewartson layer can be determined.

In unpublished experiments conducted by a colleague, Dr. Luca Montabone, a different differential-disk configuration with a large aspect ratio was studied. They were not able to observe a variety of polygonal shapes throughout their entire  $Ro$ - $E$  parameter space. Instead, only oval shaped vortices were produced. Despite the difference in the experimental configuration, it was hypothesised that the large aspect ratio of the apparatus was responsible for the formation of the oval shapes since polygonal shapes returned when the aspect ratio was decreased. The reasoning was that the Stewartson layer was either not produced or was disrupted in large aspect ratio containers, and therefore no barotropic instability exists. To investigate the effect of varying the aspect ratio, the flow structures produced in five other aspect ratios have been examined in addition to the reference aspect ratio of  $A = 2/3$  which has been presented in the previous sections. The other four aspect ratios are  $A = 1/6, 1/3, 4/3$  and  $2$ . In all cases, the radius of the disk is kept constant while the height of the container is changed.

### 4.3.1 Axisymmetric flow structure

Containers characterised by aspect ratios both lower and higher than the reference case exhibit flow structures similar to that of the reference case, except that they are scaled to their respective tank height. The contours of axial velocity and axial vorticity of the axisymmetric steady-state base flows for a variety of  $A$  are illustrated in figure 4.19. The contours of axial velocity demonstrate a pair of meridional circulation on each horizontal boundary for all  $A$  investigated, while the axial vorticity contours display a column of vorticity at  $r = 1$ . For small  $A$  (small  $H$ ), the flow is largely confined and the axial vorticity is strongly concentrated as a column. As the aspect ratio is increased, the meridional circulation and the vorticity column broadens. At larger  $A$ , the reflective symmetry about mid-depth in the axial velocity contours is maintained. It is apparent that at sufficiently large aspect ratios, the symmetry axis and side-walls begin to confine the flow. Presumably this will act to limit the Stewartson layer scaling with  $H$  (and  $A$ ). It is surprising that the column of axial vorticity does not demonstrate a weakening in regions of the interior as was suggested in the experiments. That is, the Stewartson layer appears to exist even at large aspect ratios. These characteristics are consistent through a wide range of  $E$  and  $Ro$  conditions.

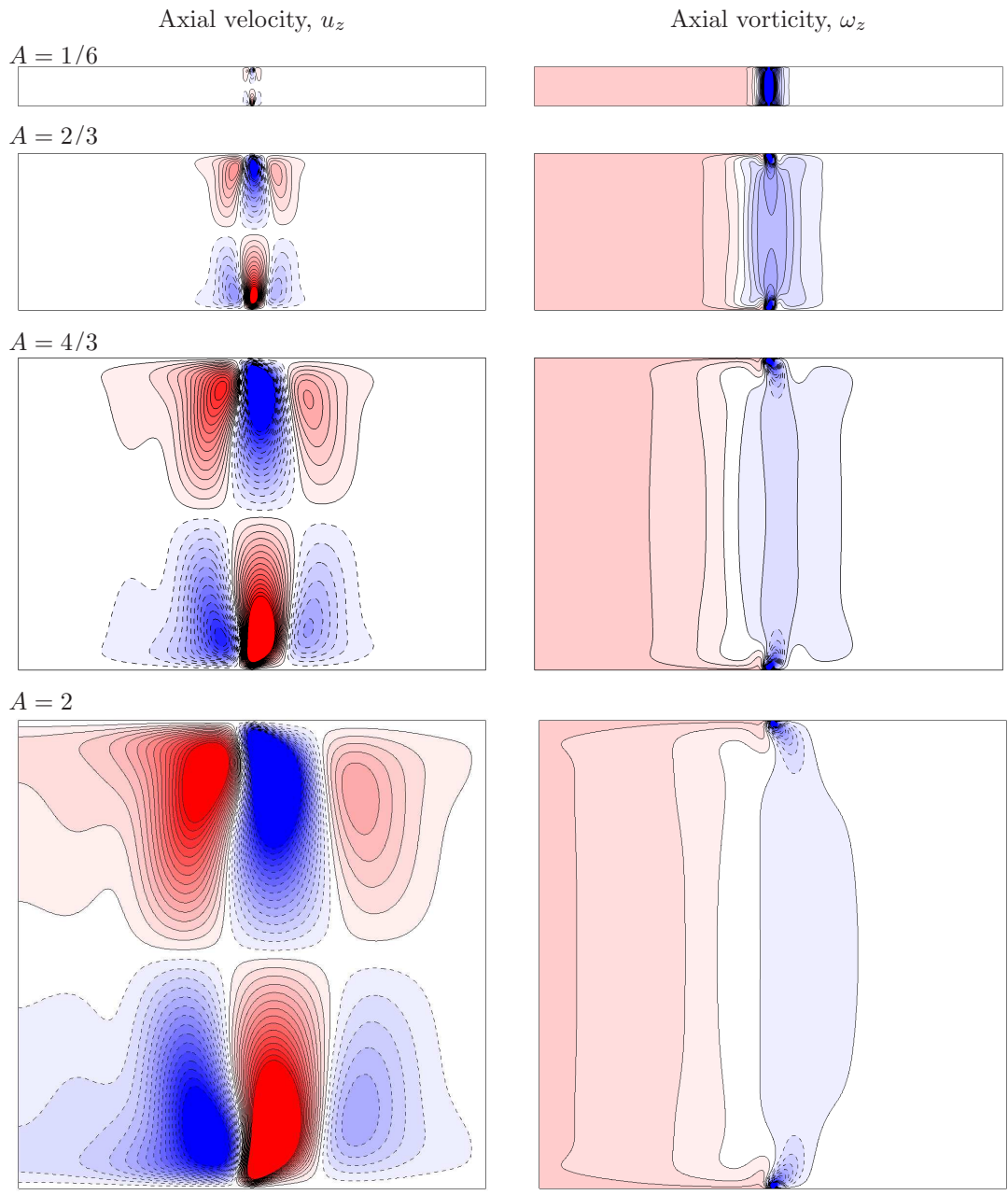


FIGURE 4.19: Structure of the axisymmetric flows visualised on the semi-meridional  $r$ - $z$  plane. Axial velocities (left) and axial vorticity (right) are shown for  $Ro = 0.3$  and  $E = 7 \times 10^{-4}$  with  $A = 1/6, 2/3, 4/3$  and  $A = 2$ . The images are to scale. Contour levels are as per figure 4.2.

### 4.3.2 Vertical shear-layer profile and thickness

Despite the visual similarities in the solutions for the various  $A$ , the profiles of axial vorticity for the smallest and largest  $A$  illustrate vast differences. For a sufficiently large  $A$ , the minimum and maximum axial vorticity values are no longer bounded by approximately  $\omega_{z,\text{tank}} = 2\Omega$  and  $\omega_{z,\text{disk}} = 2(\Omega + \omega)$ , respectively. A comparison between the axial vorticity profiles of a small and large  $A$  is illustrated in figure 4.20(*a, b*). For  $A = 1/6$ , the flow outside of the shear layer exhibits values consistent with  $\omega_{z,\text{tank}} = 2$  and  $\omega_{z,\text{disk}} = 2.21$ . Inside the shear-layer region, the axial vorticity profile demonstrates a dip across  $r = 1$  as it decreases and then increases with increasing radius. However, the profile obtained from the  $A = 2$  configuration does not exhibit vorticity values consistent with the theoretical values of  $\omega_{z,\text{tank}} = 2$  and  $\omega_{z,\text{disk}} = 8$ , nor does it demonstrate any large range of a constant value. There is a small range between  $1.7 \leq r \leq 2$  which displays a constant vorticity value of  $\omega_z = 1.9$ , which is lower than the vorticity attributed by the tank. Therefore, with increasing  $A$ , the magnitude of vorticity increases near the axis of rotation while it decreases at the disk-tank interface and beyond ( $r \geq 1$ ).

This trend is observable in figure 4.20(*c*) which provides a collapse of the axial vorticity profiles for a variety of  $A$ . The horizontal axis has been rescaled to  $(r - 1)/A$  such that the zero value represents the disk-tank interface. The magnitude of axial vorticity is seen to increase with increasing  $A$  for negative values of  $(r - 1)/A$  values while it decreases with increasing  $A$  for positive values of  $(r - 1)/A$ . For this particular flow condition, the flow is seen to deviate at  $A = 4/3$ . The similarity of the dip in the vorticity profile is apparent in the vicinity of the disk radius at all  $A$ , demonstrating strong scaling with  $1/A$ . However, the local minimum of each curve is shifted slightly towards the tank wall with increasing  $A$ . This is due to the asymmetry in the recirculation on either side of the axial jet produced at the disk-tank interface. Figure 4.20(*d*) shows a plot of the axial velocity profiles extracted at  $z/H = 0.9$  ( $z/H = 0.1$  reveals the same trends) for  $A = 1/6$  and  $A = 2$ . The profile of  $A = 1/6$  is almost symmetric about the disk radius ( $(r - 1)/A = 0$ ) with the circulations on either side of the jet exhibiting a similar strength. However, for  $A = 2$ , the jet has shifted slightly towards the tank wall in order to compensate for the stronger circulation displayed on the side closer to the axis of rotation.

An increase in  $Ro$  also reveals the same trend attributed to increasing  $A$ , although

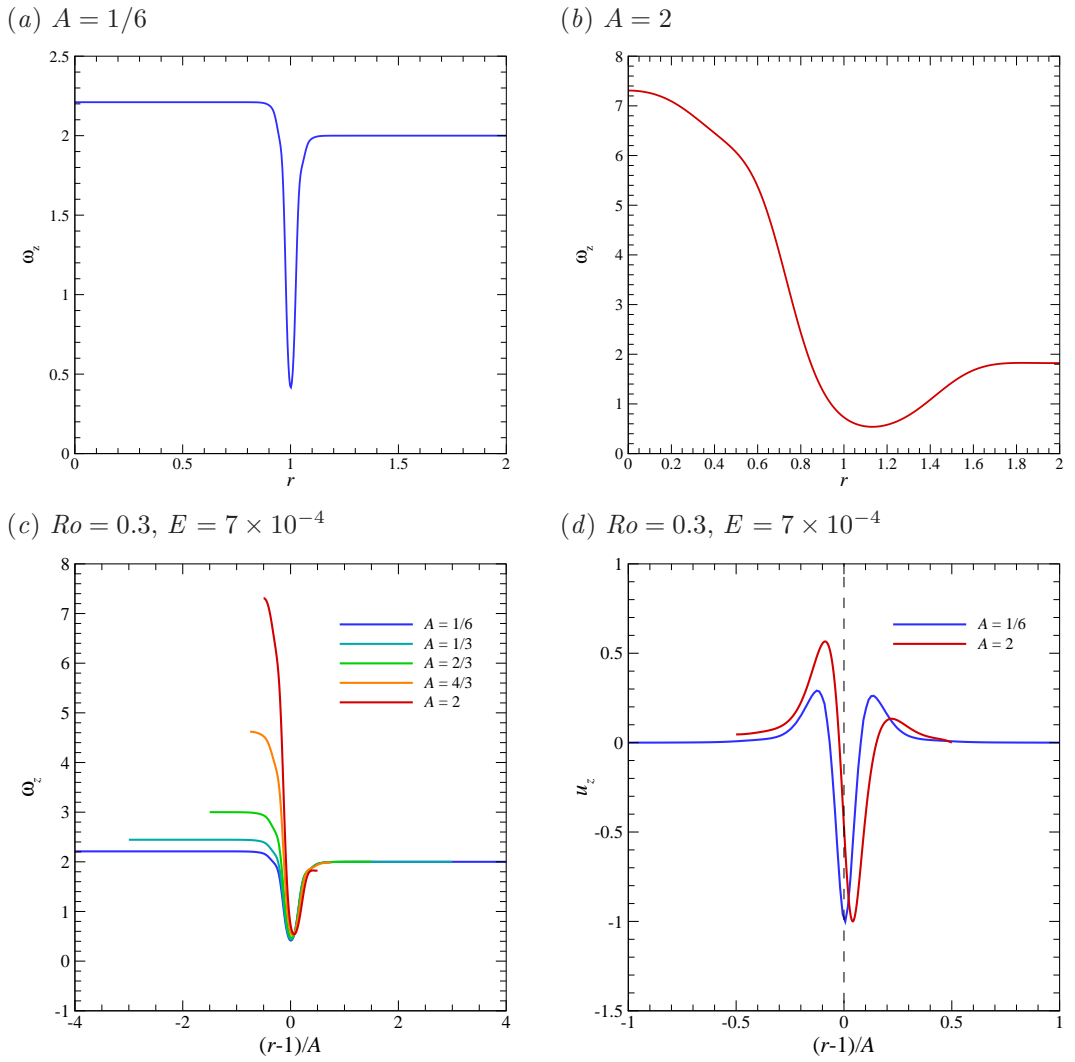


FIGURE 4.20: Profiles of axial vorticity for  $Ro = 0.3$  and  $E = 7 \times 10^{-4}$  for (a)  $A = 1/6$  and (b)  $A = 2$  extracted at  $z/H = 0.5$ . (c) A collapse of  $\omega_z$  for various  $A$  as a function of  $(r - 1)/A$ . (d) The axial velocity profiles extracted at  $z/H = 0.9$  for  $A = 1/6$  and  $A = 2$ . The axial velocities have been scaled by their relative maximums.

the changes are not as pronounced. This is likely due to the increased Stewartson layer thickness caused by increasing  $Ro$  (see figure 4.6). The effects are not as prominent because the Stewartson layer in the flow conditions studied under  $A = 2/3$  did not become large enough to experience the effects of the confining side-walls and axis of symmetry.

The shear-layer thicknesses of  $\delta_{\text{vel}}$  and  $\delta_{\text{vort}}$  have been measured following the same procedures described earlier in § 4.2.2. The shear-layer thicknesses were obtained for various Ekman number at a small Rossby number close to zero ( $Ro = 0.005$ ) for  $A = 1/6$

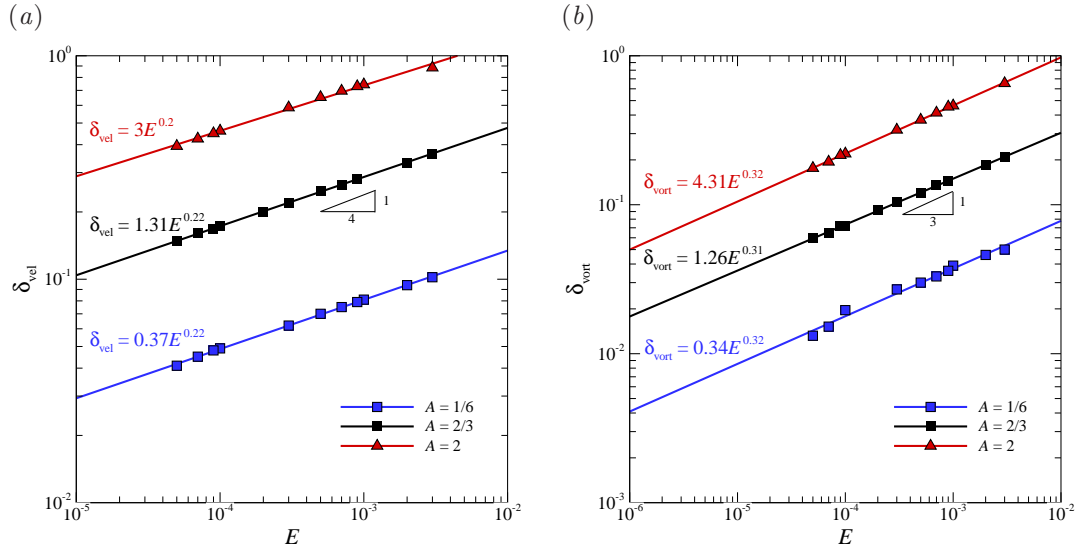


FIGURE 4.21: The thickness based on the (a) relative azimuthal velocity and (b) based on the axial vorticity as a function of  $E$ . Data for  $A = 1/6$  ( $\square$ ) and  $A = 2$  ( $\triangle$ ) are shown while the fit for  $A = 2/3$  is shown with a black solid line. The Rossby number examined is close to zero at  $Ro = 0.005$ .

and  $A = 2$ . Power-law fits of the shear-layer thicknesses as a function of  $E$  are shown in figure 4.21. For  $A = 1/6$ ,  $\delta_{\text{vort}}$  and  $\delta_{\text{vel}}$  are demonstrated to scale with  $0.34E^{0.32}$  and  $0.37E^{0.22}$ , respectively. For  $A = 2$ ,  $\delta_{\text{vort}}$  and  $\delta_{\text{vel}}$  is demonstrated to scale with  $4.31E^{0.32}$  and  $3E^{0.2}$ , respectively. For reference, it was determined that  $\delta_{\text{vort}} = 1.26E^{0.31}$  and  $\delta_{\text{vel}} = 1.31E^{0.22}$  for  $A = 2/3$ . At small  $A$ , the exponent for  $\delta_{\text{vort}}$  and  $\delta_{\text{vel}}$  displays a strong agreement with the theoretical  $1/3$  and  $1/4$  values, respectively. In fact, the exponents for both shear-layer thicknesses are comparable for  $A = 1/6$  and  $A = 2/3$ . This suggests that the Stewartson layer is present in both these aspect ratio containers. In contrast, the exponent for  $\delta_{\text{vel}}$  decreases as  $A$  increases. Surprisingly, the exponent of  $1/3$  is still maintained for  $\delta_{\text{vort}}$  at this large  $A$ . Since these thickness measurements were performed at  $Ro = 0.005$ , the profiles of axial vorticity and azimuthal velocity exhibit distinct shear-layer regions such as those shown in figure 4.5, as compared to figure 4.20(b) for which the measurements may have no physical significance. It is noted that the  $E$  exponent of  $\delta_{\text{vort}}$  across  $1/6 \leq A \leq 2$  remains fairly constant at the theoretical prediction of  $1/3$ . This may suggest that the  $E^{1/3}$  Stewartson layer may be persistent throughout a large range of  $A$ . This would not be surprising since the  $E^{1/3}$  layer functions to smooth out the discontinuity of the vorticity generated at the disk-tank interface and is thinner than the  $E^{1/4}$  layer.

For the range of  $E$  applicable to this study ( $E \ll 1$ ), empirical fits for the shear-layer thicknesses suggest that the Stewartson layers become thicker with increasing  $A$ . In turn, it is expected that the shear layer then becomes more stable as for a constant  $Ro$ , increases in  $E$  and therefore the Stewartson layer thickness has demonstrated flow approaching stability (Früh & Read 1999). According to prior studies, an unstable flow transitions from a high-wavenumber polygonal configuration to a low-wavenumber structure as the forcing is increased. The thicker Stewartson layer with the larger aspect ratio is therefore counter-intuitive to what was expressed by Dr. Luca Montabone (*personal communication*) in that unstable oval shapes were only obtained with large  $A$  containers. Results of a linear stability analysis conducted on flows produced in large aspect ratio containers explain this result and are examined later in § 5.2.

### 4.3.3 Time-dependent axisymmetric flow structure

Simulations at higher Rossby numbers in an  $A = 1/6$  container have achieved time-dependent solutions. Firstly, results at  $E = 1 \times 10^{-3}$  are discussed followed by  $E = 5 \times 10^{-4}$ . The former Ekman number case reveals aperiodic and periodic flows while the latter case demonstrates an additional type of periodic flow. For a constant  $E$ , the onset of these time-dependent flow features are characterised by the increase in  $Ro$ . A comment on flows within the  $A = 2/3$  container relating to these time-dependent phenomena is provided.

A periodic flow is obtained at  $Ro = 1$  and  $E = 1 \times 10^{-3}$ . The integral of the azimuthal velocity relative to the tank and the  $L_2$  norm of this flow condition is portrayed in figure 4.22. The periods extracted from both measures provide the same value of  $T = 37.29$ . This corresponds to a frequency of  $f = 0.0268$ , which is less than twice the frequency of the background flow ( $f = 0.9549$ ). The flow structure exhibits similar motions to that of  $Ro = 0.924$  and  $E = 1 \times 10^{-3}$  for  $A = 2/3$  (figure 4.11), where the vorticity strands stemming from the disk-tank interfaces bypass each other twice throughout a single period. Decreasing the Rossby number to  $Ro = 0.9$  achieves a chaotic-like profile for the integral of azimuthal velocity, as shown in figure 4.23(a). The axial vorticity contours for this case are illustrated in figure 4.23(b). In this case, the contours of axial vorticity display the tip of the strands fluctuating in the interior with occasional bypasses with the opposing vorticity strand. Between  $1955 < t < 1960$ , the vorticity strands are seen to bypass each other and adopt a preference of the opposing

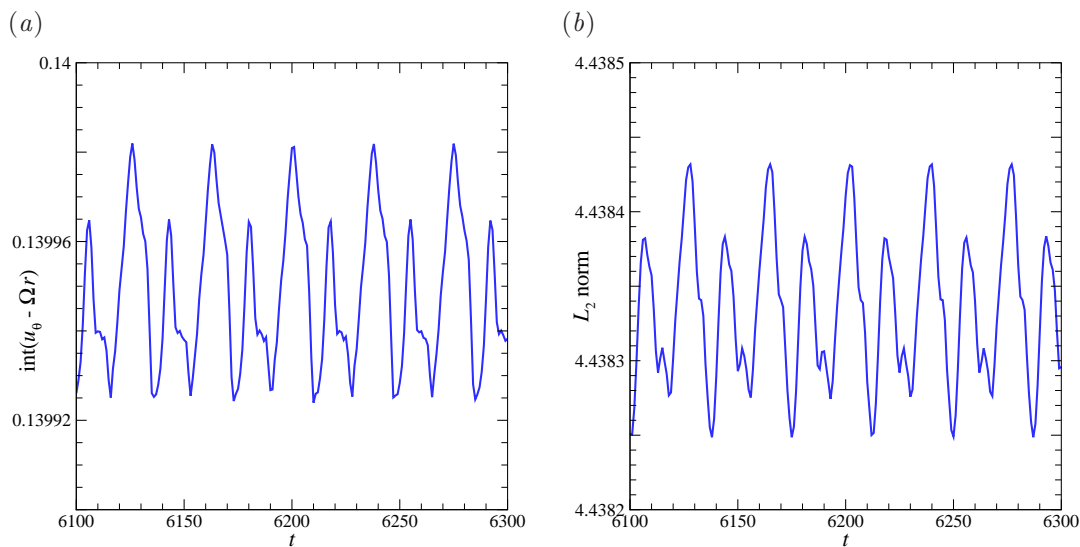
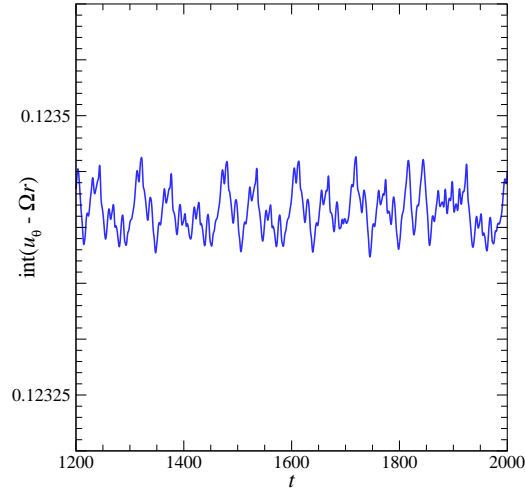


FIGURE 4.22: (a) The integral of the azimuthal velocity relative to the tank and (b) the  $L_2$  norm of the flow with conditions  $Ro = 1$  and  $E = 1 \times 10^{-3}$  with  $A = 1/6$  measured over time.

side. At  $t = 1965$ , the strands are aligned vertically with the tips of the strands coinciding at  $r = 1$ . However, the strands do not flap past each other, rather they return to their respective sides. The next bypassing of the strands occurs before  $t = 1980$ . Throughout the development of the flow, the event of the strands meeting at  $r = 1$  but not bypassing is not observed more than once consecutively. Decreasing the Rossby number further to  $Ro = 0.8$  corresponds to steady-state flow conditions. Thus, the flow of  $Ro = 0.9$  and  $E = 1 \times 10^{-3}$  portrays an aperiodic state which exists between a steady and periodic regime.

For  $E = 5 \times 10^{-4}$ , a steady-state flow is achieved for  $Ro = 0.65$  while periodic flow is seen at  $Ro = 0.85$ . An aperiodic state is observed at  $Ro = 0.8$ . Interestingly, decreasing  $Ro$  below  $Ro = 0.8$  but remaining above  $Ro = 0.65$  reveals a different type of periodic flow (e.g. at  $Ro = 0.7$ ). The integrals of azimuthal velocity for  $Ro = 0.7$ ,  $0.8$  and  $0.85$  are shown in figure 4.24. It is seen that with increasing  $Ro$ , the flow transitions from steady-state conditions to periodic, then to aperiodic, and back to periodic. Chaotic flows are expected at very large  $|Ro|$ . It is surprising that this type of rotating flow is able to recover time-periodic properties once it is lost by increasing the forcing magnitude. A period of  $T = 6.992$  is determined from two integral measures (relative azimuthal velocity and  $L_2$  norm) for  $Ro = 0.7$ . A significantly larger period of

(a)  $Ro = 0.9$ ,  $E = 1 \times 10^{-3}$

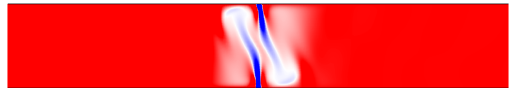


(b)

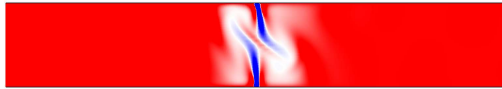
$t = 1950$



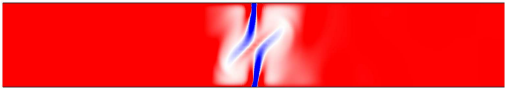
$t = 1975$



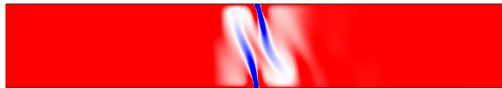
$t = 1955$



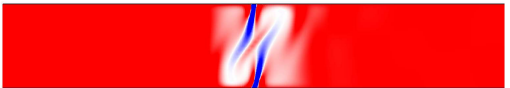
$t = 1980$



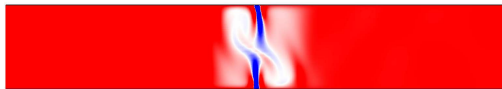
$t = 1960$



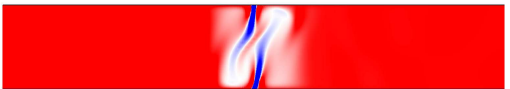
$t = 1985$



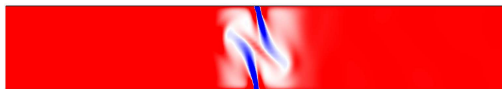
$t = 1965$



$t = 1990$



$t = 1970$



$t = 1995$

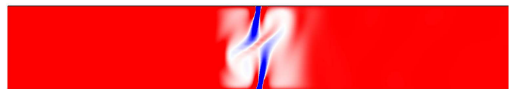


FIGURE 4.23: Flow conditions of  $Ro = 0.9$  and  $E = 1 \times 10^{-3}$  for  $A = 1/6$ . (a) The integral of the azimuthal velocity relative to the tank measured over time. (b) Snapshots of axial vorticity for the same flow conditions throughout  $1950 \leq t \leq 1995$  with intervals of  $\Delta t = 5$ . A partial domain is shown with  $0.5 \leq r \leq 1.5$  and  $0 \leq z \leq 1/6$ . Contour levels are as per figure 4.2.

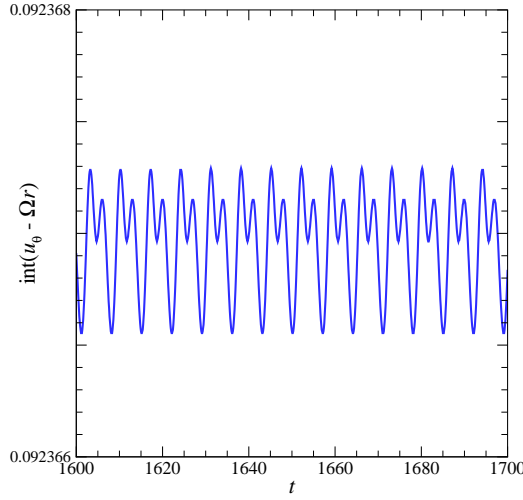
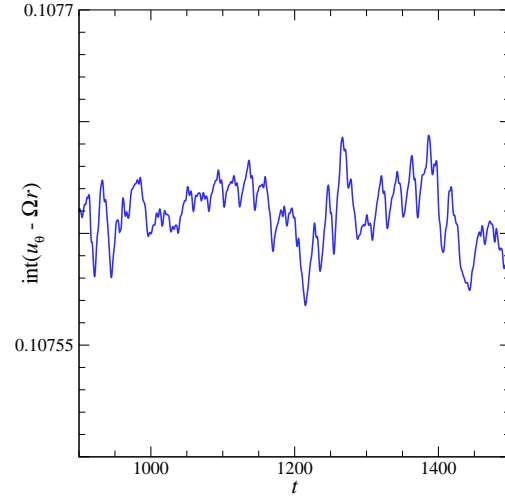
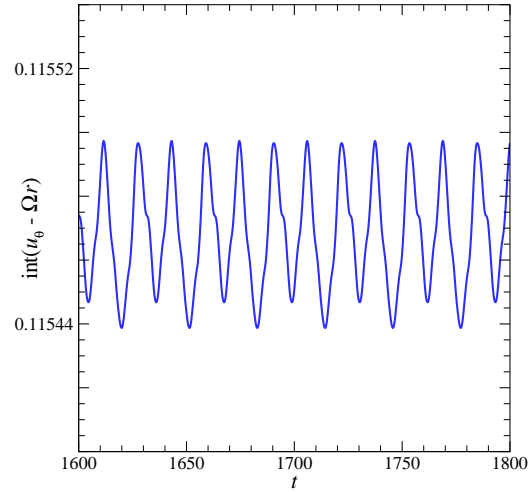
(a)  $Ro = 0.7, E = 5 \times 10^{-4}$ (b)  $Ro = 0.8, E = 5 \times 10^{-4}$ (c)  $Ro = 0.85, E = 5 \times 10^{-4}$ 

FIGURE 4.24: The integral of the azimuthal velocity relative to the tank measured over time for flow conditions of (a)  $(Ro, E)=(0.7, 5 \times 10^{-4})$ , (b)  $(Ro, E)=(0.8, 5 \times 10^{-4})$  and (c)  $(Ro, E)=(0.85, 5 \times 10^{-4})$  with  $A = 1/6$ . The flow in panels (a) and (c) exhibit periods of  $T = 6.992$  and  $T = 31.453$ , respectively.

$T = 31.453$  is exhibited from both integral measures at  $Ro = 0.85$ . Both flow cases of  $Ro = 0.7$  and  $Ro = 0.85$  demonstrate an oscillation frequency which is less than twice their background rotation frequency. At  $Ro = 0.85$ , the flow features are very similar to that of flow conditions  $(Ro, E)=(0.924, 1 \times 10^{-3})$  (figure 4.11), such that the axial vorticity strands bypass one another twice per period. The other type of periodic flow observed at  $Ro = 0.7$  demonstrates unsteady negative-vorticity strands at the disk-tank interface which favour different sides of the  $r = 1$  line similar to that of  $Ro = 0.5$  and

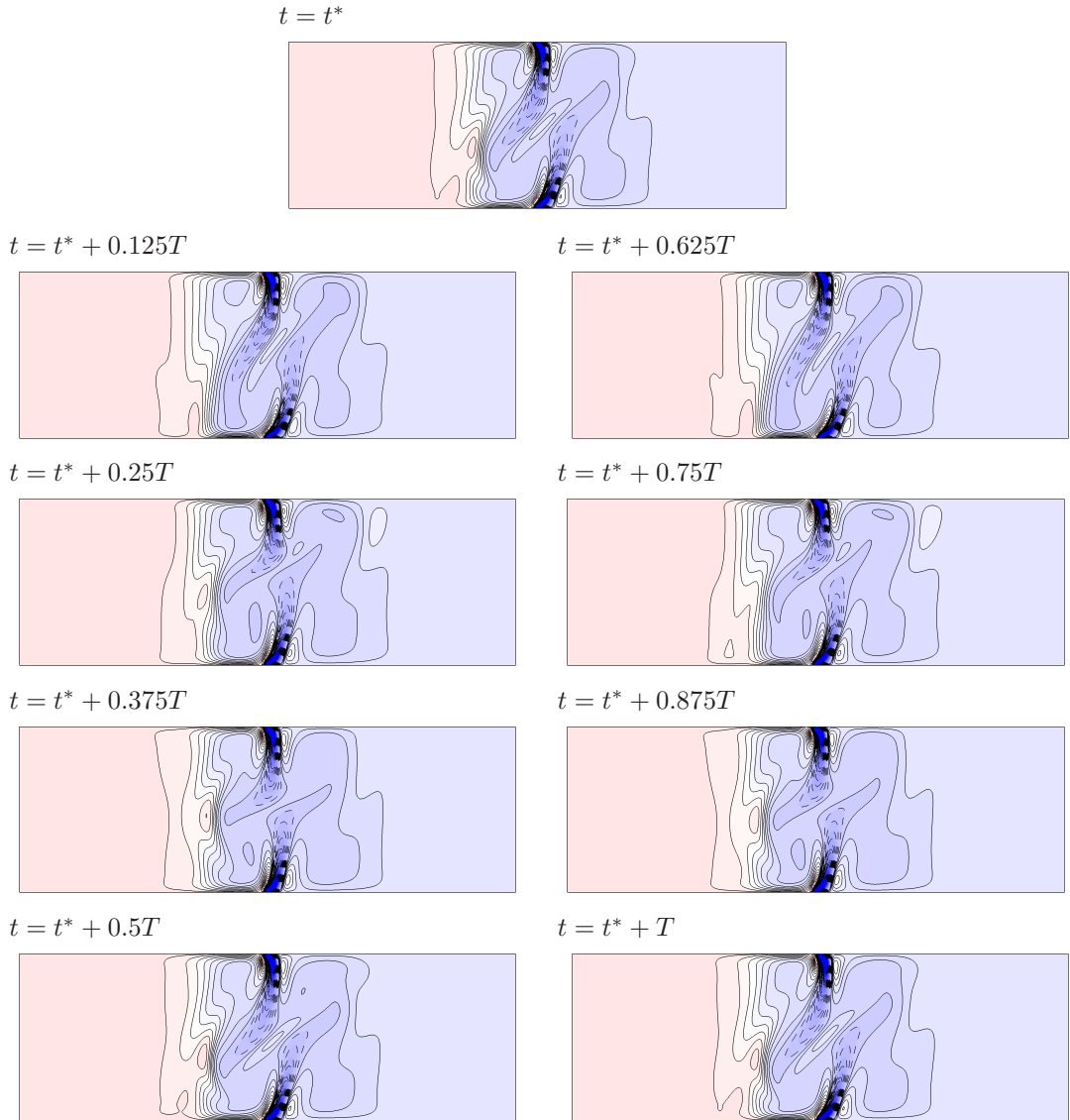


FIGURE 4.25: Snapshots of axial vorticity throughout a complete period with flow with conditions  $Ro = 0.8$  and  $E = 1 \times 10^{-3}$  for  $A = 2/3$ . The top centred panel represents the reference flow condition at  $t = t^*$ . The period of the flow is given by  $T = 17.011$ . Contour levels are as per figure 4.2.

---

$E = 3 \times 10^{-4}$  in the  $A = 2/3$  container (figure 4.2(d)). However, the length of the strands are not equivalent and the tips of the strands are angled differently; the top strand is more inclined away from the vertical while the bottom strand is largely vertical. The tips of these strands fluctuate over time but does not cross  $r = 1$  nor bypass each other as was seen in figure 4.11 of flow conditions  $Ro = 0.924$  and  $E = 1 \times 10^{-3}$ .

Referring back to the  $A = 2/3$  configuration, a closer investigation of  $E = 1 \times 10^{-3}$  has now also revealed the periodic  $\rightarrow$  aperiodic  $\rightarrow$  periodic type of transition for  $Ro =$

0.8  $\rightarrow$  0.85  $\rightarrow$  0.9. That is, the flow at  $Ro = 0.8$  demonstrates the first type of periodic flow such that there are slight fluctuations in the tips of the vorticity strands and they do not bypass each other at  $r = 1$ . This is observed in figure 4.25. At  $Ro = 0.85$ , an aperiodic flow is achieved whereby the flow illustrates irregular bypasses of the vorticity strands (see figure 4.23). For  $Ro = 0.9$  exhibits a periodic flow which involves flapping of the strands past each other twice per period (see figure 4.11). It is emphasised that although these are the only flow cases where this phenomena has been observed in our parameter space, it is possible that it could be found at other Ekman and Rossby numbers and aspect ratios.

#### 4.3.4 Universal regime diagram

A pair of non-dimensional parameters independent of height is obtained by grouping the Rossby and Ekman number with the aspect ratio. Substitution of  $H = AR_d$  into the definitions of  $Ro$  and  $E$  and seeking a group of variables independent of height yields

$$\begin{aligned} Ro &= \frac{\omega}{2\overline{\Omega}A}, \\ ARo &= \frac{\omega}{2\overline{\Omega}}, \end{aligned} \tag{4.3}$$

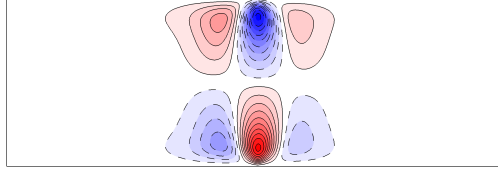
$$\begin{aligned} E &= \frac{\nu}{\overline{\Omega}A^2R_d^2}, \\ EA^2 &= \frac{\nu}{\overline{\Omega}R_d^2}. \end{aligned} \tag{4.4}$$

The non-dimensional groupings of  $ARo$  and  $EA^2$  appear, incidentally, in the coefficient of diffusion in the dimensionless governing equations, namely  $EA^2/(1 - ARo)$ . Thus, the effect of the height dependence of the flow is examined through  $ARo$  and  $EA^2$ .

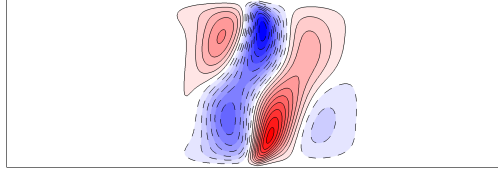
The height dependence of the flow has been visually characterised into two categories as determined through contours of axial velocity. The categories and their associated axial velocity contours are shown in figure 4.26 with both cases belonging to the positive- $Ro$  regime. Category 1 demonstrates a reflective symmetry about the mid-plane while category 2 portrays a breaking of this symmetry. With category 2, cases displayed two orientations of the primary fluid pumping and suction strands. In some instances, pumping is induced on the right side of the stronger fluid suction branch while in other instances pumping is induced on the left side of the fluid suction branch. However, both cases are the same solution, merely reflected about the horizontal mid-plane.

---

(a) Category 1



(b) Category 2



(c) Category 2

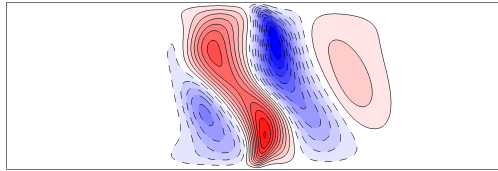


FIGURE 4.26: The three types of axial velocity contours used to characterise the height dependence of the flow. Characterisation is determined for steady-state axisymmetric flows. Category 1 is reflectively symmetric about the mid-plane while category 2 breaks the mid-plane symmetry. Examples of both category 2 orientations are shown in panels (b) and (c). The flow conditions are of (a)  $(Ro, E)=(9.97 \times 10^{-3}, 2.99 \times 10^{-3})$ , (b)  $(Ro, E)=(0.692, 2.31 \times 10^{-3})$  and (c)  $(Ro, E)=(0.9, 2 \times 10^{-3})$ .

---

Thus, category 1 and 2 represent reflectively symmetric and symmetry-broken flows, respectively.

The solution of the flow condition combined with the aspect ratio have been characterised as either category 1 or 2. A plot of  $ARo$  and  $EA^2$  and its respective category is shown in figure 4.27. The data are characterised by the shape and colour of the symbols used. The colour illustrates the categories while the symbol shape represents the aspect ratio. It is seen that for small  $ARo$ , the regime is dominated by category 1 type flows. The flow transitions to category 2 with increasing  $ARo$ . Thus, the plot illustrates a strong transition from reflectively symmetric to symmetry-broken flow with increasing  $ARo$ .

A transition between reflectively symmetric (category 1) and symmetry-broken flow (category 2) has been estimated, as shown by a solid line in figure 4.27. As the data are plotted as functions of  $ARo$  and  $EA^2$  and has demonstrated great conformity to the respective categories, it is assumed that the transition line is a function of  $A$ ,  $Ro$  and  $E$ .

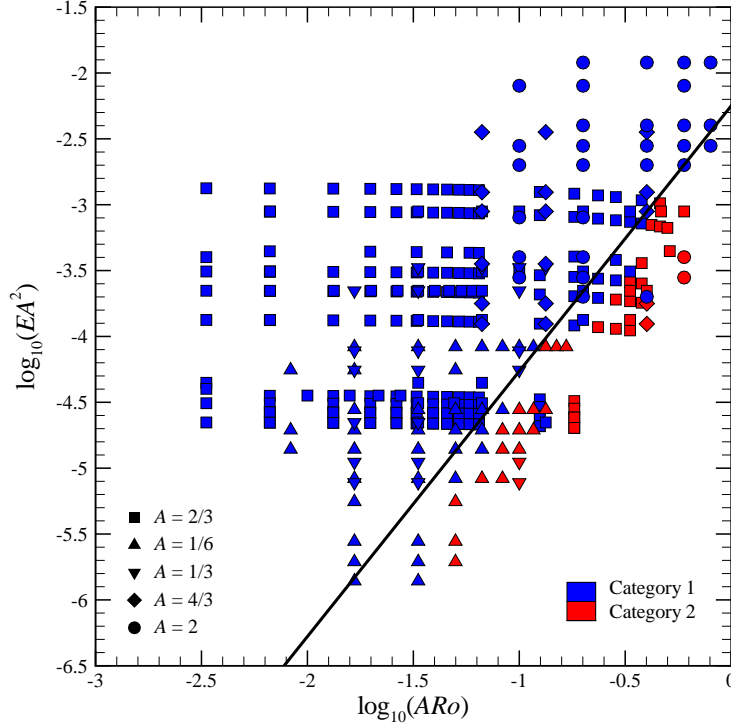


FIGURE 4.27: A plot of  $ARo$  against  $EA^2$  and its respective category. The categories are color coded such that category 1 is represented by blue and category 2 by red. Aspect ratios of  $A = 1/6$  ( $\triangle$ ),  $A = 1/3$  ( $\nabla$ ),  $A = 2/3$  ( $\square$ ),  $A = 4/3$  ( $\diamond$ ) and  $A = 2$  ( $\circ$ ) are represented by different symbols. The solid line represents the transition between reflectively symmetric (category 1) and symmetry-broken (category 2) flow, which is governed by  $Ro_{c1-c2} = 13.35E^{0.5}$ .

An initial empirical fit of the transitional line was given by  $ARo_{c1-c2} = 13.35(EA^2)^{0.483}$  which yields a relationship for  $Ro_{c1-c2} = 13.35A^{-0.034}E^{0.483}$ . Interestingly, the exponents of  $A$  and  $E$  are very close to zero and 0.5, respectively, and it is emphasised that the line has been fitted roughly by eye which can certainly be tweaked. Thus, the refined transition may be described by  $Ro_{c1-c2} \sim 13.35E^{0.5}$ , which has no dependence on the aspect ratio (solid line in figure 4.27). This suggests that the symmetry-breaking threshold can be described by a constant governed by  $Ro/\sqrt{E}$ . This parameter group can be expressed in terms of the forcing parameters through

$$\frac{Ro}{\sqrt{E}} = \frac{R_d\omega}{2\sqrt{\Omega\nu}}. \quad (4.5)$$

Furthermore, the presence of the  $E^{1/2}$  seems to suggest that the breaking of reflective symmetry may be related to the Ekman layer, or its thickness, which scales with  $E^{1/2}$ . By adopting a length scale of  $L = E^{1/2}H$  and a velocity scale of  $U = R\omega$ , a Reynolds

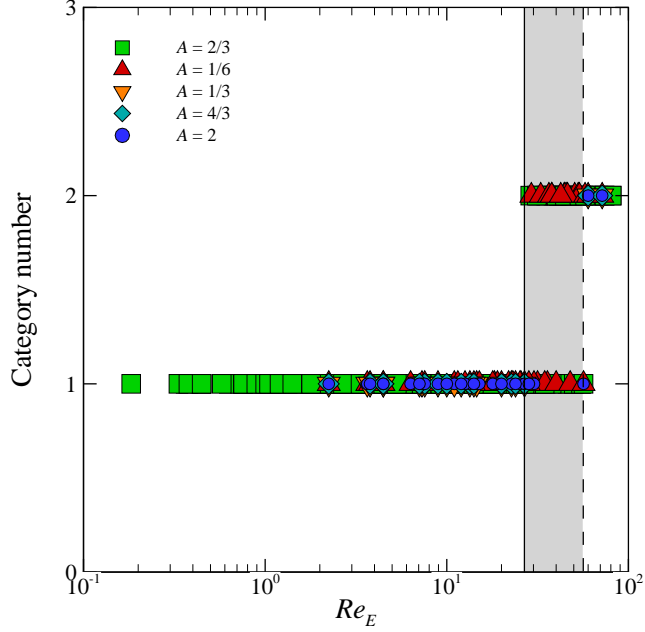


FIGURE 4.28: A plot of the category number as a function of  $Re_E$ . Aspect ratios of  $A = 1/6$  ( $\triangle$ ),  $A = 1/3$  ( $\nabla$ ),  $A = 2/3$  ( $\square$ ),  $A = 4/3$  ( $\diamond$ ) and  $A = 2$  ( $\circ$ ) are represented by different symbols. The solid line represents the transition between reflectively symmetric (category 1) and symmetry-broken (category 2) flow, which is governed by  $Re_E = 26.7$ . The grey region bounded by the solid line and the dashed line represents a transition zone which exhibits either category. The dashed line describes  $Re_E = 56.4$ .

number based on the Ekman layer thickness can be defined as

$$Re_E = \frac{UL}{\nu} = \frac{2Ro}{E^{1/2}}. \quad (4.6)$$

Thus, combining the threshold equation of  $Ro_{c1-c2} \sim 13.35E^{0.5}$  and equation 4.6 yields a constant  $Re_E \sim 26.7$ .

Plotting the category number as a function of the external Reynolds number, which considers  $H$  as the reference length, does not display any strong trends even for a constant  $A$ . The internal Reynolds number also does not exhibit any trends. This is due to the exponent of  $E$  in the symmetry breaking parameter revealing a value of a  $1/2$ , which is not equivalent to the Ekman number scales for the  $Re$  and  $Re_i$ , namely 1 and  $3/4$ , respectively. Thus the category number as a function of the Reynolds number based on the Ekman layer thickness is reproduced in figure 4.28. The different symbols correspond to the various aspect ratios investigated. The solid line represents the transition between reflectively symmetric and symmetry-broken flow, as determined to be  $Re_E \sim 26.7$ . Evidently, flow conditions for  $Re_E > 26.7$  still demonstrate category 1

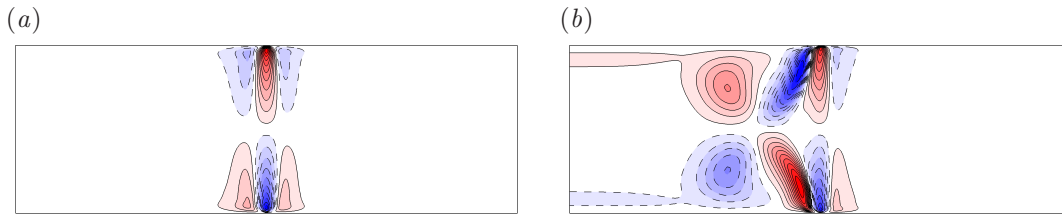


FIGURE 4.29: Axial velocity contours of (a)  $Ro = -0.3$  and (b)  $Ro = -2$  for  $E = 3 \times 10^{-4}$ .

features. However, the data displays an upper bound to the category 1 flows described by  $Re_E \sim 56.4$  and is shown by a dashed line. It is noted that this limit is present for all  $A$  in this region. Thus, the regime between  $26.7 < Re_E < 56.4$  (shaded grey) may represent a transitional regime whereby both categories are present (i.e. both reflectively symmetric and symmetry-broken flows).

All of the axisymmetric steady-state flows in the negative- $Ro$  regime demonstrated reflective symmetry about the mid-plane in the axial velocity contours. The axial velocity contours for a small and large negative- $Ro$  flow are shown in figure 4.29. As expected, the small- $Ro$  flow with  $Ro = -0.3$  demonstrates Ekman pumping and suction on the horizontal boundaries that is reflectively symmetric about the mid-plane, similar to that of the small-positive- $Ro$  cases. Increasing  $|Ro|$  in the negative- $Ro$  regime causes a deviation from this typical structure such that an extra circulation is created at the inner side of the fluid pumping and suction zone. However, this altered structure still exhibits reflective symmetry about the mid-plane in the axial velocity contours. Thus, in considering only axisymmetric steady-state flows, the negative- $ARo$  regime is characterised only by category 1 flow. Recall that at sufficiently large  $|Ro|$  in the negative- $Ro$  regime, periodic and chaotic states demonstrate a breaking of height independence of the flow (e.g. figure 4.16). In the positive- $ARo$  regime, the flow conditions are limited by  $ARo = 1$  which corresponds to  $\omega \rightarrow \infty$ . This constraint has been described in § 3.7.1.1.

#### 4.4 Flow on the $\beta$ -plane

The previous sections considered flow computed on an  $f$ -plane which behaves with a constant planetary vorticity of  $2\Omega$ . In this section, the influence of a varying planetary vorticity on the flow is investigated through the use of a linearly varying bottom topography. In theory, the lateral variation of the planetary vorticity is required for

phenomena such as Rossby waves to exist. Thus, it would not be surprising if the flow structures on the  $f$ -plane and the  $\beta$ -plane were different. The same methodology of the previous sections have been adopted here.

#### 4.4.1 Axisymmetric flow structure

Steady-state solutions were obtained on the meridional semi-plane for selected cases such that comparisons against the respective  $f$ -plane counterpart can be made. Four different bottom topographic angles of  $\theta = 2.5^\circ, 5^\circ, 7.5^\circ, 10^\circ$  have been investigated. The topographic  $\beta$  effect is defined by  $\beta = 2\bar{\Omega} \tan \theta / H$  (equation 3.61).

Comparisons between the  $f$ -plane and  $\beta$ -plane cases are shown in figure 4.30 through contours of axial velocity and axial vorticity with  $Ro = 0.3$  and  $E = 7 \times 10^{-4}$ . At these flow conditions, the flow structures in the  $f$ -plane are reflectively symmetric as illustrated by contours of velocity and vorticity. It should be noted that the contour levels are the same in each panel of their respective column. The structure of the shear layer remains seemingly unchanged in the axial vorticity contours as the angle with the bottom horizontal increases. The major difference is observed in the region of  $r < 1$  where the fluid exhibits high vorticity in the  $f$ -plane and decreases as  $\theta$  is increased. Differences in the axial velocity contours are not obvious. There is a slight asymmetry in the circulation at the top horizontal boundary where the magnitude of the axial velocity on the deeper side is larger than that on the shallower side. This is not evident on the bottom boundary as the mid-plane separating the top and bottom circulations adopts an angle of  $\theta$ . In addition, the axial velocity in the shear layer loses symmetry for  $\beta > 0$  where the downward jet from the top boundary inclines inward while the upward jet inclines outward.

Essentially, very little difference in the flow structure has been observed between the  $f$ -plane and the largest  $\beta$ -plane case for this particular flow condition. This trend is seen throughout all of the flow conditions examined, even for those which have broken height independence in the  $f$ -plane case. An example of this is demonstrated in figure 4.31 where similar velocity circulations and vorticity strands are seen between  $\theta = 0^\circ$  and  $\theta = 10^\circ$ . Larger cases of  $\theta$  were not examined due to numerical stability constraints induced by the required quadrilateral elements used in discretising the spatial domain. That is, the number of element vertices on the left and right boundaries must be equal which causes a dense cluster of elements near the axis of rotation. Despite this

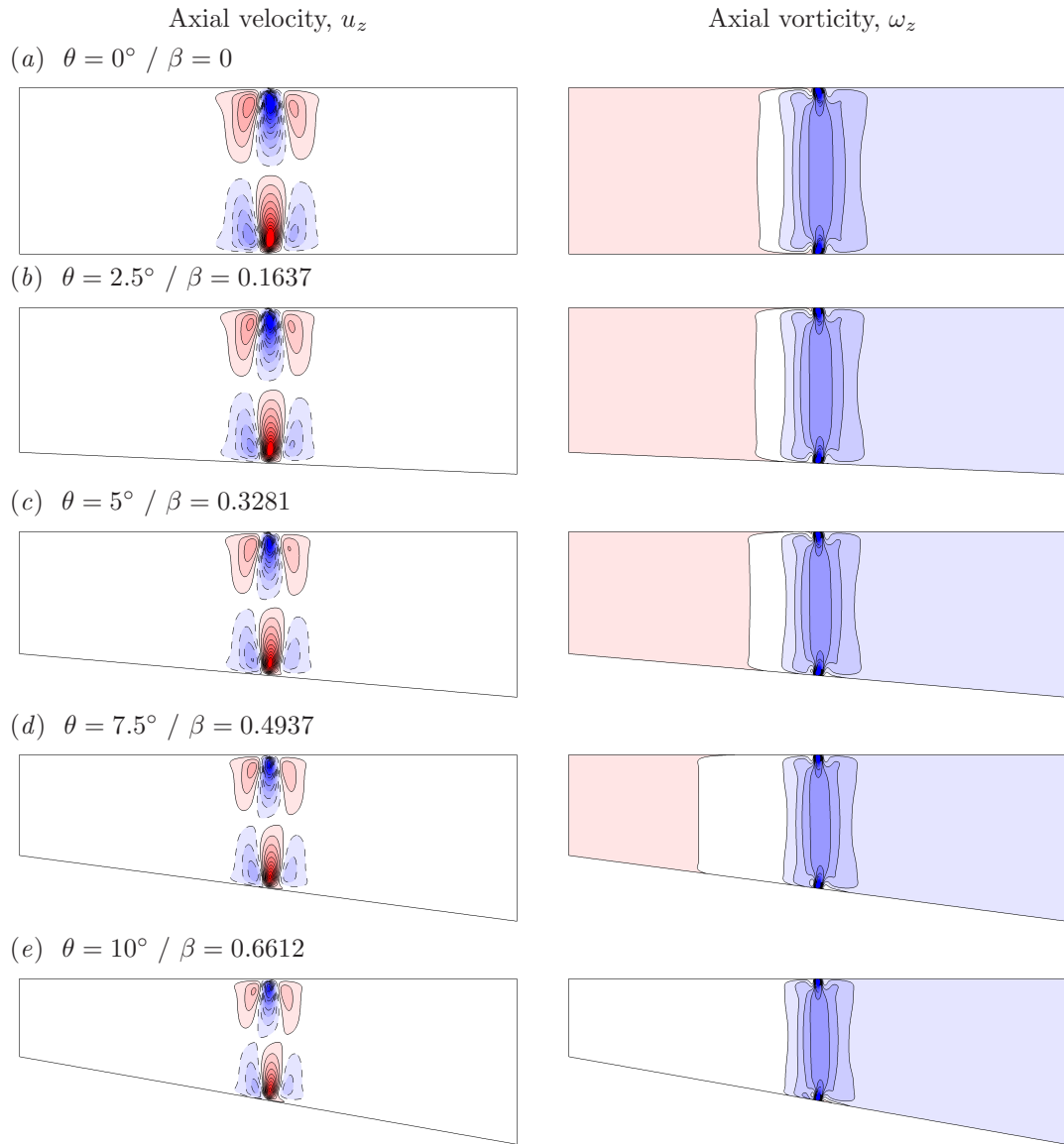


FIGURE 4.30: Structure of the axisymmetric flows visualised on the semi-meridional  $r$ - $z$  plane. Axial velocity (left) and axial vorticity (right) are shown for  $Ro = 0.3$  and  $E = 7 \times 10^{-4}$  in containers of  $\theta = 0^\circ, 2.5^\circ, 5^\circ, 7.5^\circ$  and  $10^\circ$ . Contour levels are as per figure 4.2. The same number of contour levels are used for each  $\theta$  case.

---

limitation, it is expected that higher  $\theta$  angles would not produce any structures that are largely different to those obtained in a flat container especially if the flow reaches a steady state. This is because the effect of vortex stretching on a fluid column caused by the change in fluid depth is only triggered by motions in the radial direction. Thus, differences between the cases are expected to be seen through linear stability analysis where the perturbations will stimulate the vorticity changes. Results of the linear

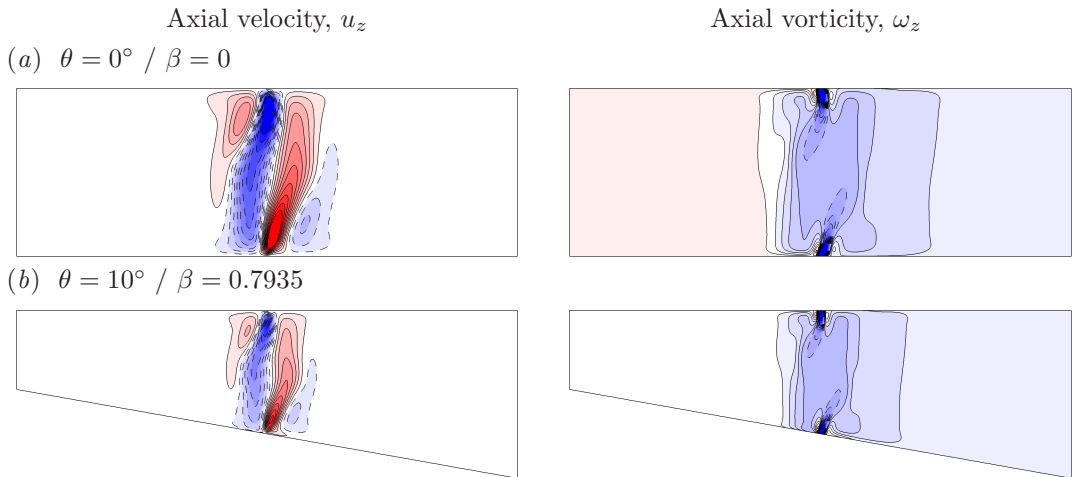


FIGURE 4.31: Structure of the axisymmetric flows visualised on the semi-meridional  $r$ - $z$  plane. Axial velocity (left) and axial vorticity (right) are shown for  $Ro = 0.5$  and  $E = 7 \times 10^{-4}$  in containers of (a)  $\theta = 0^\circ$  and (b)  $\theta = 10^\circ$ . Contour levels are as per figure 4.2. The same number of contour levels are used for each  $\theta$  case.

---

stability analysis on  $\beta$ -plane flows are covered in § 5.3.

## 4.5 Summary

The structure of the axisymmetric base flows produced by differential rotation in a cylindrical container have been examined numerically. The dimensions of the primary model are based on the laboratory apparatus used in Früh & Read (1999), which has an aspect ratio of  $A = 2/3$ . In addition, other aspect ratios ranging from  $1/6 \leq A \leq 2$  were explored.

A variety of axisymmetric steady-state base flows characterised by the governing parameters of Rossby and Ekman number were obtained. Results of both positive and negative forcing revealed several distinct base flow features. For small values of  $|Ro|$ , the flow remained highly two-dimensional following predictions from the Taylor–Proudman theorem. The height-independent velocity and vorticity profiles were analysed to determine the relationships and thickness scalings of the Stewartson layers. The results agree well with theoretical predictions in the limit of small- $Ro$ . Universal relationships for the  $\delta/E^{1/3}$  and  $\delta/E^{1/4}$  have been developed and demonstrate an approximately linear dependence against  $(\omega/\Omega)$  for negative and small-positive- $Ro$  flows. As  $|Ro|$  is increased, negative-vorticity strands are seen stemming from the disk-tank interface which demonstrates a disruption to the two-dimensionality of the flow. This breaking

of two-dimensionality occurs at a much lower  $|Ro|$  for positive  $Ro$  compared to negative  $Ro$ . A likely explanation for this may be given by the sign of the axial vorticity generated at the disk-tank interface and hence, the strength and direction of the axial jets induced by the Ekman layers.

With sufficient forcing in the positive- $Ro$  regime, the steady-state condition of the axisymmetric flow is lost and a periodic flow is observed. In a number of cases, a state of aperiodic flow between steady-state and time-periodic flow was encountered whereby the integral of the relative azimuthal velocity and the  $L_2$  norm exhibited chaotic-like features. This aperiodic state was also found between two different types of periodic flow. The first involves minor fluctuations in the axial vorticity strands and occurs at lower  $Ro$  than those describing the aperiodic regime. The second type exhibits stronger oscillations where the strands of vorticity bypass each other twice over a single period. This occurs at higher Rossby numbers. A pure periodic state was not observed in the negative- $Ro$  regime, although periodic features in the flow structures were demonstrated. This includes minor oscillations of the positive axial vorticity strands and the shedding of vortex pairs towards the axis of rotation.

The effect of a large aspect ratio container yielded a broadening of the shear layer while a more concentrated shear layer is obtained for small aspect ratio containers. Although the structure of the flow did not vary greatly throughout the various aspect ratios, it is expected that the linear stability of the flow will illustrate greater differences due to the change in the shear-layer structure. The analysis of the shear-layer thickness across the different aspect ratios revealed Ekman number exponents close to  $1/3$  for  $\delta_{vort}$ . Thus, the thin  $E^{1/3}$  is expected to exist even though the thicker  $E^{1/4}$  is disrupted at larger  $A$ . A universal diagram governed by  $\log_{10}(EA^2)$  and  $\log_{10}(ARo)$  was produced to determine the effect of the aspect ratio on the height dependence of the flow. A clear segregation between reflectively symmetric and symmetry-broken flow was observed, and the empirical fit of the transition line yielded no dependence on  $A$ , namely  $Ro_{c1-c2} \sim 13.35E^{0.5}$ .

The axisymmetric steady-state flows on a  $\beta$ -plane illustrated minor differences to the  $f$ -plane flows. It is proposed that this structural similarity is due to the lack of radial motions, which is required to induce vorticity changes across the varying depth. Thus, similar to the flows obtained across the different aspect ratios, the major differences are expected to be seen in the results of the linear stability analysis.

The next chapter will investigate the linear stability of the axisymmetric steady-state flows reported in this chapter.



## Chapter 5

# Linear instability of flow in a differential-disk rotating system

In this chapter, a linear stability analysis is used to predict the fastest-growing three-dimensional azimuthal wavenumbers that develop on the underlying axisymmetric steady-state flow, for a wide range of  $Ro$  and  $E$ . The azimuthal wavenumber is defined by  $k = 2\pi/\lambda$ , where  $\lambda$  is the angular wavelength of the instability. The zeroth wavenumber is omitted, as it has a synchronous nature that was found always to be stable. In contrast, the eigenvalues of non-zero wavenumbers are consistently complex, which correspond to quasi-periodic instability modes, where the instability introduces an incommensurate frequency into the flow (Blackburn *et al.* 2005; Blackburn & Sheard 2010). In other words, the instability invokes a Hopf bifurcation from a steady axisymmetric state to an unsteady non-axisymmetric state. This analysis predicts that flows become linearly unstable under certain combinations of  $Ro$  and  $E$ . Distinct stability characteristics are observed between positive and negative- $Ro$  flows.

§ 5.1 continues investigating the configuration used by Früh & Read (1999) through a linear stability analysis on the axisymmetric base flows obtained in the previous chapter (§ 4.2). The results at positive and negative- $Ro$  flows are detailed in § 5.1.1 and § 5.1.2, respectively, which includes growth rate data, instability mode shapes in isolation and in combination with the base flow, and the preferred linear azimuthal wavenumbers complimented by several observable trends. The same analyses are then performed for flows in containers with different aspect ratios, which are described in § 5.2. The last section § 5.3 examines the linear stability of flows on a  $\beta$ -plane.

Various results from this chapter have been published in Vo *et al.* (2014).

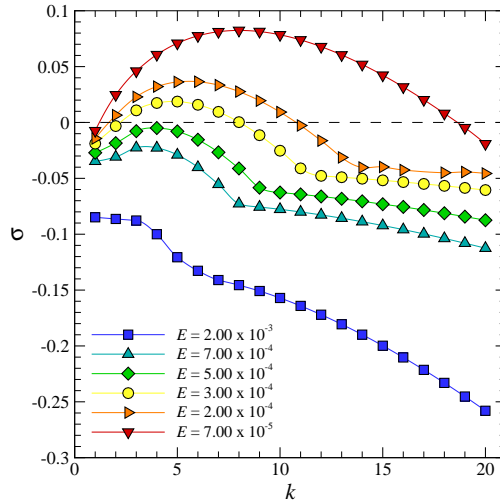


FIGURE 5.1: Growth rate  $\sigma$  as a function of azimuthal wavenumber  $k$  for various  $E$  at a small  $Ro = 0.05$ . The dashed line represents neutral stability where points above and below symbolise unstable and stable modes, respectively.

## 5.1 Simulating the configuration used by Fröh & Read

Fröh & Read (1999) considered a double end-wall differentially-rotating configuration with a disk radius of  $R_d = 15$  cm and a tank height of  $H = 10$  cm. This corresponds to a container aspect ratio of  $A = 2/3$ . This section highlights the numerical results of this configuration and aspect ratio for positive and negative- $Ro$  flows separately.

### 5.1.1 Positive-Rossby-number regime

#### 5.1.1.1 Growth rates

The growth rates for a range of azimuthal wavenumbers were obtained for numerous  $Ro$ - $E$  combinations. The fastest-growing wavenumber was established in each case, with peak unstable azimuthal wavenumbers ranging primarily from 2 to 9 in the positive- $Ro$  regime. As a comparison, unstable nonlinear azimuthal modes with wavenumbers of 2 to 8 were typically observed in laboratory experiments (Fröh & Read 1999; Aguiar *et al.* 2010).

The growth rate as a function of wavenumber for a small  $Ro = 0.05$  and several  $E$  is shown in figure 5.1. A single maximum can be seen in the  $\sigma$ - $k$  relationship. Local maxima typically represent distinct instability modes (e.g. Barkley & Henderson 1996). For wavenumbers beyond this maximum, the growth rate decreases monotonically. This behaviour is consistent with the progressively stronger viscous damping of shorter-

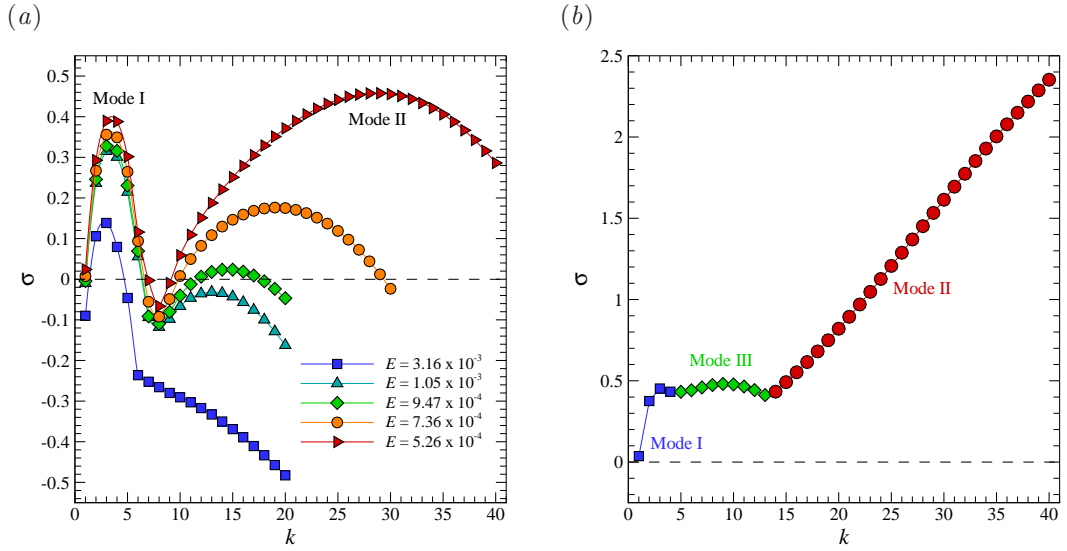


FIGURE 5.2: Growth rate  $\sigma$  as a function of wavenumber  $k$  for (a) various  $E$  at  $Ro = 0.395$  and (b)  $(Ro, E) = (0.5, 3 \times 10^{-4})$ . Two mode peaks of  $\sigma$  are present at low and high wavenumbers denoted by mode I and II, respectively in panel (a). A third mode peak, mode III, is illustrated in panel (b). The dashed line represents neutral stability where points above and below symbolise unstable and stable modes, respectively.

wavelength disturbances at higher wavenumbers. At large Ekman numbers, this peak is still present despite the growth rates always remaining negative (stable flow). The flow is only unstable for small  $E$  ( $E < 3 \times 10^{-4}$ ) at  $Ro = 0.05$ . Several trends can be observed from this figure. The growth rates and the most unstable wavenumber increases with decreasing  $E$ . Also, the profiles do not change significantly with varying  $E$ , though the range of wavenumbers over which the mode branches are detected to increase with decreasing  $E$ . For example, the mode branch covers  $1 \leq k \leq 8$  for  $E = 7 \times 10^{-4}$  while a larger range of  $1 \leq k \leq 14$  is seen for  $E = 2 \times 10^{-4}$ .

Figure 5.2(a) illustrates the growth rate as a function of wavenumber at constant  $Ro = 0.395$  for varying  $E$ . Similarly, with small- $Ro$  flows, only a single mode peak comprising small wavenumbers exists for large  $E$ . This first mode peak is shown for  $E = 3.16 \times 10^{-3}$  in figure 5.2(a), with the most unstable wavenumber predicted as  $k_{\text{peak}} = 3$ . However, unlike small- $Ro$  flows, a second mode peak emerges at higher wavenumbers as  $E$  decreases. In fact, the emergence of the second mode peak is dependent on both  $Ro$  and  $E$ , which is discussed later in this section (figure 5.3). Eventually, the growth rates of these higher wavenumbers become larger than those of the first mode peak. The dominance of the second peak is shown for the case of  $E = 5.26 \times 10^{-4}$ , where the

predicted linearly unstable wavenumber is  $k_{\text{peak}} = 29$ . These small-wavenumber and high-wavenumber modes will hereafter be referred to as modes I and II, respectively. A third mode peak (mode III) has also been observed, which comprises intermediate wavenumbers between modes I and II, as shown in figure 5.2(b). This third peak arises by further decreasing  $E$  or increasing  $Ro$ , and in a small number of small- $E$ /high- $Ro$  cases it was seen to achieve growth rates exceeding those of mode I.

The emergence of these three mode peaks may be related to the features exhibited in the base flow. Base flows on which mode I dominates are typically reflectively symmetric about the horizontal mid-plane. This is reflective of small- $Ro$  and high- $E$  flows, which is in agreement with the trends seen on growth rate against wavenumber plots. Thus, depth-independent contours of axial vorticity usually demonstrate dominance of the mode I instability. Ascendency of mode II is characterised by the elongation of the negative-vorticity strands and the symmetry breaking of the base flow. Further elongation and development of the “hooks” at the tip of the vorticity strands is associated with the emergence of mode III. It may well be possible for mode III to become the most dominant mode by sufficiently increasing  $Ro$  or decreasing  $E$ , though this has not been observed in our parameter space.

Figure 5.3 is a regime diagram depicting the dominance of either the mode I or mode II instability for specific flow conditions. It is stressed that the data represents flows for which the dominant mode is either a mode I or II, and not merely of the presence of mode I or II wavebands in the growth rate against wavenumber data. Actually, the mode I instability is always present when the mode II instability exists. There is a clear transition from flows that exhibit larger growth rates associated with the mode I instability to flows that exhibit larger growth rates from wavelengths belonging to the mode II instability. The conditions for this transition are similar to those observed with the onset of the mid-plane symmetry-broken flow such that it occurs with increasing  $Ro$  and/or decreasing  $E$ . However, the relationships are not the same. The thick line represents the transition between mode I and mode II dominated flows, which is dictated by  $Ro_{I-II} = 5.3E^{0.35 \pm 0.4}$ . It is noted that the line has been fitted visually and that there exists a range of exponents of  $E$  that fit to the available data. That is, the exponent lies somewhere between 0.31 and 0.4. Interestingly, this range includes the  $1/3$  value, which may be related to the thin  $E^{1/3}$  Stewartson layer. This equation is a refinement to the relationship that was postulated in Vo *et al.* (2014), namely  $Ro_{I-II} = 5.44E^{0.35}$ .

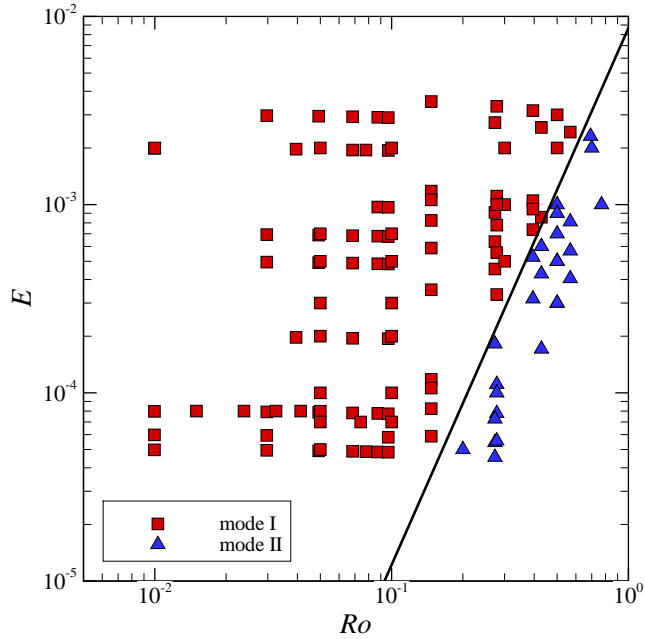


FIGURE 5.3: A regime diagram depicting the dominance of either the mode I ( $\square$ ) or mode II ( $\triangle$ ) linear instability. The thick line represents the transition line from mode I dominated flows to mode II dominated flows. The empirical relationship of the line is described by  $Ro_{I-II} = 5.3E^{0.35 \pm 0.4}$ .

It was established in § 4.3.4 that the mid-plane symmetry breaking of the axisymmetric base flow is likely related to the axial pumping induced by the Ekman layers and can be described by a constant  $Re_E$ . However, the presence of axial pumping also induces the  $E^{1/3}$  layer to complete meridional circulations. Hence, the two layers are related. Thus, from a physical point of view, as  $Ro$  is increased or  $E$  is decreased, the axial jets become stronger leading to the breaking of the reflective symmetry of the flow. Consequently, the secondary motions become stronger, which creates an unstable  $E^{1/3}$  Stewartson layer exhibiting linear growth rates larger than those associated with the  $E^{1/4}$  Stewartson layer. Therefore, this proposition suggests that the mode II instability is a manifestation of the thin Stewartson layer.

As it turns out, the onset of this instability dominance cannot be described by a Reynolds number based on a length scale of  $L = E^{1/3}H$ . Following the adaptation in defining  $Re$  as previously described in § 3.7.1.1 and § 4.3.4, this particular proposed Reynolds number can be defined as

$$Re_{E^{1/3}} = \frac{UL}{\nu} = \frac{2Ro}{E^{2/3}}. \quad (5.1)$$

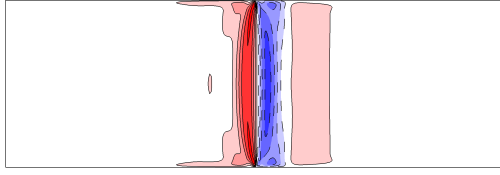


FIGURE 5.4: Contours of axial vorticity of the three-dimensional perturbation field of  $Ro = 0.05$  for  $E = 2 \times 10^{-4}$  depicted on the  $r$ - $z$  plane. The most unstable azimuthal wavenumber  $k = 6$  is shown here. Given the arbitrary scaling of linearised eigenvector fields, equi-spaced contour levels are plotted between  $\pm(|\omega_{z,\min}| + |\omega_{z,\max}|)/2$ . Dark (blue) and light (yellow) flooded contours represent negative and positive values, along with dashed and solid contour lines, respectively.

---

Thus, combining the threshold equation of  $Ro_{I-II} \propto E^{0.33}$  and equation 5.1 would not yield a constant. However, as stated earlier, the threshold represents the dominance of the linear instability modes and not their presence in the growth rate data (i.e. when mode II first arises despite having growth rates smaller than mode I). If the onset of the mode II instability is described by  $Ro_{II} \propto E^{2/3}$ , then this would suggest that this transition can be described by a constant  $Re_{E^{1/3}}$  and that the instability may be closely linked to the  $E^{1/3}$  Stewartson layer. The transition describing the first occurrences of the mode II instability remains unexplored due to the high computational cost required, which was beyond that available to this study.

### 5.1.1.2 Global instability mode shapes

The three-dimensional perturbation fields have also demonstrated axial invariance in the axial vorticity contours similar to its base flow counterpart for small- $Ro$  flows. Axial vorticity contours of the  $k_{\text{peak}} = 6$  perturbation associated with conditions of  $Ro = 0.05$  and  $E = 2 \times 10^{-4}$  are illustrated in figure 5.4. A pair of vertical vorticity strands are shown around  $r = 1$ , which extends throughout the depth of the flow. In the faster-rotating region ( $r < 1$ ), positive axial vorticity is generated, while negative axial vorticity is seen in the slower rotating region ( $r > 1$ ). It is also noted that the pair of vorticity strands is joined together closely all the way along the disk-tank interface. The pair is surrounded by weaker positive vorticity.

The joining of the positive and negative-vorticity strands is divided at higher- $Ro$  flows. An example of this is illustrated in figure 5.5, where a gap of fluid with an axial vorticity value similar to that of the surrounding flow is seen in between the pair

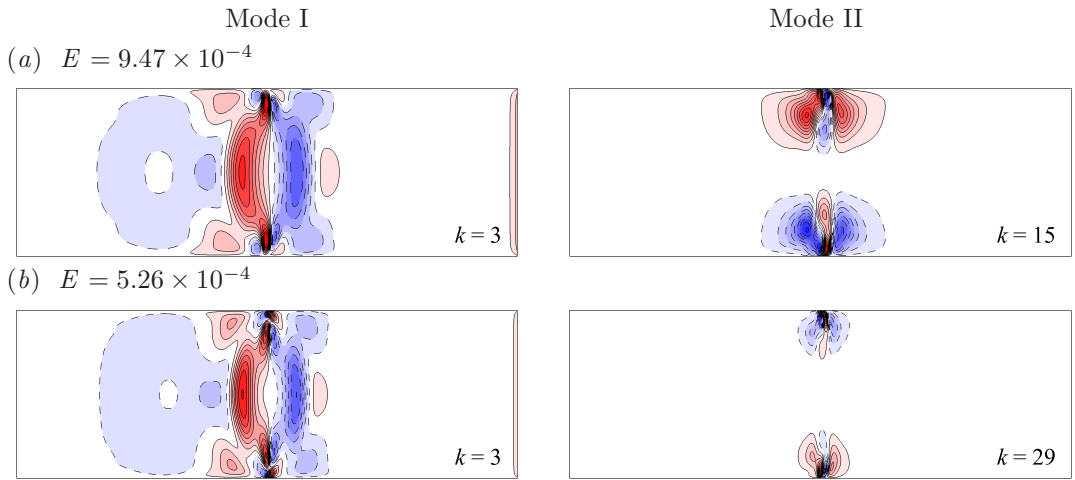


FIGURE 5.5: Contours of axial vorticity of the three-dimensional perturbation field of a given azimuthal wavenumber depicted on the  $r$ - $z$  plane. The left and right columns illustrate the most unstable wavenumber from mode I and II peaks, respectively. The perturbation fields are obtained at  $Ro = 0.395$  for (a)  $E = 9.47 \times 10^{-4}$  and (b)  $E = 5.26 \times 10^{-4}$ . Contour levels are as per figure 5.4.

---

of vorticity strands. Figure 5.5 presents the three-dimensional perturbation fields of mode I and II. Even when the base flow is no longer reflectively symmetric about the horizontal mid-plane, the unstable wavenumbers stemming from mode I still exhibit two strands of negative and positive perturbed vorticity. These strands encompass a region of positive axial vorticity, with the end of the strands connecting at the horizontal boundaries. Perturbation fields belonging to mode II display highly localised disturbances around the periphery of the ring. On each disk, a negative and positive-vorticity strand is sandwiched between contrasting vorticity patches. The strands do not extend into the interior to connect with the disturbances from the opposite disk. As such, the axial vorticity contours of mode II are not depth-independent. This is expected as the growth of the mode II instability only becomes apparent when the depth independence of the base flow is broken. The structures of the mode I and mode II instabilities do not differ significantly in these figures even though the flows are dominated by different instabilities. The similarity arises from the comparable growth rates between  $k_{\text{peak}}$  of modes I and II in figure 5.5(b).

When growth rates of wavenumbers from mode II are orders of magnitude greater than those of mode I, the structure of the perturbation field is altered. The perturbation fields are shown in figure 5.6. For the mode I waveband, the vorticity strands, which

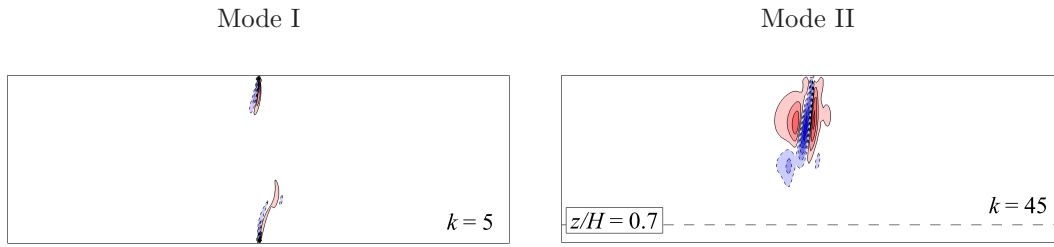


FIGURE 5.6: Contours of axial vorticity of the three-dimensional perturbation field of a given azimuthal wavenumber depicted on the  $r$ - $z$  plane. Perturbation fields of the most unstable wavenumbers from mode I (left) and mode II (right) for conditions of  $(Ro, E) = (0.273, 5.45 \times 10^{-5})$ . The mode II disturbances are localised at the top horizontal boundary, in this flow and only the domain of  $0.65 \leq r \leq 1.35$  and  $0.65 \leq z/H \leq 1$  is shown. The dashed line represents a depth level of  $z/H = 0.7$ . Contour levels are as per figure 5.4.

---

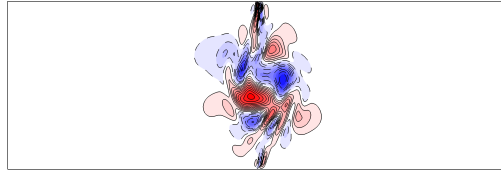


FIGURE 5.7: Contours of axial vorticity of the three-dimensional perturbation field of  $k = 9$  for  $Ro = 0.5$  and  $E = 3 \times 10^{-4}$ . The wavenumber 9 structure belongs to the mode III waveband as seen in figure 5.2. Contour levels are as per figure 5.4.

---

would otherwise extend over the entire depth, become truncated and extend diagonally into the interior. A similar trend is shown in the vorticity contours observed in the base flows (see figure 4.3(d)). However, a coupling of both positive and negative-vorticity strands stems from  $r = 1$ . For the mode II waveband, the instabilities are only encouraged to grow at the top disk-tank interface (note that mode II in figure 5.6 only represents a third of the flow depth). No structures are evident in the interior or bottom of the flow.

In the event of the mode III instability emerging and overtaking the mode I, axial vorticity in the perturbation field exhibits both signed vorticity strands arising at  $r = 1$  from the top and bottom boundaries, and extending all the way into the interior. However, the interior does not feature a clear depth-independent zone, instead adopting a complex structure comprising an amalgamation of negative and positive vorticity. An example of this is illustrated in figure 5.7.

A Floquet analysis has also been performed on a periodic flow case characterised by

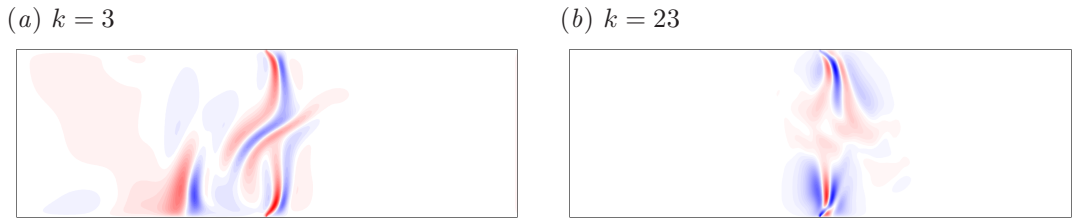


FIGURE 5.8: Contours of axial vorticity of the three-dimensional perturbation field of (a)  $k = 3$  and (b)  $k = 23$  for  $Ro = 0.924$  and  $E = 1 \times 10^{-3}$ . Contour levels are as per figure 5.4.

---

$Ro = 0.924$  and  $E = 1 \times 10^{-3}$ . This particular case reveals a wavenumber 3 structure being the most unstable in the first instability waveband (mode I). For steady-state flows, this waveband corresponds to a mode I instability. However, a different type of instability is expected for time-periodic flows, since the  $E^{1/4}$  Stewartson layer is seemingly broken, as is illustrated in the perturbation field shown in figure 5.8(a). The axial vorticity contours do not depict a pair of positive and negative vertical vorticity band about  $r = 1$ , rather the strands are broken about the mid-depth adopting a similar outline of the low vorticity strands originating at the disk-tank interface in the axisymmetric base flow (see figure 4.9). Thus, this type of instability is unlikely associated with the  $E^{1/4}$  Stewartson layer (mode I). A strong pair of opposing vorticity is evident at  $r \approx 0.66$  on the lower boundary, which is generated from a strong axial vorticity present at  $r \approx 0.66$  in the axisymmetric base flow (see figure 4.9). Additional wavebands similar to mode II and III are also evident at higher wavenumbers for this case, which exhibit greater growth rates. An illustration of the perturbation field from one of these other wavebands is shown in figure 5.8(b) for  $k = 23$ . The vorticity contours display alternating bands of vorticity at the disk-tank interface for both the upper and lower horizontal boundaries, similar to the mode II instability. However, the strands elongate further into the flow interior. Thus, time-periodic and steady-state axisymmetric base flows are unstable to different types of linear instabilities.

### 5.1.1.3 Visualising the linear instability modes on horizontal planes

In order to visualise the non-axisymmetric structure of the predicted linear instability modes, the leading eigenmodes are superimposed onto their respective axisymmetric base flow fields. Slices are then extracted in the  $r$ - $\theta$  plane for visualisation in a top-down sense. These slices do not depict the actual three-dimensional flow structure that would be observed in an experiment as nonlinear effects during the growth of the instability

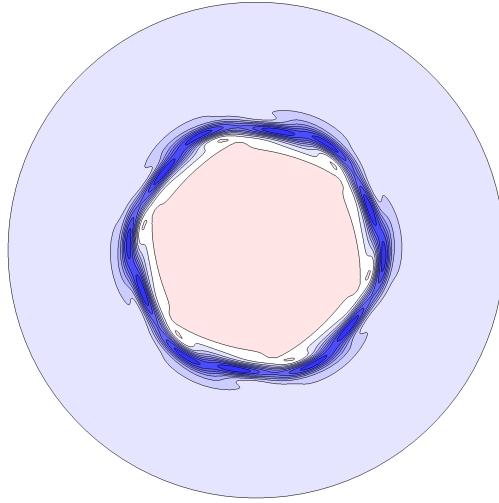


FIGURE 5.9: An  $r$ - $\theta$  slice taken at mid-depth in  $z$  is extracted from a linear axisymmetric flow approximation constructed by superposing the axisymmetric base flow and the leading instability mode with azimuthal wavenumber 6. This flow field is not representative of the three-dimensional non-axisymmetric flow since nonlinear effects are omitted here. The case shown had  $Ro = 0.05$  and  $E = 2 \times 10^{-4}$ . Contours of axial vorticity are plotted, with equispaced contour levels between  $2\bar{\Omega} \pm 10\omega$ . Blue and red contour shading represent low and high values, respectively, while solid and dashed contour lines identify positive and negative contour levels, respectively. The orientation is such that the positive  $Ro$  causes the central region to rotate *clockwise* faster than the outer region.

---

are bound to alter the flow structure. Rather, these fields demonstrate the type of distortions that these linear instabilities can induce on the axisymmetric base flow. Furthermore, it is stressed that only the leading instability eigenmode is superimposed onto the axisymmetric base state. In a real-case situation a growing perturbation is likely to include a combination of several eigenmodes. The base flow and most unstable perturbation field (shown in figure 5.4) of  $Ro = 0.05$  and  $E = 2 \times 10^{-4}$  have been superimposed to generate figure 5.9. This method gives a qualitative illustration of the azimuthal distortion incited by the instability, but because it does not capture nonlinear effects, the visualisation should not be mistaken for the actual three-dimensional modes that would be observed in practice. This flow condition has only the mode I linear instability associated with it (figure 5.1). The mode I instability exhibits an axial vorticity field which features a regular central polygon coupled with a strand of lower vorticity around the polygon border. The border is located approximately at the disk-tank interface. Here, the wavenumber 6 instability is represented by an

interior hexagon of high vorticity, which is surrounded by lower vorticity around the perimeter. This strand of lower vorticity is thin, with its borders forming a hexagonal shape. Outside of this hexagonal structure, there are intermediate levels of vorticity attributed from the rotation of the tank (base flow). A ring of satellite vorticity patches *in lieu* of a thin strand around the interior polygon is observed if the amplitude of the perturbation field is excessively large compared to the amplitude of the base flow prior to the superposition.

Several more resultant flows from superimposing the perturbation fields with their respective flows are shown in figure 5.10. The perturbation fields correspond to those illustrated in figure 5.5. For wavenumbers belonging to mode II, the central vortex is circular in shape and is surrounded by a ring of vorticity patches near the horizontal boundaries, where the number of vortices corresponds to the wavenumber of the instability. The mid-plane does not exhibit any noticeable disturbances. With increasing wavenumber, the size of the vortices decreases in order to fit into the circumference at  $r = 1$ .

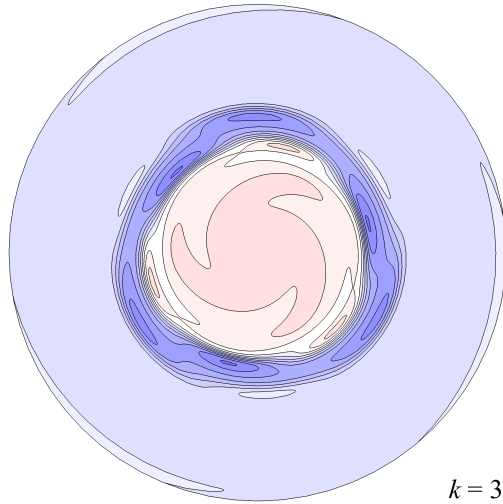
The leading instability wavenumber of the first unstable waveband for the time-periodic flow of  $Ro = 0.924$  and  $E = 1 \times 10^{-3}$  was determined to be  $k = 3$ . The perturbation field demonstrated features that differ to that of the mode I linear instability (figure 5.8). The results of superimposing the perturbation field onto its axisymmetric flow is reproduced in figure 5.11. A top-down view of the  $k = 3$  structure at mid-depth does not illustrate a triangular configuration, rather a circular structure with alternating rings of axial vorticity. Unlike a typical mode I instability, the resultant flow is not reflectively symmetric about the mid-depth and the axial vorticity contours do not demonstrate depth independence. The vertical structure of the resultant flow is depicted in figure 5.11(b). Since the contours of axial vorticity in the perturbation field closely follow the silhouette of the major structures in the axisymmetric base flow, the superposition of the two fields demonstrates features very similar to the axisymmetric base flow.

#### 5.1.1.4 Preferred azimuthal wavenumbers

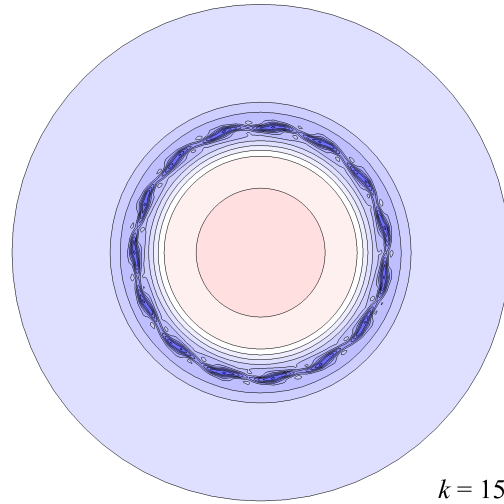
The most unstable wavenumbers for various  $Ro$  and  $E$  pairings have been mapped onto an  $Ro$ - $E$  regime diagram. The resultant regime diagram is shown in figure 5.12. Fractional peak wavenumbers and the corresponding peak growth rates were obtained

---

(a)  $E = 9.47 \times 10^{-4}$

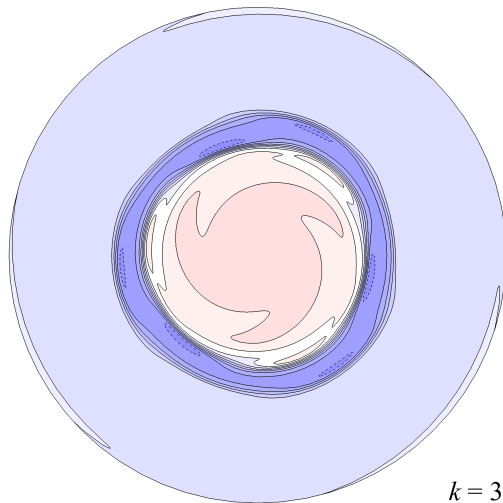


$k = 3$

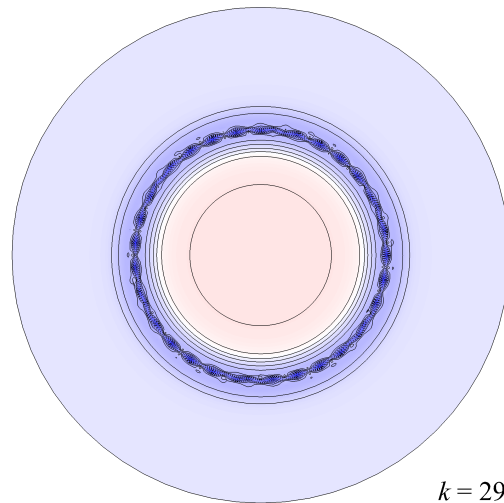


$k = 15$

(b)  $E = 5.26 \times 10^{-4}$



$k = 3$



$k = 29$

FIGURE 5.10: Slices of non-axisymmetric flows constructed by superposition of the base flow and the linear instability mode as per figure 5.9. These flow fields are not representative of the three-dimensional non-axisymmetric flow since nonlinear effects are omitted here. These cases show  $Ro = 0.395$  at Ekman numbers (a)  $E = 9.47 \times 10^{-4}$  and (b)  $E = 5.26 \times 10^{-4}$ . Left: the mode I instability is visualised on a slice extracted at mid-depth ( $z/H = 0.5$ ). Right: the mode II instability is shown at  $z/H = 0.85$  (near the top of the container). These cases correspond to the meridional semi-plane views of the perturbation fields from figure 5.5. Contour levels and the sense of rotation are as per figure 5.9.

---

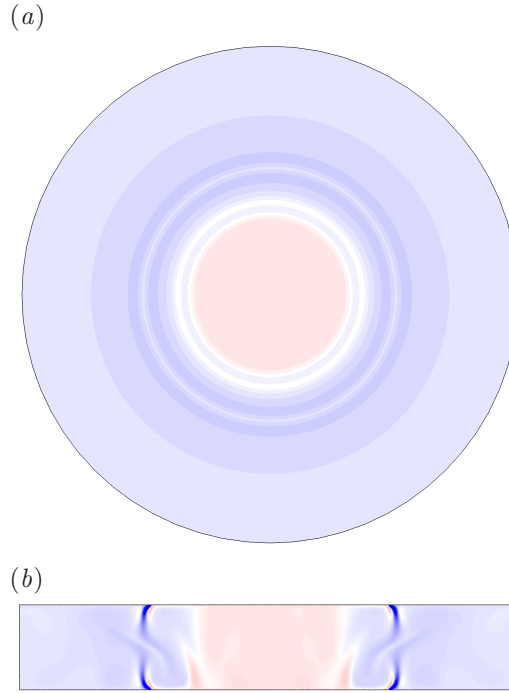


FIGURE 5.11: Flow case characterised by  $Ro = 0.924$  and  $E = 1 \times 10^{-3}$ . (a) An  $r$ - $\theta$  slice taken at mid-depth in  $z$  and (b) an  $r$ - $z$  extraction from a linear non-axisymmetric flow approximation constructed by superposing the axisymmetric base flow and the leading instability mode with azimuthal wavenumber 6. This flow field is not representative of the three-dimensional non-axisymmetric flow since nonlinear effects are omitted here. Contour levels and the sense of rotation are as per figure 5.9.

---

via the local maximum of a parabolic fitting of the peak and the adjacent wavenumbers from the  $\sigma$ - $k$  data obtained via a linear stability analysis. These data points were used to generate a contour map of preferred wavenumber for mode I over the  $Ro$ - $E$  space, allowing an accurate depiction of wavenumber segregation. As a result of using fractional peak wavenumbers, the wavenumber in the regime diagram represents a range of wavenumbers. For example, the contour band of 5 on the regime diagram represents the most unstable wavenumbers ranging from  $4.5 \leq k < 5.5$ . Only peak wavenumbers from the mode I instability have been used to construct this regime diagram, even if wavenumbers from other mode peaks have higher growth rates. The purpose of this is to illustrate the preferential wavenumbers attributed by the mode I instability (acting on the  $E^{1/4}$  Stewartson layer) for specific flow conditions as this instability is of interest in the context of polar vortex instability motivating this thesis. The map depicts a decrease in unstable wavenumber with increasing  $E$  at lower  $Ro$ . At higher  $Ro$ , the preferred wavenumber becomes independent of the Ekman number, with wavenumbers

decreasing with increasing  $Ro$ . These trends differ from those obtained experimentally. In Fröh & Read (1999), their experimental trends depict a stronger dependence on  $Ro$  compared to  $E$ . However, the experimental observations are of the saturated nonlinear flows, which are likely to differ in wavenumber from the linear predictions. The general trend is that either increasing  $Ro$  or decreasing  $E$  leads to a decreasing wavenumber state. These trends were also observed by Aguiar *et al.* (2010) using differential rings instead of disks.

The dominance of either a mode I or II for each flow has previously been mapped onto an  $Ro$ - $E$  parameter space (figure 5.3) with the transition represented by a thick-dashed line in figure 5.12. This transition is given by  $Ro_{I-II} = 5.3E^{0.35}$ . In addition, the “highly irregular” and “period-doubled” threshold flow regimes from Fröh & Read (1999) are overlaid on the regime diagram as black regions and a solid line, respectively. The overlap between the mode II instability found numerically and the time-dependent flows observed experimentally suggests that flows with a mode II dominance may be promoting this time dependence. Although the mode I-II threshold differs in exponent from the experimental non-modal flows, all of these flow regimes are seen to occur at higher  $Ro$  and lower  $E$ . In the same region of the parameter space, Aguiar *et al.* (2010) also found time-dependent flows which they denote as “chaotic” flows. Moreover, the transition from reflectively symmetric to symmetry-broken flows described by  $Ro_{c1-c2} \sim 13.35E^{0.5}$  is represented by a dotted line, beyond which encompasses the experimental time-dependent flow regimes. It is evident that this line and the  $Ro_{I-II}$  intersects at  $E \approx 2.1 \times 10^{-3}$ . This suggests that these relationships are only valid for a finite range of  $E$ .

The empirical relationship of the critical Rossby number as a function of Ekman number determined by Fröh & Read (1999) is given by  $|Ro_c| \approx 27E^{0.72}$ . This relationship was obtained using both positive and negative- $Ro$  data, as the experimental study found little differences between the positive and negative  $Ro_c$ . This similarity was predicted by the asymptotic analysis conducted by Busse (1968), who found that  $|Ro_c|$  scales with  $E^{3/4}$ . The numerical investigation here yields the threshold of stability to be  $Ro_c = 16.877E^{0.758}$  when considering positive- $Ro$  data only. The threshold equation is given by  $|Ro_c| = 18.11E^{0.767}$  when using both positive and negative- $Ro$  data. It should also be noted that the threshold obtained by Hide & Titman (1967) of  $|Ro_c| = 16.8E^{0.568}$  is shifted even further to the right with a differing slope (not shown



in the regime diagram).

There is a quantitative mismatch in the leading coefficient between the numerical result and the experimental empirical fit, although the exponent of  $E$  is in good agreement, both to the asymptotic result of  $3/4$  (Busse 1968) and to experimental results suggesting a  $0.72$  scaling. The higher coefficient causes a horizontal shift of the threshold line towards higher  $Ro$ , given that the exponent is similar. This can be seen in figure 5.12 between the solid line (numerical) and the dash-dotted line (experimental). The horizontal shifting to the right may be due to difficulty detecting instabilities at very small amplitudes due to limitations of the experimental measurements. This is revisited later in § 5.1.3 and § 6.2.2. Linear stability analysis is able to pinpoint the stability threshold via the growth rate but does not provide any information about the saturated amplitudes of the instabilities. However, the mode transition was experimentally determined to be supercritical (see Früh & Read (1999), Bergeron *et al.* (2000) and § 3.6), and therefore it is expected that the structures will be weak near to the onset of the stability threshold. The difference in coefficients causes a significant difference in the critical internal Reynolds number (equation 3.60).

To summarise, the differences in preferential wavenumber trends between numerical and laboratory results may be attributed to geometric differences, nonlinear effects, experimental observation and measurement techniques, and time dependence of flow states. The centre of the tank used in the laboratory contains a vertical rod used to drive the two horizontal disks. The addition of this rod may introduce perturbations into the flow that interact with the unstable shear layers and therefore alter the stability. Vortices were observed to shed from the central rod in simulations conducted by Früh & Nielsen (2003) and Bergeron *et al.* (2000). Nonlinear effects may also encourage competition between instability modes that cause the flow to undergo various wavenumber transitions. During this process, hysteresis effects are present, and therefore the resulting structure is highly dependent on the flow's history. In addition, the sharp changes in the contour lines of figure 5.12 are due to a number of factors, including the scatter of the data points used to construct the map and the method used to determine the peak wavenumbers. A quadratic fit to the three closest points to the local peak in the  $\sigma$ - $k$  data is used to determine the peak growth rate and wavenumbers. Preferential wavenumbers associated with mode I were obtained for more than 100 different positive- $Ro$  flow conditions, which is used to construct the positive  $Ro$ - $E$

regime diagram in figure 5.12.

## 5.1.2 Negative-Rossby-number regime

### 5.1.2.1 Growth rates

A stability analysis was conducted on negatively forced flows in a similar fashion to that conducted for the positive- $Ro$  regime. Many similarities were observed and will be briefly noted but emphasis will be placed on distinct features of the negative- $Ro$  regime that distinguish it from the positive- $Ro$  regime. Unstable wavenumbers ranging from 3 to 13 were observed for the range of  $Ro \geq -4.0$ . This implies that negative- $Ro$  flows are more sensitive to higher wavenumbers compared to positive- $Ro$  flows. In comparison, experimental observations obtained azimuthal wavenumbers ranging from 2 to 8 for  $Ro > -0.4$  (Früh & Read 1999).

As observed in the results of negative- $Ro$  base flows, a larger range of  $Ro$  demonstrates reflective symmetry about the horizontal mid-plane. Thus, it is expected that the mode I instability will dominate a large parameter space in this negative regime. Mode II is also expected to arise, as depth-dependent flows were observed for  $Ro < -1/A$ . Similar to the positive regime, the breaking of depth dependence is a function of both  $Ro$  and  $E$ . Thus, counter-rotating flows are not expected to become mode II dominant instantly at  $Ro = -1/A$ .

Growth rates for wavenumbers beyond the mode I branch illustrate a gradual decrease like that of positive- $Ro$  flows. These features are illustrated in figure 5.13 for two different  $Ro$  values. At a small  $Ro = -0.167$  and a large  $E = 4 \times 10^{-4}$ , the flow is linearly stable. As  $E$  decreases, the growth rates increase and the peak wavenumber shifts to higher wavenumbers as well as increasing the bandwidth of unstable wavenumbers. The shift in peak wavenumber with decreasing  $E$  is much more evident in the negative- $Ro$  regime compared to the positive- $Ro$  regime. As the base flows for the majority of the negative- $Ro$  regime explored do not break its depth independence, this mode peak is reflective of the mode I instability. This observation supports the hypothesis that the other mode peaks emerge due to the departure of highly vertical-independent motion. Growth rates of a higher-magnitude  $Ro = -1.46$  (relative to the positive- $Ro$  regime) shown in figure 5.13(b) exhibit only the mode I instability even for small  $E$ . The growth rates associated with  $k > 30$  have been obtained and exhibit a monotonic decrease with increasing wavenumber within the mode I waveband, although they are

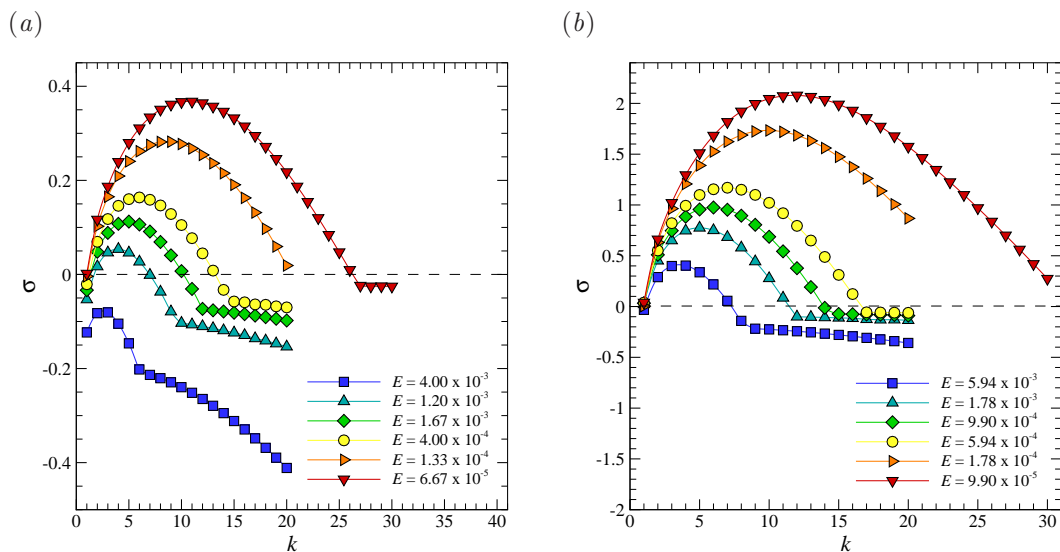


FIGURE 5.13: Growth rate  $\sigma$  as a function of wavenumber  $k$  for various  $E$  at (a)  $Ro = -0.167$  and (b)  $Ro = -1.46$ . A single maximum is seen for each  $E$  case. The dashed line represents neutral stability where points above and below symbolise unstable and stable modes, respectively.

not shown here.

Linear stability analysis results for a constant  $E = 2 \times 10^{-3}$  with varying  $Ro$  are illustrated in figure 5.14. Two maxima in the  $\sigma$ - $k$  data are evident. At small Rossby numbers, only mode I is present, which is consistent with previous findings in the positive- $Ro$  regime. For cases with  $Ro \leq -1/A$ , mode II appears and eventually dominates at sufficiently large  $|Ro|$ . This can be seen for  $Ro = -3.0$  and  $Ro = -4.0$ . Negative Rossby numbers with larger magnitude have not been investigated, so it is unknown whether additional instability modes exist (e.g. mode III).

### 5.1.2.2 Linear instability modes and visualisation on horizontal planes

An illustration of the perturbation field structure is shown in figure 5.15(a) for  $Ro = -0.167$  and  $E = 4 \times 10^{-4}$ , which was most unstable to a wavenumber  $k = 6$  (figure 5.13(a)). This flow condition only exhibits the mode I instability. The perturbations are largely vertical, with a pairing of positive and negative strands of vorticity. It should be noted that an  $r$ - $z$  plane at an arbitrary angle  $\theta$  is shown, and that may not represent flow structures at other azimuthal phase angles due to the non-axisymmetric mode structure. Further elucidation of the azimuthal mode structure is provided by superimposing this linear perturbation field onto the axisymmetric base flow (shown in

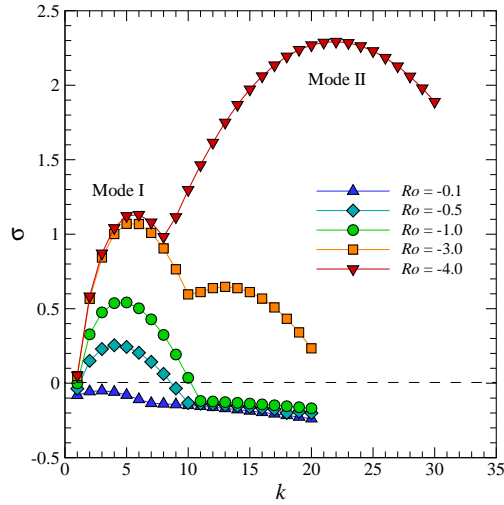


FIGURE 5.14: Growth rate  $\sigma$  as a function of wavenumber  $k$  for various  $Ro$  at (a)  $E = 2 \times 10^{-3}$ . Mode I and mode II branches are present. The dashed line represents neutral stability where points above and below symbolise unstable and stable modes, respectively.

figure 5.15(b)). Similar to figures 5.9 and 5.10, the purpose of this field is to demonstrate any flow alterations that occur as a result of the linear instability. A central hexagonal structure is present, surrounded by six closed contours of vorticity. The ring of vorticity containing the six vorticity patches contains the highest vorticity in the flow. The lowest vorticity is situated in the central region.

The instability structures of modes I and II differ between positive and negative- $Ro$  regimes. Contour plots of axial vorticity in the perturbation fields for  $Ro = -3.0$  and  $E = 2 \times 10^{-3}$  are shown in figure 5.16. For mode I, a pair of positive and negative vertical vorticity strands still exist and remain bonded (even for  $Ro = -4.0$ ). This is different from its positive counterpart, as a region of neutral vorticity grows between the strands with increasing  $Ro$  magnitude (figure 5.5). In addition to the vertical strands there are positive-vorticity strands angled towards the interior. The angle is similar to that observed in the base flow. The mode II structure also comprises of a pair of positive and negative vorticity, except that it does not extend the entire depth and is localised to the horizontal boundaries. This localisation was observed for positive- $Ro$  flows also. These strands are also angled in a similar nature to that of mode I and the base flow (figure 4.2(b)(ii)).

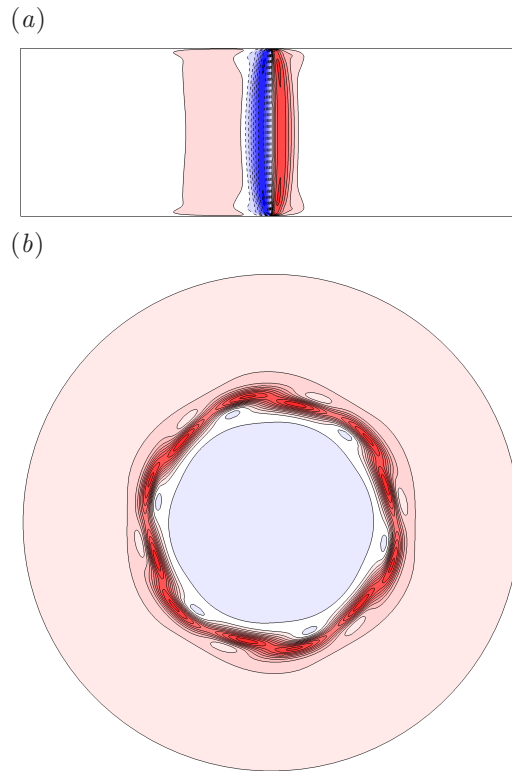


FIGURE 5.15: Axial vorticity contours of the dominant linear instability mode with azimuthal wavenumber  $k = 6$  at  $Ro = -0.167$  and  $E = 4 \times 10^{-4}$ . (a) The perturbation field of the instability mode is plotted in the  $r$ - $z$  plane, with contour levels as per figure 5.4. (b) A linear non-axisymmetric flow constructed by superposing the axisymmetric base flow and the azimuthal linear instability wavenumber as per figure 5.9. This flow field is not representative of the three-dimensional non-axisymmetric flow since nonlinear effects are omitted here. The slice shown was extracted at mid-depth, with contour levels as per figure 5.9, and the orientation is such that the negative  $Ro$  causes the central region to rotate *anti-clockwise* faster than the outer region.

---

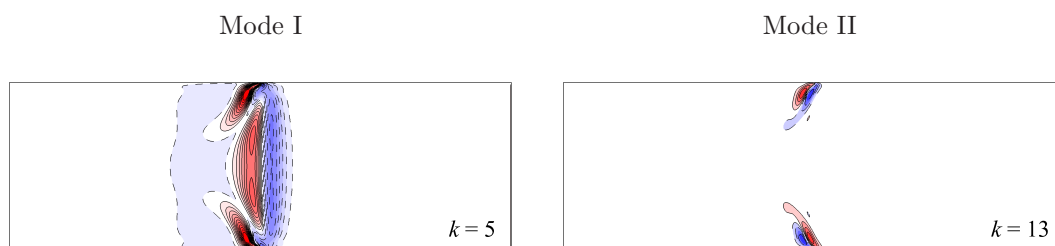


FIGURE 5.16: Contours of axial vorticity of the three-dimensional perturbation field of a given azimuthal wavenumber depicted on the  $r$ - $z$  plane. Perturbation fields of the most unstable wavenumbers from mode I (left) and mode II (right) for conditions of  $(Ro, E) = (-3.0, 2 \times 10^{-3})$ . Contour levels are as per figure 5.4.

---

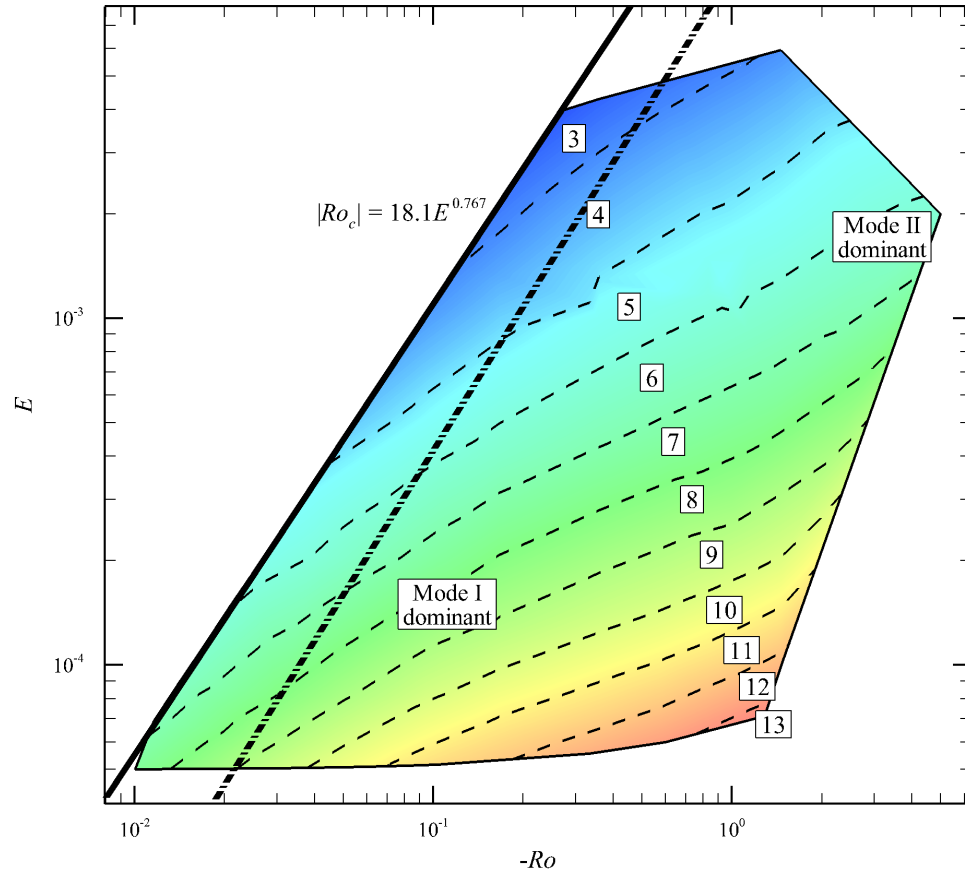


FIGURE 5.17: The same as figure 5.12 except for negative  $Ro$ .

### 5.1.2.3 Preferred azimuthal wavenumbers

Figure 5.17 shows the  $Ro$ - $E$  regime diagram of the linearly unstable azimuthal wavenumbers for negative  $Ro$ . Like figure 5.12, this diagram is also constructed only from mode I wavenumbers, even if a flow is predicted to be dominated by a mode II linear instability. The figure presents an overview of the linear stability results and suggests a decrease in unstable wavenumbers for decreasing  $Ro$  or increasing  $E$ . This is in contrast to the trend observed for the positive- $Ro$  regime, where the preferential wavenumber is dependent on both  $Ro$  and  $E$  in specific regions. In considering just the mode I dominant region, the negative and positive- $Ro$  regimes are comparable. The unstable azimuthal wavenumbers have a greater dependence on  $E$  rather than  $Ro$ , with no shift in parameter dependence.

Building upon the earlier assumption that mode II instabilities promote time-dep-

endent flows, this type of flow would not be observed unless the disks and tank were counter-rotating whereby Ekman pumping on the disks produce jets that may become unstable. However, experimental work by Früh & Read (1999) described irregular and period-doubled flows for flows with disks rotating slower than the tank (not shown in figure 5.17). Irregular flows were primarily located at very low values of  $E < 5 \times 10^{-5}$ . The flow conditions numerically investigated here do not cover this lower- $E$  space so no direct comparisons can be made. However, there are no signs in any of the  $\sigma$ - $k$  data obtained in this study to indicate the presence of other instability mode types. While the linear stability analysis conducted here implicitly considers only azimuthal Fourier modes, other instabilities such as Taylor vortices on the  $r$ - $z$  plane would be observable in the axisymmetric base flows. No indications of such structures were observed in the simulations reported, despite being seen experimentally (Früh & Read 1999). Preferential wavenumbers associated with mode I were obtained for more than 100 different negative- $Ro$  flow conditions from which the negative  $Ro$ - $E$  regime diagram was constructed.

Empirically fitting  $Ro$  and  $E$  data points corresponding to zero growth yields the relationship  $|Ro_c| = 19.8E^{0.777}$  for negative- $Ro$  data. Referring back to the asymptotic result of  $|Ro_c| \propto E^{3/4}$  and experimental result of  $|Ro_c| \propto E^{0.72}$ , the numerical relationship is quite similar. Again, the higher coefficient is due to the horizontal shifting of the threshold line towards higher  $Ro$  given that the exponent does not differ greatly. A possible explanation was given in the positive- $Ro$  results section (§ 5.1.1.4). Despite the difference in exponents of  $E$  for the instability threshold between positive and negative- $Ro$  regimes ( $Ro_c = 16.9E^{0.758}$  and  $|Ro_c| = 19.8E^{0.777}$ , respectively), the lines are indistinguishable on the log-log plot. Therefore, a stability threshold has been determined that uses both positive and negative- $Ro$  data. This concept is supported by experiments of Hide & Titman (1967) and Früh & Read (1999), which could not detect a difference in the onset of instability between positive and negative- $Ro$  flows. The threshold using both regimes is given by  $|Ro_c| = 18.1E^{0.767}$ . As can be seen in both regime diagrams (figures 5.12 & 5.17), this threshold line fits the positive and negative- $Ro$  data very well.

Study	$Re_{i,c}$	$Re_{i,c}/(Ro/E^{3/4})$	Critical $Ro/E^{3/4}$
Niino & Misawa (1984)	11.7	$1/\sqrt{2}$	16.5
van de Konijnenberg <i>et al.</i> (1999)	16.6	1	16.6
Früh & Read (1999)	10.9 (lowest point)	$1/\sqrt{2}$	15.4
Present study	$22.4 \pm 0.8$	$\sqrt{2}$	$15.8 \pm 0.57$

TABLE 5.1: Critical internal Reynolds numbers quoted by various studies, the factors by which each definition of  $Re_i$  differ, and the corresponding critical value of  $Ro/E^{3/4}$  found in each study.

### 5.1.3 The internal Reynolds number and characterisation of the preferred wavenumber regime diagrams

The internal Reynolds number is known to play an important role in characterising the stability of the Stewartson layers generated in this and similar previous studies (e.g. Niino & Misawa 1984; Früh & Read 1999). The various definitions of internal Reynolds number appearing in the literature share a common dependence between Rossby and Ekman number, namely  $Ro/E^{3/4}$ , differing only by constant factors arising from the choice of characteristic length and velocity scales (e.g. whether half or the full velocity differential across the shear layer, etc.). Unraveling the quoted critical internal Reynolds numbers from the literature shows a striking consistency. The theoretical analysis of Niino & Misawa (1984) yields a critical internal Reynolds number of 11.7, while from experiments, van de Konijnenberg *et al.* (1999) determined  $Re_{i,c} = 16.6$ . The line of best fit that Früh & Read (1999) employed to determine a critical internal Reynolds number yielded approximately 24, though their figure 8 demonstrates that they found unstable flows down to  $Re_i \approx 10.9$ . The linear stability analysis conducted in this study returns a critical internal Reynolds number of  $22.4 \pm 0.8$  across the considered range of Ekman numbers. However, dividing each of these values through by the respective prefactors to  $Ro/E^{3/4}$  employed in each definition of  $Re_i$  yields the critical values listed in table 5.1. As can be seen, these show a remarkable consistency across the analytical, experimental and numerical methods employed in the studies, all producing a critical threshold within the range  $15.4 \leq Ro/E^{3/4} \leq 16.6$ . Note that the difference between the critical  $Ro/E^{3/4} = 15.8$  and the coefficient of 18.1 in the  $Ro_c$  relationship (figure 5.12 & 5.17) is due to the difference in powers of Ekman number (namely  $E^{3/4}$  and  $E^{0.767}$  in the respective relations).

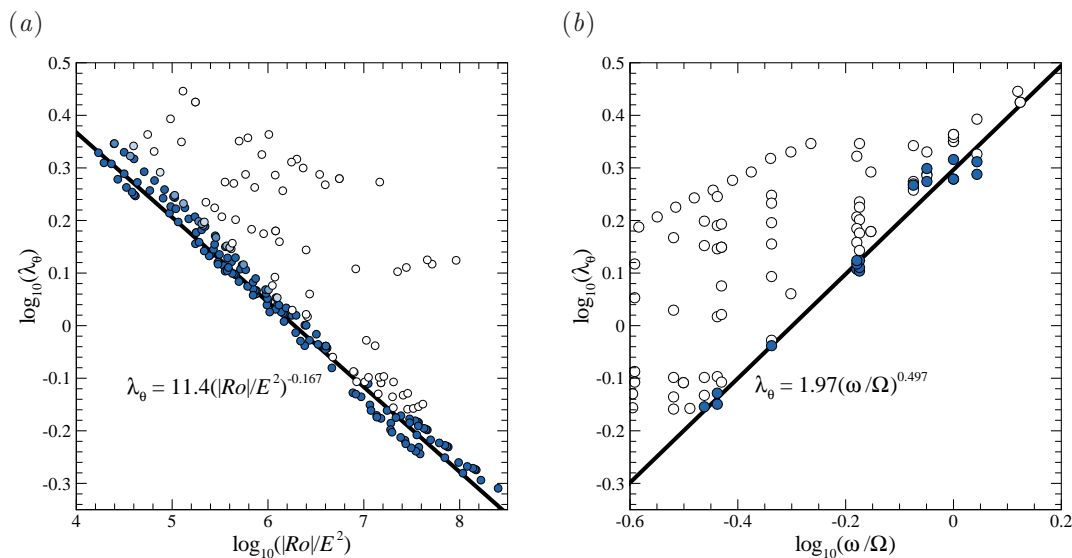


FIGURE 5.18: Regressions of the preferred azimuthal wavelength of the mode I instability. (a) Plot of the  $\log_{10}(\lambda_\theta)$  against  $\log_{10}(|Ro|/E^2)$ . The data are shaded by  $Re_i$ , with dark shading showing  $Re_i \lesssim 49$ . This captures the regime of axisymmetric flows that depict depth-independent axial vorticity contours, and a linear collapse of the data is seen. (b) Plot of  $\log_{10}(\lambda_\theta)$  against  $\log_{10}(\omega/\Omega)$ . Here dark shading identifies  $Re_i \gtrsim 194$ , which captures the regime of Ekman-number-independent instability wavelengths at large  $Ro$  and small  $E$ . The expressions obtained by least-squares power-law fitting to the data are included in each plot.

Revisiting figure 5.12 in the context of the importance of  $Re_i$  on the shear layer, it can be seen that the lines of constant preferred azimuthal wavenumber respond to changes in  $Re_i$ . For instance, the preferred wavenumbers exhibit a steady increase with increasing Reynolds number to  $Re_i \approx 49$ , beyond which the contours turn downwards. Eventually (beyond  $Re_i \gtrsim 194$ ), the lines of constant azimuthal wavenumber are approximately vertical, demonstrating that the stability of the flow (at least in terms of the dominant azimuthal wavenumbers of the instabilities) is independent of the Ekman number. Hence the flow can be divided into three regimes:  $Re_i \lesssim 49$  for reflectively symmetric flows;  $49 \lesssim Re_i \lesssim 194$ , representing a transitional zone; and  $Re_i \gtrsim 194$  an Ekman-number-independent regime. These are not precise threshold criteria; rather, they are determined approximately by inspection.

It turns out that the preferred wavenumbers obtained in the depth-independent positive- $Ro$  regime for  $Re_i \lesssim 49$  are consistent with those obtained in the negative- $Ro$  regime (i.e. figure 5.17) if the data are plotted against  $|Ro|$ . This motivated a search for a grouping of  $|Ro|$  and  $E$  that might universally collapse the data onto a single curve.

Recasting the preferred azimuthal wavenumbers  $k$  as azimuthal wavelengths  $\lambda_\theta = 2\pi/k$ , an optimisation procedure was used to maximise the correlation coefficient ( $r^2$ ) of a power-law fit to the data when plotted against  $|Ro|^\alpha E^\beta$ , where exponents  $\alpha$  and  $\beta$  were variables in the optimisation process. A highly optimal pair of exponents giving a correlation coefficient  $r^2 = 0.989$  was found to be  $\alpha = 1$  and  $\beta = -2$ . Using  $|Ro|/E^2$  as an independent variable, the universal power-law fit describing the preferred azimuthal wavelength of the mode I instability is given by

$$\lambda_\theta = 11.4 (|Ro|/E^2)^{-0.167}, \quad (5.2)$$

and this universal fit is plotted in figure 5.18(a). Interestingly, the exponent in this expression is almost precisely  $-1/6$ , which if substituted produces  $\lambda_\theta \sim E^{1/3}/|Ro|^{1/6}$  through a rearrangement of equation 5.2. Given the appearance of  $E^{1/3}$  in this expression, it is possible that the instability wavelength scales with the  $E^{1/3}$  Stewartson layer. This may have implications for the validity of quasi-geostrophic models of these flows, which do not capture the  $E^{1/3}$  layer. Results of the quasi-two-dimensional model are later described in Chapter 7.

In the Ekman-number-independent stability regime, the preferred azimuthal wavelengths vary only with Rossby number. Our analysis determined that a convenient universal collapse of the data in this regime could be obtained by adopting  $\omega/\Omega$  as the independent variable. The resulting best fit of a power-law relationship to the data with  $Re_i > 194$  was found to be

$$\lambda_\theta = 1.97 (\omega/\Omega)^{0.497}, \quad (5.3)$$

which is plotted in figure 5.18(b). This fit achieved a correlation coefficient of  $r^2 = 0.976$ . The 0.497 exponent is within 0.6% of the exponent describing a square-root relationship. Therefore, in this regime it is proposed that the preferred azimuthal wavelengths follow  $\lambda_\theta \sim \sqrt{\omega/\Omega}$ .

It is stressed that the relationships developed here for the preferred azimuthal wavelengths of the shear-layer instability are based on a linear stability analysis of the axisymmetric shear-layer solutions. It is expected that nonlinear effects will play a role in modifying the eventual azimuthal wavenumbers that would be seen in a physical experiment after the instability grows sufficiently to break into a ring of well-defined vortices (Früh & Read 1999; Aguiar 2008; Aguiar *et al.* 2010). A numerical investigation into nonlinear effects are discussed later in Chapter 6.

## 5.2 Varying the aspect ratio

The same analysis presented in the previous section has been performed here for other aspect ratios. The steady-state axisymmetric base flows provided very slight differences in the contour structure of the flow through  $1/6 \leq A \leq 2$  as described previously in § 4.3.1. This section highlights the differences in the linear stability of the flow by examining the growth rates over a wide range of azimuthal wavenumbers and therefore the most unstable wavenumber. The leading eigenvalues from the analysis are still described by complex conjugates which signify quasi-periodic instability modes.

### 5.2.1 Growth rates

The growth rates for a range of azimuthal wavenumbers have been determined via a linear stability analysis performed on steady-state axisymmetric base flows. In considering a single aspect ratio, the effect of varying the Rossby and Ekman number on the growth rate as a function of azimuthal wavenumber demonstrate the same trends observed for  $A = 2/3$ . That is, increasing the Rossby number invokes larger growth rates in the perturbations and causes a preference towards higher azimuthal wavenumbers. Plots of the growth rates as a function of wavenumber for  $A = 1/6$  with  $E = 7 \times 10^{-4}$  and varying  $Ro$ , and  $Ro = 0.1$  with varying  $E$ , are portrayed in figure 5.19. The peak wavenumbers for  $Ro = 0.05, 0.1, 0.2$  and  $0.3$  are determined to be  $k_{\text{peak}} = 12.6, 14.9, 15.7$  and  $14.7$ , respectively, for  $E = 7 \times 10^{-4}$ . Noticeably, there is a decrease in peak wavenumber from  $Ro = 0.2$  to  $0.3$ . It is proposed that this decrease may be due to the near-onset of symmetry-broken flow. The transition between reflectively symmetric and symmetry-broken flow occurs at  $Ro_{c1-c2} = 0.353$  for  $E = 7 \times 10^{-4}$  (see § 4.3.4). In the previous section which considered  $A = 2/3$ , the transition line was indicative of where the contour lines of preferred wavenumber becomes independent of the Ekman number. However, the transition to this Ekman-number-independent regime is not abrupt whereby the contour lines gradually become vertical prior to the  $Ro_{c1-c2}$  line. Thus, as  $Ro = 0.3$  is near the critical value of  $Ro_{c1-c2} = 0.353$ , it is suspected that the linear stability of the flow has started to become more dependent on the Rossby number. An example of this particular trend can be observed in figure 5.12 by moving horizontally at any constant Ekman number. Decreasing the Ekman number causes the flow to shift its linear stability preference towards higher azimuthal wavenumbers with increased growth rates, as was seen with  $A = 2/3$ .

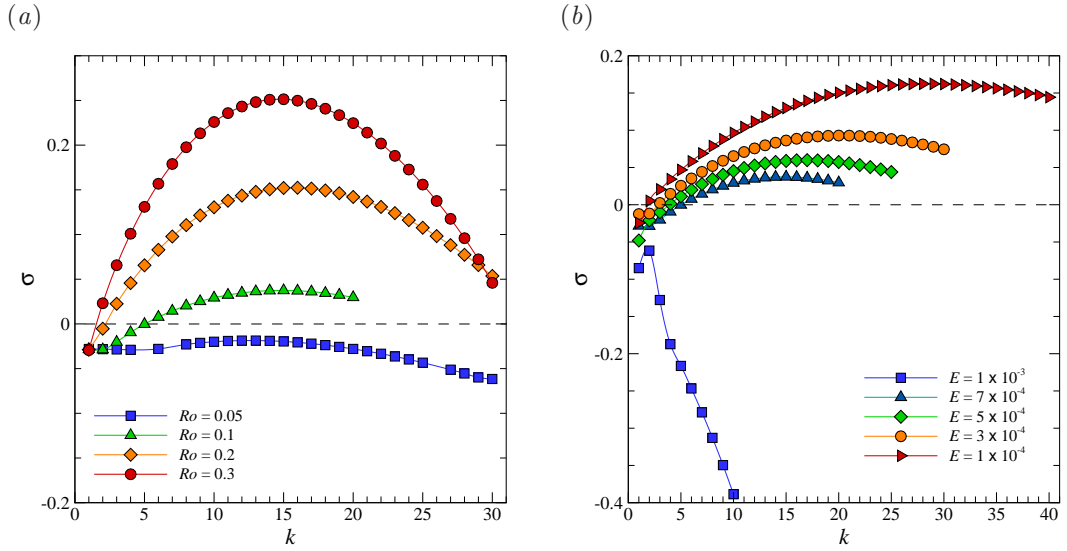


FIGURE 5.19: Growth rate  $\sigma$  as a function of azimuthal wavenumber  $k$  for  $A = 1/6$  and (a)  $E = 7 \times 10^{-4}$  for various  $Ro$  and (b)  $Ro = 0.1$  for various  $E$ . The dashed line represents neutral stability where points above and below symbolise unstable and stable modes, respectively.

Similarly, negative- $Ro$  flows display a parabolic-like profile in the growth rate data as a function of azimuthal wavenumber. A typical illustration of the data is shown in figure 5.20 for  $Ro = -1.0$ ,  $E = 7 \times 10^{-4}$  and  $A = 1/6$ . The shape of the profile suggests that the instabilities within the waveband shown are mode I. The same trends exist in that increasing the Rossby number magnitude yields an increase in both growth rate and the peak azimuthal wavenumber. Decreasing the Ekman number demonstrates the same behaviour.

Typical profiles of growth rates against wavenumber for various  $A$  are shown in figure 5.21(a), with flow conditions of  $Ro = 0.1$  and  $E = 7 \times 10^{-4}$ . The reference aspect ratio of  $A = 2/3$  described in the previous section demonstrates a single peak in the profile associated with the mode I instability, with a corresponding integer peak wavenumber of  $k_{\text{peak}} = 4$ . By decreasing  $A$ , the stability of the flow is seen to shift its preference towards higher azimuthal wavenumbers and the waveband of mode I increases. For  $A = 2/3$  this waveband ranges between  $1 \leq k \leq 9$  while for  $A = 1/3$ , this waveband ranges between  $1 \leq k \leq 18$ . For  $A = 1/6$ , a single local maxima in the profile is observed for  $k > 2$  with the integer peak wavenumber corresponding to  $k_{\text{peak}} = 15$ . The preceding wavenumbers  $k = 1$  and  $k = 2$  demonstrate a gradual

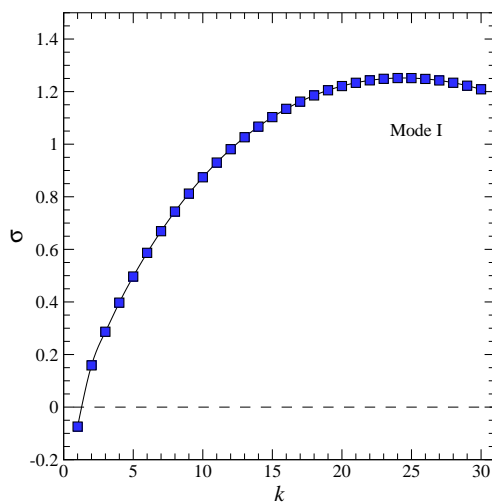


FIGURE 5.20: Growth rate  $\sigma$  as a function of azimuthal wavenumber  $k$  for  $Ro = -1.0$ ,  $E = 7 \times 10^{-4}$  and  $A = 1/6$ . The dashed line represents neutral stability where points above and below symbolise unstable and stable modes, respectively.

---

decrease that do not appear to be associated with the mode I waveband. A major difference in growth rate is also observed for the case of  $A = 2$ . Although it appears that the mode I profile is maintained and demonstrates an inclination towards low azimuthal wavenumber structures, the growth rates are smaller than those associated with  $A \leq 2/3$ . The growth rates portray a stable flow to all non-axisymmetric disturbances with the slowest decaying wavenumber characterised by  $k_{\text{peak}} = 2$ . The negative growth rates conveyed by all wavenumbers in this case demonstrates the increased stability of the flow, which is in agreement with what was expressed in § 4.3.2, namely a thicker shear layer produced by a larger  $A$  results in a more stable flow. Thus, increasing the aspect ratio decreases the observed azimuthal wavenumber, which is in agreement with the unpublished experiments of Dr. Luca Montabone who only observed oval shapes in large  $A$  containers. The trend of increasing  $A$  causing the flow to favour lower wavenumbers is seen not only for this flow condition but throughout the large parameter space covered. The profile of the growth rate data further suggests that the instability associated with the Stewartson layer is weak due to the reduction of the velocity gradients across the shear layer, as was observed in the radial profiles of axial vorticity (see figure 4.20).

The peak growth rates between  $A = 1/6$  and  $A = 2/3$  are comparable. In fact, the peak growth rates for cases of  $A \leq 2/3$  in figure 5.21(a) are similar. This suggests that

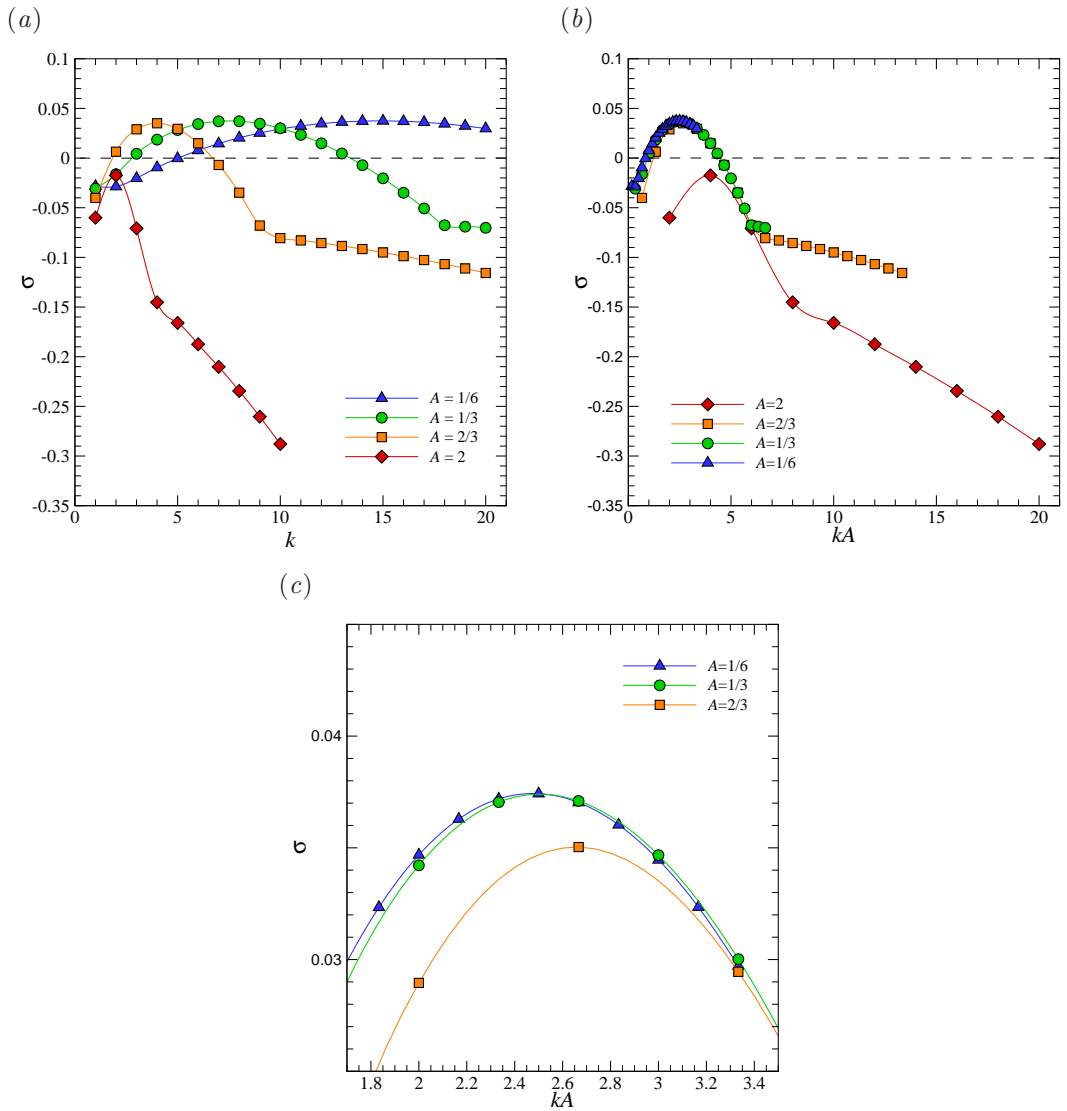


FIGURE 5.21: Growth rate  $\sigma$  as a function of (a) azimuthal wavenumber  $k$  and (b) scaled azimuthal wavenumber  $kA$ , for  $Ro = 0.1$  and  $E = 7 \times 10^{-4}$  for various aspect ratios. (c) A closeup of panel (b). The dashed line represents neutral stability where points above and below symbolise unstable and stable modes, respectively.

there is a maximum growth rate associated with a specific flow condition, for which aspect ratios under a particular threshold will exhibit. In other words, the stability of the shear layer corresponding to a particular flow is independent of the aspect ratio, provided that the shear layer is not greatly affected by the confinement. The theoretical shear-layer thickness  $\delta = (E/4)^{1/4}H$  suggests that the thickness is scaled with the enclosure height. If the dominant wavenumber scales with the thickness, then this suggests that the wavenumber can be rescaled by  $A$ , such that a universal collapse of

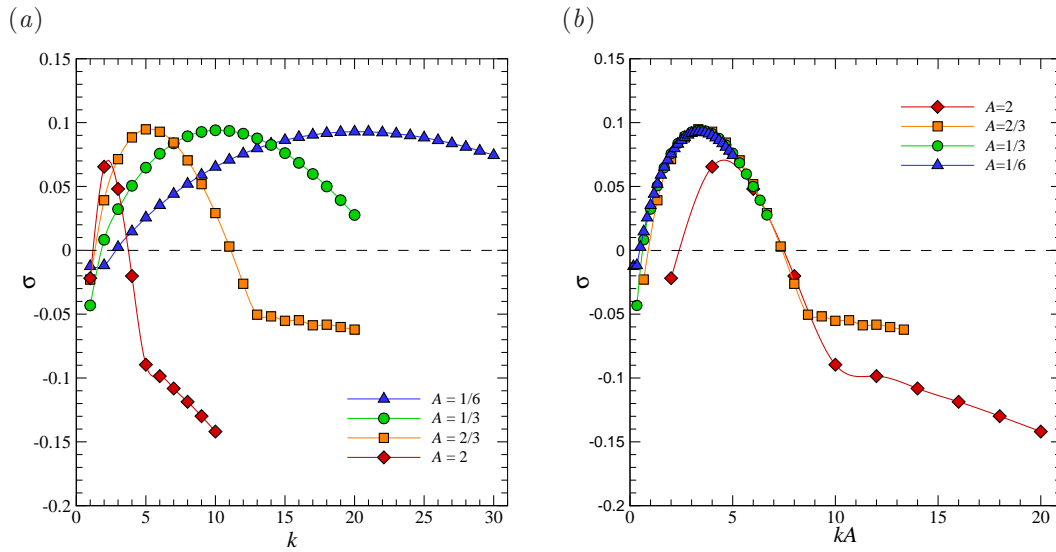


FIGURE 5.22: Growth rate  $\sigma$  as a function of (a) azimuthal wavenumber  $k$  and (b) scaled azimuthal wavenumber  $kA$ , for  $Ro = 0.1$  and  $E = 3 \times 10^{-4}$  for various aspect ratios. The dashed line represents neutral stability where points above and below symbolise unstable and stable modes, respectively.

the data is achieved for  $\sigma$  as a function of  $kA$ . This is illustrated in figure 5.21(b) with figure 5.21(c) providing a close-up image of the peak growth rates. The collapse for cases  $A \leq 2/3$  demonstrate strong agreement with each other. This can be explained by the similar profiles exhibited in the scaled axial vorticity throughout the shear layer, which is the unstable part of the flow (see figure 4.20). This also explains why the growth rate profile for  $A = 2$  does not conform with the lower aspect ratios since at this aspect ratio the  $E^{1/4}$  Stewartson layer is strongly affected by the confinement.

Another example of this universal collapse is demonstrated for  $Ro = 0.1$  and  $E = 3 \times 10^{-4}$  in figure 5.22. Again, the growth rates of the wavenumbers associated with the mode I instability in the  $A = 2$  container is lower and bounded by  $A \lesssim 2/3$  due to the Stewartson  $E^{1/4}$  layer being disrupted by the confining walls.

An axisymmetric base flow characterised by  $Ro = 0.3$  and  $E = 3 \times 10^{-4}$ , which describes a mode II instability of comparable growth rate to that of mode I instability is now considered. The axisymmetric base flow structure is reflectively symmetric for this case. The growth rates as a function of azimuthal wavenumber for this flow condition are illustrated in figure 5.23. Recall that the flows at  $A = 2$  demonstrated the existence of a  $E^{1/3}$  Stewartson layer in the thickness measurements (see figure 4.21).

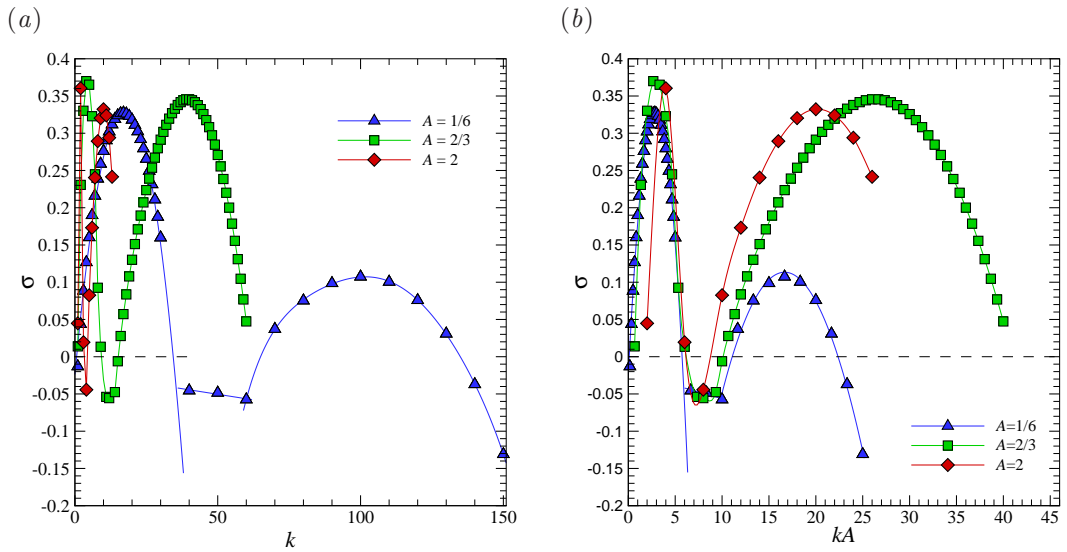


FIGURE 5.23: Growth rate  $\sigma$  as a function of (a) azimuthal wavenumber  $k$  and (b) scaled azimuthal wavenumber  $kA$ , for  $Ro = 0.3$  and  $E = 3 \times 10^{-4}$  for various aspect ratios. The dashed line represents neutral stability where points above and below symbolise unstable and stable modes, respectively.

Despite this, the growth rates associated with the mode II instability do not appear to follow the aspect ratio scaling. This is observed in figure 5.23(b) where the growth rates of wavenumbers from  $A = 2$  are no longer bound by the growth rates of  $A \lesssim 2/3$ . In fact, the growth rates of both the mode I and mode II structures in the larger container are now greater than those for  $A \lesssim 2/3$ . In addition, the maximum growth rates attributed from the mode I and mode II instability for  $A = 2/3$  and  $A = 1/6$  are no longer similar. Also, the scaled wavenumbers do not conform to each other. This difference is explained by the instability of the  $E^{1/3}$  layer and may be affected by the onset of symmetry-breaking flow, and therefore affecting the  $E^{1/4}$  Stewartson layer.

## 5.2.2 Linear instability modes and visualisation on horizontal planes

The three-dimensional perturbation fields of the most unstable wavenumber have been obtained through a linear stability analysis. A comparison between the leading eigenmodes for  $Ro = 0.1$  and  $E = 7 \times 10^{-4}$ , with  $A = 1/6$ ,  $2/3$  and  $2$  is portrayed in figure 5.24. The contours of axial vorticity for each  $A$  demonstrates a strong pair of opposing vorticity bands at the disk-tank interface, which is indicative of the mode I instability. This is not surprising since the growth rate data (figure 5.21) illustrates a single maxima that is representative of the mode I instability. Visually, there are slight

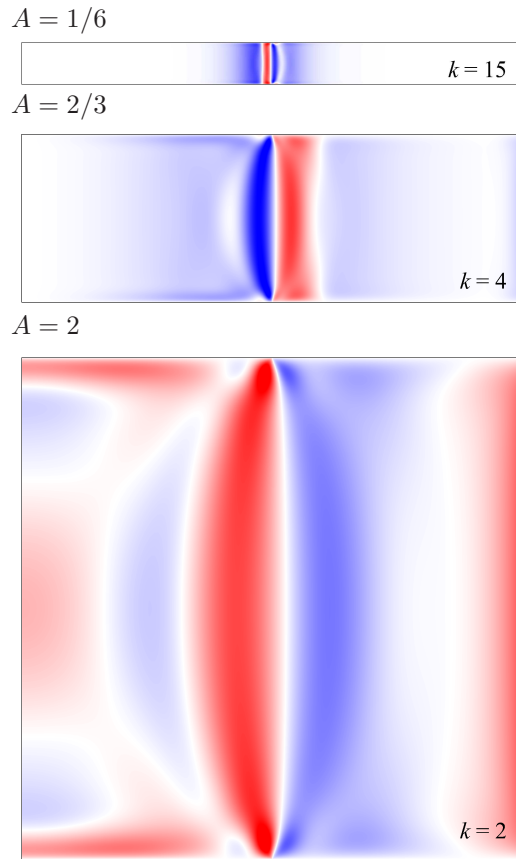


FIGURE 5.24: Contours of axial vorticity of the three-dimensional perturbation field of a given azimuthal wavenumber depicted on the semi-meridional  $r$ - $z$  plane for various aspect ratios. The flow conditions are of  $(Ro, E) = (0.1, 7 \times 10^{-4})$ . Contour levels are as per figure 5.4.

---

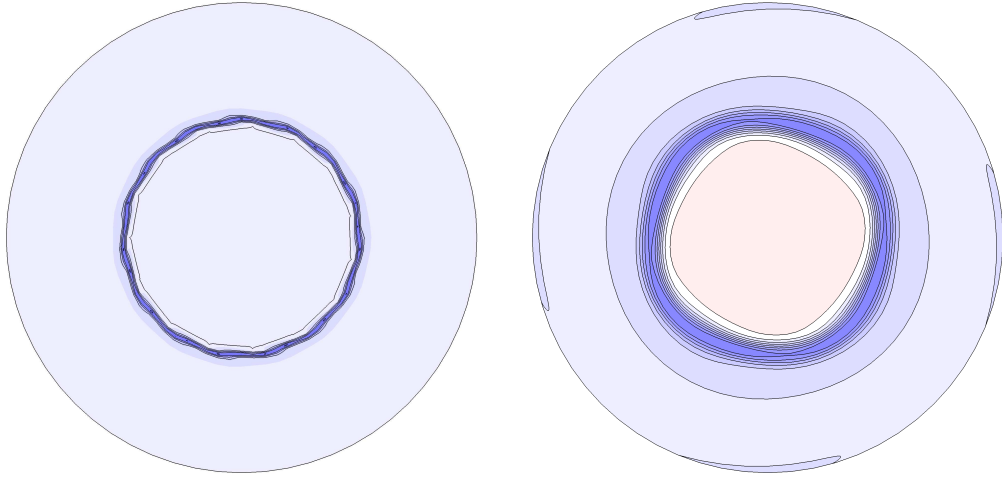
differences in  $A = 1/6$  and  $A = 2$  compared to the reference aspect ratio ( $A = 2/3$ ) in the region of  $r < 1$  which may be due to the azimuthal angle at which this  $r$ - $z$  plane is examined. In addition, the structure may be as a result of the weaker growth rates. Despite the visual differences in the structure, the contours also demonstrate that growth in the disturbances are more localised for lower  $A$ . Thus, the region that is susceptible to instability increases as  $A$  increases.

Recall that for a sufficiently small  $A$ , the smallest azimuthal wavenumbers do not appear to be a part of the mode I waveband. This is observed with  $k = 1$  for  $Ro = 0.1$  and  $E = 7 \times 10^{-4}$  with  $A = 1/6$  in figure 5.21. This particular wavenumber does not exhibit a pair of axial vorticity bands at  $r = 1$ , rather the growth and decay of perturbations are localised along the axis of rotation. The perturbation contours for  $k = 2$  exhibits growth throughout the entire domain while  $k = 3$  is localised at  $r = 1$ . Thus wavenumbers 1 and 2 are not associated with mode I, but perhaps may be closely

---

(a)  $A = 1/6, k = 15$

(b)  $A = 2/3, k = 4$



(c)  $A = 2, k = 2$

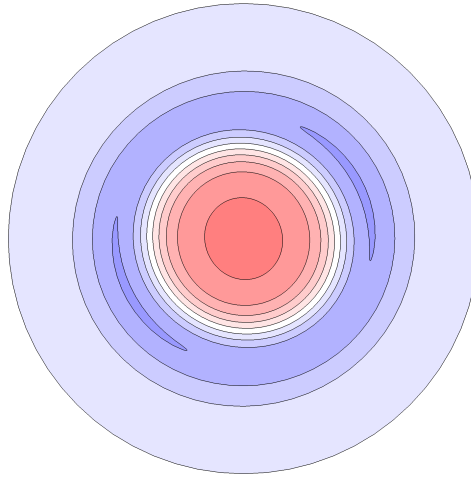


FIGURE 5.25: Linear non-axisymmetric flows constructed by superimposing the axisymmetric base flow and the most unstable azimuthal linear instability wavenumber, with flow conditions of  $Ro = 0.1$  and  $E = 7 \times 10^{-4}$ . The aspect ratios and corresponding peak wavenumber are described by (a)  $A = 1/6, k = 15$  and (b)  $A = 2/3, k = 4$  and (c)  $A = 2$  and  $k = 2$ . Contours levels as per figure 5.9.

---

related with the axisymmetric mode.

The perturbation field associated with the most unstable azimuthal wavenumber has been superimposed onto its respective base flow for visualisation purposes. The resultant contours of axial vorticity for cases in figure 5.24 are illustrated in figure 5.25. For each wavenumber associated with mode I, the flow demonstrates a polygonal configuration bordering  $r = 1$ . Similar to the structures obtained in  $A = 2/3$ , the ring of vorticity is comprised of very low vorticity surrounded by higher axial vorticity.

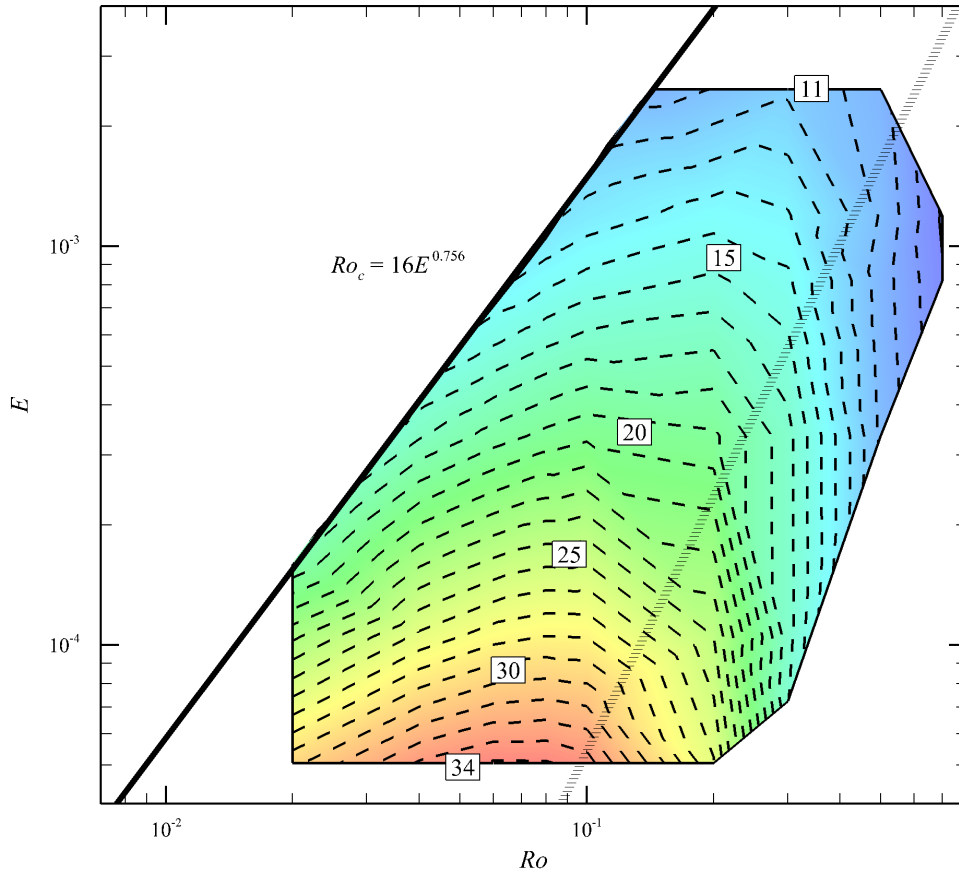


FIGURE 5.26: The same as figure 5.12 except for  $A = 1/6$ . The short-dashed lines represent the transition between one wavenumber and another, denoted by the wavenumber of the instability shown within the band. The azimuthal wavenumber of unlabelled contour bands can be determined by referencing a labelled contour band and incrementing by 1. The solid boundary lines represents the range of triangulation. The left thick boundary line represents the stability threshold, which is given by  $Ro_c \propto E^{0.756}$  (using positive data only). The dotted line represents the transition from reflectively symmetric flow to symmetry-broken flow, defined as  $Ro_{c1-c2} \sim 13.35E^{0.5}$ .

### 5.2.3 Preferred azimuthal wavenumbers

A regime diagram of the most unstable wavenumber as a function of both  $Ro$  and  $E$  has been generated for  $A = 1/6$  as shown in figure 5.26. A wide range of unstable azimuthal wavenumbers between  $7 \leq k \leq 35$  is seen throughout the computed parameter space. This range is much greater than those obtained for  $A = 2/3$  ( $2 \leq k \leq 9$ ). However, taking into consideration the aspect ratio, the scaled wavenumbers range between  $1 \leq kA \leq 6$  for both  $A = 1/6$  and  $A = 2/3$ . A pair of dashed lines encom-

passes a single azimuthal wavenumber that is denoted by a label. The increment in azimuthal wavenumber is 1 and therefore other wavenumbers can be determined from labelled contoured bands (e.g.  $k = 15, 20, 25 \dots$ ). In the low- $Ro$  regime, the preferred azimuthal wavenumbers increase with either increasing  $Ro$  or decreasing  $E$ , which is the same trend exhibited by the regime diagram for  $A = 2/3$  (figure 5.12). In addition, in the large- $Ro$  regime, the contours of preferred wavenumbers become largely independent of  $E$ . The contour lines become vertical approximately after the transition from reflectively symmetric flow to symmetry-broken flow, which is in itself independent of the aspect ratio. Thus, this feature is also exhibited for flows contained in the  $A = 2/3$  geometry.

The instability threshold for  $A = 1/6$  was determined to be  $Ro_c = 16E^{0.756}$ , which is comparable to that obtained for  $A = 2/3$  ( $Ro_c = 18.1E^{0.767}$ ). This is expected since the maximum growth rates associated with the mode I instability appeared to have no dependence on the aspect ratio (§ 5.2.1), provided the shear layer is not affected by the container walls. In fact, the cases of  $A = 1/6$  demonstrated slightly higher growth rates as compared to  $A = 2/3$ , which suggests that the  $E^{1/4}$  Stewartson layer is the most unstable in configurations of  $A \lesssim 2/3$ . Thus, the instability threshold of  $A = 1/6$  would be more representative of a pure  $E^{1/4}$  Stewartson layer becoming unstable. This explanation is reinforced by the exponent of  $E$  demonstrating an almost identical value to the theoretical prediction of  $3/4$ . This also explains the slight deviation of the Ekman number exponent from the theoretical  $3/4$  value and that predicted for  $A = 2/3$ . That is, the  $E^{1/4}$  Stewartson layer is slightly affected by the confinement in  $A = 2/3$  and therefore the instabilities are not able to grow to the maximum potential associated with the flow conditions (a pairing of  $Ro$  and  $E$ ). The instability threshold for  $A = 1/6$  corresponds to  $Re_{i,c} \approx 22.6$ , which importantly equates to a critical  $Ro/E^{3/4}$  of approximately 16. This critical value is the average value determined by prior studies (see table 5.1).

It was established that for a sufficiently small  $A$  ( $A \lesssim 2/3$ ), the growth rate data can be universally described by scaling the azimuthal wavenumber by  $A$ . Thus, a regime diagram of the scaled parameter  $kA$  can be produced as a function of  $Ro$  and  $E$ . This is illustrated in figure 5.27. The solid lines represent an integer value result of  $kA$  while the short-dashed lines represent the increments of 0.1 in  $kA$ . Therefore, this regime diagram is universal such that the linearly predicted azimuthal wavenumber can be

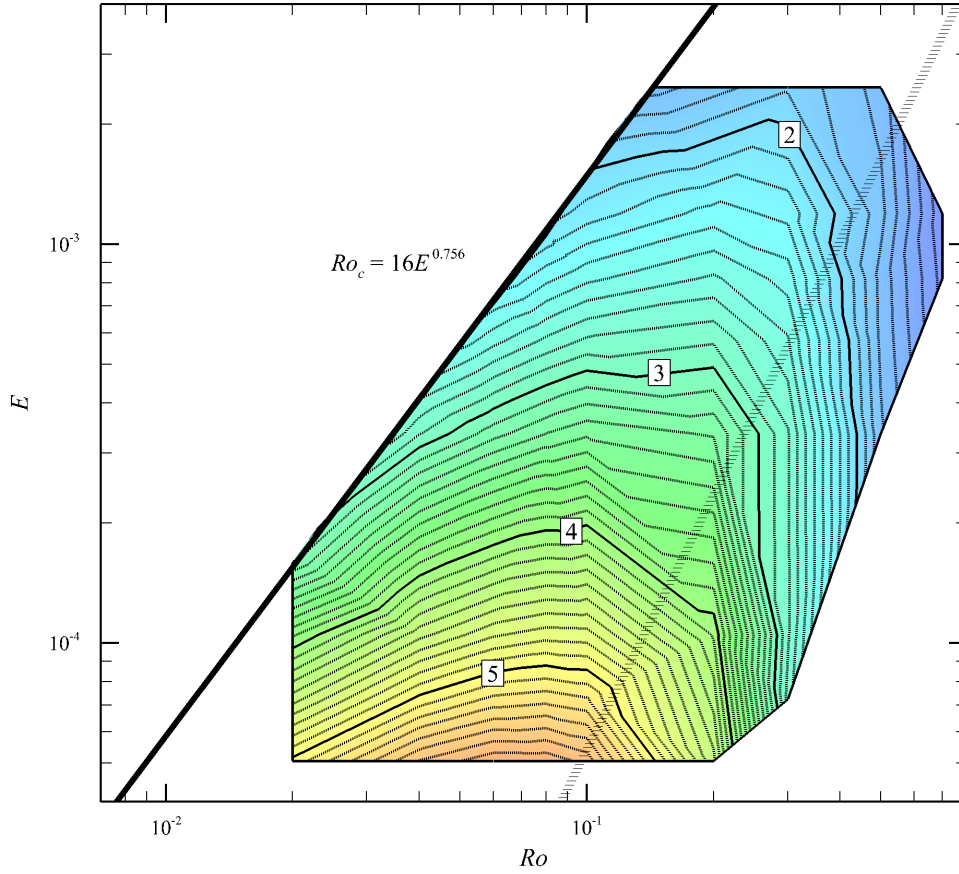


FIGURE 5.27: The same as figure 5.12 except  $kA$  is plotted instead of  $k$  generated from the  $A = 1/6$  data. This regime diagram is universal such that the linearly predicted azimuthal wavenumber can be determined by dividing the  $kA$  value by the aspect ratio considered. The solid lines denote an integer result of  $kA$  while the short-dashed lines represent a decimal value with increments of 0.1.

determined by dividing the value by the aspect ratio. That is, the regime diagram for  $A = 2/3$  as seen in figure 5.12 (and for any other aspect ratio  $A < 2/3$ ) can be reproduced by using figure 5.27 and multiplying the values by  $1/A$ .

A fit of the preferred azimuthal wavelengths ( $\lambda_\theta = 2\pi/k$ ) of the mode I instability as a function of  $Ro$  and  $E$  has been determined using the same optimisation process described in earlier in § 5.1.3. A power-law fit of the azimuthal wavelength against  $Ro^\alpha E^\beta$ , where  $\alpha = 1$  and  $\beta = -2$ , demonstrates the relationship

$$\lambda_\theta = 4.95 (Ro/E^2)^{-1/5}, \quad (5.4)$$

and is illustrated in figure 5.28. The shaded data represents cases described by  $Re_i \lesssim 49$ ,

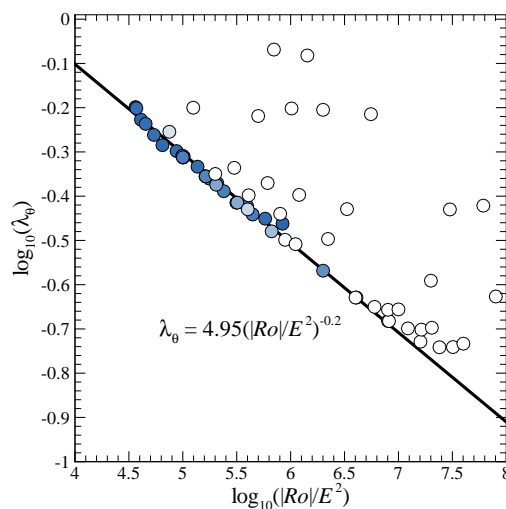


FIGURE 5.28: Regressions of the preferred azimuthal wavelength of the mode I instability for  $A = 1/6$ . Plot of the  $\log_{10}(\lambda_\theta)$  against  $\log_{10}(|Ro|/E^2)$ . The data are shaded by  $Re_i$ , with dark shading showing  $Re_i \lesssim 49$ . This captures the regime of axisymmetric flows that depict depth-independent axial vorticity contours, and a linear collapse of the data is seen. The expressions obtained by least-squares power-law fitting to the data are included in each plot.

which is the same range of values used in the earlier azimuthal wavelength analysis for  $A = 2/3$ . The wavelength relationship simplifies to  $\lambda_\theta \sim E^{2/5}/Ro^{1/5}$ , which differs to that obtained for the  $A = 2/3$  configuration, namely  $\lambda_\theta \sim E^{1/3}/Ro^{1/6}$ . This difference suggests that the  $1/3$  exponent observed for  $A = 2/3$  flows is not related to the  $E^{1/3}$  Stewartson layer. In addition, if the scaled azimuthal wavelength  $kA$  is instead used, the fitted relationship would only differ in the coefficient of  $Ro/E^2$  and not the exponent. However, it must be noted that only positive- $Ro$  data have been used in this analysis and the addition of negative- $Ro$  may affect the exponent of  $Ro/E^2$ . In fact, in considering only the positive- $Ro$  data for  $A = 2/3$  changes the exponent from  $-0.167$  to  $-0.178$ . Further discussion on the appearance of the  $1/3$  exponent in  $E$  relating to the quasi-two-dimensional model is presented later in § 7.3.4.

### 5.3 Linear stability of flow on a $\beta$ -plane

The axisymmetric base flow structures of the  $f$ -plane and the  $\beta$ -plane exhibited very little differences in their axisymmetric base flow structures. A linear stability analysis has been conducted to deduce the differences in their linear stability.

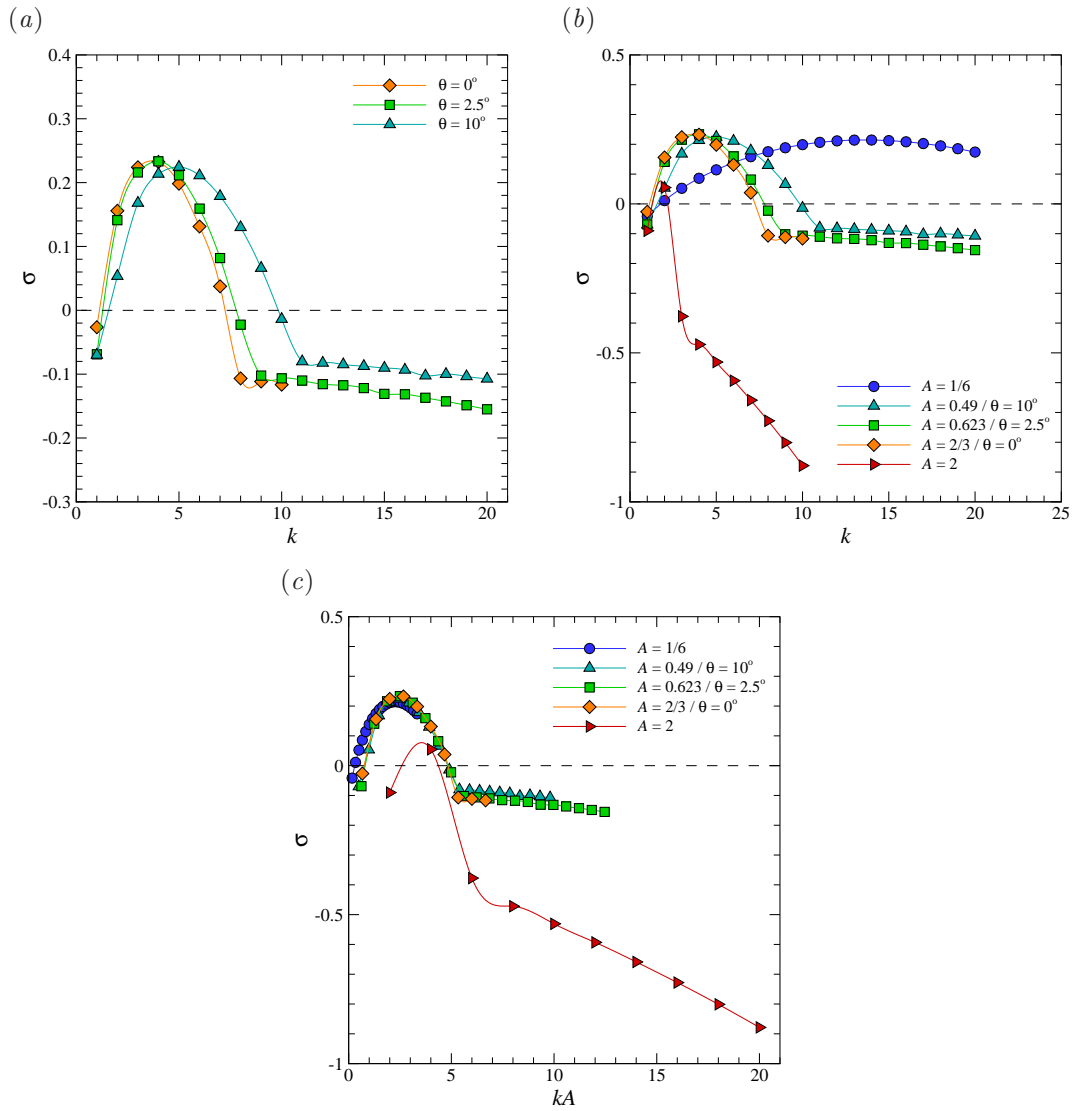


FIGURE 5.29: (a) Growth rate  $\sigma$  as a function of azimuthal wavenumber  $k$  for  $Ro = 0.3$  and  $E = 1 \times 10^{-3}$  for various angles of  $\theta$ . (b) The same plot as (a) except it is represented through the aspect ratio parameter with additional cases illustrated. (c) The growth rate data as a function of the scaled azimuthal wavenumber  $kA$ . The dashed line represents neutral stability where points above and below symbolise unstable and stable modes, respectively.

The growth rate against azimuthal wavenumber for  $Ro = 0.3$  and  $E = 1 \times 10^{-3}$  for various angles of  $\theta$  is demonstrated in figure 5.29(a). Minor differences in the growth rate magnitudes and the profile shapes are observed between the  $f$ -plane ( $\theta = 0^\circ$ ) and  $\theta = 2.5^\circ$ . Both cases illustrate a preference to an unstable wavenumber of  $k = 5$ . The flow shifts its preference to larger azimuthal wavenumbers as  $\theta$  increases while maintaining a similar peak growth rate magnitude. Thus, the trend of increasing  $\theta$  is the

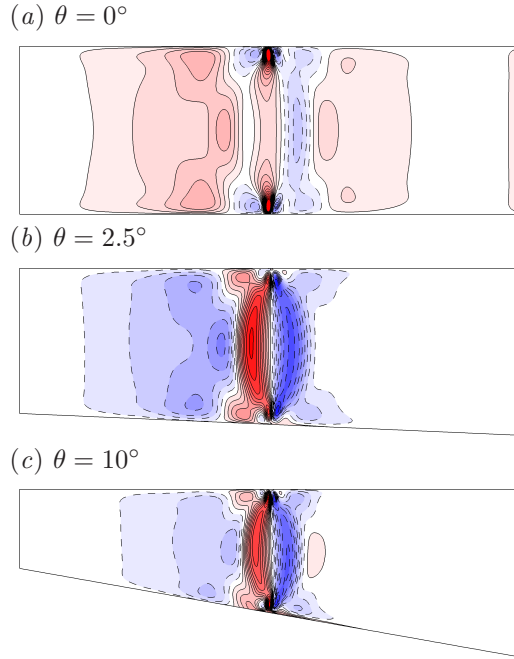


FIGURE 5.30: Contours of axial vorticity of the three-dimensional perturbation field of a given azimuthal wavenumber depicted on the semi-meridional  $r$ - $z$  plane for the (a)  $f$ -plane and (b, c)  $\beta$ -plane cases. The flow conditions are of  $(Ro, E) = (0.3, 1 \times 10^{-3})$ . Contour levels are as per figure 5.4.

---

same as that observed by decreasing  $A$  in § 5.2.1. Hence, the same plot of figure 5.29(a) has been reproduced in figure 5.29(b) as a function of the aspect ratio with additional cases to illustrate this trend more clearly. The aspect ratio is defined as the ratio of the disk radius to the depth of the fluid at the disk-tank interface ( $r = 1$ ), such that increasing  $\theta$  corresponds to decreasing  $A$  ( $H = 2/3 - R_d \tan \theta$ ). It is evident that the maximum growth rates between all of the cases except for  $A = 2$  are comparable, which eludes to the possibility that a universal relationship can be obtained by scaling the azimuthal wavenumber by the aspect ratio (as observed previously). The scaling for this set of data are shown in figure 5.29(c), which demonstrates strong agreement for  $A < 2/3$ . Thus, the growth rate data suggests that performing flows on a  $\beta$ -plane is equivalent to performing flows on an  $f$ -plane of an equivalent aspect ratio based on the radius of the disk and the height of the container at the disk-tank radius.

This suggestion is further reinforced by observing the perturbation fields both in isolation and with its superposition onto its respective axisymmetric base flow. The three-dimensional perturbation fields of the most unstable wavenumber for the various  $\beta$ -plane cases are shown in figure 5.30. The most prominent structure in the perturba-

---

(a)  $\theta = 2.5^\circ$ ,  $k = 4$

(b)  $\theta = 10^\circ$ ,  $k = 5$

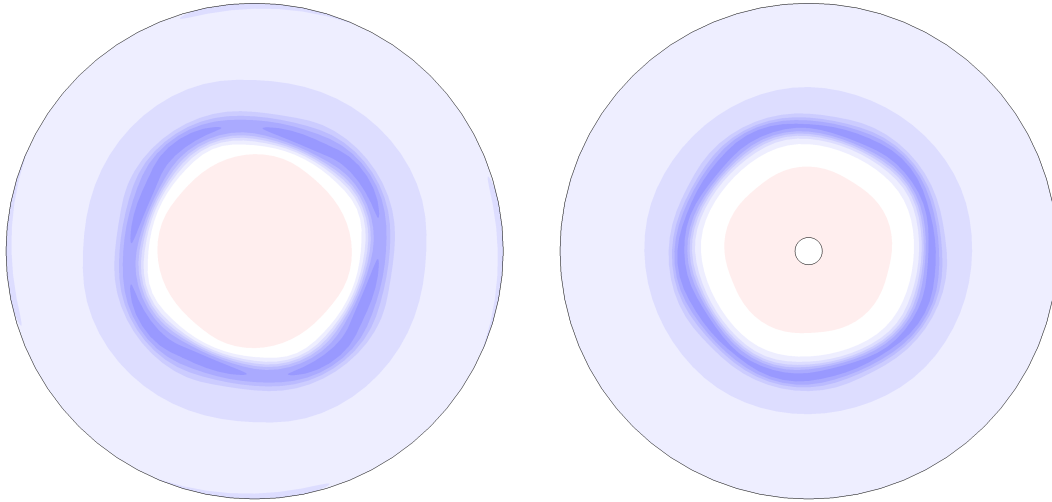


FIGURE 5.31: Linear non-axisymmetric flows constructed by superimposing the axisymmetric base flow and the most unstable azimuthal linear instability wavenumber, with flow conditions characterised by  $Ro = 0.3$  and  $E = 1 \times 10^{-3}$ . The  $\beta$ -plane configurations are (a)  $\theta = 2.5^\circ$  with  $k = 4$  and (b)  $\theta = 10^\circ$  with  $k = 5$ . The horizontal plane shown is at  $z = 1/3$  (equivalent to  $z/H = 0.5$  in the  $A = 2/3$   $f$ -plane case) with contour levels as per figure 5.9.

---

tion fields is the pair of vertical axial vorticity bands at the disk-tank interface, which is representative of a mode I instability mode. The contours of axial vorticity demonstrate depth independence except near the tank wall boundaries. The superposition of the perturbation fields onto their respective axisymmetric base flows are illustrated in figure 5.31. The horizontal planes have been extracted at mid-depth in relation to the sidewall tank height ( $z/H_{\text{tank}} = 0.5$ ). Thus the white solid circle at  $r = 0$  represents the conical extension attributed by the sloping bottom of the  $\beta$ -plane. The resulting structures portray a ring of vorticity arranged into a polygon at the periphery of the disk. This type of deformation was observed for flows on an  $f$ -plane and the structure does not change throughout the majority of the fluid depth. Since the amplitudes of the perturbation fields used are arbitrary, it is not possible to clarify whether or not the presence of the changing bottom topography causes the polygonal ring of vortices to become sharper as was observed by Aguiar *et al.* (2010).

## 5.4 Summary

The reflective symmetry breaking of the axisymmetric base flow was seen to affect the nature of its linear stability. For base flows illustrating depth-dependent and/or

reflective symmetric features, a single mode peak was present that is associated with the mode I instability. When superimposed onto the base flow, the leading unstable wavenumber for mode I demonstrated vorticity-forming polygonal structures such as triangles, pentagons and hexagons. The combination of several instability modes and nonlinear effects are likely to alter such linear patterns in real-world cases. A second and third mode peak were also observed at large  $Ro$  and small  $E$ ; the same conditions where symmetry-broken flow is observed. Modes II and III exhibited highly localised and irregular instabilities, respectively, which are atypical of the depth independence exhibited by the mode I instability. These instability modes also favored higher wavenumbers. A compilation of the results corresponding to mode I were used to construct  $Ro$ - $E$  regime diagrams.

The empirical relationship of the stability threshold for negative and positive- $Ro$  flows with  $A = 2/3$  was obtained. Both were in good agreement with the asymptotic predicted exponents obtained by Busse (1968) and little differences were observed between the threshold of positive and negative- $Ro$  flows. Consequently, the exponent for the relationship between  $|Ro|$  and  $E$  correspond to a constant  $|Re_i|$ . Although the stability of the flow can be described by  $|Re_{i,c}|$  alone, the prediction of the preferential wavenumber requires both  $|Ro|$  and  $E$  to be known. An empirical fit of the preferential azimuthal wavenumber as functions of  $(|Ro|/E^2)$  and  $(\omega/\Omega)$  have been determined for depth-independent ( $Re_i \lesssim 49$ ) and depth-dependent flows ( $Re_i \gtrsim 194$ ), respectively.

In comparison to the stability threshold obtained by Fröh & Read (1999), similarities were observed in the exponent with differences seen in the leading coefficient. This is caused by the stability onset occurring at higher  $Ro$  values, and therefore at higher  $Re_i$ . This dissimilarity may be explained by experimental observation limitations. In addition, the discrepancy observed between the values of  $Re_{i,c}$  determined in previous literature and this study is due to the different length and velocity scales used. Compensating for these differences, consistent threshold values of  $15.4 \lesssim Ro/E^{3/4} \lesssim 16.6$  are found across the theoretical, laboratory and numerical studies of Niino & Misawa (1984), van de Konijnenberg *et al.* (1999), Fröh & Read (1999) and the present simulations. The  $Ro$ - $E$  regime diagrams depict a different trend to those obtained experimentally by Fröh & Read (1999) and Aguiar *et al.* (2010). The primary reason for the differences in trends may be explained by the nonlinearity associated with these experimental flows.

The linear stability analysis results for other aspect ratios revealed that beyond a certain  $A$ , the Stewartson  $E^{1/4}$  layer becomes weaker and shifts its preference towards low azimuthal wavenumbers. In contrast, given a sufficiently small  $A$  whereby the Stewartson layer is unhindered by the confining walls, the growth rates demonstrate the same maximum. As such, the threshold of instability was determined to be  $Ro_c \propto E^{0.756}$  for  $A = 1/6$ , which is comparable to that obtained for  $A = 2/3$  ( $Ro_c \propto E^{0.767}$ ). However, a difference of results is seen in the corresponding peak azimuthal wavenumber. That is, decreasing  $A$  causes a more unstable azimuthal wavenumber to develop. Though it was determined that the data can be universally scaled by the aspect ratio. Growth rates associated with flows on a  $\beta$ -plane also adopt this universal scaling as the effect of increasing  $\theta$  demonstrated similar trends to that attributed by decreasing  $A$ . The resulting structures from this type of instability are polygonal rings of vortices, representative of the mode I instability. Thus, from a linear stability standpoint, flows on a  $\beta$ -plane are identical to flows on a  $f$ -plane given that the aspect ratios are equivalent.

The next chapter is devoted to the study of nonlinear shear-layer instability and comparisons to the linear stability results presented in this chapter.

## Chapter 6

# Non-axisymmetric flow in a differential-disk rotating system

With guidance from the linear stability analysis results presented in the previous chapter (Chapter 5), three-dimensional direct numerical simulations have been performed at various flow conditions throughout the positive- $Ro$  regime for the  $A = 2/3$  enclosure. These specific flow conditions have been selected to demonstrate the three-dimensional behaviour that manifests at parameters where the axisymmetric base flows are dominated either by the mode I or mode II linear instability. That is, flows which exhibit instability modes that are either reflectively symmetric about the mid-depth or localised near the bottom or top of the shear layer at the disk-tank interface. The selected flow conditions also serve to demonstrate nonlinear mode evolution and interactions. It is predicted that nonlinear effects become significant when flow conditions are forced well beyond the onset of instability. Thus, a flow case near the stability threshold is explored initially in § 6.1, which acts as reference case for this chapter. Flows conditions well beyond the instability onset are achieved by either increasing  $Ro$  or decreasing  $E$ , and this is investigated in § 6.2. This is followed by examining the effect of varying the Rossby number in the large and small-Ekman-number regimes, as presented in § 6.3. The sensitivity to initial conditions and hysteresis effects are explored in § 6.4 with results of a bifurcation analysis presented in § 6.5.

The threshold of instability has been determined previously in § 5.1.1.4 to be  $Ro_c = 18.1E^{0.767}$  from a linear stability analysis for  $A = 2/3$ . Figure 6.1 is a reproduction of the regime diagram of the linearly preferred azimuthal wavenumber as a function of  $Ro$  and  $E$  (figure 5.12), with additional symbols marking the referenced flow conditions investigated in this chapter. The shapes and colours of the symbols are grouped into

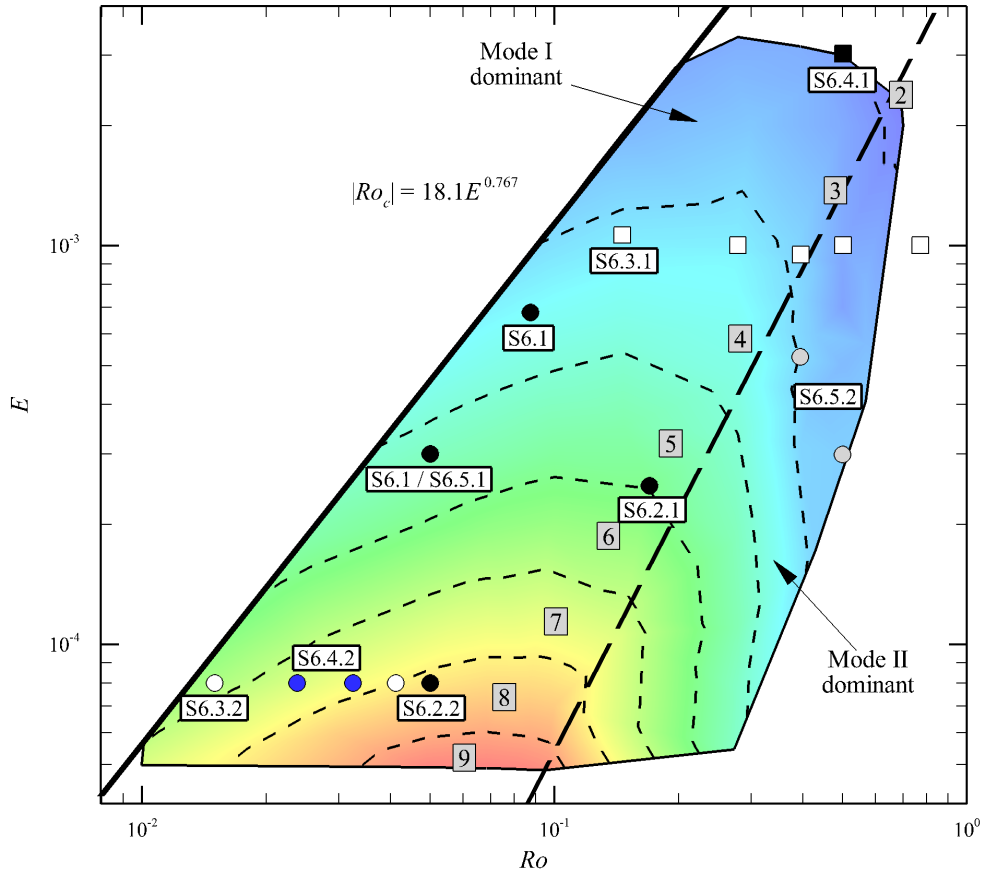


FIGURE 6.1: A regime diagram of the preferred linear wavenumber in the positive  $Ro$ - $E$  parameter space. The numerical labels on the diagram represent the unstable linear wavenumber associated with the mode I instability. Similar shaped data points and colours are generally grouped as part of a specific section which are represented by the labels  $Sx$ , where  $x$  denotes the relevant section. The long dashed line represents  $Re_E = 26.7$ . A transitional regime exists between  $26.7 \leq Re_E < 56.4$  where both reflectively symmetric and symmetry-broken flow are exhibited.

their respective sections. The thick dashed line represents the transition from base flows that are reflectively symmetric about the horizontal mid-plane and those that are not, defined by  $Re_E = 26.7$ . The reflective symmetry is important as it corresponds to flows that possess a strong depth independence of azimuthal velocity and axial vorticity through the interior of the tank. However, there exists a transitional regime ( $26.7 \leq Re_E < 56.4$ ) that encompasses both reflectively symmetric and symmetry-broken flows. Thus, flow conditions just beyond  $Re_E = 26.7$  are not certain to be reflectively symmetric about the horizontal mid-plane.

## 6.1 In the vicinity of instability onset

A flow having a moderate Ekman number and a small Rossby number described by  $(Ro, E) = (0.05, 3 \times 10^{-4})$  is investigated. For this particular  $E$ , the linear stability analysis predicts a critical Rossby number of  $Ro_c = 0.036$ . Hence, this condition is near the onset of linear instability and will be taken as the reference flow condition used for comparison throughout this chapter. Additionally, the internal Reynolds number is given by  $Re_i \approx 31$  ( $Re_{i,c} \approx 22.4$ ). Firstly, three-dimensional direct numerical simulation results at this reference flow case are presented in this section. The following sections describe two cases characterised by an increase in  $Ro$  and a decrease in  $E$  to this reference case, respectively. These flow conditions are marked by solid black circles in figure 6.1. It is expected that flow conditions in the vicinity of instability will be relatively weak, and would then be well-predicted by linear stability analysis. This is supported by experimental evidence that the instability bifurcation is supercritical (Früh & Read 1999; van de Konijnenberg *et al.* 1999; Bergeron *et al.* 2000). In contrast, flow conditions sufficiently far from the instability onset are expected to be altered by nonlinear effects, and therefore the resulting wavenumber may shift from the linearly predicted wavenumber.

For  $Ro = 0.05$  and  $E = 3 \times 10^{-4}$ , the most unstable wavenumber is predicted to be  $k = 5$  according to the linear stability analysis. The linear growth rates as a function of wavenumber and the axial vorticity contours for  $k = 5$  are illustrated in figure 6.2. The axial vorticity contours are only a depiction of the linear instabilities which have been arbitrarily amplified to finite amplitudes. Since  $k = 5$  is associated with the mode I waveband, the structure of the mode is reflectively symmetric about the mid-depth. Thus, the structure has a pentagonal appearance that extends throughout the depth of the tank.

A three-dimensional direct numerical simulation has been performed for the same flow conditions ( $Ro = 0.05$  and  $E = 3 \times 10^{-4}$ ). This simulation is initialised from the steady-state axisymmetric base flow solution seeded with white noise. This technique has been described in § 3.5. For this simulation, 24 Fourier modes have been used in the construction of the three-dimensional flow to ensure sufficient spatial resolution. Typically, increasing  $Re_i$  requires additional Fourier modes to accurately capture the small scale structures present, which has also been described in § 3.7.3. Implementing additional Fourier modes demonstrates no changes to the observed structure as larger

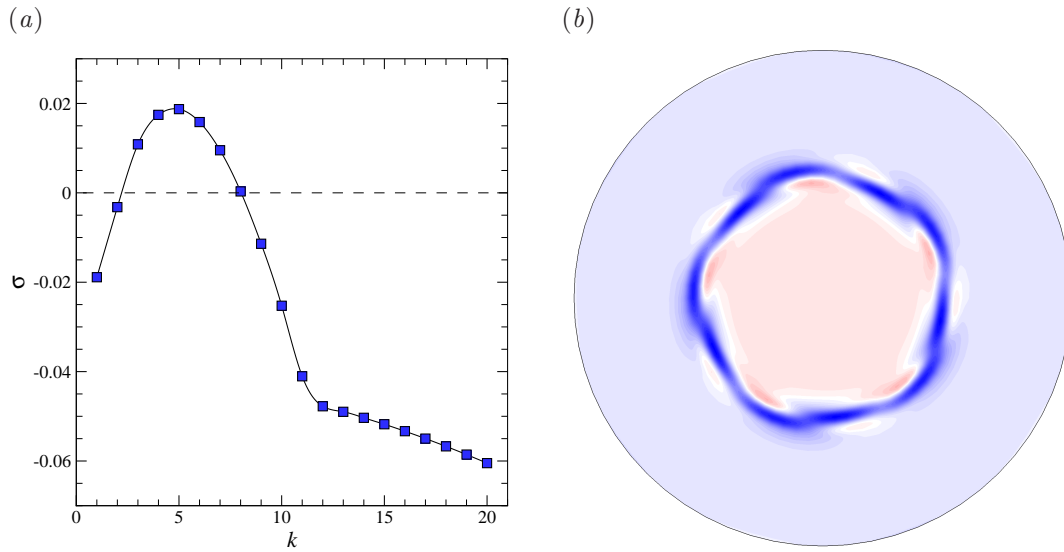


FIGURE 6.2: (a) The growth rates for a range of wavenumbers obtained through linear stability analysis for a flow condition of  $Ro = 0.05$  and  $E = 3 \times 10^{-4}$ . The dashed line represents neutral stability where points above and below symbolise unstable and stable wavenumbers, respectively. (b) Representative axial vorticity contours of linear instabilities of finite amplitude superimposed onto its respective base flow shown at  $z/H = 0.5$ . Nonlinear effects have been neglected. Contours of axial vorticity are plotted, with equi-spaced contour levels between  $2\bar{\Omega} \pm 10\omega$ . Blue and red contour shading represent low and high values, respectively, while solid and dashed contour lines identify positive and negative contour levels, respectively. The orientation is such that the positive  $Ro$  causes the central region to rotate *clockwise* faster than the outer region.

---

wavenumbers are effectively harmonics of the developing flow exhibiting lower energies. The purpose of the white noise is to add energy into all of the non-zero azimuthal Fourier modes to accelerate the development of any instabilities in the flow. In the linear regime at long times, wavelengths that are unstable will increase in energy over time while stable wavelengths will lose its energy. However, it is also possible that non-modal transient effects may briefly grow a linearly stable Fourier mode when nonlinear effects are considered (Blackburn *et al.* 2008). A time sequence of mode evolution from the initial white noise seeding is shown in figure 6.3 with contours of axial vorticity plotted on the horizontal mid-plane of the three-dimensional domain. The energies in the non-zero wavenumber structures are very small compared to the energy contained in the base flow during the initial developments. Thus, viewing the entire flow solution will only reveal an axisymmetric flow. Hence, axial vorticity contours of the perturbation field are shown in isolation. That is, the fundamental mode (zeroth azimuthal

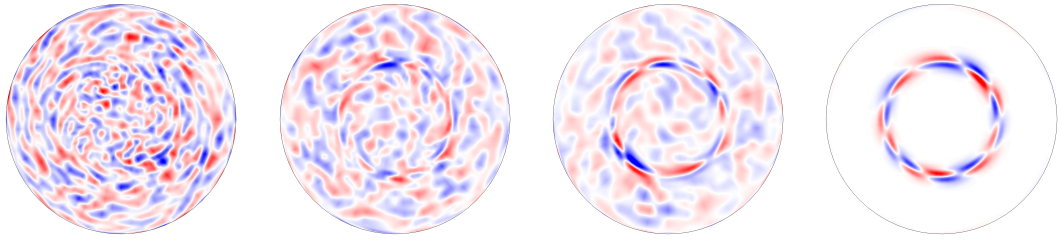


FIGURE 6.3: A flow condition of  $Ro = 0.05$  and  $E = 3 \times 10^{-4}$ . Time evolution of axial vorticity of the perturbation field alone. The initial base flow is seeded with white noise which eventually evolves into a wavenumber 5 structure. From left to right, the snapshots of axial vorticity are taken at  $t = 10, 20, 30$  and  $100$ . Equi-spaced contour levels are plotted between  $\pm(|\omega_{z,\min}| + |\omega_{z,\max}|)/2$ . Blue and red flooded contours represent negative and positive values, along with dashed and solid contour lines, respectively.

---

wavenumber) has been subtracted from the full flow solution. As expected, the flow portrays a chaotic appearance near the start of the simulation ( $t = 0$ ) since noise is distributed randomly across all Fourier modes in the simulation. As the flow evolves, the dominant instability emerges, developing into a sinusoidal structure concentrated at a radial position consistent with the disk edge. The eventual instability forms a wavenumber 5 structure which is seen at  $t = 100$ . This is in agreement with the prediction from the linear stability analysis. Since the instability adopts a sinusoidal form, a pairing of positive and negative vorticity represents a single wavelength of the disturbance. Hence, the frame at  $t = 100$  illustrates two disturbance rings representative of a wavenumber 5 structure.

For three-dimensional flows that involve modal interactions, measurements of modal parameters are typically used as an indicator in demonstrating the most dominant mode in time. Examples of modal parameters include the kinetic energy (e.g. Henderson 1997; Lopez & Marques 2011), the amplitude (e.g. Sheard *et al.* 2003; Carmo *et al.* 2010) and the enstrophy (e.g. Bergeron *et al.* 2000; Fröh & Nielsen 2003) in each Fourier mode. Here, the kinetic energy measure is adopted. The energy contained in each azimuthal wavenumber over time for  $Ro = 0.05$  and  $E = 3 \times 10^{-4}$  is displayed in figure 6.4. The zeroth wavenumber is omitted in all energy plots since changes to the axisymmetric mode energy are small in comparison to its absolute value. Indeed, the zeroth wavenumber contains the highest energy in the flow due to the large azimuthal velocities arising from the tank rotation. Initially there is a rapid energy decrease due to the decay of the white noise belonging to stable wavenumbers. Then unstable wavelengths

are seen to gain energy at an exponential rate in the linear regime ( $t \lesssim 450$ ). As the modes grow in amplitude, nonlinear effects become significant and the exponential growth of the wavelengths becomes inhibited with the dominant wavelength usually expressing saturation. It is seen that  $k = 5$  is dominant in the linear regime and remains stable as the dominant wavenumber throughout the nonlinear regime. Harmonics of the dominant wavenumber are also seen to plateau after sufficient time. Non-harmonic wavenumbers are seen to decay at varying rates with each demonstrating particular oscillations. In fact, the oscillations appear to be shared by a group of wavenumbers. That is, a wavenumber belonging to a particular group illustrates oscillations in energy over time that are synchronised with the other wavenumbers belonging to the same group. For example, wavenumbers 3, 8, 13, 18 and 23 all demonstrate the same energy frequencies over time, as is seen in figure 6.4(b). Similarly, wavenumbers 4, 9, 14 and 19 illustrate similar oscillations amongst each other. Thus, wavenumbers  $k + k_{\text{peak}}n$  share similar oscillations in their energy over time data, where  $k_{\text{peak}}$  represents the dominant wavenumber at a particular time,  $n$  is an integer ( $n \geq 0$ ) and  $k$  is an integer azimuthal wavenumber ( $1 \leq k \leq k_{\text{peak}}$ ). This relationship can be explained by the most dominant wavenumber imposing its symmetry onto all other wavelength structures. The hierarchy of these wavenumbers in terms of the energy is typically described by the lowest wavenumber containing the highest energy which then cascades down to higher-wavenumber structures.

On the horizontal plane at saturation of the instability mode, contours of axial vorticity display a pentagon-shaped interior of high vorticity that is bordered by a ring of lower vorticity. This is portrayed in figure 6.5(a) at two different heights,  $z/H = 0.1$  and  $z/H = 0.5$ . Consistent with the underlying axisymmetric base flow solution, the flow is reflectively symmetric about  $z/H = 0.5$ . The ring of lower vorticity surrounding the inner pentagon also outlines the shape of a pentagon. This vortical structure extends throughout the entire depth with little variability except in the vicinity of the horizontal boundaries (figure 6.5(b)). From a top-down view, the structure precesses clockwise while the wave oscillates about  $r = 1$ . This nonlinear flow structure is very similar to that predicted by the linear stability analysis (figure 6.2(b)). Thus, the expectation that nonlinear effects would have little effect in the vicinity of the stability threshold is supported. In addition, the velocity and vorticity flow contours in the  $r$ - $z$  plane illustrate very similar features to those obtained via the axisymmetric model.

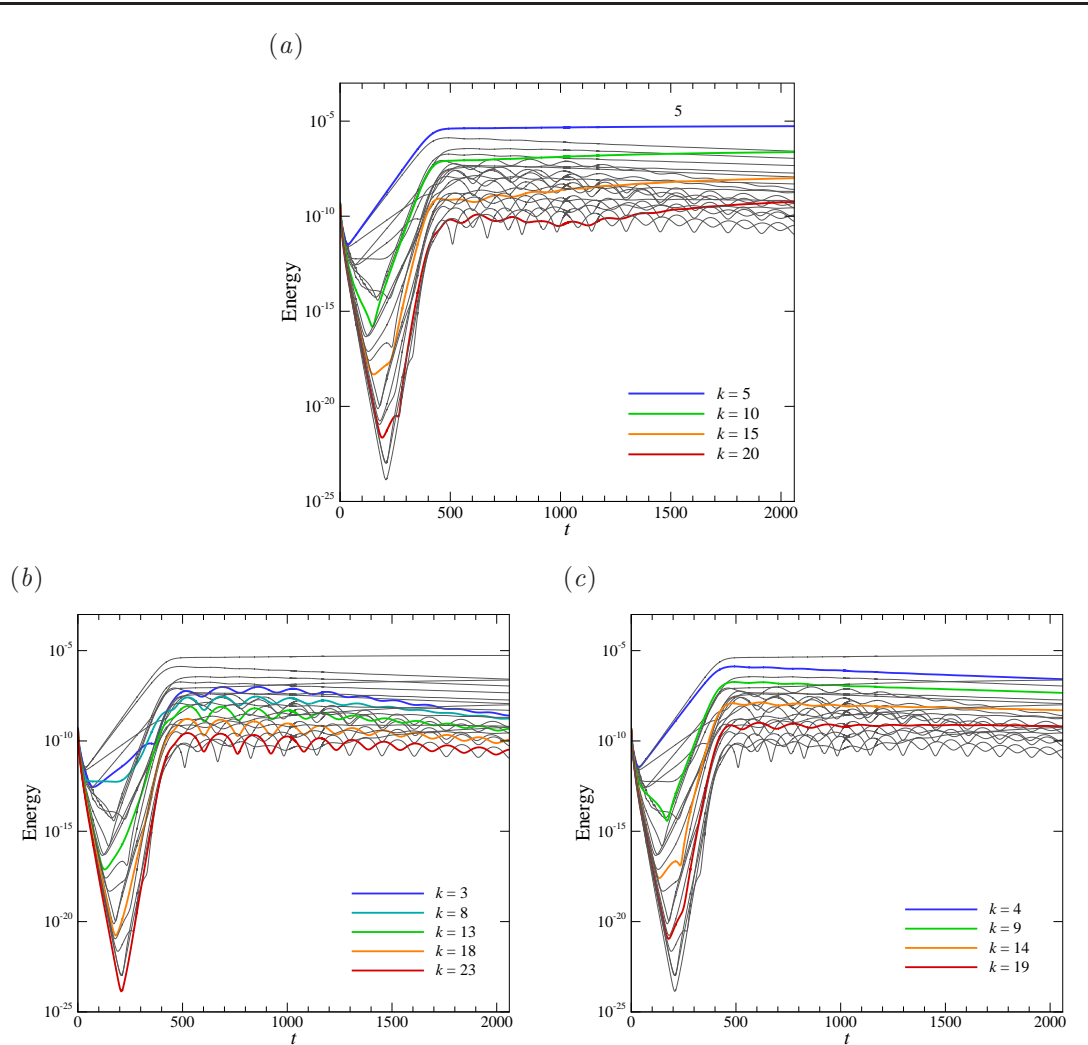


FIGURE 6.4: Energy time history of the energies contained in each azimuthal wavenumber for a flow condition of  $Ro = 0.05$  and  $E = 3 \times 10^{-4}$ . Energies of the first 23 non-zero wavenumbers are shown. (a) The bold lines represent the energies in wavenumber 5 and its harmonics. The bold lines in (b) represent the energies in wavenumbers  $k = 3, 8, 13, \dots$ , while the bold lines in (c) represent the energies in wavenumbers  $k = 4, 9, 14, \dots$

The depth independence of the wavenumber 5 configuration is illustrated in an iso-surface of axial vorticity, as shown in figure 6.5(b). The pentagonal organisation extends throughout the entire depth and rotates about the axis at a frequency of  $f = 0.162$ . The period of the polygonal structure is slightly larger than the period of the background flow ( $T = 6.2$  compared to  $T = 6.07$ , respectively). Thus, the frequency is less than twice the background frequency ( $f = 0.329$ ), which suggests that inertial waves are possible in the interior flow. The appearance of the distinct circular impression at the top of the iso-surface at  $r = 1$  is associated with the discontinuous boundary conditions

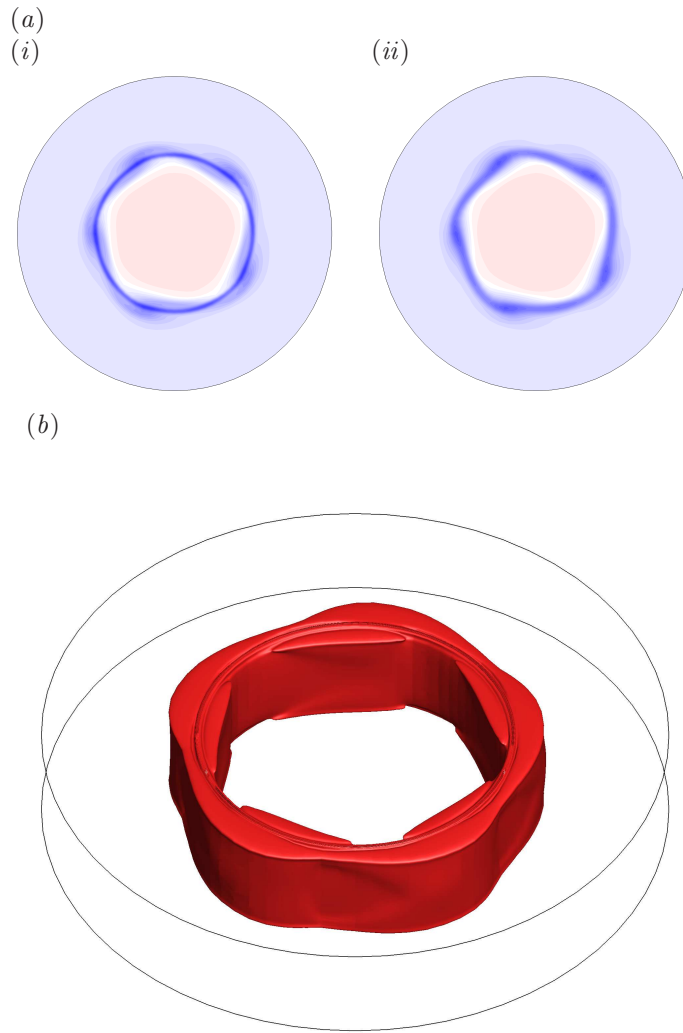


FIGURE 6.5: (a) Contours of axial vorticity at 2 different heights of (i)  $z/H = 0.1$  and (ii)  $0.5$  for a flow condition of  $Ro = 0.05$  and  $E = 3 \times 10^{-4}$ . These snapshots are taken at  $t = 910$ . The flow is reflectively symmetric about the  $z/H = 0.5$ . Contour levels are as per figure 6.2. (b) An isometric view of axial vorticity iso-surface of the saturated flow state at  $t = 2060$ . A single iso-surface of  $\omega_z = 1.96$  is shown.

---

imposed across the disk-tank interface. Although this resulting structure is observed at  $t = 2060$ , the structures at earlier times in both the linear and nonlinear regime are very similar to this. Despite the interactions between other wavenumbers in the nonlinear regime (figure 6.4), their amplitudes are not large enough to significantly affect the primary structure. In fact, all non-harmonic wavenumbers are seen to continually lose energy over time. The only wavenumbers which gain energy over time are those that are harmonics of the dominant wavenumber 5, which are observed to be approaching

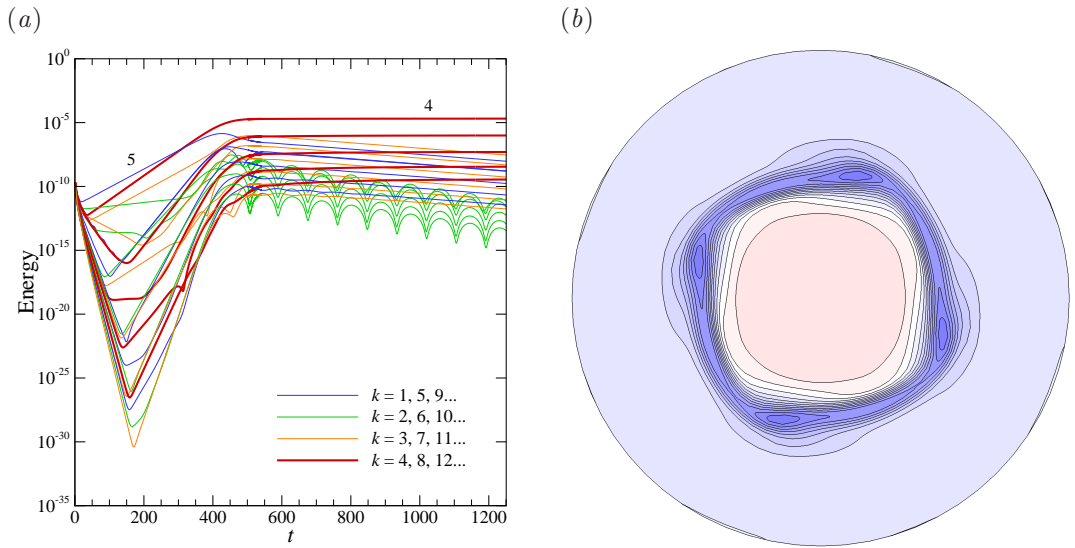


FIGURE 6.6: (a) Time series of the modal energies for a flow condition of  $Ro = 0.08738$  and  $E = 6.8 \times 10^{-4}$ . Energies of the first 23 non-zero wavenumbers are shown. (b) Contours of axial vorticity at mid-depth at  $t = 1250$  is shown. The wavenumber 4 structure is the most dominant wavenumber at this time. Contour levels are as per figure 6.2.

asymptotic values at  $t \rightarrow \infty$  in figure 6.4.

The features exhibited at  $Ro = 0.05$  and  $E = 3 \times 10^{-4}$ , which is close to the instability threshold, are also evident at other flow conditions just beyond the onset of linear instability. An example case of this occurs at  $Ro = 0.08738$  and  $E = 6.8 \times 10^{-4}$ , corresponding to  $Re_i \approx 29$ . According to the empirical equation of threshold instability (§ 5.1.1.4), the critical Rossby number for this Ekman number is given by  $Ro_c = 0.0673$  and is most unstable to a linear  $k = 4$  structure.

This flow condition has also been computed with 24 Fourier modes. The energy time history of the first 23 non-zero wavenumbers are shown in figure 6.6(a). The lines are highlighted such that each colour denotes a group of wavenumbers that share similar energy oscillations. The dominant wavenumber upon flow saturation is  $k = 4$ . However, this wavenumber is not the most stable configuration throughout the initial flow development. In the linear regime ( $0 \lesssim t \lesssim 450$ ), a  $k = 5$  structure is seen to exhibit larger energy compared to  $k = 4$  before becoming superseded. Despite the linear stability analysis predicting a  $k = 4$  structure, the random amount of energy distributed to each wavenumber upon the start up of the simulation does not guarantee that the leading  $k = 4$  eigenmode contains the highest energy. For this particular simulation,

a growing eigenmode with  $k = 5$  was seeded with more energy than the leading  $k = 4$  mode, and therefore is seen to be dominant between  $20 \lesssim t \lesssim 300$ . However, this does not change the preference of the flow as is demonstrated in the growth and eventual saturation of a  $k = 4$  structure in the flow. This saturated flow solution is illustrated in figure 6.6(b) through contours of axial vorticity on the horizontal mid-plane. A ring of low vorticity is seen comprising a square configuration encompassing an interior region of higher vorticity.

## 6.2 Flow conditions further beyond the instability onset

### 6.2.1 Increasing the Rossby number

A flow characterised by a higher  $Ro$  and an  $E$  similar to that of the reference case is now examined. A higher  $Ro$  was selected to ensure that the flow is significantly further beyond the instability onset than the reference case. It is anticipated, in part due to the difference between experimental observations (Früh & Read 1999) and the wavenumbers predicted in Chapter 5, that nonlinear effects will be predominant in this region of the  $Ro$ - $E$  parameter space, producing a deviation from the linear solution. The nonlinear effects will primarily encourage the interaction and coalescence between vortices, which will in turn result in a larger wavelength structure. A flow condition of  $Ro = 0.17$  and  $E = 2.5 \times 10^{-4}$  is studied, and is marked by a solid black circle in figure 6.1. The corresponding internal Reynolds number is given by  $Re_i \approx 120.92$ , which is well beyond the critical value of  $Re_{i,c} \approx 22.4$ .

The linear stability analysis predicts a wavenumber 5 configuration to be the most unstable structure at this flow condition. Note that although the predicted linearly unstable integer wavenumber has not changed from the reference case, the peak wavenumber is very close to  $k = 5.5$  ( $k = 6$  dashed boundary). This suggests that the growth rates of the dominant instabilities with  $k = 5$  and  $k = 6$  exhibit similar magnitudes. This can be identified in the plot of the growth rate as a function of wavenumber which is shown in figure 6.7. In addition, the axial vorticity contours of the flow superposed with the leading instability at an arbitrarily large amplitude are illustrated.

The growth rate of  $k = 5$  in this case has increased by an order of magnitude compared to the reference case and the instability mode is still characterised by mode I. Thus, the resulting deformed structure caused by the linear instability is the similar to that shown in figure 6.2(b). That is, a polygonal ring of low axial vorticity at  $r = 1$

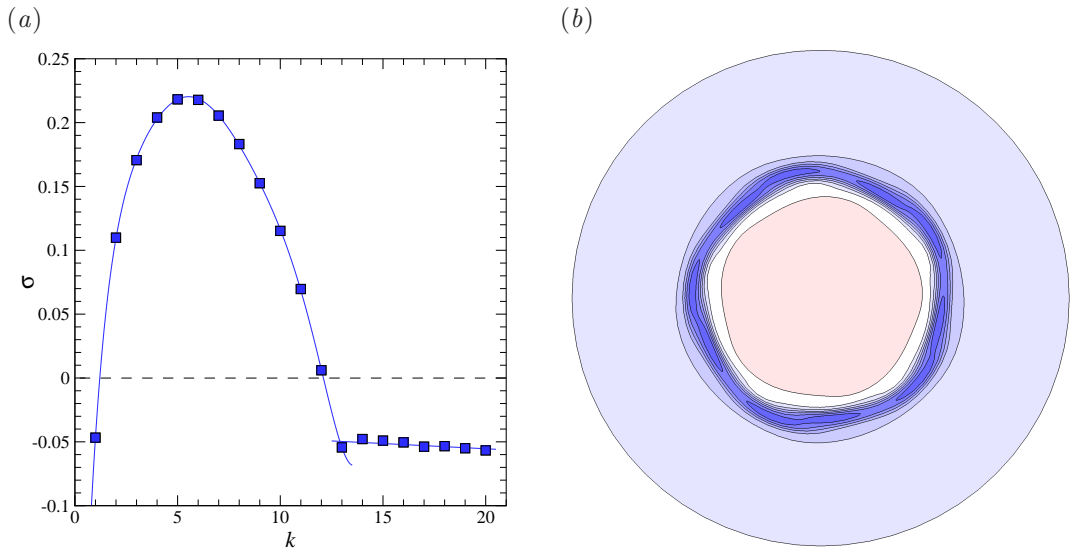


FIGURE 6.7: (a) The growth rates for a range of wavenumbers obtained through linear stability analysis for a flow condition of  $Ro = 0.17$  and  $E = 2.5 \times 10^{-4}$ . The dashed line represents neutral stability where points above and below symbolise unstable and stable wavenumbers, respectively. (b) Representative axial vorticity contours of linear instabilities of finite amplitude superimposed onto its respective base flow shown at  $z/H = 0.5$ . Nonlinear effects have been neglected. Contour levels are as per figure 6.2.

---

encompasses a region of high vorticity. This is expected since the wavenumbers are independent of each other in the linear stability analysis. Any differences between the two figures would be attributed to the arbitrary scaling used on the perturbation field before it is superimposed onto the axisymmetric base flow.

The three-dimensional flow has been computed using 40 Fourier modes in the azimuthal direction. It is anticipated that large increases in  $Ro$  or decreases in  $E$  (increasing  $Re_i$ ) will increasingly deform the shear layer. Thus, a greater spatial resolution is required to capture any time-dependent changes of the shear layer and therefore 40 Fourier modes is used here instead of the 24 implemented for the reference case. It should be noted that this flow case has also been computed using 24 Fourier modes, which described a very similar saturated solution to the case computed using 40 Fourier modes. The energy time history of the non-zero wavenumbers is shown in figure 6.8. Again, the flow is initialised with the axisymmetric base flow solution perturbed by white noise. A wavenumber 5 structure arises during the initial stages of the flow. However, the governance of the flow by the  $k = 5$  structure is short-lived as the energy in wavenumber 2 becomes larger in comparison at approximately  $t = 80$ . Beyond the

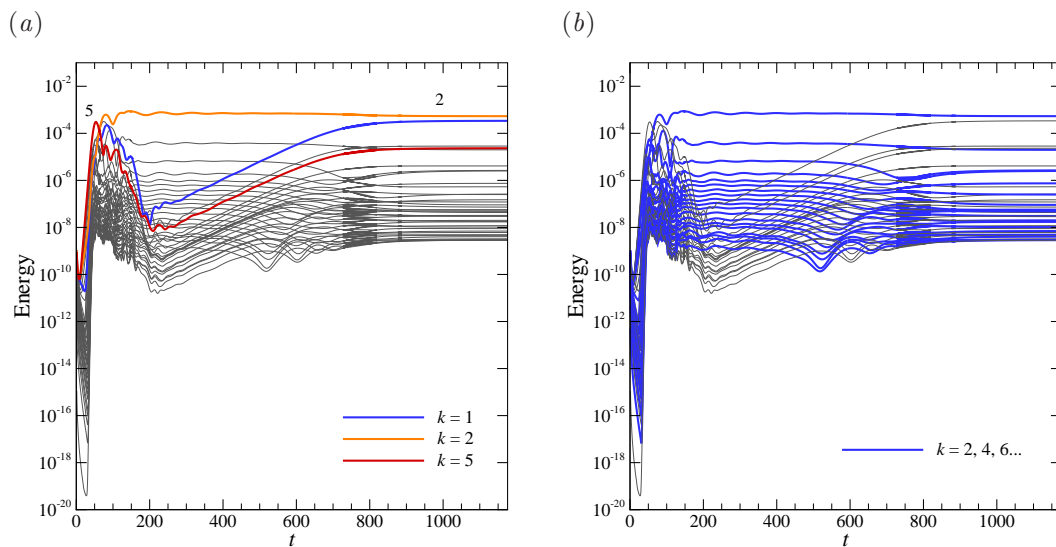


FIGURE 6.8: Time series of the modal energies for a flow condition of  $Ro = 0.17$  and  $E = 2.5 \times 10^{-4}$ . Energies of the first 39 non-zero modes are shown. (a) Azimuthal wavenumbers 1, 2 and 5 are highlighted. (b) Even-wavenumber energies are highlighted.

peaking of energy in the wavenumber 2 structure, the energy in  $k = 2$  and its harmonics plateaus over time while the energies of the odd wavenumbers decrease. At  $t \simeq 200$  the energies of the odd wavenumbers begin to increase again and plateau with comparable amplitudes to the even wavenumbers. Eventually, the flow saturates to a state which is dominated by  $k = 2$  distorted by a wavenumber 1 structure. It is also noted that the energy oscillation of a wavenumber and its  $k + k_{\text{peak}}n$  associates no longer demonstrates a very strong similarity as compared to the cases near the instability threshold described in the previous section.

The flow development represented through axial vorticity contours at mid-depth is illustrated in figure 6.9. The steady-state axisymmetric base flow solution is observed in the first frame at  $t = 5$ . A non-axisymmetric structure begins to evolve around the disk periphery at  $r = 1$  as the dominant wavelengths increase in amplitude. At  $t = 35$ , 4 vortices are seen to form on one half of the initially axisymmetric shear layer. As time is evolved, the vortices grow larger in size and the remaining semi-circle becomes distorted. Eventually, 6 vortices are observed at  $t = 45$  that are arranged irregularly, with the two vortices at the bottom of the frame being clustered close together. This pair of vortices coalesce at a future time and the structure adopts a pentagonal configuration. This initial process is reflected in the energy time history plots shown in figure 6.8.

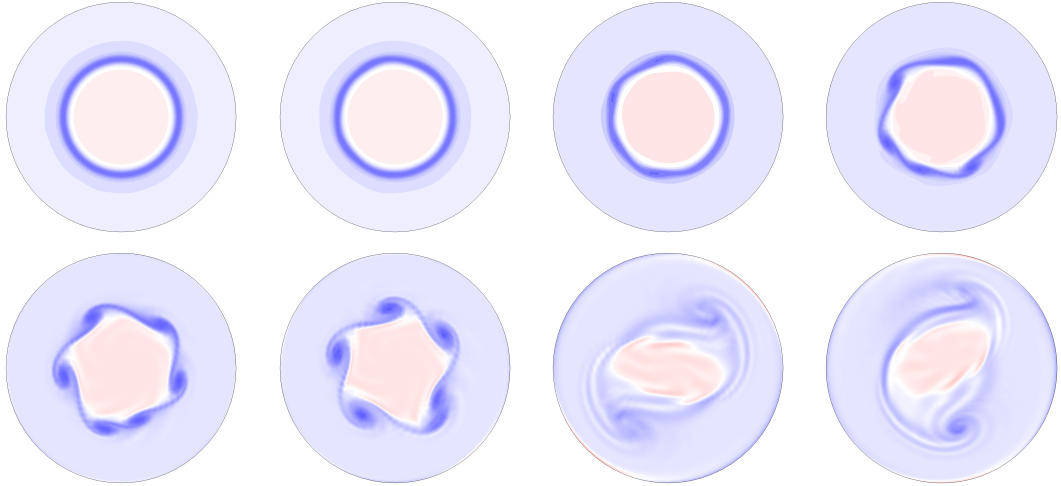


FIGURE 6.9: Flow condition of  $Ro = 0.17$  and  $E = 2.5 \times 10^{-4}$ . Time evolution of axial vorticity of the three-dimensional flow. Time increases from left to right and continues in the bottom row. The times are given by  $t = 5, 30, 35, 40, 45, 50, 145$  and  $1175$ , respectively. The starting axisymmetric base flow is seeded with white noise. Contour levels are as per figure 6.2.

---

That is, a pentagonal structure is expected during the exponential growth regime. It is noted that the wavenumber 5 structure at  $t = 50$  is an asymmetric pentagon, and that a standard pentagon was not observable at other time steps. This is due to the time dependence of the flow as the energies in many of the wavelengths are still varying at comparable amplitude. The vorticity contained within the polygon is seen to remain constant until the interior region is no longer completely contained by the low axial vorticity ring.

According to figure 6.8, a dipolar structure ( $k = 2$ ) is predicted once nonlinear effects become significant. This is observed at  $t = 145$  where two vortices exhibiting low vorticity surround a higher-vorticity oval-shaped interior. The energy of the wavenumber 1 structure continually increases and eventually becomes comparable to the dominant wavenumber 2 pattern. This results in an asymmetric dipolar structure as seen at  $t = 1175$ . This structure is characterised by a strong vortex which has a trailing tail of vorticity that is connected to a weaker opposing vortex. This solution is representative of the stable saturated flow state.

Alternating weak and strong bands of axial vorticity are observable in the panels at  $t = 145$  and  $t = 1175$ . A similar feature is observable in the interior region where alternating bands of high and mean values of vorticity are exhibited. Examination of

the discretised domain underlying the axial vorticity contours demonstrated that these waves are significantly larger than the radial and azimuthal grid spacings. Thus, it is proposed that the alternating band structures are a physical feature of the flow. It may be possible that this feature is related to inertial waves, which was described in § 4.2.3. The validity of the spatial resolution is further reinforced by the smoothness of the contours of axial velocity and azimuthal vorticity shown in figure 6.10. This is particularly the case for azimuthal vorticity contours since it is comprised of very small values ( $O(10^{-7})$ ) as compared to axial vorticity ( $O(10^0)$ ). Therefore, demonstrating similar structures to those in figure 6.9 (last panel) ensures that the structures are accurately captured. In addition, a simulation at a lower azimuthal resolution (24 Fourier modes) yielded a similar energy time history plot and the same contours of axial vorticity. It is expected that such spiral structures would be very difficult to capture experimentally using laboratory techniques such as laser Doppler velocimetry and particle image velocimetry since the azimuthal vorticity values are so much smaller than the values of axial vorticity in the flow. Additionally, the dipolar prediction by the direct numerical simulation is in agreement with the results of Früh & Read (1999). Their regime diagram suggests that they observed wavenumbers 2 to 4 for  $Ro = 0.17$  and  $E = 2.5 \times 10^{-4}$ .

Despite the complex patterns observed in the  $r$ - $\theta$  plane, the saturated flow still reveals depth-independent features. Figure 6.11(a) shows contours of the axial velocity and axial vorticity on the vertical mid-plane of the tank. These solutions are illustrated at an arbitrary azimuthal angle and are non-axisymmetric. Reflective symmetry about mid-depth is observed in the contours of axial velocity. The primary Ekman pumping is observed at the disk-tank interface in addition to recirculation zones on either side. Fluid is observed migrating from the bottom boundary and up along the tank side wall while no recirculation is present near the axis of rotation. The strong axial pumping at the disk-tank interface on the right induces a strong vertical band of axial vorticity. Furthermore, the interface between the regions of high and low values of axial vorticity demonstrates a strong degree of depth independence. An iso-surface of axial vorticity is illustrated in figure 6.11(b).

Increasing the Rossby number sufficiently beyond the instability onset has displayed azimuthal structures that are lower than those predicted by the linear stability analysis. This is due to the nonlinear effects that invoke competition between multiple

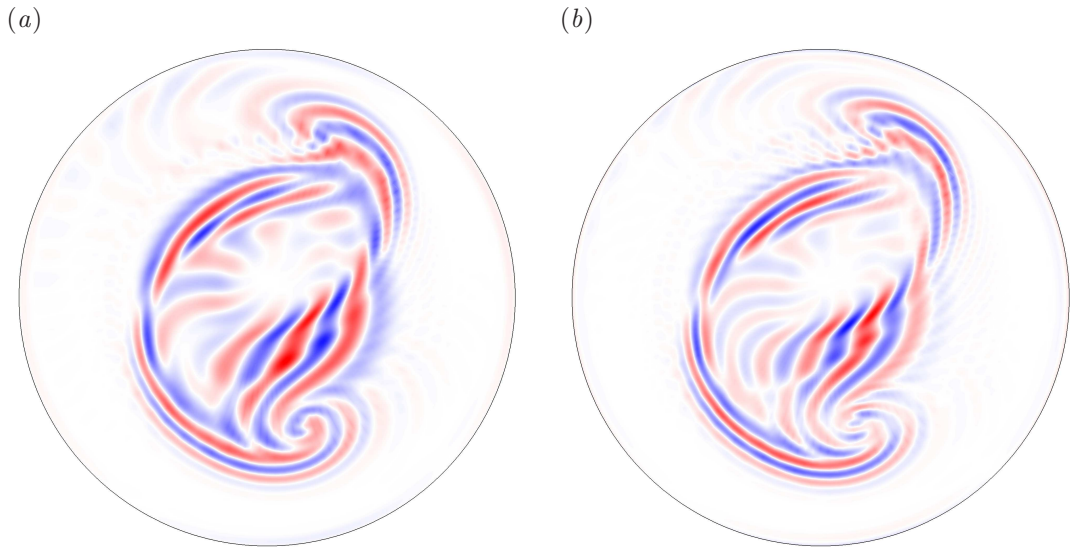


FIGURE 6.10: Contours of (a) axial velocity and (b) azimuthal vorticity for a flow condition of  $Ro = 0.17$  and  $E = 2.5 \times 10^{-4}$ . The mid-depth is illustrated at  $t = 1175$ . Contour levels are as per figure 6.2 for the axial velocity. Azimuthal vorticity contours are plotted between  $\omega_\theta = \pm|\omega_{\theta, \max}|$ .

---

wavenumbers of comparable energies. This nonlinear mode interaction was observed in figure 6.8(a) whereby the flow transitioned from a  $k = 5$  to a  $k = 2$  structure. At saturation, the secondary mode was observed to be a result of the  $k = 2$  (and its harmonics) and  $k = 5$  interaction (i.e.  $k = 5 - (2 \times 2) = 1$ ). The resultant wavenumber observed is in agreement with the wavenumbers reported by the experiments of Fröh & Read (1999). The next section also investigates a flow condition that is sufficiently beyond the onset of instability, although this is achieved instead by decreasing the Ekman number of the reference flow case, rather than increasing the Rossby number.

### 6.2.2 Decreasing the Ekman number

The effect of decreasing the Ekman number to increase  $Re_i$  is examined with flow conditions of  $Ro = 0.05$  and  $E = 8 \times 10^{-5}$ . This flow condition is also marked in figure 6.1. The decrease in  $E$  causes the investigated point to be at an internal Reynolds number of  $Re_i = 83.59$ , significantly beyond the instability threshold at  $Re_{i,c} \approx 22.4$ . Therefore, it is expected that as with the previous section, the unstable wavenumber from the three-dimensional simulations will be different to the predicted wavenumber from the linear stability analysis due to nonlinear effects. More specifically, the nonlinear state will adopt a lower azimuthal wavenumber than its linear prediction.

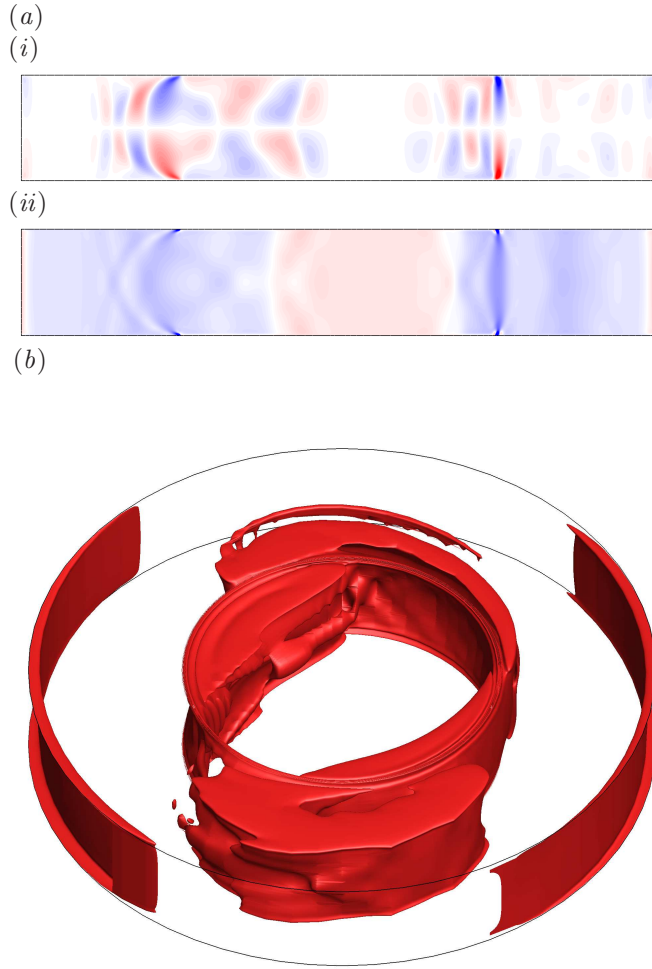


FIGURE 6.11: Flow condition of  $Ro = 0.17$  and  $E = 2.5 \times 10^{-4}$  at  $t = 1629$ . Contours of (a)(i) axial velocity and (ii) axial vorticity is displayed on the entire  $r$ - $z$  plane. Contour levels are as per figure 6.2. (b) An isometric view of an axial vorticity iso-surface of  $\omega_z = 1.88$  is shown.

---

As indicated in the regime diagram, the linear preferred wavenumber increases with decreasing Ekman number at small Rossby numbers. The predicted wavenumber here has changed from a wavenumber 5 (reference case) to a wavenumber 8. A plot of the growth rate as a function of wavenumber and the axial vorticity contours of the most unstable wavenumber at mid-depth are shown in figure 6.12. The contours depict a central octagon exhibiting high values of vorticity with a thin ring of lower vorticity surrounding it.

For this simulation, 128 azimuthal Fourier modes have been implemented to resolve the flow. The energy history of each non-zero wavenumber is shown in figure 6.13(a).

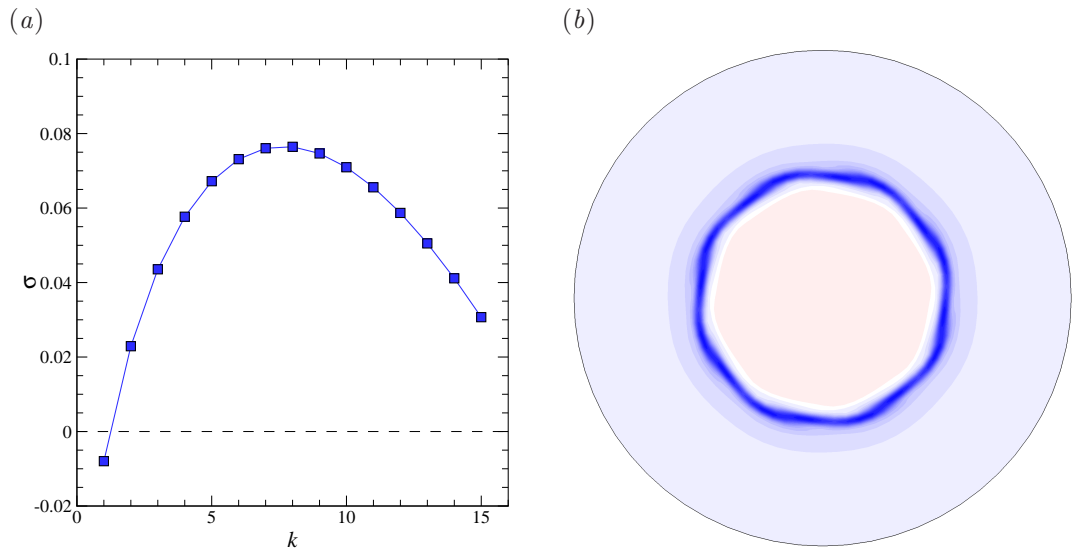


FIGURE 6.12: (a) The growth rates for a range of wavenumbers obtained through linear stability analysis for a flow condition of  $Ro = 0.05$  and  $E = 8 \times 10^{-5}$ . The dashed line represents neutral stability where points above and below symbolise unstable and stable wavenumbers, respectively. (b) Representative axial vorticity contours of the  $k = 8$  linear instability of finite amplitude superimposed onto its respective base flow shown at  $z/H = 0.5$ . Nonlinear effects have been neglected. Contour levels are as per figure 6.2.

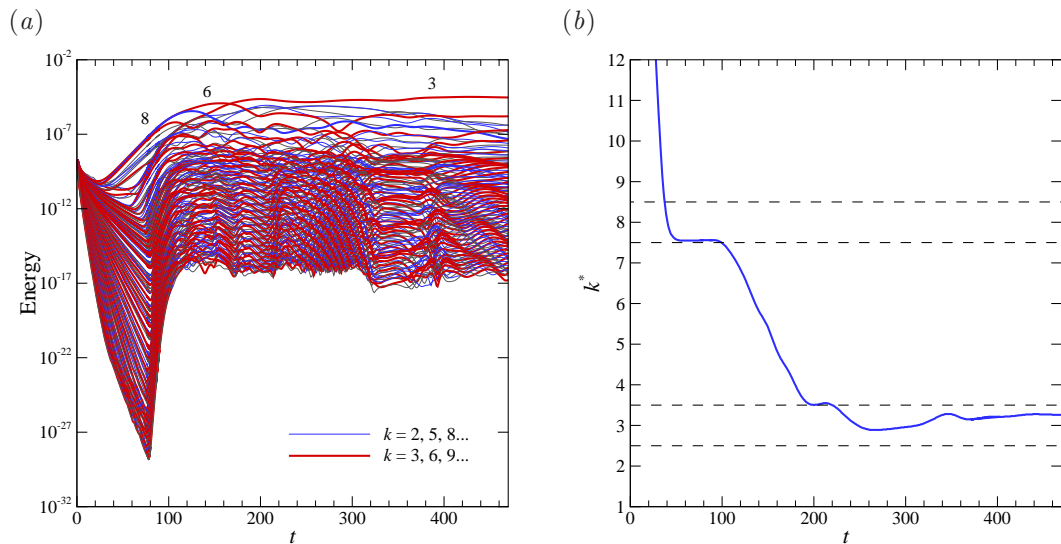


FIGURE 6.13: Flow conditions of  $Ro = 0.05$  and  $E = 8 \times 10^{-5}$ . Time series of (a) the energies contained in the first 127 azimuthal wavenumbers and (b) the averaged wavenumber weighted by energy. The dominant wavenumber transitions from  $k = 8 \rightarrow 6 \rightarrow 3$  over time represented by bold lines. The dashed lines enclosing  $2.5 \leq k^* < 3.5$  and  $7.5 \leq k^* < 8.5$  represent integer wavenumbers 3 and 8, respectively.

The three-dimensional solution has been initialised with the axisymmetric base flow solution perturbed with white noise. It can be seen that the energies contained in the wavenumber 6 and 8 structures are initially the highest throughout the linear growth regime. In fact, the energy in  $k = 6$  is the largest until it becomes surpassed by  $k = 8$  at  $t \approx 80$ . However, the energy in  $k = 8$  is superseded soon after at  $t \approx 100$ . Again, it is not surprising that the wavenumber 6 structure is observed in the linear regime rather than the linearly predicted  $k = 8$ . This is because there is little difference in the linear growth rates between  $k = 8$  and its neighbouring wavenumbers. The difference between the growth rate of  $k = 6$  and  $k = 8$  is less than 5%. For this particular simulation, the white noise has become more favourable to the  $k = 6$  wavelength. The competition between  $k = 6$  and  $k = 8$  structures weaken beyond  $t \approx 100$  as nonlinear effects become significant. At this time, the energy in  $k = 8$  begins to decrease as the energy in  $k = 6$  continues to increase. At approximately  $t = 160$ , the energy in  $k = 3$  dominates and saturates as the stable wavenumber. The difference in energy between the two most energetic wavenumbers,  $k = 3$  and  $k = 6$ , is of an order of magnitude. Thus, an undisrupted triangular structure is predicted in the three-dimensional flow.

An alternative interpretation of the energy time history is achieved by considering the average wavenumber weighted by energy over time. Figure 6.13(b) illustrates the average wavenumber weighted by energy over time, which is calculated as

$$k^* = \frac{\sum_{k=1}^N E_k k}{\sum_{k=1}^N E_k}, \quad (6.1)$$

where  $k$  is an integer azimuthal wavenumber,  $N$  is the number of Fourier modes used in the simulation and  $E_k$  is the energy contained in the  $k^{\text{th}}$  wavenumber. The energy associated with the base flow ( $k = 0$ ) is omitted in calculating  $k^*$ . The purpose of this quantity is to identify the dominant wavenumber that would be observed in the flow at a specific time, provided the amplitudes are not so small as to be swamped by the base flow. This parameter also helps to illustrate the wavenumber vacillation process when there are multiple wavenumbers competing with very large energies. The plot demonstrates a brief saturation of a wavenumber 8 structure ( $7.5 \leq k^* < 8.5$ ) between  $35 \lesssim t \lesssim 100$ . As the nonlinear effects become significant, the apparent wavenumber decreases towards  $k^* = 3$  ( $2.5 \leq k^* < 3.5$ ) and is sustained for  $t \gtrsim 220$ . Thus, a triangular configuration is predicted in the three-dimensional direct numerical simulation for this flow condition. These vacillation trends are consistent with the energies demonstrated in figure 6.13(a).

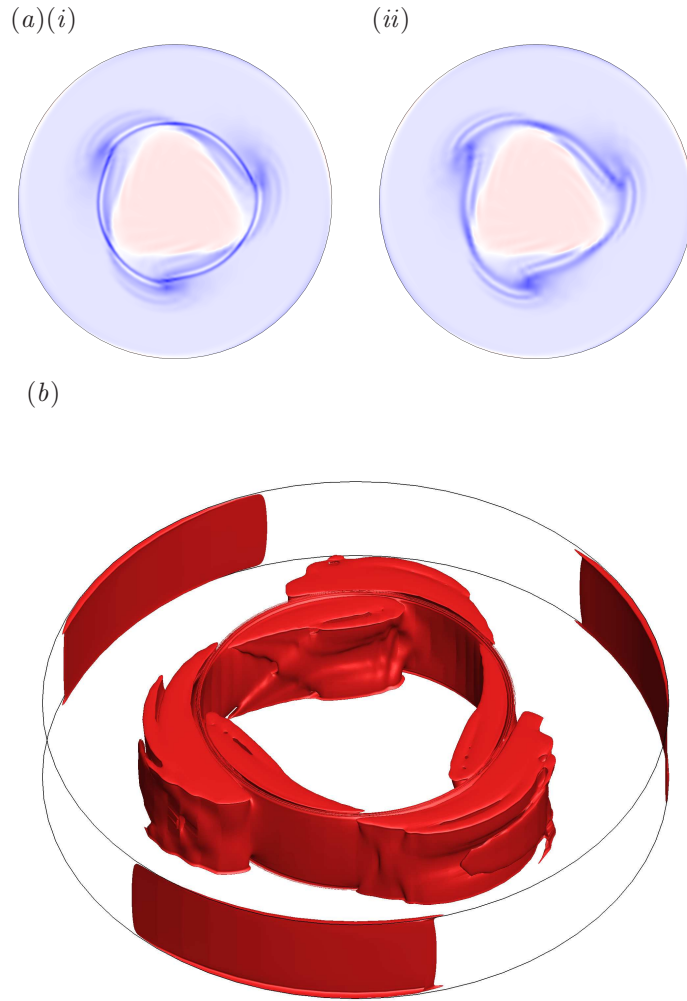


FIGURE 6.14: Flow condition of  $Ro = 0.05$  and  $E = 8 \times 10^{-5}$  at  $t = 469$ . (a) Contours of axial vorticity at 2 different heights of (i)  $z/H = 0.1$  and (ii)  $z/H = 0.5$ . The flow is reflectively symmetric about the  $z/H = 0.5$ . Contour levels are as per figure 6.2. (b) An isometric view of an axial vorticity iso-surface of  $\omega_z = 1.96$  is shown.

---

The three-dimensional wavenumber 3 structure achieved at saturation is represented in the contours of axial vorticity at two different depths, as shown figure 6.14(a). The structure at  $z/H = 0.5$  is observed over a wide range of depths as its axial vorticity is largely depth-independent. The structure is comprised of three concentrated regions of low vorticity migrating around the  $r = 1$  circumference. As described earlier, the contours near the horizontal boundary ( $z/H = 0.1$ ) illustrate a circular ring of low vorticity attributed by the discontinuity at the disk-tank interface. Also, the spirals of low and high vorticity are evident in the interior and satellite vortices. It is speculated

that these spirals may be a physical feature of the flow related to inertial waves, which was also observed in the previous flow condition of  $Ro = 0.17$  and  $E = 2.5 \times 10^{-4}$  (see figure 6.9). An iso-surface of axial vorticity at  $t = 469$  is illustrated in figure 6.14(c). The iso-surface illustrates three vortices arranged in a triangle extending the entire depth of the tank.

The resultant wavenumber 3 structure from direct numerical simulation is not in agreement with the experimental results of Fröh & Read (1999). The flow condition of  $Ro = 0.05$  and  $E = 8 \times 10^{-5}$  displayed wavenumbers 6 to 8 in the experimental environment. A possible explanation for this discrepancy may be due to the consistent change in  $Ro$  or  $E$  over time implemented in the experiments. That is, one parameter was kept constant while the other was slowly scanned. It was reported that a typical scan lasted approximately 7 to 12 hours. However, as will be observed later in § 6.4.2, slightly changing the forcing conditions of an established flow requires very long time periods for the flow to equilibrate to a new saturated state. This is particularly true for flow conditions just beyond the onset of instability. Additionally, a viscous time unit ( $R_t^2/\nu$ ) in their experiments corresponds to 25 hours. This suggests that the scans in the experiments were not performed at a low enough rate to allow the slow interactions to occur and the flow to saturate, as the time taken to scan through an entire parameter is less than that typically required for a constant flow condition to reach equilibrium (one or more viscous time units (e.g. Lopez & Marques 2011)). This could be an additional reason for why their instability threshold is further to the right (i.e. a larger  $Re_i$  is needed for instability). The linear stability analysis growth rates that are very small just beyond the instability threshold and therefore suggests that large time periods are required for the instability to grow to a noticeable amplitude. Adopting the dimensionless timescale used here to the physical scales of the set-up used by Fröh & Read (1999) ( $\Omega = 4 \times 10^{-4}$  rad/s and  $\nu = 1 \times 10^{-6}$  m<sup>2</sup>/s) would suggest that it would take approximately 174 hours ( $t = 250$ ) to exhibit a wavenumber 3 structure. This is approximately 7 viscous time units. The entire time integration of the simulation corresponds approximately to 347 hours ( $t = 500$ ). In addition, it is worth noting that this simulation has been initialised from its steady-state axisymmetric base flow and assisted by the introduction of white noise. Thus, this simulation suggests that the rate of consistent change in forcing was not low enough in the experiments, though it should be stated that there would be sources of experimental error which would accelerate to

a degree, the growth of any instabilities present.

Decreasing the Ekman number far beyond the instability onset has exhibited similar flow behaviour to that resulting from increasing the Rossby number well beyond the onset. That is, the structures of the stable flow state displays azimuthal structures that are different (lower wavenumber) than those predicted by the linear stability analysis. The comparable energy in each azimuthal wavenumber structure exacerbates nonlinear effects, which causes unstable structures of varying wavelengths to compete and interact.

### 6.3 Varying the Rossby number

In this section, the effect of varying the Rossby number in relation to nonlinearity is investigated in both the small and large-Ekman number regimes. A progression of Rossby numbers lower and higher than the reference case ( $Ro = 0.05$  and  $E = 3 \times 10^{-4}$ ) is explored. Although this section studies the effect of varying the Rossby number, the available data has minor variations in the Ekman number, which are considered to be negligible. The results of the small and large- $E$  regimes are highlighted separately in the following sections.

#### 6.3.1 Large-Ekman-number regime

The previous section examined flows which were well beyond the onset of linear instability. However, those flow conditions described axisymmetric base flows that are reflectively symmetric about the mid-depth. This section investigates increases to the Rossby number through to flows that have broken this reflective symmetry. The transition from reflectively symmetric to symmetry-broken axisymmetric base flows have been observed to be broken at large  $Ro$  and small  $E$  (equivalent to large  $Re_i$ ), and is represented by a thick dashed line in figure 6.1. The determination of this line has been described in § 5.1.1.4. An initial case of  $Ro = 0.147$  and  $E = 1.06 \times 10^{-3}$  is investigated with supplementary cases of increasing  $Ro$  at a similar Ekman number. These additional cases are characterised by  $(Ro, E) = (0.278, 1 \times 10^{-3}), (0.395, 9.47 \times 10^{-4}), (0.5, 1 \times 10^{-3})$  and  $(0.77, 1 \times 10^{-3})$ , and have been marked by solid white squares in figure 6.1. For these flow conditions, the linear stability analysis predicts a preferential azimuthal wavenumber of either  $k = 3$  or  $k = 4$  and their respectively axisymmetric base flows are reflectively symmetric characterised by  $Re_E < 31.6$ . The regime that

encompasses both reflectively symmetric and symmetry-broken flow was determined to be  $26.7 < Re_E < 56.4$  (see § 4.3.4).

The energy of the first 31 non-zero azimuthal wavenumbers over time for  $Ro = 0.147$  and  $E = 1.06 \times 10^{-3}$  is illustrated in figure 6.15(a). For this particular flow condition, the linear stability analysis predicts a wavenumber 4 structure as most unstable. It is clear from the energy plot that the flow stabilises with a wavenumber 3 structure in both the linear and nonlinear regimes. The linearly predicted  $k = 4$  structure is not observed in the linear regime due to the white noise favouring  $k = 3$  during initialisation. For this flow, there is a 7% growth rate difference between  $k = 3$  and  $k = 4$  while a the growth rate between  $k = 4$  and  $k = 5$  demonstrates a 25% difference. Thus, given the low amplitude white noise used in these simulations, it is unlikely that a wavenumber 5 would be favoured throughout the linear regime. Despite this, the wavenumber 4 structure still exhibits a larger growth rate compared to  $k = 3$  in the linear regime, which is in agreement with the linear stability analysis. The amplitude of the structures become large and nonlinear effects become apparent before the energy in  $k = 4$  has an opportunity to surpass  $k = 3$ .

Figure 6.15(b, c, d) are the supplementary flow conditions to panel (a) whereby each successive case is characterised by an increase in Rossby number. The axisymmetric base flow at these conditions are reflectively symmetric about the mid-depth. The flow condition in panel (b) is predicted to be unstable to  $k = 4$  by linear stability analysis while flow conditions in panels (c, d) are predicted to be unstable to  $k = 3$ . As nonlinear effects begin to manifest, a wavenumber 3 structure and its harmonics are seen to plateau over time, while all of the other wavenumbers decay at exponential rates. This is true for all four flow conditions. Also, the energies in the wavenumber groups of  $k + k_{\text{peak}}n$  demonstrate similar oscillations over time even though the majority of the flows are beyond the onset of instability. Thus, it is in contrast with figure 6.8, which displayed a major difference in energy oscillations at  $t \approx 550$ . However, there is a point of difference in that the primary wavenumbers are not comparable or in competition at any time, which may be a possible explanation for this discrepancy.

The contours of axial vorticity at mid-depth for  $Ro = 0.147$  and  $E = 1.06 \times 10^{-3}$  at  $t = 450$  are shown in figure 6.16(a). An interior triangular configuration is observed with three satellite vortices exhibiting low vorticity. The appearance of the flow does not change at other depths except near the horizontal boundaries where the neg-

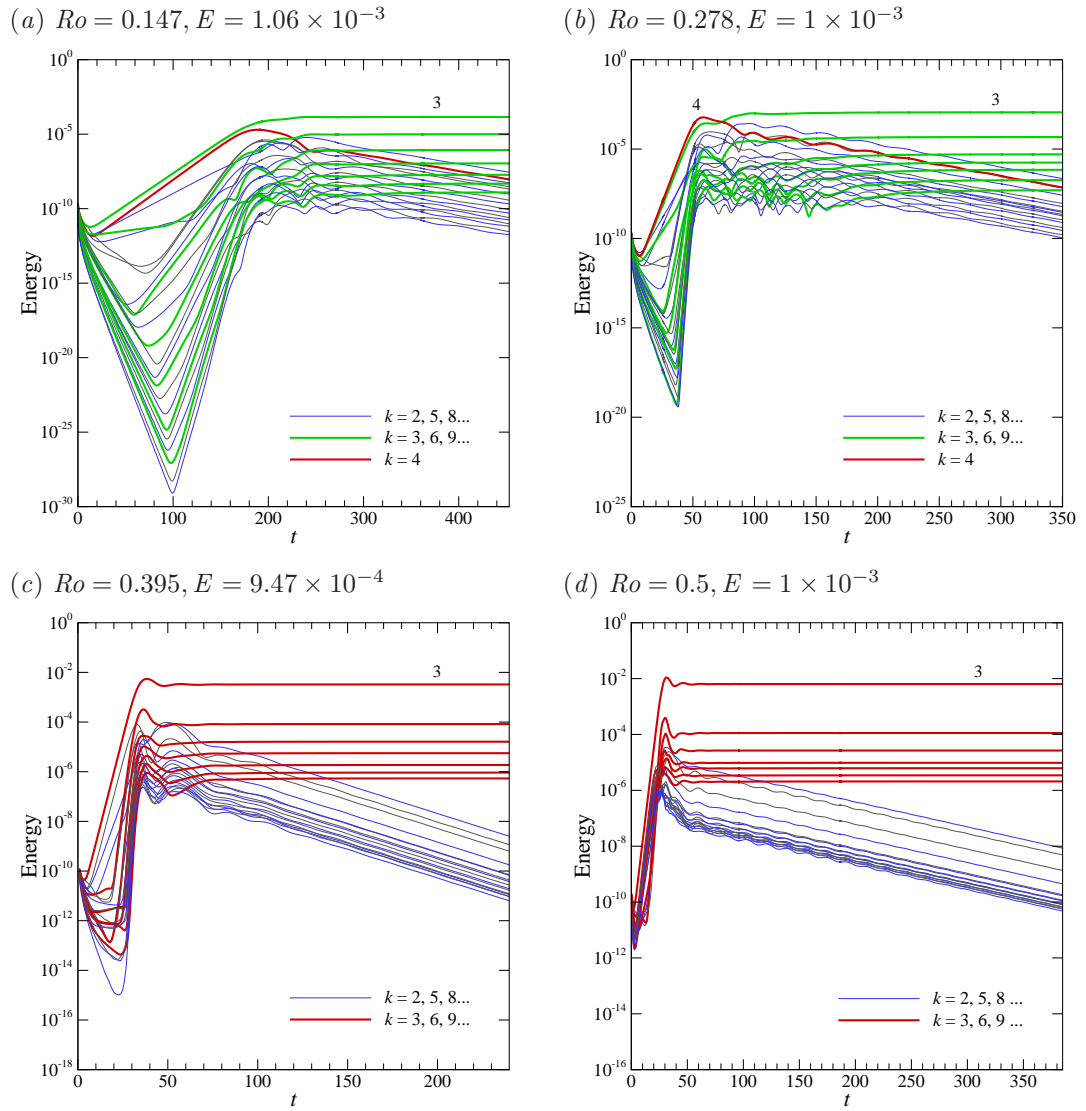
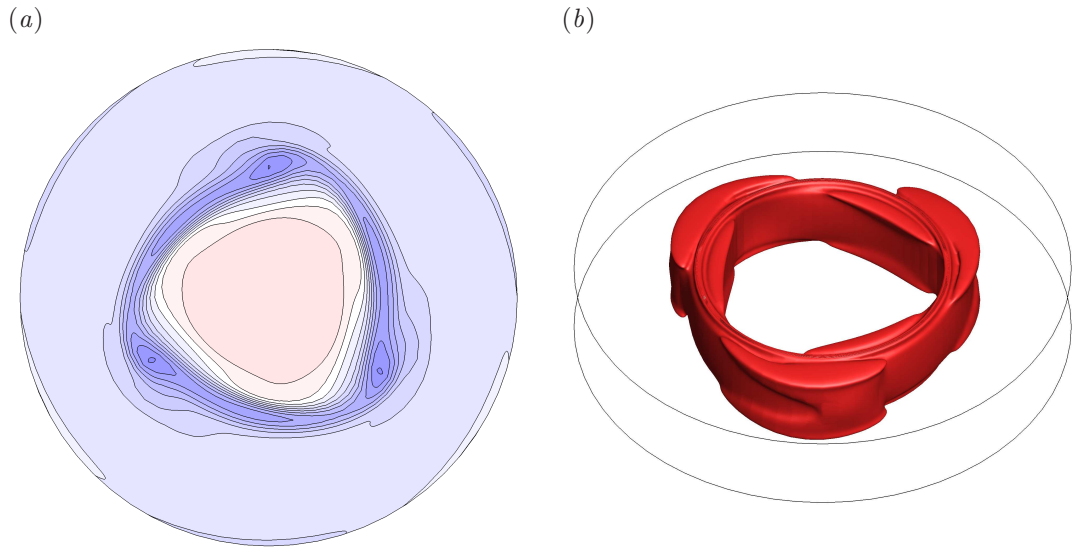


FIGURE 6.15: The energy time histories for flow conditions of  $(Ro, E) = (a) (0.147, 1.06 \times 10^{-3})$ ,  $(b) (0.278, 1 \times 10^{-3})$ ,  $(c) (0.395, 9.47 \times 10^{-4})$  and  $(d) (0.5, 1 \times 10^{-3})$ . Flows  $(a, b, c)$  have been simulated using 32 Fourier modes and flow  $(d)$  has been computed using 40 Fourier modes. Linear stability analysis predicts a an azimuthal wavenumber 4 for flows  $(a)$  and  $(b)$ , and a wavenumber 3 for flows  $(c)$  and  $(d)$ . All of these flows have been initialized with the axisymmetric base flow and seeded random noise.




---

FIGURE 6.16: Saturated flow conditions of  $Ro = 0.147$  and  $E = 1.06 \times 10^{-3}$  at  $t = 450$ . (a) Contours of axial vorticity contours viewed at  $z/H = 0.5$ . Contour levels are as per figure 6.2. (b) An isometric view of an axial vorticity iso-surface characterised by  $\omega_z = 1.86$  is shown.

---

ative vorticity produced at the disk-tank interface feeds energy into the axisymmetric structure. That is, a circular ring of very low vorticity is observed in addition to the three outer vortices. An iso-surface for the same flow is illustrated in figure 6.16(b), which elucidates a highly depth-independent structure throughout the interior with three vortices encircling the centre at  $r = 1$ . These figures are typical of all the other wavenumber 3 stable flows in figure 6.15. This is surprising since flows with  $Ro > 0.278$  and  $E = 1 \times 10^{-3}$  are well beyond instability onset, and therefore nonlinear effects are expected to become significant such that multiple wavenumbers are in competition.

Now Rossby numbers that are further increased into the symmetry-broken regime where the base flow exhibits symmetry-broken behaviour will be considered. The transition from reflectively symmetric to symmetry-broken axisymmetric base flows have been described earlier in 4.2.1. The symmetry-breaking property of the flow is typically identified by the two diagonal strands of axial vorticity generated at the disk-tank interface, and occurs for the flow condition of  $Ro = 0.77$  and  $E = 1 \times 10^{-3}$ . This flow condition corresponds to  $Re_E = 48.7$  and  $Re_i = 193.64$ , and has been marked in figure 6.1 with a solid white square. At this condition the linear stability analysis predicts an azimuthal wavenumber of  $k = 3$  as the most unstable mode I instability and  $k = 28$  as the most unstable mode II instability. The regime diagram does not encompass this

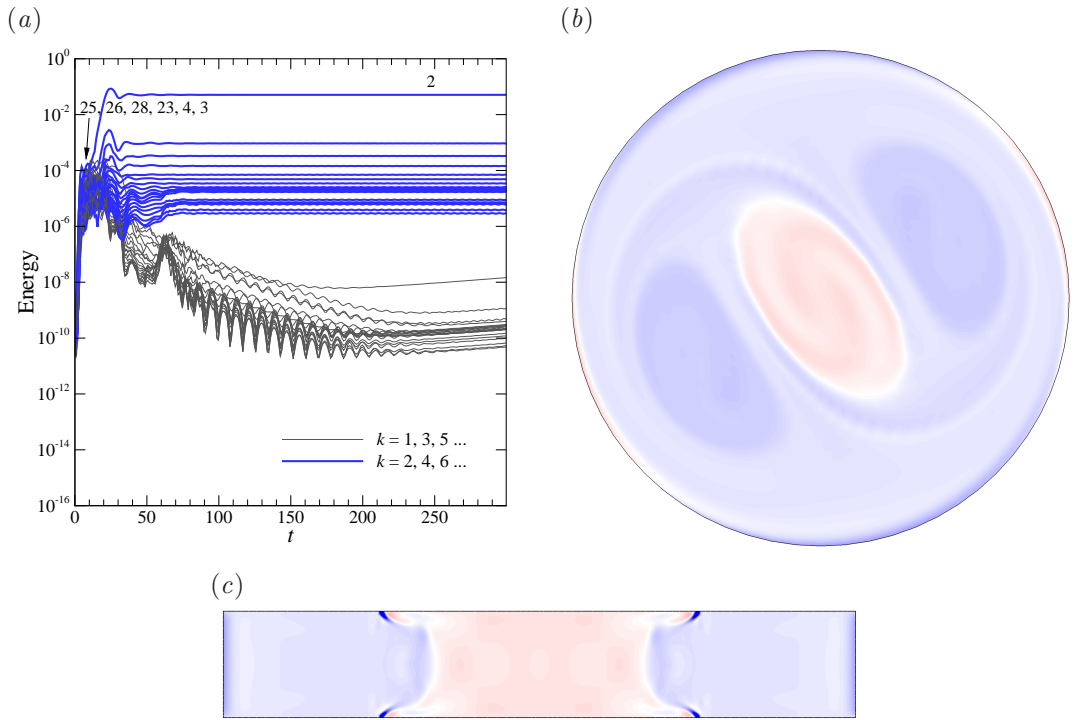


FIGURE 6.17: Flow conditions of  $Ro = 0.77$  and  $E = 1 \times 10^{-3}$ . Time series of (a) the energies contained in the first 39 non-zero azimuthal wavenumbers and (b) the axial vorticity contours extracted at  $t = 300$  for  $z/H = 0.5$ . (c) Contours of axial vorticity in the full meridional  $r$ - $z$  plane. Contour levels are as per figure 6.2.

region because limited data has been obtained in this parameter space.

The energy in each azimuthal wavenumber has been computed and is shown in figure 6.17(a). Although it is not clear from the figure, the energies in  $k = 25, 26$  and  $28$  (wavenumbers consistent with the mode II instability) are comparable and are the most dominant during the linear regime of the flow. However, these larger-wavenumber modes quickly weaken as nonlinear effects are realised. This suggests that the mode II instability has a negligible effect on the saturated flow state. Thus, the saturated stable wavenumber is lower than the predicted linear wavenumber. In the nonlinear regime, the wavenumber 2 structure becomes the primary mode and the wavenumber dominance cascades through  $k = 2, 4, 6, \dots$ , while the energies of the odd wavenumbers quickly decay over time. In addition, the energy time history of each non-zero wavenumber except for the dominant wavenumber illustrates minor oscillations for even wavenumbers and large oscillations for odd wavenumbers. Since the energy in  $k = 2$  is several orders of magnitude above  $k = 4$ , a dipolar structure is expected to appear with no distortions induced by other wavenumbers. The mid-depth axial vorticity contours of the

flow at  $t = 300$  is reproduced in figure 6.17(b). Two vortices are observed revolving around a central oval-shaped interior vortex. This structure resembles an undisturbed wavenumber 2 structure which is different to that of a competing wavenumber 2 configuration previously shown in figure 6.9. The vortices are large and fill the majority of the container, which is in contrast to the thinner characteristic ring of vortices observed previously. Despite the depth dependence of the axisymmetric base flow, the axial vorticity contours illustrated by the direct numerical simulation are typical at other heights except in the vicinity of the horizontal boundaries. The contours of axial vorticity in an entire  $r$ - $z$  plane is illustrated in figure 6.17(c). The diagonal vorticity strands are still evident at the disk-tank interface except that both strands now favour the same inward direction. In addition, the strands do not elongate far into the interior of the flow but is rather truncated and limited to the horizontal boundaries. Hence it appears that the developments of non-axisymmetric structures reverts the flow to a reflectively symmetric state about the horizontal mid-plane.

A flow condition described by an even greater  $Ro$ , which describes a time-dependent axisymmetric base flow, has been simulated via a three-dimensional direct numerical simulation. The flow is characterised by  $Ro = 0.924$  and  $E = 1 \times 10^{-3}$  with the structure of its axisymmetric base flow described in § 4.2.3. The linear stability analysis described in § 3.4 was performed over the exact period of the time-periodic flow state (known as Floquet analysis), which demonstrates a preference to a linear  $k = 3$  arrangement for the mode I instability. Mode II and mode III instabilities exist with growth rates larger than those associated with mode I. However, as portrayed earlier in the previous flow condition, only wavelengths associated with the mode I instability are significant in the nonlinear regime. As such, the flow was initialised only with 24 Fourier modes. The energy time history of this flow is reproduced in figure 6.18(a). An additional 24 Fourier modes was added at  $t = 500$  to confirm the negligible contribution of smaller mode II instability wavelengths in the nonlinear regime: the energies of the higher wavenumbers were seen to decay over time. Due to figure clarity reasons, the energies in these wavenumbers have not been shown though the flow has been simulated up to  $t = 1060$ . A wavenumber 19 associated with the mode II instability is seen dominating the linear regime while nonlinear effects are seen to encourage the stabilisation of a wavenumber 2 configuration. The energy time history for each azimuthal wavenumber demonstrates irregular increases and decreases in energy. This fluctuation in energy

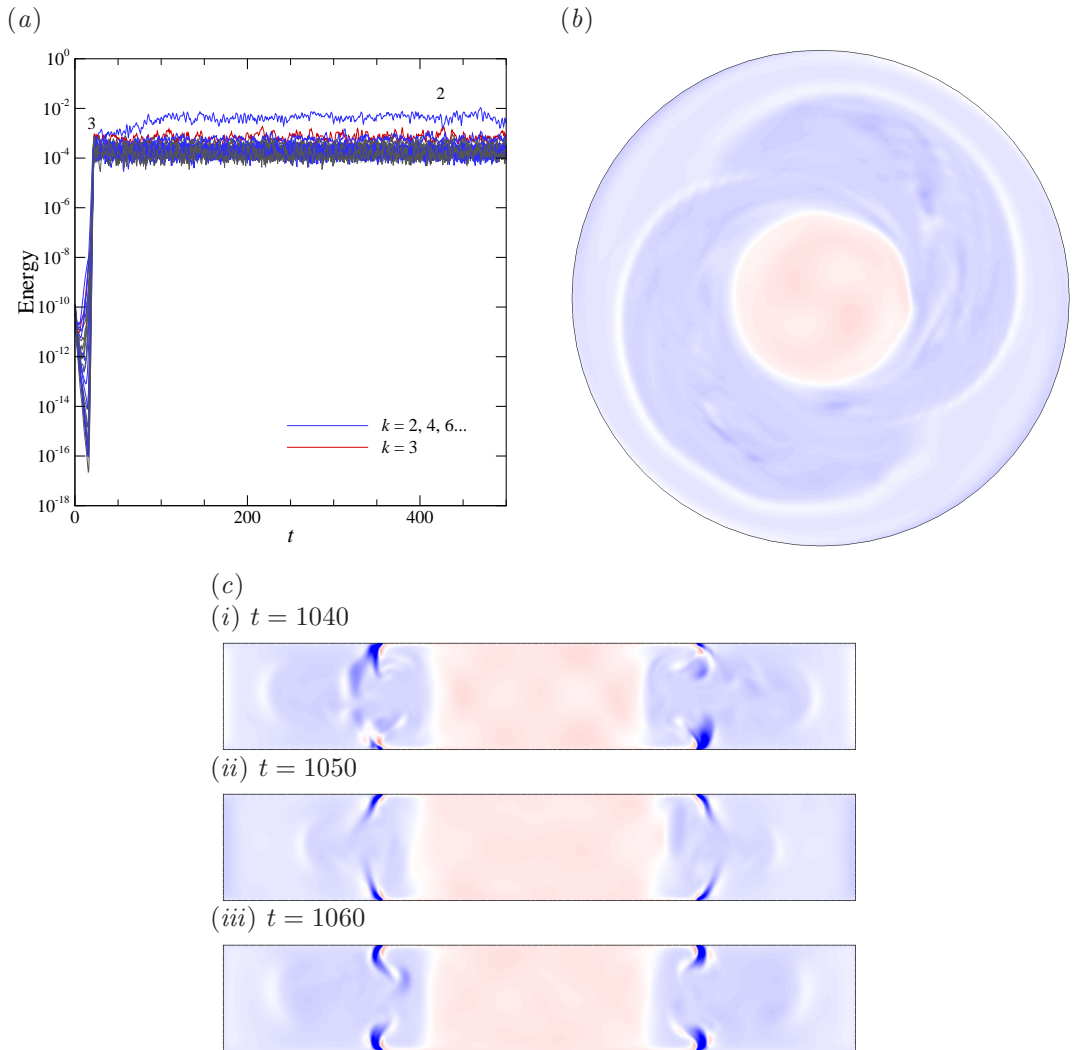


FIGURE 6.18: Flow conditions of  $Ro = 0.924$  and  $E = 1 \times 10^{-3}$ . Time series of (a) the energies contained in the first 39 non-zero azimuthal wavenumbers and (b) the axial vorticity contours extracted at  $t = 1143$  for  $z/H = 0.5$ . (c) Contours of axial vorticity in the full meridional  $r$ - $z$  plane at (i)  $t = 1040$ , (ii)  $t = 1050$  and (iii)  $t = 1060$ . Contour levels are as per figure 6.2.

was also observed for  $Ro = 0.77$ , although it is more prominent at this higher Rossby number case.

The axial vorticity contours extracted at mid-depth at  $t = 1060$  is illustrated in figure 6.18(b). From a top-down view, the axial vorticity contours portray a circular interior of high vorticity surrounded by low vorticity. The structure comprising the low vorticity illustrates two overlapping ellipses which is bounded by higher vorticity with values ranging in between that exhibited by the circular and the ellipse structures. Multiple patches of varying vorticity exists predominantly in the off-axis ellipses

which suggests that the flow structure is not coherent in time and is not reflectively symmetric about the mid-plane. The full meridional  $r$ - $z$  plane shown at various times in figure 6.18(c) reveals the symmetry-broken vertical structure of the flow. The low vorticity strands originating from the disk-tank interface have elongated further into the interior flow as compared to the  $Ro = 0.77$  case. The axial vorticity contours of the interior circular structure illustrate a region of greater depth independence.

### 6.3.2 Small-Ekman-number regime

The previous section investigated the effect of varying the Rossby number with progression into depth-dependent and time-periodic flows at large Ekman numbers. This section highlights the effect of decreasing the Rossby number towards the instability threshold in the small-Ekman-number regime. The previously investigated case of  $Ro = 0.05$  and  $E = 8 \times 10^{-5}$  in § 6.2.2 serves as a reference case here. Four additional flows of  $Ro = 0.04125, 0.0325, 0.02375$  and  $0.015$  at  $E = 8 \times 10^{-5}$  are examined. The predicted unstable azimuthal wavenumbers are  $k = 8, 8, 7$  and  $7$ , respectively. These flow conditions have been marked in figure 6.1 as solid white and blue circles.

The energy time histories for the four investigated cases are shown in figure 6.19 with the reference case ( $Ro = 0.05$  and  $E = 8 \times 10^{-5}$ ) illustrated earlier in figure 6.13. For  $Ro = 0.04125$ , the linear regime of the flow development is dictated by a wavenumber 8 structure, which is in agreement with the predicted unstable linear wavenumber. The energy in  $k = 7$  briefly becomes dominant with the onset of nonlinear effects. The flow eventually saturates to a stable wavenumber 3 at  $t \approx 1400$ . This is the same wavenumber preferred at the higher  $Ro = 0.05$  case. Decreasing  $Ro$  demonstrates an increase in saturated wavenumber which is in agreement with experimental trends (Früh & Read 1999; Aguiar *et al.* 2010) such that the observed structures are described by  $k = 4, 5$  and  $6$  at  $Ro = 0.0325, 0.02375$  and  $0.015$ , respectively. For the smallest  $Ro$  case (equivalently smallest  $Re_i$  case) of  $Ro = 0.015$  (figure 6.19(d)), the direct numerical simulation yields a stable wavenumber throughout the linear and nonlinear regime that is in agreement with the linear stability analysis results. This reinforces the trends established in the vicinity of instability onset (§ 6.1). It is clear that as the Rossby number is decreased towards the onset of instability, the nonlinear effects are less evident whereby the energies in each azimuthal wavenumber are not as comparable and the number of sides of the observed stable polygon is increased.

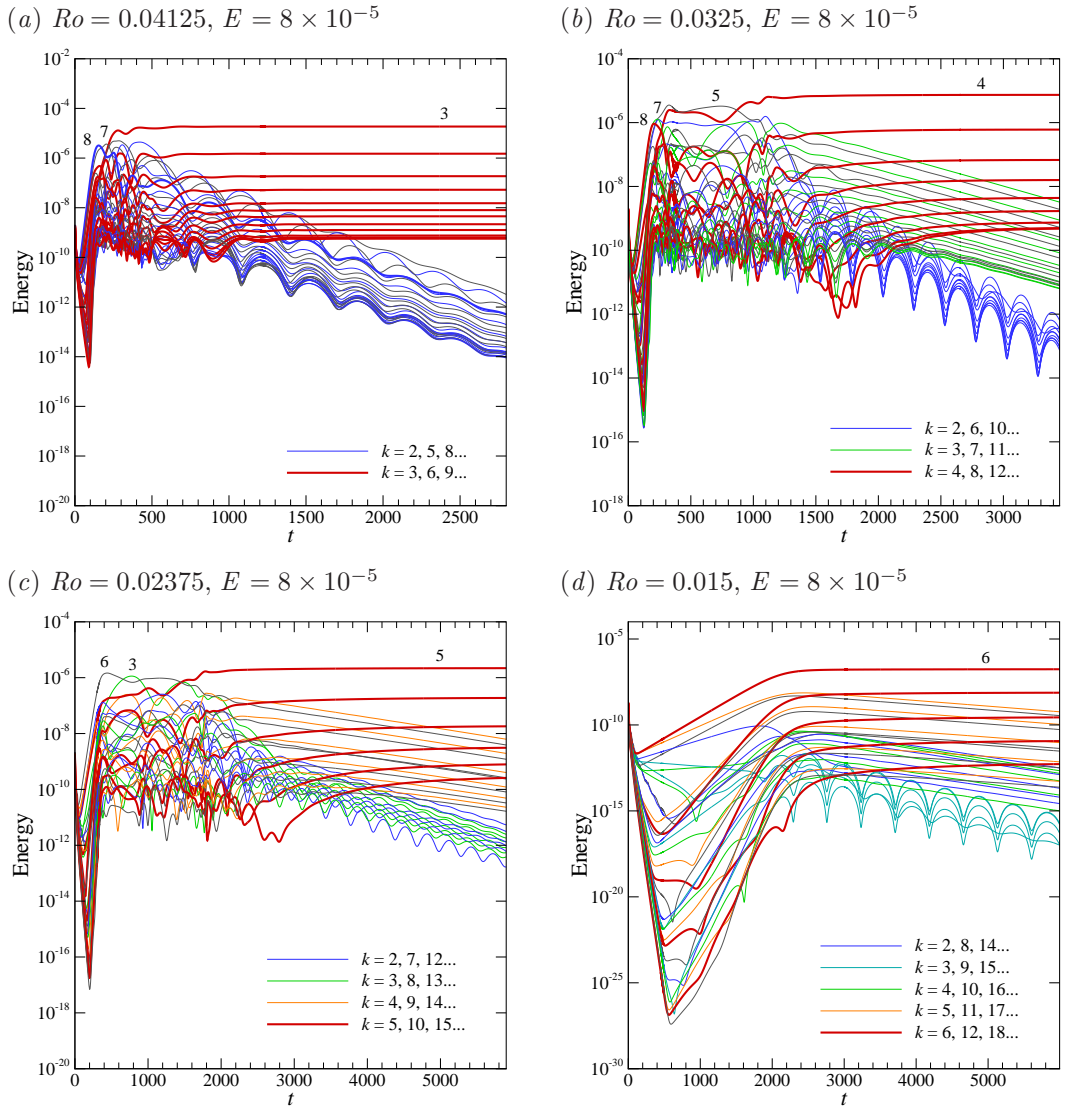


FIGURE 6.19: The energy time histories for flow conditions of (a)  $Ro = 0.04125$ , (b)  $Ro = 0.0325$ , (c)  $Ro = 0.02375$  and (d)  $Ro = 0.015$  at  $E = 8 \times 10^{-5}$ . The first 40, 40, 32 and 32 non-zero wavenumbers are shown for each flow, respectively.

The contours of axial vorticity of the flows described in figure 6.19 are illustrated in figure 6.20. For  $Ro = 0.04125$ , a triangular configuration is observed with spiral-like disturbances of alternating low and high vorticity in the interior and satellite vortices. At this flow condition, the internal Reynolds number is characterised by  $Re_i = 69$ . Decreases to the Rossby number demonstrate a weakening to the strength and presence of the spirals and a thinning of the low vorticity ring bordering the interior polygon.

Figure 6.21 presents a regime diagram of the most unstable linear and nonlinear wavenumbers, and illustrates the trends established in the previous sections. Near the

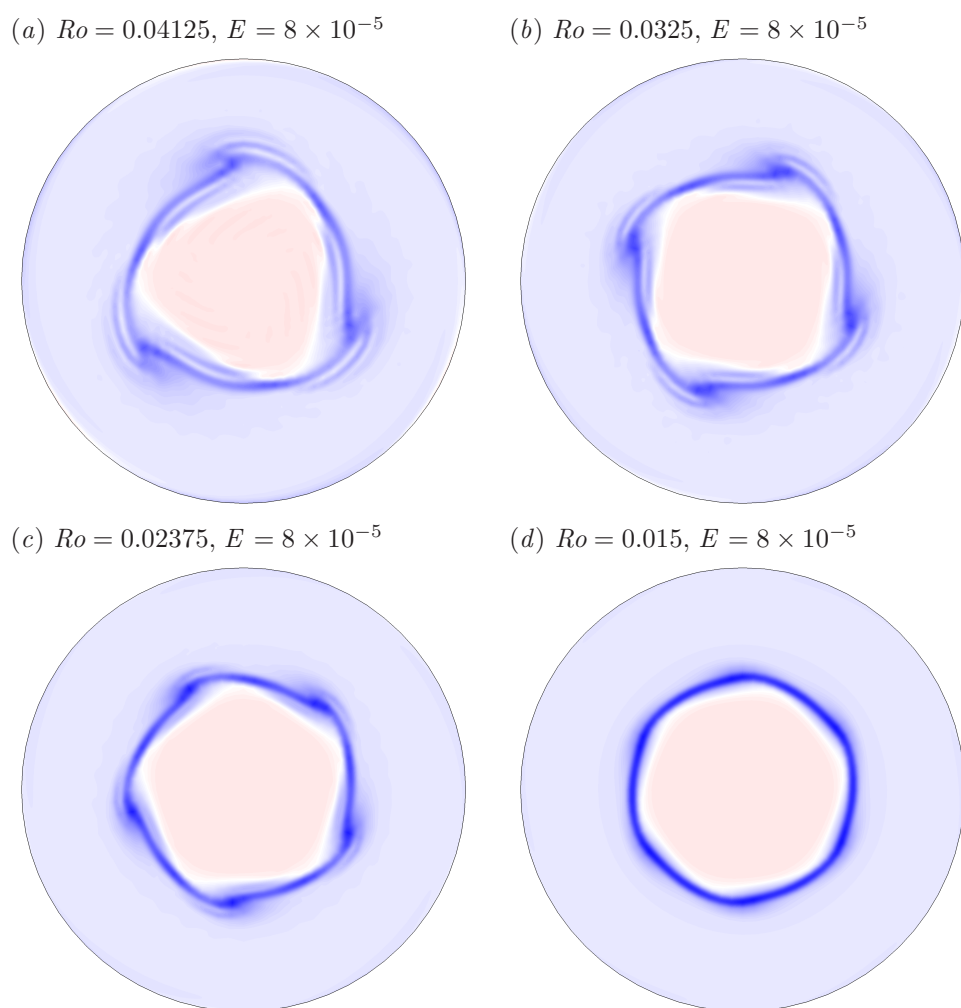


FIGURE 6.20: The mid-depth contours of axial vorticity for (a)  $Ro = 0.04125$ , (b)  $Ro = 0.0325$ , (c)  $Ro = 0.02375$  and (d)  $Ro = 0.015$  and  $E = 8 \times 10^{-5}$ . The contours are shown at  $t = 2800, 3450, 5900$  and  $5995$ , respectively. Contour levels are as per figure 6.2.

---

threshold of instability, the flow is dominated by linear instabilities and portrays a polygonal configuration characterised by the wavenumber predicted by the linear stability analysis. As the flow conditions deviate away from the instability threshold, nonlinear effects cause the satellite vortices to interact and coalesce and hence, demonstrate a lower stable wavenumber than that linear predicted wavenumber. The lowest wavenumber observed in the nonlinear dominant regime was a wavenumber 2 structure coupled with a wavenumber 1 disturbance, labelled as ‘1/2’ on the regime diagram.

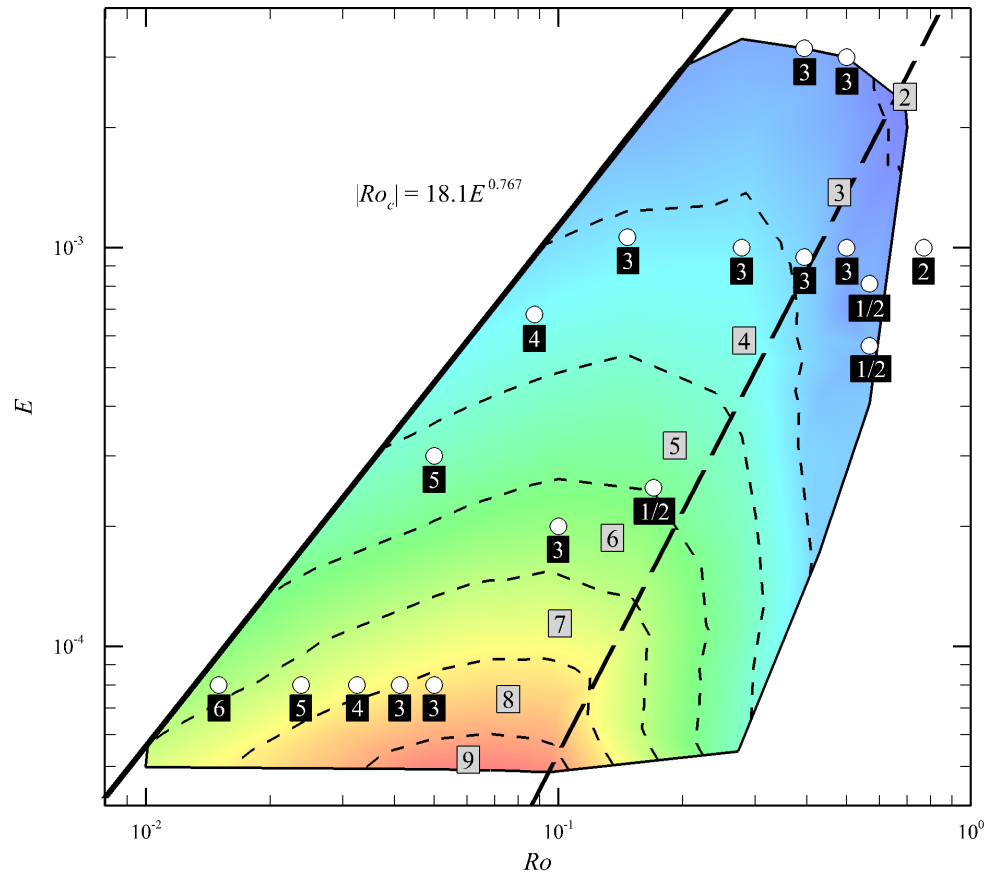


FIGURE 6.21: A regime diagram of the preferred linear wavenumber in the positive  $Ro$ - $E$  parameter space. The solid grey numerical labels on the diagram represent the unstable linear wavenumber associated with the mode I instability while the solid black labels represent the nonlinear preferred wavenumber. The long dashed line represents the transition from reflectively symmetric to symmetry-broken flow defined as  $Re_E = 26.7$ .

## 6.4 Flow sensitivity

The sensitivity of the three-dimensional flow is investigated in this section under two different studies. The first considers initialising the simulation with various initial conditions at constant  $Ro$  and  $E$  to examine the variation of the stable azimuthal wavenumbers observed upon saturation. The second considers changing the Rossby number of a saturated three-dimensional flow to investigate hysteresis effects which have been observed experimentally (e.g. Früh & Read 1999).

### 6.4.1 Perturbing the axisymmetric solution

The saturated three-dimensional flows observed in the previous sections were initialised from the evolved axisymmetric steady-state solution perturbed with white noise. Since many of the prior energy time histories demonstrated a single stable azimuthal wavenumber of very large energy compared to the other wavenumbers, it is expected that different initial conditions of the same flow condition will achieve the same stable solution. In this section, the simulations are initially seeded with various unstable linear mode solutions, with and without white noise.

A flow characterised by  $Ro = 0.5$  and  $E = 3 \times 10^{-3}$  is considered for investigation. This flow condition is marked by a solid black square in figure 6.1. According to the linear stability analysis, the most unstable wavenumber is predicted to be  $k = 3$ . The structure of this linear instability and its related growth rates are shown in figure 6.22(*b*, *c*). A three-dimensional direct numerical simulation has been initialised with its steady-state axisymmetric base flow and white noise, as per previous direct numerical simulation cases. The energies contained in each azimuthal wavenumber over time for the first 23 non-zero wavenumbers are shown in figure 6.22(*c*). The three-dimensional solution agrees with the linear prediction as the energy in the wavenumber 3 structure is dominant during the initial stages of the flow development. The structures of the linear and nonlinear wavenumber 3 are very much similar in appearance. As nonlinear effects become apparent, the even wavenumbers slowly increase in energy over time and eventually surpass the wavenumber 3 structure to become the dominant wavenumber. Thereafter, the wavenumber 2 state is stable. Meanwhile, the energies in the odd-wavenumber structures decay exponentially.

To examine the effect of a different initial condition, the steady-state axisymmetric base flow is seeded with the leading wavenumber 3 instability mode with no additional white noise. Thus, the energies of the wavenumber 3 structure and its harmonics are expected to be the highest during the initial developments of the flow. This is observed in the left panel of figure 6.23(*a*). The other azimuthal wavenumbers exhibit very low energies likely as a disturbance at the limit of machine precision, which grows exponentially over time. The slow growth is attributed to the small linear growth rate that is predicted via the linear stability analysis. Although the simulation has not reached a saturated state over the computed time domain, it is expected that energies in wavenumbers 2 and its harmonics will eventually grow to levels consistent

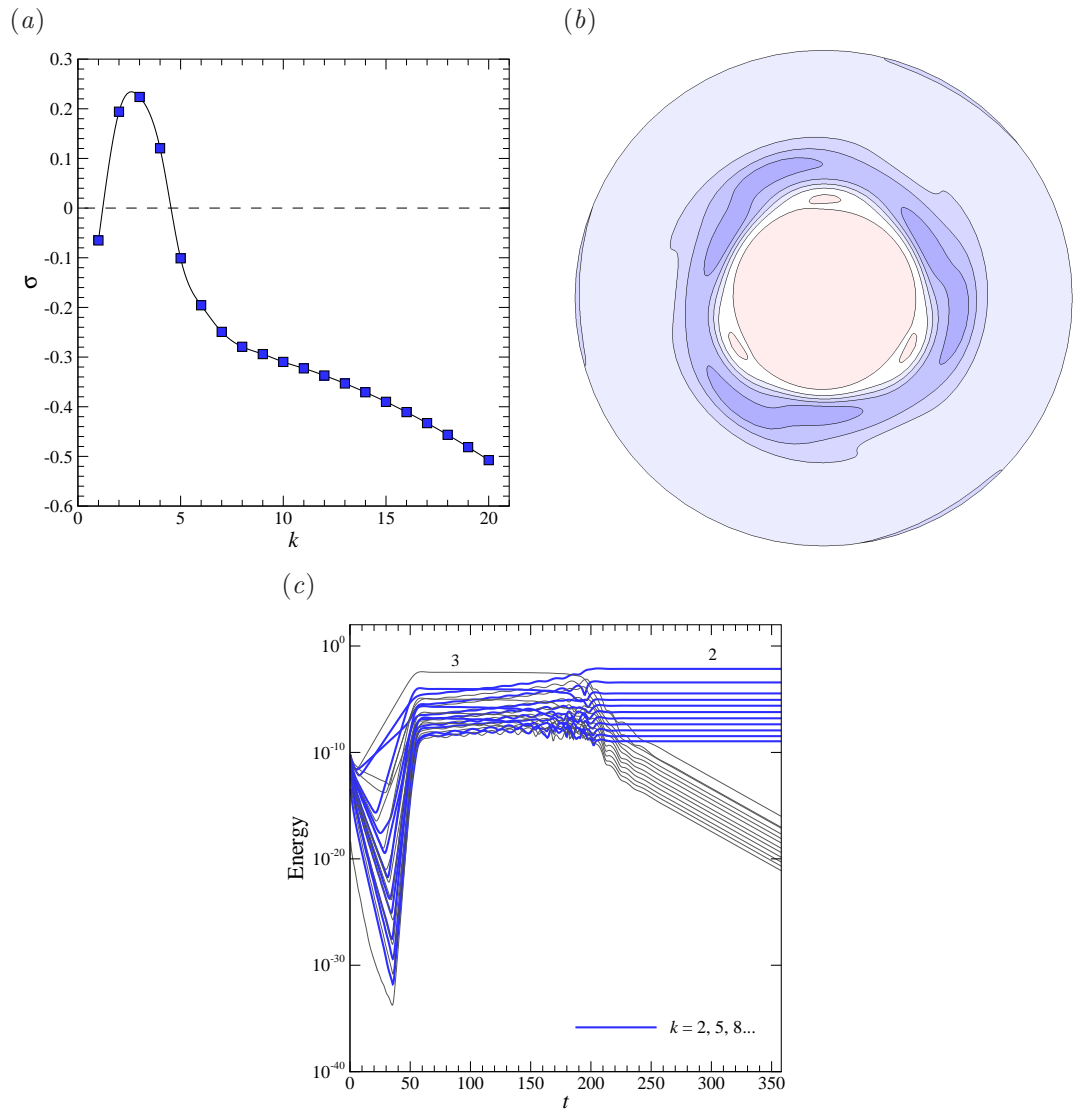


FIGURE 6.22: (a) The growth rates for a range of wavenumbers obtained through linear stability analysis for a flow condition of  $Ro = 0.5$  and  $E = 3 \times 10^{-3}$ . The dashed line represents neutral stability where points above and below symbolise unstable and stable wavenumbers, respectively. (b) Representative axial vorticity contours of linear instabilities of finite amplitude superimposed onto its respective base flow shown at  $z/H = 0.5$ . Nonlinear effects have been neglected. Contour levels are as per figure 6.2. (c) Energies of the first 23 non-zero wavenumbers over time.

with the dominant wavenumber 3 mode. At this point, it would be expected that nonlinear interactions similar to those seen in figure 6.22(c) would ultimately result in wavenumber 2 becoming the dominant stable state. To confirm this, the same case was investigated with the addition of white noise at initialisation. The purpose of the white noise is to provide all of the wavenumbers with finite energy at a level higher than machine error and significantly below nonlinear amplitudes. This accelerates the growth of any unstable wavelengths and greatly reduces the required evolution time to reach a saturated state. This particular case is illustrated in the right panel of figure 6.23(a). As expected, a stable wavenumber 2 structure is achieved at saturation whereby the energies of wavenumber 2 and its harmonics become dominant. The energy of  $k = 3$  and its harmonics have been made bold in the plots to illustrate the dominance of the seeded eigenmode in the starting phases of the flow development. It is clear that the energies of wavenumbers in their respective groups ( $k = 1, 4, 7 \dots$ ,  $k = 2, 5, 8 \dots$  and  $k = 3, 6, 9 \dots$ ) follow a similar growth trend. However, this trend is broken once the dominant wavenumber is changed. Since the primary wavenumber is shifted to  $k = 2$  at  $t \gtrsim 840$ , the initial three groupings of wavenumbers become two groups formed by odd and even wavenumbers. The bolding of odd and even wavenumber energy lines would therefore demonstrate a decay and plateau of energy, respectively, after  $t \approx 840$ .

The decay of energies in odd-wavenumber structures is also demonstrated for the case where a linearly unstable wavenumber 2 is seeded at the start of the simulation. Since it is expected that the flow saturates towards a wavenumber 2 mode, the energies of the even wavenumbers should remain dominant while the energies of the odd wavenumbers should remain very low or decay depending on whether or not white noise is seeded. The energy time histories of these are demonstrated in figure 6.23(b). In the left panel where white noise is not introduced, the energies of odd-wavenumber structures initially express values near the limit of machine precision and are not inclined to grow. Even with the injection of energy into the odd-wavenumber configurations from white noise, the energy time history still demonstrates a decay to machine error over time.

To ensure that the flow is strongly insensitive to initial conditions, several other linear unstable wavenumber solutions (e.g.  $k = 4, 5, 6$ ) have been added to the axisymmetric base flow. After a sufficient time, the wavenumber 2 and its harmonics are the only wavenumbers which contain finite energy. A typical structure of the satu-

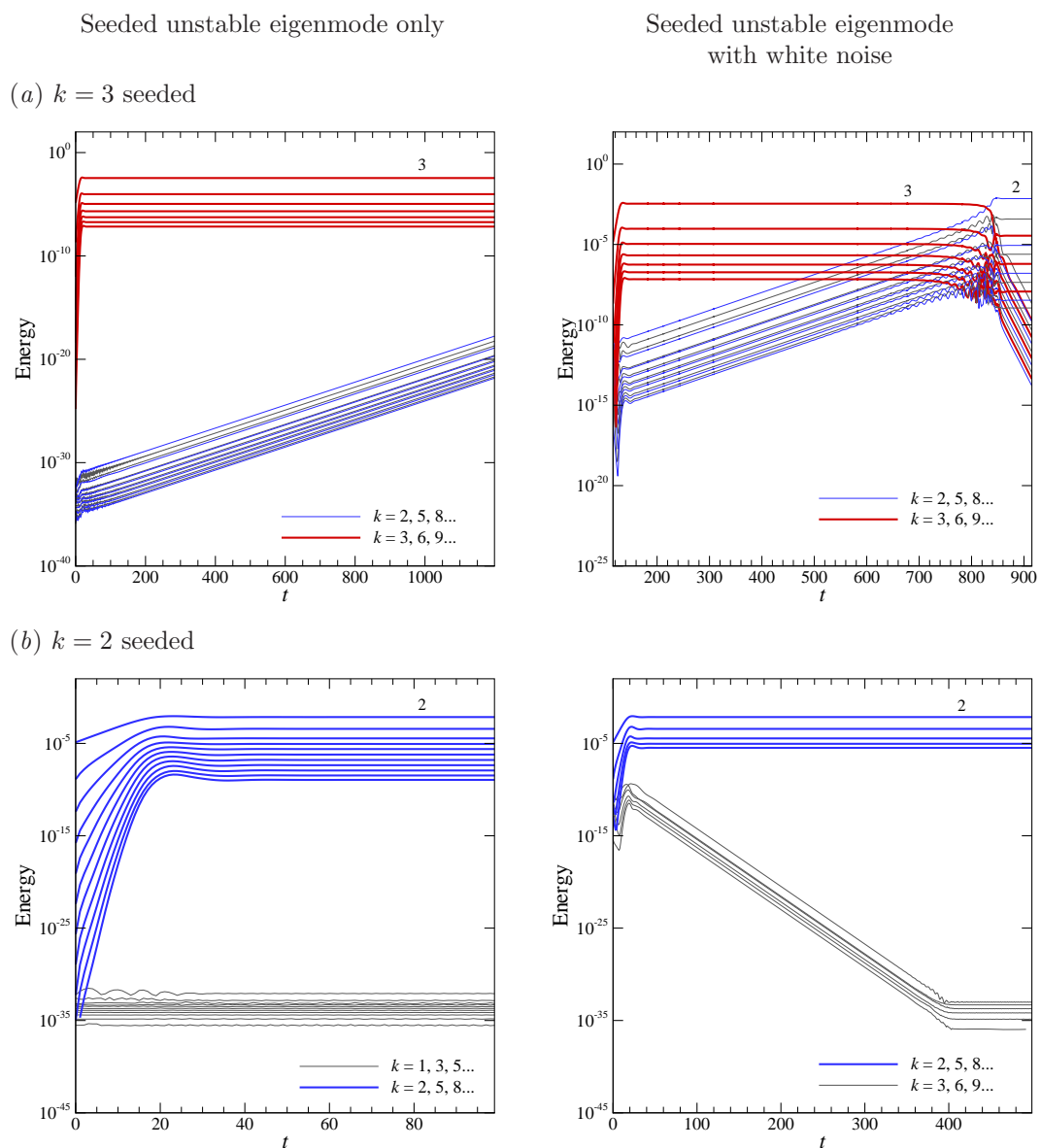


FIGURE 6.23: Energies of various non-zero wavenumbers over time for  $Ro = 0.5$  and  $E = 3 \times 10^{-3}$  initialised with (a) a wavenumber 3 eigenmode solution and (b) a wavenumber 2 eigenmode solution. The left and right columns are flows seeded with the most unstable linear eigenmode only and the eigenmode with white noise, respectively.

---

rated flow is depicted in figure 6.24. This structure resembles the linear solution of a wavenumber 2 structure. Other flow conditions have been tested for their sensitivity to initial conditions and have all shown the same insensitivity characteristics, although not shown here. This type of insensitivity has also been observed by Bergmann *et al.* (2011) who studied a different type of rotating flow. In that study, the sensitivity of the flow was examined through various initial conditions involving a flow starting from rest,

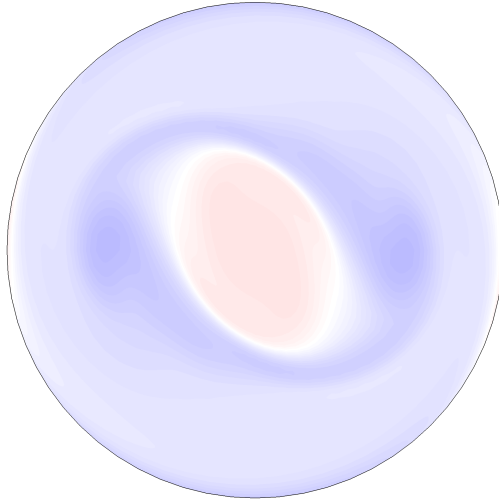


FIGURE 6.24: Contours of axial vorticity at  $z/H = 0.5$  for flow conditions of  $Ro = 0.5$  and  $E = 3 \times 10^{-3}$ . This flow state is representative of the saturated flow regardless of the initial conditions. Contour levels are as per figure 6.2.

---

initialisation by manually disrupting a developed triangular structure and commencing with a high rotation rate such that the flow was axisymmetric. The resultant flow for all three cases exhibited a “dry” triangle which suggests that the flow was insensitive to initial conditions.

#### 6.4.2 Hysteresis effects

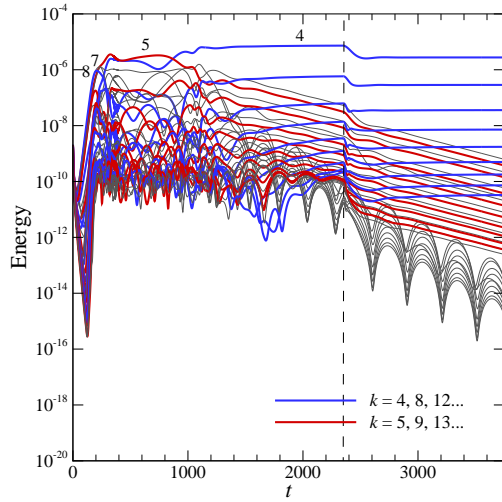
The effect of hysteresis was investigated by changing the forcing conditions of a saturated flow. Two saturated flow conditions of  $Ro = 0.0325$  and  $Ro = 0.02375$  at  $E = 8 \times 10^{-5}$  have been interchanged between each other. The Rossby number is changed instantly from  $Ro = 0.0325 \rightarrow Ro = 0.02375$  and *vice versa* at an arbitrary time that describes a stable saturated flow. These flow conditions are represented by solid blue circles in figure 6.1. The energy time histories of these saturated flow solutions have been depicted in figure 6.19(b) and 6.19(c). Stable wavenumbers 4 and 5 are exhibited in the saturated state for  $Ro = 0.0325$  and  $Ro = 0.02375$ , respectively.

The solution of  $Ro = 0.0325$  and  $E = 8 \times 10^{-5}$  at  $t = 2350$  is used as the initial condition. Although this time does not coincide with the cessation of the simulation shown in figure 6.19(b) ( $t = 3450$ ), the axial vorticity structure between these two times are very similar. At  $t = 2350$ , the flow is dominated by a wavenumber 4 structure with the energy in its harmonics saturating over time while all other wavelengths are decaying.

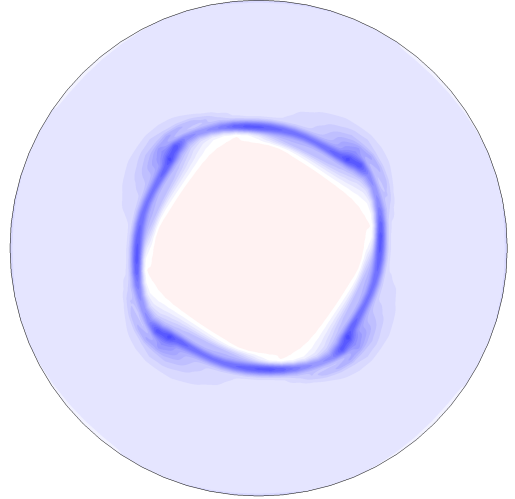
---

(a)  $Ro = 0.0325 \rightarrow Ro = 0.02375$

(i)

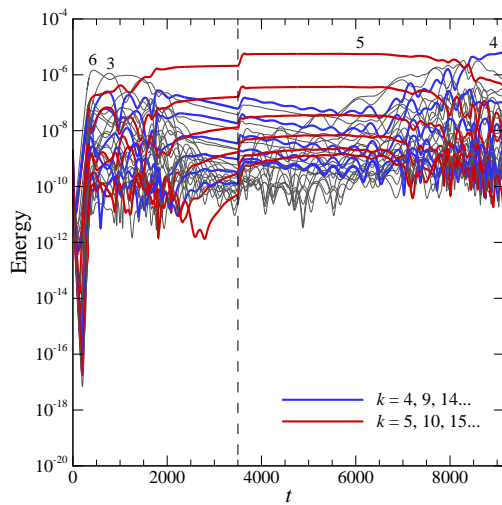


(ii)

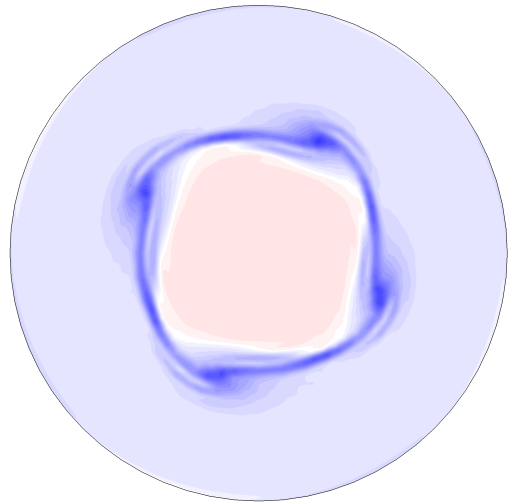


(b)  $Ro = 0.02375 \rightarrow Ro = 0.0325$

(i)



(ii)



---

FIGURE 6.25: The Rossby number is changed from (a)  $Ro = 0.0325 \rightarrow Ro = 0.02375$  and (b)  $Ro = 0.02375 \rightarrow Ro = 0.0325$  with  $E = 8 \times 10^{-5}$ . (i) Energies of various non-zero wavenumbers over time with the change in  $Ro$  occurring instantaneous at  $t = 2350$  and  $t = 3500$ , respectively, which has been marked by a vertical dashed line. (ii) The axial vorticity contours extracted at  $z/H = 0.5$  at  $t = 3750$  and  $t = 9150$ , respectively.

---

As the Rossby number is decreased to  $Ro = 0.02375$ , the energies in each azimuthal wavenumber drop gradually over a short time period. This time is marked by a vertical dashed line as shown in figure 6.25(a). The energies in each wavenumber demonstrates the same trends established before  $t = 2350$ . That is, a stable square configuration is observed and the harmonics of  $k = 5$  approach a plateau. The wavenumber 5 structure, which was determined to be most unstable mode for  $Ro = 0.02375$  (see § 6.3.2), continues to decay. Thus, hysteresis is evident for the flow condition of  $Ro = 0.02375$  and  $E = 8 \times 10^{-5}$ . The contours of axial vorticity at  $z/H = 0.5$  are illustrated in figure 6.25(a)(ii). The vortices precess at a constant frequency of  $f \approx 0.1613$  which is less than twice the frequency of the background flow ( $f = 0.3254$ ). Thus, inertial waves may be present and explain the alternating bands of vorticity in the structure.

The reverse case of increasing the Rossby number from  $Ro = 0.02375$  to  $Ro = 0.0325$  at  $E = 8 \times 10^{-5}$  was also investigated. The energy time history plot is shown in figure 6.25(b) with the change in flow conditions marked by a vertical dashed line at  $t = 3500$ . The increase in  $Ro$  causes a sharp increase in energy for all of the azimuthal wavenumbers. The flow continues to sustain the wavenumber 5 structure over a long period of time with energies from  $k = 4$  gradually decreasing. At approximately  $t = 8000$ , the energies in  $k = 4$  increases and eventually becomes dominant at  $t = 8450$ . Thus, the stable configuration observed is the same as that obtained from initialising the flow from the steady-state axisymmetric base flow with a flow condition of  $Ro = 0.0325$  and  $E = 8 \times 10^{-5}$ . That is, no major hysteresis effects have been observed for this case.

It should be noted that changing the flow from  $Ro = 0.02375$  to  $Ro = 0.0325$  takes 4500 time units for it to adjust to the new preferred state. This corresponds approximately to 3125 hours ( $\approx 130$  days) based on the maximum rotation rate of  $\Omega = 4 \times 10^{-4}$  rad/s considered by Früh & Read (1999), which is a staggering amount of time given the change in the disk speed was only of a couple of percent ( $\Omega + \omega = 1.0322 \rightarrow 1.0442$ ). Thus, in an experimental setting, the rate of change of the continuous forcing must be extremely low, impractically so, to allow the flow to adapt and develop the most stable wavenumber. This is particularly true for flow conditions near the onset of instability since the growth rate of the instability is very small. Keeping the forcing at a constant flow condition would also require long time periods for a stable azimuthal wavenumber to emerge. It is acknowledged that it would be difficult to visually detect or gauge any variables in relation to whether or not the flow has reached a truly saturated

state in the experiments. This is because the flow is still able to exhibit the wavenumber observed prior to the  $Ro$  change for long time periods. For this particular flow, a pentagonal structure is still demonstrated up until  $t = 8150$ . In addition, the remnants of the dye may display a structure that is different to the underlying evolving structure. Aguiar (2008) and Aguiar *et al.* (2010) performed experiments at constant forcing for approximately 30 minutes, which was self-reported by the latter study to be insufficient in reaching a stable flow state for some cases. This is expected to be true mostly at small  $Re_i$  due to the low growth rates. This may further explain the discrepancy observed in the small  $Re_i$  regime between the direct numerical simulation results presented in this chapter and the experimentally generated regime diagrams from Früh & Read (1999). That is, the experimental flows may not have been allowed enough time to saturate (vortex coalescence) and therefore higher stable wavenumber structures were reported instead.

## 6.5 Bifurcation analysis

The hysteretic nature of the three different linear instability transitions, namely the mode I, II and III have been investigated. The Stuart–Landau model has been applied to the most unstable linear wavenumber and its harmonics. The nonlinear behaviour is determined through the sign of the  $l$  parameter. The Stuart–Landau model has been described previously in § 3.6. The restriction of simulating a particular wavelength and its harmonics is achieved numerically through a truncation of the azimuthal range of the domain to exactly fit the wavelength of interest. As a consequence of the axisymmetry of the domain, only the considered wavenumber and its harmonics are able to fit perfectly in the truncated domain. Each numerical study has been initiated with the axisymmetric base flow solution seeded with the most unstable eigenmode with very small amplitudes.

### 6.5.1 The mode I transition

The transitional behaviour of the mode I instability of  $Ro = 0.05$  and  $E = 3 \times 10^{-4}$  is investigated. This flow point corresponds to the reference flow condition and is marked by a solid black circle in figure 6.1. A plot of the growth rate against wavenumber is shown in figure 6.2, which illustrates the existence of only the mode I instability and is most unstable to a wavenumber 5 configuration.

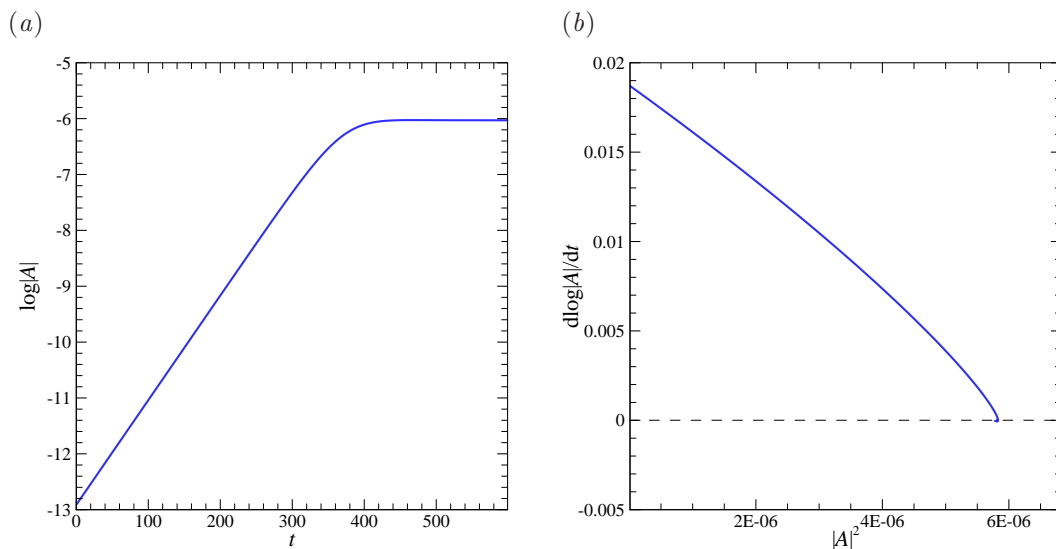


FIGURE 6.26: Flow conditions described by  $Ro = 0.05$  and  $E = 3 \times 10^{-4}$ . (a) Amplitude of the most unstable isolated mode corresponding to wavenumber 5 against time. (b) The rate of change in amplitude over time against the square of the amplitude. A negative linear gradient at the vertical axis indicates that the transition is supercritical.

The mode transition is determined to be supercritical, which can be illustrated through figure 6.26. The plots are of  $\log|A|$  over time and  $d\log|A|/dt$  against  $|A|^2$  for the  $k = 5$  instability. Initially, the amplitude of the wavenumber 5 instability is small and grows exponentially in time until it saturates at approximately  $t = 440$ . This exponential trend is representative of the linear regime, which is required to obtain an accurate gradient near the vertical axis in figure 6.26(b). The gradient at the vertical axis corresponds to the  $l$  parameter in the Stuart–Landau equation. The slope is calculated to be  $l = 4.55 \times 10^{-6}$ , which corresponds to a negative slope (the negative sign in front of  $l$  is inherited from the Stuart–Landau equation). This indicates that the mode transition is supercritical and is in agreement with the results of Früh & Read (1999), van de Konijnenberg *et al.* (1999) and Bergeron *et al.* (2000). The  $d\log|A|/dt$  curve terminates on the horizontal axis as the mode saturates. The intercept of the vertical axis has a value of 0.0187, representing the growth rate of the linear instability mode. This growth rate value is identical to that determined by the linear stability analysis (see figure 6.2(a)).

A range of other flow conditions that are dominated by the mode I instability have also been investigated. The same analysis using the Stuart–Landau model determined

the transition of the mode I instability to be supercritical consistently. Also, the growth rate predicted by the linear stability analysis demonstrates a strong agreement with those calculated from the Stuart–Landau model.

### 6.5.2 The mode II, III and $\beta$ -plane transition

A flow condition of  $Ro = 0.395$  and  $E = 5.26 \times 10^{-4}$  is investigated to study the transitional behaviour of the mode II linear instability. This flow point is marked by a solid grey circle in figure 6.1. The most unstable wavenumbers associated with modes I and II predicted by the linear stability analysis are  $k = 3$  and  $k = 29$ , respectively. The growth rate associated with wavenumber 29 is greater than that of wavenumber 3. That is, this flow condition is dominated by a mode II linear instability mode. In this particular case, the transition of the mode I and II instabilities are also determined to be supercritical. Plots of  $\log |A|$  over time and  $d \log |A|/dt$  against  $|A|^2$  for  $k = 29$  are shown in figure 6.26. The energy contained within the wavenumber 29 structure increases exponentially from initialisation at  $t = 0$  to  $t = 18$ , and plateaus over time. This results in an initial negative gradient in figure 6.26(b), which indicates that the instability is supercritical. Here,  $l = 2.46 \times 10^{-4}$  and the intercept of the vertical axis has a value of  $d \log |A|/dt = \sigma = 0.459$ . The growth rate of wavenumber 29 predicted by the linear stability analysis is determined to be  $\sigma = 0.458$ .

The same features are observed for the mode III instability. This is investigated for the flow condition of  $Ro = 0.5$  and  $E = 3 \times 10^{-4}$ , which is most linearly unstable (highest growth rate) to a wavenumber that is associated with mode II. However, there is an emergence of the mode III instability with growth rates that are comparable to wavenumbers belonging to mode I (see figure 5.2). The  $k = 9$  structure exhibits the highest exponential growth rate of the mode III waveband with  $\sigma = 0.4807$ . The value of the  $l$  parameter for this wavelength is determined to be  $l = 1.028 \times 10^{-5}$  with the same growth rate predicted by the linear stability analysis. The positive constant determines that the flow transition is supercritical.

The Stuart–Landau model has been applied to a variety of flow conditions that encourages the growth of all the three different instability modes. The  $l$  parameter has been determined to be positive in all flow cases, which suggest that the weakly nonlinear mode evolution behaviour in this type of rotating flow is supercritical. In addition, the flow transitions on a  $\beta$ -plane ( $0^\circ < \theta \leq 10^\circ$ ) also demonstrated the same bifurcation

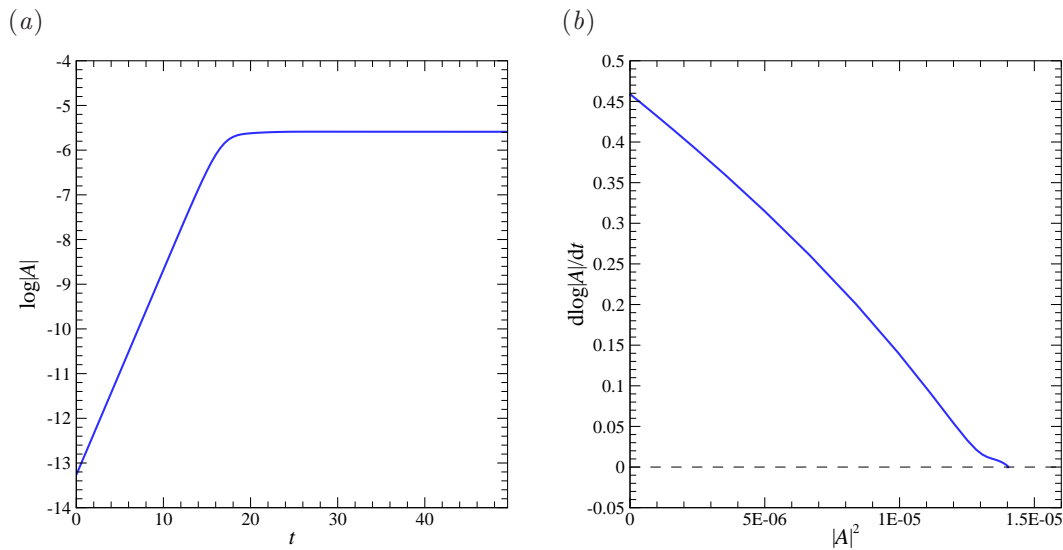


FIGURE 6.27: Flow conditions described by  $Ro = 0.395$  and  $E = 5.26 \times 10^{-4}$ . (a) Amplitude of the most unstable isolated mode corresponding to wavenumber 29 against time. (b) The rate of change in amplitude over time against the square of the amplitude. A negative linear gradient at the vertical axis indicates that the transition is supercritical.

---

characteristics. The Stuart–Landau model consistently described the growth rate very well in comparison to the linear stability analysis technique employed. This confirms and extends the experimentally determined supercritical behaviour detected for low-wavenumber instability by Fröh & Read (1999), van de Konijnenberg *et al.* (1999) and Bergeron *et al.* (2000).

## 6.6 Chapter summary

The non-axisymmetric three-dimensional flows generated in a differential-disk rotating system with an aspect ratio of  $A = 2/3$  have been investigated in this chapter. The primary purpose was to establish trends and draw comparisons with the results from the linear stability analysis presented in the previous chapter as well as the experimental trends. The energy in each azimuthal wavenumber was monitored during the flow development. Typically, the energy time history of the flow illustrates exponential growth in the initial stages of the flow (linear regime) and saturated growth in the later stages (nonlinear regime). Only the positive- $Ro$  regime was examined.

Flows characterised by small  $Re_i$  near the onset of instability ( $Re_{i,c} \approx 22.4$ ) were firstly investigated to establish a reference case. In the linear regime, the wavenumber

that contains the most energy usually corresponded to the most unstable wavenumber predicted by the linear stability analysis. However, there were instances where the unstable wavenumber in the linear regime differed by a few wavenumbers. This is due to the white noise seeded in the flow at initialisation, which feeds energy into every wavelength. Thus, it is possible that a wavenumber that is not the most linearly unstable by prediction of the linear stability analysis may be favoured in the initial developments of the flow. Despite this, linearly preferred wavenumber eventually dominates and stabilises in the nonlinear regime. Thus, nonlinear effects are considered negligible near the onset of instability. The structure of the resulting polygon is largely depth-independent when viewed through axial vorticity contours, similar to those described by the axisymmetric base flows in the same parameter regime.

Flows well beyond the onset of instability achieved by either increasing the Rossby number or decreasing the Ekman number were investigated to examine nonlinear effects. The dominant wavenumber in the linear regime was still agreeable with the results from the linear stability analysis. However, with the onset of nonlinear effects, the highest exhibited energy is quickly shifted to lower-wavenumber structures. This occurs through the coalescence of vortices. In fact, the appearance of the flow structure at the saturated state may be distorted as a result of multiple wavelengths of comparable energy competing with each other. Therefore, flows at sufficiently large  $Re_i$  portray a preference to low-wavenumber structures, which is in agreement with experimental studies (e.g. Früh & Read 1999; van de Konijnenberg *et al.* 1999; Aguiar *et al.* 2010). In addition, the contours of axial vorticity displayed alternating bands of low and high vorticity structures in the interior and satellite vortices. It is suggested that these strands have been induced by another type of instability that is present throughout the entire depth of the tank, possibly related to inertial waves.

The three-dimensional flows characterised by various  $Ro$  in the low and large  $E$  regimes reinforced the trends observed in the prior sections. That is, decreasing  $Ro$  towards the onset of instability yields a saturated wavenumber that is described by the linear stability analysis while increasing  $Ro$  away from the onset of instability decreases the resulting wavenumber. For flow conditions that describe depth-dependent axisymmetric base flows, the three-dimensional direct numerical simulation demonstrates strong depth-independent features. Furthermore, the mode II linear instabilities appeared to have no influence on the stable structure in the nonlinear regime. Despite

their dominance throughout the linear regime, the energies of the wavenumbers associated with the mode II instability quickly decayed as the amplitudes of the structures became large.

The saturated flows demonstrated a strong insensitivity to initial conditions, provided the flow does not change its Rossby and Ekman number. The flows eventually developed the same stable azimuthal wavenumber despite the flow being initially seeded with different unstable wavenumbers of large amplitude. However, changing the Rossby and Ekman number during the development of a flow has exhibited hysteresis effects such that a particular flow condition is associated with multiple stable azimuthal wavenumbers. Lastly, the transition of the mode I, II and III linear instabilities were determined to be supercritical on both the  $f$ -plane and  $\beta$ -plane configurations.

In general, the results of the three-dimensional direct numerical simulation revealed the long time periods required for these rotating flows to reach a stable state. In many cases, the corresponding physical time based on a maximum rotation rate of  $\Omega = 4 \times 10^{-4}$  employed by Fröh & Read (1999) was in the order of months! Thus, these results suggest that the experimental results reported in the literature may not be representative of the eventual stable state, especially those near the onset of instability. It should also be stated that many of the numerical simulations presented in this chapter have been computed over the time period of many physical months, some closing in on a year.

The next chapter explores many of the aspects detailed in the last three chapters using a quasi-two-dimensional model. Specifically, the axisymmetric base flows, their linear stability, and the resulting non-axisymmetric flows are investigated. The similarities and differences observed between the axisymmetric model, three-dimensional model and the quasi-two-dimensional model are examined. In turn, the validity of the quasi-two-dimensional model which has been the only model used to simulate these flows in past numerical studies, is discussed.

## Chapter 7

# Quasi-two-dimensional modelling

In the previous chapters, the flow inside a differential-disk rotating apparatus has been numerically modelled using axisymmetric and three-dimensional simulations. Due to high computation cost required to implement these models, particularly the three-dimensional simulations, previous numerical studies have considered a more efficient quasi-two-dimensional model to represent the flow. In this chapter, the flow in the differential-disk rotation system described in the previous chapters is investigated using a quasi-two-dimensional model. The flow is computed on a two-dimensional  $r$ - $\theta$  plane, with friction from the Ekman layers on the horizontal boundaries being captured by a linear friction term. That is, the flow is governed by the two-dimensional quasi-geostrophic equations (equation 3.62). Hence the axisymmetric flows described in Chapter 4 reduce to one-dimensional problems, while the non-axisymmetric flows described in Chapter 6 reduce to two-dimensional problems, greatly reducing the computational cost required to solve the flows.

A key objective of this chapter is to investigate the performance of the quasi-two-dimensional model in comparison with simulations of the full system. In particular, what effect does the  $E^{1/3}$  Stewartson layer have on the flow, given that it is excluded from the quasi-two-dimensional model. A review of the differences between the quasi-two-dimensional model and the axisymmetric model regarding the base flow structures are demonstrated in § 7.2. The linear stability of the base flows are explored in § 7.3. § 7.4 reveals the effect of imposing a smoothed forcing condition which is also implemented in the study of non-axisymmetric structures in § 7.5.

## 7.1 Grid independence study

The axisymmetric quasi-two-dimensional flows are computed on a quasi-one-dimensional domain. A bi-exponential profile is implemented for the radial discretisation of 21 vertices at the corner of elements, similar to that adopted by the two-dimensional semi-meridional  $r$ - $z$  domain, which achieved solution convergence (§ 4.1). The smallest radial edge of an element is 0.0183. A different mesh is used to simulate the non-axisymmetric quasi-two-dimensional flows. These non-axisymmetric flows are computed on a two-dimensional  $r$ - $\theta$  plane, as described in § 3.7.2. The mesh is comprised of 4000 elements with 56 element vertices along the radial direction. The radial element vertices are densely populated around  $r = 1$  to accurately capture the structure of the shear layer with the smallest radial difference of 0.0172. The number of elements stated here refer to the macro elements, which does not count the collocation points within elements.

To ensure grid independence, the convergence of several global parameters have been computed. A reference case featuring a small  $E = 5 \times 10^{-5}$  and a large  $Ro = 0.3$  is considered. This case is representative of where the flow remains quasi-two-dimensional and encapsulates very thin shear layers. Thus, a high degree of spatial resolution is required in order to capture the presence of the shear layers. Achieving grid independence for this case ensures solution accuracy for higher  $E$  cases as well as lower  $Ro$ . The aspect ratio considered in this chapter is the same as the Früh & Read (1999) configuration, which was the primary aspect ratio investigated in the previous chapters, namely  $A = 2/3$ .

Three measures for convergence have been adopted: the integral of the azimuthal velocity relative to the tank ( $u_{\theta,\text{rel}} = u_{\theta} - \Omega r$ ) across the domain, the leading eigenvalue magnitude obtained by the linear stability analysis of a perturbation with peak fractional azimuthal wavenumber  $k = 11.5$ , and the  $L_2$  norm taken as the integral of the velocity magnitude throughout the domain. The values are obtained once the base flow has reached steady-state conditions. The relative percentage error  $\varepsilon$  against a high-resolution reference case with element polynomial degree  $N_p = 14$  is plotted in figure 7.1. The results demonstrate a decreasing error with increasing  $N_p$ . A threshold criterion of  $O(1\%)$  is sought to ensure that solution error due to finite spatial resolution is much smaller than likely laboratory sources of error. This is approximately satisfied with  $N_p = 6$ , which is used hereafter. It should be noted that for this particular case, an

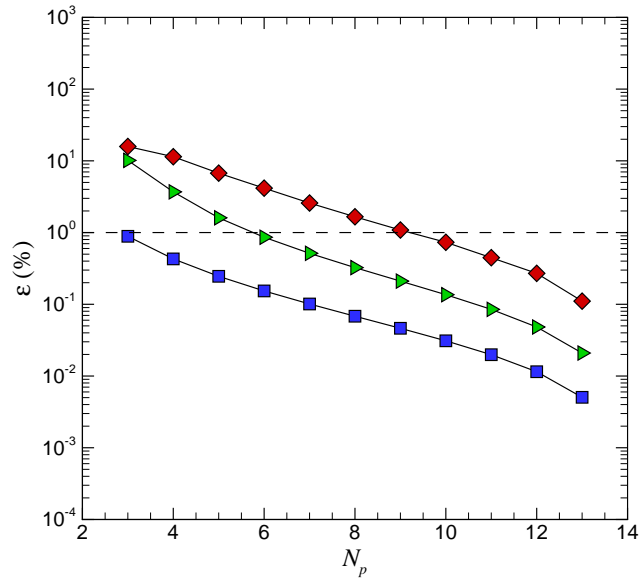


FIGURE 7.1: The relative percentage error  $\varepsilon$  in the global variables of the integral of the relative azimuthal velocity ( $\square$ ),  $L_2$  norm ( $\triangleright$ ) and the leading eigenvalue magnitude ( $\diamond$ ) of the case study  $(Ro, E) = (0.3, 5 \times 10^{-5})$ . A decreasing trend with increasing polynomial degree  $N_p$  is seen with all variables. An error of  $\varepsilon = 1\%$  is marked by the horizontal dashed line.

error of 4% (0.5/11.5) or higher is required at this fractional peak wavenumber in order for the preferential wavenumber to shift in integer value. This is satisfied with  $N_p = 6$ . The thicknesses based on the axial vorticity and azimuthal velocity demonstrated no change above  $N_p = 4$  and  $N_p = 5$ , respectively.

## 7.2 Quasi-two-dimensional axisymmetric flow structure

A variety of flow conditions for  $A = 2/3$  were obtained using the quasi-two-dimensional model. Time-evolved solutions are taken to be steady-state when velocity variations are less than  $10^{-12}$  between successive time steps. Due to the employment of a two-dimensional (quasi-one-dimensional) mesh used to capture the quasi-two-dimensional solutions, a zero variance in the axial direction is not strictly enforced (further details regarding the mesh can be found in § 3.7.2). Hence it was possible to use any loss of depth independence as an indication that the result was invalid and should be discarded. Such events were observed only at very large  $Ro$  and small  $E$ . It is further required that the radial and axial velocities and the radial and azimuthal components of vorticity are zero throughout the entire domain, which follows from the incompressible constraint and the forcing conditions imposed on the flow. Simulations are predominantly performed

for Rossby numbers between  $-1.0 \leq Ro \leq 0.6$  and Ekman numbers between  $3 \times 10^{-5} \leq E \leq 3 \times 10^{-3}$ .

Illustrations of the quasi-two-dimensional flow solutions are provided in figure 7.2(a), with  $Ro = 0.5, -1.0$  and  $-2.0$  for  $E = 3 \times 10^{-4}$ . Contours of azimuthal velocity and axial vorticity demonstrate perfect depth invariance as the one-dimensional solution is projected across the  $z$ -direction for visualisation purposes. For  $Ro = 0.5$ , the flow reveals a strand of negative vorticity at  $r = 1$  which corresponds to the radial location of the disk-tank interface. The entire shear layer remains positive for the  $Ro = -1.0$  case, which reinforces the idea that the negative-vorticity strand is induced by the decrease in angular velocity with increasing radius across the disk-tank interface. Negative axial vorticity is produced on the entire inner side of the Stewartson shear layer (closer to the axis of rotation) for  $Ro = -2.0$  in addition to the negative azimuthal velocity across the same radial extent.

The same flow conditions have been solved through the axisymmetric model and are shown in figure 7.2(b) (partial reproduction of figures 4.2 and 4.3). It is seen that the axial invariance of the flow is broken at  $Ro = 0.5$  in the axisymmetric model through the presence of the diagonal negative-vorticity strands originating from the disk-tank interface. The negative-vorticity strands in this case do not extend the entire depth of the tank and are not parallel to the axis of rotation. This illustrates a key difference between the quasi-two-dimensional model and the axisymmetric model, as the former cannot resolve depth-dependent flow features. Here the contour lines of azimuthal velocity are not perfectly vertical, especially in the vicinity of the Stewartson layer. For  $Ro = -1.0$ , the axial vorticity contours are largely depth-independent although the effects of the Ekman layers cause depth-dependent features near the horizontal boundaries. Another illustration of the difference in base flow structure between the quasi-two-dimensional and the axisymmetric model is shown for the case of  $Ro = -2.0$ . The axisymmetric flow solution presents negative patches of vorticity on the inner side of the vertical shear layer in addition to the thin negative-vorticity boundary layer along the horizontal. The interior region of  $r < 1$  exhibits both positive and negative axial vorticity. However, the quasi-two-dimensional flow exhibits only negative axial vorticity for  $r < 1$ . The depth-dependent structure is also demonstrated through the azimuthal velocity contour lines. It has been proposed in previous chapters (Chapters 4 and 5) that the breaking of the depth independence in the flow may be linked to the

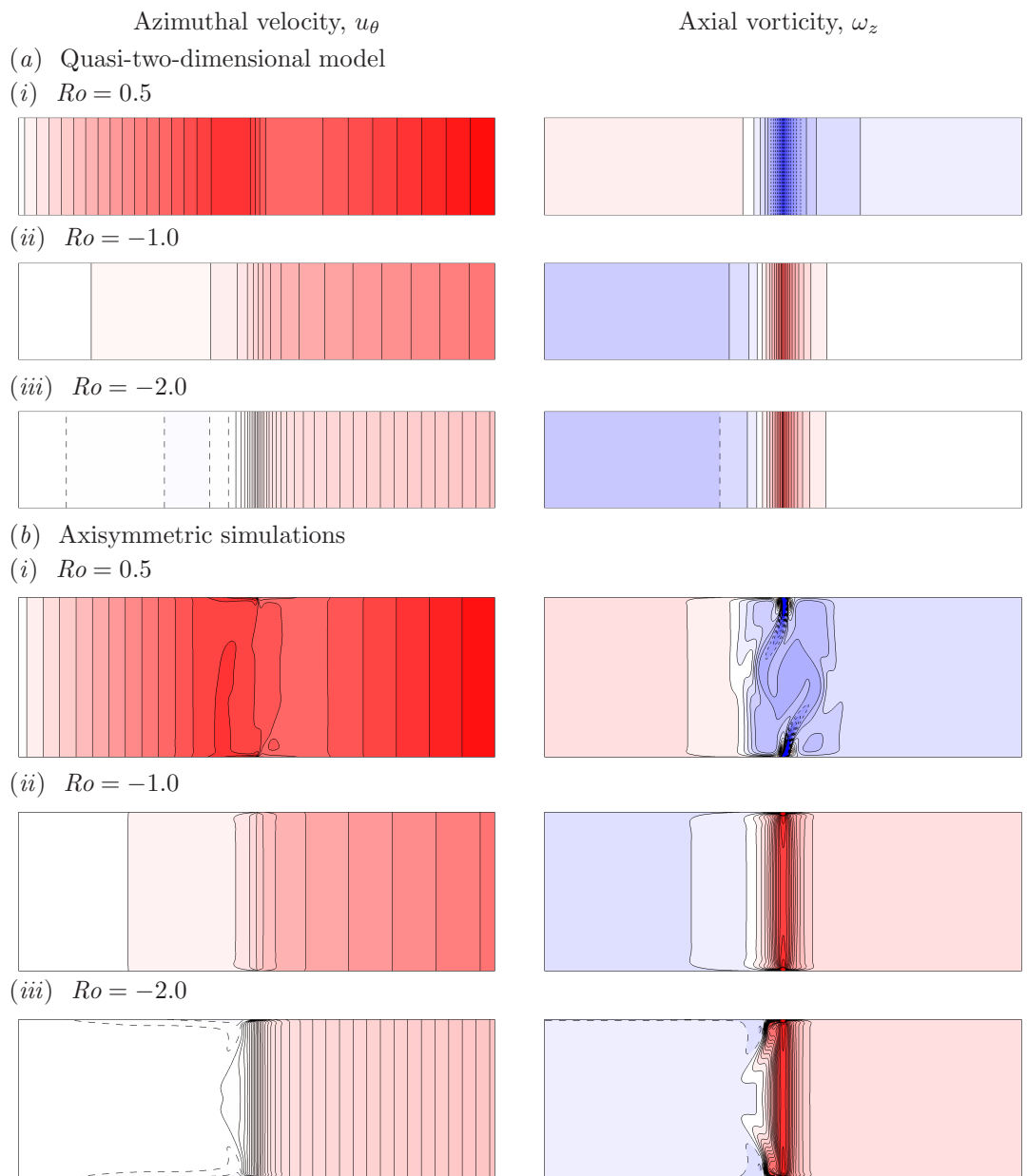


FIGURE 7.2: Structure of the axisymmetric flows visualised on the semi-meridional  $r$ - $z$  plane. Azimuthal velocities (left) and axial vorticity (right) are shown for  $E = 3 \times 10^{-4}$  at (i)  $Ro = 0.5$ , (ii)  $Ro = -1.0$  and (iii)  $Ro = -2.0$ . The flow solutions from the (a) quasi-two-dimensional model and (b) axisymmetric model are shown. For the azimuthal velocity plots, equi-spaced contour levels are plotted between  $\pm 2 |Ro| (|\Omega| + |\omega|)$ , while for the axial vorticity plots, equi-spaced contour levels are plotted between  $2\bar{\Omega} \pm 10|\omega|$ . Blue and red contour shading represent negative and positive values, respectively, while solid and dashed contour lines identify positive and negative contour levels, respectively. The domain shown represents the entire semi-meridional plane with  $0 \leq r \leq 2$ . Images are not to scale.

mode II linear instability. As depth independence is implicit in the quasi-two-dimensional model, the mode II instability is not expected to emerge in the linear stability analysis of the quasi-two-dimensional model.

### 7.2.1 Vertical shear-layer profile and thickness

Profiles of the azimuthal velocity relative to the tank and axial vorticity have been extracted from the quasi-two-dimensional flow solutions. Typical profiles of these two flow variables for  $E = 3 \times 10^{-4}$  are shown in figure 7.3. The profiles are also extracted from the axisymmetric solutions for comparison. The relative azimuthal velocity profile are very similar between the two models which is expected since the quasi-two-dimensional does not directly affect the azimuthal component of the flow. The profile demonstrates solid body rotation at a rate higher than that of the tank for the majority of  $r < 1$  while the fluid rotates at the tank rate for  $r > 1.3$ . The transition from the disk rotation rate to the tank rotation rate is achieved through the  $E^{1/4}$  Stewartson shear layer. Distinct differences between the two models are seen in the profiles of axial vorticity (figure 7.3(b)). There is no smoothing of the axial vorticity in the quasi-two-dimensional model flows since there is no meridional circulation. Within the shear layer, the axial vorticity either increases or decreases rapidly with a sharp change in gradient at  $r = 1$ . This behaviour is not seen in the axisymmetric solution as the vorticity is smoothed out via the  $E^{1/3}$  shear layer. Thus, the minimum axial vorticity value from the quasi-two-dimensional model is much lower compared to the axisymmetric solution. The presence of the sharp turning point in axial vorticity profile suggests that the flow may be susceptible to barotropic instability via the Rayleigh–Kuo criterion. That is, the radial derivative of the absolute axial vorticity changes sign somewhere within the domain.

Since there is no depth dependence in the quasi-two-dimensional modelling, there cannot be any meridional circulation within the flow. Hence, the thin  $E^{1/3}$  layer is not resolved. Therefore, the only shear layer that exists in quasi-two-dimensional flows is the  $E^{1/4}$  layer which functions to smooth out the azimuthal velocity. The discontinuity in velocity originates from the external forcing term employed to model the frictional effects invoked by the Ekman layers. Measurements for the Stewartson layer thickness were conducted using the same method performed for the axisymmetric two-dimensional base flows (§ 4.2.2). That is, the  $E^{1/4}$  layer thickness is defined as the difference in radial

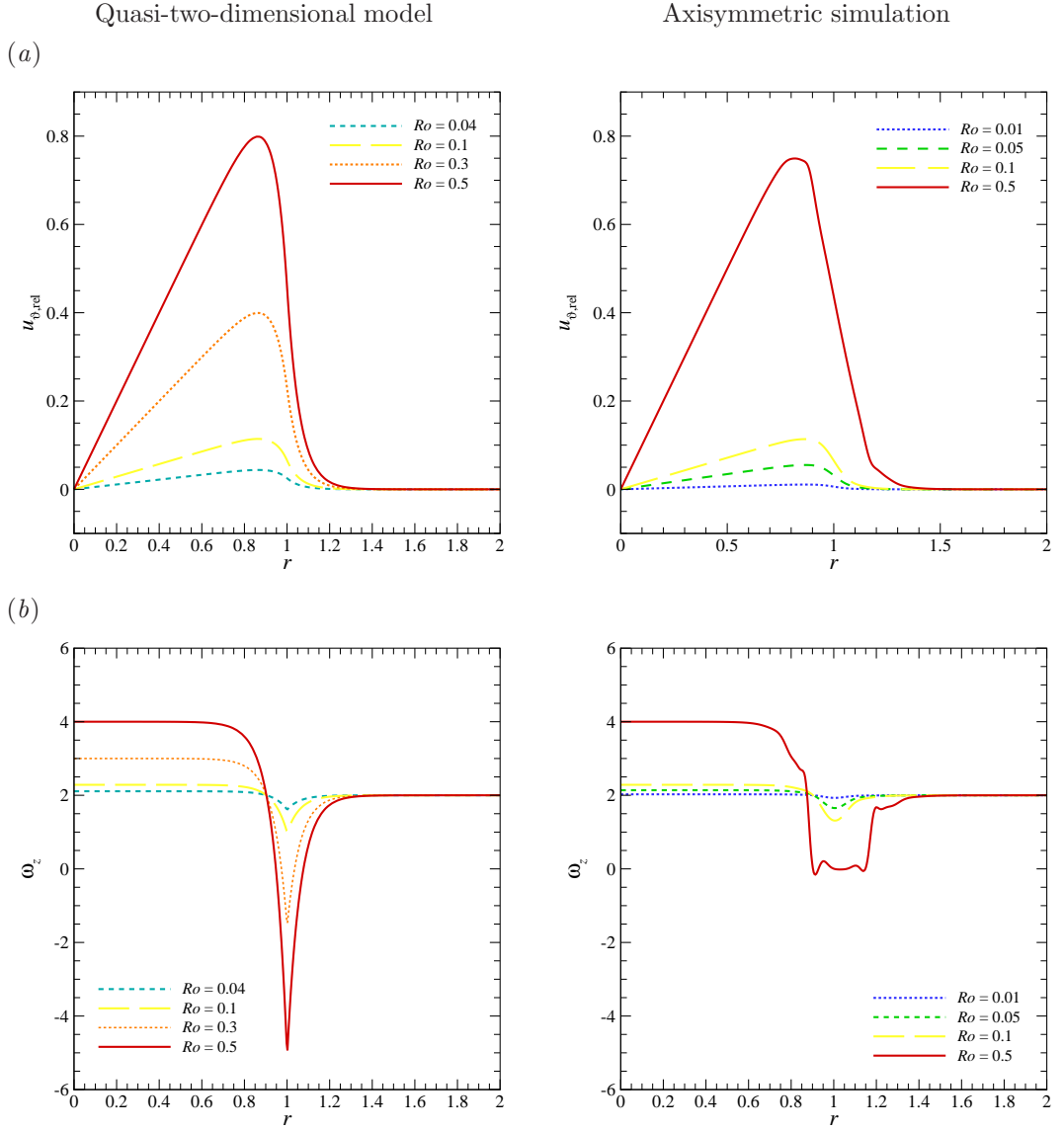


FIGURE 7.3: (a) Azimuthal velocity relative to the rotating tank against radius extracted at  $z/H = 0.5$  and (b) the axial vorticity profiles for  $E = 3 \times 10^{-4}$  at various  $Ro$ .

locations corresponding to  $(u_{\theta-\text{rel,max}} - 0.05\Delta u_{\theta-\text{rel}})$  and  $(u_{\theta-\text{rel,min}} + 0.05\Delta u_{\theta-\text{rel}})$ , where  $\Delta u_{\theta-\text{rel}}$  is the difference between the maximum and minimum values of relative azimuthal velocity. The empirical relationship between the thickness of the  $E^{1/4}$  layer  $\delta_{\text{vel}}$ , and  $E$ , is determined as  $\delta_{\text{vel}} = 1.32E^{0.219}$  which considers both the positive and negative- $Ro$  data. It is noted that the thicknesses do not differ between the positive and negative Rossby number of  $|Ro| = 0.005$ . Not surprisingly, this is extremely close to the relationship obtained for the axisymmetric flow cases, which was found to be  $\delta_{\text{vel}} = 1.31E^{0.22}$  when considering both positive and negative- $Ro$  flows. Thus, for any

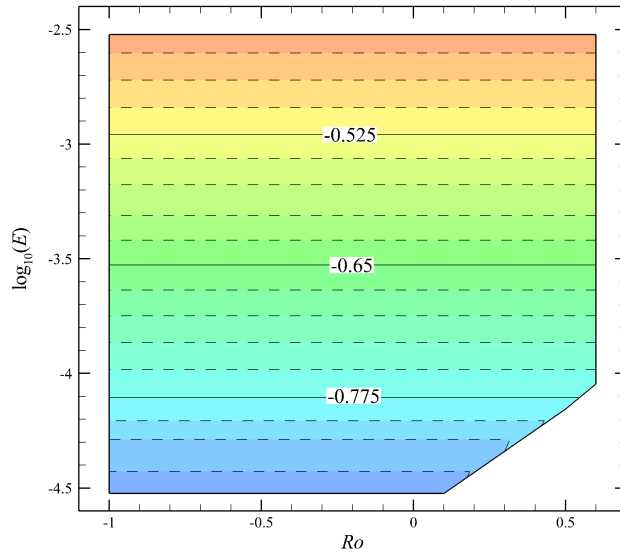


FIGURE 7.4: Contours of the base-10 logarithm of vertical shear-layer thickness measured from the relative azimuthal velocity, plotted on axes of  $\log_{10}(E)$  against  $Ro$ .

$E < 1$ , the quasi-two-dimensional model predicts a slightly thicker Stewartson layer. An approximate percentage difference of 2% is obtained at the lowest considered value of  $E = 3 \times 10^{-5}$ . The exact similarity in thickness values obtained between positive and negative- $Ro$  data in quasi-two-dimensional solutions was not seen in the axisymmetric solutions (see figure 4.6). It is unclear why there would be a difference in thickness at small  $Ro$  near zero, as the flows are highly depth-independent. A possible explanation may be that the thickness of the Stewartson layer is highly sensitive to the presence of meridional circulations, which is very weak at small  $Ro$ . This in turn may suggest that the thickness of the  $E^{1/4}$  layer may be affected by the presence of the  $E^{1/3}$  layer. Performing the thickness measurement procedures on the discontinuous axial vorticity is meaningless and results in a constant thickness for all flow conditions.

The  $\delta_{\text{vel}}$  has been calculated for every base flow condition throughout the parameter space. A regime diagram depicting the thickness for each condition characterised by  $Ro$  and  $E$  is illustrated in figure 7.4. The regime diagram is a plot of the  $\log_{10}(\delta_{\text{vel}})$  as a function of  $\log_{10}(E)$  and  $Ro$ . It is clear that the contour lines of  $\log_{10}(\delta_{\text{vel}})$  are horizontal throughout both the positive and negative- $Ro$  regime. Thus for quasi-two-dimensional flows, the  $E^{1/4}$  shear-layer thickness does not have any dependence on  $Ro$ , unlike the axisymmetric flows. It is noted that consistent with the axisymmetric

flow, the quasi-two-dimensional model also predicts a shear layer of finite thickness at  $Ro = 0$ , which represents solid-body rotation. The contour lines deviate from the horizontal at the large  $Ro$  and small  $E$  regime due to the linear triangulation used to generate the regime diagram. The thickness of the shear layer is not measured beyond this regime due to the limitations concerning the implementation of the quasi-two-dimensional model.

## 7.3 Linear stability analysis

The linear stability analysis solver used in Chapter 6 was adapted to interrogate the stability of the quasi-two-dimensional model solutions to azimuthal disturbances. This was achieved by replicating the linear forcing terms used for the one-dimensional base flow in the linearised disturbance field evolution equations.

### 7.3.1 Growth rates

#### 7.3.1.1 Positive-Rossby-number regime

The growth rates for a range of azimuthal wavenumbers were obtained throughout the explored parameter space. The fastest growing wavenumber was determined for each flow condition with unstable wavenumbers ranging from  $3 \leq k \leq 12$ . As a comparison, the axisymmetric base flows predict unstable wavenumbers ranging between  $2 \leq k \leq 9$ . This is partly explained by the smaller Ekman numbers computed, which have become feasible through the implementation of the quasi-two-dimensional model. The smaller Ekman numbers display a preference to smaller wavelengths structures.

The growth rates for flows of various  $E$  for  $Ro = 0.1$  is shown in figure 7.5(a). For large  $E$ , the base flow is not susceptible to linear instabilities as the growth rates over the entire wavenumber spectrum are negative. This is seen for  $E = 3 \times 10^{-3}$  with a peak azimuthal wavenumber of  $k_{\text{peak}} = 2.4$  and an associated growth rate of  $\sigma_{\text{peak}} = -0.089$ . The peak wavenumber and associated growth rate are determined through a parabolic fitting of the local peak in the  $\sigma$ - $k$  data and its neighbouring data points. The maximum of the fit describes  $k_{\text{peak}}$  and  $\sigma_{\text{peak}}$ . All of the cases in figure 7.5 portray a single peak in the  $\sigma$ - $k$  data which is representative of the mode I instability described for the axisymmetric flows in § 5.1.1. The growth rates of the perturbations introduced into the base flow are seen to increase with decreasing  $E$ . This is expected as decreasing the Ekman number causes the Stewartson layers to become thinner which

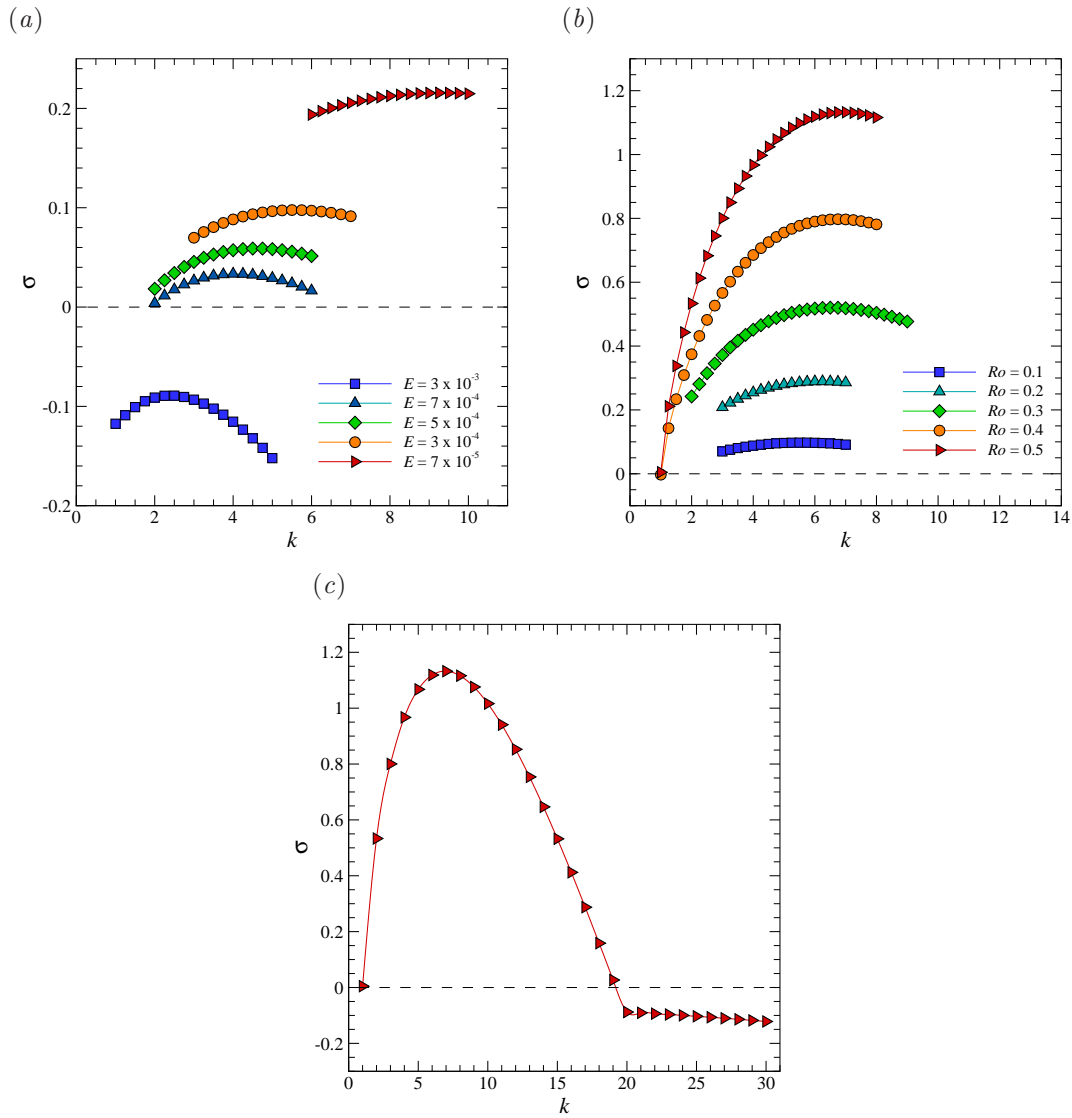


FIGURE 7.5: Growth rate  $\sigma$  as a function of azimuthal wavenumber  $k$  for (a) various  $E$  at  $Ro = 0.1$  and (b) various  $Ro$  at  $E = 3 \times 10^{-4}$ . (c) The  $\sigma$ - $k$  data for a large Rossby number of  $Ro = 0.5$  for  $E = 3 \times 10^{-4}$ . The dashed line represents neutral stability where points above and below symbolise unstable and stable modes, respectively.

leads to greater susceptibility to instability. In addition, decreasing  $E$  corresponds to a broadening of the instability waveband. A clear illustration of this can be observed through the comparison between  $E = 3 \times 10^{-3}$  and  $E = 7 \times 10^{-5}$ . It should be noted that the plotted data for each  $E$  ranges over 2 whole wavenumbers with intervals of 0.25. Furthermore, flows characterised by smaller  $E$  favours higher azimuthal wavenumbers. This is seen for  $E = 7 \times 10^{-5}$ , where the most unstable wavenumber and its associated growth rate is given by  $k_{\text{peak}} = 9.3$  and  $\sigma_{\text{peak}} = 0.2156$ , respectively.

Figure 7.5(b) illustrates the effect on the growth rates by varying the Rossby number while keeping the Ekman number constant at  $E = 3 \times 10^{-4}$ . Hence, increasing  $Ro$  causes a commensurate amplification of the growth rates, while the waveband of the instability remains relatively unaffected. As a comparison between  $Ro = 0.1$  and  $Ro = 0.5$ , the most unstable modes are characterised by  $k_{\text{peak}} = 5.57$  and  $\sigma_{\text{peak}} = 0.0977$ , and  $k_{\text{peak}} = 6.92$  and  $\sigma_{\text{peak}} = 1.1324$ , respectively. Thus, there is a shift in preference to higher wavenumbers as  $Ro$  is increased. This is surprising since the preferred azimuthal wavenumber of the instability is thought to be related to the thickness of the shear layer, for which quasi-two-dimensional flows have shown no dependence on  $Ro$  (figure 7.4). Thus, the most unstable azimuthal wavenumber is again a function of both  $Ro$  and  $E$ , as was shown with the axisymmetric results (§ 5.1.1.4).

Figure 7.5(c) demonstrates the extent of the mode I wavenumber band for a relatively large  $Ro$  at  $E = 3 \times 10^{-4}$ . A single peak is observed to be associated to the mode I instability with growth rates gradually decreasing beyond this wavenumber band ( $k > 20$ ). In contrast, the axisymmetric solution at this flow condition exhibits linear modes II and III in addition to the mode I instability (figure 5.2). This observation further reinforces the idea that the mode II and III arises from the breaking of depth independence and reflective symmetry of the axisymmetric base flow.

A comparison between the linear stability analysis results obtained from the quasi-two-dimensional model and the axisymmetric flows is demonstrated in figure 7.6 for  $Ro = 0.395$ . For the axisymmetric flows, all cases shown except for  $E = 3.16 \times 10^{-4}$  exhibit the mode II instability for wavenumbers beyond the mode I wavenumber waveband. All of the quasi-two-dimensional model solutions for this Rossby number portray  $\sigma$ - $k$  profiles that resemble the  $E = 3.16 \times 10^{-4}$  case for the axisymmetric model: a single peak is present and growth rates beyond the mode I waveband monotonically decreases. This may be explained by the absence of depth-dependent structures in the axisymmetric base flow which becomes susceptible to barotropic instability. Hence, the additional peaks in growth rate associated with the mode II and III instabilities are not present in the quasi-two-dimensional solutions. For a particular flow, the preferential azimuthal wavenumber is observed to be higher in the quasi-two-dimensional model compared to the axisymmetric simulations. The axisymmetric linear stability analysis predicts an unstable wavenumber of  $k \approx 3$  for all of the  $E$  shown at this particular  $Ro$ . In contrast, there is a shift in preferred wavenumber throughout the range of  $E$  in

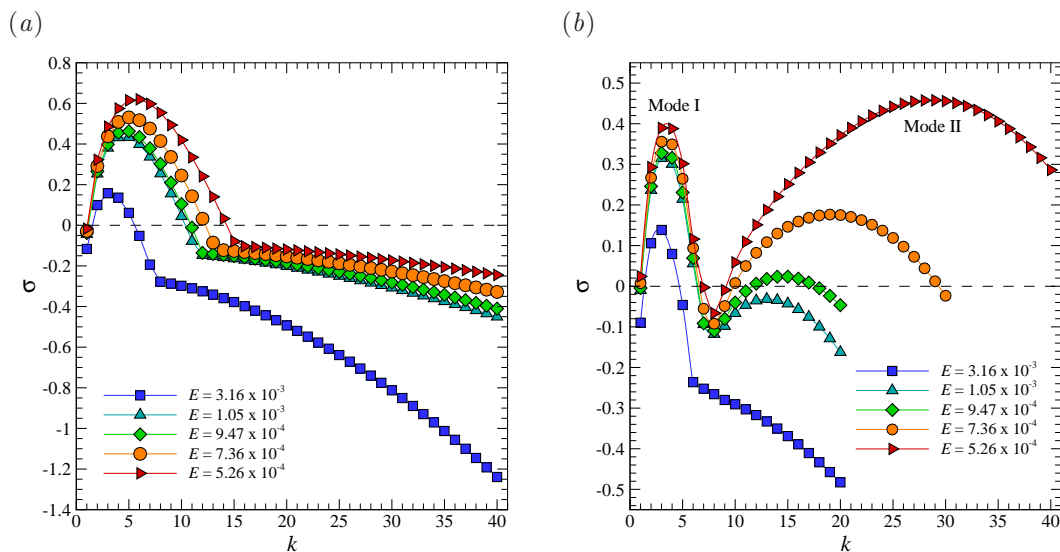


FIGURE 7.6: Growth rate  $\sigma$  as a function of wavenumber  $k$  for various  $E$  at  $Ro = 0.395$  from the (a) quasi-two-dimensional model and the (b) three-dimensional model. The quasi-two-dimensional illustrates only the mode I instability while the three-dimensional model demonstrates modes I and II. The dashed line represents neutral stability where points above and below symbolise unstable and stable modes, respectively.

the quasi-two-dimensional flows. In addition, the results of the quasi-two-dimensional flows demonstrate growth rates that are greater than those present in axisymmetric base flows. This may suggest that the depth-dependent flow features that arise in the axisymmetric flows causes a decay in the growth rate of the azimuthal instability mode.

### 7.3.1.2 Negative-Rossby-number regime

The growth rates for negative- $Ro$  flows have been obtained for the same range of  $E$  investigated in the positive- $Ro$  regime. The range of negative  $Ro$  explored is larger than that of the positive- $Ro$  regime since large negative- $Ro$  flows were less susceptible to the breaking of axial independence in the present implementation. The growth rates for the negative counterpart of the conditions illustrated in figure 7.5(a) are shown in figure 7.7. The conditions depicted are for  $Ro = -0.1$  at various  $E$ . It should be noted that the range of wavenumbers for each  $E$  are not the same between the two figures. The two plots demonstrate comparable growth rates for their common wavenumbers, although the cases associated with negative  $Ro$  consistently displays lower growth rates. This is true not only for the cases shown in figures 7.5(a) and 7.7 but also throughout the parameter space of  $0.01 \leq |Ro| \leq 0.5$  and  $3 \times 10^{-5} \leq E \leq 3 \times 10^{-3}$ . The ratio

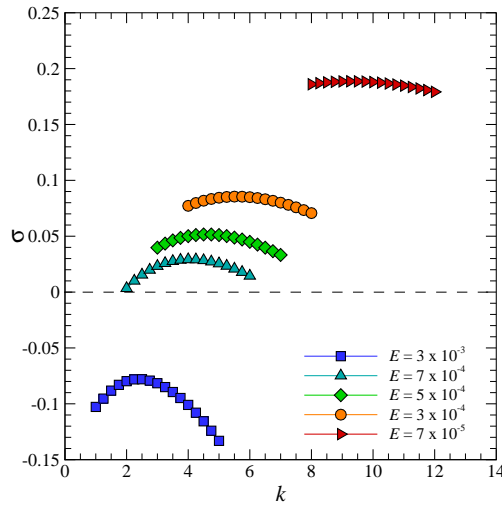


FIGURE 7.7: Growth rate  $\sigma$  as a function of azimuthal wavenumber  $k$  for various  $E$  at  $Ro = -0.1$ . The dashed line represents neutral stability where points above and below symbolise unstable and stable modes, respectively.

between the growth rates associated with positive and negative- $Ro$  flows is discussed in detail later in this section. The other trends remain the same between the positive and negative- $Ro$  regime in that with decreasing  $E$ , the growth rates increase along with a preference for higher-wavenumber structures.

Plots of the growth rate as a function of Rossby number for various Ekman numbers and for azimuthal wavenumbers  $k = 1, 2$  and  $3$  are illustrated in figure 7.8. An increase in the  $|Ro|$  causes greater velocity gradients to exist at the disk edge. This results in a base flow that is more susceptible to instability and therefore leads to a perturbation field that exhibits a larger global growth rate. It is clear that the profiles of  $\sigma-Ro$  in the negative and positive- $Ro$  regime are not symmetric about  $Ro = 0$  for any of the wavenumbers. The positive and negative- $Ro$  growth data appear to be described by different functions. That is, the growth rates increase with an increasing gradient in the positive- $Ro$  regime while the growth rates increase with a decreasing gradient in the negative- $Ro$  regime. In taking the magnitude of the growth rates and assuming that the curves adopt a power-type law of  $\sigma \propto Ro^\alpha$ , the negative and positive- $Ro$  regime would be expressed by  $\alpha < 1$  and  $\alpha > 1$ , respectively. The magnitude of  $\alpha$  becomes progressively larger for decreasing  $E$ .

The corresponding Rossby number for the minimum growth rate of a particular  $E$  is always characterised by  $Ro = 0$  which describes solid-body rotating flow. This flow is

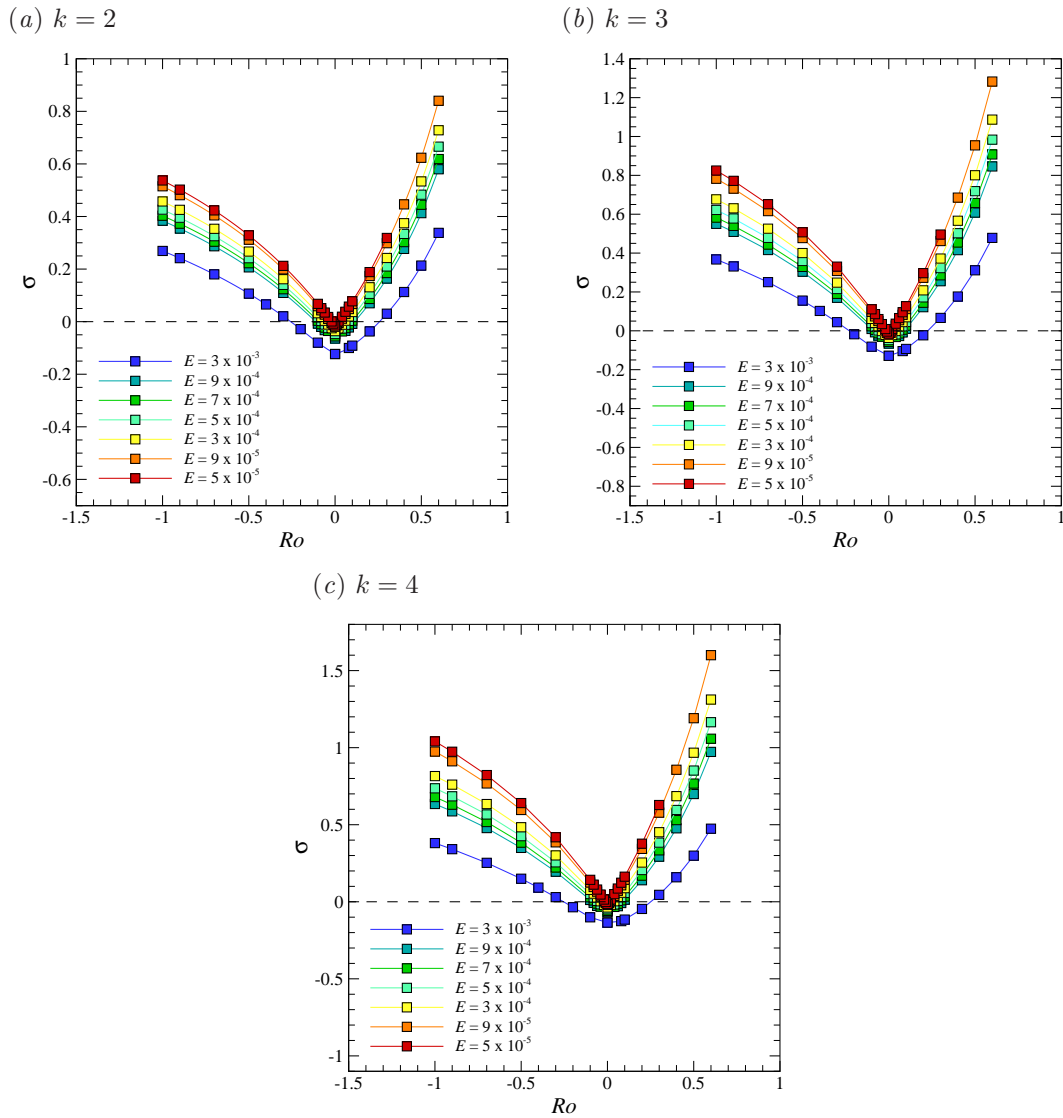


FIGURE 7.8: Growth rate  $\sigma$  as a function of  $Ro$  for various  $E$  at various azimuthal wavenumbers of (a)  $k = 2$ , (b)  $k = 3$ , and (c)  $k = 4$ . The dashed line represents neutral stability where points above and below symbolise unstable and stable modes, respectively.

always stable and therefore will always portray negative growth rates for all azimuthal wavenumbers. It is observed that the global linear stability analysis presents the zeroth azimuthal wavenumber as being the most dominant for  $Ro = 0$  over a wide range of  $E$  cases. The second leading eigenmode is consistently shown to be  $k = 1$  as seen in figure 7.9. It should be noted that the difference in growth rates between  $k = 0$  and  $k = 1$  is only of a few percent. Despite this small difference, the profiles of the growth rate as a function of wavenumber demonstrate similarity. Also, the profile of the peak growth rate and its neighbouring points do not represent a parabolic shape which has

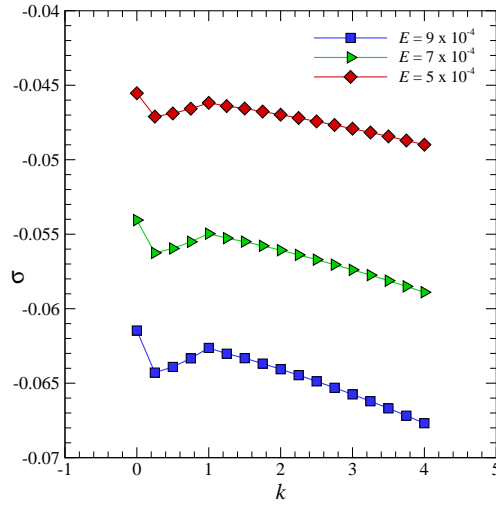


FIGURE 7.9: Growth rate  $\sigma$  as a function of  $k$  at  $Ro = 0$  for various  $E$ . The flow state of  $Ro = 0$  characterises solid-body rotation.

been indicative of the mode I instability, rather the peak point is sharp. This is because the solid-body rotating flow is unlikely to reveal a shear-layer instability and the most unstable wavenumbers would be  $k = 0$ , the axisymmetric mode, and  $k = 1$ , an oval-shaped distortion. All other azimuthal wavenumbers are less significant in terms of its growth rate. Thus, the sharp peak instead of the parabolic shape in the  $\sigma$ - $k$  profile may be explained by the absence of the mode I instability due to the insufficient horizontal shear present in solid-body rotating flows.

The ratio of the positive- $Ro$  growth rate  $\sigma_{\text{pos } Ro}$ , to the negative- $Ro$  growth rate  $\sigma_{\text{neg } Ro}$ , for every azimuthal wavenumber was calculated throughout the parameter space. A particular Rossby number demonstrates a ratio of growth rates that remain constant with varying azimuthal wavenumber. In addition to this trend, the values of the growth rate ratio also display an invariance to the Ekman number. Thus, the ratio appears to be only as a function of  $Ro$ . In fact, this trend extends into the negative- $Ro$  regime. The ratio of the growth rates as a function of  $|Ro|$  is illustrated in figure 7.10. The relationship is nonlinear, and upon closer inspection, is seen to adopt the equation describing the normalised disk speed, which is given by

$$\Omega + \omega = \frac{1 + ARo}{1 - ARo}. \quad (7.1)$$

Thus, the growth rates of negative- $Ro$  flows can be obtained directly through the relationship of the disk rotation rate if the growth rates for the positive- $Ro$  flow are known.

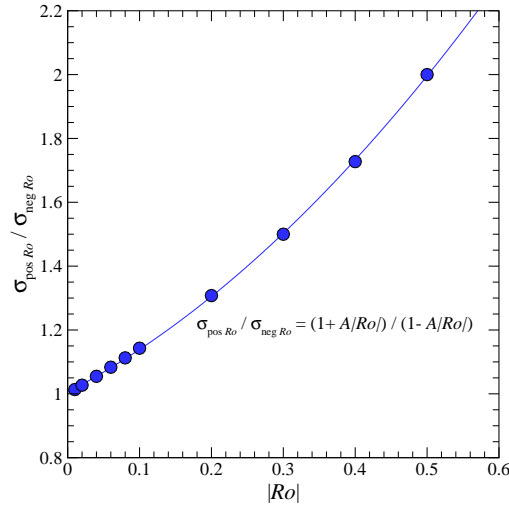


FIGURE 7.10: The relationship of the ratio between growth rates obtained from positive and negative- $Ro$  flow as a function of  $|Ro|$ . The growth rates have been computed from the quasi-two-dimensional model.

---

Similarly, positive- $Ro$  growth rates can be obtained if growth rates for its negative- $Ro$  counterparts are known and provided that the magnitude of the Rossby number is used. Thus, the physical meaning of the disk speed is lost in the latter case as the equation no longer describes the disk speed. That is, the equation which describes the ratio between positive and negative- $Ro$  growth rates is given by

$$\frac{\sigma_{\text{pos } Ro}}{\sigma_{\text{neg } Ro}} = \frac{1 + A|Ro|}{1 - A|Ro|}. \quad (7.2)$$

It is emphasised that despite the differences in growth rates between positive and negative  $Ro$ , the most unstable wavelength remains the same between the two regimes.

The relationship of the ratio (equation 7.2) demonstrates an equality between the growth rates of the positive and negative- $Ro$  cases through

$$(1 - A|Ro|)\sigma_{\text{pos } Ro} = (1 + A|Ro|)\sigma_{\text{neg } Ro}. \quad (7.3)$$

It appears then that the growth rate may be related to the sign of  $Ro$  via  $(1 - ARo)$  such that a negative  $Ro$  yields a prefactor of  $(1 + ARo)$  while a positive  $Ro$  yields a  $(1 - ARo)$  prefactor. The ratio of these results recovers the disk speed equation (equation 7.1). Plots of the  $(1 - ARo)\sigma$  as a function of  $Ro$  for three different wavenumbers are demonstrated in figure 7.11. It illustrates that the relationship in the positive and negative- $Ro$  parameter space are reflections of each other about the  $Ro = 0$  line with the

curves portraying an almost linear profile. This reflective symmetry is demonstrated for  $k = 4$  in figure 7.11(d) whereby the square and triangle symbols represent positive and negative- $Ro$  data, respectively. Thus this suggests that the product of  $(1 - ARo)\sigma$  is a function of  $|Ro|$ . The product  $(1 - ARo)\sigma$  increases with decreasing  $E$  for a given  $Ro$  as well as increasing with increasing  $|Ro|$ . Representing  $(1 - ARo)\sigma$  as a linear function demonstrates a systematic variation of the horizontal and vertical intercepts as well as the gradient of the curve with varying  $Ro$  and  $E$ .

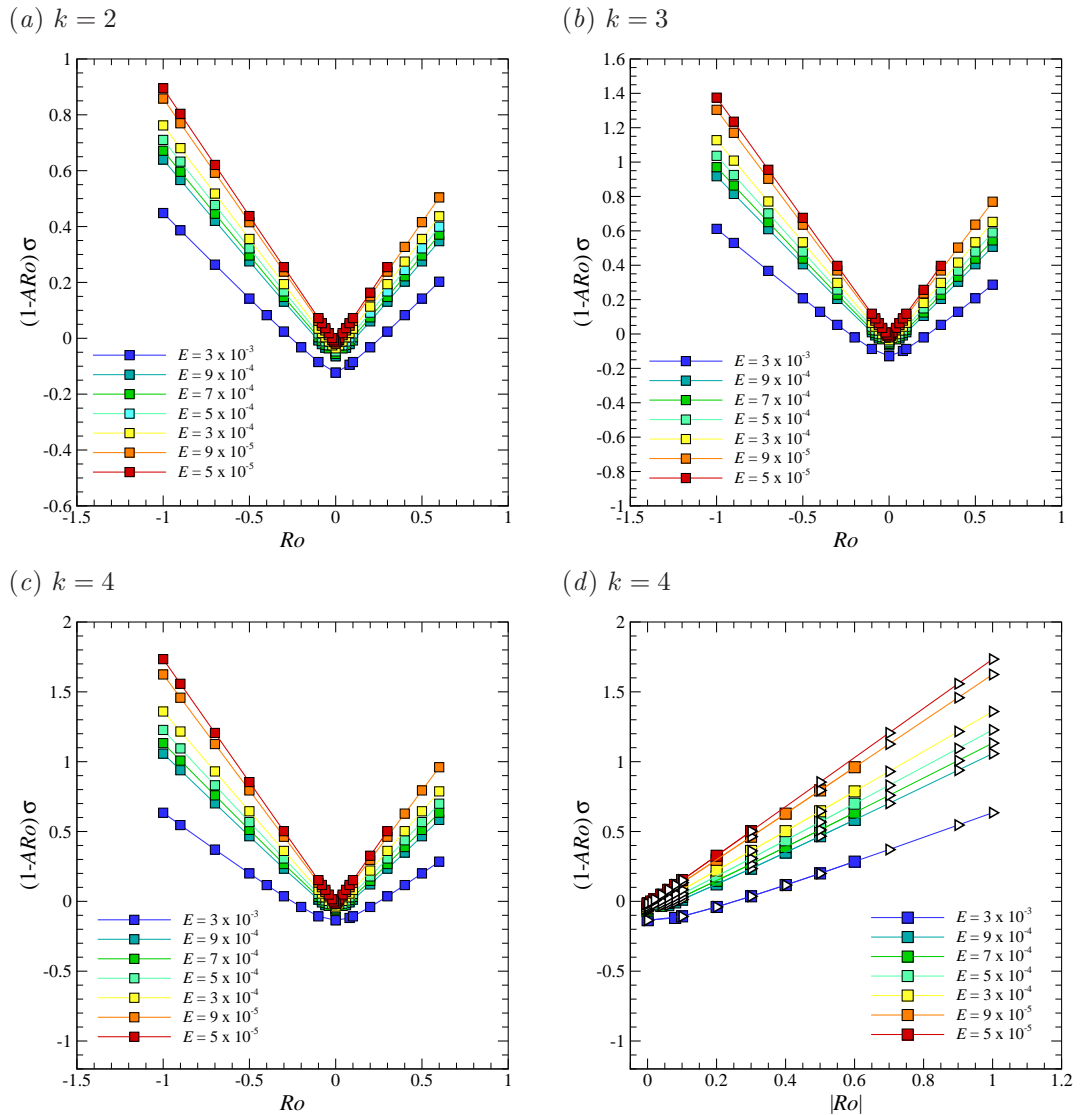


FIGURE 7.11: The product of  $(1 - ARo)$  and  $\sigma$  as a function of  $Ro$  for both the positive and negative- $Ro$  regime. Each line represents a different Ekman number with data from azimuthal wavenumbers (a)  $k = 2$ , (b)  $k = 3$  and (c)  $k = 4$  being plotted. (d) A reproduction of panel (c) except that the magnitude of  $Ro$  is used to demonstrate the reflective symmetry about the vertical axis between positive and negative- $Ro$  data.

It is noted that  $(1 - ARo)$  can be rewritten as  $\Omega/\bar{\Omega}$  through the definition of the Rossby number,  $Ro = \omega/(2\bar{\Omega}A)$  (equation 3.55). The same ratio of  $\Omega/\bar{\Omega}$  can be derived from the Navier–Stokes equations (specifically the coefficient of the diffusion term,  $EA^2/(1 - ARo)$ ) and the Ekman number definition,  $E = \nu/(\bar{\Omega}H^2)$  (equation 3.56). Noting that the growth rate has physical dimensions of the reciprocal time scale ( $\Omega$ ), the physical growth rate can be written as  $\sigma_{\text{physical}} = \Omega\sigma$ . This leads to

$$(1 - ARo)\sigma = \frac{\sigma_{\text{physical}}}{\bar{\Omega}}. \quad (7.4)$$

Since  $(1 - ARo)\sigma$  is a function of  $|Ro|$ , equation 7.4 suggests that the physical growth rate normalised by the average rotation rate is also function of the Rossby number magnitude. Thus  $\bar{\Omega}$  is the resulting variable used to normalise the growth rate in order for it to be a function of  $|Ro|$ . This is surprising since the rotation of the tank itself has been used to non-dimensionalise the governing equations. It is also interesting to note that the function is invalid if  $\bar{\Omega} = 0$  which corresponds to the differential rotation of the disk defined by  $\omega = -2\Omega$  (i.e.  $Ro = \infty$ ).

Several trends can be obtained by fitting the  $(1 - ARo)\sigma$  data against  $Ro$  with a linear relationship. That is, the data can be expressed as  $(1 - ARo)\sigma = mRo + c$  where  $m = d([1 - ARo]\sigma)/dRo$  represents the gradient and  $c = \sigma_{Ro=0}$  is the vertical intercept which represents the growth rate at  $Ro = 0$ . Figure 7.12 illustrates the vertical intercept and the gradient as a function of  $E$  for several azimuthal wavenumbers. The trends between the positive and negative- $Ro$  regime are expected to be the same according to equation 7.3. However, there are differences between the two regimes due to the number of data points used in each regime and also due to the range of  $|Ro|$  investigated. This is most clearly illustrated in figure 7.12(a) where the growth rate of  $Ro = 0$  ( $\sigma_{Ro=0}$ ) of the positive (solid) and negative (dashed) lines does not collapse perfectly on each other. Despite this, the trends are consistent throughout the regimes in that  $\sigma_{Ro=0}$  increases with decreasing  $E$  for a particular  $k$ . Similarly, the gradient of the linear fit is observed to increase in magnitude with decreasing  $E$  for a constant  $k$ .

### 7.3.2 Global instability mode shapes and visualisation on horizontal planes

The profile of the growth rate as a function of wavenumber has revealed only one type of instability mode which is suspected to be the mode I instability. The non-axisymmetric perturbation fields have been obtained and demonstrate axially invariant axial vorticity

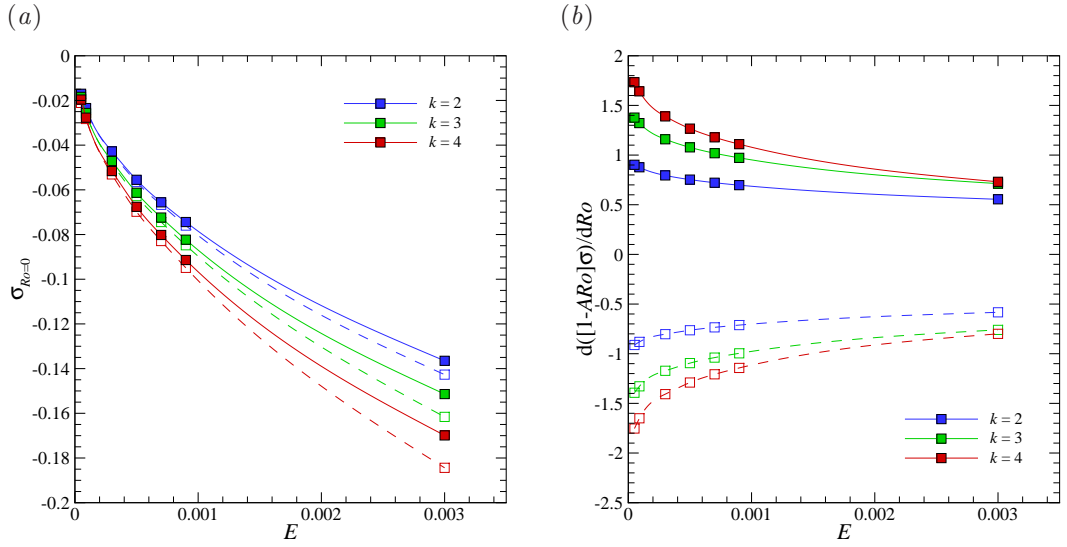


FIGURE 7.12: The (a) vertical-intercept and (b) the gradient of a linear fit through  $(1 - ARo)$  against  $Ro$ , as a function of  $E$  (figure 7.11). Each line represents a different wavenumber with both positive (solid lines with filled symbols) and negative- $Ro$  (dashed lines with hollow symbols) data shown. The vertical-intercept represents the growth rate at  $Ro = 0$ .

structures. The axial vorticity contours of  $k = 3$  and  $k = 7$  for  $Ro = 0.5$  and  $E = 3 \times 10^{-4}$  are shown in figure 7.13. Again it should be noted that the vorticity plots shown here are the quasi-two-dimensional solutions (functions of  $r$  and  $\theta$  only) projected onto the  $r$ - $z$  plane. For  $k = 3$ , there are two dominant vertical strands of vorticity at the disk-tank interface ( $r = 1$ ) that is consistent with the mode I instability portrayed through the axisymmetric solutions. Therefore, the wavenumbers composing the single branch observed in the  $\sigma$ - $k$  data are associated with  $E^{1/4}$  shear-layer instability. A direct comparison between the quasi-two-dimensional and the axisymmetric solutions cannot be made since there is no mode I instability at this flow condition from the axisymmetric modelling. That is, the base flow is sufficiently forced such that mode II and III instabilities exhibit large growth rates. Therefore, even the lower wavenumbers ranging between  $k = 1$ -3 demonstrate depth-dependent characteristics in the perturbation field. The  $k = 7$  perturbation field from the quasi-two-dimensional solution also illustrates a pair of positive and negative vertical strands of vorticity around  $r = 1$ . However, the azimuthal slice shown also reveals an extra negative-vorticity band of lower strength. This is due to the visualisation being achieved at a slice taken at the arbitrary azimuthal angle of a perturbation field which is non-axisymmetric. Thus another  $r$ - $z$  slice at a

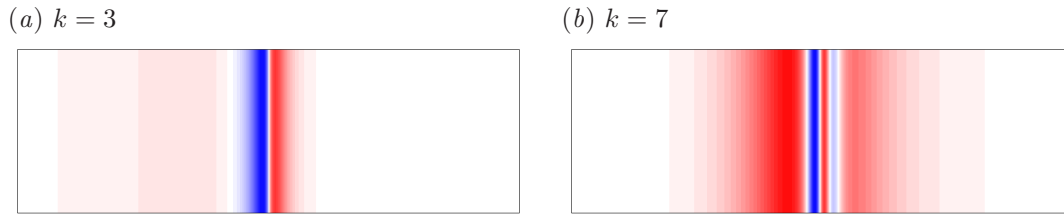


FIGURE 7.13: Contours of axial vorticity of the three-dimensional perturbation field of  $Ro = 0.5$  for  $E = 3 \times 10^{-4}$  depicted on the  $r$ - $z$  plane. The structures of (a)  $k = 3$  and (b)  $k = 7$  are shown. Given the arbitrary scaling of linearised eigenvector fields, equi-spaced contour levels are plotted between  $\pm(|\omega_{z,\min}| + |\omega_{z,\max}|)/2$ . Blue and red flooded contours represent negative and positive values, respectively.

---

different angle is likely to reproduce features similar to those in  $k = 3$ .

A visualisation of the non-axisymmetric structure predicted by the linear stability analysis is obtained by superimposing the leading eigenmodes onto their respective axisymmetric base flows. Illustrations of these structures for the instability modes from figure 7.13 are shown in figure 7.14. It is emphasised that these depictions in the  $r$ - $\theta$  plane are not representations of the actual three-dimensional flow structure, rather they are an illustration of the linear instability mode for which the amplitudes have been arbitrarily scaled. Importantly, this type of visualisation reveals the type of distortions on the base flow made capable by the most unstable azimuthal instability mode. For both  $k = 3$  and  $k = 7$  which belong to the mode I branch, the flow is seen to favour a polygon with the number of sides corresponding to that of the instability wavenumber. That is that a triangle is observed for  $k = 3$  while a heptagon is seen for  $k = 7$ . In these examples, a thin layer of axial vorticity is present and forms the border of the polygonal shape. This layer is weaker in comparison to both its interior and surrounding flow in terms of its vorticity.

Negative-Rossby-number flows display the same features as their positive- $Ro$  counterpart. For  $Ro = -0.5$  and  $E = 3 \times 10^4$ , the linear stability results predict the same preferred azimuthal wavenumber for that of  $Ro = 0.5$  at the same Ekman number, namely  $k = 7$ . The perturbation field and a visualisation of the resulting structure is presented in figure 7.15. The only difference is that the pair of negative and positive-vorticity strands around  $r = 1$  are reversed with negative vorticity residing closer to the tank side-wall while the positive vorticity is located closer to the axis of rotation. Also, the ring of vorticity forming the perimeter of the polygonal shape around  $r = 1$

---

(a)  $k = 3$

(b)  $k = 7$

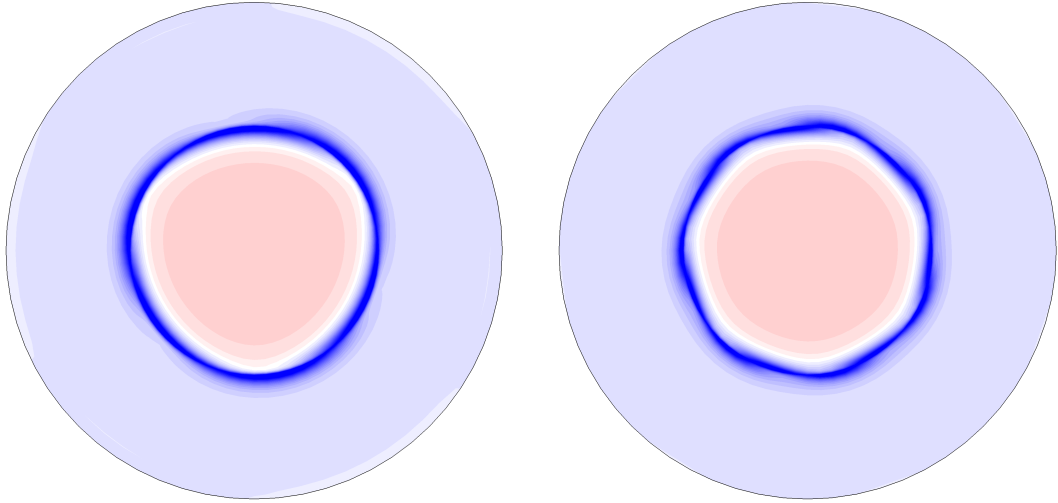


FIGURE 7.14: An  $r$ - $\theta$  slice of a  $z$ -independent flow with conditions  $Ro = 0.5$  and  $E = 3 \times 10^{-4}$  is extracted from a linear non-axisymmetric flow approximation constructed by superimposing the axisymmetric base flow and the leading instability mode with azimuthal wavenumber (a)  $k = 3$  and (b)  $k = 7$ . This flow field is not representative of the three-dimensional non-axisymmetric flow since nonlinear effects are omitted here. Contours of axial vorticity are plotted, with levels as per figure 7.2. The orientation is such that the positive  $Ro$  causes the central region to rotate clockwise faster than the outer region.

---

contains the highest axial vorticity in the domain.

The axial vorticity contours of the perturbation field and the resulting structures from the superposition of the field onto the base flow does not present any major differences between the quasi-two-dimensional solutions and the axisymmetric simulations. Since a direct comparison between quasi-two-dimensional and axisymmetric simulated solutions cannot be made at the same flow conditions due to the presence of additional instability mode types from the axisymmetric modelling, only qualitative judgements can be made. The mode I instability deforms the shear layer into polygonal configurations. This type of instability has also been observed in the axisymmetric base flows, forming polygonal configurations with their perimeter coinciding approximately with  $r = 1$ . All of these characteristics are indicative of the mode I instability.

### 7.3.3 Preferred azimuthal wavenumbers

Regimes diagrams for both the negative and positive- $Ro$  regimes have been generated and are illustrated in figure 7.16. Fractional peak wavenumbers and the corresponding

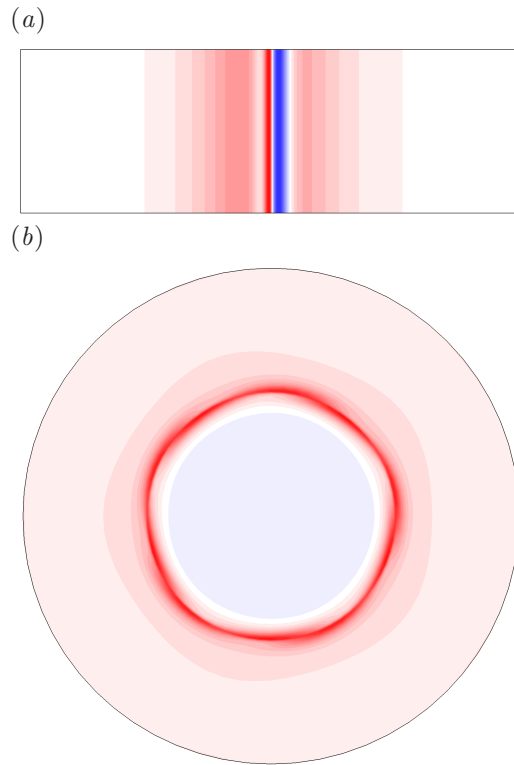


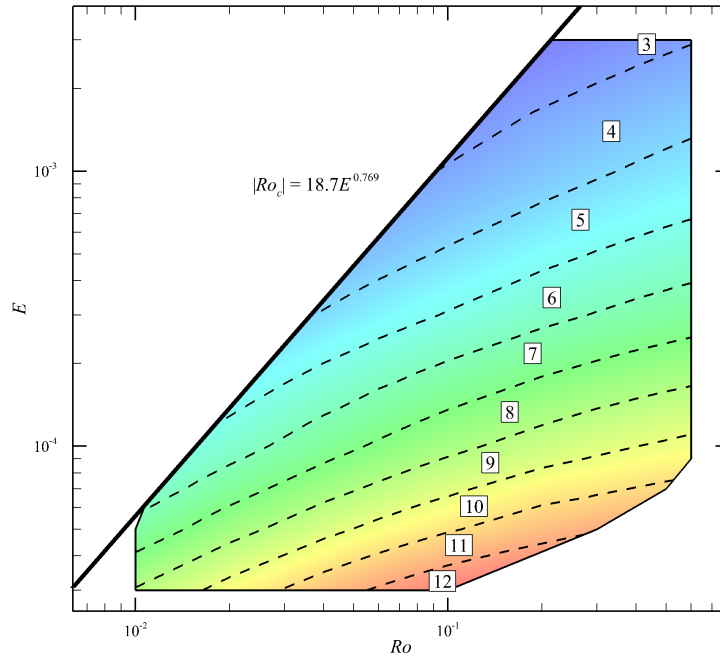
FIGURE 7.15: Axial vorticity contours of the dominant linear instability mode with azimuthal wavenumber  $k = 7$  at  $Ro = -0.5$  and  $E = 4 \times 10^{-4}$ . (a) The perturbation field of the instability mode is plotted in the  $r$ - $z$  plane, with contour levels as per figure 7.13. (b) A linear non-axisymmetric flow constructed by superimposing the axisymmetric base flow and the azimuthal linear instability wavenumber as per figure 7.14 with contours are per figure 7.2. The orientation is such that the negative  $Ro$  causes the central region to rotate anti-clockwise faster than the outer region.

---

peak growth rates were obtained via the local maximum of a parabolic fitting of the peak and the adjacent wavenumbers from the  $\sigma$ - $k$  data obtained via linear stability analysis. Thus, the number depicted within the bands on the regime diagram represents a range of fractional wavenumbers. For example, a contour band of 7 represents wavenumbers ranging between 6.5 and 7.5. Data from over 100 different flow conditions each in the positive and negative- $Ro$  regime were used to produce these regime diagrams.

Since the linear stability analysis predicted the exact same peak wavenumbers between positive and negative- $Ro$  flows, the regime diagrams look identical over the range of computed values. The analysis predicts that the preferred azimuthal wavenumber increases with increasing  $|Ro|$  and decreasing  $E$ . The trend of the preferred wavenumbers depict trends similar to those observed from the axisymmetric model (see figures 5.12

(a) Positive  $Ro$



(b) Negative  $Ro$

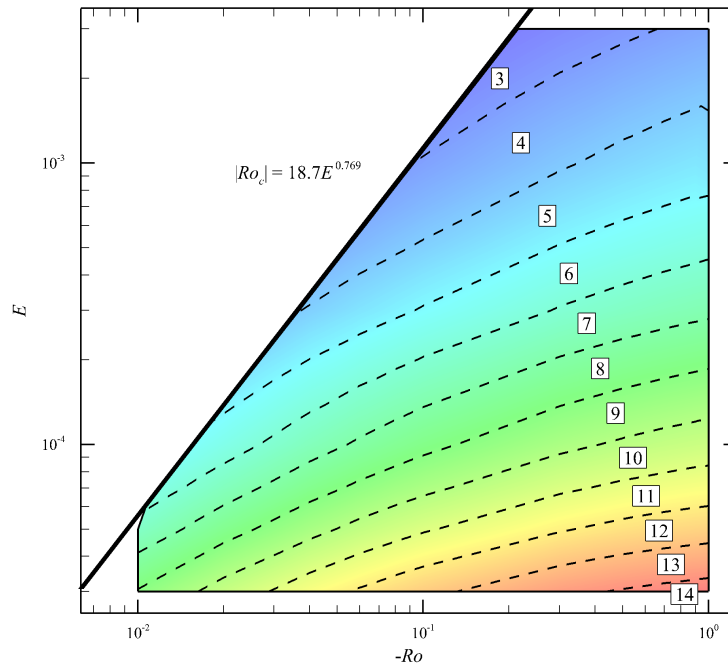


FIGURE 7.16: The regime diagram of the most unstable linear wavenumber as a function of  $E$  and (a) positive  $Ro$  and (b) negative  $Ro$ . The short-dashed lines represents the transition between one wavenumber to another, denoted by the wavenumber of the instability shown within the band. The solid boundary lines represents the range of triangulation. The left thick boundary line represents the stability threshold which is given by  $|Ro_c| \propto E^{0.769}$  (using both positive and negative- $Ro$  data).

and 5.17). The lines of constant wavenumber illustrate comparable contour lines to those in the barotropic regime from positive- $Ro$  flows produced via axisymmetric simulations. In comparison to the negative- $Ro$  axisymmetric simulations, the contour lines of the constant preferred wavenumbers from quasi-two-dimensional flows differ slightly in that the lines become horizontal at large  $Ro$  whereas the axisymmetric flows begin to display vertical contour lines. The deviation from the horizontal in the axisymmetric cases may be due to the linear interpolation technique or the limited data of  $Ro < -4.5$  used to construct the regime diagram.

The threshold line was determined by empirically fitting data points of  $Ro$  and  $E$  that correspond to zero growth rates for both positive and negative- $Ro$  flows. This yields a relationship between  $Ro$  and  $E$  given by  $|Ro_c| = 18.7E^{0.769}$ . The exponent of  $E$  is comparable to the relationship obtained from the axisymmetric model, namely 0.767, and is in good agreement with the theoretical value of  $3/4$ . This suggests that the  $E^{1/3}$  shear layer does not significantly influence the stability of the base flow to three-dimensional disturbances, particularly the onset of instability. Furthermore, the coefficient of the Ekman number of the stability threshold between the quasi-two-dimensional model and the axisymmetric simulations are comparable, namely 18.7 and 18.1, respectively. This indicates that the onset of linear instability occurs at a slightly higher  $Ro$  in quasi-two-dimensional flows, though the differences in  $Ro_c$  are negligible when plotted on the same regime diagram. A clearer comparison is seen through the internal Reynolds number which is defined as  $Re_i = \sqrt{2}Ro/E^{3/4}$  (equation 3.60). This onset relationship yields an equivalent critical internal Reynolds number of  $Re_{i,c} = 22.8 \pm 0.8$  (compared with  $Re_{i,c} = 22.4 \pm 0.8$  from the axisymmetric simulations). From figure 7.16, it is clear that this constant  $Re_{i,c}$  is not unique to a particular azimuthal wavenumber, rather it encompasses a range of unstable azimuthal wavenumbers. Thus, similar to the axisymmetric solutions, both  $Ro$  and  $E$  are required in predicting the linearly unstable azimuthal wavenumber while only  $Re_i$  is required to characterise the onset of linear instability.

### 7.3.4 The Rossby and Ekman numbers dependence on the preferred azimuthal wavenumber and wavelength

It has been demonstrated that flows governed by the quasi-two-dimensional equations do not exhibit any depth-dependent features and thereby do not exhibit any linear instabilities apart from the mode I linear instability. The preferred azimuthal wavelength

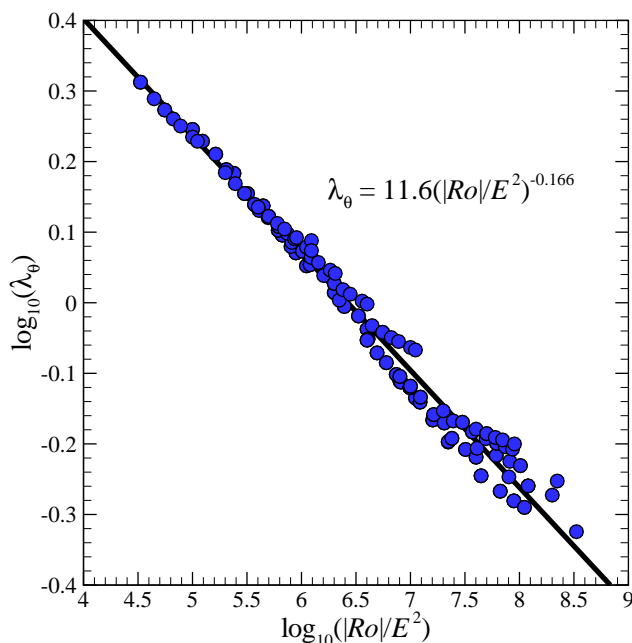


FIGURE 7.17: Regression of the preferred azimuthal wavelength of the mode I instability through a plot of  $\log_{10}(\lambda_\theta)$  against  $\log_{10}(|Ro|/E^2)$ . The data points here correspond to flow conditions of  $Re_i \lesssim 924$ .

---

as a function of both the Rossby and Ekman number is sought after following the inconspicuous  $E^{1/3}$  relationship obtained for azimuthal wavelength from the axisymmetric solutions ( $\lambda_\theta \sim E^{1/3}/|Ro|^{1/6}$ , § 5.1.3). Results from the quasi-two-dimensional simulations are grouped as  $|Ro|^\alpha E^\beta$  and correlated with  $\lambda_\theta$ . The same coefficients used in the previous procedure (§ 5.1.3) of  $\alpha = 1$  and  $\beta = -2$  is used in this analysis.

A power law is employed to fit the independent variable  $|Ro|/E^2$ , and its corresponding azimuthal wavelength  $\lambda_\theta$ . The base-10 logarithm of both variables,  $|Ro|/E^2$  and  $\lambda_\theta$ , are plotted in figure 7.17. In the axisymmetric simulations, the maximum  $Re_i$  characterising an axisymmetric base flow exhibiting reflective symmetry about the mid-depth was characterised by  $Re_i \lesssim 49$ . The highest computed internal Reynolds number for the quasi-two-dimensional model is  $Re_i \lesssim 924$ . Despite the large difference in the range of  $Re_i$ , the universal law obtained for the azimuthal wavelength from the quasi-two-dimensional flows is given by  $\lambda_\theta = 11.6(|Ro|/E^2)^{-0.166}$ , which is almost identical to the relationship obtained from axisymmetric simulations ( $\lambda_\theta = 11.4(|Ro|/E^2)^{-0.167}$ ). It is noted that the exponent of  $-0.166$  may be representative of an exact fraction of  $-1/6$  which expands the azimuthal wavelength expression to  $\lambda_\theta \sim E^{1/3}/|Ro|^{1/6}$ . Thus,

the  $E^{1/3}$  term still emerges from the quasi-two-dimensional solutions, which implies that the  $1/3$  exponent is not related to the Stewartson  $E^{1/3}$  as it does not exist in the quasi-two-dimensional model. This conclusively demonstrates that the  $E^{1/3}$  Stewartson layer does not influence the linear stability of the  $E^{1/4}$  Stewartson layer in the reflectively-symmetric regime. The significance of the  $-1/6$  exponent leading to the  $E^{1/3}$  scaling remains an open question.

## 7.4 Smoothing the imposed velocity profile

Many similarities have been observed between the quasi-two-dimensional model and the axisymmetric simulations including the thickness of the Stewartson  $E^{1/4}$  layer, the linear stability of the shear layer and its preferred azimuthal wavenumbers. A number of previous studies that have employed quasi-two-dimensional models (e.g. van de Konijnenberg *et al.* 1999; Bergeron *et al.* 2000; Fröh & Nielsen 2003) implemented a smoothed forcing profile across the disk-tank interface at  $r = 1$ . The effect of smoothing the discontinuous velocity profile which has been imposed as forcing conditions in previous sections, is investigated in this section.

A smoothed forcing function is achieved by smoothing the discontinuity at  $r = 1$  through a hyperbolic tangent function as described in § 3.7.2. The azimuthal velocity forcing is then given by

$$\mathbf{u}_\theta = \Omega r + \frac{r}{2} \left[ 1 - \tanh \left( \frac{r - R_d}{\delta} \right) \right] \omega, \quad (7.5)$$

where  $\delta$  is the thickness approximated to be  $\delta = (E/4)^{1/4}H$ . Previous studies have adopted smoothed forcing profiles due to the numerical complications arising from discontinuous profiles (e.g. high spatial resolution and small time step requirements). An investigation into the effect of employing the smoothed forcing profile for axisymmetric flows has been detailed in § 4.2.4. The established trends in this section are a precursor for the next section (§ 7.5), where non-axisymmetric structures are computed with this smoothed forcing function.

### 7.4.1 The axisymmetric flow structure, vertical profile and shear-layer thickness

The axisymmetric base flow for  $Ro = 0.5$  and  $E = 3 \times 10^{-4}$  is obtained and illustrated in figure 7.18(a). The same flow with discontinuous forcing imposed is shown in figure 7.2(a)(i). Using the same contour levels, the differences between the two imposed

forcing conditions are seen near  $r = 1$  where a wider region of negative axial vorticity (dashed lines) is observed. Also, the darker contour colours at  $r = 1$  indicates a larger axial vorticity magnitude.

The axial vorticity profiles have been extracted from both flow solutions and displayed in figure 7.18(b). The steady-state solution exhibits a smaller magnitude of axial vorticity at  $r = 1$  with the smoothed forcing condition imposed. This is also true for negative- $Ro$  flows whereby the positive axial vorticity shear layer demonstrates a smaller value in the smoothed forcing function solution compared to the discontinuous velocity imposed solution. A similar trend is seen with the azimuthal velocity relative to the tank where the peak velocity of the smoothed solution is lower than that of the discontinuous solution. Also, there is a slight shift of the maximum towards the centre of the tank. These factors result in a thicker measure of the  $E^{1/4}$  Stewartson layer. For the specific case of  $Ro = 0.5$  and  $E = 3 \times 10^{-4}$ , the smoothed solution produces a shear layer of thickness  $\delta_{\text{vel}} = 0.277$  compared to  $\delta_{\text{vel}} = 0.224$  obtained from its discontinuous counterpart. A thicker shear layer has a similar effect of increasing the Ekman number which in turn is expected to be unstable to a lower azimuthal wavenumber. A power-law fit of the Stewartson  $E^{1/4}$  layer thickness at  $Ro = 0.005$  provides the relationship  $\delta_{\text{vel}} = 1.71E^{0.226}$ , which is larger than for the discontinuous solution,  $\delta_{\text{vel}} = 1.32E^{0.219}$ . In addition, the effect of  $Ro$  variation for the smoothed forcing condition does not affect the thickness of the shear layer. This effect was also observed in the flows with discontinuous velocity conditions imposed (see figure 7.4).

#### 7.4.2 Linear instability and visualising global instability modes on horizontal planes

A linear stability analysis was conducted on base flows obtained using the smoothed forcing condition. The growth rates as a function of wavenumber for the smoothed and discontinuous forcing conditions are shown in figure 7.19 for two flow conditions:  $(Ro, E) = (0.2, 1 \times 10^{-3})$  and  $(Ro, E) = (0.5, 3 \times 10^{-4})$ . The plots suggest that the smoothed forcing condition yields an axisymmetric base flow which induces lower growth rates and a preference to lower azimuthal wavenumbers. This reinforces the expectation of the base flow being more susceptible to lower wavenumbers as a consequence of the thicker shear layer produced. At smaller wavenumbers, the growth rates predicted by the analysis between the two different forcing conditions are comparable. The trends often depart at wavenumbers higher than the peak wavenumber associated

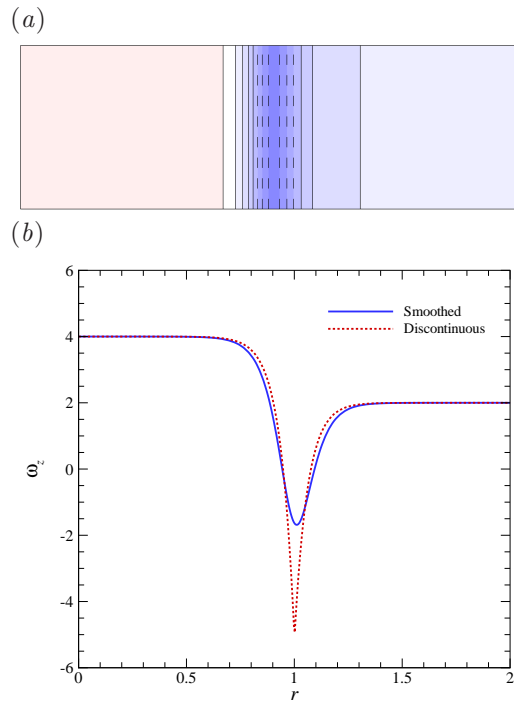


FIGURE 7.18: (a) Contours of axial vorticity of the axisymmetric flow visualised on the semi-meridional  $r$ - $z$  plane with a smoothed forcing condition imposed. The flow condition is of  $Ro = 0.5$  and  $E = 3 \times 10^{-4}$ . Contours levels are as per figure 7.2. (b) The axial vorticity profile against radius for  $Ro = 0.5$  and  $E = 3 \times 10^{-4}$  from the discontinuous (dashed) and smoothed (solid) forcing conditions.

with the smoothed forcing profile case. This data suggests that instability onset will occur at a slightly larger Rossby number for a constant Ekman number for smoothed forcing flows.

The absolute difference between the growth rates from the discontinuous solutions and the smoothed solutions have been plotted against the azimuthal wavenumber for various Ekman number cases. An example typical of the curves obtained is shown in figure 7.19(c) for flow conditions of  $Ro = 0.2$  and  $E = 1 \times 10^{-3}$ . The data illustrates an increase in the difference in growth rate with increasing azimuthal wavenumber. The curves appear to exhibit a power-law like relationship. However, the exponent of the wavenumber differs for each Ekman number, and the relationship indicates that there is no difference between the growth rates for  $k = 0$ , which is the axisymmetric mode. The varying exponent with varying Ekman number demonstrates that a more appropriate fit would involve  $k$ ,  $A$ ,  $Ro$ , and  $E$ .

Since the linear instability mode has been determined to be the mode I instability,

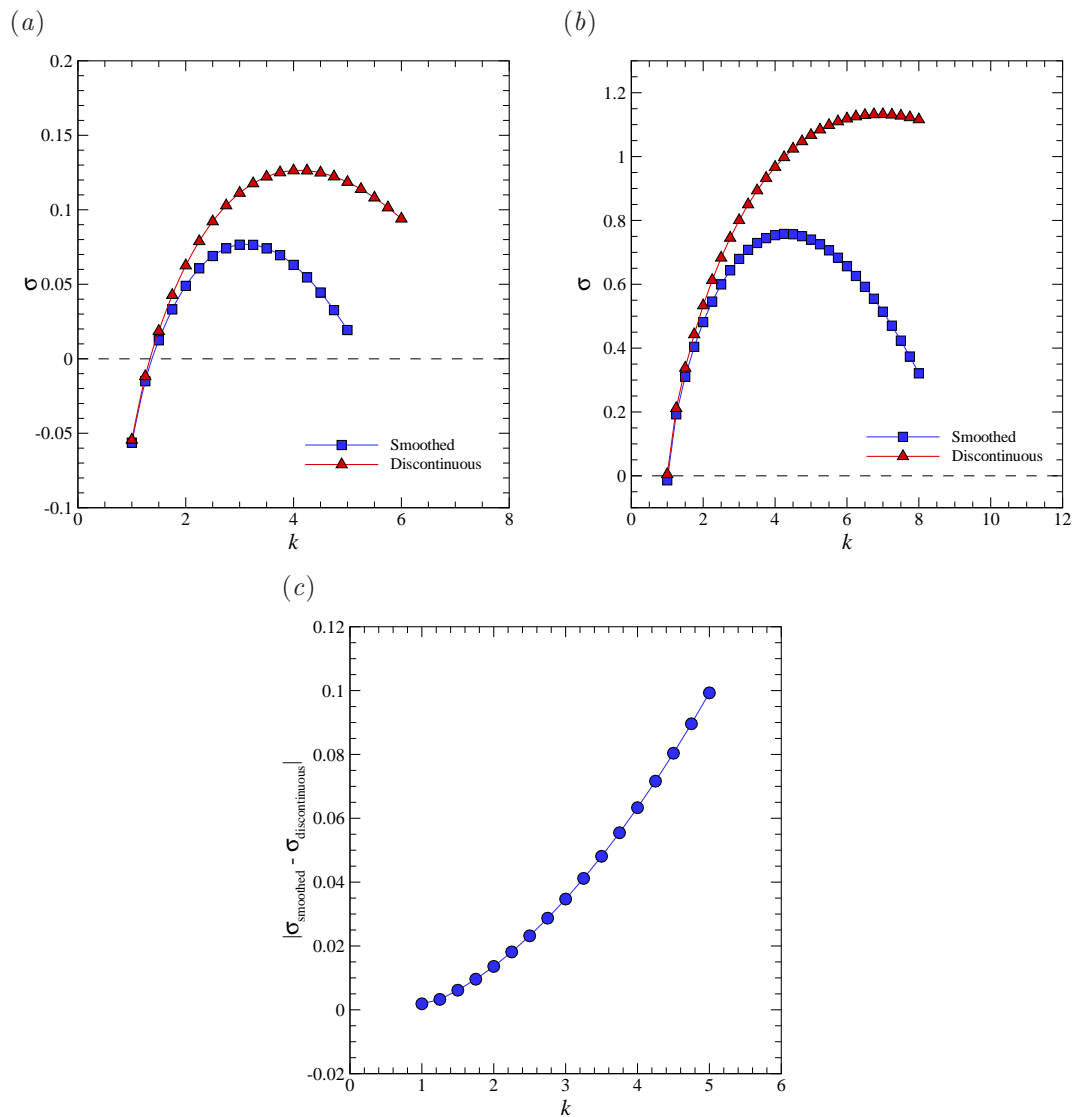


FIGURE 7.19: Growth rate as a function of wavenumber for (a)  $Ro = 0.2$  and  $E = 1 \times 10^{-3}$  and (b)  $Ro = 0.5$  and  $E = 3 \times 10^{-4}$  obtained from axisymmetric base flow solutions based on the smoothed and discontinuous forcing functions. The dashed line represents neutral stability where points above and below symbolise unstable and stable modes, respectively. (c) The absolute difference in growth rate between the smoothed and discontinuous forcing solutions as a function of wavenumber for flow conditions of (a).

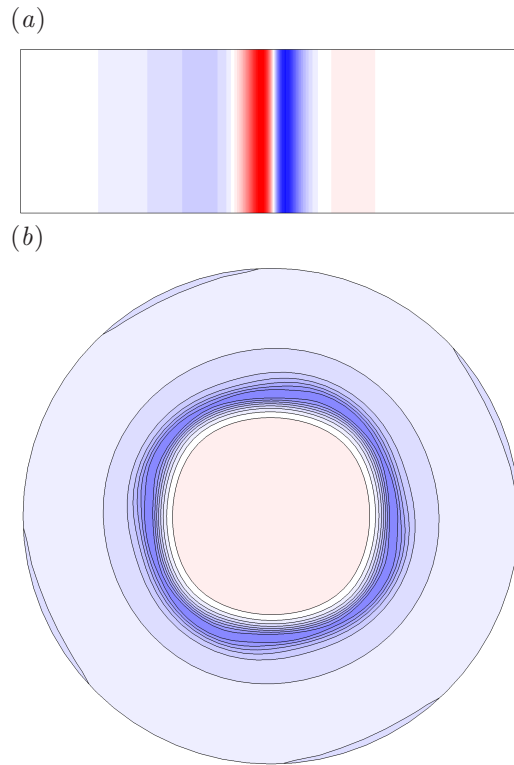


FIGURE 7.20: Axial vorticity contours of the dominant linear instability mode with azimuthal wavenumber  $k = 4$  at  $Ro = 0.5$  and  $E = 3 \times 10^{-4}$ . (a) The perturbation field of the instability mode is plotted in the  $r$ - $z$  plane, with contour levels as per figure 7.13. (b) A linear non-axisymmetric flow constructed by superimposing the axisymmetric base flow and the azimuthal linear instability wavenumber as per figure 7.14 with contours are per figure 7.2.

---

it is expected that the perturbation field and the genesis of the instability on the base flow will appear similar to that of figure 7.15 (provided the peak wavenumber is the same). Shown in figure 7.20 are the axial vorticity contours of the perturbation field of an azimuthal wavenumber  $k = 4$  and the superposition on its respective base flow. Two strong bands of opposite-signed vorticity appear around  $r = 1$ , which noticeably encompasses a wider radial region compared to the solution derived with discontinuous forcing conditions. It is believed that these perturbations evolve over a larger region due to the greater availability on which the barotropic instability can be sustained. That is, the Stewartson layer is thicker in this case. The  $k = 4$  instability causes the base flow to generate a four-sided polygon around the circumference of  $r = 1$ , which is comprised of very low axial vorticity. In contrast, its interior is composed of the highest vorticity in the entire domain. The ring of low vorticity which makes up the polygonal border is not indicative of the shear-layer thickness since an arbitrary scale

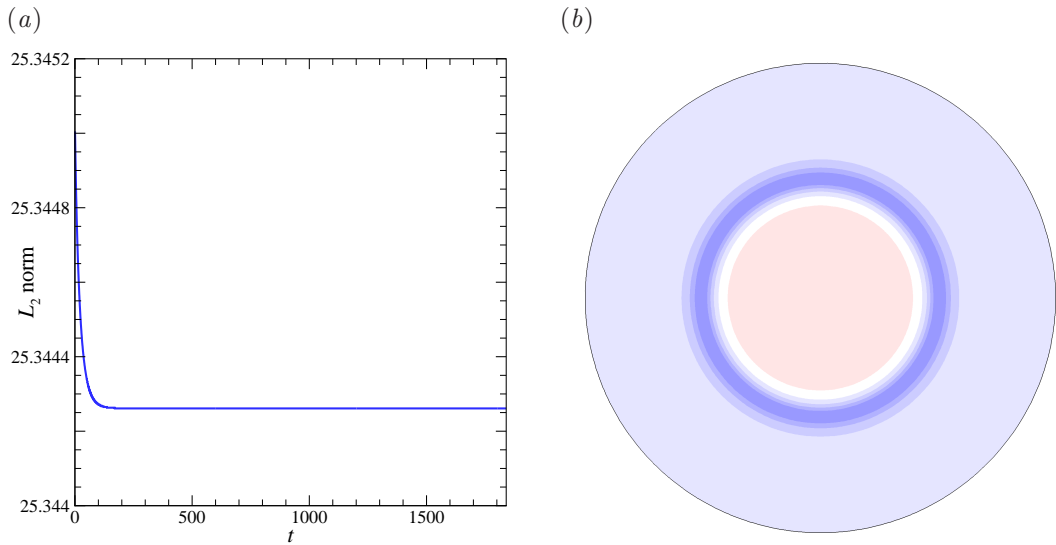


FIGURE 7.21: Flow conditions characterised by  $Ro = 0.05$  and  $E = 3 \times 10^{-4}$ . (a) The  $L_2$  norm of the quasi-two-dimensional flow measured over time. (b) Axial vorticity contours of the flow represented at  $t = 1500$ .

---

of the perturbations has been used for the superposition.

## 7.5 Non-axisymmetric flow structure

The non-axisymmetric structures that evolve from these rotating flows have been investigated to illustrate the significance of nonlinear effects. Unlike the previous simulations of non-axisymmetric structures computed via three-dimensional direct numerical simulation, the non-axisymmetric flow computed for the quasi-two-dimensional model is computed on a two-dimensional  $r-\theta$  plane, and by definition there can be no depth dependence. The forcing conditions used here are smoothed (previously described in § 3.7.2 and § 7.4) and are different to those employed in the three-dimensional direct numerical simulation. The flows simulated in this section correspond to those computed in Chapter 6, which investigated non-axisymmetric flow via three-dimensional direct numerical simulation.

The three-dimensional flow described by  $Ro = 0.05$  and  $E = 3 \times 10^{-4}$  was studied in § 6.1, corresponding to the reference case in the vicinity of instability onset. The direct numerical simulation illustrated a wavenumber 5 structure upon saturation. In contrast, the quasi-two-dimensional solution for the same flow condition demonstrates an axisymmetric stable state. The  $L_2$  norm measured over time and the axial vorticity

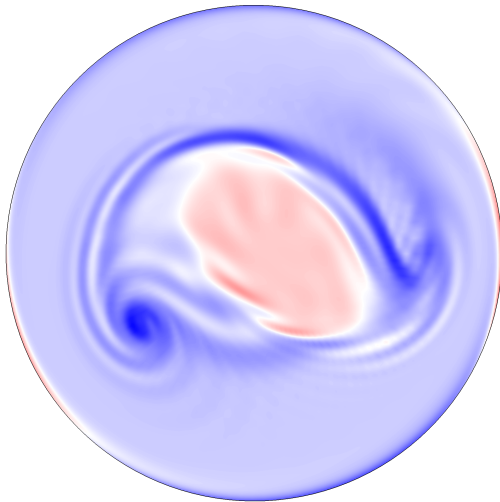
contours of the saturated flow are shown in figure 7.21. The  $L_2$  norm data indicates that the axisymmetric state observed in figure 7.21(b) is maintained from  $t \gtrsim 100$ . The axisymmetric structure is comprised of a ring exhibiting low vorticity encompassing a circular region of high vorticity. This same structure is observed over 1500 time units, which would correspond to 43 days based on a physical rotation rate of  $4 \times 10^{-4}$  in the laboratory rig used by Fröh & Read (1999). The discrepancy in the observed states between the three-dimensional and quasi-two-dimensional models is explained by the smoothed forcing condition employed in the latter model. As revealed in the previous section (§ 7.4.2), the effect of smoothing the forcing condition causes the base flow to become more stable towards non-axisymmetric perturbations. Thus, as this condition is already near the critical internal Reynolds number for instability in the three-dimensional model, adopting a smoothed forcing has caused the flow to become stable in the quasi-two-dimensional model.

The greater stability exhibited in the quasi-two-dimensional non-axisymmetric flows as a result of the smoothed forcing condition imposed was also observed for other flow conditions near the onset of instability. These cases include  $(Ro, E) = (0.015, 8 \times 10^{-5})$ ,  $(0.02375, 8 \times 10^{-5})$ ,  $(0.147, 1.06 \times 10^{-3})$  and  $(0.08738, 6.8 \times 10^{-4})$ , for which their saturated non-axisymmetric structures have been detailed previously in Chapter 6 (§ 6.1, § 6.3.1 and § 6.3.2). The  $L_2$  norm and the structure of these cases appear very similar to those presented in figure 7.21(a).

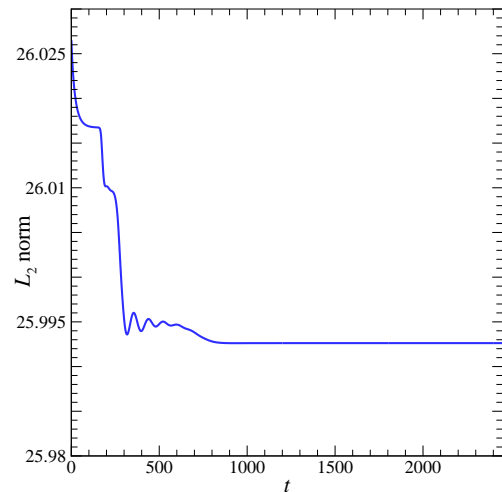
Considering flow conditions further away from the instability threshold highlights the excellent agreement in the qualitative results between the three-dimensional direct numerical simulation and the quasi-two-dimensional flows. The flow characterised by  $Ro = 0.17$  and  $E = 2.5 \times 10^{-4}$  demonstrated a wavenumber 2 consistently disturbed by a wavenumber 1 structure in the three-dimensional solution. This structure is portrayed in figure 7.22(a). The same resulting structure was observed in the quasi-two-dimensional model. The  $L_2$  norm data and a time sequence of the evolving axial vorticity structures from the quasi-two-dimensional model are shown in figure 7.22(b, c), respectively. The  $L_2$  norm data displays several sharp decreases over time, which is typically attributed to the vacillation of the evolving wavenumber structure. This is most evident in the beginning 700 time units of the simulation whereby the initial axisymmetric structure evolves to a wavenumber 4 structure, then a wavenumber 2 structure, and subsequently transforming into an unequal dipole structure. Between

---

(a) Three-dimensional solution



(b) Quasi-two-dimensional model -  $L_2$  norm



(c) Quasi-two-dimensional solution

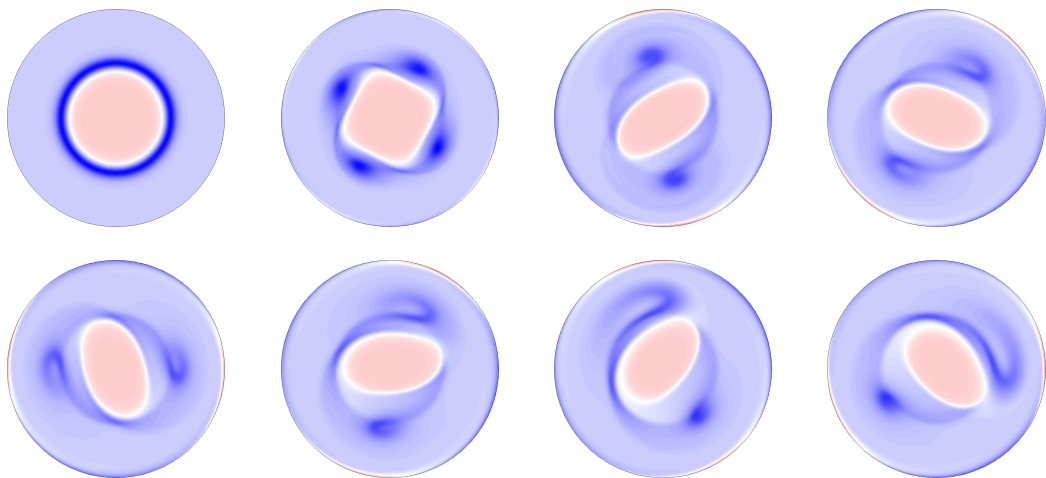


FIGURE 7.22: Flow condition of  $Ro = 0.17$  and  $E = 2.5 \times 10^{-4}$ . (a) Contours of axial vorticity at mid-depth computed from the three-dimensional direct numerical simulation at  $t = 1629$ . Quasi-two-dimensional results of the (b)  $L_2$  norm and the (c) time evolution of axial vorticity. Time increases from left to right and continues in the bottom row. The times are given by  $t = 100, 200, 300, 400, 500, 700, 1000$  and  $2000$ , respectively. Equi-spaced axial vorticity contour levels are plotted between  $2\bar{\Omega} \pm 5\omega$ . Blue and red contour shading represent low and high values, respectively.

---

$t = 300$  and  $t = 500$ , the two vortices forming the dipole structure appear to be of the same strength and gain vorticity equally. However, as seen at  $t = 700$ , one of the vortices decreases its axial vorticity to the state at  $t = 300$  while the other vortex is now elongated. This stable structure seems to persist indefinitely after  $t = 800$  where the  $L_2$  norm data exhibits a plateau. The qualitative agreement between figure 7.22(a) and the last panel of figure 7.22(c) is remarkable. It should be noted that the simulations of the two models have been computed using two different meshes. The only clear difference is attributed to the ripples in the vorticity present in the three-dimensional solution. This result reinforces the idea that these ripples may be related to inertial waves, which would be suppressed in the quasi-two-dimensional simulations as they propagate on the  $r$ - $z$  plane oblique to a plane of constant  $z$ .

The qualitative agreement of the saturated structures between the two models has also been observed for other flow conditions that are far beyond the instability onset. A few examples are highlighted in figure 7.23. Again, the inertial-like waves are not evident in the quasi-two-dimensional solutions. These non-axisymmetric results suggests that the quasi-two-dimensional model is very capable of determining the eventual stable mode at flow conditions that are well beyond the instability onset. Given a mesh that does not adopt a four-fold symmetry, it is anticipated that the quasi-two-dimensional model would be able to generate  $Ro$ - $E$  regime diagrams of the observed stable azimuthal wavenumbers similar to those produced via the three-dimensional direct numerical simulations.

## 7.6 Chapter summary

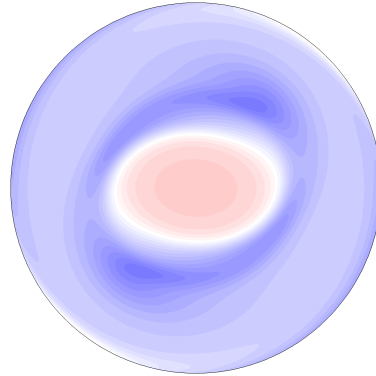
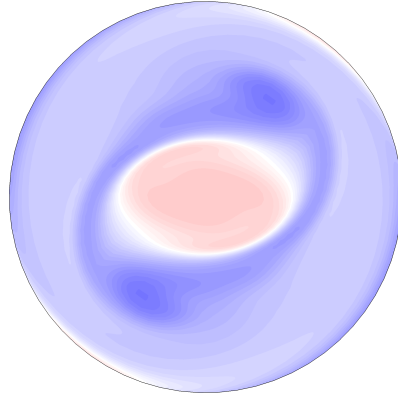
In this chapter, the axisymmetric base flow, linear instability and non-axisymmetric flow governed by quasi-two-dimensional equations have been examined in detail. There has not yet been a direct comparison between the axisymmetric solutions and the quasi-two-dimensional solutions. The primary difference in these flows is that the meridional circulation is not present in the quasi-two-dimensional solutions as depth independence is strictly enforced. Most importantly, this means that the Stewartson  $E^{1/3}$  layer is not produced in these flows, which has had thought to have implications for the linear stability of the flow.

Flows with Rossby numbers ranging between  $-1.0 \leq Ro \leq 0.6$  and Ekman numbers between  $3 \times 10^{-5} \leq E \leq 3 \times 10^{-3}$  were investigated. The same flow features were

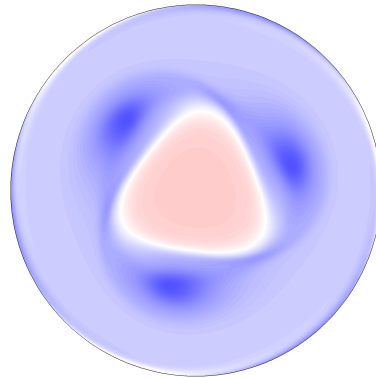
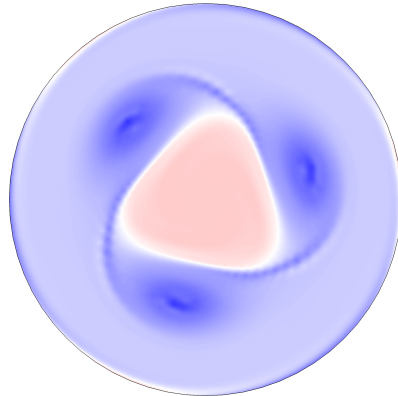
---

Three-dimensional solution  
(a)  $Ro = 0.5, E = 3 \times 10^{-3}$

Quasi-two-dimensional solution



(b)  $Ro = 0.5, E = 1 \times 10^{-3}$



(c)  $Ro = 0.05, E = 8 \times 10^{-5}$

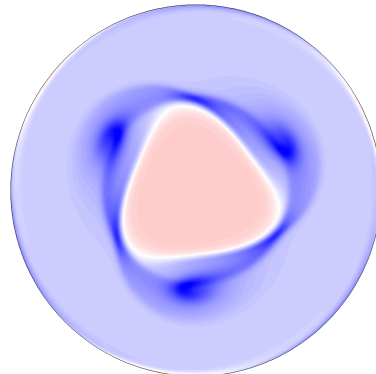
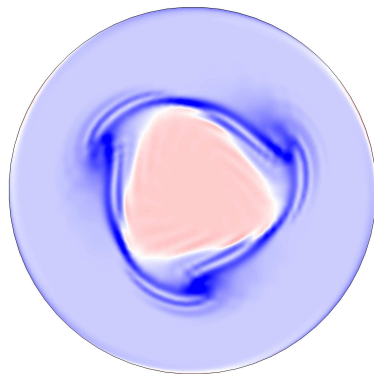


FIGURE 7.23: Flow conditions of (a)  $(Ro, E)=(0.5, 3 \times 10^{-3})$ , (b)  $(Ro, E)=(0.5, 1 \times 10^{-3})$  and (c)  $(Ro, E)=(0.05, 8 \times 10^{-5})$ . Axial vorticity contours of the saturated flow states from the three-dimensional direct numerical simulation and quasi-two-dimensional solutions are illustrated in the left and right columns, respectively. Contour levels as per figure 7.22.

---

obtained between the axisymmetric and quasi-two-dimensional models for small  $|Ro|$  with differences observed at large  $|Ro|$ . A shear layer is produced at the disk-tank interface for positive- $Ro$  flows, which is exhibited by a negative axial vorticity band. For negative- $Ro$  flows, the axisymmetric simulations exhibit negative axial vorticity patches on the inner side of the Stewartson layer. This feature is represented by a vertical strand of negative vorticity on the inner side of the  $E^{1/4}$  layer due to the depth independence imposed. The profiles of relative azimuthal vorticity displayed little differences between the two models. In contrast, the absence of secondary motions in the quasi-two-dimensional model caused a sharp turning point in the axial vorticity profile, which exhibits a greater magnitude. The similarity in the azimuthal velocity is reflected in the measured  $E^{1/4}$  thickness whereby the axisymmetric and the quasi-two-dimensional solutions yield  $\delta_{\text{vel}} = 1.31E^{0.22}$  and  $\delta_{\text{vel}} = 1.32E^{0.219}$ , respectively. It is interesting to note that the thickness relationship for the quasi-two-dimensional model is independent of  $Ro$ , rather than being limited to  $Ro \rightarrow 0$ .

Despite the independence of  $Ro$  for the shear-layer thickness, the azimuthal wavenumber preference for the linear instability of the flow remains dependent on both  $Ro$  and  $E$ . The growth rate as a function of wavenumber demonstrates the usual trend of increasing growth rate and corresponding azimuthal wavenumber with increasing  $Ro$  and decreasing  $E$ . More importantly, the results only reveal the mode I instability branch which is associated with the depth independence and reflective symmetry of the flow. The absence of the mode II and III instabilities reinforce the argument that these instabilities are generated as a consequence of the breaking of depth independence in the axisymmetric base flow proposed in Chapter 5. The ratio between the growth rate of the positive and negative  $Ro$  was found to be  $\sigma_{\text{pos } Ro}/\sigma_{\text{neg } Ro} = (1 + A|Ro|)/(1 - A|Ro|)$ . For positive  $Ro$ , this relationship exactly describes the rotation rate of the disk. In relation to the preferred azimuthal wavenumber, no difference was observed between positive and negative  $Ro$ . The superposition of the axisymmetric base flow and the perturbation field highlighted the resulting deformed structures which were consistent with the mode I instability. That is, various polygon shapes were observed with its borders coinciding with the disk-tank interface. A fit of the azimuthal wavelength as a function of  $|Ro|/E^2$  suggested that  $\lambda_\theta$  scales with  $E^{1/3}/|Ro|^{1/6}$ . Although it is unknown whether the  $1/3$  exponent has any real significance, it is clear that it is not related to the  $E^{1/3}$  layer. The same relationship was obtained for the axisymmetric solutions

which suggest that the  $E^{1/3}$  has little or no effect on the linear stability of the base flow.

The effect of smoothing out the imposed velocity forcing was examined, since previous studies have only considered smoothed forcing profiles. This demonstrated little influence on the features observed in the axisymmetric base flow. The major observable difference is seen in the shear-layer thickness. This is reinforced numerically through the relationship  $\delta_{\text{vel}} = 1.71E^{0.226}$ , which produces a larger thickness for a given  $E$ , as compared to the discontinuous forcing. As a consequence, the thicker Stewartson layer stabilises the base flow. That is, lower growth rates for the wavenumbers are achieved along with smaller peak wavenumbers.

The smoothed forcing function was also employed in the non-axisymmetric quasi-two-dimensional simulations. Consequently, flow conditions near the onset of instability were found instead to be stable resulting in an axisymmetric flow (due to the thicker shear layer). In contrast, flow conditions well beyond the instability threshold demonstrated strong qualitative agreement between the quasi-two-dimensional model and the three-dimensional direct numerical simulation. Overall, similar trends were seen between the quasi-two-dimensional simulations and the three-dimensional direct numerical simulations in that increasing  $Re_i$  causes a shift to lower wavenumbers. These trends differ to that of the linear stability analysis and are attributed to nonlinear effects. It was also observed that without the addition of random noise at the initialisation of the quasi-two-dimensional simulations, the flows required long time periods to produce and sustain stable polygonal vortex structures.



## Chapter 8

# Conclusions and direction for future research

The flow in a differentially rotating cylindrical container has been numerically investigated. The flow is differentially forced by two disks located flush with the base and lid of the container. This rotating flow is characterised primarily by two non-dimensional parameters described by the Rossby and Ekman number. The parameter space largely investigated in this thesis includes Rossby numbers between  $-4.0 \leq Ro \leq 1$ , and Ekman numbers ranging between  $5 \times 10^{-5} \leq E \leq 3 \times 10^{-3}$ . In addition, aspect ratios ranging between  $1/6 \leq A \leq 2$  have been explored. Previous studies relating to the stability of the flow have predominantly been conducted experimentally with past numerical studies limited to quasi-two-dimensional models only. Thus, the studies have been limited to investigating only the nonlinear aspects of the unstable flow and largely in a horizontal plane. The present study delivers the first elucidation of the three-dimensional flow including its vertical structure, and the first linear stability analysis of the axisymmetric base flow to non-axisymmetric disturbances. Furthermore, flow solutions from three-dimensional direct numerical simulation and quasi-two-dimensional modelling have provided significant insight relating to reported experimental results and the validity of the simple quasi-two-dimensional model.

The key conclusions from this study are outlined in the following sections in addition to suggestions for future research. The majority of the results are original and have not been realised in the literature.

## 8.1 Key results from axisymmetric base flow simulations

### 8.1.1 The vertical structure of the flow and universality of the aspect ratio

The structures of the axisymmetric base flows produced by a differential rotation in a cylindrical container have been examined numerically. Distinct features have been observed and have been determined to be dependent primarily on the sign and magnitude of  $Ro$ . For small- $|Ro|$  flows in the positive and negative-Rossby-number regime, the axial vorticity contours of the flow are depth-independent following the Taylor–Proudman theorem. The resultant flow illustrates a vertical band of vorticity originating from the disk-tank interface. As the magnitude of the Rossby number increases in the positive regime, the negative vorticity band is broken yielding diagonal strands originating from each disk-tank interface. Thus, the reflective symmetry about mid-depth is broken. In contrast, sufficiently large- $|Ro|$  flows in the negative regime maintains the reflective symmetry and demonstrates a pair of positive and negative vorticity structures adjacent to the vertical positive axial vorticity band. The breaking of reflective symmetry is likely a consequence of the axial pumping induced by the Ekman layers over  $Ro > 0$  and  $Ro < 1/A$ . That is, the hyperbolic point on the  $r$ - $z$  plane at mid-depth becomes unstable at sufficiently large opposing axial velocities.

The same features were observable throughout the entire range of  $A$ . The results revealed a transition line between reflectively symmetric and symmetry-broken flow, which is scaled by a ratio of  $Ro/E^{1/2}$ . Equivalently, this corresponds to a Reynolds number based on the Ekman layer thickness, and the threshold was determined as  $Re_E \sim 26.7$ . Moreover, the relationship is independent of the aspect ratio. A transitional regime was determined between  $26.7 \lesssim Re_E \lesssim 56.4$ , which encompasses both reflectively symmetric and symmetry-broken flow.

### 8.1.2 Scaling of the Stewartson layer thickness

The thicknesses of the Stewartson layers have been determined from the velocity and vorticity profiles extracted from the flow. The thicker  $E^{1/4}$  layer was established from the relative azimuthal velocity profile while the thinner  $E^{1/3}$  layer was determined from the axial vorticity profile. For flows characterised by a very small  $Ro$  close to zero, the exponents of the Ekman number was found to be in agreement with the theoretically predicted exponents. As the Rossby number magnitude is increased, the thickness

of the Stewartson layer also increases and becomes predominantly dependent on the Rossby number. In contrast, decreasing the Rossby number yields a thinner shear layer and becomes dependent primarily on the Ekman number.

The shear-layer thickness as  $Ro \rightarrow 0$  is also described by  $\delta_{\text{vel}} \propto E^{1/4}$  and  $\delta_{\text{vort}} \propto E^{1/3}$ . However, as the aspect ratio is increased sufficiently, the shear layer becomes affected by the confining walls. According to the thickness measurements, the shear layer responsible for smoothing out the angular velocity no longer adopts a thickness that scales with  $E^{1/4}$  at  $A = 2$ . Interestingly at the same aspect ratio, the thinner Stewartson layer is still well defined as represented through an Ekman number exponent of  $1/3$ .

### 8.1.3 Time-dependent flow structure

Time-dependent flows have been realised at large positive Rossby numbers. With increasing  $Ro$ , the axisymmetric base flow transitions from steady-state  $\rightarrow$  periodic  $\rightarrow$  aperiodic (mixed) state  $\rightarrow$  periodic. The onset of periodic flow originates from the instability of the axial jets induced by the Ekman layer. The periodic flows before and after the aperiodic mixed state are different. The periodic flow described by the lower  $Ro$  illustrates negative vorticity strand tips that fluctuate slightly in the radial direction within a period. Also, the strands do not fluctuate past  $r = 1$  and therefore does not bypass each other. This is in contrast to the periodic flow characterised by the higher  $Ro$  whereby the strands bypass each other twice per period.

## 8.2 Key results from the linear stability analysis

### 8.2.1 Mode I and II linear instabilities

A linear stability analysis revealed two dominant types of linear instabilities, namely mode I and mode II. The former is associated with the instability of the  $E^{1/4}$  layer, while the latter is suggested to be related to the instability of the  $E^{1/3}$  layer. The two instability modes are identified by their respective local maxima in the growth rate data: mode I favours low wavenumbers while mode II has a preference towards higher wavenumbers. The flow initially becomes unstable to mode I and with increasing  $Ro$  or decreasing  $E$ , the growth rate of the mode II wavelengths eventually exhibit the largest values. The presence of the mode II instability develops from the breaking of depth independence and reflective symmetry about the horizontal mid-plane in the flow. Both

instabilities have the similar effect on the axisymmetric base flow such that the shear layers deform into a chain of vortices in a polygonal arrangement.

### 8.2.2 Scaling the azimuthal wavenumber against the aspect ratio

It was determined that the thickness of the shear layer at the disk-tank interface was affected by the confining walls through axisymmetric simulations. This result was also reflected in the linear stability analysis whereby the larger aspect ratio produced flows that exhibit small growth rates. In contrast, flows of aspect ratios ranging  $A \lesssim 2/3$  generated linear modes that were similar in peak magnitude, despite the corresponding azimuthal wavenumber being different. This difference could be accounted for by scaling the azimuthal wavenumber against the aspect ratio (i.e.  $kA$ ). Thus, given growth-rate data for a particular flow condition, the growth rates and corresponding azimuthal wavenumbers can be determined for flows which generate a shear layer unhindered by the confinement ( $A \lesssim 2/3$ ).

### 8.2.3 Scaling of the unstable azimuthal wavelength

The preferred azimuthal wavenumbers associated with the mode I instability where reflective symmetry is exhibited in the axisymmetric base flow are consistent with those obtained in the negative- $Ro$  regime if the magnitude of  $Ro$  is considered. That is, at low  $Re_i$ , the predicted linear wavenumber is the same for both the positive and negative- $Ro$  regime. The preferred azimuthal wavelength of the mode I instability is described by  $\lambda_\theta \sim E^{1/3}/|Ro|^{1/6}$  for  $A = 2/3$ . It is determined that the  $E^{1/3}$  parameter is not associated with the  $E^{1/3}$  Stewartson layer as an almost identical relationship is obtained from the quasi-two-dimensional model, which does not capture the  $E^{1/3}$  layer.

### 8.2.4 The critical $Ro/E^{3/4}$ parameter

The threshold of instability was determined to be  $Ro_c = 18.1E^{0.767}$  for  $A = 2/3$ , which is in agreement with the theoretical scaling of  $Ro_c \propto E^{3/4}$  and the experimental determination of  $Ro_c \propto E^{0.72}$  (Früh & Read 1999). The determined relationship corresponds to a constant Reynolds number whose length scale is based on the thickness of the Stewartson  $E^{1/4}$  layer. Hence, the onset of instability is equivalently characterised by  $Re_{i,c} = 22.4 \pm 0.8$ . However, since a number of different length, time and velocity scales have been used to define the governing parameters across the literature, the reported internal Reynolds numbers have varied. A more consistent comparison was achieved

by instead considering the critical  $Ro/E^{3/4}$  parameter. The results from the linear stability analysis dictate a critical  $Ro/E^{3/4} = 15.8 \pm 0.57$ , which lies in between the determined values from literature of 15.4 and 16.6. A better indication of the threshold was determined using a smaller aspect ratio of  $A = 1/6$ , which yielded  $Re_{i,c} \approx 22.6$  corresponding to  $Ro/E^{3/4} = 16$ .

### 8.3 Key results from three-dimensional direct numerical simulation

#### 8.3.1 Significance of nonlinear effects

Flow conditions just beyond the onset of instability have demonstrated a very strong dominance of linear instability. Thus, the preferred azimuthal wavenumber of these flow conditions can be accurately predicted by a linear stability analysis. However, nonlinear effects become significant as the Rossby number is increased or the Ekman number is decreased further beyond the stability threshold. As a consequence, the vortices are encouraged to interact and coalesce leading to a larger wavelength structure. This trend has also been observed in the experiments. Furthermore, flow conditions that predict a dominant mode II instability via a linear stability analysis revealed the insignificant contributions from the wavelengths associated with the mode II waveband in the nonlinear regime. That is, the nonlinear effects always revealed a decay in the growth of mode II wavelengths. In addition, these rotating flows demonstrated a high insensitivity to initial conditions. However, hysteresis effects were evident in that multiple states existed for a single flow condition. This occurred when a flow condition was changed with an existing saturated flow state being used as the initial flow state.

#### 8.3.2 Experimental implications and limitations

The three-dimensional direct numerical simulation results have demonstrated unstable growth comprised of two stages: exponential growth and saturation. The exponential growth phase is accurately predicted by the linear solution obtained via the linear stability analysis, which describes very small growth rates. Thus, the amplitudes of the instability are very small and would be very difficult to detect in an experimental setting. This explains why the experimentally determined instability threshold occurs at a higher  $Re_i$  as compared to the numerical prediction. In addition, the three-dimensional direct numerical simulation results have also demonstrated very small growth rate

instabilities in the nonlinear regime, which would require an extreme amount of time for the flow to saturate towards the ultimate stable state in an experiment. This suggests that experimental results reported in the literature thus far may not necessarily be representative of the eventual stable state. This also explains the discrepancy between the numerically predicted azimuthal wavenumbers and the observed wavenumber structures in the laboratory, especially in the vicinity of the onset of instability.

## 8.4 Key results from quasi-two-dimensional modelling

### 8.4.1 The vertical flow structure and $E^{1/4}$ layer thickness

A direct comparison between the flows modelled by the axisymmetric and the quasi-two-dimensional model was conducted. The two models exhibited similar flow structures at small  $Ro$  with differences observed at large  $Ro$ . This is due to the depth independence breaking of the flow in the axisymmetric model as compared to the depth independence is enforced by the quasi-two-dimensional model. Thus, the differences reside at the disk-tank interface where a column of vorticity was seen in the quasi-two-dimensional model while the column of vorticity is broken into two diagonal strands the axisymmetric model. The similarity between the two models is reflected in the measured  $E^{1/4}$  layer as  $Ro \rightarrow 0$ , with both displaying very similar coefficients and exponents of  $E$ . However, the thickness of the  $E^{1/4}$  layer does not vary with  $Ro$  in quasi-two-dimensional flows. This is likely explained by the presence of meridional circulations produced by the Ekman layers in the axisymmetric simulations.

### 8.4.2 Significance of $|Ro|$ in describing positive and negative-Rossby-number growth rates and the preferred azimuthal wavenumbers

The growth rates of non-axisymmetric disturbances on the base flows were obtained using a linear stability analysis. The growth rate as a function of azimuthal wavenumber demonstrates the usual trend of increasing growth rate and corresponding azimuthal wavenumber with increasing  $Ro$  and decreasing  $E$ . Also, the results only reveal the mode I instability since the base flows always exhibit reflective symmetry about the mid-plane, due to the depth independence enforced by the model. Interestingly, the ratio between positive and negative growth rates for a particular flow can be described by the disk speed  $\Omega + \omega$ , provided that the magnitude of  $Ro$  is used.

Despite the constant Stewartson layer thickness across  $Ro$ , the preferred azimuthal

wavenumbers predicted by linear stability analysis varies with  $Ro$ . In fact, the predicted wavenumbers between the axisymmetric and quasi-two-dimensional models are exactly the same. Thus, the quasi-two-dimensional model can be used to accurately describe the predicted linear instability wavenumber structure associated with the  $E^{1/4}$  layer. The corresponding unstable wavelengths are described by  $\lambda_\theta \sim E^{1/3}/|Ro|^{1/6}$ , which is identical in exponents compared to that obtained for the axisymmetric simulations. Thus, the  $E^{1/3}$  result is determined not to be related to  $E^{1/3}$  layer as it is absent in the quasi-two-dimensional model. In addition, the threshold of linear instability is the same in both the positive and negative- $Ro$  regimes, namely  $|Ro_c| = 18.7E^{0.769}$ , which is comparable to the axisymmetric simulations.

### 8.4.3 Non-axisymmetric flow structure

Comparisons between the non-axisymmetric structures observed in the three-dimensional and quasi-two-dimensional solutions were performed to elucidate the differences and the validity of the quasi-two-dimensional model. In using smoothed forcing conditions for the quasi-two-dimensional simulations, the qualitative results demonstrated strong agreement in the observed stable azimuthal wavenumber provided that the flow conditions were well beyond the instability threshold. Flow conditions described near the onset of instability displayed axisymmetric structures with the  $L_2$  data providing no indication of structural change for extremely long time periods. In addition, the spatial structure between the two models are almost identical with the exception that inertial-like waves are present in the three-dimensional solution, for which the quasi-two-dimensional is not capable of capturing. The quasi-two-dimensional model was able to capture non-axisymmetric structures representative of  $k \leq 5$  and illustrated the same trends observed in the three-dimensional model. That is, either increasing  $Ro$  or  $E$  resulted in a decrease in the stable azimuthal wavenumber as a consequence of nonlinear effects.

## 8.5 Future research

The present research has revealed the flow structures and transitions in a differentially-rotating container of various aspect ratios. This thesis reports the first simulations of the axisymmetric and non-axisymmetric flows within this system. Despite the novel findings in this thesis, some unanswered questions remain.

Axisymmetric base flows described by both positive and negative  $Ro$  were thoroughly investigated. However, subsequent analysis of the linear stability of the flow and the nonlinear effects were focused primarily on positive- $Ro$  flows. Thus, additional studies are required to elucidate trends in the negative- $Ro$  regime. In particular, exploring the mode II instability present at high magnitudes of negative  $Ro$  and identifying the dependence of the Rossby and Ekman number on the preferred azimuthal wavenumbers. In addition, it would be interesting to verify that the growth rate as a function of azimuthal wavenumber is consistent across all aspect ratios provided that the shear layer is unconstrained by the confinement, similar to that observed for positive- $Ro$  flows. Although the limited results suggest that the trends established in the positive- $Ro$  regime are also applicable in the negative- $Ro$  regime, the results need to be substantiated. The study of negative- $Ro$  flows can be extended by analysing the nonlinear effects in a three-dimensional direct numerical simulation. That is, establishing the prominence of nonlinear effects in the negative- $Ro$  regime and the presence of inertial-like waves at large negative  $|Ro|$ .

Regarding the linear stability of the flow, it would be interesting to confirm if the onset of the mode II instability is described by the proposed relationship  $Ro_{\text{mode II}} \propto E^{2/3}$ , corresponding to a constant Reynolds number based on the thickness of the  $E^{1/3}$  Stewartson layer. This would reinforce the suggestion that the mode II instability is associated with  $E^{1/3}$  layer.

The computational costs required were extremely high in simulating the flow via three-dimensional direct numerical simulation. As such, it was not possible to explore all aspects of the three-dimensional flow. In particular, ideally a greater number of Fourier modes should be implemented to capture the harmonics of the preferred small wavelength structures and confirm the negligible effect of the mode II linear instability in the nonlinear growth regime. Also, flow conditions that exhibit time-dependent flow characteristics should be further explored to compare against time-dependent behaviours reported in the experiments. It would also be interesting to see direct numerical simulation being utilised to study the three-dimensional flows at other aspect ratios, especially those at large aspect ratios where the instability of the  $E^{1/4}$  layer is thought to be different or in some cases non-existent. Moreover, investigations into whether the presence of a sloping bottom demonstrates any major differences beyond effectively changing the aspect ratio as suggested by the linear stability analysis would

further the understanding of these differentially rotating flows.



## Appendix A

# The Ekman solution

This section details the velocity solution in an Ekman layer, following Pedlosky (1987). The Ekman layer is a frictional layer which appears on a surface perpendicular to the rotational vector. Consider an incompressible rotating flow with angular velocity  $\Omega$  with a horizontal uniform flow sufficiently far ( $z \rightarrow \infty$ ) from a stationary plate at  $z = 0$ . The horizontal velocity is given by  $\mathbf{u} = (u, v, w)(x, y, z) = (U_\infty, 0, 0)$ . On the rigid boundary, the velocity components are zero ( $u = v = w = 0$ ). The equations governing the flow are given by

$$\frac{\partial u}{\partial t} + u \frac{\partial u}{\partial x} + v \frac{\partial u}{\partial y} + w \frac{\partial u}{\partial z} - fv = -\frac{\partial P}{\partial x} + \nu \left( \frac{\partial^2 u}{\partial x^2} + \frac{\partial^2 u}{\partial y^2} + \frac{\partial^2 u}{\partial z^2} \right), \quad (\text{A.1})$$

$$\frac{\partial v}{\partial t} + u \frac{\partial v}{\partial x} + v \frac{\partial v}{\partial y} + w \frac{\partial v}{\partial z} + fu = -\frac{\partial P}{\partial y} + \nu \left( \frac{\partial^2 v}{\partial x^2} + \frac{\partial^2 v}{\partial y^2} + \frac{\partial^2 v}{\partial z^2} \right), \quad (\text{A.2})$$

$$\frac{\partial w}{\partial t} + u \frac{\partial w}{\partial x} + v \frac{\partial w}{\partial y} + w \frac{\partial w}{\partial z} = -\frac{\partial P}{\partial z} - g + \nu \left( \frac{\partial^2 w}{\partial x^2} + \frac{\partial^2 w}{\partial y^2} + \frac{\partial^2 w}{\partial z^2} \right), \quad (\text{A.3})$$

$$\frac{\partial u}{\partial x} + \frac{\partial v}{\partial y} + \frac{\partial w}{\partial z} = 0, \quad (\text{A.4})$$

where  $f = 2\Omega$  represents the Coriolis parameter,  $P$  is the kinematic pressure and  $\nu$  is the kinematic viscosity. Assuming steady-state flow, and that the components  $u$ ,  $v$  and  $w$  are functions of  $z$  only, equations A.1 to A.4 simplify to

$$w \frac{\partial u}{\partial z} - fv = -\frac{\partial P}{\partial x} + \nu \frac{\partial^2 u}{\partial z^2}, \quad (\text{A.5})$$

$$w \frac{\partial v}{\partial z} + fu = -\frac{\partial P}{\partial y} + \nu \frac{\partial^2 v}{\partial z^2}, \quad (\text{A.6})$$

$$0 = -\frac{\partial P}{\partial z} - g, \quad (\text{A.7})$$

$$\frac{\partial w}{\partial z} = 0. \quad (\text{A.8})$$

Note that equation A.8 states that  $w$  does not vary with  $z$ . Given that  $w = 0$  at the boundary,  $w$  is therefore zero everywhere in the flow. Thus, the  $w\partial u/\partial z$  and  $w\partial v/\partial z$

terms equate to zero. Since the fluid is homogeneous, the  $z$  derivatives of the  $x$  and  $y$  pressure gradients are zero. That is, the horizontal pressure gradients are independent of  $z$ . Applying the conditions at  $z \rightarrow \infty$ , the horizontal pressure gradients are given by

$$0 = -\frac{\partial P}{\partial x}, \quad (\text{A.9})$$

$$fU_\infty = -\frac{\partial P}{\partial y}, \quad (\text{A.10})$$

which are also applicable near  $z = 0$  as the pressure gradients are independent of  $z$ .

Thus the governing equations are described by

$$-fv = \frac{\partial^2 u}{\partial z^2}, \quad (\text{A.11})$$

$$f\hat{u} = \nu \frac{\partial^2 v}{\partial z^2}, \quad (\text{A.12})$$

where  $\hat{u} = u - U_\infty$ , which represents the departure from geostrophic flow.

Eliminating  $v$  from equations A.11 and A.12 yields

$$\frac{d^4 \hat{u}}{dz^4} + \frac{f^2}{\nu^2} \hat{u} = 0, \quad (\text{A.13})$$

whose general solution is the sum of the four independent homogenous solutions. That is, the general solution for  $\hat{u}$  is characterised as

$$\hat{u} = C_1 e^{(1+i)z/\delta} + C_2 e^{(1-i)z/\delta} + C_3 e^{-(1+i)z/\delta} + C_4 e^{-(1-i)z/\delta}, \quad (\text{A.14})$$

where  $C_1, C_2, C_3$  and  $C_4$  are constants, with  $\delta = \sqrt{\nu/\Omega}$  representing the Ekman layer thickness. The first two terms on the right side of equation A.14 grow exponentially without bound for increasing  $z$ . Thus, the constants  $C_1$  and  $C_2$  are required to be zero which also satisfies  $\hat{u} = v = 0$  at  $z \rightarrow 0$ . Therefore,  $\hat{u}$  is given by

$$\hat{u} = C_3 e^{-(1+i)z/\delta} + C_4 e^{-(1-i)z/\delta}. \quad (\text{A.15})$$

Substitution of equation A.15 into equation A.12 yields

$$v = -iC_3 e^{-(1+i)z/\delta} + iC_4 e^{-(1-i)z/\delta}. \quad (\text{A.16})$$

Applying the boundary conditions at  $z = 0$  ( $\hat{u} = -U_\infty$  and  $v = 0$ ), equation A.16 states that  $C_3 = C_4$ . Hence, equation A.15 declares that

$$C_3 = C_4 = -\frac{U_\infty}{2}. \quad (\text{A.17})$$

Therefore, the horizontal velocities are given by

$$u = U_{\infty}(1 - e^{-z/\delta} \cos(z/\delta)), \quad (\text{A.18})$$

$$v = U_{\infty}e^{-z/\delta} \sin(z/\delta). \quad (\text{A.19})$$

The velocity solutions implies that the flow consists of a uniform geostrophic region for  $z > \delta$  while a thin Ekman layer exists for  $0 < z < \delta$ .



## Appendix B

# Scaling of the governing equations

This section highlights the process of non-dimensionalising the governing equations of the flow in a differential rotating configuration using two different sets of reference scales. The only difference between the two scaling sets is the angular rate used to scale velocity, time and pressure. That is, either the tank rotation rate or the disk rotation rate is implemented. The two paradigms and their numerical tractability are presented here, with the former being adopted throughout the thesis.

Consider a closed cylindrical rotating tank with disks located at the top and bottom boundaries whose axes are aligned with the axis of rotation. The tank rotates at an angular speed of  $\Omega$ , while the disks rotate at a speed of  $\Omega + \omega$ . The tank has dimensions of  $R_t$ ,  $R_d$  and  $H$ , which correspond to the radius of the tank, the radius of the disks and the height of the tank, respectively. The aspect ratio of the container is given by

$$A = \frac{H}{R_d}. \quad (\text{B.1})$$

The governing parameters of the flow are the Rossby and Ekman numbers, which are defined respectively as

$$Ro = \frac{R_d \omega}{2\bar{\Omega}H}, \quad (\text{B.2})$$

$$E = \frac{\nu}{\bar{\Omega}H^2}, \quad (\text{B.3})$$

where  $\bar{\Omega}$  represents the mean rotation rate of the flow. The parameter  $\bar{\Omega}$  is calculated by averaging the rotation rate prescribed in each quadrant in the  $r$ - $z$  plane, such that

$$\begin{aligned} \bar{\Omega} &= \frac{\Omega + \Omega + (\Omega + \omega) + (\Omega + \omega)}{4}, \\ &= \Omega + \omega/2. \end{aligned} \quad (\text{B.4})$$

The dimensional governing equations describing the conservation of momentum and mass are written in vector form, respectively, as

$$\frac{\partial \mathbf{u}}{\partial t} + (\mathbf{u} \cdot \nabla) \mathbf{u} = -\nabla P + \nu \nabla^2 \mathbf{u}, \quad (\text{B.5})$$

$$\nabla \cdot \mathbf{u} = 0, \quad (\text{B.6})$$

where  $\mathbf{u}$  is the velocity field,  $P = p/\rho$  is the kinematic pressure,  $p$  is the pressure,  $\rho$  the fluid density and  $\nu = \mu/\rho$  is the fluid kinematic viscosity.

## B.1 Governing equations scaled by the tank rotation rate

The flow quantities are non-dimensionalised through the following relationships,

$$\mathbf{u} = R_d \Omega \hat{\mathbf{u}}, \quad (\text{B.7})$$

$$\nabla = \hat{\nabla} / R_d, \quad (\text{B.8})$$

$$t = \hat{t} / \Omega, \quad (\text{B.9})$$

$$P = R_d^2 \Omega^2 \hat{P}, \quad (\text{B.10})$$

where the hat accents denote dimensionless quantities. Substituting equations B.7 - B.10 into equation B.5 and B.6 yields the non-dimensional governing equations

$$\frac{\partial \hat{\mathbf{u}}}{\partial \hat{t}} + (\hat{\mathbf{u}} \cdot \hat{\nabla}) \hat{\mathbf{u}} = \hat{\nabla} \hat{P} + \frac{\nu}{R_d^2 \Omega} \hat{\nabla}^2 \hat{\mathbf{u}}, \quad (\text{B.11})$$

$$\hat{\nabla} \cdot \hat{\mathbf{u}} = 0. \quad (\text{B.12})$$

The Ekman number definition can be rearranged through the following

$$\begin{aligned} EA^2 &= \frac{\nu}{\Omega R_d^2}, \\ \frac{\nu}{R_d^2} &= EA^2 \left( \Omega + \frac{\omega}{2} \right), \\ \frac{\nu}{R_d^2 \Omega} &= EA^2 \left( 1 + \frac{\omega}{2\Omega} \right), \end{aligned} \quad (\text{B.13})$$

to obtain an expression for  $\nu/R_d^2\Omega$ . Similarly, the Rossby number definition can be rearranged through the following

$$\begin{aligned}
Ro &= \frac{\omega}{2A\left(\Omega + \frac{\omega}{2}\right)}, \\
Ro &= \frac{\omega}{A(2\Omega + \omega)}, \\
\frac{1}{ARo} &= \frac{2\Omega + \omega}{\omega}, \\
\frac{1}{ARo} &= \frac{2\Omega}{\omega} + 1, \\
\frac{\omega}{2\Omega} &= \frac{ARo}{1 - ARo},
\end{aligned} \tag{B.14}$$

to obtain an expression for  $\omega/(2\Omega)$ . Thus, the coefficient of diffusion in equation B.11 can be expressed in terms of the governing parameters through equations B.13 and B.14 as

$$\begin{aligned}
\frac{\nu}{R_d^2\Omega} &= EA^2 \left( 1 + \frac{ARo}{1 - ARo} \right), \\
\frac{\nu}{R_d^2\Omega} &= \frac{EA^2}{1 - ARo}.
\end{aligned} \tag{B.15}$$

The limitation in the potential  $Ro$  range of numerical investigation originates from the coefficient of diffusion. That is, the coefficient must be positive. Since  $A$  and  $E$  are always positive, it is required that the denominator remain positive and must not equate to zero. Thus,  $(1 - ARo) > 0$  implies the requirement of  $Ro < 1/A$  and therefore, this paradigm is convenient in simulating negative- $Ro$  flows. The resulting non-dimensional momentum equations expressed in terms of the governing parameters are given by

$$\frac{\partial \hat{\mathbf{u}}}{\partial \hat{t}} + (\hat{\mathbf{u}} \cdot \hat{\nabla}) \hat{\mathbf{u}} = \hat{\nabla} \hat{P} + \frac{EA^2}{1 - ARo} \hat{\nabla}^2 \hat{\mathbf{u}}. \tag{B.16}$$

It should be noted here that  $Ro = 1/A$  is the upper limit of Rossby number, as to approach this number, the ratio of  $\omega$  to  $\Omega$  goes to infinity. That is,  $\omega \rightarrow \infty$  for a constant  $\Omega$ .

The following section follows the same procedure presented here except that the angular speed of the disk is used as the reference scale.

## B.2 Governing equations scaled by the disk rotation rate

The flow quantities are non-dimensionalised through the following relationships,

$$\mathbf{u} = R_d \omega^* \hat{\mathbf{u}}, \quad (\text{B.17})$$

$$\nabla = \hat{\nabla} / R_d, \quad (\text{B.18})$$

$$t = \hat{t} / \omega^*, \quad (\text{B.19})$$

$$P = R_d^2 \omega^{*2} \hat{P}, \quad (\text{B.20})$$

where  $\omega^* = \Omega + \omega$  represents the angular speed of the disk and the hat accents denote dimensionless quantities. Substituting equations B.17 - B.20 into equation B.5 and B.6 yields the non-dimensional governing equations

$$\frac{\partial \hat{\mathbf{u}}}{\partial \hat{t}} + (\hat{\mathbf{u}} \cdot \hat{\nabla}) \hat{\mathbf{u}} = \hat{\nabla} \hat{P} + \frac{\nu}{R_d^2 \omega^*} \hat{\nabla}^2 \hat{\mathbf{u}}, \quad (\text{B.21})$$

$$\hat{\nabla} \cdot \hat{\mathbf{u}} = 0. \quad (\text{B.22})$$

The Ekman number definition can be rearranged through the following

$$\begin{aligned} EA^2 &= \frac{\nu}{R_d^2 \left( \Omega + \frac{\omega^* - \Omega}{2} \right)}, \\ EA^2 &= \frac{2\nu}{R_d^2 (\Omega + \omega^*)}, \\ \frac{\nu}{R_d^2} &= \frac{EA^2}{2} (\Omega + \omega^*), \\ \frac{\nu}{R_d^2 \omega^*} &= \frac{EA^2}{2} \left( \frac{\Omega}{\omega^*} + 1 \right), \end{aligned} \quad (\text{B.23})$$

to obtain an expression for  $\nu / R_d^2 \omega^*$ . Similarly, the Rossby number definition can be rearranged through the following

$$\begin{aligned} Ro &= \frac{\omega^* - \Omega}{2A \left( \Omega + \frac{\omega^* - \Omega}{2} \right)}, \\ \omega^* - \Omega &= 2A \left( \Omega + \frac{\omega^* - \Omega}{2} \right) Ro, \\ \omega^* - \Omega &= A\Omega Ro + A\omega^* Ro, \\ \Omega(A Ro + 1) &= \omega^*(1 - A Ro), \\ \frac{\Omega}{\omega^*} &= \frac{1 - A Ro}{A Ro + 1}, \end{aligned} \quad (\text{B.24})$$

to obtain an expression for  $\Omega/\omega^*$ . Thus, the coefficient of diffusion in equation B.21 can be expressed in terms of the governing parameters through equations B.23 and B.24 as

$$\begin{aligned}\frac{\nu}{R_d^2\omega^*} &= \frac{EA^2}{2} \left( \frac{1 - ARo}{ARo + 1} + 1 \right), \\ \frac{\nu}{R_d^2\omega^*} &= \frac{EA^2}{ARo + 1}.\end{aligned}\tag{B.25}$$

The limitation in the potential  $Ro$  range of numerical investigation originates from the coefficient of diffusion. That is, the coefficient must be positive. Since  $A$  and  $E$  are always positive, it is required that the denominator remain positive and must not equate to zero. Thus,  $(1 + ARo) > 0$  implies the requirement of  $Ro > -1/A$  and therefore, this paradigm is convenient in simulating positive- $Ro$  flows. Similar to the paradigm presented in the previous section, the limit of  $Ro > -1/A$  corresponds to a physical situation where the disk speed approaches infinity for a constant tank speed (i.e.  $\omega/\Omega = \infty$ ). The resulting non-dimensional momentum equations expressed in terms of the governing parameters are given by

$$\frac{\partial \hat{\mathbf{u}}}{\partial \hat{t}} + (\hat{\mathbf{u}} \cdot \hat{\nabla}) \hat{\mathbf{u}} = \hat{\nabla} \hat{P} + \frac{EA^2}{ARo + 1} \hat{\nabla}^2 \hat{\mathbf{u}}.\tag{B.26}$$



# References

- ABDERRAHAMNE, H., SIDDIQUI, K. & VATISTAS, G. 2009 Transition between Kelvin's equilibria. *Physical Review E* **80** (6), 066305.
- ABDERRAHMANE, H., SIDDIQUI, K. & VATISTAS, G. 2011 Rotating waves within a hollow vortex core. *Experiments in fluids* **50** (3), 677–688.
- AGUIAR, A. C. B. 2008 Instabilities of a shear layer in a barotropic rotating fluid. PhD thesis, University of Oxford.
- AGUIAR, A. C. B., READ, P. L., WORDSWORTH, R. D., SALTER, T. & HIRO YAMAZAKI, Y. 2010 A laboratory model of Saturn's north polar hexagon. *Icarus* **206** (2), 755–763.
- ALLISON, M., GODFREY, D. A. & BEEBE, R. F. 1990 A wave dynamical interpretation of Saturn's polar hexagon. *Science* **247** (4946), 1061.
- ANDERECK, C. D., LIU, S. S. & SWINNEY, H. L. 1986 Flow regimes in a circular Couette system with independently rotating cylinders. *Journal of Fluid Mechanics* **164** (3), 155–183.
- ANDERSON, J. D. 2007 *Fundamentals of Aerodynamics*. McGraw-Hill.
- DEL ARCO, E. C., SERRE, E., BONTOUX, P. & LAUNDER, B. E. 2005 Stability, transition and turbulence in rotating cavities. *Advances in Fluid Mechanics* **41**, 141–196.
- AVILA, K., MOXEY, D., DE LOZAR, A., AVILA, M., BARKLEY, D. & HOF, B. 2011 The onset of turbulence in pipe flow. *Science* **333** (6039), 192–196.
- AVILA, M. 2012 Stability and angular-momentum transport of fluid flows between corotating cylinders. *Physical Review Letters* **108** (12), 124501.
- BAINES, K., MOMARY, T., ROOS-SEROTE, M., ATREYA, S., BROWN, R., BURATTI, B., CLARK, R. & NICHOLSON, P. 2007 Saturn's polar hexagon at depth: New images of stationary planetary waves in the north polar region by Cassini/VIMS. In *Geophys. Res. Abstracts*, , vol. 9, p. 02109.

- BAINES, K. H., MOMARY, T. W., FLETCHER, L. N., SHOWMAN, A. P., ROOS-SEROTE, M., BROWN, R. H., BURATTI, B. J., CLARK, R. N. & NICHOLSON, P. D. 2009 Saturn's north polar cyclone and hexagon at depth revealed by Cassini/VIMS. *Planetary and Space Science* **57** (14-15), 1671–1681.
- BAKER, D. J. 1967 Shear layers in a rotating fluid. *Journal of Fluid Mechanics* **29** (01), 165–175.
- BARCILON, V. 1967 On the motion due to sources and sinks distributed along the vertical boundary of a rotating fluid. *J. Fluid Mech* **27** (part 3), 551–560.
- BARKLEY, D., GOMES, M. G. M. & HENDERSON, R. D. 2002 Three-dimensional instability in flow over a backward-facing step. *Journal of Fluid Mechanics* **473**, 167–190.
- BARKLEY, D. & HENDERSON, R. D. 1996 Three-dimensional Floquet stability analysis of the wake of a circular cylinder. *Journal of Fluid Mechanics* **322**, 215–241.
- BAYLY, B. J., ORSZAG, S. A. & HERBERT, T. 1988 Instability mechanisms in shear-flow transition. *Annual review of fluid mechanics* **20** (1), 359–391.
- BECKERS, M. & VAN HEIJST, G. J. F. 1998 The observation of a triangular vortex in a rotating fluid. *Fluid Dynamics Research* **22**, 265.
- BERGERON, K., COUTSIAS, E. A., LYNØV, J. P. & NIELSEN, A. H. 1996 Self-organization in circular shear layers. *Physica Scripta* **67**, 33–37.
- BERGERON, K., COUTSIAS, E. A., LYNØV, J. P. & NIELSEN, A. H. 2000 Dynamical properties of forced shear layers in an annular geometry. *Journal of Fluid Mechanics* **402** (1), 255–289.
- BERGMANN, R., TOPHØJ, L., HOMAN, T., HERSEN, P., ANDERSEN, A. & BOHR, T. 2011 Polygon formation and surface flow on a rotating fluid surface. *Journal of Fluid Mechanics* **679** (1), 415–431.
- BILLANT, P., GALLAIRE, F. *et al.* 2005 Generalized Rayleigh criterion for non-axisymmetric centrifugal instabilities. *Journal of Fluid Mechanics* **542**, 365.
- BLACKBURN, H. M., BARKLEY, D. & SHERWIN, S. J. 2008 Convective instability and transient growth in flow over a backward-facing step. *Journal of Fluid Mechanics* **603**, 271–304.
- BLACKBURN, H. M., MARQUES, F. & LOPEZ, J. 2005 Symmetry breaking of two-dimensional time-periodic wakes. *Journal of Fluid Mechanics* **522**, 395–411.
- BLACKBURN, H. M. & SHEARD, G. J. 2010 On quasiperiodic and subharmonic Floquet wake instabilities. *Physics of Fluids* **22**, 031701.

- BLACKBURN, H. M. & SHERWIN, S. J. 2004 Formulation of a Galerkin spectral element–Fourier method for three-dimensional incompressible flows in cylindrical geometries. *Journal of Computational Physics* **197** (2), 759–778.
- BURNS, A. G., MASLOWE, S. A. & BROWN, S. N. 2002 Barotropic instability of the Bickley jet at high Reynolds numbers. *Studies in Applied Mathematics* **109** (4), 279–296.
- BUSSE, F. H. 1968 Shear flow instabilities in rotating systems. *Journal of Fluid Mechanics* **33** (03), 577–589.
- CARDIN, P. & OLSON, P. 1994 Chaotic thermal convection in a rapidly rotating spherical shell: consequences for flow in the outer core. *Physics of the Earth and planetary interiors* **82** (3), 235–259.
- CARLSON, D. R., WIDNALL, S. E. & PEETERS, M. F. 1982 Flow-visualization study of transition in plane Poiseuille flow. *Journal of Fluid Mechanics* **121**, 487–505.
- CARMO, B. S. & MENEGHINI, J. R. 2006 Numerical investigation of the flow around two circular cylinders in tandem. *Journal of Fluids and Structures* **22** (6), 979–988.
- CARMO, B. S., MENEGHINI, J. R. & SHERWIN, S. J. 2010 Secondary instabilities in the flow around two circular cylinders in tandem. *Journal of Fluid Mechanics* **644**, 395–431.
- CARNEVALE, G. F., BRISCOLIN, M., KLOOSTERZIEL, R. C. & VALLIS, G. K. 1997 Three-dimensionally perturbed vortex tubes in a rotating flow. *Journal of Fluid Mechanics* **341** (1), 127–163.
- CHAKRABORTY, P., BALACHANDAR, S. & ADRIAN, R. J. 2005 On the relationships between local vortex identification schemes. *Journal of Fluid Mechanics* **535** (1), 189–214.
- CHANDRASEKHAR, S. 1961 *Hydrodynamic and hydromagnetic stability*. Oxford University.
- CHARLTON, A. J., O’NEILL, A., LAHOZ, W. A. & BERRISFORD, P. 2005 The splitting of the stratospheric polar vortex in the southern hemisphere, September 2002: Dynamical evolution. *Journal of the atmospheric sciences* **62** (3), 590–602.
- CHIRIAC, V. A. & ORTEGA, A. 2002 A numerical study of the unsteady flow and heat transfer in a transitional confined slot jet impinging on an isothermal surface. *International Journal of Heat and Mass Transfer* **45** (6), 1237–1248.

- CHOMAZ, J. M., RABAUD, M., BASDEVANT, C. & COUDER, Y. 1988 Experimental and numerical investigation of a forced circular shear layer. *Journal of Fluid Mechanics* **187**, 115–140.
- CHONG, M. S., PERRY, A. E. & CANTWELL, B. J. 1990 A general classification of three-dimensional flow fields. In *Topological fluid mechanics: proceedings of the IUTAM Symposium, Cambridge, UK, 13-18 August 1989*, p. 408. Cambridge Univ Pr.
- COGAN, S. J., RYAN, K. & SHEARD, G. J. 2011 Symmetry breaking and instability mechanisms in medium depth torsionally driven open cylinder flows. *Journal of Fluid Mechanics* **672**, 521–544.
- COLES, D. 1965 Transition in circular Couette flow. *Journal of Fluid Mechanics* **21** (03), 385–425.
- CONLISK, A. & WALKER, J. 1981 Incompressible source-sink flow in a rapidly rotating contained annulus. *The Quarterly Journal of Mechanics and Applied Mathematics* **34** (1), 89–109.
- CUCITORE, R., QUADRIO, M. & BARON, A. 1999 On the effectiveness and limitations of local criteria for the identification of a vortex. *European Journal of Mechanics-B/Fluids* **18** (2), 261–282.
- DAVIAUD, F., HEGSETH, J. & BERGÉ, P. 1992 Subcritical transition to turbulence in plane Couette flow. *Physical review letters* **69** (17), 2511–2514.
- DESHPANDE, A. P., KRISHNAN, J. M. & S., K. P. B. 2010 *Rheology of complex fluids*. Springer.
- DIMOTAKIS, P. E. 2005 Turbulent mixing. *Annu. Rev. Fluid Mech.* **37**, 329–356.
- DRAZIN, P. G. 2002 *Introduction to Hydrodynamic Stability*. Cambridge University Press.
- DRAZIN, P. G. & HOWARD, L. N. 1966 *Hydrodynamic stability of parallel flow of inviscid fluid*, , vol. 9. Academic Press New Delhi.
- DRAZIN, P. G. & REID, W. H. 2004 *Hydrodynamic stability*. Cambridge university press.
- DUBIEF, Y. & DELCAYRE, F. 2000 On coherent-vortex identification in turbulence. *Journal of Turbulence* **1** (1), 011–011.
- DUCK, P. W. & FOSTER, M. R. 1980 The inviscid stability of a trailing line vortex. *Zeitschrift für Angewandte Mathematik und Physik (ZAMP)* **31** (4), 524–532.

- DUNST, M. 1973 An experimental and analytical study of instability of asymmetric jetstream-like currents in a rotating fluid. *J. Fluid Mech* **60** (2).
- DYUDINA, U. A., INGERSOLL, A. P., EWALD, S. P., VASAVADA, A. R., WEST, R. A., BAINES, K. H., MOMARY, T. W., DEL GENIO, A. D., BARBARA, J. M., PORCO, C. C. *et al.* 2009 Saturn's south polar vortex compared to other large vortices in the solar system. *Icarus* **202** (1), 240–248.
- DYUDINA, U. A., INGERSOLL, A. P., EWALD, S. P., VASAVADA, A. R., WEST, R. A., DEL GENIO, A. D., BARBARA, J. M., PORCO, C. C., ACHTERBERG, R. K., FLASAR, F. M. *et al.* 2008 Dynamics of Saturn's south polar vortex. *Science* **319** (5871), 1801.
- ELSTON, J. R., SHERIDAN, J. & BLACKBURN, H. M. 2004 Two-dimensional Floquet stability analysis of the flow produced by an oscillating circular cylinder in quiescent fluid. *European Journal of Mechanics-B/Fluids* **23** (1), 99–106.
- ENGEVIK, L. 2004 A note on the barotropic instability of the Bickley jet. *Journal of Fluid Mechanics* **499**, 315–326.
- FJØRTOFT, R. 1950 Application of integral theorems in deriving criteria of stability for laminar flows and for the baroclinic circular vortex. *Geofys. Publ* **17** (6), 1–52.
- FLETCHER, L. N., IRWIN, P. G. J., ORTON, G. S., TEANBY, N. A., ACHTERBERG, R. K., BJORAKER, G. L., READ, P. L., SIMON-MILLER, A. A., HOWETT, C., DE KOK, R. *et al.* 2008 Temperature and composition of Saturn's polar hot spots and hexagon. *Science* **319** (5859), 79.
- FRÜH, W. G. & NIELSEN, A. H. 2003 On the origin of time-dependent behaviour in a barotropically unstable shear layer. *Nonlinear Processes in Geophysics* **10** (3), 289–302.
- FRÜH, W. G. & READ, P. L. 1999 Experiments on a barotropic rotating shear layer. Part 1. Instability and steady vortices. *Journal of Fluid Mechanics* **383**, 143–173.
- GARATE-LOPEZ, I., HUESO, R. & SÁNCHEZ-LAVEGA, A. 2013 A chaotic permanent vortex in Venus' southern pole. In *Highlights of Spanish Astrophysics VII, Proceedings of the X Scientific Meeting of the Spanish Astronomical Society (SEA), held in Valencia, July 9-13, 2012, Eds.: JC Guirado, LM Lara, V. Quilis, and J. Gorgas., pp. 746-746*, , vol. 1, pp. 746–746.
- GODFREY, D. A. 1988 A hexagonal feature around Saturn's north pole. *Icarus* **76**, 335–356.
- GRAY, W. M. 1998 The formation of tropical cyclones. *Meteorology and Atmospheric Physics* **67** (1-4), 37–69.

- GREEN, S. I. 1995 *Fluid Vortices: Fluid Mechanics and Its Applications*, , vol. 30. Springer.
- GROOSS, J.-U., KONOPKA, P. & MÜLLER, R. 2005 Ozone chemistry during the 2002 antarctic vortex split. *Journal of the atmospheric sciences* **62** (3), 860–870.
- HALLER, G. 2005 An objective definition of a vortex. *Journal of Fluid Mechanics* **525**, 1–26.
- HAMMEL, H. B. & LOCKWOOD, G. W. 2007 Long-term atmospheric variability on Uranus and Neptune. *Icarus* **186** (1), 291–301.
- HARRIS, N., LEHMANN, R., REX, M. & VON DER GATHEN, P. 2010 A closer look at arctic ozone loss and polar stratospheric clouds. *Atmospheric Chemistry and Physics* **10**, 8499–8510.
- HASHIMOTO, K. 1975 A source-sink flow of an incompressible rotating fluid. *J. Phys. Soc. Japan* **38**, 1508–1515.
- HENDERSON, R. D. 1997 Nonlinear dynamics and pattern formation in turbulent wake transition. *Journal of Fluid Mechanics* **352**, 65–112.
- HIDE, R. 1968 On source-sink flows in a rotating fluid. *Journal of Fluid Mechanics* **32** (04), 737–764.
- HIDE, R. & TITMAN, C. W. 1967 Detached shear layers in a rotating fluid. *Journal of Fluid Mechanics* **29** (01), 39–60.
- HOLLERBACH, R. 2003 Instabilities of the Stewartson layer Part 1. The dependence on the sign of  $Ro$ . *Journal of Fluid Mechanics* **492**, 289–302.
- HOLLERBACH, R. & FOURNIER, A. 2004 End-effects in rapidly rotating cylindrical Taylor-Couette flow. In *MHD Couette flows: Experiments and models* (ed. R. Rosner, G. Rüdiger & A. Bonanno), *AIP conference proceedings*, vol. 733, pp. 114–121.
- HOLLERBACH, R., FUTTERER, B., MORE, T. & EGBERS, C. 2004 Instabilities of the Stewartson layer Part 2. Supercritical mode transitions. *Theoretical and Computational Fluid Dynamics* **18** (2), 197–204.
- HOPFINGER, E. J. & VAN HEIJST, G. J. F. 1993 Vortices in rotating fluids. *Annual Review of Fluid Mechanics* **25** (1), 241–289.
- HOWARD, L. N. & GUPTA, A. S. 1962 On the hydrodynamic and hydromagnetic stability of swirling flows. *Journal of Fluid Mechanics* **14** (03), 463–476.

- HSIEH, F. C., WU, J. H., HSIEH, J. C. & LIN, T. F. 2006 Unstable vortex flow and new inertia-driven vortex rolls resulting from an air jet impinging onto a confined heated horizontal disk. *International journal of heat and mass transfer* **49** (25), 4697–4711.
- HUNT, J. C. R., WRAY, A. A. & MOIN, P. 1988 Eddies stream, and convergence zones in turbulent flows. *Center for Turbulence Research* p. 193.
- IALONGO, I., SOFIEVA, V., KALAKOSKI, N., TAMMINEN, J. & KYRÖLÄ, E. 2012 Ozone zonal asymmetry and planetary wave characterization during antarctic spring. *Atmos. Chem. Phys* **12**, 2603–2614.
- JANSSON, T. R. N., HASPANG, M. P., JENSEN, K. H., HERSEN, P. & BOHR, T. 2006 Polygons on a rotating fluid surface. *Physical review letters* **96**, 174502.
- JEONG, J. & HUSSAIN, F. 1995 On the identification of a vortex. *Journal of Fluid Mechanics* **285** (1), 69–94.
- JI, H., BURIN, M., SCHATMAN, E. & GOODMAN, J. 2006 Hydrodynamic turbulence cannot transport angular momentum effectively in astrophysical disks. *Nature* **444** (7117), 343–346.
- JIANG, M., MACHIRAJU, R. & THOMPSON, D. 2005 Detection and visualization of vortices. *The visualization handbook* p. 295.
- JIMÉNEZ, J. 2004 Turbulent flows over rough walls. *Annu. Rev. Fluid Mech.* **36**, 173–196.
- KARNIADAKIS, G. E. 1990 Spectral element-Fourier methods for incompressible turbulent flows. *Computer Methods in Applied Mechanics and Engineering* **80** (1), 367–380.
- KARNIADAKIS, G. E., ISRAELI, M. & ORSZAG, S. A. 1991 High-order splitting methods for the incompressible Navier–Stokes equations. *Journal of Computational Physics* **97**, 414–443.
- KARNIADAKIS, G. E. & SHERWIN, S. J. 2005 Spectral/hp element methods for computational fluid dynamics. *Numerical Mathematics and Scientific Computation. Oxford University Press, New York* .
- KAROLY, D. J. 2003 Ozone and climate change. *Science* **302** (5643), 236–237.
- KLOOSTERZIEL, R. C. & VAN HEIJST, G. J. F. 1991 An experimental study of unstable barotropic vortices in a rotating fluid. *J. Fluid Mech* **223** (1).
- KOLÁŘ, V. 2011 Brief notes on vortex identification. In *Proceedings of the 8th WSEAS international conference on fluid mechanics, 8th WSEAS international conference on*

*Heat and mass transfer*, pp. 23–28. World Scientific and Engineering Academy and Society (WSEAS).

VAN DE KONIJNENBERG, J. A., NIELSEN, A. H., JUUL RASMUSSEN, J. & STENUM, B. 1999 Shear-flow instability in a rotating fluid. *Journal of Fluid Mechanics* **387**, 177–204.

KOSSIN, J. P. & SCHUBERT, W. H. 2001 Mesovortices, polygonal flow patterns, and rapid pressure falls in hurricane-like vortices. *Journal of the Atmospheric Sciences* **58**, 2196–2209.

KOSSIN, J. P. & SCHUBERT, W. H. 2004 Mesovortices in hurricane Isabel. *Bulletin of the American Meteorological Society* **85** (2), 151–153.

KUIK, D. J., POELMA, C. & WESTERWEEL, J. 2010 Quantitative measurement of the lifetime of localized turbulence in pipe flow. *Journal of Fluid Mechanics* **645** (1), 529–539.

KUO, H. 1949 Dynamic instability of two-dimensional nondivergent flow in a barotropic atmosphere. *Journal of Atmospheric Sciences* **6**, 105–122.

LE GAL, P., NADIM, A. & THOMPSON, M. 2001 Hysteresis in the forced Stuart–Landau equation: application to vortex shedding from an oscillating cylinder. *Journal of fluids and structures* **15** (3), 445–457.

LEHOUCQ, R. B., SORENSSEN, D. C. & YANG, C. 1989 *ARPACK Users'É Guide: Solution of Large-Scale Eigenvalue Problems with Implicitly Restarted Arnoldi Methods*. SIAM, Philadelphia.

LEIBOVICH, S. & STEWARTSON, K. 1983 A sufficient condition for the instability of columnar vortices. *Journal of Fluid Mechanics* **126** (1), 335–356.

LESSEN, M., SINGH, P. J. & PAILLET, F. 1974 The stability of a trailing line vortex. Part 1. Inviscid theory. *J. Fluid Mech* **63** (4), 753–763.

LEUTHEUSSER, H. J. & CHU, V. H. 1971 Experiments on plane Couette flow. *Journal of the Hydraulics Division* **97** (9), 1269–1284.

LEWIS, B. M. & HAWKINS, H. F. 1982 Polygonal eye walls and rainbands in hurricanes. *Bulletin of the American Meteorological Society* **63** (11), 1294–1300.

LOPEZ, J. M. & MARQUES, F. 2011 Instabilities and inertial waves generated in a librating cylinder. *Journal of Fluid Mechanics* **687**, 171.

LOPEZ, J. M. & MARQUES, F. 2014 Rapidly rotating cylinder flow with an oscillating sidewall. *Physical Review E* **89** (1), 013013.

- LOPEZ, J. M., MARQUES, F., HIRSA, A. H. & MIRAGHAIE, R. 2004 Symmetry breaking in free-surface cylinder flows. *Journal of Fluid Mechanics* **502**, 99–126.
- LOPEZ, J. M., MARQUES, F., RUBIO, A. M. & AVILA, M. 2009 Crossflow instability of finite Bödewadt flows: Transients and spiral waves. *Physics of Fluids* **21**, 114107.
- LUGT, H. J. 1979 The dilemma of defining a vortex. *Recent developments in theoretical and experimental fluid mechanics: compressible and incompressible flows* **1**, 309–321.
- LUNDBLADH, A. & JOHANSSON, A. V. 1991 Direct simulation of turbulent spots in plane Couette flow. *Journal of Fluid Mechanics* **229**, 499–516.
- LUZ, D., BERRY, D. L., PICCIONI, G., DROSSART, P., POLITI, R., WILSON, C. F., ERARD, S. & NUCCILLI, F. 2011 Venus’s southern polar vortex reveals precessing circulation. *Science* **332** (6029), 577–580.
- MASLOWE, S. A. 1991 Barotropic instability of the Bickley jet. *Journal of Fluid Mechanics* **229** (1), 417–426.
- MATSUDA, T., SAKURAI, T. & TAKEDA, H. 1975 Source-sink flow in a gas centrifuge. *Journal of Fluid Mechanics* **69**, 197–208.
- MCWILLIAMS, J. C. 1991 Geostrophic vortices. *Nonlinear Topics in Ocean Physics* pp. 5–50.
- MEKSYN, D. & STUART, J. 1951 Stability of viscous motion between parallel planes for finite disturbances. *Proceedings of the Royal Society of London. Series A. Mathematical and Physical Sciences* **208** (1095), 517–526.
- MEYERS, S. D., SOMMERIA, J. & SWINNEY, H. L. 1989 Laboratory study of the dynamics of Jovian-type vortices. *Physica D: Nonlinear Phenomena* **37** (1), 515–530.
- MIRAGHAIE, R., LOPEZ, J. M. & HIRSA, A. H. 2003 Flow induced patterning at the air–water interface. *Physics of Fluids* **15**, L45.
- MONTABONE, L., WORDSWORTH, R., AGUIAR, A., JACOBY, T., MCCCLIMANS, T., READ, P. L. & WILSON, C. 2009 Coherent structures in planetary polar vortices: A laboratory view. In *International Conference on Comparative Planetology: Venus-Earth-Mars*.
- MONTABONE, L., WORDSWORTH, R., AGUIAR, A., JACOBY, T., READ, P. L., MCCCLIMANS, T. & ELLINGSEN, I. 2010a Barotropic instability of planetary polar vortices: Concept, experimental set-up and parameter space analysis. In *Proceedings of the HYDRALAB III Joint Transnational Access User Meeting, Hannover*.

- MONTABONE, L., WORDSWORTH, R., AGUIAR, A. C. B., JACOBY, T., MANFRIN, M., READ, P. L., CASTREJON-PITA, A., GOSTIAUX, L., SOMMERIA, J., VIBOUD, S. & DIDELLE, H. 2010b Barotropic instability of planetary polar vortices: CIV analysis of specific multi-lobed structures. In *Proceedings of the HYDRALAB III Joint Transnational Access User Meeting, Hannover*, p. 191.
- MONTGOMERY, M. T. & FARRELL, B. F. 1993 Tropical cyclone formation. *Journal of the atmospheric sciences* **50** (2), 285–310.
- MOXEY, D. & BARKLEY, D. 2010 Distinct large-scale turbulent-laminar states in transitional pipe flow. *Proceedings of the National Academy of Sciences* **107** (18), 8091–8096.
- MURAMATSU, T. 1986 The structure of polygonal eye of a typhoon. *Journal of the Meteorological Society of Japan* **64** (6), 913–921.
- MURPHY, B. F. & TIMBAL, B. 2008 A review of recent climate variability and climate change in southeastern Australia. *International Journal of Climatology* **28** (7), 859–879.
- MURRAY, B. C., WILDEY, R. L. & WESTPHAL, J. A. 1963 Infrared photometric mapping of Venus through the 8- to 14-micron atmospheric window. *Journal of Geophysical Research* **68**, 4813–4818.
- NEWMAN, P. A. & NASH, E. R. 2005 The unusual southern hemisphere stratosphere Winter of 2002. *Journal of the atmospheric sciences* **62** (3), 614–628.
- NIINO, H. & MISAWA, N. 1984 An experimental and theoretical study of barotropic instability. *Journal of Atmospheric Sciences* **41** (12), 1992–2011.
- NISHIOKA, M., IIDA, S. & ICHIKAWA, Y. 1975 An experimental investigation of the stability of plane Poiseuille flow. *J. Fluid Mech* **72** (73), 1.
- ORR, W. M. 1907 The stability or instability of the steady motions of a perfect liquid and of a viscous liquid. Part II: A viscous liquid. In *Proceedings of the Royal Irish Academy. Section A: Mathematical and Physical Sciences*, , vol. 27, pp. 69–138. JSTOR.
- ORSZAG, S. A. 1971 Accurate solution of the Orr–Sommerfeld stability equation. *J. Fluid Mech* **50** (4), 689–703.
- ORSZAG, S. A. & KELLS, L. C. 1980 Transition to turbulence in plane Poiseuille and plane Couette flow. *Journal of Fluid Mechanics* **96** (01), 159–205.

- ORTON, G. S., ENCRENAZ, T., LEYRAT, C., PUETTER, R. & FRIEDSON, A. J. 2007 Evidence for methane escape and strong seasonal and dynamical perturbations of Neptune’s atmospheric temperatures. *Astronomy and Astrophysics* **473** (1), 5–8.
- ORTON, G. S. & YANAMANDRA-FISHER, P. A. 2005 Saturn’s temperature field from high-resolution middle-infrared imaging. *Science* **307** (5710), 696.
- PAOLETTI, M. S., VAN GILS, D. P. M., DUBRULLE, B., SUN, C., LOHSE, D. & LATHROP, D. P. 2012 Angular momentum transport and turbulence in laboratory models of Keplerian flows. *Astronomy and Astrophysics* **547** (A64).
- PAOLETTI, M. S. & LATHROP, D. P. 2011 Angular momentum transport in turbulent flow between independently rotating cylinders. *Physical Review Letters* **106** (024501).
- PEDLOSKY, J. 1987 *Geophysical fluid dynamics*. Springer.
- PICCIONI, G., DROSSART, P., SANCHEZ-LAVEGA, A., HUESO, R., TAYLOR, F. W., WILSON, C. F., GRASSI, D., ZASOVA, L., MORICONI, M., ADRIANI, A. *et al.* 2007 South-polar features on Venus similar to those near the north pole. *Nature* **450** (7170), 637–640.
- PONCET, S., CHAUVE, M. *et al.* 2007 Shear-layer instability in a rotating system. *Journal of Flow Visualization and Image Processing* **14** (1), 85–105.
- POTHÉRAT, A., SOMMERIA, J. & MOREAU, R. 2000 An effective two-dimensional model for MHD flows with transverse magnetic field. *J. Fluid Mech* **424**, 75–100.
- POTHÉRAT, A., SOMMERIA, J. & MOREAU, R. 2005 Numerical simulations of an effective two-dimensional model for flows with a transverse magnetic field. *Journal of fluid mechanics* **534**, 115–143.
- PROUDMAN, I. 1956 The almost-rigid rotation of viscous fluid between concentric spheres. *Journal of Fluid Mechanics* **1** (05), 505–516.
- PROVANSAL, M., MATHIS, C. & BOYER, L. 1987 Bénard-von Kármán instability: transient and forced regimes. *Journal of Fluid Mechanics* **182**, 1–22.
- PROVENZALE, A. 1999 Transport by coherent barotropic vortices. *Annual review of fluid mechanics* **31** (1), 55–93.
- RABAUD, M. & COUDER, Y. 1983 Shear-flow instability in a circular geometry. *Journal of Fluid Mechanics* **136**, 291–319.
- RAO, A., THOMPSON, M. C., LEWEKE, T. & HOURIGAN, K. 2013 The flow past a circular cylinder translating at different heights above a wall. *Journal of Fluids and Structures* **41**, 9–21.

- RASMUSSEN, J. J., GARCIA, O. E., NAULIN, V., NIELSEN, A. H., STENUM, B., BOKHOVEN, L. J. A. & DELAUX, S. 2006 Generation of zonal flows in rotating fluids and magnetized plasmas. *Physica Scripta* **2006**, 44.
- RAYLEIGH, L. 1880 On the stability, or instability, of certain fluid motions. *Proceedings of the London Mathematical Society* **11**, 57–72.
- REICHARDT, H. 1956 Über die geschwindigkeitsverteilung in einer geradlinigen turbulenten couetteströmung. *ZAMM-Journal of Applied Mathematics and Mechanics/Zeitschrift für Angewandte Mathematik und Mechanik* **36** (S1), S26–S29.
- REYNOLDS, O. 1883 An experimental investigation of the circumstances which determine whether the motion of water shall be direct or sinuous, and of the law of resistance in parallel channels. *Proceedings of the Royal Society of London* **35** (224-226), 84–99.
- ROBINSON, S. K. 1991 Coherent motions in the turbulent boundary layer. *Annual Review of Fluid Mechanics* **23** (1), 601–639.
- ROMANOV, V. A. 1973 Stability of plane-parallel Couette flow. *Functional analysis and its applications* **7** (2), 137–146.
- SANCHEZ-LAVEGA, A., LECACHEUX, J., COLAS, F. & LAQUES, P. 1993 Temporal behavior of cloud morphologies and motions in Saturn’s atmosphere. *Journal of Geophysical Research* **98** (E10), 18857.
- SANSÓN, L. Z. & VAN HEIJST, G. 2002 Ekman effects in a rotating flow over bottom topography. *Journal of Fluid Mechanics* **471** (1), 239–255.
- SCHAEFFER, N. & CARDIN, P. 2005 Quasigeostrophic model of the instabilities of the Stewartson layer in flat and depth-varying containers. *Physics of Fluids* **17**, 104111.
- SCHÄR, C. & DAVIES, H. C. 1990 An instability of mature cold fronts. *Journal of the atmospheric sciences* **47** (8), 929–950.
- SCHARTMAN, E., JI, H., BURIN, M. J. & GOODMAN, J. 2012 Stability of quasi-Keplerian shear flow in a laboratory experiment. *Astronomy and Astrophysics* **543** (A94).
- SCHLICHTING, H. 1979 *Boundary-Layer Theory*. McGraw-Hill, USA.
- SCHMID, P. J. & HENNINGSON, D. S. 2001 *Stability and transition in shear flows*, , vol. 142. Springer Verlag.
- SCHUBERT, W. H., MONTGOMERY, M. T., TAFT, R. K., GUINN, T. A., FULTON, S. R., KOSSIN, J. P. & EDWARDS, J. P. 1999 Polygonal eyewalls, asymmetric eye

- contraction, and potential vorticity mixing in hurricanes. *Journal of the Atmospheric Sciences* **56**, 1197–1223.
- SHEARD, G. J. 2009 Flow dynamics and wall shear-stress variation in a fusiform aneurysm. *Journal of Engineering Mathematics* **64** (4), 379–390.
- SHEARD, G. J. 2011 Wake stability features behind a square cylinder: Focus on small incidence angles. *Journal of Fluids and Structures* **27**, 734–742.
- SHEARD, G. J. & RYAN, K. 2007 Pressure-driven flow past spheres moving in a circular tube. *Journal of Fluid Mechanics* **592**, 233–262.
- SHEARD, G. J., THOMPSON, M. & HOURIGAN, K. 2003 From spheres to circular cylinders: the stability and flow structures of bluff ring wakes. *Journal of Fluid Mechanics* **492**, 147–180.
- SHEARD, G. J., THOMPSON, M. C. & HOURIGAN, K. 2004 Asymmetric structure and non-linear transition behaviour of the wakes of toroidal bodies. *European journal of mechanics. B, Fluids* **23** (1), 167–179.
- SHEARD, G. J., THOMPSON, M. C. & HOURIGAN, K. 2005 Subharmonic mechanism of the mode C instability. *Physics of Fluids* **17**, 111702.
- SMITH, S. H. 1984 The development of nonlinearities in the  $E^{1/3}$  Stewartson layer. *The Quarterly Journal of Mechanics and Applied Mathematics* **37** (1), 75–85.
- SMYTH, W. D. & PELTIER, W. R. 1994 Three-dimensionalization of barotropic vortices on the  $f$ -plane. *Journal of Fluid Mechanics* **265** (1), 25–64.
- SOMMERIA, J., MEYERS, S. D. & SWINNEY, H. L. 1988 Laboratory simulation of Jupiter’s Great Red Spot. *Nature* **331** (6158), 689–693.
- SOMMERIA, J., MEYERS, S. D. & SWINNEY, H. L. 1989 Laboratory model of a planetary eastward jet. *Nature* **337** (6202), 58–61.
- SOMMERIA, J., MEYERS, S. D. & SWINNEY, H. L. 1991 Experiments on vortices and Rossby waves in eastward and westward jets. *Nonlinear Topics in Ocean Physics* **109**, 227–269.
- SOMMERIA, J. & MOREAU, R. 1982 Why, how, and when, mhd turbulence becomes two-dimensional. *Journal of Fluid Mechanics* **118** (1), 507–518.
- STEGMAIER, S., RIST, U. & ERTL, T. 2005 Opening the can of worms: An exploration tool for vortical flows. In *Visualization, 2005. VIS 05. IEEE*, pp. 463–470. IEEE.
- STEWARTSON, K. 1957 On almost rigid rotations. *Journal of Fluid Mechanics* **3**, 17–26.

- STEWARTSON, K. 1966 On almost rigid rotations. Part 2. *Journal of Fluid Mechanics* **26**, 131–144.
- SYNGE, J. L. 1933 The stability of heterogeneous fluids. *Chaos: An Interdisciplinary Journal of Nonlinear Science* **4**, 203.
- TAYLOR, F. W., BEER, R., CHAHINE, M. T., DINER, D. J., ELSON, L. S., HASKINS, R. D., MCCLEESE, D. J., MARTONCHIK, J. V., REICHEL, P. E., BRADLEY, S. P. *et al.* 1980 Structure and meteorology of the middle atmosphere of Venus: infrared remote sensing from the Pioneer Orbiter. *Journal of Geophysical Research* **85** (A13), 7963–8006.
- TAYLOR, G. I. 1923 Stability of a viscous liquid contained between two rotating cylinders. *Philosophical Transactions of the Royal Society of London. Series A, Containing Papers of a Mathematical or Physical Character* **223**, 289–343.
- THOMPSON, D. W. J. & SOLOMON, S. 2002 Interpretation of recent Southern Hemisphere climate change. *Science* **296** (5569), 895.
- THOMPSON, M. C. & LE GAL, P. 2004 The Stuart–Landau model applied to wake transition revisited. *European Journal of Mechanics-B/Fluids* **23** (1), 219–228.
- TILLMARK, N. & ALFREDSSON, P. H. 1992 Experiments on transition in plane Couette flow. *J. Fluid Mech* **235**, 89–102.
- TOMBOULIDES, A. G. & ORSZAG, S. A. 2000 Numerical investigation of transitional and weak turbulent flow past a sphere. *Journal of Fluid Mechanics* **416** (1), 45–73.
- TOPHØJ, L., MOUGEL, J., BOHR, T. & FABRE, D. 2013 Rotating polygon instability of a swirling free surface flow. *Physical review letters* **110** (19), 194502.
- TORY, K. J. & FRANK, W. M. 2010 Tropical cyclone formation. *Global Perspectives on Tropical Cyclones: From Science to Mitigation* **4**, 55.
- VALLIS, G. K. 2006 *Atmospheric and Oceanic Fluid Dynamics*. Cambridge, U.K.: Cambridge University Press.
- VAN HEIJST, G. J. F. 1984 Source-sink flow in a rotating cylinder. *Journal of engineering mathematics* **18** (3), 247–257.
- VAN HEIJST, G. J. F. 1994 Topography effects on vortices in a rotating fluid. *Meccanica* **29** (4), 431–451.
- VAN HEIJST, G. J. F. & CLERCX, H. J. H. 2009 Laboratory modeling of geophysical vortices. *Annual Review of Fluid Mechanics* **41**, 143–164.

- VATISTAS, G., WANG, J. & LIN, S. 1992 Experiments on waves induced in the hollow core of vortices. *Experiments in fluids* **13** (6), 377–385.
- VATISTAS, G. H. 1990 A note on liquid vortex sloshing and Kelvin’s equilibria. *Journal of Fluid Mechanics* **217** (1), 241–248.
- VATISTAS, G. H., ABDERRAHMANE, H. A. & SIDDIQUI, M. H. K. 2008 Experimental confirmation of Kelvin’s equilibria. *Physical review letters* **100** (17), 174503.
- VO, T., MONTABONE, L. & SHEARD, G. J. 2014 Linear stability analysis of a shear layer induced by differential coaxial rotation within a cylindrical enclosure. *Journal of Fluid Mechanics* **738**, 299–334.
- VOOREN, A. I. 1992 The Stewartson layer of a rotating disk of finite radius. *Journal of Engineering Mathematics* **26** (1), 131–152.
- WAUGH, D. W. & POLVANI, L. M. 2010 Stratospheric polar vortices. *The Stratosphere: Dynamics, Transport, and Chemistry, Geophys. Monogr. Ser* **190**, 43–57.
- WILLOUGHBY, H. E., CLOS, J. A. & SHOREIBAH, M. G. 1982 Concentric eye walls, secondary wind maxima, and the evolution of the hurricane vortex. *J. Atmos. Sci* **39** (2), 395–411.
- ZHOU, J., ADRIAN, R. J., BALACHANDAR, S. & KENDALL, T. M. 1999 Mechanisms for generating coherent packets of hairpin vortices in channel flow. *Journal of Fluid Mechanics* **387** (1), 353–396.